Novel Strategies for Electrochemical Ion Sensing at Functional Interfaces

Sophie C. Patrick

St John's College, University of Oxford



A thesis submitted for the degree of Doctor of Philosophy

Department of Chemistry, University of Oxford

Hilary Term 2024

“Life need not be easy, provided only that it is not empty.”-Lise Meitner

“Well-behaved women seldom make history.”-Laurel Thatcher Ulrich

This thesis is dedicated to my family: to Mum, Dad, Lisa and Marie, for their steadfast love and support. In loving memory of Nana, Grandma Share and Grandad.

Novel Strategies for Electrochemical Ion Sensing at Functional Interfaces

Sophie C. Patrick, St John's College, University of Oxford

Abstract of thesis submitted for the degree of D.Phil., Hilary Term 2024.

This thesis explores novel strategies for electrochemical ion sensing with supramolecular host-guest systems in solution and at functional interfaces.

Chapter 1 introduces general design principles for supramolecular hosts, as well as the basic operational principles that underpin common electrochemical techniques for ion sensing (potentiometry, voltammetry and impedance spectroscopy).

Chapter 2 explores the impact of incorporating discrete halogen bonding or hydrogen bonding-mediated receptive units into a polymeric scaffold on their anion binding and sensing performance, as assessed through systematic ^{1}H NMR and voltammetric studies in multiple organic/aqueous solvent systems. The impact of tuning local dielectric on anion binding/sensing performance is explored.

Chapter 3 describes the development of a continuous voltammetric anion sensing method to follow anion binding in real-time at redox-active, anion receptive self-assembled monolayers, as well as an accompanying data analysis method to semi-automate processing of the resulting large data sets. A custom-designed microfluidic cell enables continuous flow assays that can be conducted over multiple hours.

Chapter 4 presents the first comprehensive example of redox capacitive ion sensing, which uniquely demonstrates an unprecedented ability to simultaneously monitor and modulate key anion binding (binding affinity) and sensing (sensitivity) parameters at redox-active, anion receptive self-assembled monolayers. This methodology is widely applicable to receptive, electroactive interfaces and can be operated continuously with a high temporal resolution for multiple hours.

Chapter 5 outlines a novel, continuous non-Faradaic capacitive ion sensing method to continually monitor interfacial binding events in a reagentless manner. The superb baseline stability of an exemplary benzo-15-crown-5-based self-assembled monolayers supports ion sensing assays over multiple days in pure water.

Chapter 6 summarises the main conclusions from Chapters 2-5 and outlines the future outlook for the work described in this thesis.

Chapter 7 describes experimental considerations, as well as synthetic procedures and characterisation of key receptors relevant to this thesis.

Chapter 8 lists all references cited within this thesis.

The appendices contain a variety of supplementary information, including raw data and further sensor and surface characterisation.

Acknowledgements

After nearly 8 years in Oxford, I'm incredibly grateful to have a lot of wonderful people to thank for both my professional and personal development during this time. This thesis marks the culmination of more than three years of hard work, late nights, good times and even a global pandemic, so the memories forged every step of the way are ones that I will treasure forever.

I would like to first and foremost sincerely thank **Prof. Jason J. Davis** for his continued guidance and supervision. Thank you for always making time for a "quick" chat about my endless supply of complicated data and crazy ideas. Above all else, thank you for believing in my potential and encouraging me to strive for levels of success I didn't think were possible. I have no doubt that the skills you've conferred to me throughout my DPhil are ones that will see me through any hardship in the future, and for that I am so grateful.

I would also like to thank **Prof. Paul D. Beer** for his support and mentorship throughout my DPhil, I am so glad to have had the opportunity to learn from you and your group.

I am also indebted to a number of outstanding scientists that I was lucky enough to collaborate with: **Dr. Robert Hein, Dr. Mohamed Sharafeldin, Dr. Xiaoxiang Li, Dr. Krzyzstof Bąk**, without whom the work in this thesis would not be possible. You all set the bar for academic and professional excellence so high, I learned so much during my time working with each of you. In particular, I am immensely grateful to **Dr. Robert Hein** for the wisdom and advice he has shared, you are a constant

source of strength and inspiration for me. Also, sunset > watermelon, no contest. I'd also like to thank **Dr. Andrew Docker, Andrew Taylor, Shaoyu Kang** and **Xuanxiao Chen** for collaborations outside of my field, in which I also learned a great deal.

I cannot understate that this thesis would not have been possible without the advice and encouragement of a wonderful support system. Though we never officially collaborated on any projects, I am so grateful to **Tara Lurshay**, **Connor Ellis**, **Felix Fleschhut**, **Daohe Yuan**, **Dr. Robert Barber**, **Lilli Leutloff**, **James Smith**, **Anna Duncan** and **Sophia Abusamra** for being the best lab mates. The assorted sweet treats and Kaffeeklatsch sessions during my inevitable monthly meltdowns are so appreciated. I hope you all know how incredibly talented and capable you are, I'm honoured to call you friends, as well as colleagues.

I would like to extend my gratitude to my other friends in Oxford and at home, you have been such a comfort to me throughout this degree. **Jess Thomson**, I truly don't know what I'd do without you, the yang to my yin, always. **Joe Elliott**, **Harriet Haysom**, **Molly Lewis**, **Alex Stainsby**, **Oliver Brown** and **Serena Alagappan** thank you for being so supportive and standing by me when things got tough.

Finally, the biggest thank you to my family. **Mum**, **Dad**, **Lisa** and **Marie**. No matter the barrier in my way, you've always convinced me it was surmountable and given the best advice to approach it with grace and a whole lot of grit. I may not have always managed the grace bit very often but I would be lost without you all. Thank you for pushing me to be the best version of myself.

An additional thank you to **Cezza** for drowning me in love and fluff, I always said I'd include you in this thesis and I always keep my promises...



Perhaps it is the sentimentality of this moment now, but when I reflect back on my time at Oxford, I only feel immense pride and joy for what I have accomplished here. I hope that any legacy I leave behind will be one of determination and resilience, but also of empathy and collaboration (and immaculate colour schemes, of course). I have been so lucky to be surrounded by people that choose to share their sunshine rather than cast a deeper shadow on a tough situation, and I hope to carry that approach with me wherever I go next.

List of Publications

Publications pertaining to this thesis:

Chapter 1:

S. C. Patrick, P. D. Beer, J. J. Davis, "Solvent effects in anion recognition", *Nat. Rev. Chem.*, **2023**, https://doi.org/10.1038/s41570-024-00584-4.

Chapter 2:

S. C. Patrick,† K. Bąk,† X. Li, P. D. Beer, J. J. Davis, "Engineered binding microenvironments in halogen bonding polymers for enhanced anion sensing", *Angew. Chem. Int. Ed.*, **2023**, e202300867

Chapter 3:

S. C. Patrick,† R. Hein,† M. Sharafeldin, X.Li, P. D. Beer, J. J. Davis, "Real-time Voltammetric Anion Sensing Under Flow", *Chem. Eur. J.*, **2021**, 27, 17700-17706

Chapter 4:

S. C. Patrick,† R. Hein,† P. D. Beer, J. J. Davis, "Continuous and polarization-tuned redox capacitive anion sensing at electroactive interfaces", *J. Am. Chem. Soc.*, **2021**, 143, 19199-19206

Chapter 5:

S. C. Patrick,† R. Hein,† P. D. Beer, J. J. Davis, "Non-Faradaic Capacitive Ion Sensing Under Flow", *Chem Sci.*, **2024**, Accepted.

†- equal contribution

Other publications:

A. J. Taylor, R. Hein, **S. C. Patrick**, J. J. Davis, P. D. Beer, "Anion Sensing through Redox-Modulated Fluorescent Halogen Bonding and Hydrogen Bonding Hosts", *Angew. Chem. Int. Ed.*, **2023**, e202315959

S. Kang, M. Sharafeldin, **S. C. Patrick**, X. Chen, J. J. Davis, "Ultrafast Biomarker Quantification through Reagentless Capacitive Kinetics", *Anal. Chem.*, **2023**, 95, 4721-4727

S. C. Patrick, R. Hein, A. Docker, P. D. Beer, J. J. Davis, "Solvent effects in halogen and hydrogen bonding mediated electrochemical anion sensing in aqueous solution and at interfaces", *Chem. Eur. J.*, **2021**, 27, 10201-10209

†- equal contribution

Glossary of Abbreviations

ACN	Acetonitrile
AIBN	Azobisisobutyronitrile
ATR-FTIR	Attenuated total reflectance-Fourier transform infrared
ATRP	Atom transfer radical polymerisation
β_2	Association constant of the 2:1 host–guest complex
BEF	Binding enhancement factor
BuA	Butyl acrylate
Cf.	*Confer*
ChB	Chalcogen bonding
CuAAC	Copper(I)-catalysed azide-alkyne cycloaddition
CV	Cyclic voltammetry
Da	Dalton
DCM	Dichloromethane
DDMAT	2-dodecylthiocarbonothioylthio)-2-methylpropionic acid
DEGA	Di(ethyleneglycol)ethyletheracrylate
DMAP	4-Dimethylaminopyridine
DMF	Dimethylformamide
DMSO	Dimethyl sulfoxide
DNA	Deoxyribonucleic acid
DPV	Differential pulse voltammetry
ε_r	Dielectric constant
ε_0	Permittivity of free space

$E_{1/2}$	Half-wave potential
EDC	1-Ethyl-3-(3-dimethylaminopropyl)carbodiimide
EIS	Electrochemical impedance spectroscopy
E.m.f.	Electromotive force
E.g.	*Exempli gratia*
Et al.	*Et alia*
Etc.	*Et cetera*
Fc/Fc^+	Ferrocene/ferrocenium
GPC	Gas permeation chromatography
h	hour(s)
HB	Hydrogen bonding
I.e.	*Id est*
ISE	Ion-selective electrode
J	Joule
K_a	Association binding constant
K_{Ox}	Binding constant to the oxidised receptor
K_{Red}	Binding constant to the reduced receptor
M	Molar, mega
M_{CTA}	Molecular weight of chain transfer agent
Me	Methyl
M_n	Number average molecular weight
$M_{n,th}$	Maximum theoretical number average molecular weight
M_M	Molecular weight of monomer

M_w	Molecular weight
Mol	mole
NDI	Naphthalenetetracarboxylic diimide
NMR	Nuclear magnetic resonance
P	Monomer conversion
PDI	Polydispersity index
pH	$-\log_{10}[H^+]$
PnB	Pnictogen bonding
POPC	1-Palmitoyl-2-oleoyl-sn-glycero-3-phosphocholine
RAFT	Reversible addition-fragmentation chain-transfer
R_{ct}	Charge transfer resistance
RDRP	Reversible deactivation radical polymerisation
RNA	Ribonucleic acid
RPM	Revolutions per minute
SAM	Self-assembled monolayer
SWV	Square wave voltammetry
TBA	Tetrabutylammonium
TEA	Tetraethylammonium
THF	Tetrahydrofuran
TrB	Tetral bonding
TTF	Tetrathiafulvalene
UV-Vis	Ultraviolet-visible spectroscopy
Vs.	*Versus*

V	Volt
w.r.t.	With respect to
XB	Halogen bonding
XBF	Halogen bonding enhancement factor
ΔE	Change in potential (typically change in $E_{1/2}$)
$\Delta H°_{hyd}$	Anion hydration enthalpy
ΔH	Enthalpy change
ΔS	Entropy change
π	Pi

Table of Contents

Abstract ..... **IV**

Acknowledgements ..... **VI**

List of Publications ..... **IX**

Glossary of Abbreviations ..... **XI**

Chapter 1: Introduction **1**

1.1 Relevance of Ion Recognition for Sensing Applications **2**

1.2 Considerations for Supramolecular Host Design **4**

1.2.1 General Considerations 4

1.2.2 Supramolecular Design Principles 5

1.2.3 Non-covalent Interactions 8

1.3 Solvent Effects at Anion Binding Microenvironments **16**

1.3.1 Solution-phase Approaches 17

1.3.2 Surface Immobilisation 23

1.4 Electrochemical Techniques **30**

1.4.1 Potentiometry for Ion Sensing 30

1.4.2 Voltammetry for Ion Sensing 33

1.4.3 Impedance-derived Techniques for Ion Sensing 42

1.5 Thesis Aims **47**

Chapter 2: Polymers for Enhanced Anion Binding & Sensing Performance **50**

2.1 Introduction & Chapter Aims **51**

2.2 Synthesis of Monomeric Hosts **58**

2.3 Synthesis of Polymeric Hosts **59**

2.3.1 Optimisation of Polymerisation Procedure 59

2.3.2 UV-initiated RAFT Polymerisation 61

2.3.3 Thermally-initiated RAFT Polymerisation 65

2.4 Characterisation of Monomers and Polymers **69**

2.5 ^{1}H NMR Anion Binding Studies **74**

2.5.1 Anion Binding Performance of Monomeric Hosts 74
2.5.2 Anion Binding Performance of Polymeric Hosts & Comparisons with Monomeric Hosts 81
2.6 Electrochemical Analyses of Monomeric & Polymeric Hosts 93
2.6.1 Voltammetric Characterisation of Monomeric & Polymeric Hosts..... 93
2.6.2 Electrochemical Anion Sensing Performance of Monomeric & Polymeric Hosts 104
2.7 Conclusions & Future Work..... 113
2.7.1 Conclusions 113
2.7.2 Future Work..... 114

Chapter 3: Continuous Voltammetric Anion Sensing.....116

3.1 Introduction & Chapter Aims 117
3.2 3.XB/HB_{SAM} Film Generation & Characterisation 120
3.3 Static Voltammetric Anion Sensing Performance of 3.XB/HB_{SAM} 122
3.4 Microfluidic Flow Cell Design 127
3.5 Continuous Voltammetric Anion Sensing..... 129
3.6 Data Analysis 136
3.7 Sensing of Other Anions & Analytical Performance of the Flow Sensors 142
3.8 Conclusions & Future Work..... 147
3.8.1 Conclusions 147
3.8.2 Future Work..... 148

Chapter 4: Redox Capacitive Ion Sensing.....150

4.1 Introduction & Chapter Aims 151
4.2 Principles of Redox Capacitive Anion Sensing..... 154
4.3 Comparison of Continuous Voltammetric & Redox Capacitive Methods 161
4.4 Pseudo-flow Redox Capacitive Anion Sensing..... 165
4.5 Continuous Redox Capacitive Anion Sensing Under Flow 170
4.6 Tuning Sensor Performance Through Surface Polarisation..... 174

4.7 Redox Capacitive Sensing of Other Anions 178
4.8 Redox Capacitive Measurements at Multiple Potentials & Frequencies 186
4.9 Conclusions & Future Work 191
4.9.1 Conclusions 191
4.9.2 Future Work 192

Chapter 5: Continuous Non-Faradaic Capacitive Ion Sensing ...193
5.1 Introduction & Chapter Aims 194
5.2 Synthesis of B15C5, Film Formation & Characterisation 198
5.2.1 Synthesis of B15C5 198
5.2.2 $B15C5_{SAM}$ Film Formation & Physical Characterisation 199
5.2.3 Electrochemical $B15C5_{SAM}$ Film Characterisation 202
5.3 Origin of Non-Faradaic Capacitive Ion Sensing Mechanism 205
5.4 Practical Considerations for Non-Faradaic Capacitive Ion Sensing 211
5.5 Non-Faradaic Capacitive Cation Sensing 214
5.5.1 Static Non-Faradaic Capacitive Cation Sensing 214
5.5.2 Continuous Flow Non-Faradaic Capacitive Cation Sensing 219
5.5.3 Temporal Resolution of Cation-dependent Binding Modes 231
5.6 Conclusions & Future Work 234
5.6.1 Conclusions 234
5.6.2 Future Work 235

Chapter 6: Conclusions & Future Outlook 239

Chapter 7: Experimental 245
7.1 General Considerations 246
7.2 NMR Spectroscopy & High-Resolution Mass-Spectrometry 246
7.3 Gas Permeation Chromatography (GPC) Measurements 247
7.4 Water Contact Angle Measurements 248
7.5 Ellipsometry 248

7.6 Fourier-Transform Infrared Attenuated Total Reflection (FTIR-ATR) Spectroscopy 248
7.7 X-ray Photoelectron Spectroscopy 249
7.8 Electrochemical Measurements 250
7.8.1 Considerations for Electrochemical Measurements 250
7.8.2 Electrode Cleaning Procedure & SAM Formation 253
7.8.3 Molecular Surface Coverage Determination 253
7.8.4 Square Wave Voltammetry (SWV) 255
7.8.5 Capacitance Measurements 255
7.9 Continuous Electrochemical Measurements & Microfluidics 257
7.9.1 Pseudo-flow Set-up 257
7.9.2 Flow Cell Designs 257
7.9.3 Continuous Flow Set-up 259
7.10 Data Analysis & Model Fitting 261
7.10.1 Analysis of Errors Associated with Determining Binding Constants at Polymeric Hosts 261
7.10.2 Response Isotherm & Sensogram Analysis 268
7.11 Synthesis 272
7.11.1 Synthesis for Chapter 2 272
7.11.2 Synthesis for Chapters 3 & 4 291
7.11.3 Synthesis for Chapter 5 291

Chapter 8: References 295

Appendices 305
A1 Appendices for Chapter 1 306
A2 Appendices for Chapter 2 308
A3 Appendices for Chapter 3 319
A4 Appendices for Chapter 4 324
A5 Appendices for Chapter 5 330

Chapter 1

Introduction

Chapter 1: Introduction

1.1 Relevance of Ion Recognition for Sensing Applications

Ionic species are as diverse as they are ubiquitous, and are accordingly integral to a broad range of industrial, medicinal and environmental scenarios.[1-3] Table 1.1-1 highlights the relevance of a select range of inorganic ions within these fields, with some playing pivotal roles as structural components (phosphates in the sugar-phosphate backbone of DNA),[4] or as messengers in communication pathways through ion transport across cell membranes (Na^+/K^+ channels for cell signal transduction), for example.[5] Alternatively, the presence (or excess amounts) of certain ions can have catastrophic implications for local environments. For instance, elevated levels of nitrates/phosphates induce eutrophication of aquatic habitats,[6] and industrial by-products such as N_3^-, CN^- or radioactive $^{99}TcO_4^-$ are highly toxic to local ecosystems.[7, 8]

Table 1.1-1. A list of pertinent ionic species which are common targets when designing and developing ion receptors or sensors, and their role in biological/industrial/environmental scenarios.

Ion	Role
Na^+	**Regulation of osmotic pressure and cell signalling-** major extracellular cationic electrolyte, critical component (along with K^+) for cell signalling pathways.[5]
K^+	**Heart function and smooth muscle contraction-** crucial for normal heart, digestive and muscular function, major intracellular cationic electrolyte.[5]
Cl^-	**Cystic fibrosis-** misregulation of Cl^- transmembrane channels.[9] **Anti-cancer treatments-** enhanced Cl^- transport to acidify the cytoplasm of cancerous cells and initiate apoptosis.[10]
Br^-	**Environmental trends-** trends in fossil fuel activity are reflected in concentration changes of Br^- in surface seawater.[11]
I^-	**Thyroid function-** required for the synthesis of the thyroid hormones thyroxine (T_4) and triiodothyronine (T_3).[12]
Organo-phosphates	**Nerve agents-** phosphorylation of acetylcholinesterase causes seizures, miosis and eventually death.[13]
SO_4^{2-}	**Sulfate binding protein-** active transport system in Gram-negative bacteria.[14] **Groundwater contaminant-** increased SO_4^{2-} levels due to seawater intrusion.[15]

There is, then, significant demand to be able to detect and quantify ionic targets effectively, particularly in aqueous conditions given the prevalence of these ions in both medically-relevant (*i.e.*, biofluids such as sweat, saliva or blood) and environmental (*e.g.*, river water, ground water or potable water sources) media.[2] This remains a formidable challenge in host-guest chemistry, and understanding/controlling the impact of water on ion binding strength and/or selectivity is essential to progress in supramolecular host design. In parallel, scoping out novel transduction methodologies that are able to follow or even control ion binding events with precision would provide a powerful avenue towards translating these potent hosts into functional sensors for the applications outlined above.

These objectives are, however, non-trivial, and necessitate a deeper understanding of the impact of receptor design and solvent on ion recognition behaviour, as well as an exploration of sensing techniques and how best they can be exploited to optimise analytical performance (sensitivity, temporal resolution, limits of detection *etc*.). Downstream sensor development is also crucial to translate potent ion-receptive motifs into functional devices to enable facile, continuous ion sensing modes.

This thesis aims to address these issues by first exploring the role of the local environment on anion binding performance, to provide insight into the utility of established microenvironments to exclude solvent from anion binding sites to enhance binding affinities and/or improve tolerance to increasing external solvent polarity. Then, multiple novel, continuous ion sensing methodologies based on

electrochemical techniques will be outlined, which are capable of sensitively following ion binding in real-time and even modulate key ion binding and sensing parameters. All ion-receptive motifs are supramolecular in nature, allowing for facile sensor reuse which in turn improves the downstream sustainability of these approaches. The design considerations for these ion receptors are initially discussed below, followed by an outline of the electrochemical techniques and principles which govern the sensing methodologies presented herein.

1.2 Considerations for Supramolecular Host Design

1.2.1 General Considerations

Ion recognition at abiotic receptors typically proceeds via one of two routes: an irreversible (or occasionally partially reversible) reaction transduced through an observable signal (chemodosimeters), or a fully reversible binding event mediated by non-covalent interactions (chemosensor).[16] Chemodosimeters have been broadly applied to sense a range of cationic and anionic targets in a cost-effective, facile and fast manner, but are typically restricted by poor selectivity preferences as numerous other ionic species can often react with the functional site(s) to an extent.[16] Furthermore, the irreversible nature of the sensing mechanism inherently prohibits sensor-reuse, resulting in an unsustainable, resource intensive technique which cannot be operated in real-time; a critical objective for medical or environmental monitoring applications.

In contrast, chemosensors derived from supramolecular host architectures bind guest ionic species in an entirely reversible manner, and additionally boast a substantially higher degree of tuneability and versatility to impart a greater degree

of selectivity for a given target ion.[3, 17] This is especially crucial for the recognition of anionic species, as they typically exhibit considerably lower charge-to-radius ratios with respect to their isoelectronic cationic counterparts, as well as greater pH sensitivity, more complex geometries, poorly defined coordination preferences, and high solvation enthalpies.[18] The latter is especially prohibitive in polar solvents and is often related to the Hofmeister series, which is a "salting-out" series that indirectly reports on anion solvation, as depicted in Figure 1.2.1-1.[19] The series predicts that poorly hydrated anions such as I^- or ClO_4^- would be preferentially bound over highly hydrated anions such as F^- as SO_4^{2-} in polar media as their de-solvation enthalpies are comparably small, and *vice versa* in non-polar media wherein these de-solvation penalties are much less significant and the strength of host-guest non-covalent interactions dominates.

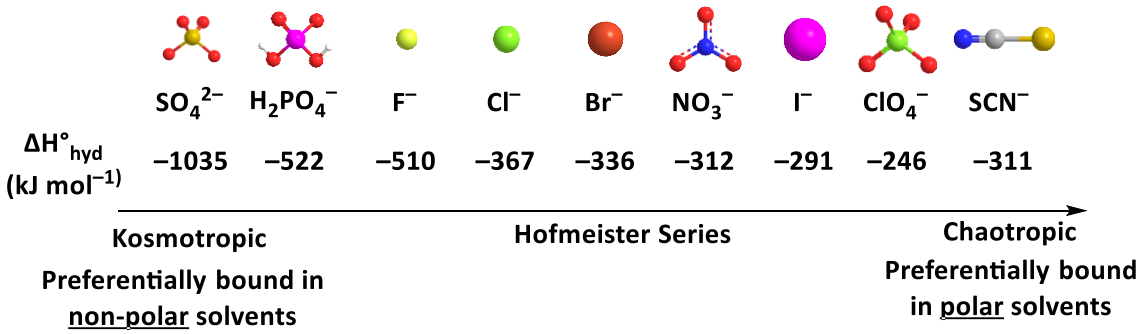


Figure 1.2.1-1. The Hofmeister series and associated anion hydration enthalpies ($\Delta H°_{hyd}$).[20, 21]

In order to effectively and selectively bind the target (an)ion of choice, a range of supramolecular design principles can be applied to establish a Lewis acidic binding site that complements the geometry or size of the target species, as outlined below.

1.2.2 Supramolecular Design Principles

As highlighted above, the breadth of (an)ion characteristics (*e.g.*, geometry: linear, bent, tripodal, tetrahedral, octahedral *etc.*, as visualised in Figure 1.2.1-1) has

inspired a rapid evolution of synthetic receptor designs for each target, from molecular, acyclic scaffolds to macromolecular, interlocked, or hierarchical structures.[22, 23] In order to compensate for the often formidable (an)ion desolvation penalties, the interaction energy between the host and guest must be maximised (see Figure 1.2.2-1 for common approaches to achieve this).

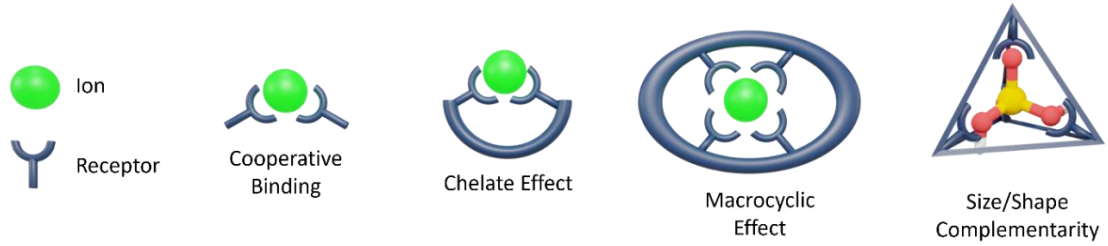


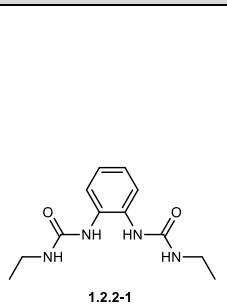
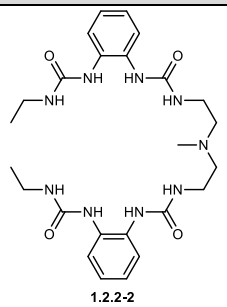
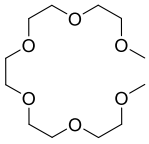
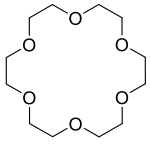
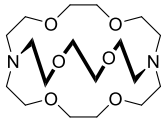
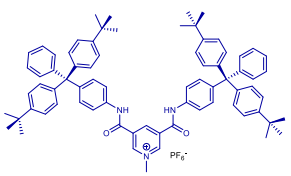
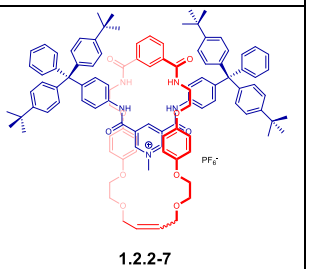
Figure 1.2.2-1. Fundamental concepts for supramolecular abiotic receptor design, from left to right: cooperative binding modes, the chelate effect, the macrocyclic effect and shape complementarity.

Cooperative binding modes, whereby multiple binding motifs are intentionally directed towards a central, organised binding site have been shown to substantially improve (an)ion binding strengths.[24] This approach is often used in conjunction with the concept of complementarity (*i.e.*, tailoring the shape, size and other characteristics of the binding site to promote the best fit to the target ion), as both the directionality and spatial arrangement of the constituent binding units can markedly augment both (an)ion binding strength and selectivity when an excellent size/shape match is made.

More generally, these concepts reflect the role of host preorganisation in promoting the stability of the resulting host-guest complex by optimising both the enthalpic and entropic components of binding.[25] Specifically, by rigidifying or preorganising the host structure into a conformation that is conducive to binding at the point of synthesis, much of the enthalpic cost associated with bringing multiple binding units close in space is paid prior to the binding event. This results in a considerably

more favourable overall enthalpic change upon ion binding. Furthermore, limiting the receptor's conformational degrees of freedom via preorganisation also reduces the entropic penalties associated with confining the host to the lowest energy conformation for (an)ion binding.[26] Host preorganisation can be achieved via a number of established approaches, with Table 1.2.2-1 highlighting the most common routes and examples thereof, from least to most preorganised.

Table 1.2.2-1. Common approaches to increase the degree of preorganisation at a host.

Approach	Definition	Example
Chelate Effect	The manner in which polydentate acyclic hosts form more stable complexes than the equivalent number of monodentate ligands with the same donor atom.[27]	 **1.2.2-1**  **1.2.2-2** K_a in 3:1 DMSO-d_6/H_2O for SO_4^{2-} = 294 M^{-1} for **1.2.2-1** and 7025 M^{-1} for **1.2.2-2**.[28]
Macrocyclic Effect	The increase in stabilisation of a complex when n monodentate ligands are replaced by a macrocyclic ligand containing the same n coordinating atoms connected in a cyclical arrangement.[29]	 **1.2.2-3**  **1.2.2-4**  **1.2.2-5** LogK_a in MeOH for K^+ = 2.2 for **1.2.2-3**, 6.1 for **1.2.2-4** and 9.8 for **1.2.2-5.**[30-33]
Mechanical Bond Effect	A mechanical bond enforces a high effective molarity of donor components in multi-donor systems, creating a highly solvent-excluding binding cavity in order to overcome the entropic and enthalpic penalties conventionally experienced upon host-guest binding.[34]	 **1.2.2-6**  **1.2.2-7** K_a in 1:1 $CDCl_3$/CD_3OD for Cl^- = 125 M^{-1} for **1.2.2-6** and 1130 M^{-1} for **1.2.2-7**.[35]

1.2.3 Non-covalent Interactions

The aforementioned design principles are especially impactful when used in conjunction with potent non-covalent interactions. A number of different non-covalent interactions have been applied for ion recognition, with the following being most relevant to anion recognition: coulombic interactions with incorporated cationic sites (*e.g.,* with coordinatively-unsaturated metal cations),[36] hydrogen bonding (HB) through O-H-, N-H-, S-H- or C-H-based donor sites ((thio)ureas, amides, (thio)squaramides, *inter alia*),[37] sigma-hole based interactions such as those provided by halogen bonding (XB), chalcogen bonding (ChB) or pnictogen bonding (PnB) (*e.g.,* iodo- or telluro-triazoles),[38] or anion-π interactions with an electron deficient (π-acidic) aromatic system.[39]

Non-directional Coulombic Interactions

Exploiting coulombic (or electrostatic) interactions between a charged host and guest is a well-established approach for achieving effective anion recognition. Inclusion of a positively charged centre, or multiple centres appropriately arranged to perform in a cooperative manner, can engender strong anion binding even in highly polar and aqueous media.[40] Frequently employed motifs include polyammonium-,[41-43] polyguanidinium[44-46] or metal-based[47-49] anion receptors, though it should be noted that the latter can also participate in dative bonding to the anionic species. Whilst these highly charged receptors can be associated with high anion binding strengths, the inherent non-directionality of coulombic interactions typically affords poor selectivity for a given target.[40] Furthermore, charged hosts are necessarily accompanied by counter-anions to ensure charge neutrality, which

may interfere with specific anion binding interactions through competitive ion pairing effects, for example.

Such effects are well-known to complicate binding equilibria in low polarity solvents, and can typically only be diminished/avoided by moving to more polar solvents (to increase ion dissociation during binding studies) where coulombic interaction strengths are greatly attenuated. As detailed above, though, this brings about its own problem as specific binding interactions are also substantially diminished. Recent investigations have started to quantify the impact of these effects in different solvent media,[50-54] including a report from Bhattacharjee *et al.* who explored solvation effects on the strength of ion-ion interactions at complexes of a positively charged (quinolinium), aryl-triazole host, **1.2.3-1** and Cl^- across multiple solvents (DCM, ACN and DMSO).[55] Expectedly, the charged receptor **1.2.3-1** performed well in non-polar solvents ($K_a = 2 \times 10^7\ M^{-1}$ (DCM) with **1.2.3-1** (*cf.* $K_a = 5 \times 10^3\ M^{-1}$ (DCM) with **1.2.3-2**, both for Cl^-) but quickly weakened in more polar solvents ($K_a = 5 \times 10^3\ M^{-1}$ (ACN) and $K_a = 80\ M^{-1}$ (DMSO), both for Cl^-). This loss of performance was especially apparent in comparison to more preorganised, neutral hosts such as **1.2.3-3** which essentially maintained its Cl^- binding affinity from ACN ($K_a = 1.6 \times 10^5\ M^{-1}$) to DMSO ($K_a = 2 \times 10^4\ M^{-1}$).

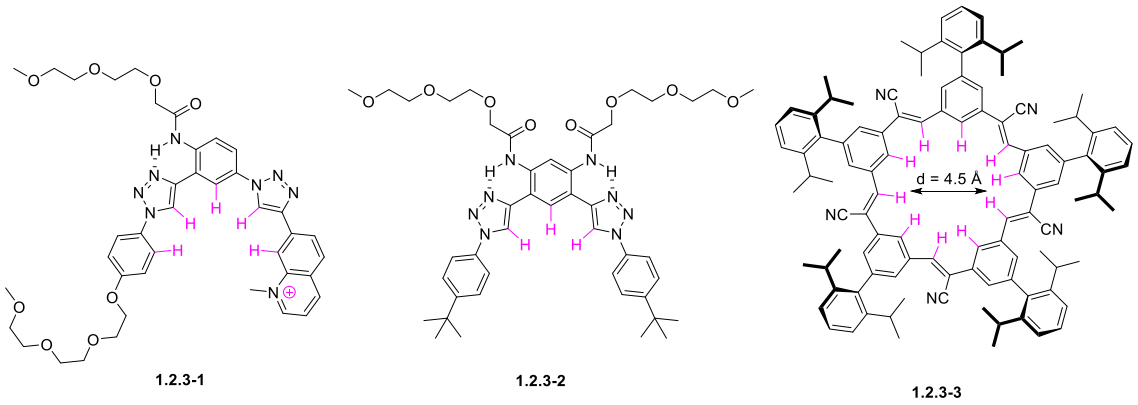


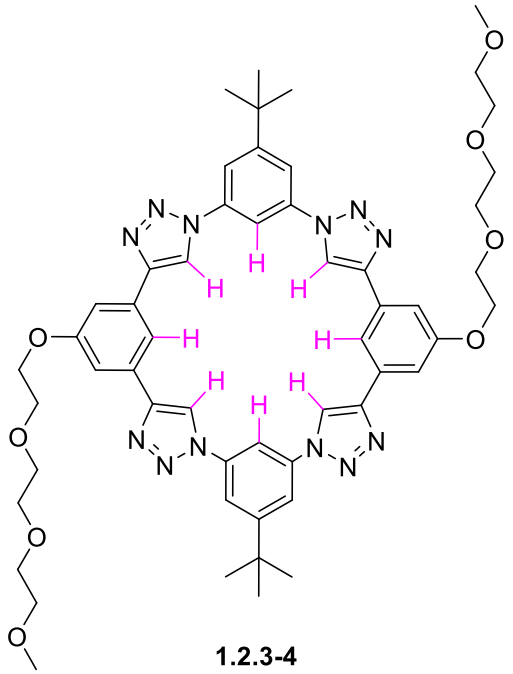
Figure 1.2.3-1. Schematics of hosts with increasing degrees of preorganisation, from an asymmetric, acyclic binding cavity **1.2.3-1**, to an intramolecularly HB, convergent receptor **1.2.3-2**, to a macrocyclic host, **1.2.3-3**.[55]

It is important to note, however, that comprehensive, systematic studies concerning these solvation effects at charged hosts are unfortunately still rare,[56] and a greater depth of understanding is still required in order to universally account for this behaviour. As such, neutral host scaffolds and associated non-covalent interactions have established themselves as promising alternatives, or even improvements, to existing charged host architectures to avoid these issues.

Hydrogen Bonding

Hydrogen bonding (HB)-based receptors are perhaps the most ubiquitous class of anion-receptive host, employing a broad range of binding motifs bearing O-H-, N-H-, S-H- or C-H-based donors ((thio)ureas, amides, (thio)squaramides, *inter alia*).[37, 57, 58] Hydrogen bonding is described as the net attractive interaction between a positively polarised hydrogen atom (through inductive effects from appended electron-withdrawing groups) and a Lewis base (anionic species). In contrast to coulombic interactions, hydrogen bonding is directional, enabling the construction of more defined anion binding sites for anions of different sizes or geometries.[59] For example, Liu *et al*. reported a neutral, shape-persistent, macrocyclic triazolophane

host, **1.2.3-4** which features a preorganised binding cavity defined by 8 HB interactions that effectively binds Cl^- (K_a = 1.3 x 10^5 M^{-1} in ACN).[50, 60]



1.2.3-4

Figure 1.2.3-2. A neutral, shape-persistent, macrocyclic triazolophane host, **1.2.3-4** featuring a preorganised binding cavity with 8 convergent HBs for Cl^- binding.[50, 60]

Hydrogen bonding motifs are also synthetically facile to incorporate into a host scaffold and can also be used to direct secondary host structures via intramolecular hydrogen bonding to further preorganise the host for binding, as exemplified above by **1.2.3-2**. It should also be noted that ion binding studies with HB-based hosts can be restricted to certain pH ranges, as high external pH levels may result in deprotonation of the HB donor. However, this is unlikely to induce issues unless the target application requires operation at a particularly high pH.

Sigma-hole Bonding

Sigma-hole bonding has emerged in recent decades as a particularly promising and potent family of non-covalent interactions termed halogen bonding (XB), chalcogen bonding (ChB), pnictogen bonding (PnB) and tetral bonding (TrB). In analogy to

hydrogen bonding, sigma-hole bonding is defined as a net attractive interaction between an electrophilic region of a halogen/chalcogen/pnictogen/tetral atom, and a Lewis base (anionic species). Amongst sigma-hole interactions, halogen bonding is the most widely studied interaction and has been the focus of a number of fundamental binding studies and applications.[61-63] Examples of anion receptors based on its sister analogues: ChB and PnB, bearing one/two or up to three sigma-holes depending on hybridisation, respectively, are distinctly more rare, predominantly due to the synthetic complexity associated with incorporating them into stable, receptive scaffolds.[38, 64, 65] As halogen bonding is most relevant to the discussions later in this thesis, its characteristics will be described below.

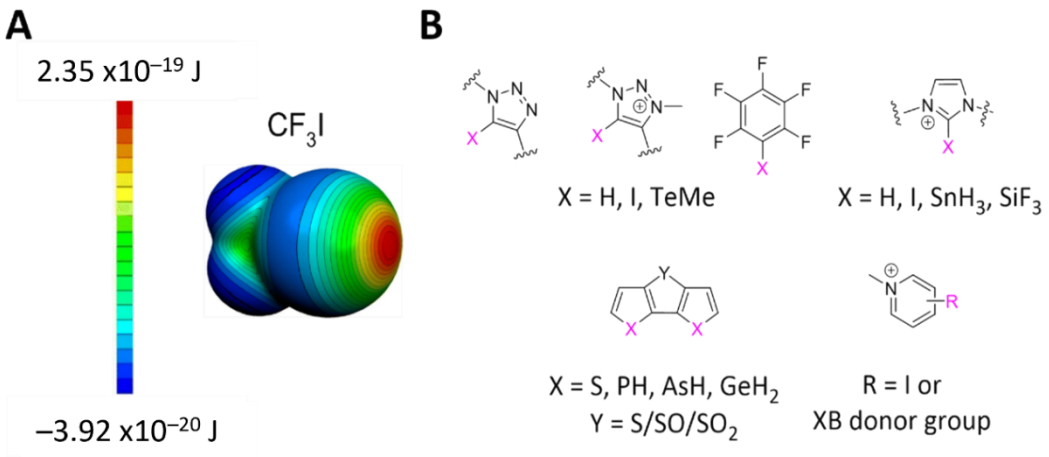


Figure 1.2.3-3. (A) Schematic displaying the molecular electrostatic potential of CF_3I in J (at the 0.001 electrons $Bohr^{-3}$ isodensity surface) displaying the localisation of positive potential (red) termed the sigma-hole. Adapted with permission from Springer-Verlag.[66] (B) Common sigma-hole based analogues of HB binding motifs, as well as electrostatic potential mapping of the sigma holes of a typical halogen bond (I-F) and chalcogen bond (F-Te-F).

Covalently linking a halogen atom to an electron-withdrawing group (*e.g.*, a triazole, perfluoroaryl or more electronegative atom such as fluorine) results in an anisotropic distribution of electron density with a localised positive electrostatic potential along the covalent bond axis, termed a sigma-hole. This electron-deficient

region is expectedly more pronounced with the more polarisable halogens (I particularly, followed by Br), and interacts with electron-rich Lewis bases through a combination of electrostatic and orbital interactions (Figure 1.2.3-3A).[61] XB interactions are often considered to have a greater degree of covalency to their binding behaviour, which is often borne out in selectivity preferences for soft, lipophilic anions (particularly the halides) such as I^-.

XB is typified by a strict linearity in binding (R-X---A^- binding angle of 180°),[67] tuneability of binding strength by modulating the sigma-hole permanently with judicious choice of electron-withdrawing group or *in situ* (see later),[68-70] and higher inherent hydrophobicity compared to HB analogues. The latter can be productively exploited to modulate the lipophilicity of anion transporters (receptors capable of reversibly transporting anions across cell membranes/biomimetic analogues *e.g.*, lipid bilayers), for example.[71-73] As is immediately notable from Figure 1.2.3-3B, synthetic analogues of XB and HB-based hosts can be prepared with relative synthetic ease, with their structures only differing by the donor atom (*i.e.*, -X or -H, respectively). This crucially enables direct, comparative studies to investigate the potency of both interactions in different scenarios (for different anions, solvents, *etc.*); a crucial step towards gaining a better understanding of how non-covalent interactions perform more generally in different solvents and environments. These studies have elucidated that XB often outperforms HB analogues in both anion binding strength and selectivity, marking XB and the other classes of sigma-hole interactions as potent options to improve anion recognition performance (as defined by high anion binding strengths and selectivity preferences).[62, 74]

Anion-π Interactions

Anion-π interactions are notably underdeveloped in comparison to cation-π interactions, but have been used in conjunction with electrostatic or HB motifs for anion recognition.[75-79] An advantage of this approach is that the electron-deficient, π-aromatic surfaces that are utilised to enable binding, can often concomitantly transduce the binding event through optical means. For example, strong electronic interactions between the lone-pair electrons of F^- and π*-orbitals of a π-electron deficient naphthalenetetracarboxylic diimide (NDI) unit was shown to produce an orange coloured $NDI^{\bullet-}$ radical anion.[80] Further reduction of $NDI^{\bullet-}$ by another F^- then produced a pink coloured NDI^{2-} dianion, rendering NDI a colorimetric F^- sensor.

Solvophobic Interactions

The solvophobic effect (hydrophobic; when uniquely related to water) is a well-established and frequently cited phenomenon in anion recognition.[81-83] In addition to mediating host conformational change (see below),[84] solvophobic effects have been used to rationalise a broad range of solvation effects including solvent-dependent dynamic anion binding modes at molecular interlocked host structures,[85] or even the inherent affinities of chaotropic anions for hydrophobic surfaces (with interaction strengths that rival those of established HB motifs).[86-88]

Solvophobic interactions are described as the net attractive force between a solvophobic surface and the guest ionic species, which is often itself solvophobic to minimise unfavourable interactions with the surrounding solvent (*cf*. aggregation of oil droplets in water).[81] Classically, this effect has been ascribed to the favourable entropy gained from the release of "high-energy" (coordinatively unsaturated

compared to bulk) solvent molecules that are bound/confined to the host, or around a non-polar guest, in accordance with the Frank-Evans description (see Figure 1.2.3-4).[89]

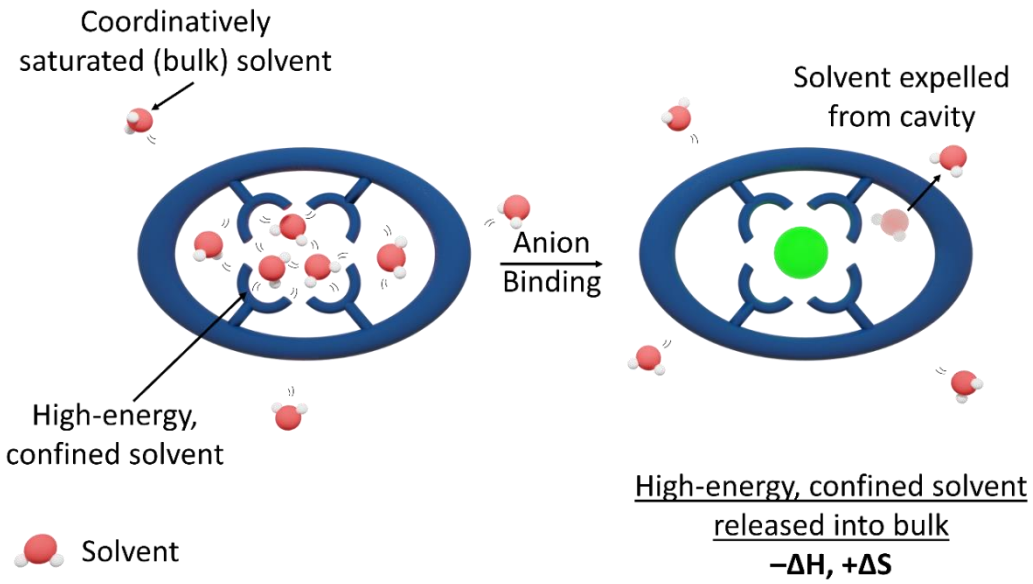


Figure 1.2.3-4. Schematic depiction of "high-energy" solvent from binding cavity (left) being dispelled upon guest binding (right).

This favourable entropic change upon complexation is principally the driving force for solvophobic interactions between non-polar species (e.g., a binding cavity and non-polar species), though favourable enthalpic changes can contribute. For example, water molecules residing in a hydrophobic cavity cannot form fully satisfied HB networks in this confined space, so an enthalpically favourable change is expected upon their displacement into bulk.[89-93] Evidence of this in the context of guest complexation has been obtained through calorimetric analyses,[89, 94, 95] as well as simulations.[81] In rare cases, these enthalpic contributions (deemed "non-classical" effects) have been shown to be significant,[96] arising from particularly strong interactions formed between the liberated solvent molecules and bulk compared to the weaker interactions between confined, "frustrated" solvent

molecules within the host cavity.[94, 97-99] The exact origins of the solvophobic effect are likely more complex than this, and its origins have been greatly debated within the supramolecular community and beyond.[100] Some work has suggested that references to "high-energy" water are only appropriate if a physical (kinetic) barrier to water egression exists (*e.g.*, a single water molecule trapped within a C_{60} molecule).[101] An alternative Lum-Chandler-Weeks theory of hydrophobicity (describing the tendency of non-polar surfaces to de-wet) has been proposed to explain the origin of these effects at concave surfaces (*e.g.*, within binding cavities of hosts).[102-104]

1.3 Solvent Effects at Anion Binding Microenvironments

As is evident from the discussions above, one of the most impactful factors on anion recognition studies in solution or at surfaces is the solvent media used. The suppression of anion binding strength in more polar, competitive media is a well-established (though often empirical) phenomenon and is predominantly attributed to the combined effects of more severe de-solvation penalties and electrostatic screening. This has major implications for designing more effective anion receptors for recognition/sensing applications in aqueous media, which is, of course, relevant for all environmental and medicinal scenarios. To this end, one can take inspiration from biotic anion receptors such as sulfate-specific binding proteins,[105-109] which rely on established binding microenvironments that are shielded from the high screening power of the surrounding bulk media. In doing so, the electrostatic components of all contributing non-covalent interactions and solvation effects more generally are less screened, leading to markedly enhanced anion binding

strengths. Predictably, these effects are greatest when lower local dielectric constant microenvironments are generated.[110] Numerous routes have been reported for this purpose, which can generally be divided into solution-phase and surface-bound approaches.

1.3.1 Solution-phase Approaches

Cage-like structures[111] have shown great promise for anion recognition, operating through highly preorganised, 3D binding environments that can effectively encapsulate anionic targets, concomitantly increasing selectivity biases based on preferred target size or geometry. Examples of this include a triazole-based cage (**1.3.1-1**) from Liu *et al*. which binds Cl^- selectively with a remarkable attomolar (10^{17} M^{-1}) affinity in DCM,[112] or cavitands[92, 93] such as bambusuril **1.3.1-2** which have demonstrated the highest I^- binding strengths in water to date (K_a = 3.2 x 10^7 M^{-1} (H_2O) for I^-).[113]

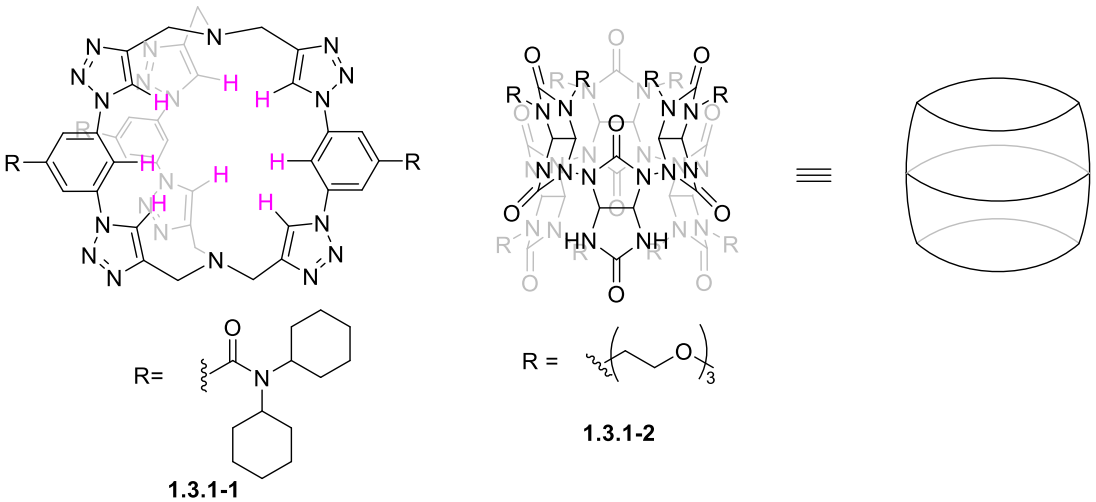


Figure 1.3.1-1. A triazole-based cage, **1.3.1-1**[112] and bambusuril, **1.3.1-2**[113] as representative hosts for highly preorganised 3D binding sites.

Another approach is through the mechanical bond effect,[114, 115] as representatively shown below for XB/HB bis-triazole pyridinium rotaxanes **1.3.1-3.XB/HB** from

Langton *et al*.[116] In this example, significant solvent exclusion from the **1.3.1-3.XB** interlocked cavity prior to anion binding prevented the entropically favourable expulsion of "high-energy" water molecules upon I^- binding, but enabled particularly strong (highly enthalpically favourable) XB-anion interactions. The thermodynamic aspects of this binding event were confirmed and quantified by van't Hoff analysis (analysing how binding constants vary with temperature to estimate ΔH and ΔS for complex formation),[117] demonstrating the positive and negative magnitudes of the entropic and enthalpic contributions, respectively. Conversely, the HB host exhibited the opposite thermodynamic behaviour, which was attributed to efficient "high-energy" water release from the comparably hydrophilic (more hydrated) HB site, highlighting a productive exploitation of XB to enhance anion binding.

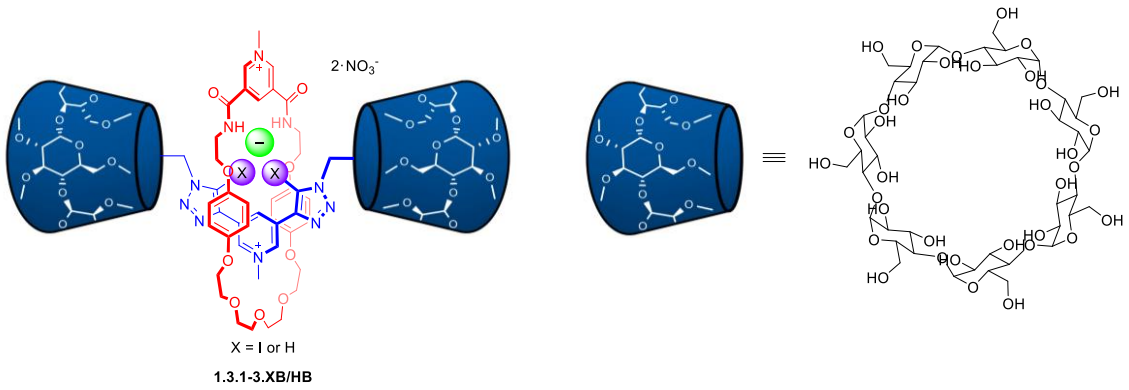


Figure 1.3.1-2. XB/HB bis-triazole pyridinium rotaxanes **1.3.1-3.XB**/**HB**.[116]

Alternatively, solvent-excluded binding cavities may be generated upon a solvent-triggered host conformational change through solvophobic collapse of flexible, macromolecular receptors such as foldamers or polymers. Advantageously, this approach imbues a promotion of anion binding strength within the established local

binding environment, and potentially the generation of highly preorganised, convergent binding sites which may be more selective (Figure 1.3.1-3).[118]

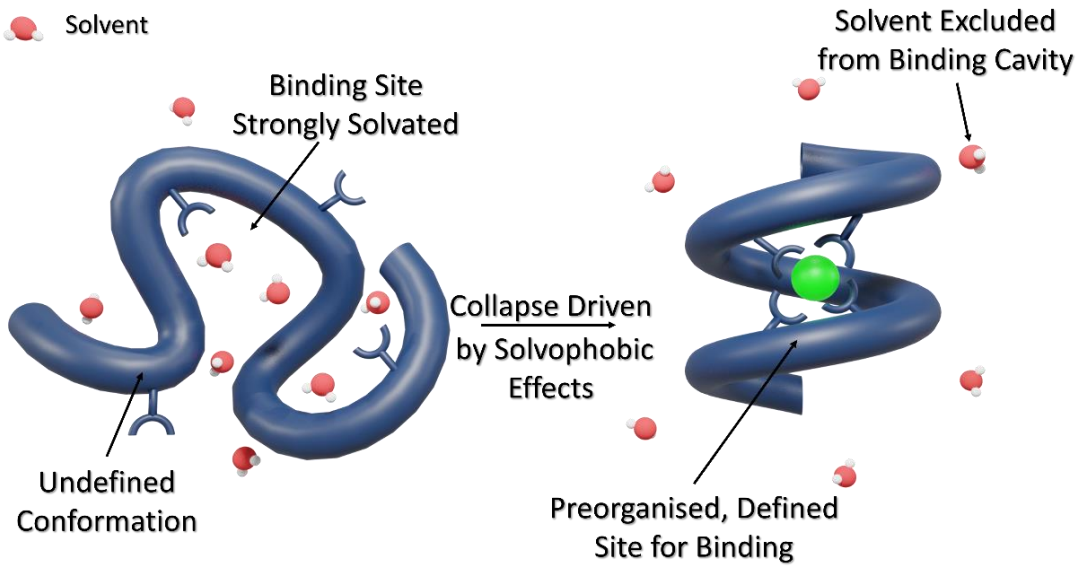


Figure 1.3.1-3. Schematic depiction of conformational changes in solution driven by solvophobic effects to generate a solvent-excluded, preorganised anion binding site with convergent receptive motifs.

A notable example of this concept includes that of Suk *et al.*, who reported respectable halide binding constants with **1.3.1-4** (K_a = 65 M^{-1} (D_2O), 46 M^{-1} (D_2O) and 19 M^{-1} (D_2O) for $Cl^- > F^- > Br^-$, respectively), *cf.* its molecular analogue, **1.3.1-5** whose ^1H NMR spectrum was unchanged upon the addition of any of the halides, due to a combination of reduced screening effects within the binding site and convergent N-H indole HB interactions.[119]

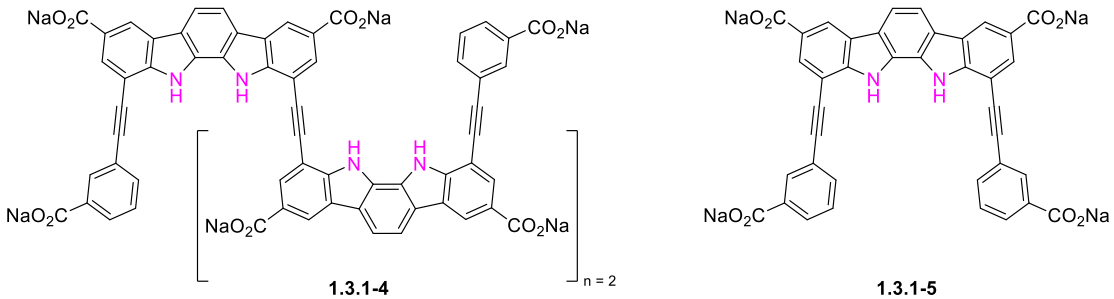


Figure 1.3.1-4. Foldameric HB-based host, **1.3.1-4** capable of binding halides in D_2O, whereas negligible binding was observed at its consituent monomer **1.3.1-5**.[119]

Further still, hosts bearing solvent-excluded binding sites tend to, by definition, demonstrate anion binding strengths which are more tolerant to an increasing solvent polarity. Examples corroborating these predictions include foldameric hosts produced by Hua *et al.* (**1.3.1-6**)[120] and Liu *et al.* (**1.3.1-7**)[110] which demonstrated persistent Cl^- binding in ACN/H_2O mixtures (K_a = 0.5 x10^6 M^{-1} (ACN), 3.8 x10^6 M^{-1} (3:1 ACN/H_2O), 3.8 x10^7 M^{-1} (1:1 ACN/H_2O) for 2:1 host-guest binding at **1.3.1-6**) and a range of solvents spanning a broad dielectric range ($K_a \approx 10^5$ M^{-1} at **1.3.1-7** across ε_r = 9 (DCM) to 36 (ACN)), respectively. In the latter example, the resolved solvent tolerance of **1.3.1-7** as a foldameric receptor was directly contrasted with macrocyclic (**1.3.1-8**) and pentad (**1.3.1-9** and **1.3.1-10**) receptors which displayed a significant dependence on solvent polarity.

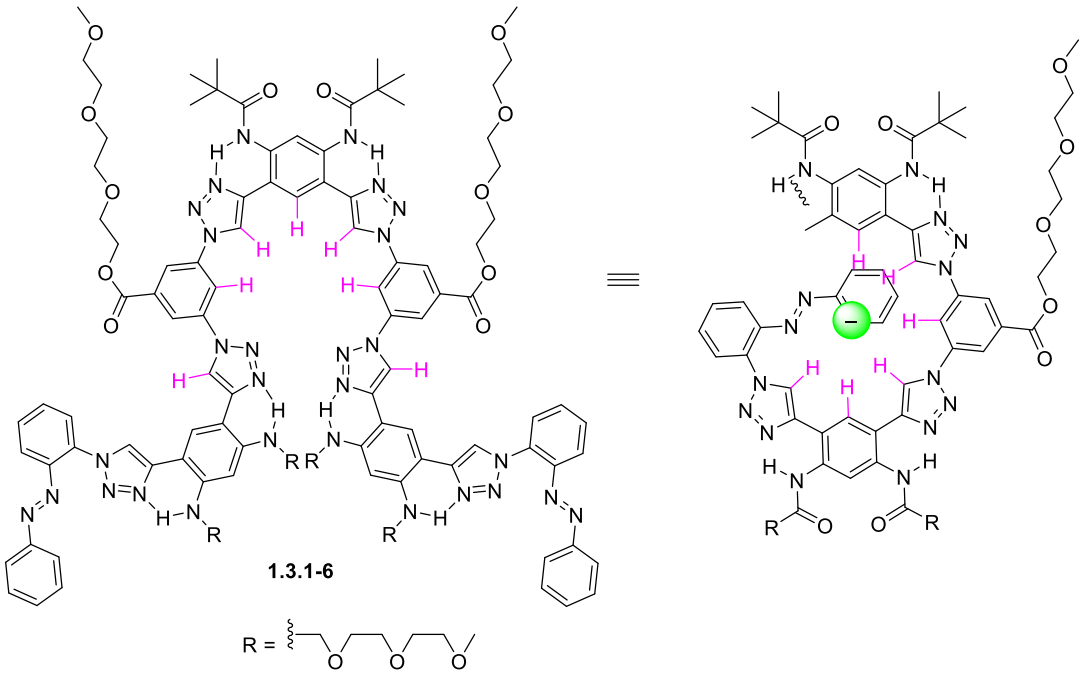


Figure 1.3.1-5. Foldameric HB-based host, **1.3.1-6** which displayed persistent Cl^- binding in a range of ACN/H_2O mixtures.[120]

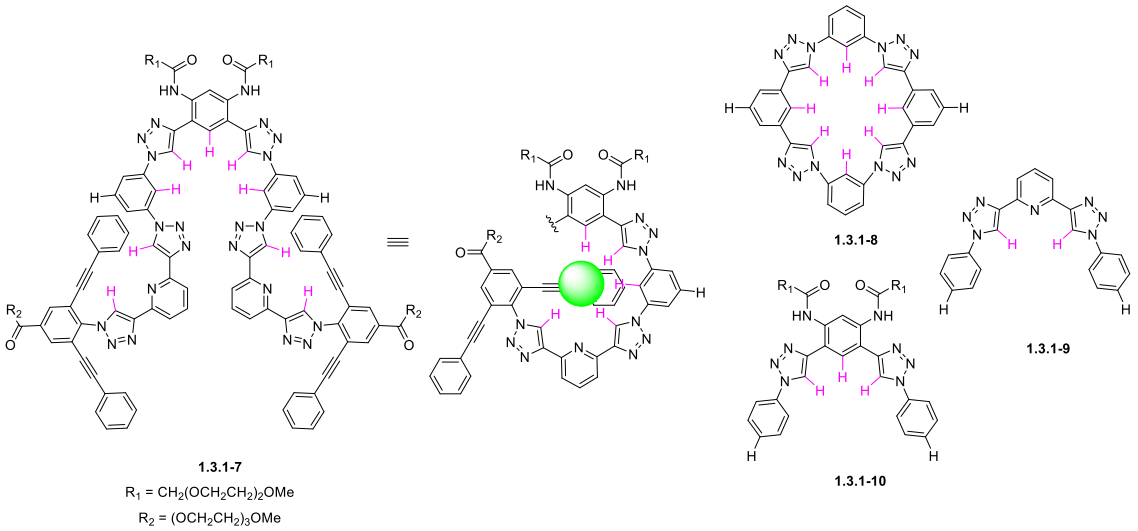
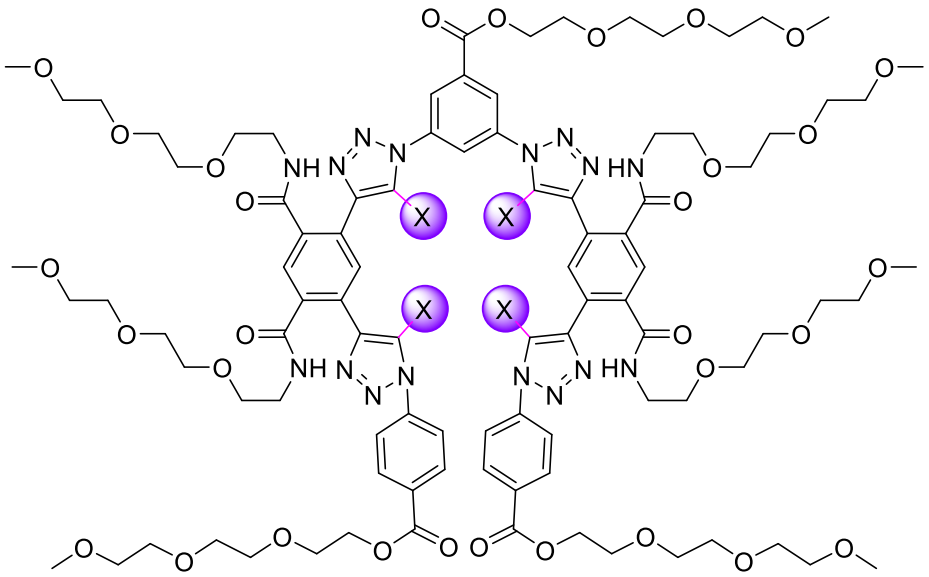


Figure 1.3.1-6. Foldameric HB-based host, **1.3.1-7** which displayed persistent Cl^- binding across a solvent dielectric range of ε_r = 9 (DCM) to 36 (ACN), unlike macrocyclic (**1.3.1-8**) or acyclic (**1.3.1-9** or **1.3.1-10**) analogues.[110]

As one might expect, binding units bearing more hydrophobic non-covalent interactions can also assist in the generation of a solvent excluded binding site. This was demonstrated by Borissov *et al.* with water-soluble charge-neutral, sigma-hole-based XB and ChB foldameric hosts and a HB analogue (**1.3.1-11.XB**/**ChB**/**HB**), whereby the XB/ChB foldamers exhibited significantly higher binding affinities with I^- than the HB analogue in water.[121, 122] This observation was directly attributed to enhanced binding within the binding cavity imbued by the inherently higher hydrophobicity of the sigma-hole motifs, as well as efficient size complementarity. Notably, this highly preorganised binding mode (with 2:1 host-guest stoichiometry) presented by four convergent neutral sigma-hole donor units per host within a solvent-excluded core afforded strong I^- binding constants which impressively exceed all known cationic charge assisted XB receptors ($\beta_2 = 1.45 \times 10^{10}\ M^{-2}$ (H_2O) for I^- with **1.3.1-11.XB**, as assessed by ITC); surpassing even a natural Na^+/I^- symporter protein (NIS, $K_a \approx 4.5 \times 10^4\ M^{-1}$ (H_2O)).[123]



X = I, Te-Me or H

1.3.1-11.XB/ChB/HB

Figure 1.3.1-7. Water-soluble charge-neutral XB/ChB/HB foldameric hosts, **1.3.1-11.XB/ChB/HB** to bind I^- with high affinity in H_2O.[121, 122]

These examples clearly demonstrate the value in augmenting anion binding strengths through the generation of hosts with solvent-excluded binding microenvironments, but generating such hosts can be synthetically taxing. The reason for this is two-fold: producing a host with multiple binding motifs appropriately oriented in space (to enable cooperative binding) is synthetically challenging itself (*e.g.*, to produce mechanically interlocked molecules or cages),[124-126] but flexible host structures are also susceptible to assuming numerous conformations in solution, some of which may not effectively form a solvent-excluded binding pocket. Alternative and promising routes to address this includes incorporation into a tuneable polymeric scaffold or surface immobilisation, through which solvent-excluded receptive films can be generated.

1.3.2 Surface Immobilisation

Receptive motifs can be appended to surfaces in a number of ways, but common approaches include chemisorption of thiol- or disulfide-based hosts to Au surfaces, exploiting the well-established strength of S-Au interactions,[127] or electrografting diazonium salts onto a range of conductive surfaces.[128] A number of benefits are afforded by immobilising receptive architectures to a surface. From a practical perspective, a considerably lower amount of material is required to perform binding/sensing studies (typically µg *vs*. mg amounts) and any host solubility issues are bypassed. These factors are especially pertinent when using abiotic receptors, as considerable synthetic effort is often required to add neutral solubilising groups such as polyethylene glycol (PEG) chains or sulfobetaines, or charged groups including carboxylates, phosphonates, sulfonates or tetra-alkyl ammoniums.[129, 130] However, as highlighted above in Section 1.2.3 in the context of coulombic interactions, incorporating charged groups can introduce other issues through ion pairing effects, for example, and is thus best avoided.

Another crucial benefit in the context of ion sensing, is that surface-immobilised hosts also enable receptor/sensor reusability; taking full advantage of the reversibility of the non-covalent interaction-mediated binding that takes place at a supramolecular host in a way which is significantly more difficult or even impossible to realise in solution. In conjunction with (micro)fluidic setups, which can be easily designed and constructed in a cost-effective manner, (an)ionic targets can be simply introduced and subsequently removed to/from the receptive interface under continuous flow (see Figure 1.3.2-1).[131]

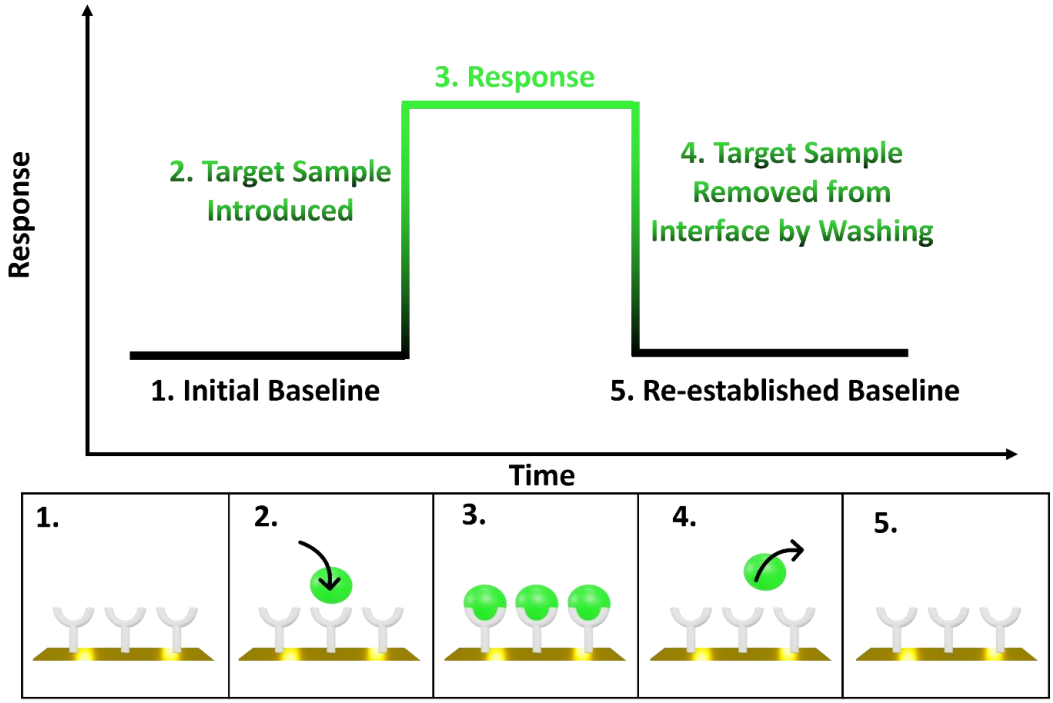


Figure 1.3.2-1. Schematic depiction of surface-immobilised receptors in a (micro)fluidic setup, highlighting the steps to 1. establish the initial baseline, 2. introduce the target sample by flowing it over the receptive interface until 3. the response reaches equilibrium, then 4. the target can be removed from the interface by washing to 5. re-establish the baseline in the absence of target.

In addition to the practical considerations above, there are also important advantages pertaining to interfacial ion binding/sensing. Often, these surface-immobilisation techniques are used to generate self-assembled monolayers (SAMs), which are homogenous, well-defined architectures that have found application in a broad range of scenarios including anti-fouling, batteries, biosensing and ion sensing.[132-134] Providing that a densely packed SAM is formed (typically ≈ x10^{10} mol cm^{-2}), a new microenvironment at the surface can be generated which is often associated with a lower dielectric than the surrounding solvent due to significant solvent exclusion (*e.g.*, SAMs often display film $\varepsilon_r \approx 10$, see Figure 1.3.2-2).[135, 136] Furthermore, immobilising receptors onto a surface can preorganise the host structure by limiting the number of energetically accessible conformations, which has been associated with an amplification in binding strength and/or sensor response.[137, 138]

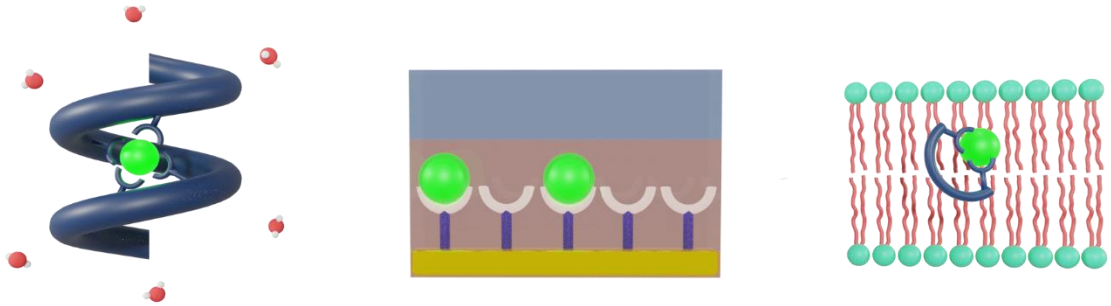
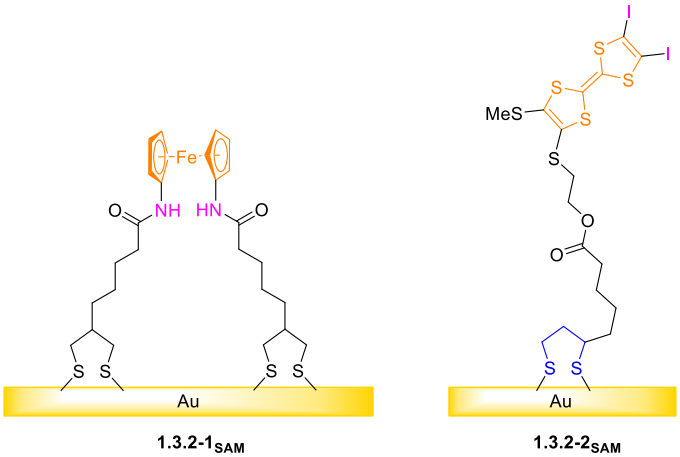


Figure 1.3.2-2. Depiction of defined binding microenvironments within a macromolecular structure in solution (left), at a receptive molecular film (centre) and within a lipid bilayer (right).

For example, early work from Beer *et al.* demonstrated this surface-amplification effect with 1,19-bis(alkyl-N-amido)ferrocene receptors (**1.3.2-1**), which displayed interfacial anion-induced voltammetric responses that were significantly greater than those obtained in solution (ΔE = –40 mV (2:1 ACN/$CHCl_3$) and ΔE = –100 mV (2:1 ACN/$CHCl_3$) for Cl^- with **1.3.2-1** in solution and **1.3.2-1$_{SAM}$** films, respectively) for the same receptor (further detail regarding the use of voltammetry as a sensing method is provided in Section 1.4.2).[139] Similarly, an iodo-tetrathiafulvalene (TTF) sensor (**1.3.2-2**) has also displayed a larger cathodic shift for Cl^- when immobilised in a SAM than in solution (ΔE = –160 mV in ACN *vs* –78 mV in 7:3 DMF/ACN, respectively).[140]



1.3.2-1$_{SAM}$ 1.3.2-2$_{SAM}$

Figure 1.3.2-3. 1,19-bis(alkyl-N-amido)ferrocene receptors (**1.3.2-1$_{SAM}$**)[139] and iodo-TTF XB-based sensors (**1.3.2-2$_{SAM}$**)[140] which demonstrate greater voltammetric responses at the surface over those in solution.

The exact origins of these effects are not yet fully understood, but are primarily attributed to the aforementioned surface preorganisation effects, as well as the relatively low local dielectric constant that is predicted to be generated within the SAM. Hein *et al.* explored these concepts further by presenting an in-depth analysis of the effects within local dielectric environments in ferrocene-isophthalamide-(iodo)triazole (XB/HB) SAMs, **3.XB/HB$_{(SAM)}$** in ACN or ACN/H_2O 99:1.[141] Notably, redox-promoted electrostatic binding (always observed for receptors of this type in which redox units are in close proximity to Lewis acidic receptor units) was enhanced with the positively-charged host state (upon in situ oxidation of Fc to Fc^+) in a low dielectric environment, resulting in an amplification of the resolved electrochemical sensing response at the receptive films compared to the solution-phase hosts (ΔE = –63 mV (99:1 ACN/H_2O) and ΔE = –118 mV (99:1 ACN/H_2O) for Cl^- with **3.XB** in solution and **3.XB$_{SAM}$** films, respectively).

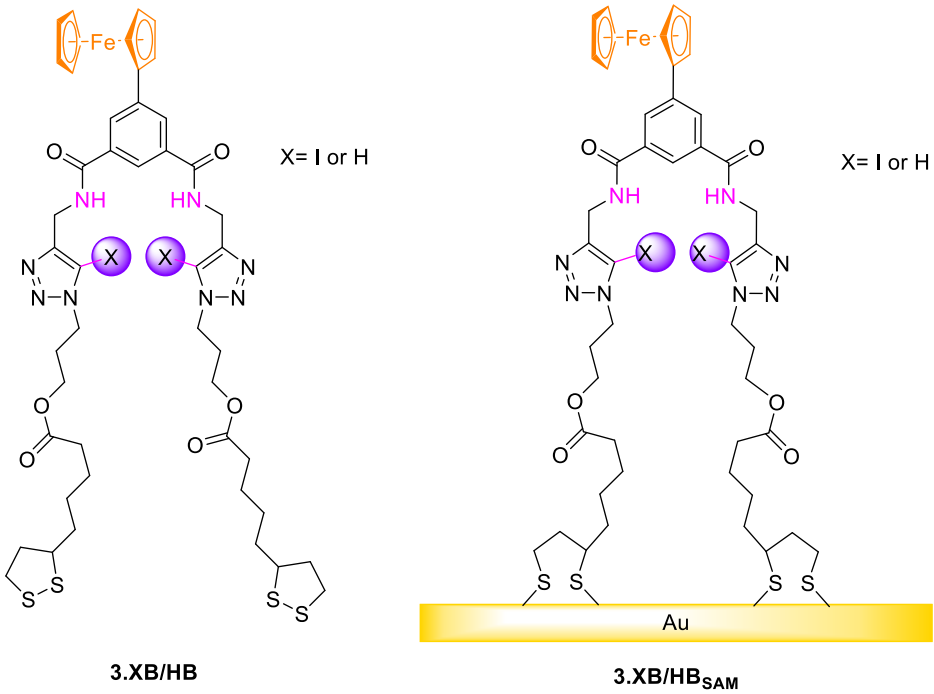
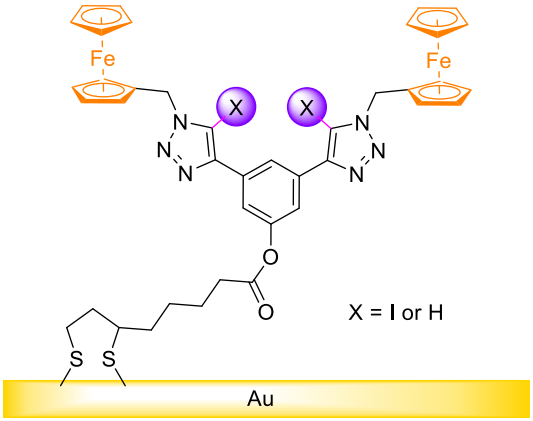


Figure 1.3.2-4. Ferrocene-isophthalamide-(iodo)triazole (XB/HB) SAMs, **3.XB/HB$_{(SAM)}$.**[141]

Film-based solvent exclusion effects have been further demonstrated by Patrick *et al.* with bis-ferrocene-(iodo)triazole receptors, **2.XB/HB$_{SAM}$** across a broad range of solvents.[135] In solution, the XB sensor markedly outperformed the HB analogue, and once again demonstrated a greater tolerance to increasing solvent polarity (see above) for halide recognition. In derived films of both, substantially larger responses to anionic guests were displayed compared to those resolved for the solution-phase hosts ($\Delta E = -60$ mV (9:1 ACN/H_2O) and $\Delta E = -120$ mV (9:1 ACN/H_2O) for $H_2PO_4^-$ with **2.XB** in solution and **2.XB$_{SAM}$** films, respectively), and significant binding responses were retained in up to ACN/30% H_2O (past the solubility limit of the hosts in solution). Notably, this work marks the highest water content that significant anion-induced voltammetric responses have been reported.



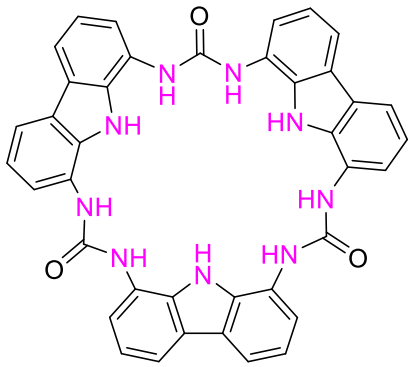
2.XB/HB$_{(SAM)}$

Figure 1.3.2-5. Bis-ferrocene-(iodo)triazole receptors, **2.XB/HB$_{SAM}$**, used for systematic anion sensing studies in a broad range of solvent media up to ACN/30% H_2O.[135]

Significant work has also explored analogous effects within lipid bilayers where solvent exclusion and dielectric effects in line with their biomimetic character have been noted with embedded ion transporters.[142] The environment within a lipid bilayer is has been noted to be of lower polarity ($\varepsilon_r \approx 2$ within the hydrophobic interior, *cf.* $\varepsilon_r \approx 35$ at the periphery)[143] than that of the surrounding (almost exclusively

aqueous) solvent media.[144] The expected role this has in enhancing ion binding has been observed for both cation[143] and anion recognition, with examples of the latter demonstrating a 10,000-fold increase in binding affinity compared to solution, at an air-water interface between phosphate (phospholipid monolayer) and arginine.[145]

In a rare example of a direct, quantitative comparison between anion recognition in solution and within a lipid bilayer, Wu *et al.* report the use of a fluorescent trimeric carbazole-urea macrocycle, **1.3.2-3** to rationalise the anion binding strengths and selectivity preferences for a range of anions in solution-phase, biphasic micelles and lipid bilayer environments.[146] Once again, significant differences in the anion binding behaviour in solution and membrane environments were displayed, as charge-dense anions such as $H_2PO_4^-$ and Cl^- were observed to bind relatively strongly in solution (DMSO/0.5% H_2O), but not within the lipid bilayer membrane (*e.g.,* K_a = 2000 M^{-1} and <1 M^{-1} for Cl^- in DMSO/0.5% H_2O solution and within 1-palmitoyl-2-oleoyl-sn-glycero-3-phosphocholine (POPC) vesicles, respectively). Conversely, anions that were poorly bound in solution (ClO_4^- and I^-) show surprisingly large affinities with macrocycle **1.3.2-3**, when embedded in the membrane of different vesicles (*e.g.,* K_a = 6.1 M^{-1} (DMSO-d_6/0.5% H_2O) and 24 M^{-1} (within POPC vesicles) for I^- with **1.3.2-3**).



1.3.2-3

Figure 1.3.2-6. Fluorescent trimeric carbazole-urea macrocycle, **1.3.2-3**, used to rationalise the anion binding strength/selectivity in solution and within a bilayer.[146]

These bilayer-bound examples and surface-immobilised anion receptive scaffolds support the profound benefits of engineering solvent exclusion in formats that additionally lend themselves to translational application/sensing. They do, however, concomitantly highlight the need for analytical techniques which can transduce ion binding at surfaces.

In solution, more often than not interaction strengths between the host-guest complex are assessed through titration binding studies by ^{1}H NMR spectroscopy, whereby the extent to which the signals of protons within or close to the binding cavity are perturbed is used to determine (an)ion binding constants. Whilst this approach reliably quantifies binding affinity and supports further analyses of host-guest binding stoichiometries and selectivity preferences in solution, it must be performed with expensive and highly specialist equipment (NMR spectrometers, mass spectrometers *etc.*) and cannot be easily applied for interfacial ion sensing studies. This marks a significant drawback when seeking to detect/quantify (an)ions for either environmental or medical applications, which would both hugely benefit from ion quantification in real-time to enable continuous target monitoring.

Therefore, alternative routes which enable continuous and/or real-time monitoring, in a facile and cost-effective manner are highly sought after. Electrochemical approaches have met this challenge in recent decades, resulting in powerful techniques for ion sensing.

1.4 Electrochemical Techniques

Electrochemical techniques are cheap[147-149] experimentally straight-forward and scalable, affording a high information density and sensitivity in reporting both solution-phase and interfacial events.[148] As aforementioned, the latter differentiates electrochemical methods from other sensing techniques, as interfacial ion sensing is otherwise challenging (necessitating optically transparent substrates, for example) or impossible to probe with routinely used techniques such as NMR or optical methods (UV-Vis spectroscopy, colourimetry, fluorescence *etc*.).[150] Electrochemical ion sensing methods can be separated into potentiometric, voltammetric and impedance-derived techniques, and each are outlined in turn below.[151]

1.4.1 Potentiometry for Ion Sensing

Potentiometric approaches for ion sensing rely on the measurement of the potential (specifically the electromotive force, e.m.f.) between an indicator (working) and reference electrode when both are immersed in an analyte solution. In most case the indicator electrode is an ion-selective electrode (ISE) which contains a membrane separating the inner filling solution and the external analyte solution selectively (see Figure 1.4.1-1).

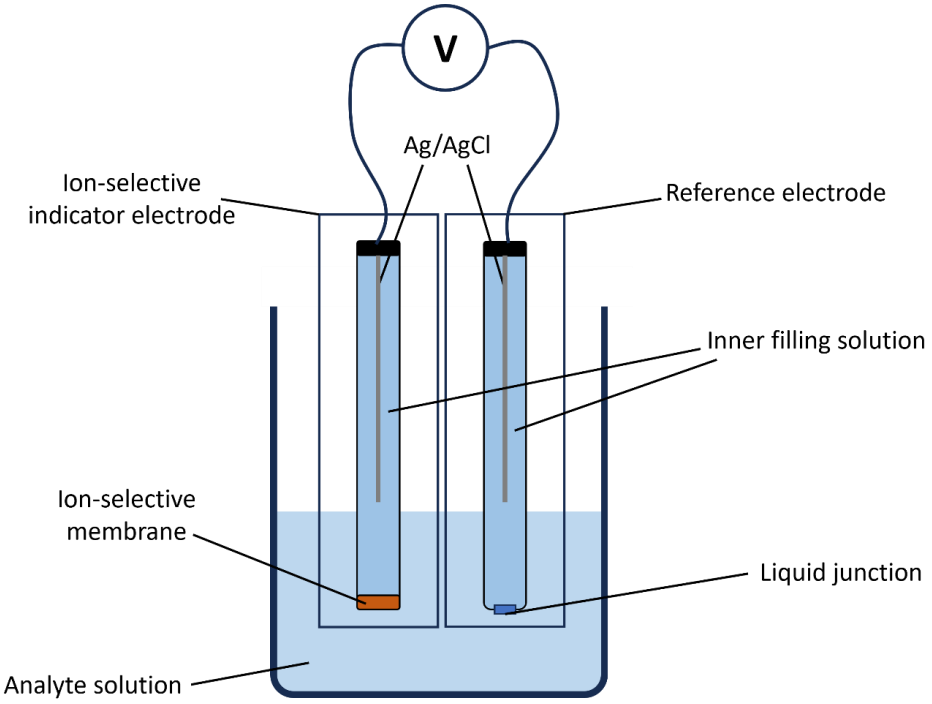


Figure 1.4.1-1. Schematic depiction of a typical setup for potentiometric ion sensing measurements with a membrane-based ion-selective electrode.

The ISE response to target concentration (or more accurately, the activity) is generated once a membrane potential is established when the target (an)ion selectively partitions into the membrane, inducing a charge separation at the membrane boundary and a measurable e.m.f. Selectivity for the target ion directly relies upon the selectivity of the membrane to only allow the target (an)ion too pass. Therefore, the resolved response of the system is solely dependent on the potential across the membrane of the indicator electrode. All other potentials, including junction potentials and that of the reference electrode, which should be unresponsive during measurements, can be assumed to be constant or be corrected for. The membrane potential, E can be described by Equation 1.4.1-1, where E^0 is a constant which encompasses all phase boundary or junction potentials, excluding the outer membrane interface potential, and a_I and z_I are the activity and charge of the target (an)ion, respectively.

$$E = E^0 + \frac{RT}{z_I F} \ln a_I \qquad \textbf{Equation 1.4.1-1}$$

Providing that the concentration of target ion in the inner filling solution is known and constant, Equation 1.4.1-1 holds true in that any measured emf is only dependent on a_I at the outer membrane, *i.e.*, a_I in the analyte solution. Given the logarithmic nature of Equation 1.4.1-1, 10-fold increments in target ion activity result in a change in emf of 59.2 mV/z_I; a so-called "Nernstian response". Deviations from ideality are most often attributable to interference from other ions, reinforcing the need for highly selective membrane materials. A variety of membranes have been applied for this purpose, including glass, crystalline LaF_3 (for F^- ISEs), liquid or polymeric membranes. The latter two types also rely on ion-exchangers and/or ionophores (ion carriers) to impart selectivity for the target, which are often based on supramolecular principles such as the convergent, hydrogen bonding motifs displayed in Figure 1.4.1-2 (selective for Cl^-,[152] SO_4^{2-},[153] HPO_4^{2-},[154] I^-,[155] and ClO_4^-)[156] as well as many others.[151, 157, 158] Importantly, the frequency with which supramolecular motifs are used to improve selectivity and performance of these ISEs reinforces the desire to continue developing more potent supramolecular hosts.

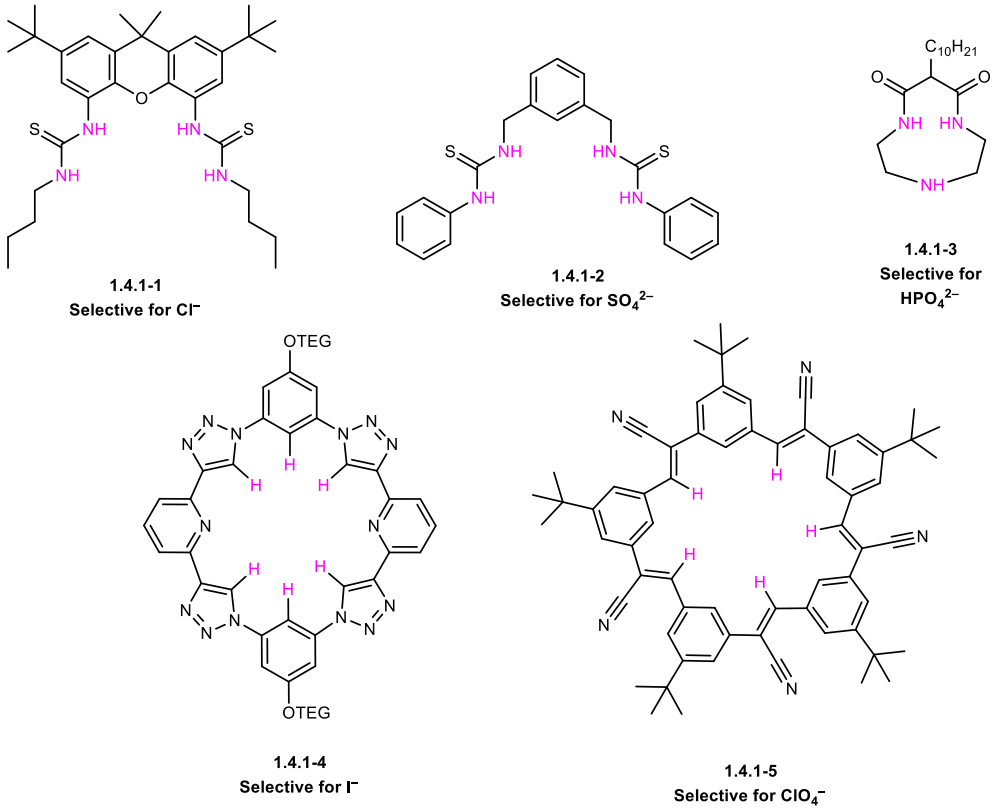


Figure 1.4.1-2. Exemplary ionophores used in ISEs for common anionic targets, **1.4.1-1** for Cl^-,[152] **1.4.1-2** for SO_4^{2-},[153] **1.4.1-3** for HPO_4^{2-},[154] **1.4.1-4** for I^-,[155] and **1.4.1-5** for ClO_4^-.[156]

1.4.2 Voltammetry for Ion Sensing

Voltammetric techniques such as cyclic voltammetry (CV), square wave voltammetry (SWV) and differential pulse voltammetry (DPV) are some of the most routinely employed techniques for electrochemical ion sensing. Their operation relies on an electrochemically addressable, redox-active transducer unit appended to the host, whose electrochemical properties are also sensitive to and actively modulated by the target (an)ionic species. These information-rich methods (providing further information on binding processes beyond a simple e.m.f. to ion activity readout)[151] afford a great deal of insight for both the local environment around the transducer (see Figure 1.4.2-1A, highlighting some of the most relevant information gained from a CV), as well as binding events, whereby typically the half-wave potential ($E_{1/2}$) is used to directly report on binding (see Figure 1.4.2-1B).

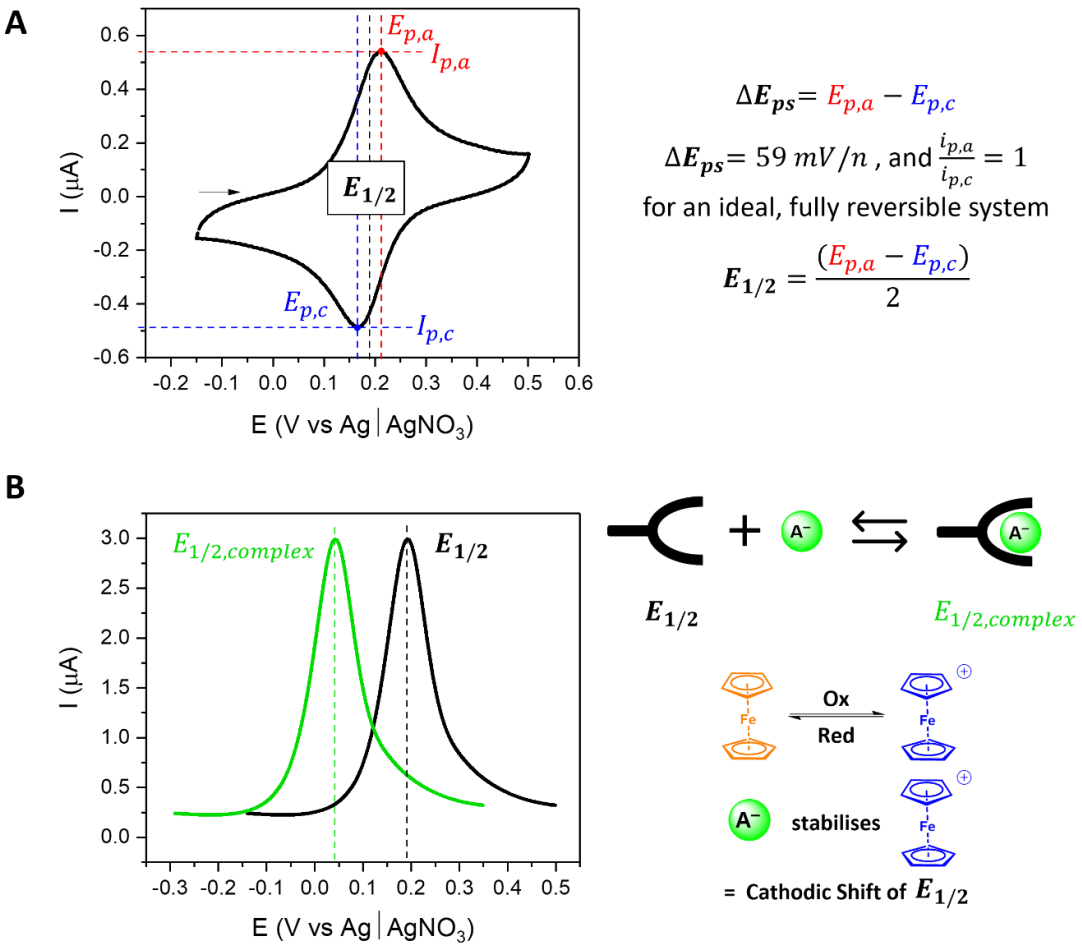
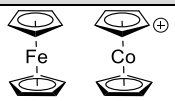
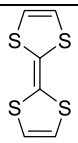
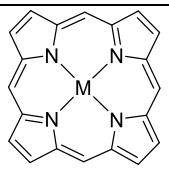
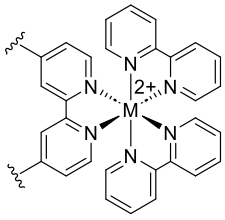
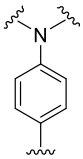
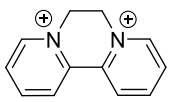
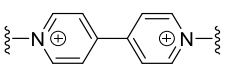


Figure 1.4.2-1. (A) Schematic depiction of the relevant parameters which can be extracted from a typical cyclic voltammogram, and the expectations for an ideal, fully reversible system. (B) The sensing mechanism for voltammetric anion sensing, highlighting the cathodic perturbation of the host $E_{1/2}$ upon anion binding.

A range of redox-active transducers are used for this purpose, including ferrocene ($Fc|Fc^+$, of interest here), tetrathiafulvalene, metal complexes and organic transducers.[151] A summary of the most commonly used transducers is given in Table 1.4.2-1, including the advantages and disadvantages of each transducer type.

Table 1.4.2-1. Table Aummarising the most common redox-active transducers used to report on anion recognition.

Redox-active Transducer	Structure(s)	Redox Couple(s)	Notable characteristics
Metallocenes		Ferrocene/ferrocenium ($Fc|Fc^{+}$)[159, 160] Cobaltocene/ cobaltocenium ($Cp_2Co|Cp_2Co^{+}$)[161]	1. Well-defined, reversible one-electron redox properties at low/moderate oxidation potentials 2. Ease of synthetic incorporation
Tetrathiafulvalene		Neutral/radical cation/dication ($TTF|TTF^{+\cdot}|TTF^{2+}$)[162-165]	1. Two-stage oxidation at moderate/high oxidation potentials 2. Rich spectro(electro)chemistry 3. Conductive 4. Second oxidation process often poorly reversible and solvent dependent 5. Non-trivial synthetic integration
Metal complexes	 M = Zn(II), Fe(III), Co (III) etc.  M^{2+} = Ru^{2+} or Os^{2+}	Porphyrin: Neutral/radical cation/dication ($P|P^{+\cdot}|P^{2+}$)[166-170] Metal-centred oxidative couples (e.g. $Ru^{2+}|Ru^{3+}$, $Os^{2+}|Os^{3+}$)	1. Highly tuneable through metal substitution 2. Rich photophysical properties (e.g., luminescence, can provide dual sensor readout) 3. Can be biomimetic (e.g. porphyrin) 4. Synthetically challenging 5. Second oxidation process often poorly reversible and solvent dependent
Organic Transducers	 *p*-phenylenediamine  Diquat  Paraquat	*p*-phenylenediamine (neutral|+1 state)[171] Diquat ($DQ^{2+}|DQ^{+\cdot}$)[172] Paraquat ($PQ^{2+}|PQ^{+\cdot}$)[173]	1. Tuneable redox potentials through synthetic functionalisation 2. Redox properties are often solvent and/or pH-dependent 3. Often synthetically challenging

Ferrocene is often the transducer of choice for anion sensing applications, primarily due to its ease of synthetic incorporation into receptive scaffolds (Fc and numerous substituted analogues are commercially available) and highly reversible, well-behaved one-electron redox couple that is compatible with a broad range of solvent media.[174] In the context of anion recognition with $Fc|Fc^+$, a cathodic perturbation of $E_{1/2}$ can thus be expected upon anion binding due to stabilisation of the positively-charged ferrocenium state. This stabilisation has been proposed to result from both through-bond and through-space effects upon binding, where the former is expected to be most relevant to more polarisable binding sites (such as those based on sigma-hole interactions), and the latter is most potent with charge-dense anions (*e.g.*, those bearing multiple negative charges).[175, 176] The mechanism by which the $E_{1/2}$ of the redox-active transducer is modulated upon anion binding is likely a combination of both but, crucially, transduction always relies on either spatial or electronic coupling between the binding site and transducer in order to directly report on binding.

The relevant binding equilibrium for the simplest case: 1:1 host-guest binding stoichiometry, can be described by Equation 1.4.2-1, but in the case of a redox-active host this must be adapted to account for the dependence of binding affinity on the redox state of the host (introducing the individual binding constants K_{Ox} and K_{Red}, representing the binding affinity to the host in its oxidised and neutral/reduced redox states, respectively).

$$K = \frac{[HG]}{[H][G]} \qquad \textbf{Equation 1.4.2-1}$$

In doing so, the square scheme given in Figure 1.4.2-2 is afforded, highlighting that the $E_{1/2}$ of the host alone and the host-guest complex are not expected to be equal. An analogous square scheme can also be derived for 1:2 host-guest binding with a host bearing two of the same transducer units, for example, which is relevant to the discussions in Chapter 2 and can be found in Appendices A1, Figure A1.1.

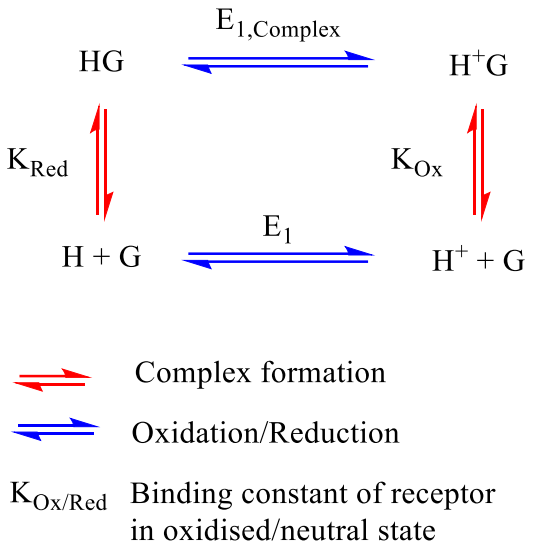
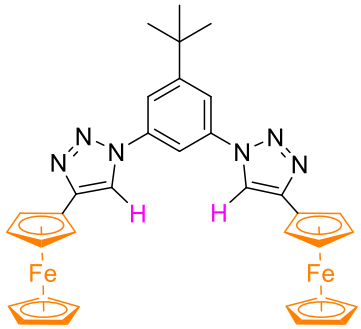


Figure 1.4.2-2. Square scheme describing the binding and redox equilibria involved in 1:1 host-guest binding with a host bearing a single one-electron redox transducer.

Though the binding equilibria of redox-active hosts are inevitably more complex than redox-inactive receptors because of the separate binding affinities to the neutral and oxidised species, the benefits for anion sensing are manifold. By introducing positive charge in situ, in a highly controlled and reversible manner (by oxidising Fc up to Fc^+), anion binding affinity can be "switched-on" (augmented substantially) with respect to the neutral (*cf.* redox-inactive) receptor through two complementary mechanisms. Firstly, the additional electron-withdrawing power of the ferrocenium group (w.r.t. ferrocene) polarises adjacent HB or sigma-hole-based groups, enhancing the HB/XB donor strength for an anionic target. Secondly, attractive coulombic interactions through-space between the two oppositely

charged species are also expected to contribute, particularly in non-polar solvents. This was shown to be especially powerful upon incorporation of two Fc transducers within a bis(Fc-triazole) sensor (**1.4.2-1**), indicating that the inclusion of two transducers can induce a larger "switch-on" enhancement of response due to the additional electrostatic contributions of the oxidised receptor bearing two positive charges rather than one.[177]



1.4.2-1

Figure 1.4.2-3. Bis-(Fc-triazole) HB receptor, **1.4.2-1** for $H_2PO_4^-$ and $HP_2O_7^{3-}$ voltammetric sensing in DCM.[177]

The dependence of anion affinity on redox state is, in fact, the very parameter that results in the observed perturbation in $E_{1/2}$ (*i.e.*, the voltammetric response, ΔE) from which a range of other analytical parameters can be calculated. The relative enhancement from the neutral to charged receptor states is most often represented by the ratio of their respective binding constants: K_{Ox}/K_{Red}, also termed the binding enhancement factor (BEF). BEF values can be directly determined from the maximum cathodic shift observed at each concentration (or at saturation) according to Equation 1.4.2-2. Alternatively, when [Guest] >> [Host] (often satisfied during solution-phase binding studies, and certainly true during interfacial binding studies, see above in Section 1.3.2) Equation 1.4.2-3 can be applied to extract K_{Ox} and K_{Red} separately through non-linear least-squares fitting to determined binding

isotherms.[178] This statement in itself highlights a benefit of voltammetry over ^{1}H NMR spectroscopy, for example, to resolve anion binding in polar media as binding to the neutral host can be almost negligible in competitive solvents, but isolation of the more potent charged host can be challenging or it may be paramagnetic, preventing analyses. From Equation 1.4.2-2, it is clear that the largest responses arise when the difference between K_{Ox} and K_{Red} is greatest, further corroborating the importance of strong spatial or electronic coupling between the transducer and binding site when seeking to resolve measurable voltammetric responses. What is perhaps less obvious, though, is that the lack of an observable response does not necessary mean that binding does not occur, only that there is very little difference in binding affinity to the oxidised and reduced hosts (K_{Ox}/K_{Red} (BEF) ≈ 1).

$$\Delta E = -\frac{RT}{nF}\ln\left(\frac{K_{Ox}}{K_{Red}}\right) \qquad \textbf{Equation 1.4.2-2}$$

$$\Delta E = -\frac{RT}{nF}\ln\left(\frac{1+K_{Ox}[G]}{1+K_{Red}[G]}\right) \qquad \textbf{Equation 1.4.2-3}$$

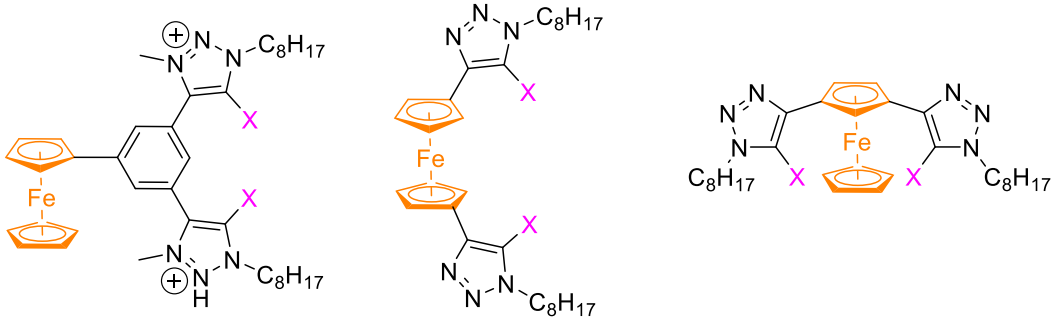
Other considerations for voltammetric anion sensing include the use of a supporting electrolyte to limit errors associated with solution-phase resistance (*i.e.*, ohmic drop) to voltammetric peak positions. To address this, a large excess (≥ 100 mM) of a non-coordinating supporting electrolyte is used to not interfere with the ion binding event. Typically, these are sterically bulky ions (tetraalkylammonium salts such as tetraethylammonium or tetrabutylammonium; bulky anions such as ClO_4^-, BF_4^- or PF_6^-) that are not to expected to fit within the host's binding cavity. It should be noted though, that there is an inherent electrostatic (de)stabilisation of the neutral/charged redox states in the presence of different identities and

concentrations of supporting electrolyte, as well as the solvent media used. Expectedly, this can have a considerable impact on the voltammetric characteristics of the redox-active host which can be problematic when these parameters are used as the sensor readout. For example, the $E_{1/2}$ of the host is used to report on specific anion binding, but it is also inherently sensitive to changes in salt concentration or solvent. These effects are particularly pronounced in non-polar solvents (*e.g.*, chloroform or DCM) where charge screening is minimal. To counteract these non-specific effects, it is preferable to maintain a constant ionic strength during both characterisation and anion sensing studies, and compare all specific responses to a non-receptive model host to ensure certainty in these response magnitudes.

Voltammetric techniques are some of the most commonly used electrochemical techniques to transduce anion binding both in solution and at interfaces. Notable examples of voltammetric anion sensors have been reviewed extensively else,[151, 179] but a key subgroup of sensors that are highly relevant in the context of this thesis include those mediated by XB, particularly those with direct HB analogues for comparative studies. These are of particular interest here, as XB interactions are distinctly more polarisable than HB and the strength of these sigma-hole interactions can be disproportionately enhanced over HB analogues via the use of adjacent electron-withdrawing groups such as perfluorophenyls.[68] Notably, this concept is directly translatable to an anion sensor whereby a Fc unit is appended close to the XB/HB binding site (within a few bond lengths), as in situ oxidation of the Fc transducer increases its electron withdrawing ability, polarising the X-R or H-R bonds for a XB or HB interaction, respectively. As stated above, the higher

polarisability of XB interactions typically leads to a disproportionate enhancement in binding strength for the XB-based sensor over its HB-based analogue, reflected in greater anion-induced voltammetric response magnitudes (*i.e.*, greater ΔE).

This has been demonstrated, for example, with Fc-bis-(iodo)triazole HB/XB sensors (**1.4.2-2.XB/HB** and **1.4.2-3.XB/HB**)[180] and structurally analogous 1,3-bis-(iodo)triazole-Fc sensors (**1.4.2-4.XB/HB**).[181] These receptors all demonstrated significantly larger cathodic perturbations in the presence of Cl^- and Br^- in ACN than the corresponding HB analogues (*e.g.,* cathodic shifts observed for Cl^- with **1.4.2-2.XB** *vs.* **1.4.2-2.HB** were –32 and –17 mV respectively), to the extent that only **1.4.2-2.XB** displayed a response for Cl^- in ACN/10% H_2O. Similar XB enhancements in response were observed at 1,3-bis-(iodo)triazole-Fc receptors (**1.4.2-3.HB/XB**), with cathodic shifts of –40 and –18 mV, observed in response to N_3^- at **1.4.2-3.XB** *vs.* **1.4.2-3.HB**, respectively (99:1 ACN/H_2O).[181]



X= I or H
1.4.2-2.XB/HB

X = I or H
1.4.2-3.XB/HB

X = I or H
1.4.2-4.XB/HB

Figure 1.4.2-4. Fc-HB/XB receptors with (iodo)triazolium binding motifs (**1.4.2-2.XB/HB**) and Fc-XB/HB receptors (iodo)triazole unit and Fc transducer directly linked (**1.4.2-3.XB/HB**). Both **1.4.2-2.XB/HB** and **1.4.2-3.XB/HB** were utilised for voltammetric sensing of halides in ACN and ACN/10% H_2O.[180] 1,3-bis-(iodo)triazole-Fc HB/XB receptors for voltammetric sensing of halides and AcO^- in ACN/1% H_2O (**1.4.2-4.XB/HB**).[181]

Voltammetric anion sensing studies can equally be conducted at receptive, redox-active interfaces, with notable examples prior discussed in the context of surface

immobilisation (see Section 1.3.2 for descriptions of the voltammetric sensing behaviour of redox-active, receptive interfaces **1.3.2-1$_{SAM}$**, **1.3.2-2$_{SAM}$**, **2.XB/HB$_{SAM}$** and **3.XB/HB$_{SAM}$**). Additionally, it should be noted that the disproportionate enhancements in response often observed for the XB-based hosts over HB analogues extends to both solution-phase and interfacial analyses, confirming the potential of XB-based hosts to improve anion sensor performance in both scenarios. However, further analyses are still required to quantify this effect fully, as XB-based interfacial anion sensors remain rare.[140, 182]

1.4.3 Impedance-derived Techniques for Ion Sensing

Impedance-derived techniques mark some of the most sensitive approaches for probing the resistive and capacitive characteristics of a range of interfacial events, including ion recognition.

Impedance, Z is the resistance a circuit experiences to an alternating current (AC), and is defined by Equation 1.4.3-1:

$$Z(t) = \frac{E(t)}{i(t)} \qquad \textbf{Equation 1.4.3-1}$$

Where E(t) is the time-dependent potential and i(t) is the time-dependent current.

Potentiostatic electrochemical impedance spectroscopy (EIS) refers to the technique whereby a potentiostat applies a sinusoidal potential (Equation 1.4.3-2) to an electrochemical cell and measures a corresponding sinusoidal current (Equation 1.4.3-3). The measured sinusoidal current has the same ω as the applied sinusoidal potential signal, but may be shifted in phase, φ.

$$E(t) = E_0 \sin(\omega t) \qquad \textbf{Equation 1.4.3-2}$$

$$i(t) = i_0 \sin(\omega t + \varphi)$$ **Equation 1.4.3-3**

Where E(t) is the applied, time-dependent (t) potential, E_0 is the amplitude of the applied signal, i(t) is the measured, time-dependent current, ω is the angular frequency of an oscillating sine wave (ω = 2πf, where f is frequency) and φ is the phase shift (phase angle) between the applied and measured sine waves.

Therefore, substituting Equations 1.4.3-2 and 1.4.3-3 into Equation 1.4.3-1 yields Equation 1.4.3-4:

$$Z(t) = \frac{E(t)}{i(t)} = \frac{E_0 \sin(\omega t)}{i_0 \sin(\omega t + \varphi)} = Z_0 \frac{\sin(\omega t)}{\sin(\omega t + \varphi)}$$ **Equation 1.4.3-4**

Utilising Euler's formula (Equation 1.4.3-5):

$$e^{ix} = \cos(x) + i\sin(x)$$ **Equation 1.4.3-5**

Z(t) can thus be expressed as Equation 1.4.3-6:

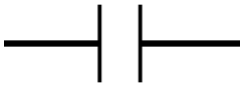
$$Z(t) = Z_0\big(\cos(\varphi) - i\sin(\varphi)\big) = Z' + iZ''$$ **Equation 1.4.3-6**

Where Z' is the real part, and Z'' is the imaginary part of the impedance.

The phase angle strongly depends upon the nature of the circuit. In a purely ohmic resistor, the applied E(t) signal waveform is in-phase (phase angle = 0°) with the measured i(t) signal. Alternatively, in a pure inductor or capacitor the E(t) signal waveform is shifted by a phase angle of +90° or –90°, respectively.

Equivalent circuit modelling is often used to model electrochemical systems, so that relevant, useful information can be extracted. A range of circuit elements are used for this purpose, some of which are summarised in Table 1.4.3-1 below.

Table 1.4.3-1. Summary of relevant circuit elements and their symbols. Note: $j = \sqrt{i}$. α = 0 to 1, with 1 being an ideal capacitor.

Circuit Element	Symbol	Equation
Resistor (R)- element which opposes the flow of charge, here this represents electron transfer across an interface		$Z_R = R$
Capacitor (C)- element which stores charge, typically this represents non-Faradaic charging at an interface		$Z_C = \frac{1}{j\omega C}$
Inductor (L)- element which stores energy in the form of a magnetic field		$Z_L = j\omega L$
Warburg element (W)-element to represent diffusion of electrons/ions		$Z_W = \frac{W}{(j\omega)^{0.5}}$
Constant phase element (Q or CPE)- element to represent a non-ideal capacitor		$Z_Q = \frac{1}{Q(j\omega)^{\alpha}}$

These elements can be combined in a manner to best represent the electrochemical system in question, but the Randles circuit (see Figure 1.4.3-1 below) is most commonly employed. EIS measurements are performed across a range of frequencies (typically 0.1-100,000 Hz), and the resulting spectra can be plotted in a number of ways such as a Bode plot (|Z| *vs*. f, and/or φ *vs*. f) or a Nyquist plot (–Z'' *vs*. Z).

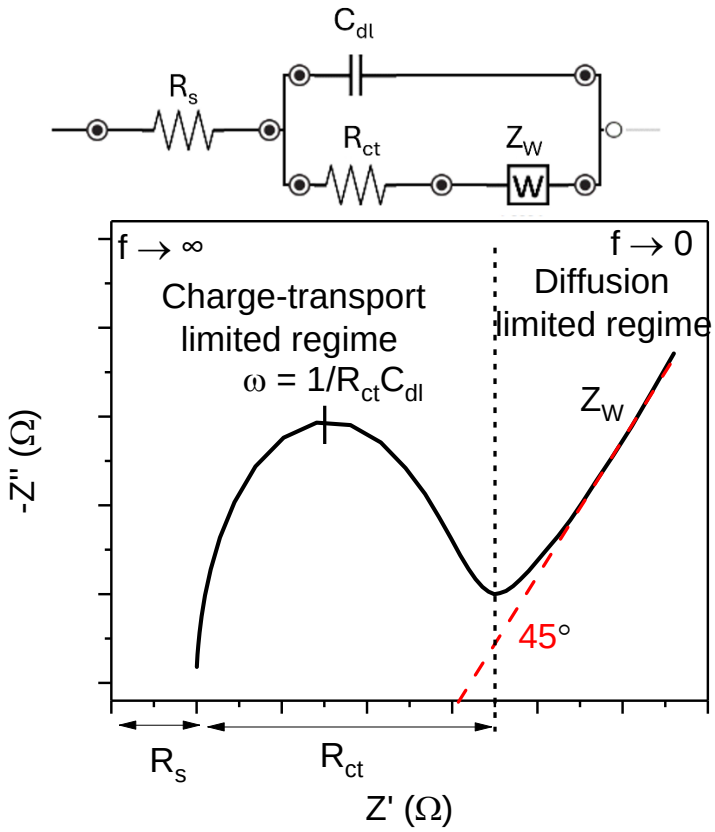


Figure 1.4.3-1. Randles circuit and corresponding Nyquist plot, containing the elements R_s (solution resistance), R_{ct} (charge-transfer resistance), W (Warburg element) and C_{dl} (double layer capacitance).

A small amplitude AC perturbation is applied at a fixed bias potential across a range of frequencies (typically 0.1-100,000 Hz) resulting in a high density of information about the interfacial characteristics, with minimal perturbation to the interface. Importantly, these small perturbations enable investigation of systems at equilibrium, unlike transient techniques such as voltammetry (see Section 1.4.2). Impedance-derived techniques can be further separated into Faradaic and non-Faradaic approaches, whereby the former necessitates the use of a redox-active transducer in solution or appended to the surface, and the latter detects changes in dielectric effects at the surface.

Electrochemical impedance spectroscopy (EIS) is well-established for sensing biologically-relevant molecules such as antigens, proteins or RNA/DNA strands.

Frequently, the charge transfer resistance (R_{ct}) of a receptor-modified electrode is monitored in the presence of a solution-phase redox probe (usually $[Fe(CN)_6]^{3+/4+}$ or $[Ru(NH_3)_6]^{2+/3+}$) to transduce binding. In the case of large biorecognition elements, target binding to the interface is expected to result in an increase in R_{ct} due to increased steric crowding at the electrode interface, dampening electron transfer between the probe and electrode. Notably, this concept has also been applied to the sensing of ions, for which different responses magnitudes are expected based on the resulting electrostatic interactions (*i.e.*, repulsive or attractive) between the utilised redox transducer and target. For example, when a positively charged redox transducer (*e.g.*, $[Ru(NH_3)_6]^{2+/3+}$) and a cation-receptive interface is utilised, R_{ct} would be expected to increase upon cation recruitment due to the enhanced electrostatic repulsion present at the interface. This concept has been applied in particular for cation sensing,[183] especially at crown ether-modified electrodes,[184-186] and has also been demonstrated in rare cases for anion sensing.[187-190]

Another impedance-derived technique of note is redox capacitance, in which the capacitance of a surface-appended redox transducer is used to report on interfacial processes, including target recruitment. As in the case above, this technique is also most commonly used to transduce biorecognition events with large biological targets such as proteins or antigens.[191, 192] Notable advantages of utilising redox capacitance for sensing, are that the only redox-active transducers present are those at the surface, negating the use of solution-phase probes, and the high sensitivity demonstrated with this technique.[193, 194] Despite these advantages, using redox capacitance for ion sensing is almost unknown, with preliminary investigations into sensing cations at crown ether-based receptive films,[195] and

unpublished reports of anion sensing.[179] Further detail regarding the transduction mechanism of this technique will be provided in Chapter 4.

Finally, the use of a redox transducer can be entirely avoided in non-Faradaic capacitive formats, whereby changes in film capacitance upon ionic recruitment to a redox-inactive, receptive film are justified by changes in the dielectric constant of the film. For instance, ion binding at the receptive film increases the charge stored at the interface, increasing local ε_r and, in turn, the film capacitance. Once again, more comprehensive theoretical considerations regarding the transduction mechanism of this technique will be detailed in Chapter 5.

1.5 Thesis Aims

This thesis concerns the development of multiple, novel ion sensing methodologies based on electrochemical techniques, as well as quantifying the impact of imparting a low local dielectric around an ion binding site, on the strength of ion binding and tolerance to increasing bulk solvent polarity. Considerable focus is given to developing ion sensing methodologies which can be performed in a facile manner under flow with high sensitivity, as well as gaining an ability to both follow and even control ion binding thermodynamics and kinetics in real-time.

Chapter 2 explores the impact of incorporating discrete anion-receptive units into a macromolecular co-polymeric scaffold on the anion binding and sensing performance of the resulting hosts. The synthesis and characterisation of the redox-active, XB/HB-based monomeric (**1.XB**/**HB**) and polymeric hosts (**pDEGA-1.XB**/**HB**, **pDEGA-1.XB$_{0.5}$** and **pDEGA-BuA-1.XB**) will be outlined. Systematic anion binding

and sensing studies will be conducted across a range of competitive organic/aqueous solvent mixtures to quantify the influence of the modulated local binding environment imbued by the surrounding co-polymeric architecture. Investigations into whether varying the polymer composition (with less polar co-monomeric units, for example) could influence the local environment and tune anion binding/sensing performance will be conducted for the first time.

Chapter 3 describes the derivation of a continuous voltammetric methodology for anion sensing under continuous flow. An established ferrocene-(iodo)triazole-isophthalamide SAM (**3.XB**/**HB**$_{\mathbf{SAM}}$) will be utilised as a model redox-active, anion-receptive interface to continually monitor specific anion-induced voltammetric responses in real-time. A custom-designed, 3D-printed microfluidic cell will be described, as well as a semi-automated data analysis approach to process the substantial data sets afforded by this technique.

Chapter 4 concerns the development of a novel, real-time redox capacitive ion sensing methodology, conducted under continuous flow. As in **Chapter 3**, **3.XB**/**HB**$_{\mathbf{SAM}}$ will be used as a model redox-active, anion-receptive interface, which will enable a direct comparison of the capabilities of this method with that described in **Chapter 3**. The impact on anion binding and sensing performance will be assessed upon modulation of both the applied potential and frequency.

Chapter 5 outlines a novel, reagentless impedimetric-derived ion sensing methodology based on non-Faradaic capacitance under continuous flow. A benzo-15-crown-5 SAM, **B15C5**$_{\mathbf{SAM}}$ will first be characterised, then utilised as a model cation-receptive interface for continuous non-Faradaic capacitive cation sensing

studies in pure water. The potential of this reagentless method for long-term ion monitoring will then be explored, as well as the cation sensing performance of **B15C5$_{SAM}$** in real, complex media (*e.g.*, river water or tap water samples).

Chapter 2

Polymers for Enhanced Anion Binding & Sensing Performance

Chapter 2: Polymers for Enhanced Anion Binding & Sensing Performance

2.1 Introduction & Chapter Aims

Polymeric hosts represent a promising means to address the synthetic strain associated with generating functional, macromolecular hosts, as less synthetically demanding receptor units can be incorporated into a comparably simple polymeric backbone. Whilst the degree of control associated with polymerisation can differ from that accessible with synthetically-complex receptors, a polymeric scaffold represents an almost infinitely tuneable architecture that can be tailored towards a specific application (by incorporating cation *vs*. anion binding sites, optical or electrochemical transducers, solubilising co-monomers *etc*.).[196, 197] Furthermore, polymeric anion receptors have been associated with several advantages over their monomeric counterparts, such as those imparted by multivalent effects, cooperative binding and enhanced guest selectivity (schematically depicted in Figure 2.1-1).[198]

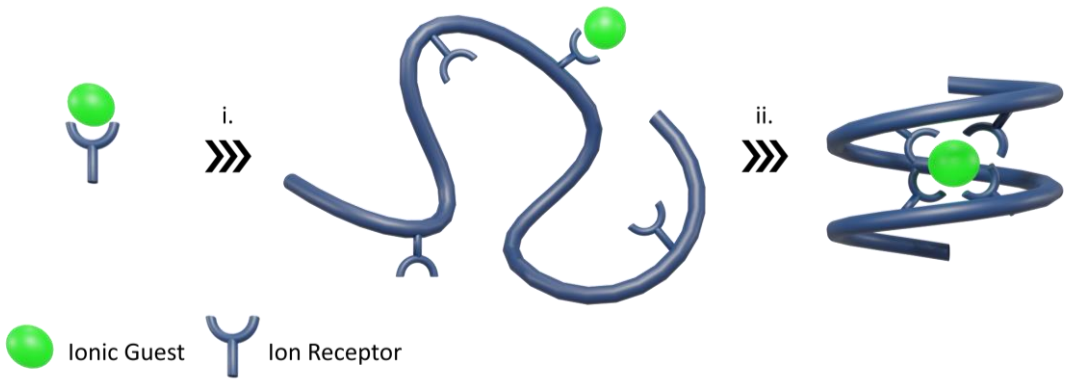


Figure 2.1-1. Schematic depiction of i. the incorporation of ion-receptive (monomeric) units within a polymeric scaffold, which *may* ii. result in a secondary host structure with additional functionality (through solvent- or structurally-driven conformational changes, for example).

A range of polymeric hosts for anion binding/sensing have been reported thus far, from which two prominent categories of polymeric host structures can be defined: covalent or supramolecular. Briefly, the former describes polymers in which each of the repeat monomer units are linked together by permanent, covalent bonds, and the latter are defined as systems which extend beyond the polymeric molecule itself, utilising non-covalent interactions to direct or manipulate their assembly (*e.g.*, to control their conformational arrangements, or to define their behaviour).[199] As outlined later in Section 2.3, covalent polymers are of greater interest here due to their structural tolerance to variable solvent polarity, but interested readers may find examples of supramolecular polymers for anion recognition in the reviews cited here and references therein.[199-201]

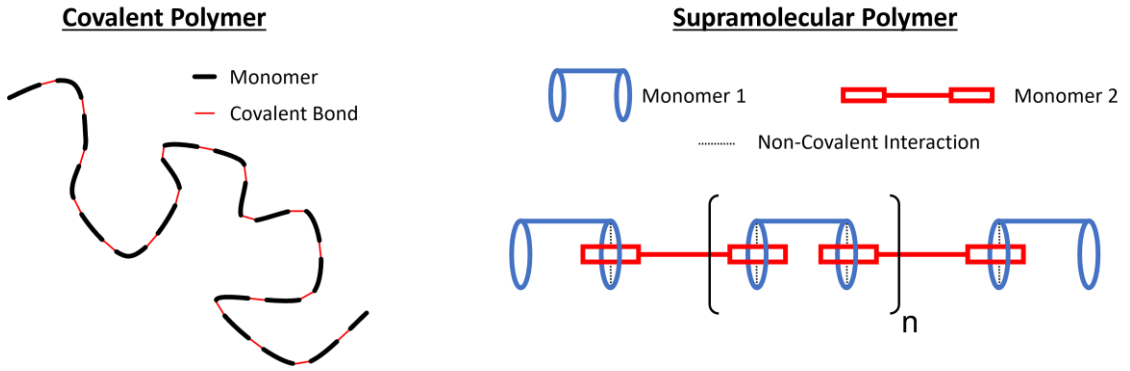
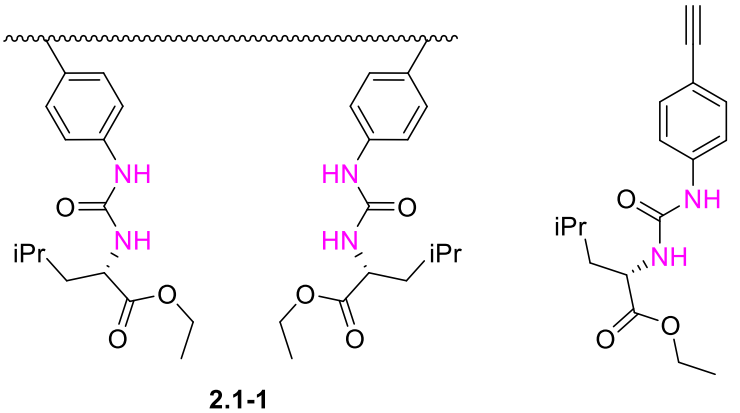


Figure 2.1-2. Schematic depiction of a covalent, linear polymer (left) and supramolecular (right) polymer.

Covalent polymeric hosts for anion recognition typically bear defined binding sites within the structure of at least one of their repeating units (see Figure 2.1-2),[202] although rare examples have also demonstrated the ability of polymeric chains to bind or extract weakly hydrated ionic targets (*e.g.*, SCN^- or I^-) from H_2O without specific receptor units. These examples attributed this behaviour to the polymer backbone disrupting local H_2O HB networks,[203, 204] and could indicate the utility of

using the polymeric backbone itself to facilitate or enhance anion binding. Importantly, numerous reports of polymeric hosts have indicated their promise as candidates for hosts for anion recognition or extraction in polar media.

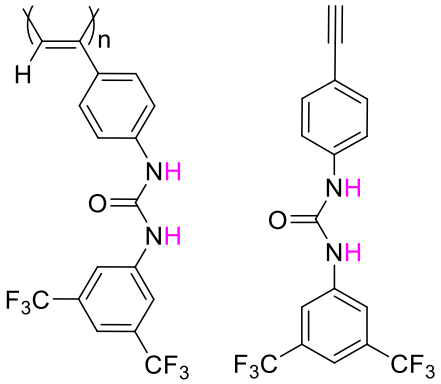
For example, a poly(phenylacetylene) polymeric host with urea and L-leucine functionalities, **2.1-1** was shown to bind anions in a size-specific manner due to a cooperative binding mode.[205] In this mode, two binding units were brought close in space by virtue of being appended to the same polymer chain, enabling strong anion binding with Br^-, Cl^- and AcO^- which was resolved by strong colourimetric responses from pale blue to red in THF.



2.1-1

Figure 2.1-3. Poly(phenylacetylene) polymeric host, **2.1-1** with urea and L-leucine functionalities (left) and its constituent monomer (right).[205]

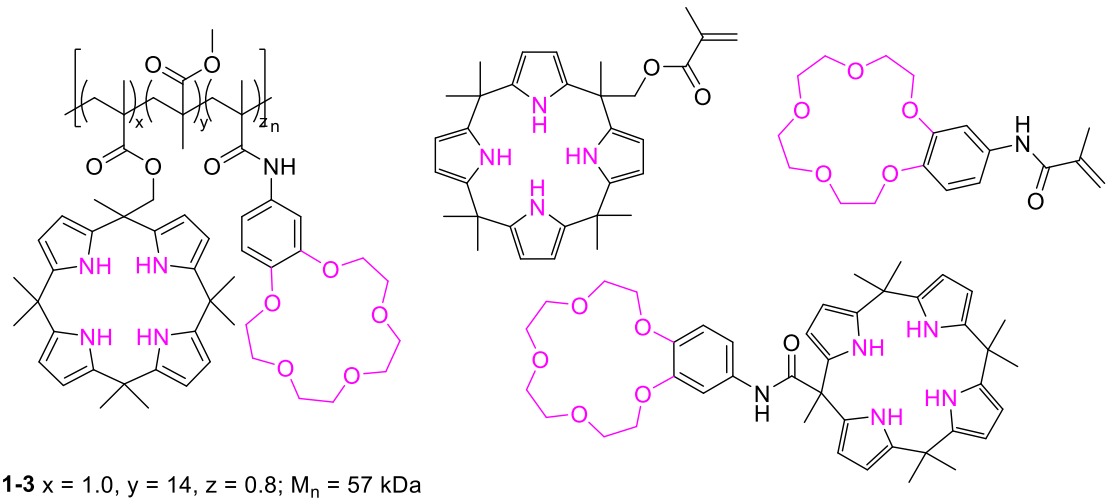
Additionally, a urea-functionalised poly(phenylacetylene) polymer, **2.1-2** produced by Sakai *et al.* displayed anion-induced colorimetric responses for a variety of species (*e.g.*, $C_6H_5CO_2^-$, $CH_3CO_2^-$, Cl^- and Br^-) in DMF.[206] This particular system demonstrated significant positive cooperativity (Hill coefficient = 8.4 for $C_6H_5CO_2^-$ binding to **2.1-2**), indicating that binding was driven by a positive homotropic allosterism whereby the initial binding event induced a change in the main polymer scaffold to promote additional anion binding.



2.1-2

Figure 2.1-4. Poly(phenylacetylene) polymer backbone with [bis(fluoromethyl)phenyl]urea pendants, **2.1-2** (left) and its constituent monomer (right).[206]

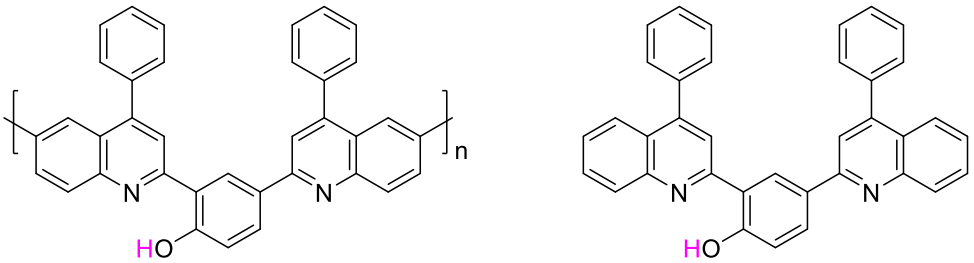
Previous reports also indicate that incorporating receptive monomers into a polymeric scaffold may improve the anion binding/extraction performance with respect to its discrete monomeric, receptive unit. For example, Aydogan *et al.* reported a calix[4]pyrrole and benzo-15-crown-5-based co-polymer, **2.1-3** which was able to extract KF and KCl from aqueous media, with efficiencies greater than that of the effective concentration of the constituent monomers (extraction efficiencies: percentage of extractant populated with KF upon exposure to saturated aqueous solution of KF = 67% (**2.1-3**), *cf.* 0% with a discrete, molecular analogue containing both binding units).[207] Furthermore, no quantifiable fluorine signal was observed in ^{19}F NMR spectra (expected upon successful extraction of KF) when the individual components were used as hosts, suggesting that only the polymeric host was effective at extracting KF/KCl salts.



2.1-3 x = 1.0, y = 14, z = 0.8; M_n = 57 kDa

Figure 2.1-5. Calix[4]pyrrole and benzo-15-crown-5-based co-polymeric host, **2.1-3** (left), and its constituent monomers and a molecular analogue combining both motifs (right).[207]

Alternatively, different or enhanced selectivity preferences may be observed at polymeric hosts. For example, a greater selectivity preference for F^- and $H_2PO_4^-$ was observed at a poly-hydroxyquinoline chemosensor (**2.1-4**) compared to its monomeric analogue, whereby deprotonation of the acidic OH group induced an emissive fluorescence response in DMSO. In addition to this improvement in selectivity, a 147-fold increase of the characteristic emission intensity at 590 nm towards F^- was also observed for **2.1-4** in comparison to its monomer.[208]

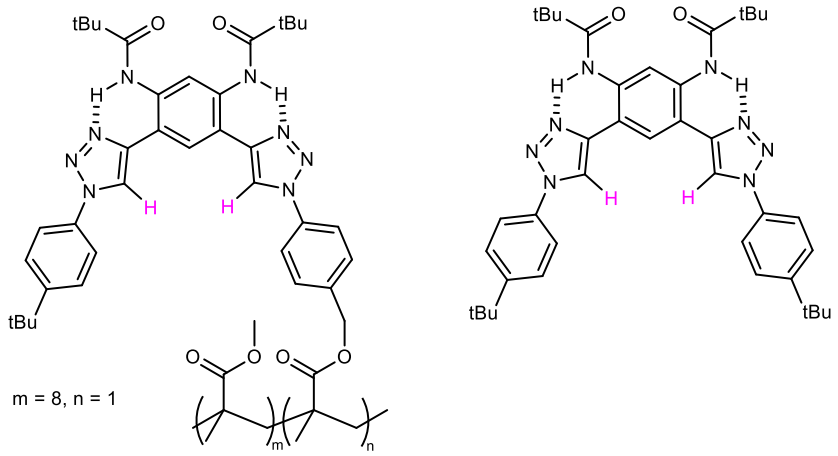


2.1-4

Figure 2.1-6. Poly-hydroxyquinoline chemosensor, **2.1-4** (left) and its constituent monomer (right).[208]

These examples demonstrate the potential and efficacy of polymeric hosts for anion recognition over their monomeric counterparts, but it should be noted that exceptions exist which suggest that incorporating discrete receptors into a

polymeric scaffold has minor/negligible implications on anion binding performance. For example, McDonald *et al.* showed that the anion binding characteristics of an aryl-triazole-based control compound and derived polymeric host, **2.1-5** demonstrated very similar binding affinities for Cl^-, as assessed from shifts of relevant proton signals in their ^1H NMR spectra in CD_2Cl_2 ($K = 5 \times 10^4\ M^{-1}$, for both when normalised per binding unit).[202]



2.1-5

Figure 2.1-7. Aryl-triazole-based polymeric host, **2.1-5** (left) and its constituent monomer (right).[202]

Therefore, it is evident that a more comprehensive and comparative quantification of the anion binding performance of monomeric and polymeric hosts is required to better understand the implications of translating discrete receptors into a polymeric scaffold.

This chapter explores the use of polymeric scaffolds for anion recognition and sensing, with a particular focus on comparisons with monomeric, discrete receptors. The relative ease and versatility of polymer synthesis provides an auspicious means of generating potent anion receptors by incorporating polymerisable anion binding units whose binding performance can be tuned via judicious choice of non-receptive, commercially available co-monomers. A family

of monomeric and polymeric hosts were designed, synthesised and comprehensively characterised, and their anion binding performance in a range of solvents were systematically evaluated and contrasted in a range of solvents. The impact of incorporating stand-alone monomeric hosts into a macromolecular, polymeric scaffold on anion binding ability was quantified, for the first time, via complimentary ^{1}H NMR binding and electrochemical sensing studies. Additionally, halogen bonding and hydrogen bonding analogues of these receptors were generated, to investigate whether a polymeric host structure exerts distinct effects on anion binding when different types of non-covalent interactions are utilised. These effects could include stronger binding with the interaction which is less dominated by electrostatic contributions to binding (*e.g.,* XB *vs* HB), or the influence of local dielectric on these interactions. Furthermore, the solvent dependence of both the monomeric and polymeric hosts were assessed, consolidating the potential of generating engineered binding microenvironments within polymeric architectures for more effective anion recognition in polar, aqueous media.

In summary, the key aims of Chapter 2 are:

- Synthesise XB/HB-based anion-receptive, redox-active monomeric hosts with a polymerisable functionality
- Generate a family of XB/HB-based anion-receptive, redox-active polymeric hosts with different non-receptive co-monomers
- Perform systematic, comparative ^{1}H NMR anion binding studies and voltammetric anion sensing studies with the monomeric and polymeric hosts

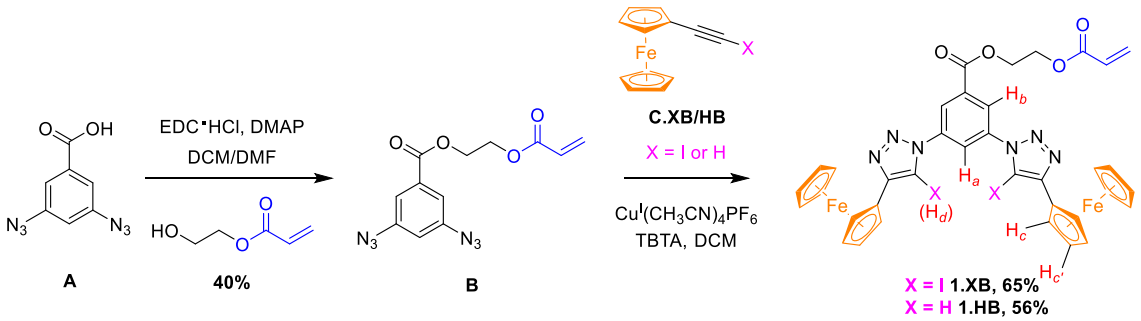
- Assess the impact of varying local ε_r (by virtue of incorporating different non-receptive co-monomers of different relative hydrophobicity) on anion binding/sensing performance

2.2 Synthesis of Monomeric Hosts

The synthesis of the monomeric and polymeric hosts was carried out by Dr. Krzysztof Bąk (see Section 7.11.1), as well as ^{1}H NMR anion binding studies and analyses thereof.

Receptive monomeric units (**1.XB**/**HB**) were designed with three functional components in mind: i. an anion-receptive group, ii. a redox-active reporter unit and iii. a polymerisable functionality. 3,5-bis-(iodo)triazolebenzene XB/HB motifs were incorporated as established, potent anion binding sites.[209] Ferrocene units were then directly appended as redox-active groups with well-defined electrochemical characteristics to effectively transduce anion binding events, as well as potentially "switch-on" anion binding upon oxidation to the positively charged Fc^+ state. The close proximity both through-bond and through-space between the binding site and reporter group ensures that each Fc unit sensitively reports on specific anion binding events.[210] The acrylate functionality at the terminus of the monomeric host structure enables polymerisation through a free radical polymerisation process, herein reversible addition-fragmentation chain-transfer (RAFT),[211] which proceeds away from the steric bulk of the binding site and susceptible functional groups (ferrocene, C-I *etc*.) that may be vulnerable to/interfere with propagating radical species.[212]

1.XB/**HB** were synthesised according to Scheme 2.2-1. 3,5-diazidobenzoic acid (**A**) was first coupled to 2-hydroxyethyl acrylate through an EDC/DMAP-mediated Steglich esterification to generate a 3,5-diazidobenzoate bearing the polymerisable acrylate functionality (**B**). **B** was then reacted with (iodo)ethynylferrocene (**C.XB**/**HB**, to generate the XB and HB receptors, respectively) via an established copper(I)-catalysed azide-alkyne cycloaddition (CuAAC) "click" reaction to form the target receptors **1.XB**/**HB** in good yields (65/56%, respectively). Further details regarding the specific synthetic protocols to produce **1.XB**/**HB**, as well as characterisation data (HR-MS, ^{1}H and ^{13}C NMR) can be found in Section 7.11.1.



Scheme 2.2-1. Synthetic scheme detailing the protocols carried out to produce **1.XB**/**HB**, and the relevant proton signals used to follow binding: H_a, H_b, H_c and H_d (or control signal, $H_{c'}$).

2.3 Synthesis of Polymeric Hosts

2.3.1 Optimisation of Polymerisation Procedure

Covalent polymers were targeted in this work to ensure that a robust and consistent polymeric structure was maintained throughout anion binding studies regardless of the solvent media utilised (*cf.* supramolecular polymers whose macromolecular structures are intimately solvent-directed). This in turn facilitated more direct and accurate comparisons of the monomeric and polymeric hosts' anion

binding/sensing performance by excluding contributions from changes in the secondary structure/order of the polymeric hosts.

Covalent polymers can be reliably generated via a range of well-established techniques which are tolerant to a broad range of monomers, including ring-opening polymerisation[213] or reversible-deactivation radical polymerisation (RDRP) techniques such as atom transfer radical polymerisation (ATRP)[214] or reversible addition fragmentation chain-transfer (RAFT) polymerisation.[211, 215] RDRP techniques, also known as living polymerisation processes, facilitate the synthesis of polymeric architectures with predictable molecular weights (M_n or M_W, defined by Equations 2.3.1-1 and 2.3.1-2, respectively), low polydispersity (PDI, given by Equation 2.3.1-3) and ability for progressive chain growth.[211]

$$M_n = \frac{\Sigma N_i M_i}{\Sigma N_i} \qquad \textbf{Equation 2.3.1-1}$$

$$M_w = \frac{\Sigma N_i {M_i}^2}{\Sigma N_i M_i} \qquad \textbf{Equation 2.3.1-2}$$

$$PDI = \frac{M_w}{M_n} \qquad \textbf{Equation 2.3.1-3}$$

Where M_i is the molecular weight of a polymer chain, and N_i is the number of chains of that molecular weight.

RAFT polymerisation was selected due to its high tolerance to a range of monomer structures, as well as its high degree of control over physical polymer characteristics such as M_n, M_w and PDI.[211] The polymerisation procedure was first optimised with homopolymerisations of commercially available, non-receptive monomers and later applied to copolymerisations with **1.XB**/**HB**. The non-receptive

monomers in question were di(ethyleneglycol)ethyl ether acrylate (DEGA) and butyl acrylate (BuA), as somewhat non-polar and highly non-polar monomers, respectively, to impart different local dielectric properties around the binding sites confined within the polymeric hosts.[216] The predicted effect of changes to local dielectric on anion binding is discussed in greater detail in Section 2.5.

Polymerisation reactions were deemed successful if they resulted in polymers with a high molecular weight (>10,000 Da) and low dispersity (PDI < 1.5). Generating a sufficient number of repeating units ensured that the polymeric architecture had a significant effect on the material properties of the polymeric host compared to the receptive monomer alone. Low polydispersity indices (PDI) ensured that all individual polymer chains displayed similar chemical properties (consistent host properties throughout). Thus, high M_n and low PDIs were prioritised as the most important parameters to obtain during optimisation of the polymerisation procedure. Two approaches were considered: (1) UV-initiated RAFT polymerisation and (2) thermally-initiated RAFT polymerisation. Both initiation methods are well-established and have been applied for a wide range of monomers, with UV-initiated RAFT emerging as a promising option due to considerably shorter polymerisation times (often 1-2 h, *cf.* 12-24 h for thermally-initiated RAFT). Thus, this technique was explored first.

2.3.2 UV-initiated RAFT Polymerisation

pDEGA and **pBuA** homopolymers were generated according to the following procedure: Solutions of monomer (DEGA or BuA; 1 M), chain transfer agent (2-dodecylthiocarbonothioylthio)-2-methylpropionic acid, DDMAT; 5 mM) and radical

initiator (azobisisobutyronitrile, AIBN; 2 mM) were prepared in 0.5 mL DMF ([monomer]:[chain transfer agent]:[initiator] = 200:1:0.2), sealed in a microwave vial and degassed with Ar for 15 min. The reaction vessels were then irradiated with 390 nm light for 0.5-4 h. The resulting polymers were purified by removing residual solvent in vacuo (n.b. this process also removes residual BuA monomer), then resolubilised in a small amount of THF (≈1 mL), before precipitating in cold hexane (≈5 mL). The resulting suspension was then centrifuged at 3900 RPM for 12 min, from which the supernatant was removed and the precipitate resolubilised in a small amount of THF. This washing procedure was repeated three times in total, before removing residual solvent in vacuo to obtain the pure homopolymers. The purity of the polymers was confirmed by ^{1}H NMR from the loss of residual monomer acrylate signals at ≈ 6-6.5 ppm in $CDCl_3$.

As shown in Figures 2.3.2-1 – 2.3.2-3, **pDEGA** and **pBuA** polymers were afforded within only 30 min of irradiation, and a progressive increase in chain length was observed with longer irradiation durations (up to ≈ 3 h, see Figure 2.3.2-1), as is consistent with a "living" polymerisation process. A range of relevant parameters (M_n, M_w, PDI; determined by GPC, and monomer conversion; quantified via integration of ^{1}H NMR signals of the monomer and polymer) were ascertained for each of the afforded polymers (see Table 2.3.2-1). Briefly, M_n, M_w and monomer conversion all increased with longer irradiation times (following a pseudo-first order relationship), and the PDI remained relatively constant for all generated homopolymers. PDIs of less than 1.3 were acquired in all cases, showcasing the control afforded by the UV-initiated RAFT polymerisation approach (*cf.*, PDIs < 1.2

are generally considered acceptable for commercial production). The theoretical number mass of the polymers ($M_{n,th}$) produced by this polymerisation protocol was then calculated according to Equation 2.3.2-1. As shown in Table 2.3.2-1, the acquired and calculated M_n values are in good agreement and are within 30% of each other in all cases, showing that the living RAFT polymerisation proceeds according to expectations.[211]

$$M_{n,th} = \frac{[M]_0 p M_M}{[CTA]_0} + M_{CTA} \qquad \textbf{Equation 2.3.2-1}$$

p = monomer conversion, M_M and M_{CTA} are molecular weights of monomer and chain transfer agent, respectively.

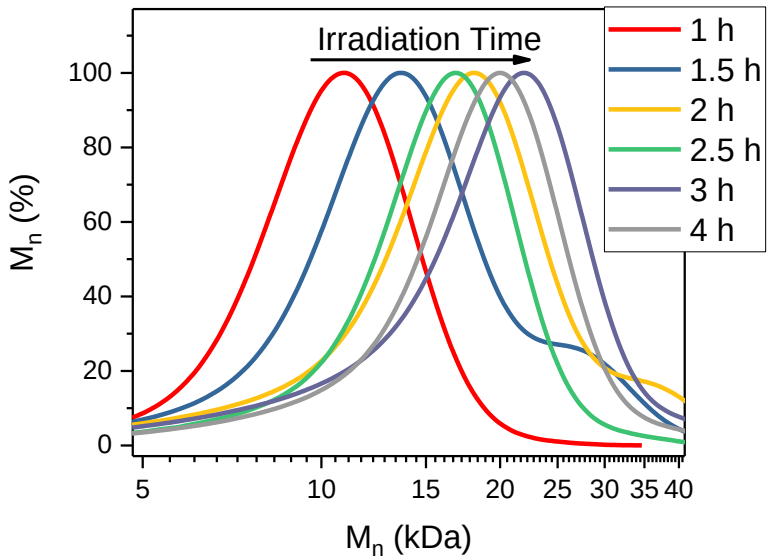


Figure 2.3.2-1. GPC traces of **pBuA** polymers generated by UV-initiated RAFT polymerisation with increasing durations of irradiation, highlighting the direct correlation between polymer chain length and irradiation time.

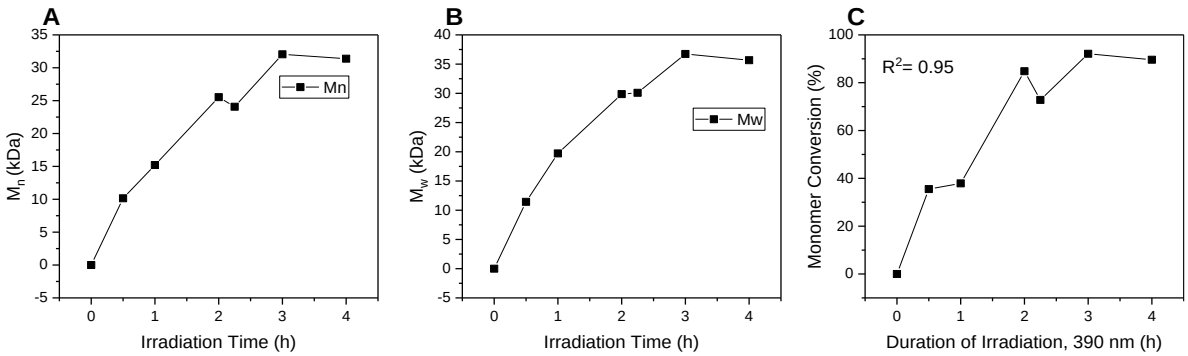


Figure 2.3.2-2. (A) M_n (B) M_w and (C) monomer conversion determined for **pDEGA** polymers afforded by UV-initiated RAFT polymerisation of DEGA with different durations of irradiation.

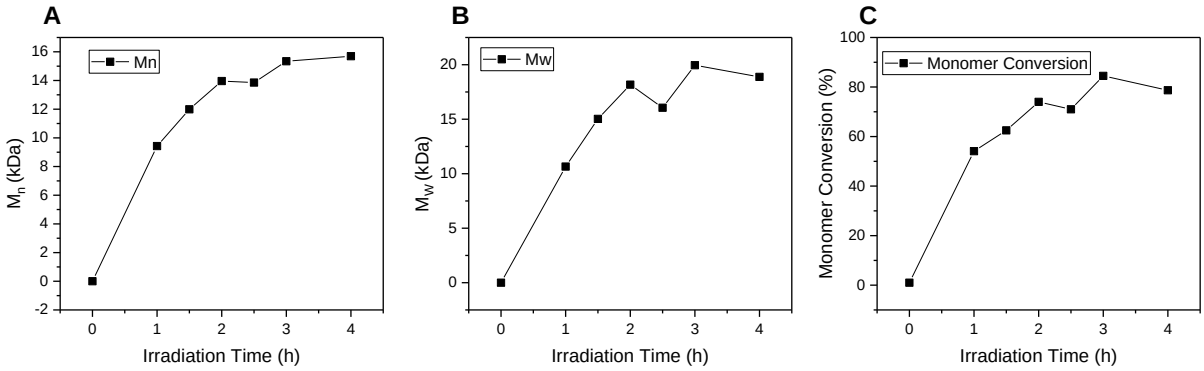


Figure 2.3.2-3. (A) M_n (B) M_w and (C) monomer conversion determined for **pBuA** polymers afforded by UV-initiated RAFT polymerisation of BuA with different durations of irradiation.

Table 2.3.2-1. Tabulated data (M_n, M_w, PDI and monomer conversion) from the characterisation of **pDEGA** and **pBuA** polymers generated by UV-initiated RAFT polymerisation with various hours of irradiation. $M_{n,th}$ was calculated according to Equation 2.3.2-1.

Irradiation Time	M_n (kDa)	M_w (kDa)	Polydispersity (PDI)	Monomer conversion (%)	$M_{n,th}$ (kDa)
pDEGA					
0.5	10.1	11.4	1.30	35.5	13.7
1	15.2	19.7	1.13	37.9	14.6
2	25.5	29.9	1.17	84.8	32.3
2.25	24.1	30.1	1.25	72.8	27.8
3	32.0	36.7	1.15	92.1	35.0
4	31.4	35.7	1.14	89.6	34.1
pBuA					
1	9.43	10.7	1.13	54.1	14.2
1.5	12.0	15.0	1.25	62.5	16.4
2	14.0	18.2	1.21	74.0	19.3
2.5	13.9	16.1	1.16	71.0	18.6
3	15.3	20.0	1.30	84.5	22.0
4	15.7	18.9	1.20	78.7	20.5

However, upon moving to more complex monomers containing Fc moieties and anion binding sites, the UV-initiated RAFT polymerisation reactions failed. No measurable polymer growth was observed (negligible precipitation observed during purification) for a monomer ratio of 9:1 DEGA:**1.XB** following 4 h of irradiation.

One explanation for this is could be degradation of the **1.XB** monomer upon irradiation with 390 nm light (by breaking one of the relatively weak C-I bonds, for example). To investigate this, a solution of 50 mM **1.XB** in DMF was placed in a microwave vial (reflecting the solvent and vessel used for polymerisation reactions) and exposed to 390 nm light for 3 h, from which aliquots were taken each hour and analysed via ^{1}H NMR. The resulting spectra, which are shown in Appendices A2, Figure A2.1, are generally consistent (no signals are lost or gained) throughout the 3 h irradiation, suggesting that **1.XB** does not degrade under these conditions. Alternatively, the rate of polymerisation with **1.XB** may be extremely slow under these conditions, due to the additional steric bulk of the ferrocene-decorated monomers w.r.t. DEGA or BuA,[217] or slow chain growth due to a high rate of chain transfer resulting from electron transfer from the ferrocene group to the radical chain end.[218]

2.3.3 Thermally-initiated RAFT Polymerisation

To address this lack of compatibility with the functional monomers, attention then turned to using a thermally-initiated RAFT polymerisation approach, which is compatible with a broad range of monomers, including those containing ferrocene.[219-221] **pDEGA** homopolymers were generated first via this method, which exhibited similar characteristics to those produced by UV-initiated RAFT

polymerisation both in terms of chain length and PDI (see Figure 2.3.3-1 and Table 2.3.3-1 for comparison).

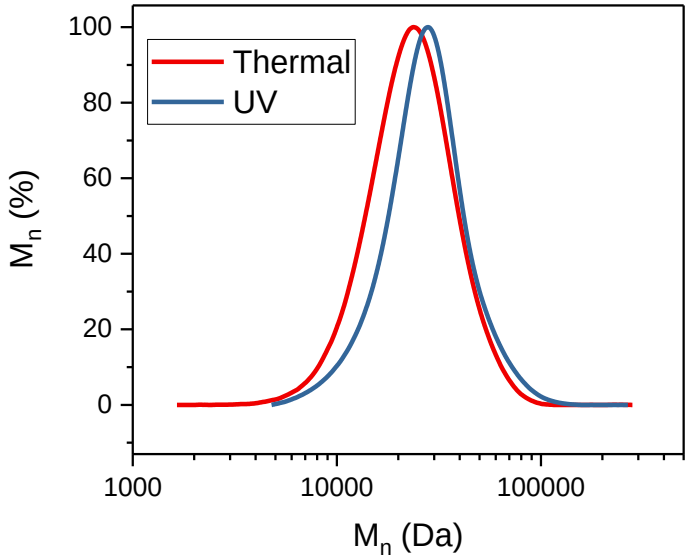


Figure 2.3.3-1. GPC traces of **pDEGA** polymers generated by thermally- (red line) and UV- (blue line) initiated RAFT polymerisation.

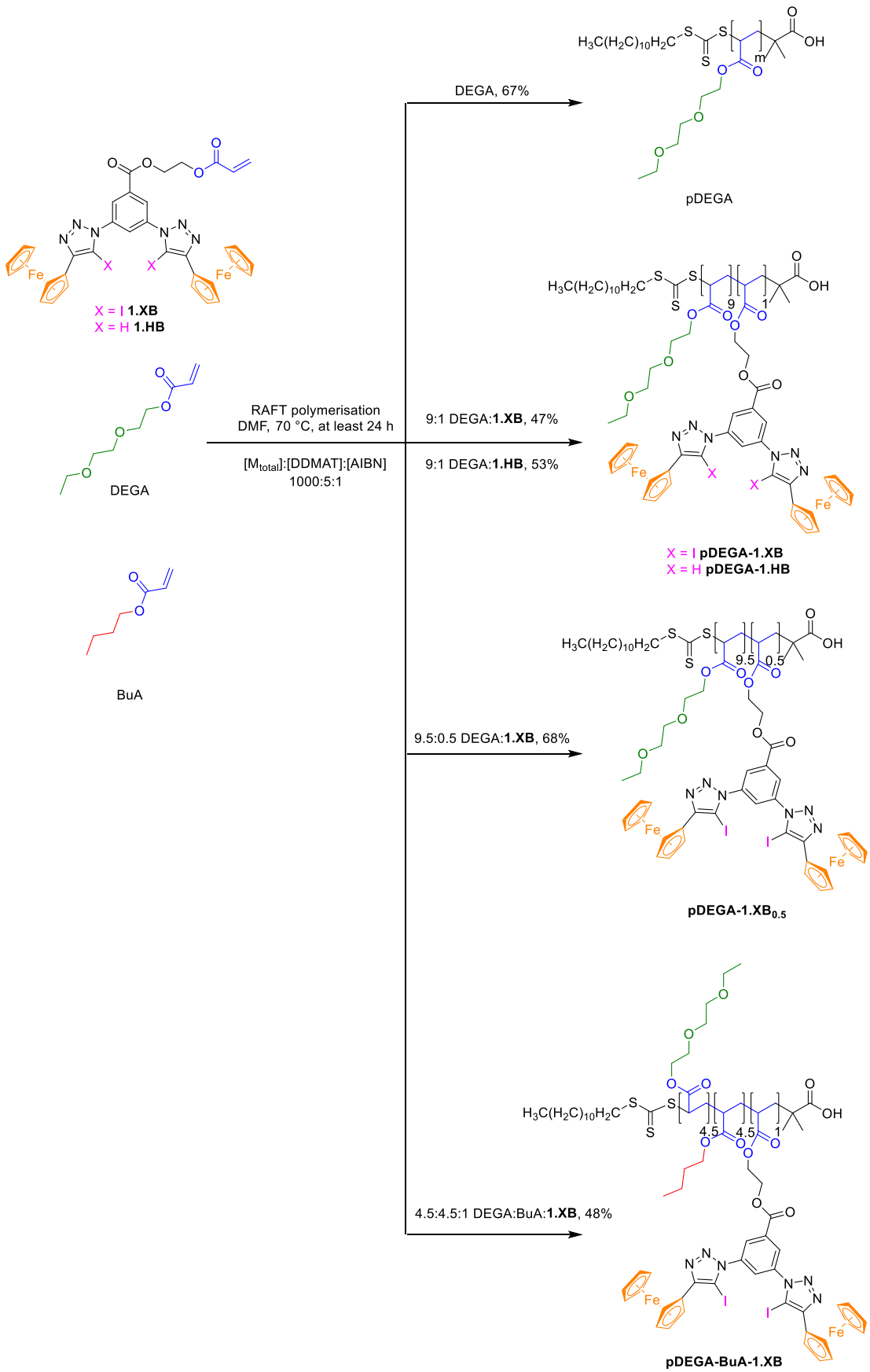
Table 2.3.3-1. Tabulated data (M_n, M_w and PDI) to compare **pDEGA** polymers generated by UV-initiated (2 h irradiation time) and thermally-initiated (12 h) RAFT polymerisation.

RAFT Method	M_n (kDa)	M_w (Da)	Polydispersity (PDI)
UV-initiated (2 h)	25.5	29.9	1.17
Thermally-initiated (12 h)	20.3	25.7	1.27

Then, a family of co-polymeric redox-active, anion-receptive hosts were generated according to Scheme 2.3.3-1: **pDEGA-1.XB** (the primary host of interest, whereby anion binding is mediated by XB), **pDEGA-1.HB** (a HB analogue to **pDEGA-1.XB**), **pDEGA-1.XB$_{0.5}$** (an analogue of **pDEGA-1.XB** which has half the number of incorporated receptive **1.XB** units) and **pDEGA-BuA-1.XB** (an analogue of **pDEGA-XB** co-comprised of relatively hydrophobic DEGA units, and highly hydrophobic BuA units which are expected lower the local ε_r within the polymeric scaffold). Further details regarding the specific synthetic protocols to produce **pDEGA-1.XB/HB**,

pDEGA-BuA-1.XB and **pDEGA-1.XB$_{0.5}$** as well as characterisation data (HR-MS, ^{1}H- and ^{13}C NMR) can be found in Section 7.11.1.

In an analogous manner to the UV-initiated RAFT polymerisations, all thermally-initiated RAFT polymerisation reactions were performed in microwave vials containing 0.5 mL of the appropriate RAFT polymerisation solution (molar ratio of 200:1:0.2 [monomer]:[DDMAT]:[AIBN] in DMF), and subsequently sealed with aluminium seals with PTFE septa to ensure airtight conditions. Each vial and polymerisation solution were then thoroughly degassed with Ar for 15 min, then placed in an oil bath at 70 °C to initiate polymerisation which continued for at least 24 h. Reaction progress was monitored by ^{1}H NMR through extraction of aliquots taken periodically with a degassed (Ar) syringe and needle. Unless stated otherwise, all polymers were purified by size exclusion with a column filled with Bio-Beads™ S-X1 Support (styrene divinylbenzene beads, 1% cross-linkage, 40-80 μm bead size, 600-14,000 MW exclusion range) and $CHCl_3$ as an eluent. **pDEGA** homopolymers generated by thermally-initiated RAFT polymerisation were purified in the same way as those produced by UV-initiated RAFT polymerisation (*vide infra*).



Scheme 2.3.3-1. Reaction scheme highlighting the ratio of monomers used in each respective RAFT polymerisation reaction to afford **pDEGA**, **pDEGA-1.XB/HB**, **pDEGA-1.XB$_{0.5}$** and **pDEGA-BuA-1.XB**.

2.4 Characterisation of Monomers and Polymers

Following purification, the resulting monomers and polymers were characterised by a number of techniques including ATR-FTIR, ^{1}H and ^{13}C NMR, high resolution mass spectroscopy, GPC and voltammetric approaches (see Chapter 7 for details regarding the procedures for each of these techniques). ATR-FTIR spectra of monomers **1.XB/HB** and polymers **pDEGA-1.XB/HB** were consistent with expectations, as evident from the range of characteristic features shown in Figure 2.4-1 (*e.g.*, vinyl ester C-O stretches at 1260-1290 cm^{-1} and ester C=O stretches at 1720-1740 cm^{-1}). Importantly, the characteristic acrylate C=C stretch band at 1610 cm^{-1} is lost upon polymerisation (*i.e.*, A to B, or C to D, highlighted for the XB hosts in Figure 2.4-2), confirming that the monomeric units are incorporated into the polymeric backbone. M_n, M_w and PDI values were resolved by GPC (see Figures 2.4-3 and 2.4-4), which are tabulated in Table 2.4-1.

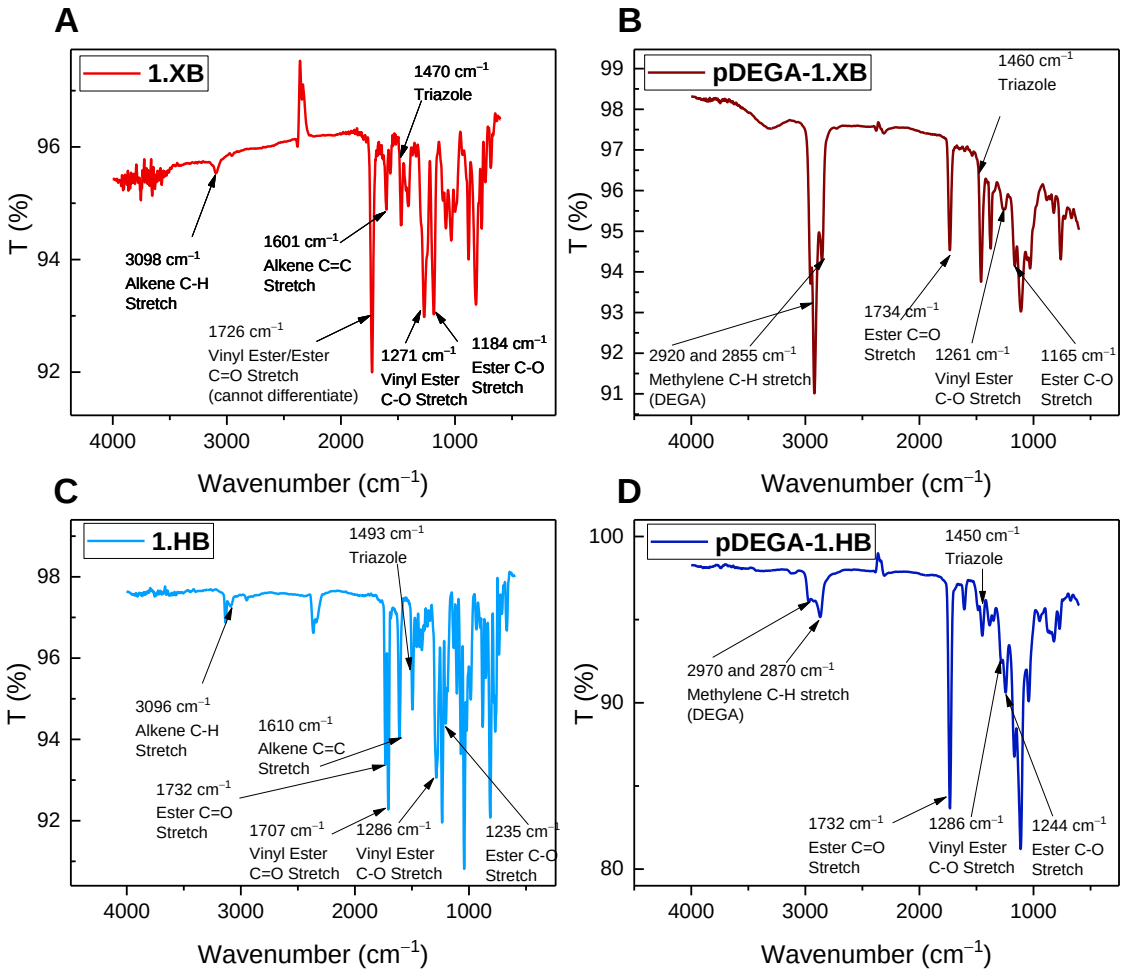


Figure 2.4-1. ATR-FTIR spectra of (A) **1.XB** (B) **pDEGA-1.XB** (C) **1.HB** and (D) **pDEGA-1.HB**.

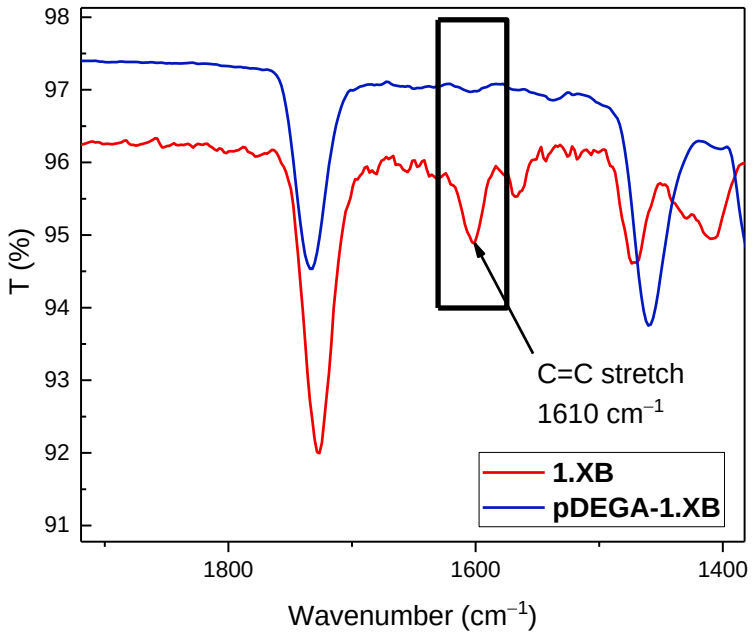


Figure 2.4-2. ATR-FTIR spectra of **1.XB** and **pDEGA-1.XB**, highlighting the loss of the C=C stretch signal at 1610 cm^{-1}, attributed to polymerisation of the acrylate functionality from **1.XB** into the **pDEGA-1.XB** polymer backbone.

Table 2.4-1. Physical characterisation data of all polymeric hosts and control non-receptive polymer **pDEGA** including M_n and PDI obtained by GPC, and associated information about the composition of each polymeric host.

Host	M_n (kDa)	PDI	Average Total no. Units	Average No. Receptive Units	Yield
pDEGA-1.XB	15.7	1.37	57	5.7	47%
pDEGA-1.HB	27.7	1.38	115	11.5	53%
pDEGA-1.XB$_{0.5}$	12.2	1.40	52	2.6	68%
pDEGA-BuA-1.XB	16.7	1.40	70	7.0	48%
pDEGA	32.0	1.15	168	N.A	67%

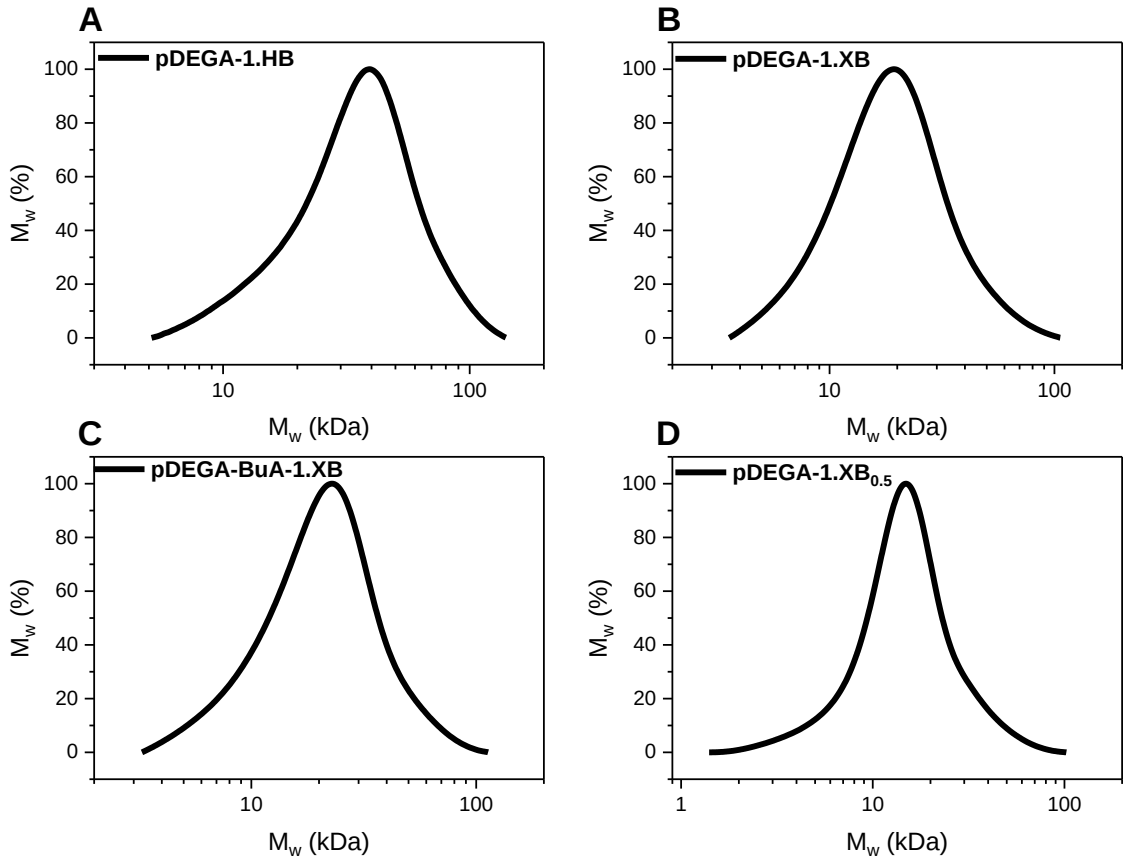


Figure 2.4-3. GPC data for all receptive co-polymers (A) **pDEGA-1.HB**, (B) **pDEGA-1.XB**, (C) **pDEGA-BuA-1.XB** and (D) **pDEGA-1.XB$_{0.5}$**.

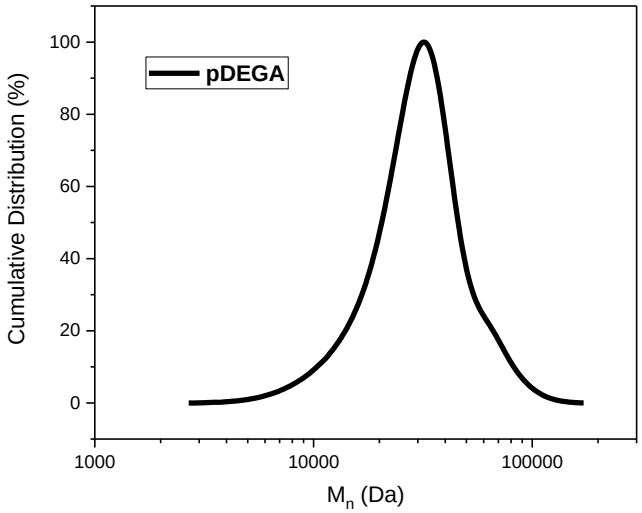


Figure 2.4-4. GPC data for non-receptive homopolymer **pDEGA**.

It should be noted that the ^{1}H NMR signals corresponding to each of the polymeric hosts were significantly broader than those of the monomers, due to the polymers being macromolecular species with a considerable number of repeating units. As each repeat unit is statistically distributed along the length of each polymer chain, each signal experiences marginally different chemical environments, resulting in signal broadening. Whilst signal broadening typically makes analysing spectral changes more difficult, extensive and systematic analyses confirmed that in this case integrating broader, polymeric signals did not introduce additional error with respect to the monomeric hosts. The details regarding these analyses can be found in Section 7.10.1.

The ratio of binding unit to non-receptive monomer was governed at the point of synthesis by strictly controlling the stoichiometry during polymerisation reactions (*i.e.*, 9:1 [co-monomer]:[binding unit]). Integration of characteristic binding unit signals from ^{1}H NMR spectra of the resulting polymers, in conjunction with determined M_n values, confirmed that these predicted ratios were attained (see Table 2.4-1 for determined average number of binding units per polymer). These

results also confirmed a broadly equivalent monomer reactivity for incorporation within the polymer backbone. In addition to fixing the stoichiometry of co-monomers during synthesis, characteristic co-monomer and binding unit signals were integrated and compared in order to calculate the ratio of [co-monomer]:[binding unit]. For example, there are on average 5.7 anion-receptive, redox-active units per polymer chain for the polymer **pDEGA-1.XB** (M_n of 15.7 kDa). This average density of binding units per polymer (with a ratio of 9:1 [co-monomer]:[binding unit]) is consistent with previous reports of polymers of a similar molecular weight that have also been utilised for anion binding. For example, **2.1-5** (see Figure 2.1-7 above) displays effective Cl^- binding with an M_n of 12.5 kDa, and a [co-monomer]:[binding unit] of 8:1.[202] To the best of our knowledge, the anion-receptive, redox-active units are assumed to be statistically distributed along the length of the polymer chain. This is supported by the lack of evidence for any cooperative binding modes in the binding analyses discussed in Section 2.5 that may be expected if the binding units were in close proximity, as would be the case in a block polymer, for example.

The accurate determination of the density of binding units per polymer is, of course, crucial in enabling a fair comparison for the anion binding performance comparisons of the monomeric and polymeric hosts made below. Therefore, the concentration of binding units during titrations with tetrabutylammonium (TBA) salts was also further confirmed through comparison of the ratio of integrals from polymer and TBA+ signals (*i.e.*, host:guest), with TBA+ serving as an internal standard of known concentration. This process is described in further detail in Chapter 7.10.1.

Referring back to the ideal criteria laid out for these polymeric hosts, all of the polymers generated via this method were of high quality (PDI ≤ 1.4), with chains of significant length (M_n > 12 kDa) and multiple binding units per chain in all cases. The physical characteristics (*e.g.*, M_n, M_w or PDI) of the XB polymeric hosts were all in close agreement, but there were slight discrepancies observed between the HB and XB hosts in that the HB chains were longer on average. These marginal differences could be attributed to the comparably higher difficulty experienced with co-polymerising **1.XB** *vs.* **1.HB**, whereby significantly longer reaction times were required to generate halogen-bonding polymers of comparable chain length to their hydrogen bonding analogues (≈ 3 d *vs*. 1 d, respectively). This observation was hypothesised to result from the weak C-I bond interfering the radical polymerisation mechanism.[222] Nevertheless, all of the polymeric hosts, XB/HB or otherwise, were sufficiently similar to take forward for comparative anion binding/sensing studies.

2.5 ^{1}H NMR Anion Binding Studies

2.5.1 Anion Binding Performance of Monomeric Hosts

The anion binding performance of monomers **1.XB**/**HB** was assessed by ^{1}H NMR titration studies in three organic/aqueous solvent systems of increasing polarity ranging from ε_r = 26 – 39, determined as molar linear combinations of reported ε_r values of each pure, constituent solvent (97.5:2.5 acetone-d_6/D_2O, 48.75:48.75:2.5 acetone-d_6/ACN-d_3/D_2O and 97.5:2.5 ACN-d_3/D_2O). Addition of TBA salts with **1.XB**/**HB** ([**1.XB**/**HB**] = 1 mM, starting volume = 0.5 mL) induced a significant downfield shift of the receptor's central aryl proton, H_a and triazole proton, H_d (relevant only for the HB analogues), and upfield perturbations of the adjacent aryl,

H_b, and ferrocenyl, H_c protons in all solvent systems investigated (see Figure 2.5.1-1 for a representative example of such a titration). Given the substantial and specific perturbations of the signals associated these protons, anion binding was confirmed to take place within the central binding cavity defined by the two ferrocenyl-(iodo)triazole arms of the receptor. Anion binding was primarily mediated by XB/HB interactions donated by the (iodo)triazole groups, with minor contributions from HB interactions with the central aryl proton H_a. Negligible shifts were observed for any of the signals associated with protons further removed from the binding cavity. The downfield (de-shielded) shift of the central aryl proton, H_a was attributed to hydrogen bonding between H_a and the target anion, which is fully consistent with the behaviour of similar 3,5-bis-(iodo)triazolebenzene XB/HB-based anion receptors.[209] The upfield (shielded) shifts displayed for the adjacent aryl proton, H_b were attributed to increased electron density from the proximal anionic guest.

Interestingly, greater perturbation magnitudes (|Δδ|) were observed in acetone-d_6:D_2O (97.5:2.5 v/v) for the adjacent aryl proton, H_b with respect to the internal H_a proton (see Figure 2.5.1-2), despite H_b being further removed from the predicted location of the binding cavity (*i.e.*, between the two ferrocenyl-(iodo)triazole arms of the receptor). However, upon moving to acetone-d_6:acetonitrile-d_3:D_2O (48.75:48.75:2.5, v/v/v) and acetonitrile-d_3:D_2O (97.5:2.5, v/v), the difference in shift magnitude (|Δδ|) between protons H_a and H_b becomes negligible in almost all cases (see Figures 2.5.1.3 and 2.5.1-4). These results indicate that **1.XB** may assume a slightly different, solvent-dependent conformation upon anion binding in the least polar solvent system. For example, if the two ferrocenyl-(iodo)triazole arms were

forced closer in space in this new conformation then the size of the binding site would be constricted, forcing anion binding to take place slightly closer to the neighbouring aryl group. This slight variation on the expected binding mode could explain why the anionic guests interact with H_b to a greater extent than in the other solvent systems, an effect which is particularly noticeable for the largest anionic guest: I^- (ionic radii: I^- (2.20 Å), Br^- (1.96 Å), Cl^- (1.81 Å) and $H_2PO_4^-$(2.00 Å)).[223] Nevertheless, the substantial differences between the resolved anion binding constants for the XB and HB receptors (see later) strongly suggest that anion binding is primarily mediated by the XB/HB interactions with the (iodo)triazole units, validating the systematic XB *vs*. HB comparative studies described below.

Signal perturbations (using signals H_a & H_b and H_b & H_d in the case of **1.XB** and **1.HB**, respectively) were assessed over a guest concentration range of 0-10 equivalents and Bindfit analyses were performed on the resulting binding isotherms (see Figure 2.5.1-2), elucidating that all binding events proceed with 1:1 host-guest stoichiometry as 2:1 host-guest fittings failed in all cases, in line with similar hosts.[209, 210] 1:1 host-guest association constants were afforded through these analyses and are presented in Table 2.5.1-1 for **1.XB**/**HB** across all solvent systems and anions investigated. All ^{1}H NMR spectra and resulting binding isotherms (fitted to a 1:1 host-guest model) can be found in the Supporting Information of the publication corresponding to this work.[224]

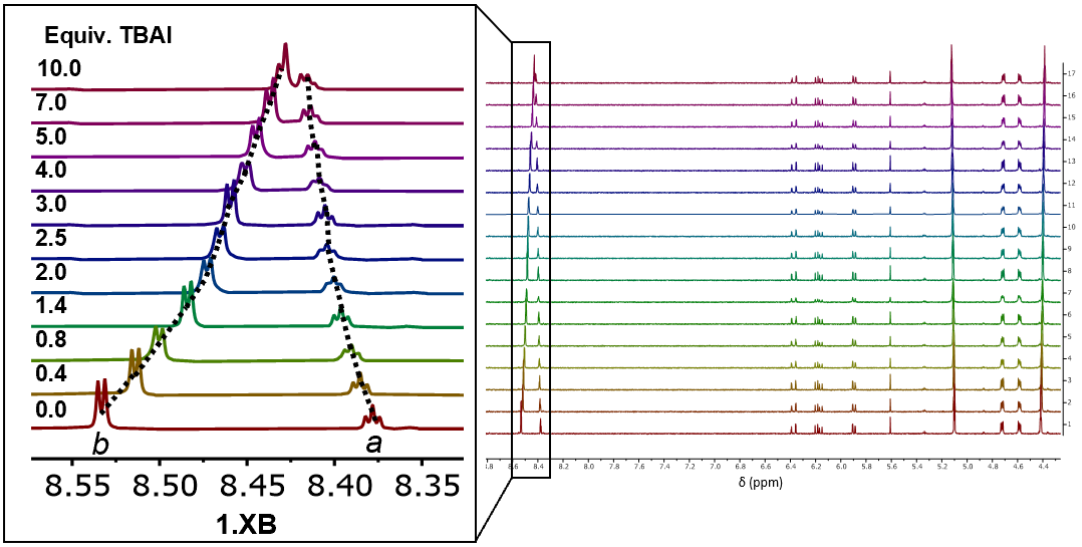


Figure 2.5.1-1. Stacked ^{1}H NMR spectra (right) and expanded view of the spectra highlighting the shifts of relevant protons, *a* and *b* (left) from titration of **1.XB** with TBAI in acetone-d_6:D_2O (97.5:2.5, v/v), 500 MHz, 298 K. Spectrum no. 1 – 0 equivalents of the guest; spectrum no. 17 – 10 equivalents of the guest.

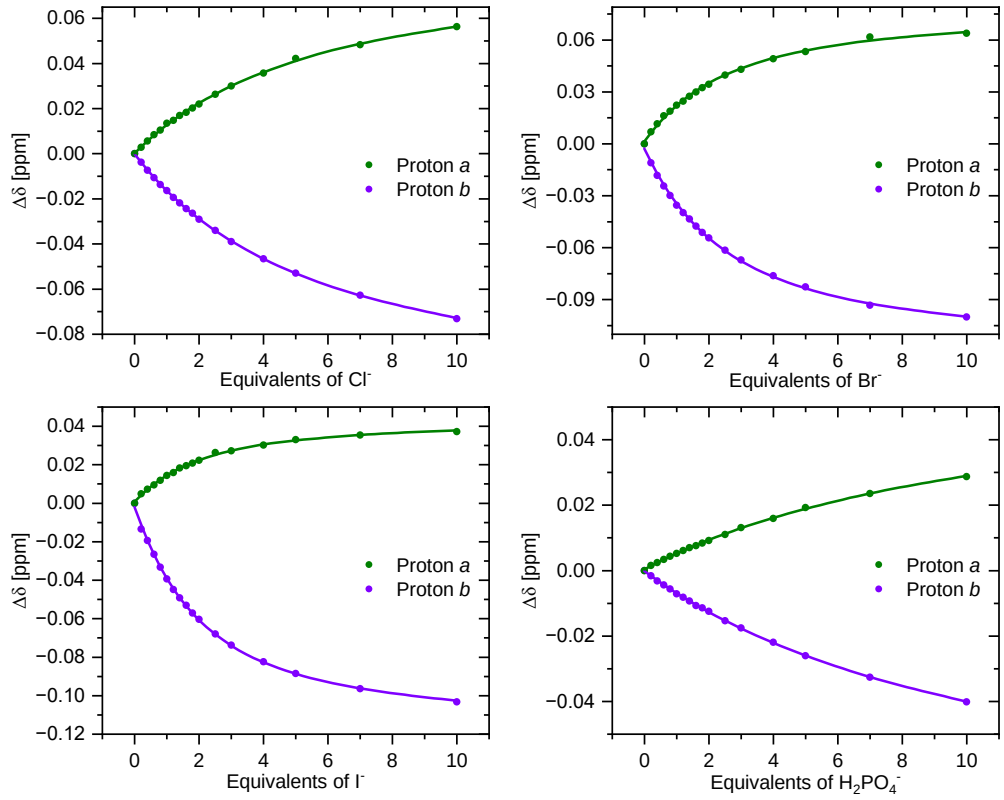


Figure 2.5.1-2. Anion binding isotherms for **1.XB** in response to Cl^-, Br^-, I^- and $H_2PO_4^-$ in acetone-d_6:D_2O (97.5:2.5, v/v), where circles represent experimental data and the lines represent the fitted isotherm.

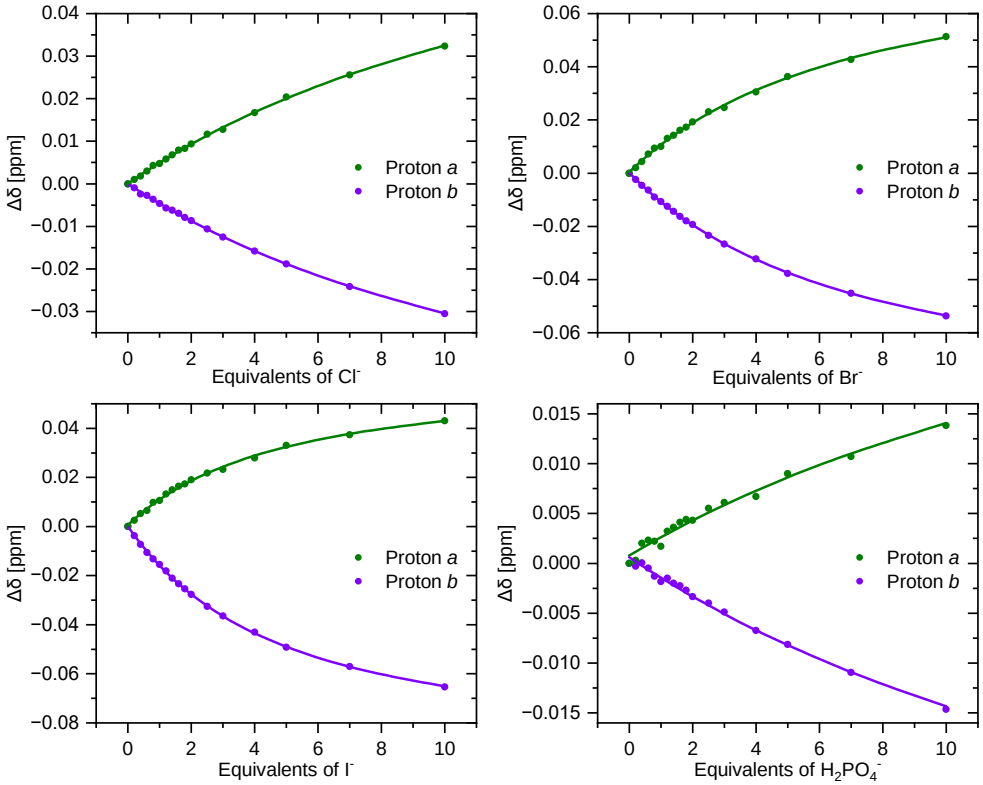


Figure 2.5.1-3. Anion binding isotherms for **1.XB** in acetone-d_6:acetonitrile-d_3:D_2O (48.75:48.75:2.5, v/v/v), where circles represent experimental data and the lines represent the fitted isotherm.

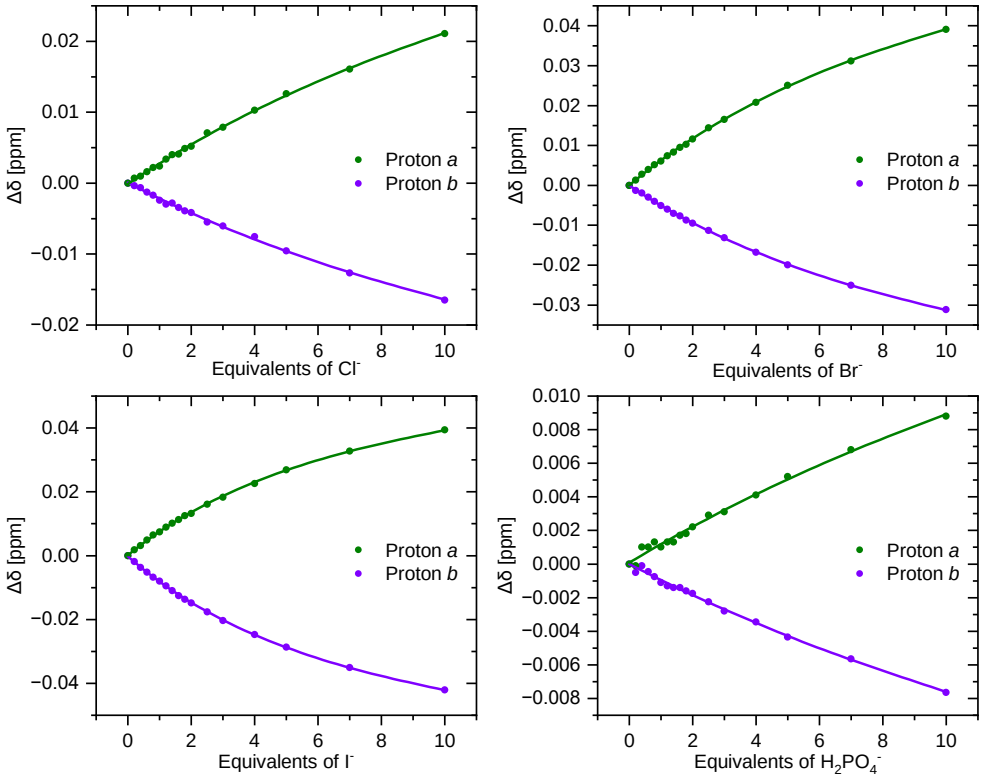


Figure 2.5.1-4. Anion binding isotherms for **1.XB** in acetonitrile-d_3:D_2O (97.5:2.5, v/v), where circles represent experimental data and the lines represent the fitted isotherm.

Table 2.5.1-1. Anion association constants, K_a of monomeric receptors **1.XB** and **1.HB**, as determined by ^{1}H NMR titrations in 97.5:2.5 acetone-d_6:D_2O, 48.75:48.75:2.5 acetone-d_6/ACN-d_3/D_2O and 97.5:2.5 ACN-d_3/D_2O. Errors estimated to be 10%. n.d. – not determined.

	K_a (M^{-1})					
	97.5:2.5 acetone-d_6/D_2O		48.75:48.75:2.5 acetone-d_6/ACN-d_3/D_2O		97.5:2.5 ACN-d_3/D_2O	
	1.XB	**1.HB**	**1.XB**	**1.HB**	**1.XB**	**1.HB**
Cl^-	170	30	40	n.d.	20	n.d.
Br^-	470	50	130	n.d.	60	n.d.
I^-	640	50	220	n.d.	110	n.d.
$H_2PO_4^-$	60	30	25	n.d.	< 10	n.d.

Regardless of the solvent system utilised, a clear selectivity trend of $I^- > Br^- > Cl^- > H_2PO_4^-$ was resolved for **1.XB**, following the Hofmeister bias of anion hydration energies in polar media (*i.e.*, strongest binding is predicted for the anion which exhibits the lowest penalty to desolvation), which is consistent with the previously reported XB preference for softer halides, particularly I^-. In contrast, **1.HB** does not exhibit a clear selectivity trend, further reinforcing that this observed halide selectivity is a phenomenon that is unique to the XB-based hosts. Of further note, is that the clear difference in association constant magnitude and resolved selectivity preference between the XB and HB analogues confirms that anion binding must be mediated by specific XB/HB interactions, and not a simple Hofmeister-directed bias through non-specific interactions or solvation effects with the hosts (through the hydrophobic effect, for example). In the least polar solvent system investigated (97.5:2.5 acetone-d_6/D_2O) respectable association constants of up to 640 M^{-1} (for I^- at **1.XB**) were determined. These values notably exceed those ascertained for **1.HB** (*cf.* K_a = 50 M^{-1} for I^- at **1.HB**), highlighting the superior binding performance afforded by XB hosts over HB analogues. Halogen bonding enhancement factors (XBF = K_{XB}/K_{HB}) were determined for all of the anions investigated in 97.5:2.5 acetone-

d_6/D_2O with **1.XB**/**HB** and are collated in Table 2.5.1-2. In all cases, the XBF for monomers **1.XB** and **1.HB** is greater than unity, signifying the dominance of the halogen bonding receptor over its hydrogen bonding analogue. The greatest enhancement was observed for I^- with an XBF of 12, further corroborating that halogen bonding-mediated anion binding is especially strong for the halides, particularly for the softer, lipophilic anions for which there is a greater degree of covalency in the XB-A^- interaction.[225]

Table 2.5.1-2. Ratio of anion association constants of monomeric receptors **1.XB** and **1.HB**, representing the halogen bonding enhancement factor (XBF = K_{XB}/K_{HB}) for the monomeric hosts, as determined by ^{1}H NMR titrations in 97.5:2.5 acetone-d_6/D_2O. Errors estimated to be 15%.

	$K_{1.XB}/K_{1.HB}$
Cl^-	5.7
Br^-	9.4
I^-	12.8
$H_2PO_4^-$	2.0

Given the already modest magnitudes of the association constants measured for **1.HB** in 97.5:2.5 acetone-d_6/D_2O, further anion binding studies were not conducted with **1.HB** in more polar media. The impact of solvent on the anion binding performance of **1.XB** was, however, evaluated. Upon moving to progressively more polar solvent systems, first to 48.75:48.75:2.5 acetone-d_6/ACN-d_3/D_2O then to 97.5:2.5 ACN-d_3/D_2O, anion binding strengths at **1.XB** were expectedly diminished due to more effective charge screening effects which attenuated the potency of XB/HB interactions towards anionic targets. Contrasting the effect of solvent polarity, ε_r on halide binding, the observed attenuation in K with increasing ε_r was highest for Cl^- ($Cl^- > Br^- > I^-$), as is consistent with expectations that the electrostatic component of binding is greatest for the most charge dense anions. Halogen

bonding interactions with soft, lipophilic anions such as I^- have been suggested to proceed with a higher degree of covalency and are therefore expected to be less affected by increasing ε_r, as corroborated here.[62, 74]

To summarise the anion binding performance of the monomers **1.XB**/**HB**:

- Relevant signals within the predicted binding cleft of both **1.XB** and **1.HB** displayed significant shifts upon addition of target anions (Cl^-, Br^-, I^- and $H_2PO_4^-$)
- Modest anion binding strengths were observed, with K_a values of up to 640 M^{-1}
- **1.XB** outperformed **1.HB** in terms of anion binding strength in all cases, highlighting the potency of XB-based motifs vs. HB analogues
- As expected, anion binding strength decreased with increasing external solvent polarity

2.5.2 Anion Binding Performance of Polymeric Hosts & Comparisons with Monomeric Hosts

The anion binding performance of the polymeric hosts was then similarly assessed by ^{1}H NMR spectroscopy in identical solvent systems to those used for the monomeric hosts: 97.5:2.5 acetone-d_6/D_2O, 48.75:48.75:2.5 acetone-d_6/ACN-d_3/D_2O and 97.5:2.5 ACN-d_3/D_2O. To enable accurate and direct comparisons between the polymeric and monomeric hosts, it is critical that analogous anion binding studies be performed at the same effective concentration of binding unit throughout. To this end, the concentration of each polymeric host was normalised with respect to the number of average binding units per polymer. For example, **pDEGA-1.XB** has an average of 5.7 binding units per polymer, henceforth the

polymer concentration was normalised by a factor of 5.7 to [**pDEGA-1.XB**] = 0.174 mM (see Table 2.5.2-1 for absolute polymer concentration).

Table 2.5.2-1. Concentration of polymeric host used during titrations with TBAX (X = I^-, Br^-, Cl^- or $H_2PO_4^-$) and list of signals used for fitting.

	[Polymeric host] (mM)	Signals used for fitting
pDEGA-1.XB	0.174	*b, c*
pDEGA-1.XB$_{0.5}$	0.246	*b, c*
pDEGA-BuA-1.XB	0.143	*b, c*
pDEGA-1.HB	0.0871	*a, d*

Analogously to the shift patterns described above for the monomeric hosts, addition of TBA halide salts induced significant perturbations to H_a and H_d (downfield: central aryl proton and triazole proton (**pDEGA-1.HB** only), respectively), H_b and H_c (upfield: adjacent aryl proton and ferrocenyl proton, respectively) of the polymeric hosts (see Figures 2.5.2-2 and 2.5.2-3). The protons corresponding to these signals are labelled in Figure 2.5.2-1.

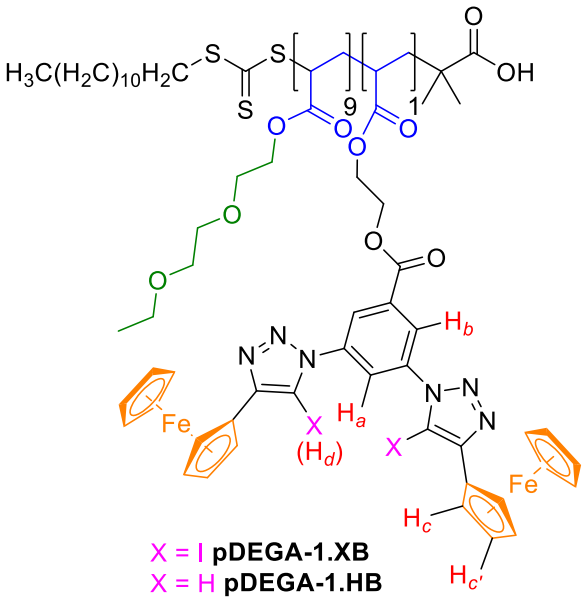


Figure 2.5.2-1. Schematic to show the relevant proton signals used to follow binding at the polymeric hosts: H_a, H_b, H_c and H_d (or control signal, $H_{c'}$), as exemplified for **pDEGA-1.XB**/**HB**.

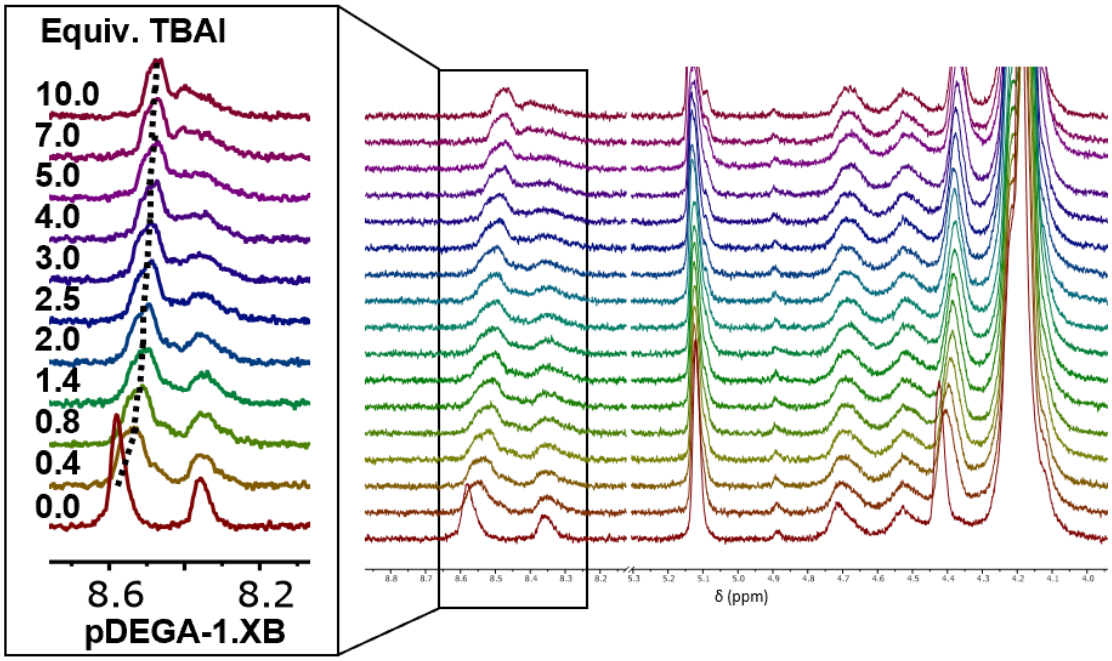


Figure 2.5.2-2. Stacked ^{1}H NMR spectra (right) and expanded view of the spectra highlighting the shifts of relevant protons, *a* and *b* (left) from titration of **pDEGA-1.XB** with TBAI in acetone-d_6:D_2O (97.5:2.5, v/v), 500 MHz, 298 K. Spectrum no. 1 – 0 equivalents of the guest; spectrum no. 17 – 10 equivalents of the guest.

As this behaviour directly reflects the spectral changes observed for **1.XB**/**1.HB**, it can be assumed that anion binding at both the monomeric or polymeric hosts proceeds via the same binding mode (*i.e.*, binding takes place in the cavity defined between the ferrocenyl-(iodo)triazole arms of the receptor). It is important to note that no measurable perturbation to either the DEGA co-monomer or polymer backbone signals were observed throughout these titrations, once again confirming that anion binding was restricted to the binding cleft of the **1.XB**/**HB** units. All titration spectra and associated anion binding isotherms for the monomeric and polymeric hosts can be found in the Supporting Information of the publication corresponding to this chapter.[224]

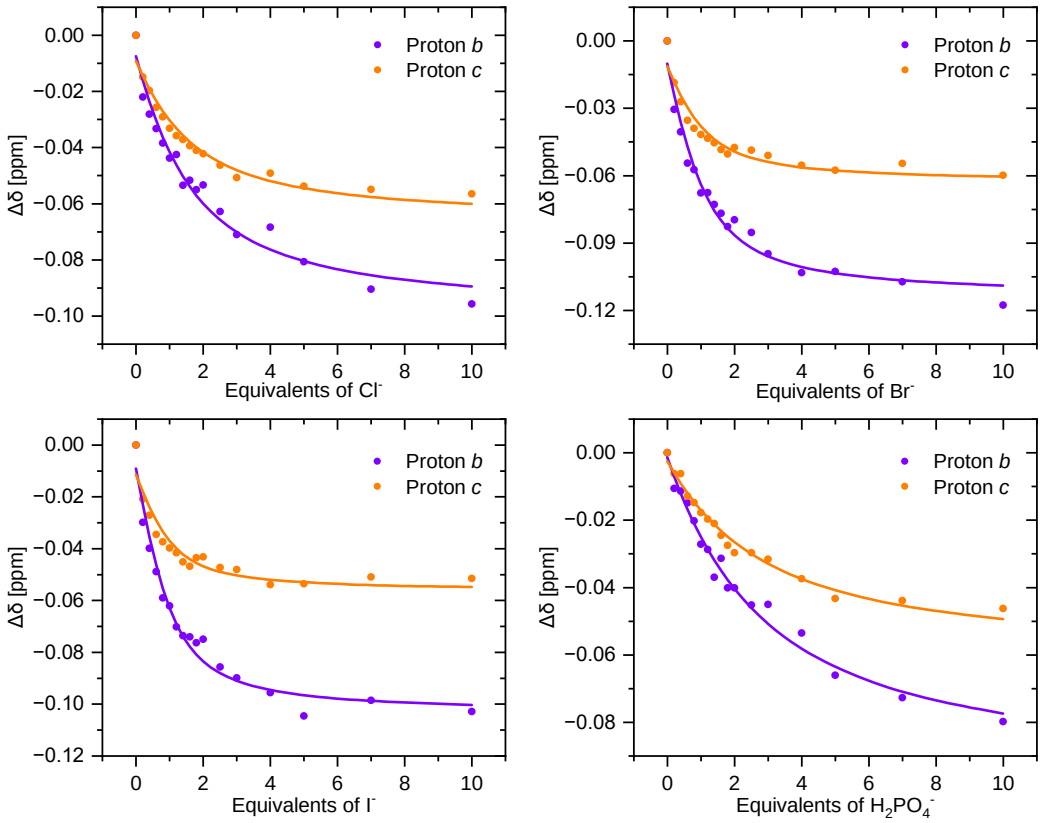


Figure 2.5.2-3. Examples of anion binding isotherms for **pDEGA-1.XB** in response to Cl^-, Br^-, I^- and $H_2PO_4^-$ in acetone-d_6:D_2O (97.5:2.5, v/v), where circles represent experimental data and the lines represent the fitted isotherm.

1:1 host-guest model fittings to the resulting binding isotherms afforded anion binding constants of up to 3000 M^{-1} for **pDEGA-1.XB** which were greater than that of either **1.XB**/**HB** in all cases. An interesting observation to note is that once again fittings with 2:1 host-guest binding models failed in all cases, confirming that cooperative binding between individual binding units does not occur. This independent, 1:1 host-guest binding mode can be justified by the assumption that each of the binding units are statistically distributed and therefore each **1.XB**/**HB** receptor is on average surrounded by 9 non-receptive DEGA units. Thus, 2:1 host-guest binding modes are prevented based on distance and steric constraints of bringing two receptive units sufficiently close in space to enable this mode. Additionally, the 1:1 host-guest binding mode is fully consistent with that observed

for the monomeric hosts in all cases, enabling direct comparisons between the monomeric and polymeric anion association constants. Furthermore, the absence of such cooperative binding modes indirectly confirms that the receptive binding units are statistically distributed along the length of the polymer chain (and not in "islands" or blocks, for example), given that a close proximity between binding units is presumably required to facilitate 2:1 host-guest binding events.

Table 2.5.2-2 displays the acquired halide binding constants for **pDEGA-1.XB** in all 3 solvent systems investigated, as well as the values for **pDEGA-1.HB** obtained in 97.5:2.5 acetone-d_6/D_2O which serve as a comparison of XB and HB analogues for these polymeric hosts (*infra vide,* for XB/HB comparisons).

Table 2.5.2-2. Anion association constants K_a (M^{-1}) of **pDEGA-1.XB** and **pDEGA-1.HB**, as determined by ^1H NMR titrations in 3 competitive solvent systems: 97.5:2.5 acetone-d_6/D_2O, acetone-d_6/ACN-d_3/D_2O and ACN-d_3/D_2O.

	97.5:2.5 acetone-d_6/D_2O		48.75:48.75:2.5 acetone-d_6/ACN-d_3/D_2O	97.5:2.5 ACN-d_3/D_2O
Anion	**pDEGA-1.XB**[a]	**pDEGA-1.HB**[a]	**pDEGA-1.XB**[a]	**pDEGA-1.XB**[a]
Cl^-	1100	65	320	240
Br^-	2800	110	1300	880
I^-	3000	120	1800	1650
$H_2PO_4^-$	410	n.d.	240	80

[a] Standard errors estimated to be < 20%. Error approximation is detailed in Section 7.10.1. n.d.-not determined.

The halogen bonding enhancement factors of **pDEGA-1.XB**/**HB** for the halides are given in Table 2.5.2-3 (*cf.* Table 2.5.1-2 for the monomeric hosts), once again highlighting the substantial (up to x25) enhancement in anion binding performance for XB-mediated hosts (**pDEGA-1.XB**) with respect to HB analogues (**pDEGA-1.HB**). Of immediate note is that the XBFs of the polymeric hosts (**pDEGA-1.XB**/**HB**) exceed all those of the monomeric hosts (**1.XB**/**HB**) in 97.5:2.5 acetone-d_6/D_2O by a substantial margin. For example, XBFs of 12.8 and 25 were obtained for the

monomers and polymers, respectively, marking a near two-fold enhancement of halogen bonding-mediated binding over hydrogen bonding analogues.

Table 2.5.2-3. Ratio of anion association constants of polymeric receptors **pDEGA-1.XB** and **pDEGA-1.HB**, representing the halogen bonding enhancement factor, XBF for the polymeric hosts, as determined by ^{1}H NMR titrations in 97.5:2.5 acetone-d_6/D_2O. Errors estimated to be 30%. Error approximation is detailed in Section 7.10.1.

	$K_{pDEGA\text{-}1.XB}/K_{pDEGA\text{-}1.HB}$
Cl^-	14
Br^-	20
I^-	25

A striking observation is that the anion binding constants for the polymeric hosts exceed those of their monomers in all cases, whilst the anion selectivity trends observed for the monomers persist ($I^- > Br^- > Cl^- > H_2PO_4^-$). A so-called polymeric enhancement factor, PEF can be calculated from the ratio of the binding constants of the polymeric host:monomer host (PEF = $K_{polymer}/K_{monomer}$, *e.g.*, $K_{pDEGA\text{-}1.XB}/K_{1.XB}$), which can be found in Table 2.5.2-4. As evidenced by all PEFs being greater than unity, a significant enhancement in anion binding is observed in all cases (to all anions, in all solvent systems, with either XB or HB-based hosts), signifying that the incorporation of monomeric receptive units into a unique polymeric environment greatly enhances their ability to bind anions more strongly (see Figure 2.5.2-4).

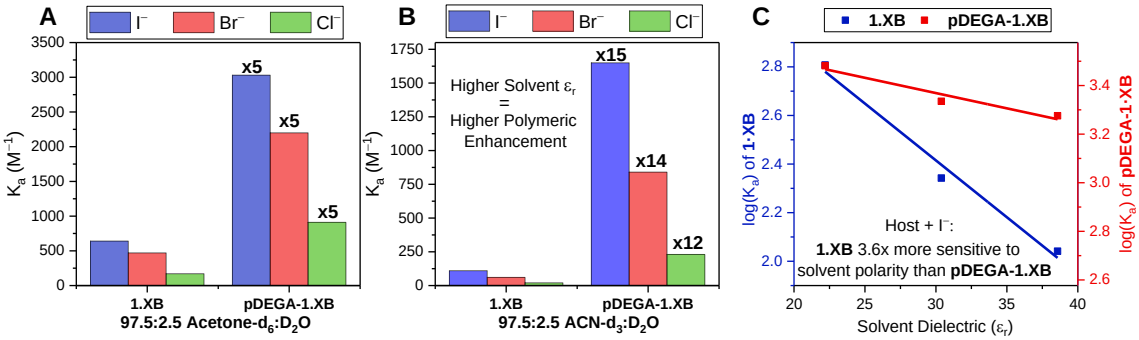


Figure 2.5.2-4. Comparison of halide binding constants with **1.XB** and **pDEGA-1.XB** in (A) 97.5:2.5 acetone-d_6/D_2O and (B) 97.5:2.5 ACN-d_3/D_2O. (C) Comparison of the log(K_a) vs. solvent dielectric constant for binding constants with **1.XB** and **pDEGA-1.XB** in response to I^-.

These results are especially impressive given the electro-neutrality of the hosts, and that the binding unit itself is not directly altered in any way to induce these enhancements (*e.g.*, synthetically enhancing anion binding strength by methylating the triazole moieties).

The polymeric enhancement effect is still pronounced (with average enhancements of x2) but generally lower for the HB hosts, which was attributed to discrepancies in the binding site solvation of the XB/HB receptors due to stronger interactions between the proto-triazole units and surrounding solvent molecules, especially given the strong HB-accepting nature of the solvents used here. Alternatively, there may be a greater extent of interaction between the HB units and DEGA co-monomers compared to the XB-based hosts. Regardless, the distinct and significant difference in local environment exhibited by the XB and HB hosts was also supported by electrochemical analyses of the hosts, through an assessment and comparison of native $E_{1/2}$ values in different solvent media (see later in Section 2.6.1).

Impressively, the PEFs only increase in more polar media, displaying a maximum PEF of 15.0 for I^- with **pDEGA-1.XB** *vs*. **1.XB** in 97.5:2.5 ACN-d_3/D_2O. Crucially, these observations demonstrate the greater tolerance of the polymeric hosts to increasing solvent polarity. This in turn has implications for future host design approaches, as the unique local binding environment imparted by incorporating receptors into polymeric or similar architectures (*e.g.*, self-assembled monolayers, see later) uniquely augments anion binding strengths without significant additional synthetic cost.

Table 2.5.2-4. Polymeric enhancement in binding constant ($K_{pDEGA\text{-}1.XB}/K_{1.XB}$), as determined by ^{1}H NMR titrations in competitive polar media.

	97.5:2.5 acetone-d_6/D_2O		48.75:48.75:2.5 acetone-d_6/ACN-d_3/D_2O	97.5:2.5 ACN-d_3/D_2O
Anion	$K_{pDEGA\text{-}1.XB}/K_{1.XB}$[a]	$K_{pDEGA\text{-}1.HB}/K_{1.HB}$[a]	$K_{pDEGA\text{-}1.XB}/K_{1.XB}$[a]	$K_{pDEGA\text{-}1.XB}/K_{1.XB}$[a]
Cl^-	6.5	2.2	8.0	12.0
Br^-	6.0	2.2	10.0	14.7
I^-	4.7	2.4	8.2	15.0
$H_2PO_4^-$	5.8	n.d.	9.6	> 8.0

[a] Standard errors estimated to be 22.5%. n.d. – not determined. Error approximation is detailed in Section 7.10.1.

The solvent tolerance of anion binding strength at the polymeric hosts was ascribed to the generation of a unique binding micro-environment which exhibits a lower, local dielectric constant, ε_r than that of the surrounding bulk media (which ranges from ε_r = 26 – 39). This local dielectric is imparted by the DEGA (or BuA) co-monomeric units, which effectively shield the **1.XB**/**HB** units from the surrounding bulk solvent, affording a less competitive binding site and increasing anion binding strength.

To further explore the impact of an induced local binding microenvironment, two additional, contrasting polymeric hosts were studied: **pDEGA-1.XB$_{0.5}$** and **pDEGA-BuA-1.XB**. The former represents a "diluted" form of **pDEGA-1.XB**, whereby weaker anion binding would be expected due to a higher local concentration of polar, flexible DEGA units around each **1.XB** receptor, increasing both local solvation and dielectric. The latter marks a more potent analogue of **pDEGA-1.XB**, whereby the inclusion of notably more non-polar BuA co-monomer units would be expected to markedly enhance anion binding through improved solvent exclusion; lowering local ε_r. Gratifyingly, both of these predictions were borne out in resolved I^- binding constants for these hosts in acetonitrile-d_3:D_2O 97.5:2.5, with weaker anion binding

observed for **pDEGA-1.XB$_{0.5}$** (K = 570 M^{-1}, *cf.* 1650 M^{-1} at **pDEGA-1.XB**) and stronger anion binding at **pDEGA-BuA-1.XB** (K = 4900 M^{-1}, *cf.* 1650 M^{-1} at **pDEGA-1.XB**). The value obtained for I$^-$ binding to **pDEGA-BuA-1.XB** is especially impressive when compared to I$^-$ recognition at **1.XB** (K = 4900 M^{-1}, *cf.* 110 M^{-1} at **1.XB**), as a 47-fold increase in anion binding strength was revealed. Once again, it should be noted that the binding unit is identical in both cases, therefore only the unique modulation of local hydrophobicity through judicious co-monomer inclusion that can be credited with these striking enhancements in anion binding potency (see Figure 2.5.2-5 for a schematic representation of these effects).

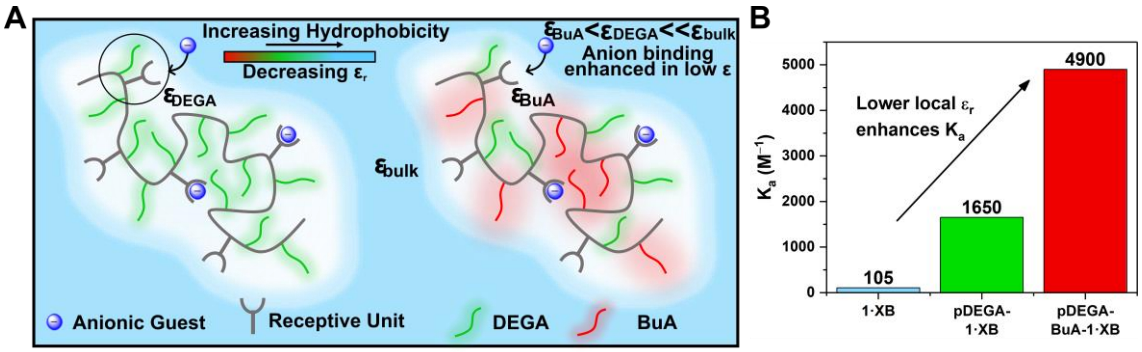


Figure 2.5.2-5. (A) Schematic representation of binding microenvironment tuning by the strategic use of more hydrophobic co-monomers. (B) Enhancement of I$^-$ binding constants with a series of hosts: **1.XB**, **pDEGA-1.XB** and **pDEGA-BuA-1.XB**, as determined from ^{1}H NMR titrations.

To provide further support for this proposed mechanism of modulated local dielectric constant, additional studies were conducted to eliminate other possible factors which may contribute to enhanced binding at the polymeric hosts.

One such factor is the countercation used during titrations, as significant incorporation of countercations into the polymeric structure (especially pertinent for lipophilic cations such as TBA$^+$ due to potential solvophobic effects, for example, see Section 1.2.3 for further detail) could, in principle, enhance anion binding through additional stabilising electrostatic interactions. This was refuted, however,

by the lack of any significant perturbation to the TBA^+ ^1H NMR signals throughout the course of a titration, confirming that TBA^+ does not interact significantly with the polymer or target anion in all three solvent systems investigated. Furthermore, the chemical shifts of these TBA^+ signals following the final addition of target anion (I^-, Br^- or Cl^-) were near-identical regardless of whether **1.XB** or **pDEGA-1.XB** acted as host (see Table 2.5.2-5). It should be noted, however, that the same TBA^+ signals are expectedly sensitive to the external environment, as illustrated by the ≈ 0.2 ppm difference in the chemical shifts of N^+CH_2 signals between acetone/D_2O 97.5:2.5 and acetone/acetonitrile/D_2O 48.75:48.75:2.5, and a further ≈ 0.1 ppm change between acetone/acetonitrile/D_2O 48.75:48.75:2.5 and acetonitrile/D_2O 97.5:2.5.

Table 2.5.2-5. Chemical shifts (ppm) of selected TBA signals at the last titration point of monomeric host **1.XB** and polymeric host **pDEGA-1.XB** titrations with halides (added as TBA salts) in different solvent systems.

ACN-d_3:D_2O 97.5:2.5						
	I^-		**Br^-**		**Cl^-**	
	$N\mathbf{CH_2}CH_2$-	$NCH_2\mathbf{CH_2}$-	$N\mathbf{CH_2}CH_2$-	$NCH_2\mathbf{CH_2}$-	$N\mathbf{CH_2}CH_2$-	$NCH_2\mathbf{CH_2}$-
1.XB	3.4311	1.8109	3.4326	1.8113	3.4330	1.8116
pDEGA-1.XB	3.4314	1.8103	3.4310	1.8105	3.4313	1.8100
Acetone-d_6:ACN-d_3:D_2O 48.75:48.75:2.5						
	I^-		**Br^-**		**Cl^-**	
	$N\mathbf{CH_2}CH_2$-	$NCH_2\mathbf{CH_2}$-	$N\mathbf{CH_2}CH_2$-	$NCH_2\mathbf{CH_2}$-	$N\mathbf{CH_2}CH_2$-	$NCH_2\mathbf{CH_2}$-
1.XB	3.2068	1.6704	3.2070	1.6700	3.2016	1.6700
pDEGA-1.XB	3.1792	ND	3.1785	1.6424	3.1792	1.6433
Acetone-d_6:D_2O 97.5:2.5						
	I^-		**Br^-**		**Cl^-**	
	$N\mathbf{CH_2}CH_2$-	$NCH_2\mathbf{CH_2}$-	$N\mathbf{CH_2}CH_2$-	$NCH_2\mathbf{CH_2}$-	$N\mathbf{CH_2}CH_2$-	$NCH_2\mathbf{CH_2}$-
1.XB	3.0708	1.5875	3.0709	1.5871	3.0997	1.6164
pDEGA-1.XB	3.0705	1.5872	3.0708	1.5880	3.0714	1.5880

Additionally, an additional control titration was performed for a representative data set (**pDEGA-1.XB** for I^- in acetonitrile-d_3/D_2O) which utilised Na^+ as the countercation. Unfortunately, precipitation occurred beyond 5 equivalents of NaI, preventing further studies. Nonetheless, 1:1 host-guest binding model fitting to the data collected up to this point afforded a binding constant of 1350 ± 270 M^{-1} (Figure 2.5.2-5); close to that determined for the analogous titration with TBAI (K = 1650 ± 330 M^{-1}). In summary, these results conclusively confirm that the countercation (either TBA^+ or Na^+) has a negligible contribution to anion binding. Crucially, this implies that the observed differences in monomeric and polymeric host's anion binding strength must result from the inherent difference between monomer and polymer binding environment, as proposed.

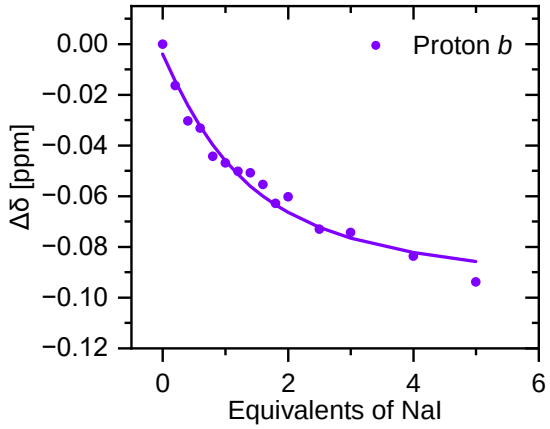


Figure 2.5.2-6. Representative example of a binding isotherm determined for iodide with a different countercation (added as NaI) for **pDEGA-1.XB** in acetonitrile-d_3:D_2O (97.5:2.5, v/v), where circles represent experimental data and the lines represent the fitted isotherm. Precipitation beyond 5 equivalents of NaI prevented further analyses.

Another factor to consider is whether the binding unit must be directly incorporated into the polymeric backbone in order to benefit from the lower local dielectric constant imbued by the surrounding monomers. To investigate this, a control ^1H NMR titration was performed for I^- at **1.XB** in the presence of a **pDEGA** homopolymer, ensuring a 9:1 ratio of DEGA:**1.XB** units to directly mimic the conditions in a titration

with **pDEGA-1.XB** (see Figure A2.9 and A2.10 in the Appendices A2). These analyses afforded a binding constant of 110 M^{-1}, in near-perfect agreement with that of **1.XB** alone (105 M^{-1}). Furthermore, none of the **pDEGA** signals were perturbed significantly ($\Delta\delta$ < 0.05 ppm), implying once again that the DEGA groups do not contribute meaningfully to anion binding. The combination of these observations suggest that the receptive **1.XB**/**HB** units must be integrated into the polymeric scaffold to experience the substantial polymeric enhancement afforded by the generation of a low dielectric microenvironment within the polymeric hosts.

To summarise the anion binding performance of the polymeric hosts:

- Relevant signals within the predicted binding cleft of both **1.XB** and **1.HB** when incorporated within a polymeric scaffold once again displayed significant shifts upon addition of target anions (Cl^-, Br^-, I^- and $H_2PO_4^-$), mirroring the shift patterns observed for the monomers
- High anion binding affinities were displayed, with K_a values of up to 4900 M^{-1}
- Consistent with the monomers, **pDEGA-1.XB** outperformed **pDEGA-1.HB** in terms of anion binding strength in all cases, once again supporting the reportedly high potency of XB-based motifs vs. HB analogues
- In direct comparative studies, the polymeric hosts (**pDEGA-1.XB**/**HB**) substantially outperformed their monomeric analogues (**1.XB**/**HB**) in all cases, displaying polymeric enhancement factors of up to 15x
- By incorporating more hydrophobic non-receptive, co-monomers (1:1 BuA:DEGA *vs*. DEGA) anion binding strengths were augmented 3-fold (**pDEGA-BuA-1.XB** *vs*. **pDEGA-1.XB**), and 47-fold w.r.t. the monomer alone (**pDEGA-BuA-1.XB** *vs*. **1.XB**)

2.6 Electrochemical Analyses of Monomeric and Polymeric Hosts

2.6.1 Voltammetric Characterisation of Monomeric and Polymeric Hosts

By virtue of the appended redox-active ferrocene units of **1.XB**/**HB**, a high density of information can be obtained regarding the local environment and anion recruitment through voltammetric analyses. As introduced in Section 1.4.2, voltammetric techniques such as cyclic voltammetry and square wave voltammetry can be utilised to reversibly oxidise/reduce the ferrocene/ferrocenium (Fc/Fc^+) species in situ, and analyses thereof provide a number of relevant electrochemical parameters (see Figures 2.6.1-1 – 2.6.1-6 and Figures A2.4 – S2.9 for the voltammograms measured in 97.5:2.5 acetone/H_2O and 97.5:2.5 ACN/H_2O, respectively, for the full range of hosts). For example, Figures 2.6.1-1A and 2.6.1-3A display the well-defined, single-electron voltammetric traces of **1.XB** and **pDEGA-1.XB**, respectively, as resolved by cyclic voltammetry (and square wave voltammetry, in the insets), depicting the reversible oxidation and reduction of the ferrocene/ferrocenium couples for these species in 97.5:2.5 acetone/H_2O. It is immediately notable that the voltammetric characteristics of both the monomeric and polymeric analogues, representatively exemplified here for **1.XB** and **pDEGA-1.XB**, are near identical (as is also the case for **1.HB** and **pDEGA-1.HB**, see Figures 2.6.1-2 and 2.6.1-4). Such characteristics include: 1) the number of peaks, 2) the peak shape, 3) the peak separation, 4) the current magnitudes, and 5) the

dependence of peak current magnitude on scan rate (see Figures 2.6.1-1B-D to 2.6.1-6B-D).

Exploring each of these in turn: the observation of a single peak in the voltammograms of the monomeric and polymeric receptors confirms that each of the two affixed ferrocene units per receptive unit were addressed simultaneously. If this were not the case, one would expect to see two separate peaks (or the presence of a significant shoulder to the major peak) in CV/SWV voltammograms, indicating a discrepancy in local environment for each of the units which thereby alters their individual redox properties. Two peaks could arise, in theory, if the receptor does not assume a symmetrical conformation, which would place the arms of the receptors, and therefore the redox-active ferrocene units, in unique, distinct environments from each other.

Secondly, a consistent peak shape was displayed in the SWVs of all hosts, in all cases, namely a symmetrical, Gaussian peak, which reflects the expected shape for a redox distribution of states (as detailed in Section 1.4.2). These characteristics convey that, as expected, both the forward (oxidation) and reverse (reduction) processes for Fc/Fc^+ were reversible and proceed with similar kinetics.

Thirdly, the peak separations, ΔE_p between the peaks associated with the oxidation of ferrocene (forward sweep) and the reduction of ferrocenium (reverse sweep) for all hosts were close to that of the ideal ΔE_p for an ideal, electrochemically reversible, one electron oxidation/reduction process for a freely diffusing redox-active species: 59 mV (ΔE_p = 37 mV and 36 mV, for example, for **1.XB** and **pDEGA-1.XB**, respectively in 97.5:2.5 acetone/H_2O).

The penultimate characteristic highlighted here is that the maximum currents passed ($I_{p,a}$ or $I_{p,c}$ for the anodic, oxidative peak and cathodic, reductive peak, respectively) in CVs/SWVs for each of the hosts are generally similar (≈ 4 μA), suggesting that the diffusion properties (*e.g.*, the diffusion constant, D) were broadly consistent across the family of receptors investigated here (both monomeric and polymeric). As $I_{p,a/c}$ is directly related to the concentration of redox-active units (which corresponds to the receptor concentration here) the consistency in maximum current magnitude across the monomeric and polymeric hosts also semi-quantitatively supports that the receptive unit normalisation calculations performed for the polymeric hosts are accurate. This enables direct comparisons between the monomeric and polymeric hosts as they can be assumed to be at identical effective receptor concentrations (see Section 7.10.1 for further quantitative evidence for effective receptor concentrations of monomeric/polymeric hosts).

Finally, the measured peak current ($I_{p,a/c}$) was, in general, directly proportional to the square root of the scan rate (see Figures 2.6.1-1D – 2.6.1-6D) which, as described by the Randles-Ševčík equation below (Equation 2.6.1-1), indicates that this redox process is both diffusion-controlled and reversible.

$$I_{p,a/c} = 0.4463\, nFAC\sqrt{\frac{nFvD}{RT}} \qquad \textbf{Equation 2.6.1-1}$$

n = no. electrons, F = Faraday's constant, A = surface area of the working electrode (in cm^2), C = concentration of redox-active species (in M), v = scan rate (in $V\ s^{-1}$), D = diffusion coefficient of redox-active species ($cm^2\ s^{-1}$), R = gas constant, T = temperature.

Any deviations from linearity with these $I_{p,a/c}$ *vs.* ν fits were attributed to a slight degree of quasi-reversibility of the redox couple, presumably due to physisorption of material onto the surface of the working electrode. This was also later identified as an issue during anion titration studies, but was easily remedied by mechanically polishing the working electrode (herein, glassy carbon) surface prior to every individual measurement.

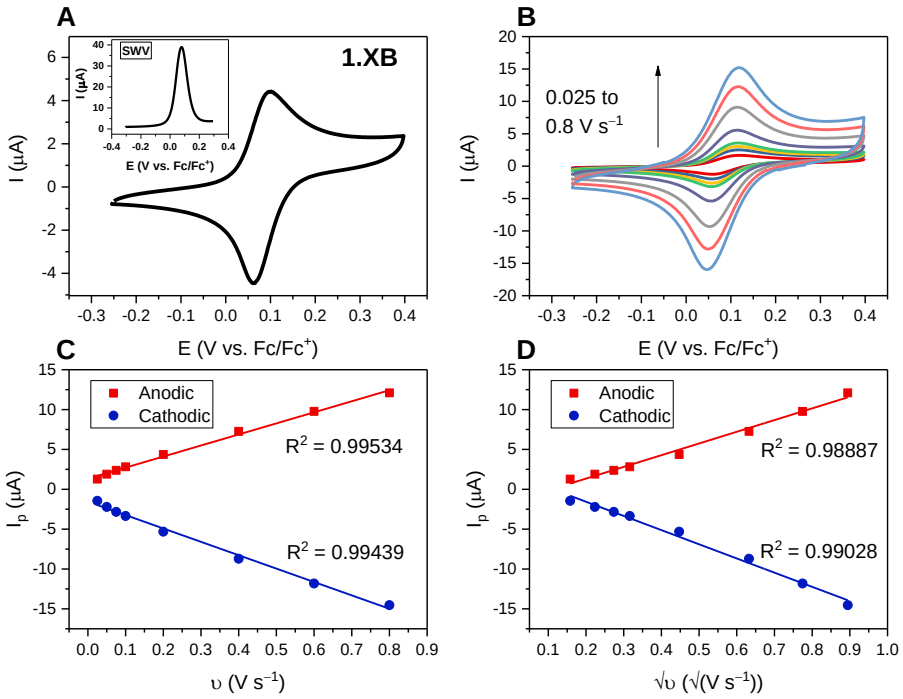


Figure 2.6.1-1. (A) Cyclic voltammogram and square wave voltammogram (inset) of 0.1 mM **1.XB** in 97.5: 2.5 acetone/H_2O, 100 mM $TBAClO_4$, at a scan rate of 0.1 V s^{-1}. (B) Cyclic voltammograms of the same system at varying scan rates from 0.025 to 0.8 V s^{-1}, and plots of peak current vs. (C) scan rate (D) the square-root of the scan rate in the same solvent system. All potentials wrt. external $Fc|Fc^+$ couple.

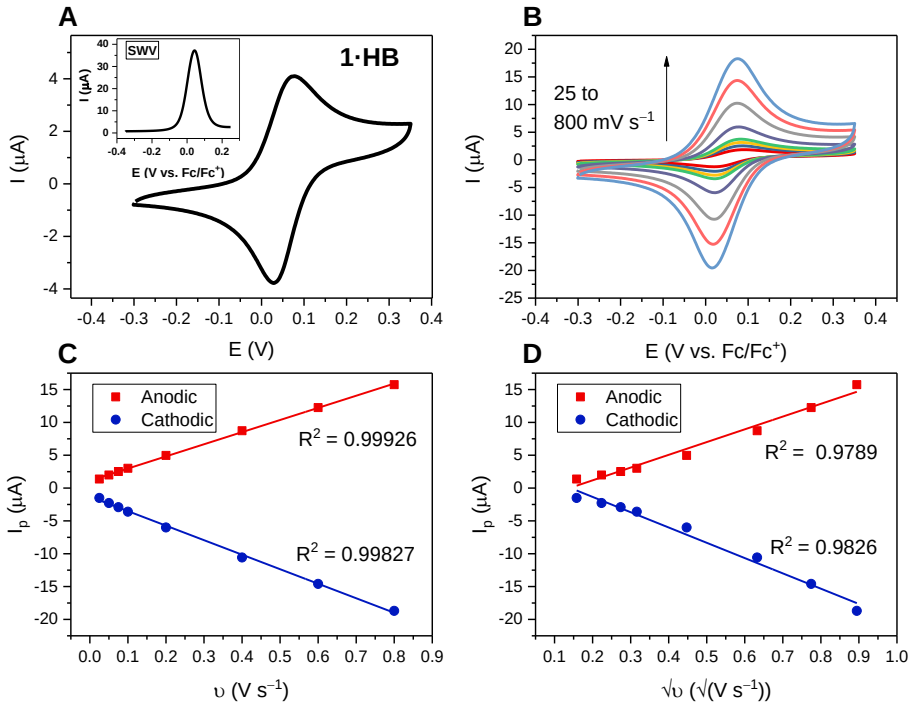


Figure 2.6.1-2. (A) Cyclic voltammogram and square wave voltammogram (inset) of 0.1 mM **1.HB** in 97.5: 2.5 acetone/H_2O, 100 mM $TBAClO_4$, at a scan rate of 0.1 V s^{-1}. (B) Cyclic voltammograms of the same system at varying scan rates from 0.025 to 0.8 V s^{-1}, and plots of peak current vs. (C) scan rate (D) the square-root of the scan rate in the same solvent system. All potentials wrt. external $Fc|Fc^+$ couple.

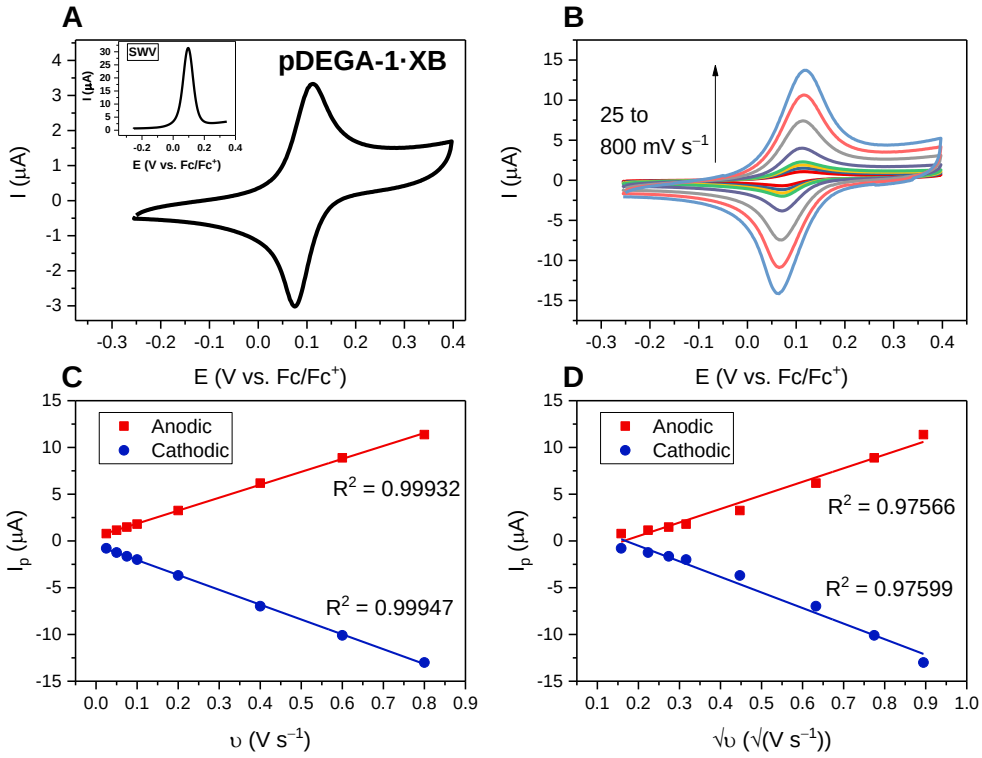


Figure 2.6.1-3. (A) Cyclic voltammogram and square wave voltammogram (inset) of 0.1 mM **pDEGA-1.XB** in 97.5: 2.5 acetone/H_2O, 100 mM $TBAClO_4$, at a scan rate of 0.1 V s^{-1}. (B) Cyclic voltammograms of the same system at varying scan rates from 0.025 to 0.8 V s^{-1}, and plots of peak current vs. (C) scan rate (D) the square-root of the scan rate in the same solvent system. All potentials wrt. external $Fc|Fc^+$ couple.

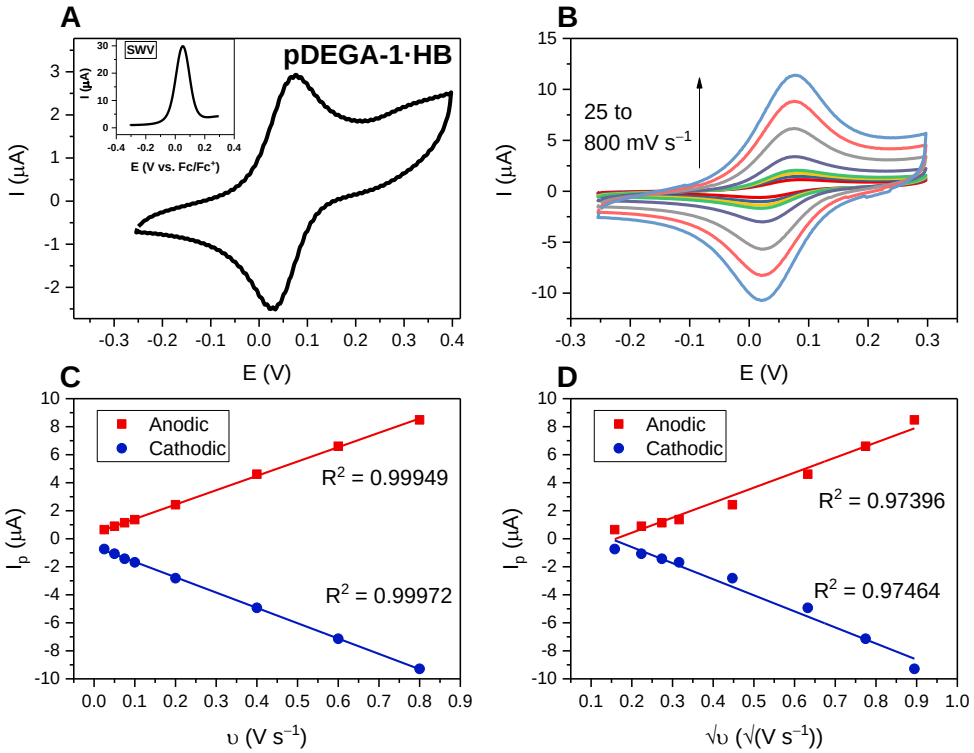


Figure 2.6.1-4. (A) Cyclic voltammogram and square wave voltammogram (inset) of 0.1 mM **pDEGA-1.HB** in 97.5: 2.5 acetone/H_2O, 100 mM $TBAClO_4$, at a scan rate of 0.1 V s^{-1}. (B) Cyclic voltammograms of the same system at varying scan rates from 0.025 to 0.8 V s^{-1}, and plots of peak current vs. (C) scan rate (D) the square-root of the scan rate in the same solvent system. All potentials wrt. external $Fc|Fc^+$ couple.

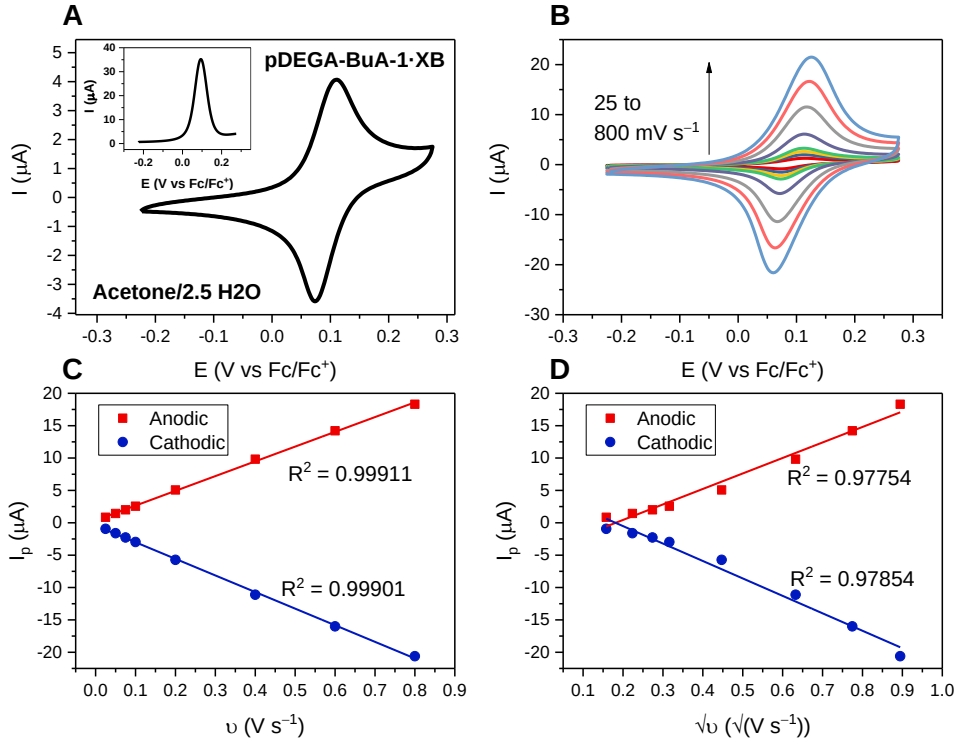


Figure 2.6.1-5. (A) Cyclic voltammogram and square wave voltammogram (inset) of 0.1 mM **pDEGA-BuA-1.XB** in 97.5: 2.5 acetone/H_2O, 100 mM $TBAClO_4$, at a scan rate of 0.1 V s^{-1}. (B) Cyclic voltammograms of the same system at varying scan rates from 0.025 to 0.8 V s^{-1}, and plots of peak current vs. (C) scan rate (D) the square-root of the scan rate in the same solvent system. All potentials wrt. external $Fc|Fc^+$ couple.

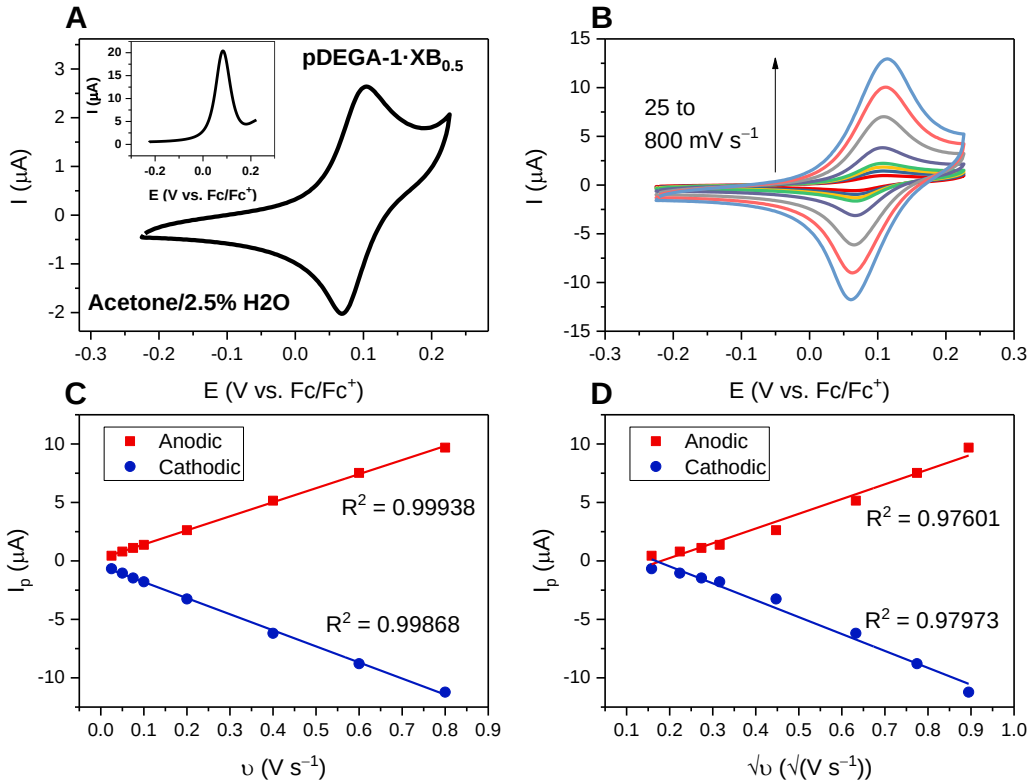


Figure 2.6.1-6. (A) Cyclic voltammogram and square wave voltammogram (inset) of 0.1 mM **pDEGA-1.XB$_{0.5}$** in 97.5: 2.5 acetone/H_2O, 100 mM $TBAClO_4$, at a scan rate of 0.1 V s^{-1}. (B) Cyclic voltammograms of the same system at varying scan rates from 0.025 to 0.8 V s^{-1}, and plots of peak current vs. (C) scan rate (D) the square-root of the scan rate in the same solvent system. All potentials wrt. external $Fc|Fc^+$ couple.

In contrast, one of the properties to vary substantially between hosts was the half-wave potential ($E_{1/2}$s), which reports on the predictably different local binding environments imparted by the XB/HB or monomeric/polymeric hosts (see Table 2.6.1-1). As introduced in the Section 1.4.2, the half wave potential ($E_{1/2}$) of each redox-active host represents the relative stabilisation of the $Fc|Fc^+$ oxidation states. As such, these characteristic $E_{1/2}$ values are in turn modulated by both through-bond (*e.g.*, impact of iodo- or proto-triazole functionalities) and through-space effects (*e.g.*, polymer *vs.* monomer comparisons or by varying solvent polarity).

Table 2.6.1-1. Half-wave potentials ($E_{1/2}$s, mV) of all hosts (**1.XB**/**HB**, **pDEGA-1.XB**/**HB**, **pDEGA-BuA-1.XB** and **pDEGA-1.XB$_{0.5}$**) in 97.5:2.5 ACN/H_2O, as determined from the peak potential of their corresponding SWV voltammograms. *a*-error represents 5 independent repeats, *b*- error represents 2 independent repeats.

	Host					
Solvent System	**1.XB**	**1.HB**	**pDEGA-1.XB**	**pDEGA-1.HB**	**pDEGA-BuA-1.XB**	**pDEGA-1.XB$_{0.5}$**
$E_{1/2}$ in 97.5:2.5 Acetone/H_2O (mV)	[a]79 ± 3	[a]49 ± 3	[a]96 ± 3	[a]51 ± 1	94	82
$E_{1/2}$ in 97.5:2.5 ACN/H_2O (mV)	[a]125 ± 2	[a]88 ± 2	[a]144 ± 2	[a]99 ± 2	[b]154 ± 1	149

Starting with the former: as discussed in Section 1.4.2, the greater electron-withdrawing ability of iodo-triazole motifs with respect to their proto-triazole analogues is expected to be borne out in more anodic native $E_{1/2}$s for these hosts (*i.e.*, in the absence of any target guest). This is a well-established phenomenon with numerous reports of this type of behaviour, exhibiting differences of up to 76 mV.[226] Expectedly, the same behaviour was observed here but, interestingly, there is a greater relative difference between the $E_{1/2}$s of the XB and HB analogues in this work compared to previous studies, which can be best exemplified through comparison with the monomeric hosts to a similar bis-((iodo)-triazole-ferrocenyl) receptor (ΔE = 41 mV for **1.XB** *vs.* **1.HB**, *cf*. ΔE = 14 mV for **2.XB** *vs.* **2.HB**, both in ACN, see Figures 2.6.1-7 and 2.6.1-8).[227] This result was justified by the fact that the Fc transducer unit and (iodo)-triazole motif are directly linked/conjugated in the case of **1.XB**/**HB**, but are separated by an additional methyl spacer at **2.XB**/**HB**. Therefore, the electron-withdrawing ability of the (iodo)triazole group is predicted to have a more substantial impact on resolved $E_{1/2}$ values for **1.XB**/**HB** with respect to **2.XB**/**HB**. These effects are, expectedly, disproportionately more pronounced for the XB

sensors over their HB analogues due to the inherently greater polarisability of C-I bonds compared to C-H bonds.

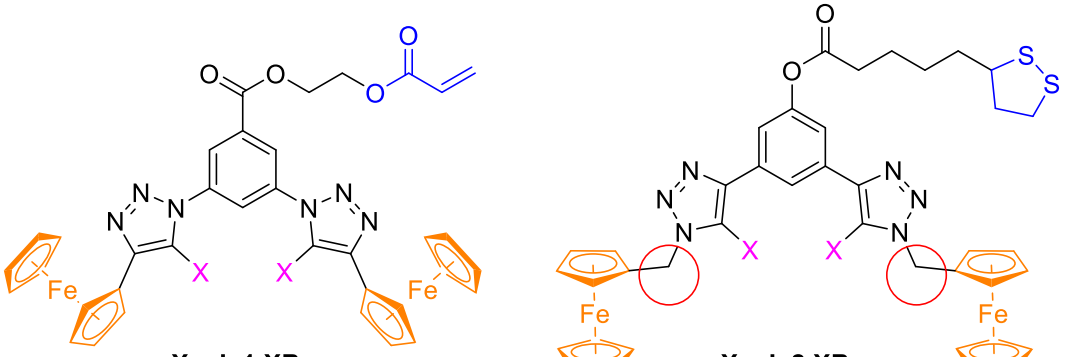


Figure 2.6.1-7. Comparison of the structures of **1.XB/HB** and another similar bis-((iodo)-triazole-ferrocenyl) sensor, **2.XB/HB**. The methyl spacers separating the Fc transducer unit and (iodo)-triazole groups in **2.XB/HB** are circled in red.

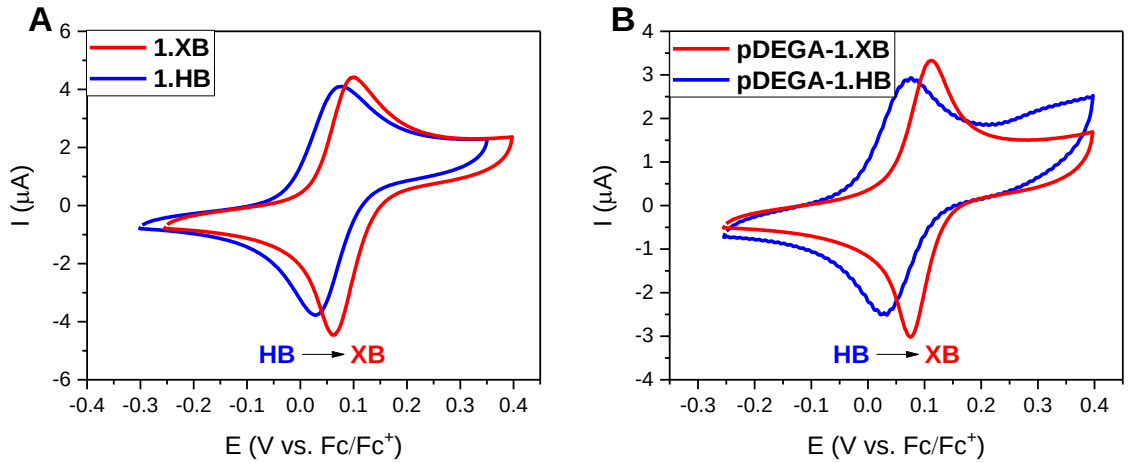


Figure 2.6.1-8. Comparison of the voltammograms of the XB and HB analogues of the (A) monomeric and (B) polymeric receptors in 97.5:2.5 acetone/H_2O, 100 mM $TBAClO_4$. The arrows depict the anodic shift in $E_{1/2}$ for the XB hosts due to the greater electron-withdrawing nature of the iodo-triazole motifs.

Moving on to through-space effects on $E_{1/2}$, a critical point of interest in this work lies in the quantification of the impact of incorporating individual monomeric, receptive units into a polymeric scaffold on anion binding/sensing performance. In particular, how this influences the characteristics of the local binding environment (by modulating local ε_r, for example) and the resulting effect this may have on anion binding stoichiometry, selectivity and strength. Incorporating the receptive units (**1.XB/HB**) into a polymeric scaffold comprised of comparably hydrophobic

monomer units (w.r.t. the polarity of the surrounding solvent media) is expected to hinder Fc oxidation (due to diminished electrostatic stabilisation of Fc^+) and be associated with a corresponding anodic shift of half wave potential with respect to the monomer alone.

Gratifyingly, these predictions were corroborated when the $E_{1/2}$ of **pDEGA-1.XB** was observed to be 19 mV more anodic than that of **1.XB** (144 ± 2 mV *vs*. 125 ± 2 mV in 97.5:2.5 ACN/H_2O, respectively, see Figure 2.6.1-9) with **pDEGA-BuA-1.XB** more anodic still (154 ± 1 mV *vs*. 144 ± 2 mV in 97.5:2.5 ACN/H_2O, for **pDEGA-BuA-1.XB** and **pDEGA-1.XB**, respectively).

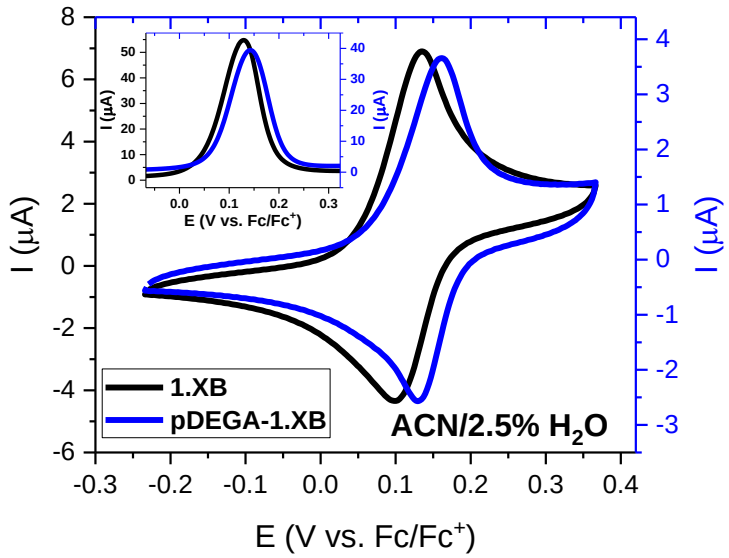


Figure 2.6.1-9. Cyclic voltammograms and square wave voltammograms (inset) of 0.1 mM **1.XB** (black lines) and **pDEGA-1.XB** (blue lines) in 97.5:2.5 ACN:H_2O, 100 mM $TBAClO_4$, at a scan rate of 0.1 V s^{-1}. Potentials w.r.t. $Fc|Fc^+$.

Furthermore, the anodic perturbation observed upon incorporating **1.XB**/**HB** into a polymeric architecture is greater for the XB sensors compared to the HB hosts, in accordance with the greater hydrophobicity of XB-based motifs compared to HB analogues ($\Delta E_{1/2}$ = 19 mV moving from **1.XB** to **pDEGA-1.XB** *vs*. $\Delta E_{1/2}$ = 11 mV for **1.HB** to **pDEGA-1.HB** in 97.5:2.5 ACN/H_2O). This concept is schematised below in Figure 2.6.1-10.

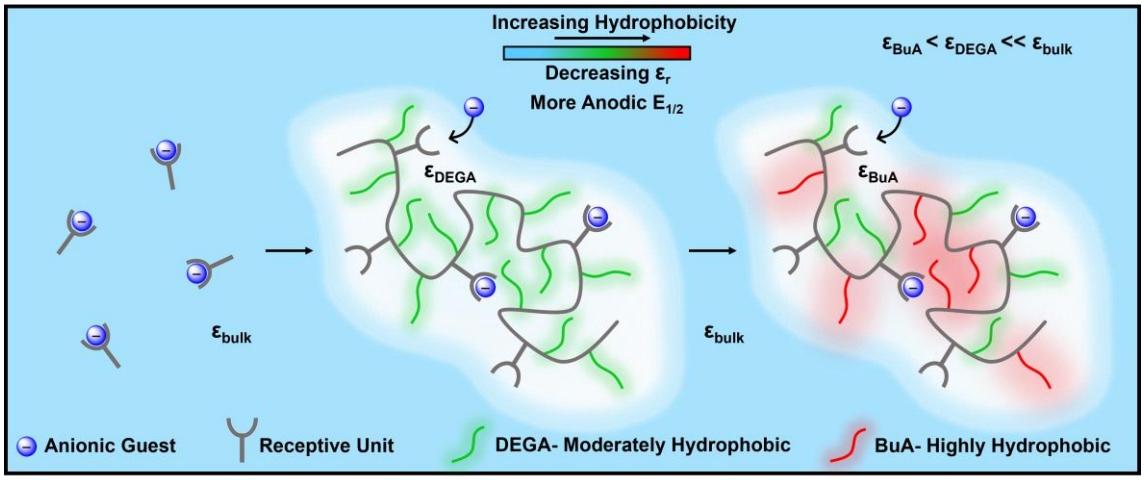


Figure 2.6.2-10. Schematic depiction of the effect of incorporating monomeric hosts (left) within a moderately hydrophobic polymeric scaffold (centre) and a highly hydrophobic polymeric scaffold (right) on the determined $E_{1/2}$ for each host. With increasing hydrophobicity (lower local ε_r) around each receptive unit, $E_{1/2}$ is progressively shifted to more anodic potentials.

Interestingly, when exploring the solvent dependence of $E_{1/2}$ of these hosts it was revealed that the disparity between the $E_{1/2}$s of **1.XB**/**HB** and **pDEGA-1.XB**/**HB** was most pronounced in more polar solvent systems, with this difference contracting, and then disappearing, on decreasing polarity (Figure 2.6.1-11). At the point of convergence ($E_{1/2,poly} = E_{1/2,mon}$), the transducers of each host can be assumed to be in near identical local environments and this enables an semi-quantitative approximation of microenvironment local dielectric. As such, the dielectric constants of the polymer binding sites can be estimated as being ≈12 for **pDEGA-1.XB** and ≈16 for **pDEGA-1.HB**. As the local dielectric around the binding unit in a polymer likely results from a combination of material contributions (i.e. the dielectric properties of the co-monomer) and the extent of solvent penetration, the slightly higher local ε_r determined for **pDEGA-1.HB** may result from the more pronounced penetration of HB-accepting solvents (acetone, ACN and/or H_2O) within the polymeric scaffold (making the local environment more polar in comparison to **pDEGA-1.XB**). Presumably, this can be attributed to enhanced

solvent-proto-triazole interactions compared to those at the iodo-triazole motifs at **pDEGA-1.XB**.

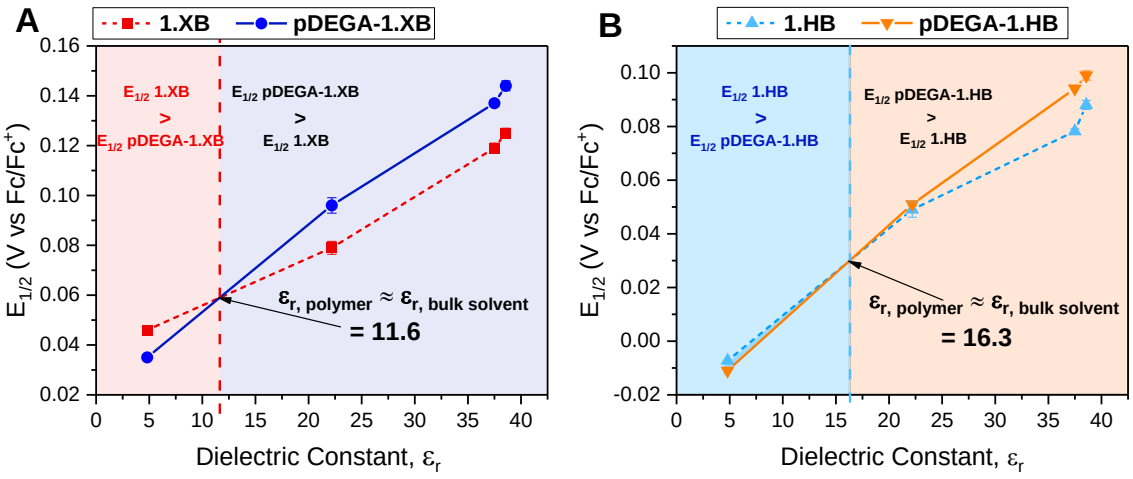


Figure 2.6.1-11. Half wave potentials of (A) **pDEGA-1.XB** and **1.XB**, and (B) **pDEGA-1.HB** and **1.HB** determined in a range of solvent media of differing polarity. Connecting lines are shown to guide the eye only. Error bars represent one standard deviation of three independent repeats. All potentials wrt. Fc|Fc+. The labelled crossover points at ≈ 12 and ≈ 16 are hypothesised to represent the approximate dielectric constants within **pDEGA-1.XB** and **pDEGA-1.HB**, respectively.

2.6.2 Electrochemical Anion Sensing Performance of Monomeric and Polymeric Hosts

The anion sensing performance of the monomeric and polymeric hosts was then assessed in two of the solvent systems (97.5:2.5 acetone/H_2O and 97.5:2.5 ACN/H_2O) used for the ^{1}H NMR anion binding studies detailed in Section 2.5. As introduced above, the half-wave potential of these redox-active receptors are sensitive to both through-bond and through-space effects. Crucially, the electrochemical properties of these hosts are also modulated in the presence of a target anionic guest species, as discussed in Section 1.4.2. Namely, the cathodic perturbations to the native $E_{1/2}$s of these hosts upon addition of target anions directly report on anion binding events. As $E_{1/2}$ can also be sensitive to changes in ionic strength, the host concentration (100 μM) and ionic strength (100 mM) was

held constant throughout all anion sensing studies to ensure that all measured responses were reliably attributed to specific anion binding.

In both solvent systems investigated, significant cathodic perturbations of all host $E_{1/2}$s ($\Delta E_{1/2}$) were displayed (see Tables 2.6.2-1 and 2.6.2-2, and Figures 2.6.2-1 and 2.6.2-2) in response to a range of anions: Cl^-, Br^-, HSO_4^- and $H_2PO_4^-$, up to –201 mV for the response of **pDEGA-1.XB** to $H_2PO_4^-$ in 97.5:2.5 acetone/H_2O. The magnitude of the voltammetric shift, ΔE is in its most general form given according to the Nernst equation (Equation 1.4.2-2) and is primarily determined by the ratio of the anion binding constants to the different receptor oxidation states K_{Ox}/K_{Red}. This ratio is often denoted as the binding enhancement factor (BEF), and provides insight into the anion binding strengths to the charged and neutral receptors.[228, 229] It should be noted that this simple model does not yield absolute values for K_{Ox} or K_{Red} and can only afford accurate BEFs when the maximum voltammetric perturbation ΔE_{max} is known, *i.e.*, when a plateauing response is reached. However, especially in increasingly competitive, aqueous solvent systems, this is often not the case, even at relatively high anion concentrations.

$$\Delta E = -\frac{RT}{nF}\ln\left(\frac{K_{Ox}}{K_{Red}}\right) \qquad \text{Equation 1.4.2-2}$$

A derived, extended model (Equation 1.4.2-3), which is applicable under fast-exchange, continuous shift (*i.e.*, not two-wave behaviour) conditions and when $[A^-] >> [H]$ (where $[A^-]$ and [H] are the concentrations of the anion and host, respectively), can also be utilised to determine absolute values for K_{Ox} or K_{Red} (discussed later in further detail).[230]

$$\Delta E = -\frac{RT}{nF}\ln\left(\frac{1+K_{Ox}[A^-]}{1+K_{Red}[A^-]}\right) \qquad \text{Equation 1.4.2-3}$$

Issues with overlapping oxidation potentials between $Fc|Fc^+$ and $2I^-|I_2$ precluded anion sensing studies at these hosts with I^- under the conditions utilised here. Nevertheless, a consistent anion selectivity trend was observed across all monomeric/polymeric hosts ($H_2PO_4^-$ > HSO_4^- > Cl^- > Br^-), as assessed from the determined maximum cathodic shifts, which mirrored predicted anion basicity trends. It should be noted that the XB hosts typically exhibited larger responses for the halides compared to the HB receptors, in accordance with previous reports of the preference of XB receptors for the halides over oxoanions. Similarly, the HB hosts generally displayed a preference for the oxoanions; consistent with previous XB/HB comparative studies.

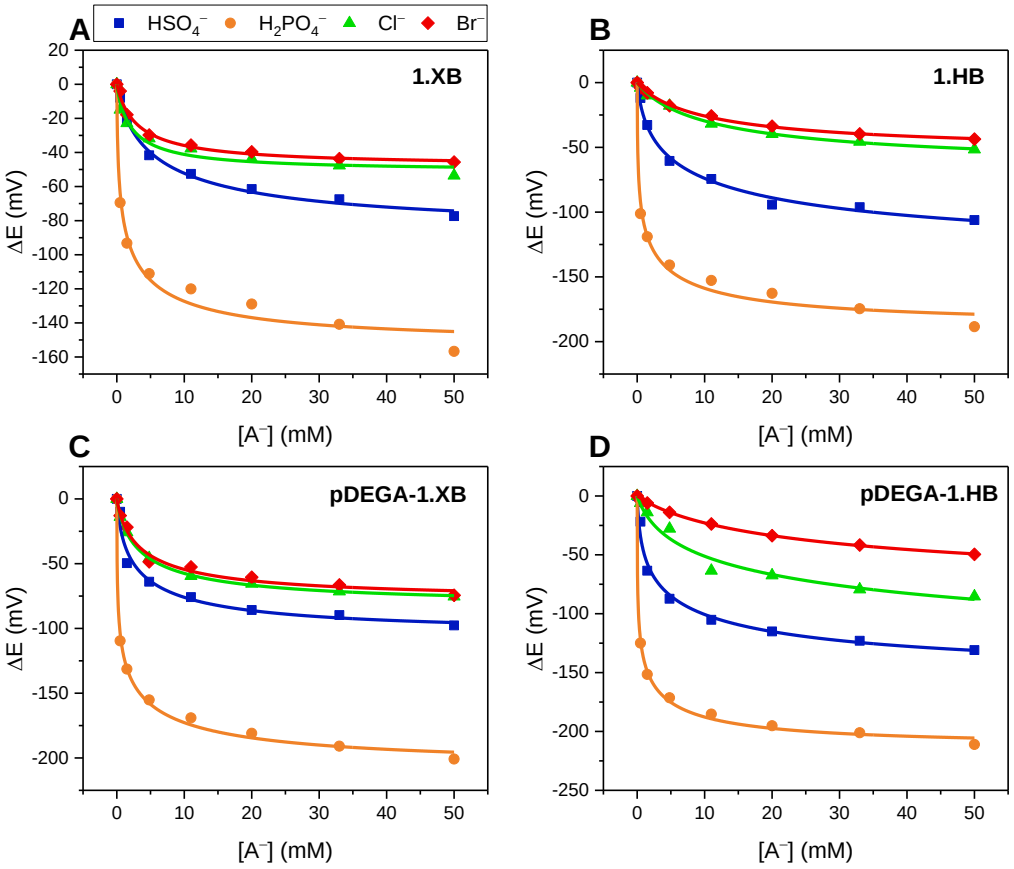


Figure 2.6.2-1. Response isotherms in 97.5:2.5 acetone/H_2O of (A) **1.XB** (B) **1.HB** (C) **pDEGA-1.XB** and (D) **pDEGA-1.HB** in response to increasing concentrations of HSO_4^- (blue), $H_2PO_4^-$ (orange), Cl^- (green) and Br^- (red) up to 50 mM. All isotherms were fitted to a derived Nernst model (Equation 1.4.2-3).

Table 2.6.2-1. Maximum $\Delta E_{1/2}$ of monomeric receptors **1.XB**/**HB**, and polymeric receptors **pDEGA-1.XB**/**HB** in response to a range of anions (HSO_4^-, $H_2PO_4^-$, Cl^- and Br^-), as determined by SWV titrations in 97.5:2.5 acetone/H_2O. Errors estimated to be ± 5 mV.

	ΔE_{max} (mV)			
Anion	**1.XB**	**pDEGA-1.XB**	**1.HB**	**pDEGA-1.HB**
HSO_4^-	–77.4	**–97.7**	–106	**–131**
$H_2PO_4^-$	–157	**–201**	–188	**–211**
Cl^-	–53.6	**–75.4**	–51.6	**–85.3**
Br^-	–45.6	**–74.4**	–43.6	**–49.6**

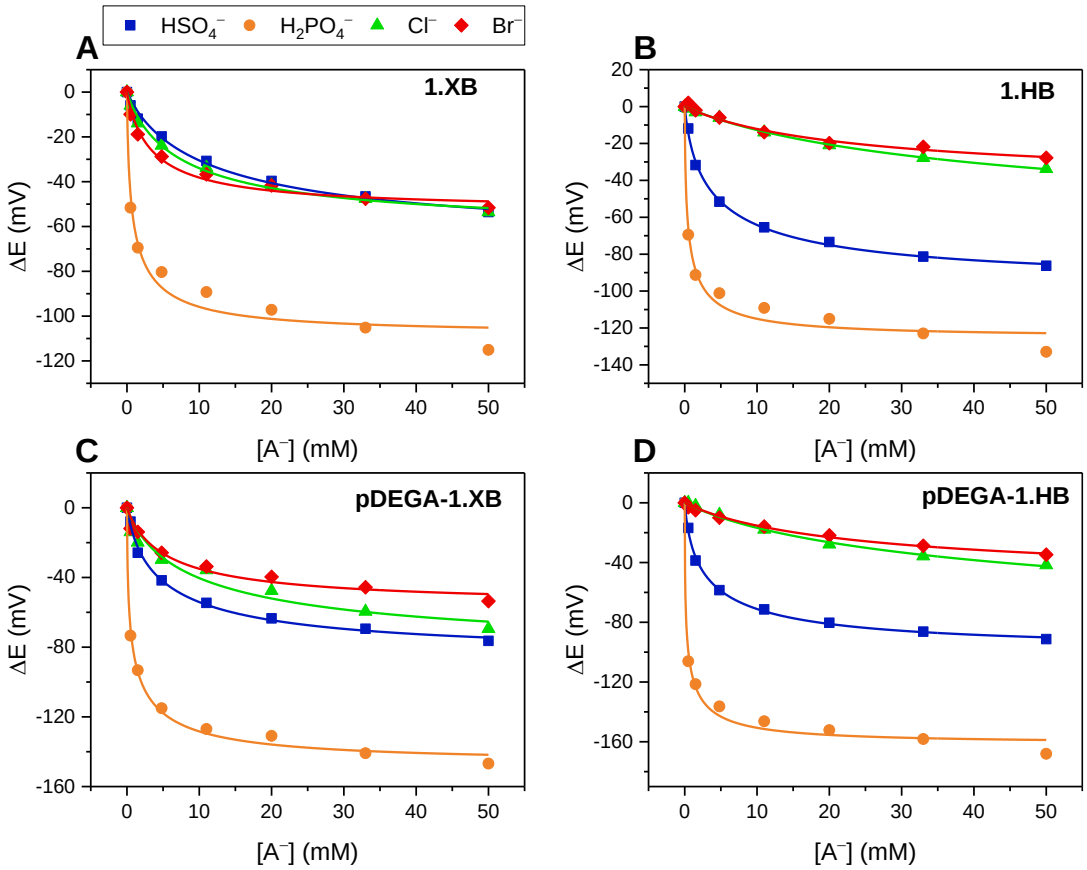


Figure 2.6.2-2. Response isotherms in 97.5:2.5 ACN/H_2O of (A) **1.XB** (B) **1.HB** (C) **pDEGA-1.XB** and (D) **pDEGA-1.HB** in response to increasing concentrations of HSO_4^- (blue), $H_2PO_4^-$ (orange), Cl^- (green) and Br^- (red) up to 50 mM. All isotherms were fitted to a derived Nernst model (Equation 1.4.2-3).

Table 2.6.2-2. Maximum $\Delta E_{1/2}$ of monomeric receptors **1.XB**/**HB**, and polymeric receptors **pDEGA-1.XB/HB** in response to a range of anions (HSO_4^-, $H_2PO_4^-$, Cl^- and Br^-), as determined by SWV titrations in 97.5:2.5 ACN:H_2O. Errors estimated to be ± 5 mV.

	ΔE_{max} (mV)			
Anion	**1.XB**	**pDEGA-1.XB**	**1.HB**	**pDEGA-1.HB**
HSO_4^-	–53.6	**–76.4**	–86.3	**–91.3**
$H_2PO_4^-$	–115	**–147**	–133	**–168**
Cl^-	–53.6	**–69.4**	–33.7	**–41.7**
Br^-	–51.6	**–53.6**	–27.8	**–34.7**

Of immediate note, are the significant enhancements in response from the monomeric (**1.XB**/**HB**) hosts to their polymeric counterparts (**pDEGA-1.XB**/**HB**), as quantified in Table 2.6.2-3 and representatively shown in Figure 2.6.2-3. In all cases, the ratio of the maximum cathodic shift of $E_{1/2}$ (ΔE_{max}) for the monomer and polymer, the so-called polymeric enhancement factor (PEF = $\Delta E_{max,\,poly}/\Delta E_{max,mon}$) is above unity, signifying the outperformance of the polymeric hosts over their constituent receptive monomer. Interestingly, this polymeric enhancement effect also appears to be most impactful for the halides, with a PEF of up to 1.6 for **pDEGA-1.XB** *vs*. **1.XB** in response to Br^- and 1.7 for **pDEGA-1.HB** *vs*. **1.HB** in response to Cl^-, both in 97.5:2.5 acetone/H_2O.

Table 2.6.2-3. Ratio of maximum change in $E_{1/2}$ (ΔE_{max}) of polymeric hosts **pDEGA-1.XB**/**HB** and monomeric receptors **1.XB**/**HB**, representing the polymeric enhancement factor (PEF = $\Delta E_{max,\,poly}/\Delta E_{max,mon}$ determined by SWV titrations in 97.5:2.5 acetone/H_2O, and 97.5:2.5 ACN/H_2O. Errors estimated to be 10%.

	Polymeric Enhancement Factor ($\Delta E_{max,\,poly}/\Delta E_{max,mon}$)			
	97.5:2.5 acetone/H_2O		**97.5:2.5 ACN/H_2O**	
	pDEGA-1.XB/1.XB	**pDEGA-1.HB/1.HB**	**pDEGA-1.XB/1.XB**	**pDEGA-1.HB/1.HB**
HSO_4^-	1.3	1.2	1.3	1.1
$H_2PO_4^-$	1.3	1.1	1.3	1.3
Cl^-	1.4	1.7	1.3	1.2
Br^-	1.6	1.1	1.0	1.2

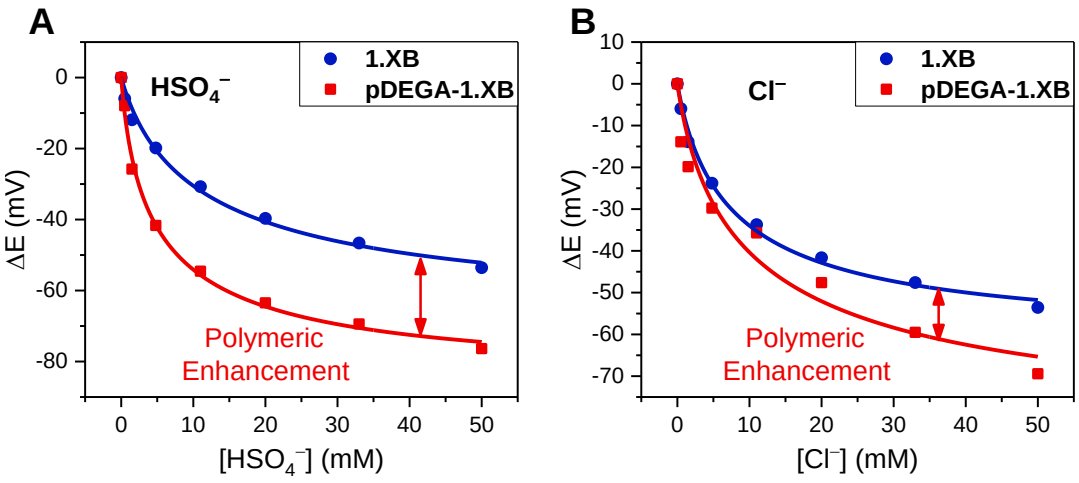


Figure 2.6.2-3. Binding isotherms for **1.XB** (blue circles) and **pDEGA-1.XB** (red squares) in 97.5:2.5 ACN/H_2O with 100 mM $TBAClO_4$ as supporting electrolyte, demonstrating the enhanced binding responses of the polymeric system as observed in response to (A) HSO_4^- and (B) Cl^-.

Analogously to the control experiment performed above for ^{1}H NMR anion binding studies, a control study was undertaken with **1.XB** in the presence of 9 eqvs. of a **pDEGA** non-receptive, homopolymer (mimicking the stoichiometry and local concentration of binding units in **pDEGA-1.XB**). Initially, the native $E_{1/2}$s of **1.XB** and **1.XB** + 9 eqvs. of **pDEGA** were compared and found to be near-identical ($E_{1/2}$ = 127 mV vs. 123 mV, respectively, in 97.5:2.5 ACN/H_2O). These are notably different from **pDEGA-1.XB** ($E_{1/2}$ =144 ± 2 mV), suggesting that the uniquely low local ε_r environment is only established around **1.XB** when it is covalently incorporated within the polymeric scaffold of **pDEGA-1.XB** (see Figure 2.6.2-4A). Further support for this arises from the fact that the anion sensing behaviour of **1.XB** is once again near-identical for Br^- in 97.5/2.5 ACN/H_2O whether used alone, or in the presence of 9 eqvs. of **pDEGA** (ΔE_{max} values within 2 mV, < 4% difference w.r.t. **1.XB** alone, see Figure 2.6.2-4B).

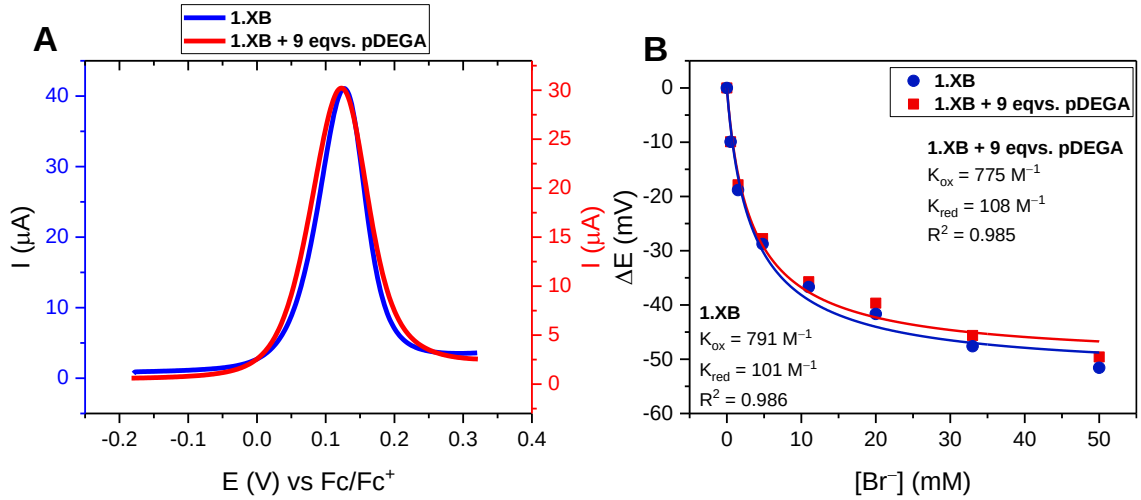


Figure 2.6.2-4. (A) Square wave voltammograms of 0.1 mM **1.XB** (blue line) and 0.1 mM **1.XB** + 9 eqvs. **pDEGA** (red line) in 97.5:2.5 ACN/H_2O with 100 mM $TBAClO_4$ as supporting electrolyte. (B) Response isotherms in 97.5:2.5 ACN/H_2O of **1.XB** (blue symbols) and **1.XB** + 9 eqvs. **pDEGA** (red symbols) in response to increasing concentrations of Br^- up to 50 mM. All isotherms were fitted to a derived Nernst model (Equation 1.4.2-3).

Crucially, the results described above corroborate the analogous observations from the ^{1}H NMR anion binding studies, confirming that this polymeric enhancement effect is applicable and significant for both the neutral and charged (upon oxidation of Fc to Fc^+) polymeric species. Once again, this augmentation of binding/response is attributed to the comparatively lower local ε_r environment afforded by the surrounding DEGA comonomer units, which are expected to shield the binding microenvironment and result in stronger binding/greater perturbations to $E_{1/2}$.

Although the substantial polymeric enhancements described above are well supported by both ^{1}H NMR and electrochemical analyses, the supplementary augmentation in anion binding strength observed by ^{1}H NMR at **pDEGA-BuA-1.XB** with respect to **pDEGA-1.XB** could not be replicated by electroanalyses. Instead, both polymeric hosts exhibit very similar resolved responses to the target anions in either solvent system, as representatively shown in Figure 2.6.2-5. This may be a result of electrolyte ingression into the polymeric scaffold to some extent during electrochemical studies, which is not present during ^{1}H NMR analyses. Considerable further studies would be required to better understand these effects by repeating all titrations (both ^{1}H NMR and voltammetric studies) at different ionic strengths, or using different supporting electrolytes, for example.

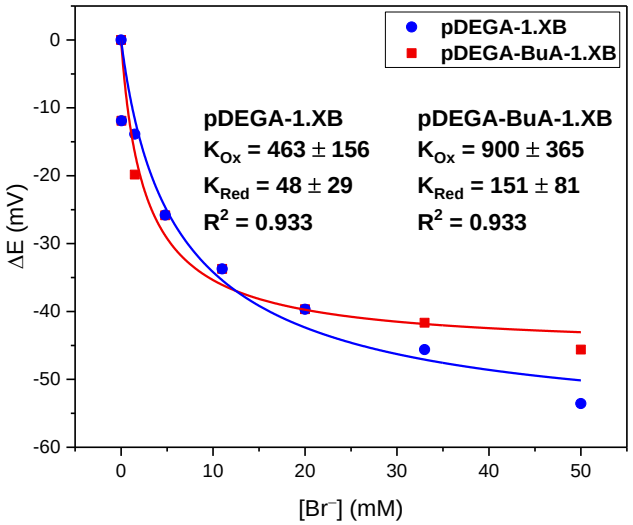


Figure 2.6.2-5. Voltammetric response isotherms for **pDEGA-1.XB** (blue circles) and **pDEGA-BuA-1.XB** (red squares) in response to increasing concentrations of Br^- up to 50 mM in 97.5:2.5 ACN/H_2O, 100 mM $TBAClO_4$ as supporting electrolyte.

As highlighted above, individual anion binding constants for the neutral (K_{Red}) and oxidised (K_{Ox}) receptors can be extracted by fitting the resolved anion response isotherms to Equation 1.4.2-3 (all tabulated data can be found in Appendices A2, Tables A2.1 – S2.4). On first consideration, one would expect the neutral K_{Red} values to equate to those determined by ^1H NMR and in several cases for **1.XB**, this is true (see Tables 2.6.2-4 and 2.6.2-5). However, greater deviations are displayed for **pDEGA-1.XB** which reflects the complexity of the binding equilibria involved for these species (see Section 1.4.2 for further detail), as well as other potential contributing factors, such as the presence and relative penetration of electrolyte within receptor structure, the extent of solvent penetration or the impact of deuterated *vs*. hydrogenated solvents.

Table 2.6.2-4. Comparison of the K_a values for **1.XB** and **pDEGA-1.XB** determined from ^{1}H NMR and voltammetric titrations (K_{Red}, as determined from fitting isotherms with a 1:1 host-guest Nernst model (K_{Ox}/K_{Red}, Equation 1.4.2-3) in 97.5:2.5 acetone/H_2O (deuterated for NMR titrations).

	1.XB		pDEGA-1.XB	
	NMR	**Echem**	**NMR**	**Echem**
HSO_4^-	N/A	31	N/A	46
$H_2PO_4^-$	60	59	410	36
Cl^-	170	170	910	55
Br^-	470	124	2200	58

Table 2.6.2-5. Comparison of the K_a values for **1.XB** and **pDEGA-1.XB** determined from ^{1}H NMR and voltammetric titrations (K_{Red}, as determined from fitting isotherms with a 1:1 host-guest Nernst model (K_{Ox}/K_{Red}, Equation 1.4.2-3) in 97.5:2.5 ACN/H_2O (deuterated for NMR titrations).

	1.XB		pDEGA-1.XB	
	NMR	**Echem**	**NMR**	**Echem**
HSO_4^-	N/A	22	N/A	38
$H_2PO_4^-$	10	159	80	95
Cl^-	20	38.5	230	18
Br^-	60	101	840	58

Summarising the electrochemical analyses of the monomeric and polymeric hosts:

- Well-resolved, single-electron voltammetric traces were resolved for all monomeric and polymeric hosts, signifying that both Fc transducers are addressed simultaneously
- Comparison of the dependence of the host's $E_{1/2}$ values on external solvent polarity is proposed to present a semi-quantitative approach to assess the local ε_r constant within the polymeric host, with lower ε_r values representing shielded micro-environments that would be expected to augment anion binding strength
- Greater voltammetric responses were observed in all cases for the polymeric hosts upon addition of target anions (Cl^-, Br^-, $H_2PO_4^-$ and HSO_4^-) w.r.t. their monomeric analogues, but polymeric enhancements were generally lower than those displayed in ^{1}H NMR anion binding studies

2.7 Conclusions & Future Work

2.7.1 Conclusions

This chapter presents, for the first time, a comprehensive characterisation and comparison of the anion binding performance of monomeric and polymeric hosts based on XB or HB-mediated binding. A family of redox-active, anion-receptive polymers were generated from constituent XB/HB bis((iodo)-triazole-ferrocenyl) monomeric units and extensively characterised by a range of physical and electrochemical techniques. The anion binding and sensing performance of both classes of host were then systematically investigated and contrasted through ^{1}H NMR binding studies and voltammetric sensing studies. Importantly, this revealed that incorporation of relatively simple XB binding motifs into a co-polymeric architecture enabled a substantial augmentation of anion binding strength in highly competitive organic-aqueous solvent systems. The magnitude of this so-called polymeric enhancement effect was corroborated and quantified through complimentary ^{1}H NMR and voltammetric approaches, revealing enhancements of up to 15x greater binding strength for I^- from the XB monomer **1.XB** to the copolymer **pDEGA-1.XB**, and greater still (47x) at **pDEGA-BuA-1.XB** upon judicious incorporation of more hydrophobic BuA units (schematised in Figure 2.7.1-1). Furthermore, the more shielded, low ε_r binding microenvironment established within the copolymeric scaffold also offered a greater tolerance for anion binding strength to increasing bulk solution polarity, signifying a promising avenue towards effective anion recognition/sensing in aqueous, polar media. These effects were particularly pronounced for the XB polymers which significantly outperformed their

HB counterparts, consolidating the use of XB binding motifs over HB units in competitive media. By virtue of the resolved $E_{1/2}$ values from the appended redox-active ferrocene units, semi-quantitative assessments of the local dielectric constants within the polymeric structures could be ascertained, corroborating the observed anion binding enhancements and providing a means to probe local physical characteristics. Additionally, this versatile and comparably synthetically facile approach (with respect to highly preorganised and structurally complex discrete molecular hosts), offers a promising and powerful alternative to more traditional approaches in supramolecular designs for ion receptors.

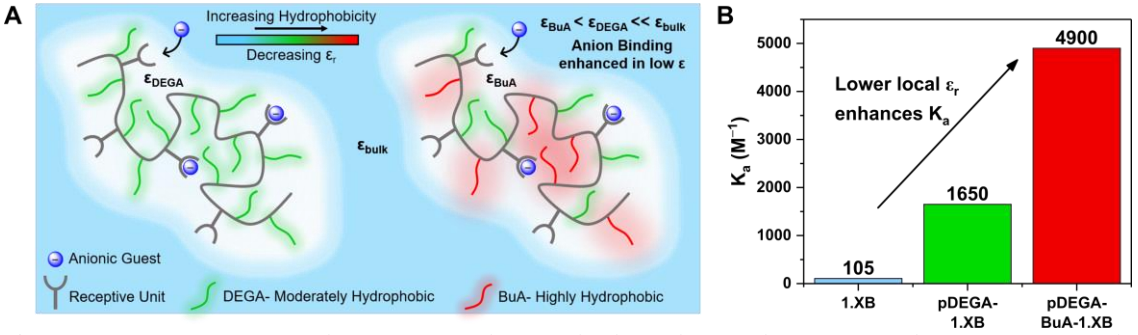


Figure 2.7.1-1. (A) Schematic representation of binding microenvironment tuning by the strategic use of more hydrophobic co-monomers. (B) Enhancement of I^- binding constants with a series of hosts: **1.XB**, **pDEGA-1.XB** and **pDEGA-BuA-1.XB**, as determined from ^{1}H NMR titrations.

2.7.2 Future Work

As speculated above, further tuning of the anion binding performance through judicious choice of functional co-monomers would be a key target for future work. For example, per-fluorinated monomers (1H,1H,2H,2H-nonafluorohexyl acrylate, for example) would be expected to impart an even lower polarity on the local binding environment, in turn enhancing anion binding strength beyond the 47-fold augmentation observed between **1.XB** and **pDEGA-BuA-1.XB**. In order to achieve this, though, consideration must be given to the reaction conditions as well as the

resulting polymer's characteristics to ensure that it remains adequately soluble in competitive organic-aqueous solvent media. To circumvent this issue, and probe the impact of modified local environments further, the polymeric hosts could be surface-immobilised onto electrode surfaces (*e.g.*, Au or glassy carbon) via physisorption by drop-casting or spin-coating. By confining the polymers to a 2D surface, host solubility issues can be all but avoided, thus expanding the scope of solvent media which can be used. Furthermore, surface-immobilisation of receptive motifs is well-established to enhance response magnitudes and/or ion binding strengths, which is proposed to proceed through a similar mechanism to that discussed above; by establishing a local ε_r within the generated film which is distinctly lower than that of the surrounding bulk media (amongst other factors, see Section 1.3 for further details). Multivalent effects could also be explored by increasing the ratio of receptive to non-receptive monomer within a polymeric host, bringing the receptive units closer in space to promote higher order host-guest binding modes (*e.g.*, 2:1). Upon confirmation of these higher order host-guest binding modes, anion binding strengths could then be further modified through crosslinking to investigate multivalent effects on anion binding performance as a function of polymer conformational rigidity.

Together, these investigations would provide additional insight into the role of local binding microenvironments, and how they can be engineered and tuned to afford the most effective anion binding sites for recognition in competitive, aqueous media.

Chapter 3

Continuous Voltammetric Anion Sensing

Chapter 3: Continuous Voltammetric Anion Sensing

3.1 Introduction & Chapter Aims

Substantial progress has been made in augmenting the potency of supramolecular hosts by improving target specificity and binding strength in polar, competitive media. In order to translate these potent receptors into practically tenable methods for continuous ion monitoring, effective and complementary sensing techniques must also be developed.

Despite the pertinence of real-time ion sensing to a wide variety of environmental and technical scenarios (*e.g.*, long-term health and water monitoring), progress has been impeded by attempts to effectively translate existing methodologies into appropriate (low-cost, scalable, sustainable *etc.*) microfluidic setups, whilst maintaining a high degree of sensitivity that can rivel established analytical techniques such as ^{1}H NMR or high resolution mass spectrometry.[231, 232] Progress is crucial, however, as these established techniques are often prohibitively expensive to run frequently, are highly resource intensive and are either impossible or extremely challenging to run continuously for real-time monitoring applications. Owing to their scalability, ease of use, high sensitivity and low cost, electrochemical ion sensing methodologies are ideally suited to address this challenge.[150, 233] To date, the only electroanalytical ion sensing approach which has demonstrated any significant applicability toward real-world-relevant applications are ion-selective electrodes (ISEs) (see Section 1.4.1 for more information on their operation).[234-236]

As noted in Section 1.4.1, though, ISEs often suffer from slow response times, poor selectivity and an inherently limited sensitivity (thermodynamically limited by the Nernst equation).[237, 238] Therefore, alternative electroanalytical ion sensing methodologies that address these limitations are highly sought after.

Aside from potentiometric (*i.e.*, ISE-based) approaches, voltammetric ion sensors based on redox-active, ion-receptive hosts have emerged as a powerful means to probe host-guest binding events, both in solution[180, 181, 230, 239-248] and at receptive interfaces.[137, 140, 141, 227, 249-254] A notable advantage of these supramolecular redox sensors is an intimate binding transduction mechanism that is natively coupled to a (redox) modulation of ion binding strength. For example, anion binding can be significantly enhanced upon the *in situ* electrochemical generation of an oxidised, cationic receptor state, which in turn has enables anion binding, and sensing, in more polar, competitive (and real-world-relevant) solvents.[141, 150] As highlighted in Section 1.3.2, there are numerous benefits to surface-immobilising hosts, and accordingly, interfacial voltammetric ion sensing has, garnered significant attention in recent years.[140, 141, 227, 254-256] Notably, these advantages include enhanced response magnitudes, removed solubility limitations, practical real-world translation and sensor re-use.[141, 257] In spite of these advantages, the application of such potent sensors for continuous ion monitoring purposes remains unrealised.

In order to achieve this, two main challenges have to be addressed; firstly, the sensor must operate continuously and secondly, the system must output a simple and calibratable ion-specific response signal. The transient, non-equilibrium nature of voltammetry (where responses are obtained via analysis of acquired

voltammograms) makes this a significant challenge. This is rarely of concern in academic studies, where the manual analysis of small data sets is not problematic, but is highly relevant to practical translation where large data sets must be processed and stored appropriately.

This chapter aims to address both of these challenges by incorporating a model redox-active, anion-receptive sensing film (ferrocene-isophthalamide-(iodo)triazole SAMs **3.XB**/**HB$_{SAM}$**) into a custom 3D-printed flow cell, marking the first example of systematic anion sensing assays under continuous flow as assessed via voltammetry. Additionally, a method for semi-automatic data analysis of the resulting sensograms will be developed, to handle the large data sets (100s of voltammograms per assay) acquired over multiple hours.

To summarise, the aims for Chapter 3 are:

- Develop a voltammetric method based on square wave voltammetry that can be operated continuously to monitor anion binding in real-time
- Design and generate a 3D-printed microfluidic flow cell to facilitate continuous voltammetric measurements under continuous flow
- Produce a data processing method using MATLAB to semi-automate the data analysis of the substantial data sets that result from continuous voltammetric measurements
- Compare relevant anion binding and sensing parameters of the continuous voltammetric method w.r.t. standard, static analyses
- Assess the use of continuous voltammetric measurements for long-term sensing applications (over hours, for example)

3.2 3.XB/HB$_{SAM}$ Film Generation & Characterisation

Receptors **3.XB**/**HB** were synthesised by Dr. Robert Hein, following a synthetic protocol designed by Dr. Xiaoxiong Li (see Section 7.11.2 for more details).

In this work a model redox-active, anion-receptive sensing film was utilised, based on previously reported ferrocene-isophthalamide-(iodo)triazole SAMs **3.XB**/**HB$_{SAM}$** (Figure 3.2-1A). Both the synthesis and film characterisation data of these receptors and derived SAMs can be found elsewhere,[179, 210] but briefly, SAMs of **3.XB**/**HB$_{SAM}$** were generated by incubating clean gold electrodes in 0.25 mM **3.XB**/**HB** in ACN overnight in the dark. Importantly, this affords densely-packed (1.01 ± 0.18 x10^{-10} mol cm^{-2} and 1.15 ± 0.22 x10^{-10} mol cm^{-2} for **3.XB**/**HB$_{SAM}$**, respectively) and reproducible SAMs, with associated $E_{1/2}$ values of 193 ± 1 mV and 183 ± 2 mV, for **3.XB**/**HB$_{SAM}$**, respectively, that are sensitive to anion binding in ACN/H_2O solvent mixtures. Specifically, substantial cathodic perturbations to the $E_{1/2}$ of the hosts were displayed in response to increasing concentrations of targets anions: HSO_4^-, $H_2PO_4^-$, NO_3^-, Cl^- and Br^- (see Figure 3.2-1B for a representative example of the response of **3.XB$_{SAM}$** to HSO_4^-).[210]

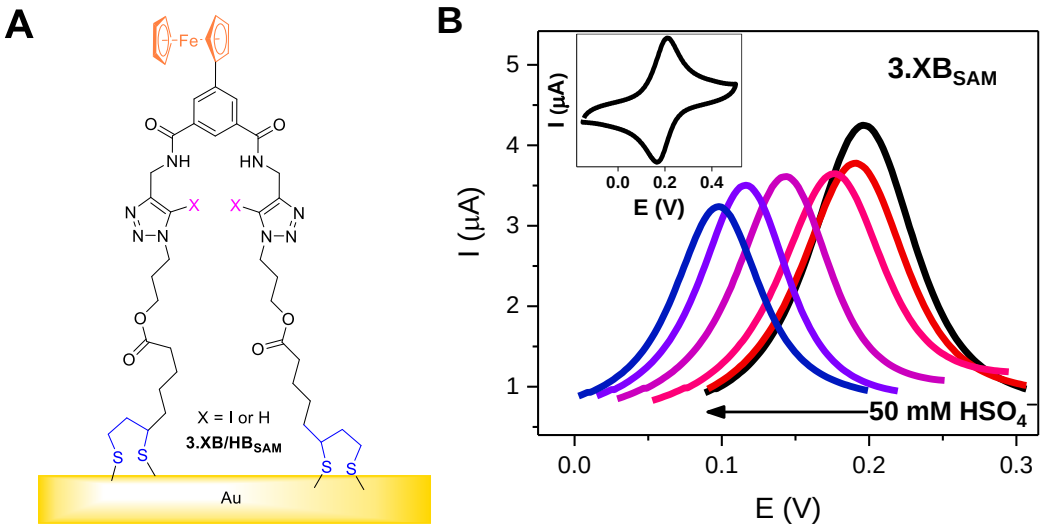


Figure 3.2-1. (A) Schematic depiction of **3.XB/HB$_{SAM}$** on a gold electrode. (B) SWVs showing cathodic voltammetric shifts of SWVs of **3.XB$_{SAM}$** upon titration with HSO_4^- up to 50 mM in ACN/H_2O 99:1, 100 mM $TBAClO_4$, 10 mM $HClO_4$. The inset shows the CV of **3.XB$_{SAM}$** in the same solvent system.

Of note here, is that previous studies of these receptors identified that acidification of the electrolyte with small amounts of $HClO_4$ significantly alleviated the otherwise significant loss of signal upon repeat cycling due to voltammetric degradation (see Figure 3.2-2A). As alluded to in Section 1.4.2, this well-known problem arises from nucleophilic attack of ferrocenium (Fc^+) by adventitious nucleophiles or electrolyte anions. Therefore, degradation can be significantly impeded by adding small amounts of an aqueous electrolyte of low pH, to protonate basic nucleophiles and scavenge them.[258-261] This results in a peak current retention of 99% after 100 cycles and 91% after 500 cycles for **3.HB$_{SAM}$** with the addition of 10 mM $HClO_4$ (see Figure 3.2-2A), whilst signal loss in the absence of acid was much larger (only 36% current retention after 100 cycles). This high voltammetric stability enables sensor re-use with high signal integrity as shown in Figure 3.2-2B. Importantly, this is possible with minimal detriment to anion sensing, as discussed below.

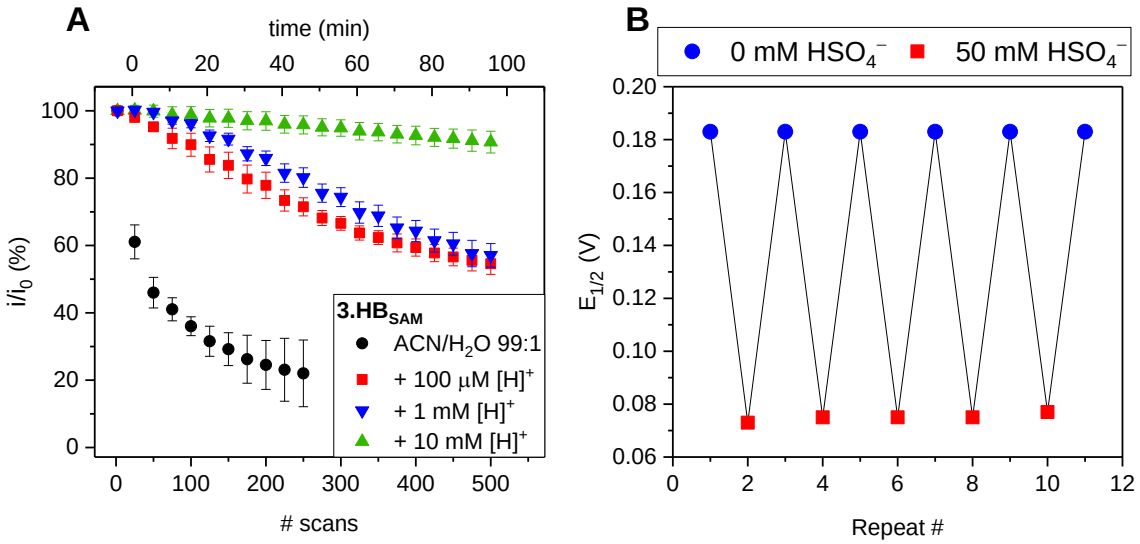


Figure 3.2-2. (A) Redox stability, as assessed by the relative decrease in peak currents (i/i_0), of **3.HB$_{SAM}$** upon repeated cycling in ACN/H_2O 99:1, 100 mM $TBAClO_4$ in the presence of various concentrations of $HClO_4$. The measurements in the absence of acid (black circles) were stopped after 250 scans. The measurements in the absence of acid were terminated after 250 scans. (B) Potential response to the HSO_4^- anion of **3.HB$_{SAM}$** in ACN/H_2O 99:1, 10 mM $HClO_4$ in the alternating absence and presence of 0 or 50 mM HSO_4^-.

3.3 Static Voltammetric Anion Sensing Performance of 3.XB/HB$_{SAM}$

Static anion sensing studies were performed by Dr. Robert Hein and Dr. Xiaoxiong Li.[210]

Whilst acidification of the electrolyte does substantially improve long-term signal retention by suppressing voltammetric degradation, it would be remiss to not consider the potential effects of this on anion binding/sensing performance. For example, it is necessary to consider the protonation state of the target anionic species (dependent on [H^+] and anion basicity), given that the conjugate acid is not expected to bind to the receptors. However, the specific degree of protonation of the target anions is difficult to assess in the mixed electrolyte system used herein (ACN/H_2O 99:1), as it is likely that the well-known acidity trends in water ($HClO_4$ > HCl > H_2SO_4 > H_3PO_4) do not directly translate to an organic/aqueous system. For

example, in pure ACN the following trend would be expected: $HClO_4$ > HBr > H_2SO_4 > HNO_3 > HCl.[262] Nevertheless, approximate trends can be extrapolated from these series, such that $HClO_4$ can be assumed to be the strongest acid, capable of almost complete protonation of $H_2PO_4^-$, but minimal protonation of anions of low basicity such as HSO_4^- and Cl^-. The sensing performance of **3.XB/HB$_{SAM}$** in response to HSO_4^- or Cl^- was therefore relatively unchanged upon increasing electrolyte acidification (see Figures 3.3-1A-B and 3.3-2A-B), whereas a noticeable delay was observed in the voltammetric response to $H_2PO_4^-$ (*i.e.*, significant responses to $H_2PO_4^-$ are only observed when $[A^-] > [H^+]$, see Figures 3.3-1C and 3.3-2C). These results are explored in greater detail elsewhere,[210] but, crucially, the response patterns of both **3.XB/HB$_{SAM}$** in the presence of various acid concentrations were identical. Therefore, it can be concluded that the acid only influences the solution-phase composition (*i.e.*, the degree of anion protonation), which does not directly influence the binding/response behaviour of the films.

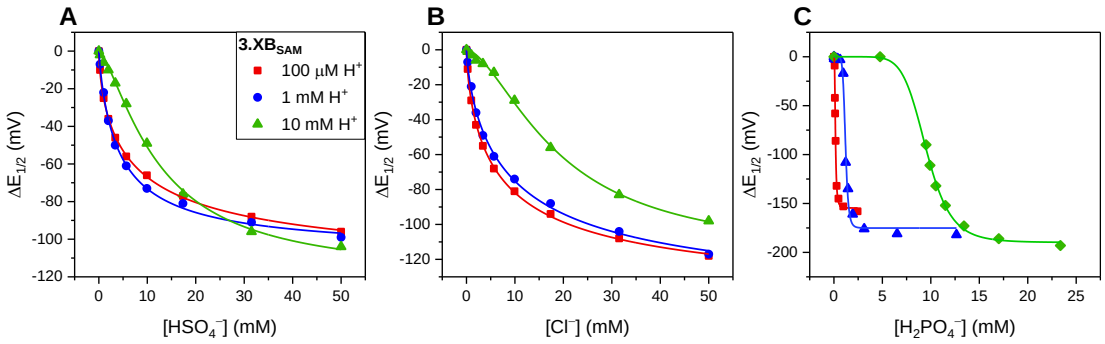


Figure 3.3-1. Cathodic voltammetric shifts of **3.XB$_{SAM}$** upon titration with (A) HSO_4^- (B) Cl^- and (C) $H_2PO_4^-$ in ACN/H_2O 99:1 and various concentrations of acid. Lines represent fits to the Langmuir-Freundlich model (Eqn. 3.3-1).

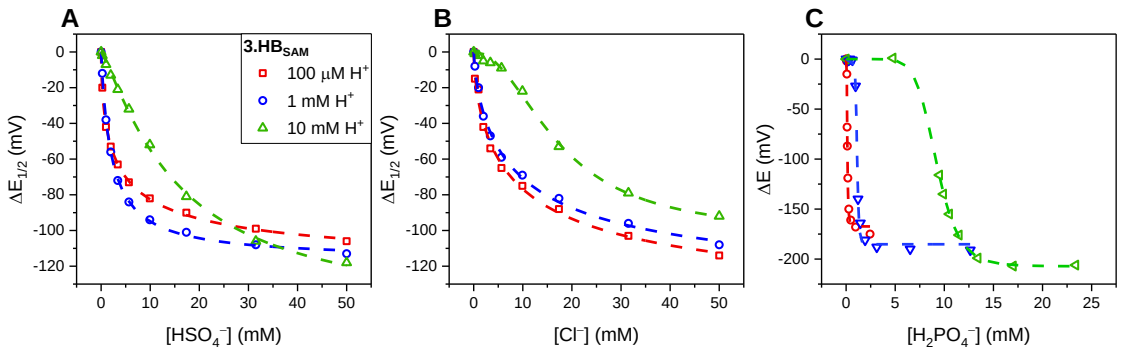


Figure 3.3-2. Cathodic voltammetric shifts of **3.HB$_{SAM}$** upon titration with (A) HSO_4^- (B) Cl^- and (C) $H_2PO_4^-$ in ACN/H_2O 99:1 and various concentrations of acid. Lines represent fits to the Langmuir-Freundlich model (Eqn. 3.3-1).

The only notable implication of this for this work is that standard binding models (*i.e.*, the 1:1 Nernst model, Equations 1.4.2-2 or 1.4.2-3) do not accurately describe the resolved response isotherms in the presence of 10 mM $HClO_4$ (as used for all following anion sensing studies in Chapters 3 and 4, unless stated otherwise). This arises because the pK_a, and therefore the concentration of free anion in this solvent system are not known, thus, no correction or adjusted binding model can be applied to accurately account for this. Therefore, a Langmuir-Freundlich model (Equation 3.3-1), derived from the classical Langmuir model (Equation 3.3-2), is utilised instead as a semi-quantitative, semi-empirical model to describe the voltammetric sensor response to anionic targets.

$$\theta = \frac{(K_{app} * [A^-])^n}{1+(K_{app} * [A^-])^n} \qquad \textbf{Equation 3.3-1}$$

$$\theta = \frac{K_{app} * [A^-]}{1+K_{app} * [A^-]} \qquad \textbf{Equation 3.3-2}$$

The classical use of the Langmuir model was to describe adsorption processes from the gas or liquid phase to surfaces,[263] but here it is used to describe guest binding to a surface composed of a monolayer of receptors. The major assumptions for the Langmuir model are that there are a fixed number of binding sites and that none of the binding sites or recruited guests interact with each other (binding occurs

independently at each site), each site has an equal affinity for the guest, each of the defined binding sites only accepts one guest (1:1 host-guest binding occurs), and finally that the surface is a monolayer (multilayers are not formed). The interaction between each host, H and guest, G can be represented by the equilibrium given by Equation 3.3-3, where k_a and k_d are the rate constants for adsorption (binding) and desorption (release), respectively.

$$H + G \underset{k_d}{\overset{k_a}{\rightleftharpoons}} HG$$

Equation 3.3-3

Given that binding is expected to occur much faster than the electrochemical processes involved to assess binding herein, host-guest binding can be considered at equilibrium in all cases. Therefore, the equilibrium constant (or binding constant, K_{app} here) can be given by Equation 3.3-4:

$$K_{app} = \frac{[HG]}{[H]*[G]}$$

Equation 3.3-4

K_{app} here represents neither the anion binding constants to the oxidised (**3.XB/HB$_{SAM}^{+}$**, K_{Ox}) nor reduced (neutral) receptor states (**3.XB/HB$_{SAM}$**, K_{Red}), but lies in between both and represents a measure of general anion binding/sensing performance.

The fraction of binding sites that are occupied by guests can be defined by the surface coverage, θ (Equation 3.3-5):

$$\theta = \frac{[G]_{bound}}{[H]_{total}} = \frac{[HG]}{[H]_{free}+[HG]}$$

Equation 3.3-5

Substituting according to the relationship given in Equation 3.3-6, θ can then be given as:

$$\theta = \frac{K_{app}*[G]}{1+K_{app}*[G]} = \frac{K_{app}*[A^-]}{1+K_{app}*[A^-]} \qquad \textbf{Equation 3.3-6}$$

The Langmuir-Freundlich model is an adapted form of the Langmuir model, which accounts for surface heterogeneity by describing the distribution of adsorption energy onto heterogeneous surfaces with a parameter, n, that lies between 0-1.[264] Expectedly, Equation 3.3-1 simplifies to a classical Langmuir model (Equation 3.3-2), when n = 1 (*i.e.*, the surface is homogeneous). In the context of this work in Chapters 4 and 5, n accounts for the "heterogeneity" imposed by partial anion protonation.

In the case of $H_2PO_4^-$, it can be assumed that full protonation occurs until $[Anion] = [H^+]$, such that at concentrations of $[Anion] > [H^+]$ no acid is present and the subsequent response obeys standard binding models. In this case the binding isotherm is largely identical to that obtained in the absence of acid but is shifted (*i.e.*, offset) by $\approx [H^+]$. For sake of simplicity and comparisons with the other anions, Equation 3.3-1 is still utilised to describe the $H_2PO_4^-$ sensing isotherms. Nevertheless, for quantitative analyses according to this model (*i.e.*, to obtain K_{app}), all $H_2PO_4^-$ isotherms were corrected by –10 mM $H_2PO_4^-$ prior to fitting (see Figure 3.7-4). Similarly, the LODs given for $H_2PO_4^-$ are "apparent" LODs in the "absence" of acid, *i.e.*, are also corrected by –10 mM.

To summarise thus far, the capability of **3.XB/HB$_{SAM}$** to reversibly recruit and respond to anions with high levels of signal stability has been established in a

standard ("static") electrochemical set-up. With a proof-of-principle application of these sensory interfaces for real-time and continual anion sensing in mind, microfluidic flow cells were thus designed to enable anion sensing under continuous flow, *vide infra*.

3.4 Microfluidic Flow Cell Design

The custom-designed and 3D-printed electrochemical flow cell was produced by Dr. Mohamed Sharafeldin.

An efficient route to obtaining a continuous sensing mode is via studies under continuous flow, whereby the target species is delivered to the receptive interface where it induces a significant response, and is then subsequently removed upon washing the interface with fresh electrolyte. This procedure is schematised in Section 1.4.2, which displays the predicted, ideal response profile displayed in resulting sensograms (plots of signal/response *vs*. time).

To this end, a custom electrochemical flow cell (see Figure 3.4-1) was designed and subsequently 3D-printed in photocurable resin to house a standard 3-electrode cell (Pt wire counter electrode, Ag|$AgNO_3$ reference electrode and Au disc electrode which is functionalised with **3.XB**/$\mathbf{HB_{SAM}}$). Specific details regarding the dimensions and production of the flow cell, and the supporting components of the microfluidic setup (tubing, syringe pump and manual injector) can be found in Section 7.9.2 (Figures 7.9.2-1 and 7.9.2-2).

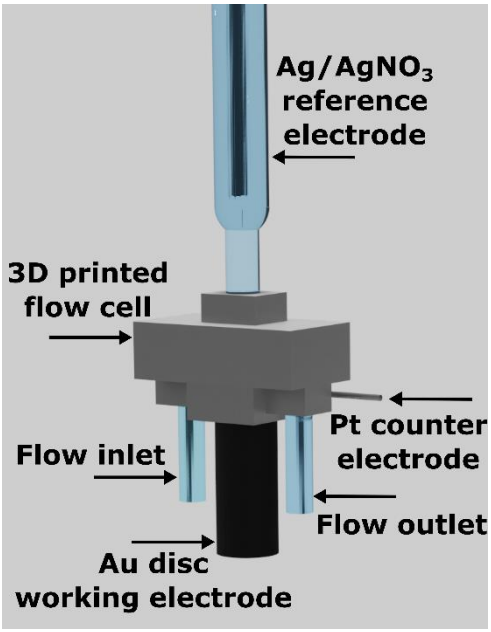


Figure 3.4-1. Schematic depiction of the 3D-printed electrochemical flow cell with an internal chamber of 100 µL was designed.

A syringe pump was used to continuously pump electrolyte (ACN/H_2O 99:1, 100 mM $TBAClO_4$, 10 mM H^+) through the flow cell, and sample aliquots ([A^-] = 0 – 50 mM, typically 500 µL) were delivered via a manual injector valve system at a flow rate of 500 µL min^{-1} (Reynolds number = 38, *cf*. less than 2000 signifies laminar flow). This flow rate was selected to ensure a rapid and complete replacement of the internal cell chamber by the injected sample aliquots, thereby confirming that any measurable changes in signal (*i.e.*, $\Delta E_{1/2}$) result from specific anion binding at the interface. Additionally, a rapid mixing stage ensures that the intended concentration of the target analyte is consistently maintained at **3.XB/HB_{SAM}**. Furthermore, this flow rate exposed **3.XB/HB_{SAM}** to the sample analyte for a sufficient duration of time to observe the response plateau, ensuring that the maximum response magnitude induced at each target concentration was reliably obtained. It should also be noted that this flow cell was tolerant to a large range of

flow rates (0.1 - 2 mL min^{-1}) and displayed a stable, flow rate-independent voltammetric response (see Figure 3.4-2).

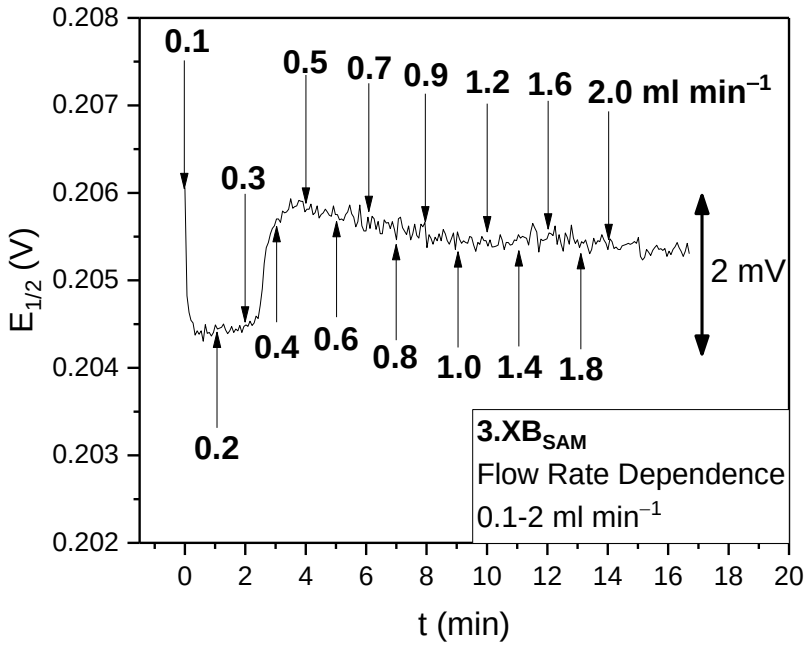


Figure 3.4-2. Dependence of $E_{1/2}$ of **3.XB$_{SAM}$** on flow rate, over a range of 100 to 2000 µl min^{-1}. Arrow indicates that the total potential fluctuation is within ±2 mV.

3.5 Continuous Voltammetric Anion Sensing

In analogy to those performed under standard, static conditions, anion sensing studies under continuous flow were carried out by monitoring changes in the $E_{1/2}$ (determined here as the peak potential of the SW voltammogram) of the $Fc|Fc^+$ couple of the **3.XB/HB$_{SAM}$s** ($\Delta E_{1/2}$) via repeat SWV cycling. SWV was selected as the electroanalytical technique of choice here, both for consistency with the static experiments but also its high sensitivity over other pulse techniques such as differential pulse voltammetry (DPV) or linear sweep voltammetry (LSV) due to minimal contributions from background, non-Faradaic currents.[265]

The continuous SWV experiments were conducted with a step potential (E_{step}) of 5 mV, an amplitude of 20 mV and a frequency (f) of 50 Hz over a potential range (E_{range})

of 550 mV (-0.25 – 0.3 V). This window was chosen as it encompasses the original $E_{1/2}$ (≈0.2 V) as well as cathodic perturbations of the Fc/Fc^+ couple by up to -200 mV. These parameters were optimised in order to minimise t_{scan}, whilst still maintaining confidence in accurately determining $E_{1/2}$ (*i.e.*, maintaining a suitable resolution of each SW scan). To reduce the time between each SW voltammogram, all pre/post-equilibration times were set to 0 s. A SW amplitude of 20 mV was used throughout; variation in applied amplitude does not affect measuring time. Initially, continuous SWV studies were performed under identical conditions as typically employed for standard, static titrations, *i.e.*, with a step potential (E_{step}) of 2 mV, an amplitude of 20 mV and a frequency (f) of 25 Hz over a potential range (E_{range}) of 550 mV (–0.25 – 0.3 V).

However, with these parameters a single SW scan took ≈12.6 s to record, which, under the experimental flow conditions represents a temporal resolution that is slightly too low to accurately measure the anion specific cathodic shifts (see Figure 3.5-1). With this in mind, the SWV parameters were optimised in order to reduce t_{scan}, which is theoretically given by Equation 3.5-1. However, in reality a SWV takes somewhat longer to record, as empirically represented by Equation 3.5-2, where c is a constant, instrument-dependent delay upon repeat SWV cycling (≈1 s with the hardware used herein).

Specifically, f was increased to its hardware limit of 50 Hz, thereby approximately halving t_{scan} to ≈7.2 s. Similarly, E_{step} was increased from 2 to 5 mV, affording a further reduction in t_{scan} to ≈3.7 s. Note that the sensing isotherms are completely identical for E_{step} = 2 or 5 mV (when data analysis is carried out with the AsymFit approach).

$$t_{scan} = \frac{E_{range}}{f \times E_{step}} \qquad \textbf{Equation 3.5-1}$$

$$t_{scan} = \frac{E_{range}}{f \times E_{step}} + c \qquad \textbf{Equation 3.5-2}$$

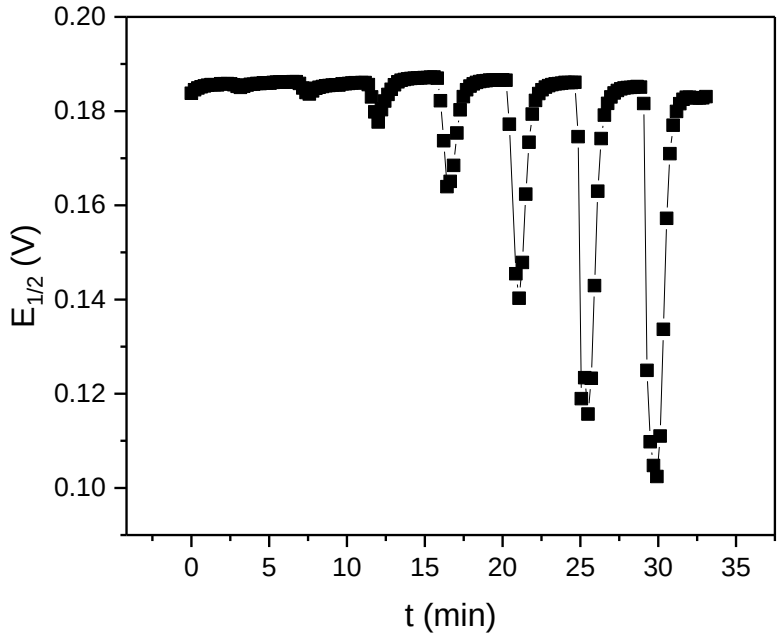


Figure 3.5-1. Sensogram afforded by an initial titration experiment under continuous flow (f = 25 Hz, E_{step} = 2 mV) shown for the response of **3.XB$_{SAM}$** to increasing concentrations of HSO_4^- (up to 50 mM) in ACN/H_2O 99:1 (100 mM $TBAClO_4$, 10 mM $HClO_4$). Notably, as a result of the comparably low temporal resolution of ≈12.6 s not many data points fall within each response peak arising from analyte addition, such that errors will be larger.

This measurement mode presents a comparably rapid and straight-forward way of probing the voltammetric properties of the sensor, and enables real-time analyses, as can be visualised in Figure 3.5-2 by the resolved redox distribution shifting cathodically upon exposure to HSO_4^-, then returning to the original $E_{1/2}$ upon washing the interface with supporting electrolyte. As expected, control injections of a non-coordinating anion (20 mM PF_6^-) or blank injections of the running electrolyte did not induce significant voltammetric responses (Figure 3.5-3), and are negligible with respect to responses attributed to specific binding events (i.e., 20 mM HSO_4^- in Figure 3.5-3).

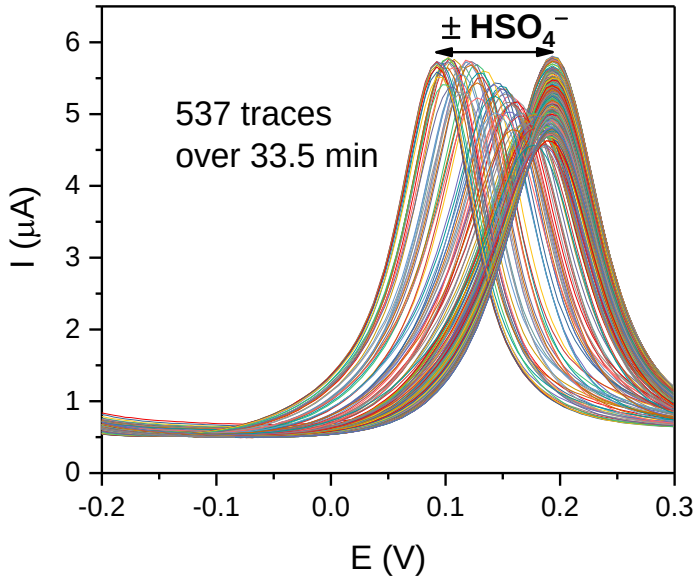


Figure 3.5-2. Overlay of all the recorded SWV traces afforded from a typical titration experiment (537 traces in 33.5 min), under continuous flow.

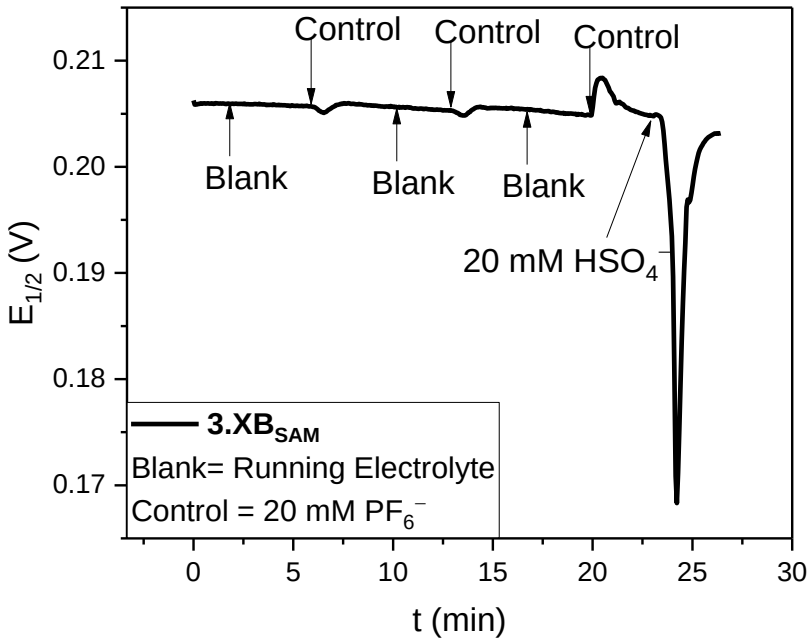


Figure 3.5-3. Voltammetric response of **3.XB$_{SAM}$** towards blank samples (running electrolyte, 100 mM $TBAClO_4$), controls (20 mM $TBAPF_6$) and 20 mM HSO_4^- under continuous electrolyte flow, flow rate = 500 µL min^{-1}. Each spike represents the response towards aliquots (V_{Sample} = 0.5 mL) of the blanks, controls or HSO_4^- as indicated, showing a negligible response to both the blank and control samples but a significant response to HSO_4^-.

The $E_{1/2}$ from each of the measured SW voltammograms can then be determined via an optimised data analysis method (further details later in Section 3.6), and translated into a sensogram showing notable cathodic response spikes ($\Delta E_{1/2}$) over time, as representatively shown for **3.XB$_{SAM}$** in response to HSO_4^- in Figure 3.5-4.

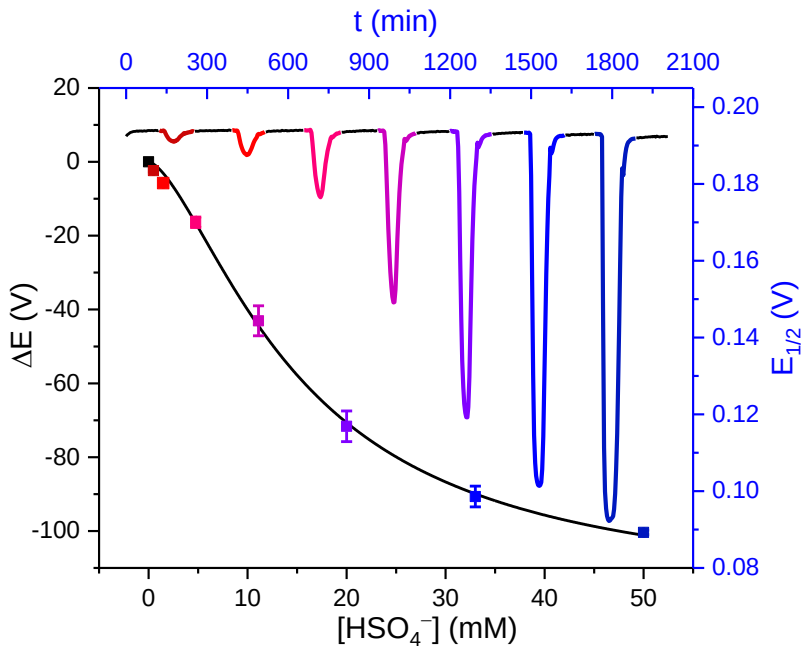


Figure 3.5-4. Sensogram (blue axes) and corresponding isotherm (black axes) from a typical titration experiment (Figure 3B) under continuous flow of **3.XB$_{SAM}$** to increasing concentrations of HSO_4^- in ACN/H_2O 99:1 (100 mM $TBAClO_4$, 10 mM $HClO_4$). Each spike corresponds to injections of increasing [HSO_4^-] up to 50 mM. Data analysis of the voltammograms was carried out according to the AsymFit method as discussed in Section 3.6 below. The solid line represents a fit according to the Langmuir-Freundlich model (Eqn. 3.3-1). Error bars represent one standard deviation of independent triplicate measurements.

As highlighted above under static conditions, the voltammetric stability of **3.XB/HB$_{SAM}$** is greatly increased by virtue of acidifying the supporting electrolyte. A key objective of this work was to develop a methodology which was capable of operating continuously for multiple hours; a crucial prerequisite for environmental or medicinal ion sensing applications. The voltammetric stability of a redox-active, receptive interface is of course highly sensitive to both the presence of target anions, particularly those which are basic, and the surrounding solvent media but, empirically, often the long-term sensing potential of such an interface is limited to approximately 100 SW voltammograms (*circa* 6 minutes with this method) before confidence in accurately determining $E_{1/2}$ is lost. In contrast here, long-term anion sensing assays with **3.XB$_{SAM}$** under the conditions described above were capable of operating for multiple hours (4.5 h), corresponding to 3700 SW voltammogram

scans. Figure 3.5-5 displays both the high signal integrity of this measurement with a drift of ≤5 mV over the whole 4.5 h, as well as highly consistent response spike magnitudes for repeat injections of 20 mM HSO_4^- (5 x 20 mM HSO_4^-, average $\Delta E_{1/2}$ = -82.4 ± 0.6 mV).

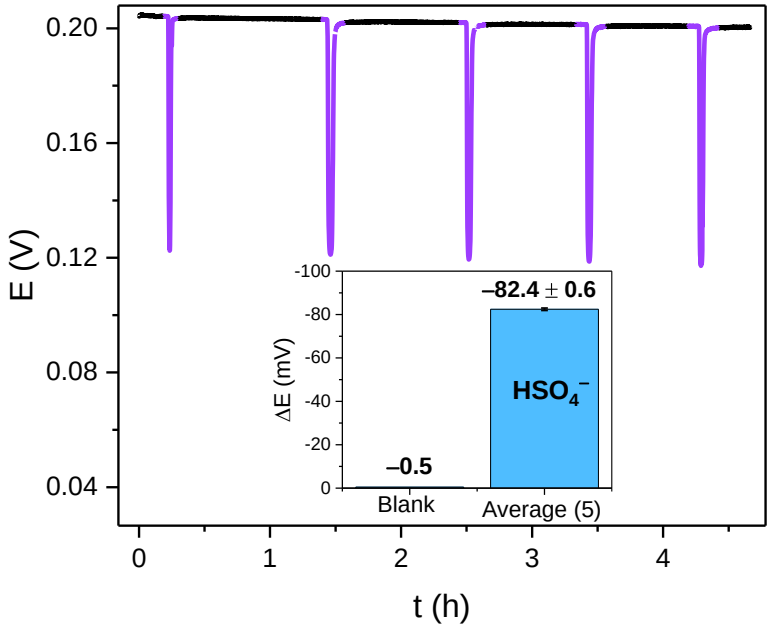


Figure 3.5-5. Voltammetric response of **3.XB$_{SAM}$** towards five additions (V_{Sample} = 0.5 mL) of 20 mM HSO_4^- (visualised as purple response spikes) under continuous electrolyte flow (flow rate = 200 µL min^{-1}) over 4.5 h. The inset shows the voltammetric shift in response to the blank sample and the average of all five HSO_4^- additions. Data analysis was carried out according to the AsymFit method.

It should be noted that, expectedly, significant voltammetric degradation was inevitably observed during this extensive time period (Figure 3.5-6), but this does not appear to have any significant impact on either the $E_{1/2}$ baseline or its responsiveness to anion recruitment, further highlighting the general utility of these interfaces as potential long-term sensors.

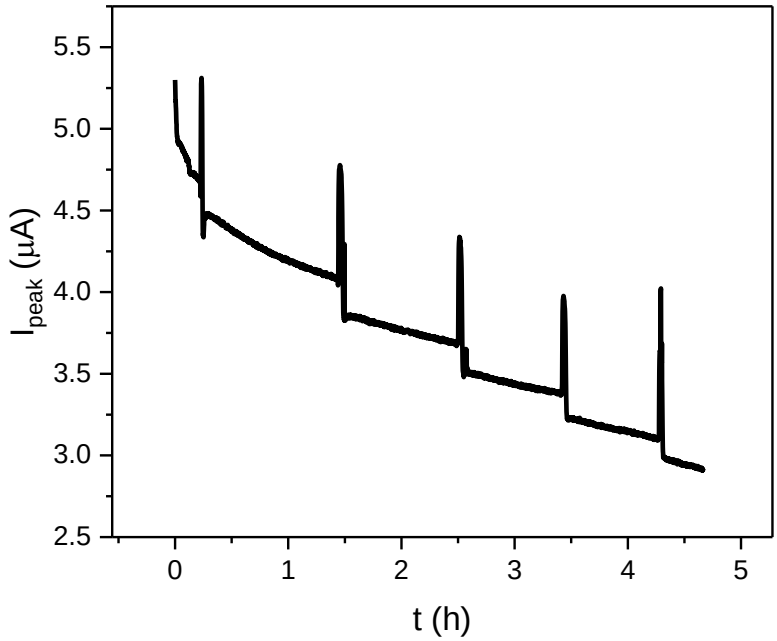


Figure 3.5-6. Current response of **3.XB$_{SAM}$** in response to five additions of 20 mM of HSO_4^- over 4.5 h, analysed with the AsymFit method.

In summary:

- A continuous voltammetric method was developed that generates a SW voltammogram every ≈ 3.7 s, enabling real-time monitoring of anion binding through changes in the measured $E_{1/2}$ values (assessed from the peak potential)

- Over the course of a standard titration, 100s of voltammograms are generated but a simple sensor output of $E_{1/2}$ *vs*. time is afforded through an optimised data analysis method (see below)

- Due to the high voltammetric stability of the **3.XB$_{SAM}$** interface, long-term measurements displaying reproducible responses to a target anion (HSO_4^-) over the course of more than 4.5 h, marking the first example of continuous voltammetric ion sensing that can operate, with accuracy, over multiple hours

3.6 Data Analysis

As alluded to above, the final method parameters for acquiring repeat SW voltammograms were optimised according to a number of considerations. The accuracy and performance of this methodology is directly dependent on the accurate determination of the $E_{1/2}$ (*i.e.*, peak potential) of each scan. However, these voltammetric measurements do not provide a direct sensor output in the sense that the raw data does not directly provide $E_{1/2}$, it must instead be determined by post-measurement analysis of the SW voltammograms. For the standard, static measurements described above (Section 3.3) this analysis is trivial to carry out manually as there are typically ≈ 10 SW voltammograms obtained during an anion titration study. This is in stark contrast to the continuous flow anion sensing method, which typically affords more than 500 SW voltammograms for each ≈ 30 min anion titration (Figure 3.5-2). In order to process this large of a data set, custom MATLAB scripts were applied to automate the analysis of the raw voltammograms (*i.e.*, to determine $E_{1/2}$ for each trace) according to two different approaches: a simple data extraction method ("PeakPick"), as well as a more advanced peak fitting ("AsymFit") method. Descriptions of both models can be found below.

PeakPick Method: The PeakPick method estimates $E_{1/2}$ as the potential which corresponds to the peak maximum (maximum current, I_{max}) of the recorded SWV (akin to peak detection functions in common electrochemical software), as exemplified in Figure 3.6-1. Whilst straightforward and easy to implement, the potential resolution of this method is inherently restricted to the magnitude of the step potential (5 mV used herein). As shown in Figure 3.6-1A, this results in large

errors in the determination of $E_{1/2}$ and is predictably associated with a poor analytical performance (Figure 3.6-1B) and high limits of detection (LODs, *vide infra*). Additionally, this method is also generally more sensitive to noise which can induce further deviations from the true $E_{1/2}$. Nevertheless, the PeakPick method serves as a useful starting point for more accurate data analysis via data fitting as described in the following.

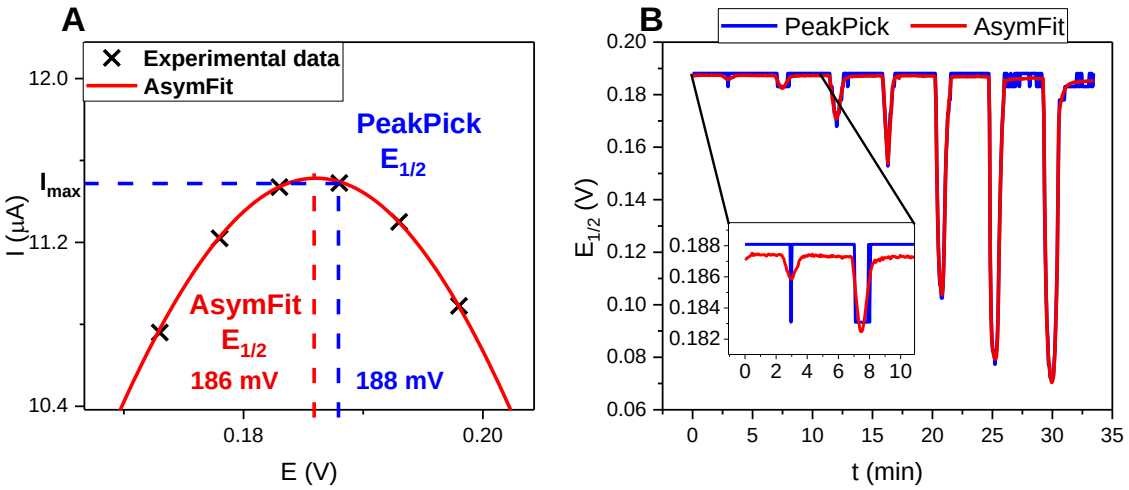


Figure 3.6-1. (A) Schematic representation of $E_{1/2}$ determination via the PeakPick and AsymFit methods. Real data points, recorded with E_{step} = 5 mV are shown as black crosses with the fitted peak function (Equation 3.6-1) shown in red. (B) Comparison of sensograms in response to increasing concentrations of HSO_4^- (0.5-50 mM) analysed with the PeakPick (black) and AsymFit (red) methods. The inset displays a magnification for the first two additions. As depicted, the $E_{1/2}$ obtained by peak picking is significantly less accurate than that obtained by the AsymFit method.

AsymFit Method: To improve on the PeakPick approach, an alternative method was devised whereby all SWV traces were fitted to an appropriate peak model from which a more accurate $E_{1/2}$ can be determined. An asymmetric double sigmoidal model was selected (Equation 3.6-1) as it provided excellent empirical fits to the data (Figure 3.6-1A, red line). Fitting of all voltammograms to this model was carried out with a custom MATLAB script (see Appendix S3 for details of the code), according to the following steps (visualised in Figure 3.6-2): An initial estimate for $E_{1/2}$ was obtained via the PeakPick method. Subsequently all data points ±50 mV

around this estimated value were isolated (*i.e.*, the baseline was removed) and the peak fitted to Eqn. 3.6-1. $E_{1/2}$ was then extracted as the peak potential from this fitted, continuous peak fit.

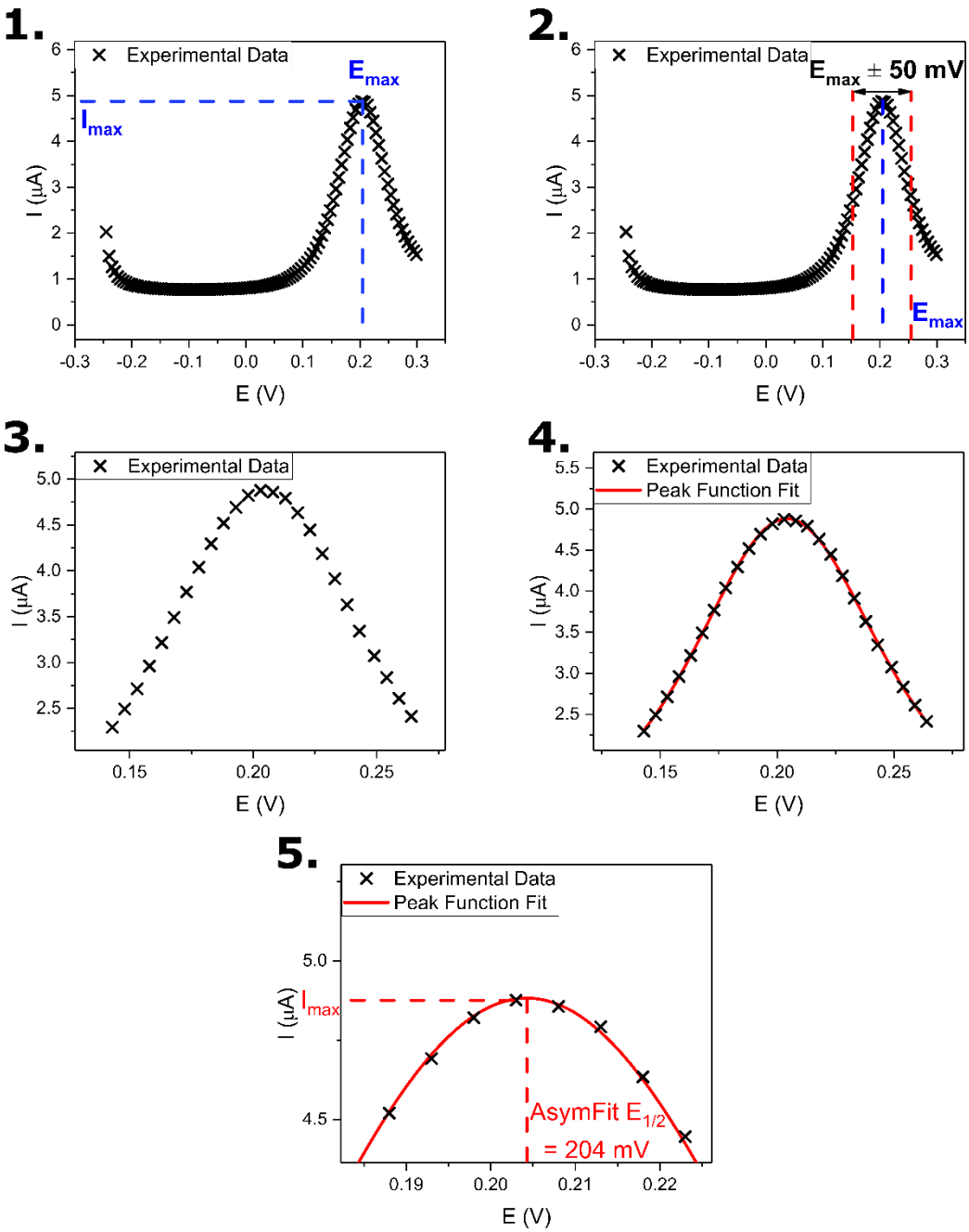


Figure 3.6-2. Schematic depiction of the steps for the AsymFit data analysis method. 1. An initial estimate for $E_{1/2}$ was obtained from the PeakPick method of the raw data. 2. and 3. All data points ±50 mV around this estimated value were isolated (i.e. the baseline was removed). 4. The isolated peak was fitted according to the asymmetric double sigmoidal function (Equation 3.6-1). 5. The $E_{1/2}$ of this fitted, continuous peak distribution was obtained by the PeakPick method (as $E_{1/2}$ at I_{max}).

$$y = y_0 + A\left[\frac{1}{\left(1+e^{(-(x-x_c+\frac{c_1}{2}))/c_2}\right)} \times \left(1 - \frac{1}{\left(1+e^{(-(x-x_c-\frac{c_1}{2}))/c_3}\right)}\right)\right] \quad \textbf{Equation 3.6-1}$$

Initialisation parameters for each variable in Equation 3.6-1 were estimated for each SWV as follows: y_0 (alpha), is the initial current value from the isolated data set around each peak. A (beta), is the peak height given by the difference between the maximum current and y_0. x_c (Guessxpeak) is the estimated peak potential, as determined via the PeakPick method. c_1, c_2 and c_3 (full width at half maximum, FWHM) are all given by an estimation for the full width half maximum value, here as the difference between the potential at the 6th and 16th data points from the isolated data set around each peak.

Importantly, this AsymFit method enables accurate determination of $E_{1/2}$, even if the $E_{1/2}$ falls in between two experimentally measured data points; whereby the PeakPick method is associated with significant error, Figure 3.6-1A. Thus, the resulting sensograms display a significantly higher potential-resolution, as shown in Figures 3.5-3, 3.6-1B, 3.6-3 and 3.6-4. It is important to note that this methodology can be readily adapted to fit voltammetric data to any desired function, such as Gaussian or *ab initio*-derived voltammetric models from which electrochemically relevant parameters, such as the full width at half maximum (FWHM) can be obtained.[266, 267]

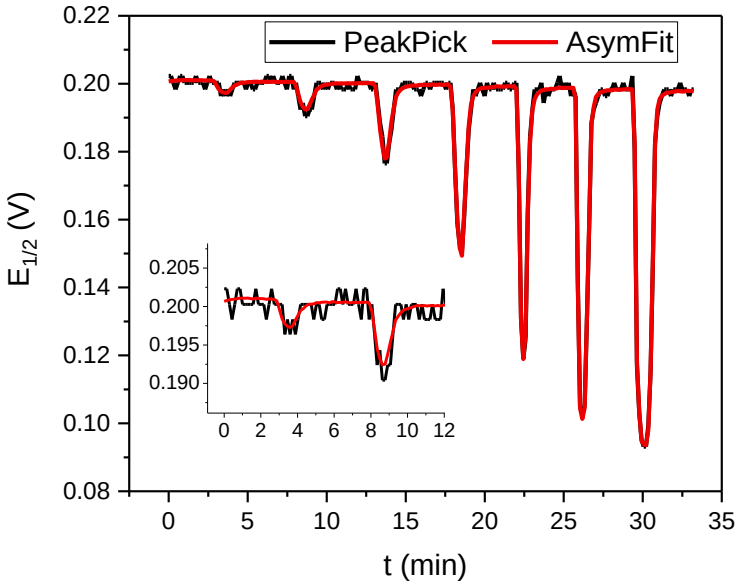


Figure 3.6-3. Comparison of continuous SWV sensograms for **3.XB$_{SAM}$** in response to increasing concentrations of HSO_4^- up to 50 mM (E_{step}= 2 mV) analysed via the PeakPick method (black line) and AsymFit method (red line). Inset displays the improved fit with the AsymFit method for the first two additions (0.5 and 1.5 mM HSO_4^-).

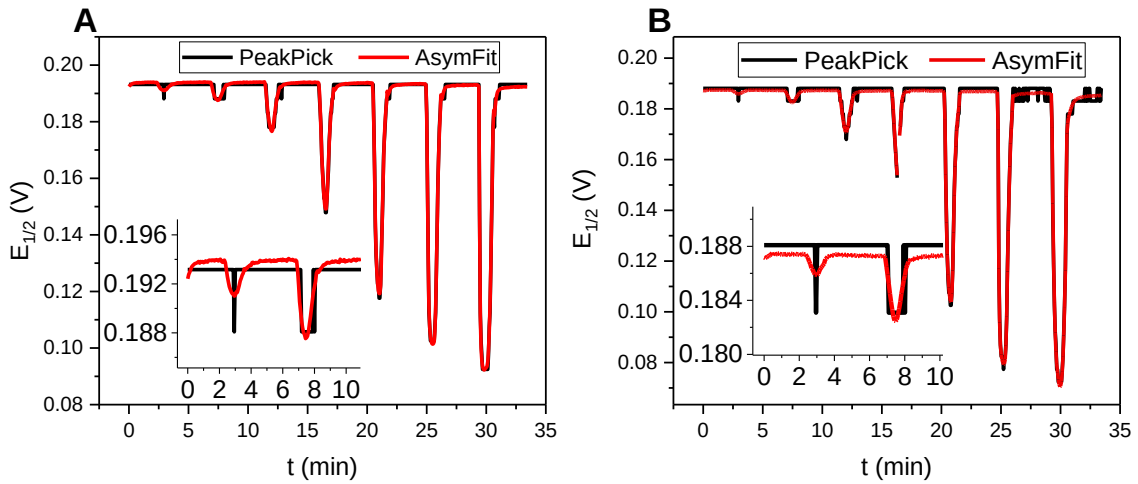


Figure 3.6-4. Comparison of continuous SWV sensograms for **3.XB$_{SAM}$** in response to increasing concentrations of HSO_4^- up to 50 mM (E_{step}= 5 mV) analysed via the PeakPick method (black line) and AsymFit method (red line). Inset displays the improved fit with the AsymFit method for the first two additions (0.5 and 1.5 mM HSO_4^-). The Figures Ahow examples where PeakPick (A) overestimates and (B) underestimates $E_{1/2}$.

It is important to note that analyses via the simple PeakPick algorithm affords LODs that are significantly worse than those obtained from the AsymFit method, see Table 3.6-1. For example, even with the smaller, more accurate E_{step} = 2 mV, the PeakPick analysis affords a high LOD of 825 ± 138 µM, for flow sensing of HSO_4^- with **3.XB$_{SAM}$**, 15-fold worse than that of the AsymFit method (53.0 ± 20.8 µM). This can

be attributed to a significantly poorer signal-to-noise ratio (*i.e.*, larger baseline fluctuation) obtained from the PeakPick methodology as its potential-resolution is inherently limited to E_{step}. In essence, the LOD for the PeakPick method for E_{step} = 5 mV is significantly worse than that of PeakPick with E_{step} = 2 mV (825 µM), but cannot be easily obtained, because fluctuations in the baseline are <5 mV such that the standard deviation of the baseline is 0, preventing accurate LOD determination. Consequently, an improvement in LOD via PeakPick is only possible by significantly decreasing E_{step}, which is, however, associated with a significant loss in temporal resolution (see Equation 3.5-1). In contrast, the AsymFit analysis is not sensitive to the value of E_{step}; the LOD for E_{step} = 5 mV is with 59.8 ± 5.5 µM identical to that for E_{step} = 2 mV. These findings validate the choice of E_{step} = 5 mV as the chosen experimental parameter and saliently illustrates the value of the AsymFit method, not only enabling sensing with a significantly improved temporal resolution and a simple, automated signal readout, but also improved LODs.

Table 3.6-1. Comparison of LODs determined via PeakPick and AsymFit data analysis methods for **3.XB$_{SAM}$** in response to HSO_4^- under static conditions (E_{step}= 2 mV) and continuous flow (E_{step}= 2 or 5 mV). Errors represent one standard deviation of triplicate independent measurements.

3.XB$_{SAM}$	**Analysis Method**	**LOD (µM)**
Flow	**AsymFit, E_{step}= 5 mV**	59.8 ± 5.5
	Asymfit, E_{step}= 2 mV	53.0 ± 20.8
	PeakPick, E_{step}= 2 mV	825 ± 138
Static	**AsymFit**	67.7 ± 25.8
	PeakPick	509 ± 151

Therefore, obtaining $E_{1/2}$ values via the AsymFit method by fitting the resulting SW voltammograms to an appropriate Gaussian-type model significantly improves the accuracy with which each $E_{1/2}$ is determined w.r.t the comparably simple PeakPick method. In turn, this improves the sensitivity of the overall voltammetric

methodology (static or continuous) by an order of magnitude when the AsymFit data processing method is applied.

3.7 Sensing of Other Anions and Analytical Performance of the Flow Sensors

With a highly efficient continuous anion sensing methodology and accompanying data analysis approach in hand, attention then turned to quantifying the analytical performance of **3.XB**/**HB$_{SAM}$** for flow ion sensing. As displayed in Figures 3.7-1 – 3.7-5, both the XB and HB sensing interfaces responded sensitively to increasing concentrations of HSO_4^-, $H_2PO_4^-$ and Cl^-. Crucially, the maximum response magnitudes of **3.XB**/**HB$_{SAM}$** for HSO_4^-, $H_2PO_4^-$ and Cl^- were near-identical under static or continuous flow conditions (see Figures 3.7-1B, 3.7-2B and 3.7-3),[141] confirming that physically translating the 3-electrode cell from a vial of static solution to a microfluidic cell does not affect the sensing performance of either interface. Any slight disparities between the static and continuous flow response isotherms are attributed to the fact that minor baseline drifts can be directly accounted for under continuous flow, which is not possible for static titrations. Sensing studies with Cl^- were limited to a slightly narrower concentration range (0 up to 33 mM Cl^-) due to the inherent electroactivity of Cl^- at the moderate potentials used here. At higher concentrations, the resolved activity of the Fc and Cl^- redox processes overlap too significantly to reliably determine the $E_{1/2}$ of the Fc/Fc^+ couple through MATLAB analysis.

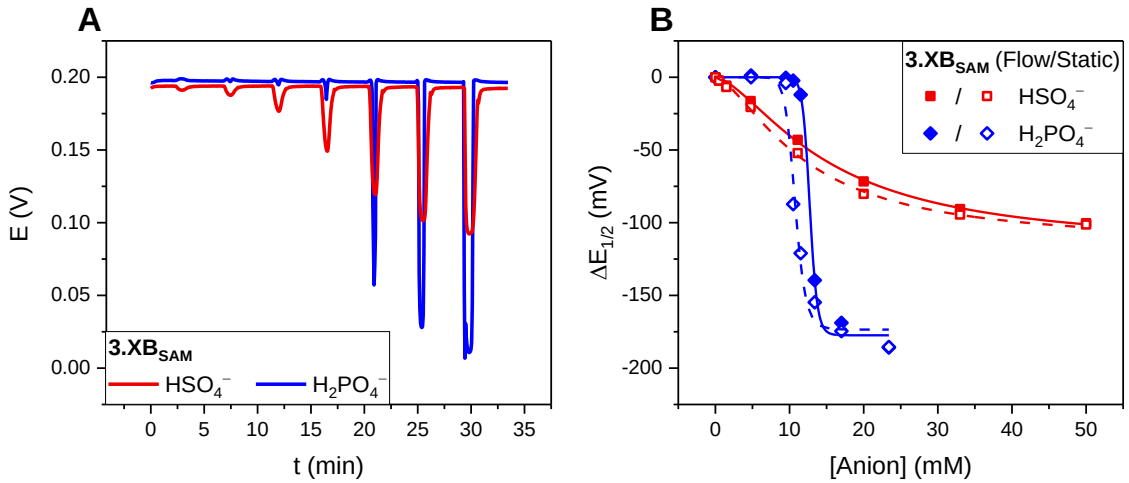


Figure 3.7-1. (A) Sensograms of **3.XB$_{SAM}$** in response to increasing concentrations of HSO_4^- (red line) and $H_2PO_4^-$ (blue line), analysed with the AsymFit method. (B) Comparison of static (empty symbols) and continuous flow isotherms (filled symbols) of **3.XB$_{SAM}$** in response to HSO_4^- (red squares) and $H_2PO_4^-$ (blue diamonds). Lines represent fits to the Langmuir-Freundlich model (Equation 3.3-1). The response towards $H_2PO_4^-$ is "delayed" until ≈10 mM due to protonation. Error bars for HSO_4^- are omitted here as they are too small to be resolved on this scale, see Figure 3.7-3.

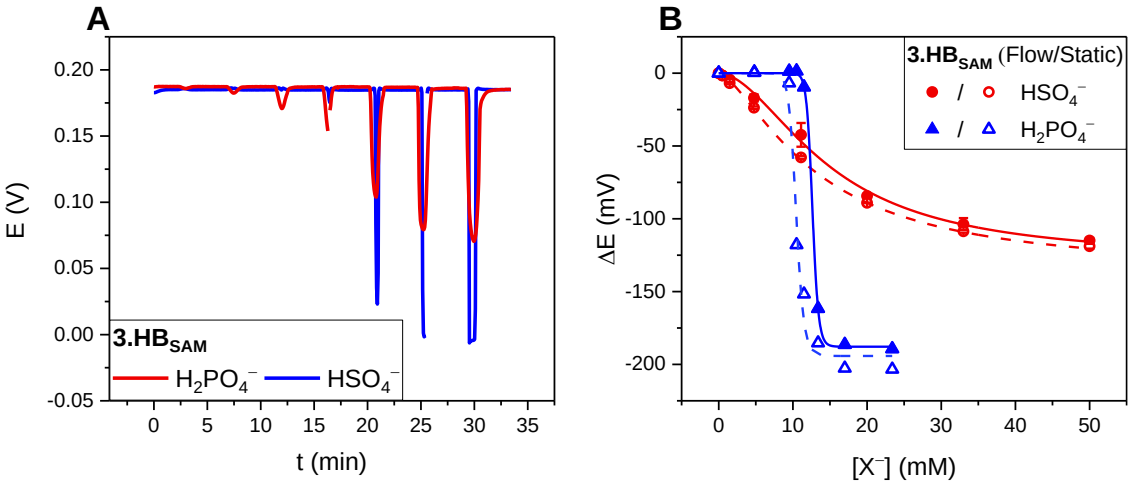


Figure 3.7-2. (A) Sensograms of **3.HB$_{SAM}$** in response to increasing concentrations of HSO_4^- (red) and $H_2PO_4^-$ (blue), analysed with the AsymFit method. (B) Comparison of static (empty symbols) and continuous titrations (filled symbols) with **3.HB$_{SAM}$** in response to HSO_4^- (red circles) and $H_2PO_4^-$ (blue triangles). All isotherms were fitted to the Langmuir-Freundlich model (Eqn. 3.3-1). Error bars for HSO_4^- are omitted here as they are too small to be resolved on this scale, see Figure 3.7-3.

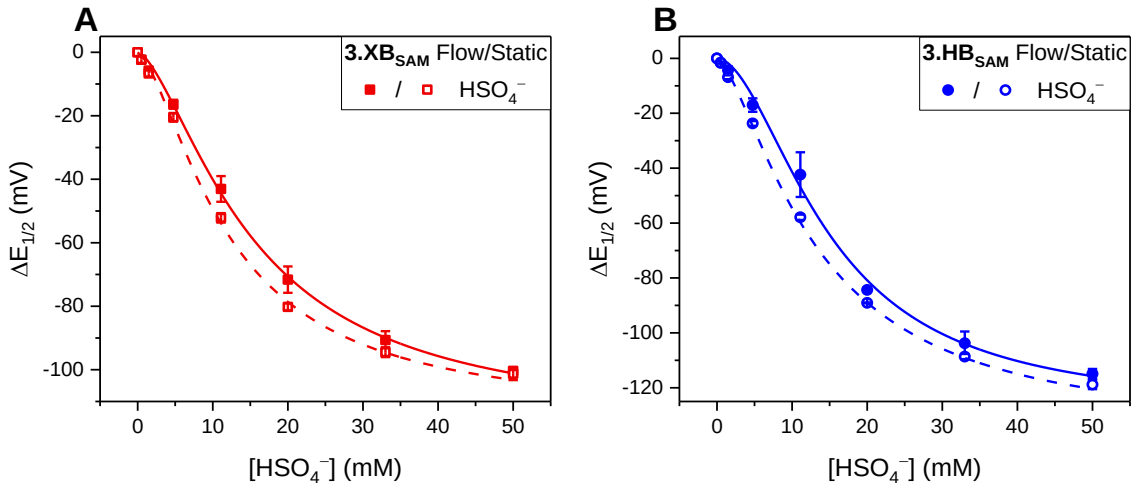


Figure 3.7-3. Comparison of static (empty symbols) and continuous isotherms (filled symbols) of (A) **3.XB$_{SAM}$** and (B) **3.HB$_{SAM}$** in response to increasing concentrations of HSO_4^- up to 50 mM. All isotherms were fitted to the Langmuir-Freundlich model (Eqn. 3.3-1). Error bars represent one standard deviation of triplicate independent measurements.

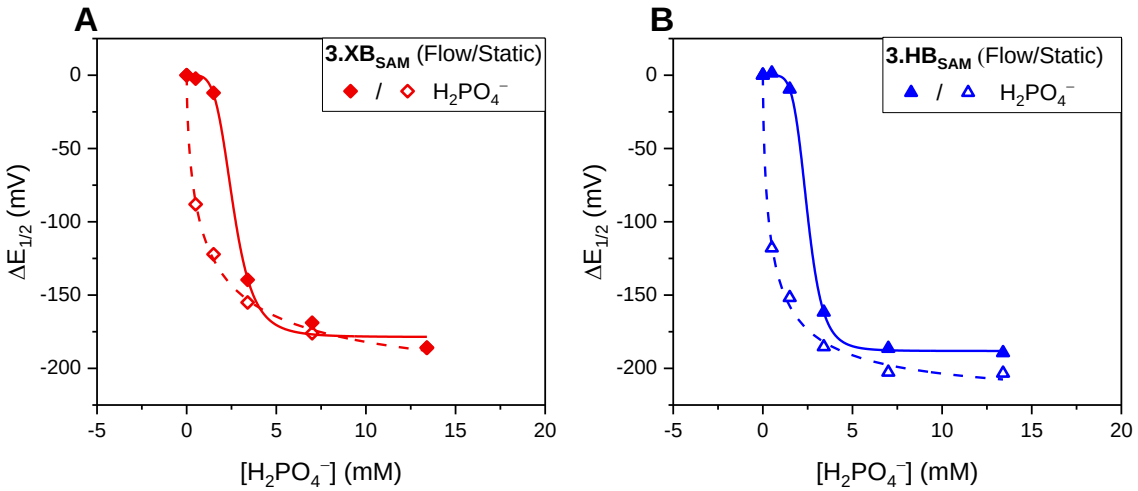


Figure 3.7-4. Comparison of corrected static (empty symbols) and continuous isotherms (filled symbols) of (A) **3.XB$_{SAM}$** and (B) **3.HB$_{SAM}$** in response to $H_2PO_4^-$ up to 23.4 mM. All isotherms were fitted to the Langmuir-Freundlich model (Equation 3.3-1), and were corrected by –10 mM. The uncorrected isotherms are shown in Figures 3.7-1B and 3.7-2B.

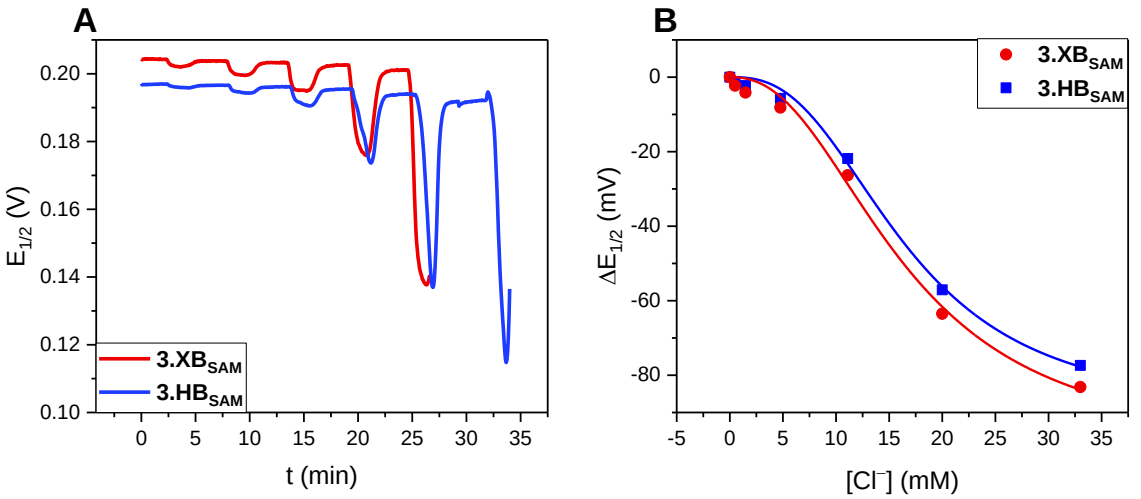


Figure 3.7-5. (A) Sensograms of **3.XB/HB$_{SAM}$** in response to increasing concentrations of Cl^- (0.5-33 mM, V_{sample}= 1 mL), analysed with the AsymFit method and (B) corresponding isotherms. All isotherms were fitted to the Langmuir-Freundlich model (Equation 3.3-1). The redox activity of Cl^- at high concentrations interfered with the AsymFit method applied, therefore data is shown for the SWVs for which the code was successful up to the point of failure.

The excellent agreement between the maximum response magnitude (ΔE_{max}), sensitivity and limit of detection (LOD) for both the static and continuous anion sensing approaches is further demonstrated in Table 3.7-1, confirming good analytical performance of the sensory interfaces under flow. For example, the cathodic shift of **3.XB$_{SAM}$** in the presence of 50 mM HSO_4^- was –100 ± 1 mV measured under continuous flow, which was found to be not only highly reproducible, but also identical to the response magnitudes under static conditions (–101 ± 2 mV; Table 3.7-1).

Table 3.7-1. Maximum shifts ΔE_{max} (mV) obtained at the highest measured concentration for each anion, sensitivities (slope of linear region) and limits of detection (LOD) of **3.XB/HB$_{SAM}$** under continuous flow (E_{step} = 5 mV) and under standard, static conditions (E_{step} = 2 mV). Data analysis was carried out according to the AsymFit method. Errors, where shown, represent the average and one standard deviation of independent triplicate experiments. Additional data is compiled in Tables A3.1 –A3.8 in the Appendices A3.

Anion		Continuous Flow Voltammetry		Static Voltammetry	
		3.XB$_{SAM}$	**3.HB$_{SAM}$**	**3.XB$_{SAM}$**	**3.HB$_{SAM}$**
HSO_4^-	**ΔE_{max} (mV)[a]**	-100 ± 1	-115 ± 2	-101 ± 2	-119 ± 2
	Sensitivity (mV mM^{-1})[b]	4.08 ± 0.13	3.84 ± 0.73	4.68 ± 0.13	5.26 ± 0.09
	LOD (µM)	59.8 ± 5.5	35.0 ± 16.4	67.7 ± 25.8	44.6 ± 13.5
$H_2PO_4^-$	**ΔE_{max} (mV)[c]**	-186	-189	-186	-203
	Sensitivity (mV mM^{-1})	49.9[e]	59.3[e]	36.0[f]	41.8[f]
	LOD (µM)[d]	3.77	0.894	20.1	8.58
Cl^-	**ΔE_{max} (mV)[g]**	-83[d]	-77	-94	-88
	Sensitivity (mV mM^{-1})[b]	2.27	1.93	2.71	2.08
	LOD (µM)	89.6	48.0	210	195

a – at [HSO_4^-] = 50 mM. b – for range of 0 – 11 mM. c – at [$H_2PO_4^-$] = 23.4 mM. d – for binding isotherms that were corrected by –10 mM. e – for range of 10.5 –13.4 mM. f – for range of 9.5 –13.4 mM. g – at [Cl^-] = 33 mM.

Interestingly, the high temporal resolution (≈3.7 s) of this flow methodology also appears to aid in elucidating binding kinetics; an almost entirely unexplored area of interest for host-guest chemistry in solution or at interfaces. Namely, Cl^- (de)complexation was empirically observed to proceed significantly more slowly than either HSO_4^- or $H_2PO_4^-$, which marks an unexpected yet potentially insightful observation for interfacial ion recognition. Specifically, under the standard flow measurement conditions (flow rate of 500 µL min^{-1} and analyte volume of 500 µL) the response magnitude of both **3.XB$_{SAM}$** and **3.HB$_{SAM}$** towards Cl^- was significantly lower than under static conditions (see Figures 3.6-5 and 3.7-6), attributable to insufficient exposure time of this analyte to the interface. To address this, the

sample injection volume was increased to 1 mL (thus resulting in double the exposure time) was sufficient to reach the static, equilibrium response.

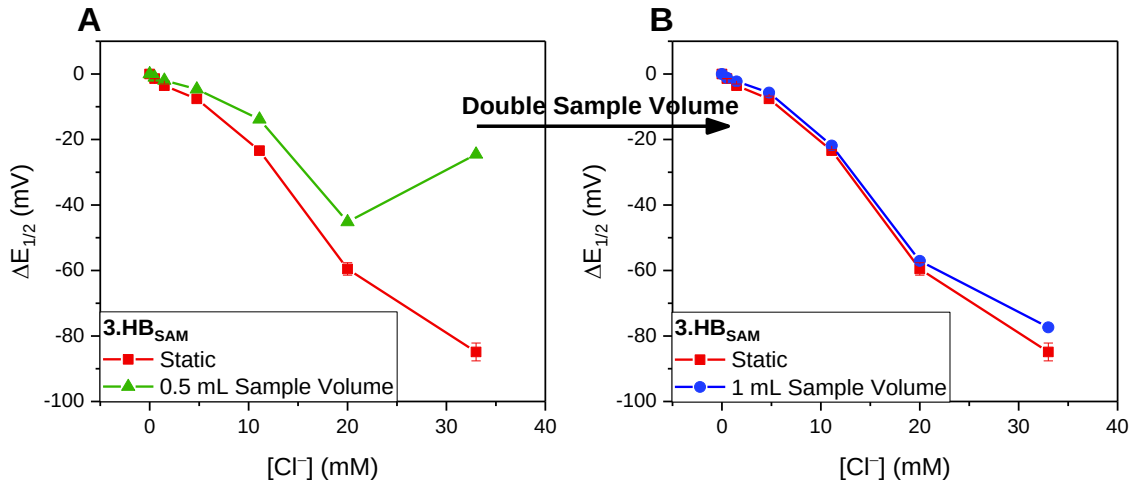


Figure 3.7-6. Comparison of static (red squares) and continuous titrations (A) green triangles for 0.5 mL aliquot volumes and (B) blue circles for measurements with 1 mL aliquot volumes with **3.HB$_{SAM}$** in response to Cl^-. Connecting lines are to guide the eye only. (B) Shows that doubling the aliquot volume to 1 mL was sufficient time to reach the static, equilibrium response.

3.8 Conclusions & Future Work

3.8.1 Conclusions

In summary, Chapter 3 describes the development and assessment of the first proof-of-principle example of real-time, continuous flow ion sensing at redox-active, anion-receptive molecular films. A custom-designed, 3D-printed flow cell housing a standard 3-electrode electrochemical cell was produced to enable a facile route towards electrochemistry, specifically square wave voltammetry, under continuous flow. This approach facilitated measurement of 100s of square wave voltammograms over a typical sensing period of ≈ 30 min, affording a high temporal resolution of ≈ 3.7 s. Custom scripts were written in MATLAB to handle these large data sets by applying two separate data analysis methods in order to semi-

automate the analysis of the raw voltammograms and determine $E_{1/2}$ of each. The two methods included one in which the $E_{1/2}$ is simply picked as the potential with the highest current in a scan and a more elaborate, but considerably more accurate method, which fitted the peak in each SW voltammograms to a model and identified $E_{1/2}$ from this. Consistent with prior studies,[210] significant cathodic perturbations of the $E_{1/2}$s of ferrocenyl-isophalamide-(iodo)triazole-based SAMs were displayed in response to HSO_4^-, $H_2PO_4^-$ and Cl^- under continuous flow conditions, with excellent agreement between the maximum response magnitudes, sensitivity, limits of detection and binding constants. The high temporal resolution of this methodology may also support further fundamental studies pertaining to interfacial ion binding kinetics, which is an essentially unexplored field of study hitherto these observations. Crucially, this voltammetric flow methodology is applicable to sensing of any analyte that can reversibly induce a voltammetric response of an electroactive interface and presents an important step in the translation of such sensors from lab to real-life applications.

3.8.2 Future Work

Future work building on the results described in Chapter 3 could therefore further explore the empirical differences observed for the responses of **3.XB**/$\mathbf{HB_{SAM}}$ through studies with other anionic targets. Perhaps the greatest limitation of the results described above, however, is the unproven ability for the method to operate in media which is more relevant to real applications. Development of a redox-active host which can demonstrate improved voltammetric stability in pure water, whilst still maintaining strong and selective ion binding is critical in this endeavor.

Progress in this is directly related to advancements in supramolecular synthetic strategies, and could include preorganising the host's binding cavity to a greater extent via macrocyclisation or mechanically interlocking components. Alternatively, even more potent non-covalent interactions could be applied by polarising the existing XB units further with more electron-withdrawing groups adjacent to the iodo-triazole groups, or using ChB bonding, for example. Additionally, whilst Fc is already a reasonably stable redox probe, there may be merit in exploring other redox transducers which can still sensitively transduce ion binding events at the host whilst maintaining a high signal ($E_{1/2}$) and current integrity during ion sensing studies.

Chapter 4

Redox Capacitive Ion Sensing

Chapter 4: Redox Capacitive Ion Sensing

4.1 Introduction & Chapter Aims

As highlighted in Chapter 3, the generation of more powerful and practical anion sensing technologies is crucial to the advancement of many natural and technological processes for environmental, industrial and healthcare applications.[150, 268, 269] This has led to the continued exploration of a range of electroanalytical methodologies for anion sensing, including potentiometric and voltammetric approaches, as prior discussed in Section 1.4.1, and Section 1.4.2, respectively. The latter has been shown to be especially promising due to the transduction mechanism being natively coupled to a (redox) modulation of ion binding strength, leading to enhanced anion binding affinity upon *in situ* electrochemical oxidation of the transducer that can enable anion binding/sensing in competitive media.[141, 150] Additionally, as noted, the surface immobilisation of redox-active ion receptors is often associated with significant response enhancement effects, and also presents a more useful platform for real-life device integration.[141, 257, 270]

Nevertheless, it must be noted that continuous ion sensing via voltammetric techniques, such as cyclic voltammetry (CV), differential pulse (DPV) or square-wave voltammetry (SWV) can be challenging. Specifically, these are transient, non-equilibrium techniques which cannot generally be utilised in a simple, continuous signal generating fashion, or they require significant data analysis/processing, as outlined in Chapter 3.[271] More recently, alternative methodologies including

chemiresistive[272] and impedance-based techniques have been investigated for sensing applications.[182, 273-278] The latter has emerged as a particularly sensitive means of reporting interfacial binding events and is most often applied for biosensing applications with biorecognition elements (*e.g.*, proteins or antibodies).[279-282] Impedance-derived techniques are notably versatile, as they can be conducted at a freely chosen constant electrode potential in both Faradaic and non-Faradaic formats. As a result, these techniques are ideally and uniquely suited to study a plethora of interfacial phenomena at equilibrium.[283] Nevertheless, this capability remains largely unexplored for the study of interfacial host-guest recognition.[151, 195]

As outlined in Section 1.4.3, Faradaic impedimetric sensing formats typically employ an excess of a solution-phase redox probe (*e.g.*, $[Fe(CN)_6]^{2+/3+}$) as a signal amplifier, but several drawbacks are associated with this: sensing studies are limited to solvents in which the redox probe is soluble, the redox probe itself may compete with binding (through direct competition for the binding site or through ion pairing to the target guest), and the presence of high background concentrations of highly charged complexes is not representative of real-world media, *inter alia*. Crucially, these factors can in turn prohibit accurate quantification of low levels of specific ion binding. To circumvent these issues, non-Faradaic impedimetric formats can be utilised for interfacial ion sensing based on an analysis of the interfacial capacitance of receptor-modified electrodes which entirely preclude the need for a redox probe (in solution or appended to a surface).[182, 273] This method is explored in detail in Chapter 5. A promising alternative approach is the direct

integration of redox-transducers into receptive films to enable sensing using the film's redox capacitance as a sensitive readout for specific binding events. Notably, this facilitates a highly sensitive and reagentless sensing mode that does not require the supporting electrolyte to be doped with high levels of a redox-active probe. Thus far, this methodology has only been applied to the sensing of (large) biomolecules[284-286] and is largely unexplored in the context of host-guest sensing.[195]

This chapter therefore explores the fundamental development of a redox-capacitive methodology for ion sensing, from the operational principles that underpin the method to its implementation into a microfluidic format to enable continuous flow ion sensing. This technique combines the advantages of both voltammetric and impedimetric techniques to not only enable a direct tuning of the ion binding (and sensing performance) via specific surface polarisation, but also real-time ion sensing with high sensitivity and a simple, direct sensor readout. Furthermore, the method is envisaged to be widely applicable to a broad range of redox-active, receptive interfaces for cationic, anionic or even neutral target species. The utility of this novel methodology was demonstrated at a model anion-receptive, redox-active interface, namely the same ferrocene-isophthalamide-(iodo)triazole SAMs, **3.XB**/**HB**$_{\mathbf{SAM}}$ described in Chapter 3, which enabled a direct comparison of the continuous voltammetric and redox capacitive anion sensing techniques outlined in Chapters 3 and 4, respectively.

In summary, the aims of Chapter 4 are:

- Comprehensively assess the use of redox capacitance to transduce interfacial anion binding events, for the first time
- Apply the redox capacitive anion sensing methodology under both pseudo-flow (fixed solution volume, stirred) and continuous flow conditions to monitor anion binding in real-time
- Compare relevant anion binding and sensing parameters of the continuous redox capacitive method w.r.t. the continuous voltammetric method derived in Chapter 3
- Assess the use of continuous redox capacitive measurements for long-term sensing applications (over hours, for example)
- Explore how varying the applied, fixed potential affects the anion sensing performance of established anion-receptive SAMs and associated analytical parameters including sensitivity and LODs

4.2 Principles of Redox Capacitive Anion Sensing

Redox capacitance sensing is an impedance-derived technique used to report on interfacial events (*e.g.*, binding) by utilising the capacitance arising from a surface-immobilised redox transducer. The redox capacitance of the electroactive SAM is inherently related to the redox activity of the interface. Specifically, the redox capacitance, C_r at a given potential is directly proportional to the redox density of

states g_r, *i.e.*, $C_r(E) \sim g_r(E)$.[287] In a generalised form, C_r of a redox-active SAM is then given by the following equation:

$$C_r = \frac{\Gamma 4 k_B T}{eF} \qquad \textbf{Equation 4.2-1}$$

Where Γ is the molecular surface coverage of redox active molecules (Γ = (1.01 ± 0.18) x 10^{-10} mol cm^{-2} for **3.XB$_{SAM}$**)[141] and all other parameters are standard constants. A decrease in redox activity (*i.e.*, a decrease in Γ/g_r) is thus directly reflected in a decreased redox capacitance. Thus, any film instability resulting from voltammetric degradation will directly translate to an instability of the baseline C_r, however this is, as previously discussed in Chapter 3, is mitigated here by acidification of the electrolyte and can be corrected for. Additionally, as this Faradaic transduction method can be carried out at any chosen potential, it is envisaged that polarising the interface at cathodic potentials w.r.t. the redox-active window of **3.XB/HB$_{SAM}$** could also reduce voltammetric degradation (see Section 4.6 for further details).

An electroactive film's redox capacitance is typically represented in one of two ways: a capacitive Nyquist plot (see Figure 4.2-1C), or the redox density of states (DOS): the variance of C_r as a function of potential (see Figure 4.2-2). Specifically, capacitive Nyquist plots are obtained at a fixed electrode polarisation (DC potential), upon which a small amplitude (10 mV) AC perturbation of a specific frequency is superimposed and scanned across a large range of different AC frequencies (100 kHz – 1 Hz).

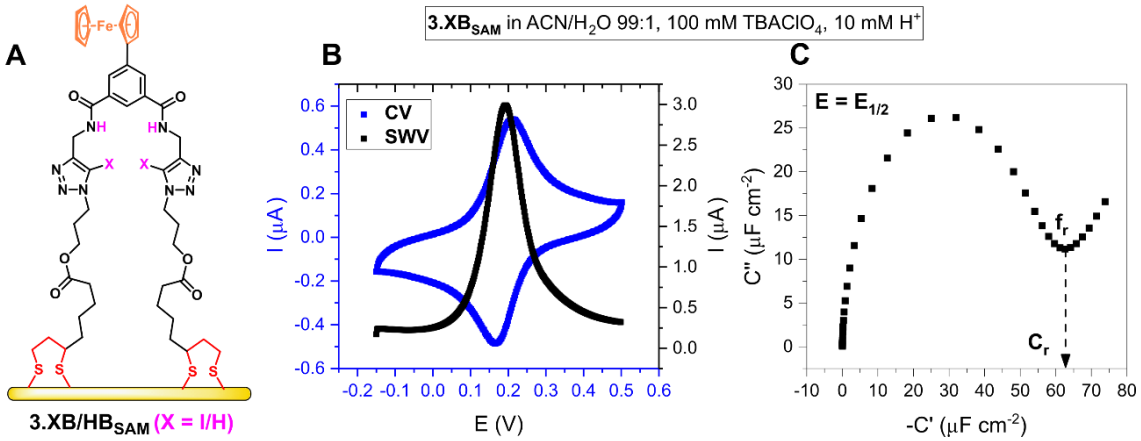


Figure 4.2-1. (A) Schematic representation of **3.XB/HB$_{SAM}$** on a gold electrode. (B) CV and SWV of **3.XB$_{SAM}$** in ACN/H_2O 99:1, 100 mM $TBAClO_4$, 10 mM $HClO_4$. (C) Capacitive Nyquist plots of **3.XB$_{SAM}$** in ACN/H_2O 99:1, 100 mM $TBAClO_4$, 10 mM $HClO_4$, at $E_{1/2}$ (black squares). Each data point represents a measurement at a different AC frequency. The film (redox) capacitance, C_r is then obtained as the real capacitance C´ at the frequency of the inflection point (f_r), approximately the semicircle diameter.

The redox density of states was resolved by a single frequency capacitance measurement (at f_r, see Figure 4.2-1C) at different potentials, $C_r(E)$, as shown in Figure 4.2-2 (green triangles) and reports on the relative proportion of oxidised and reduced receptor states (analogously to a SW voltammogram). Schematically depicted in Figure 4.2-2 is the ratio of oxidised and reduced anion receptors at different potential regimes where ferrocene/ferrocenium units are highlighted in orange and blue, respectively.

As is evident from Figure 4.2-2, the redox density of states directly reflects the redox distribution obtained via SWV for **3.XB$_{SAM}$**. Accordingly, the maximum value of $C_r(E)$ is obtained at the $E_{1/2}$ of the redox couple and sampling outside the redox-active window of **3.XB/HB$_{SAM}$** reports on the non-Faradaic capacitance, which is expectedly smaller than the redox capacitance ($C_{E1/2}$ = 62.6 µF cm^{-2} *vs*. C_{-240} = 3.4 µF cm^{-2}, C_{-240} is 5.4% of $C_{E1/2}$), as shown in Figure 4.2-3.

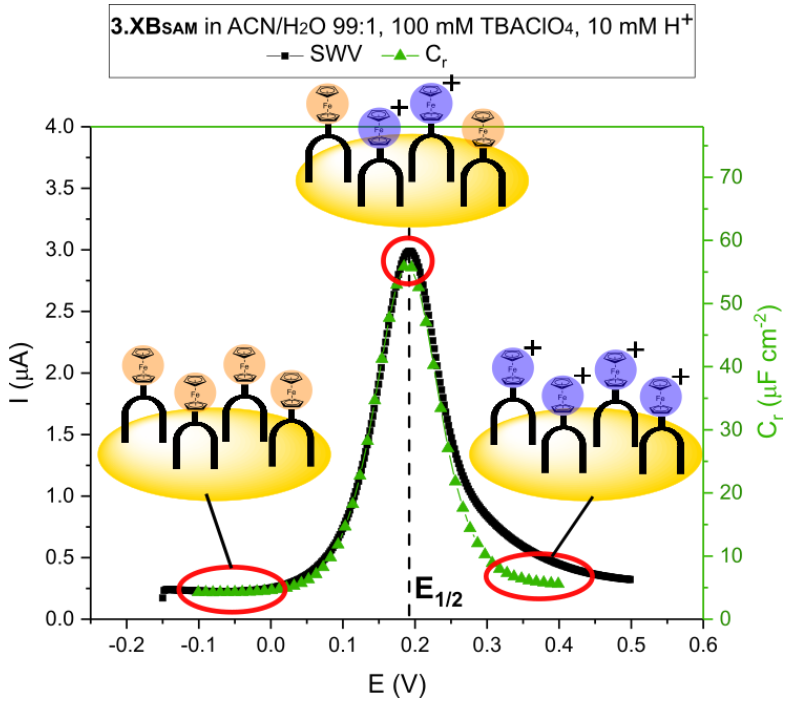


Figure 4.2-2. Comparison of SWV (black) and redox capacitance, C_r (green triangles) as a function of electrode potential (*i.e.*, redox density of states (DOS)) of **3.XB$_{SAM}$** in ACN/H_2O 99:1, 100 mM $TBAClO_4$, 10 mM $HClO_4$. C_r(E) was obtained at a fixed frequency f_r (determined at $E_{1/2}$, see Figure 4.2-1C).

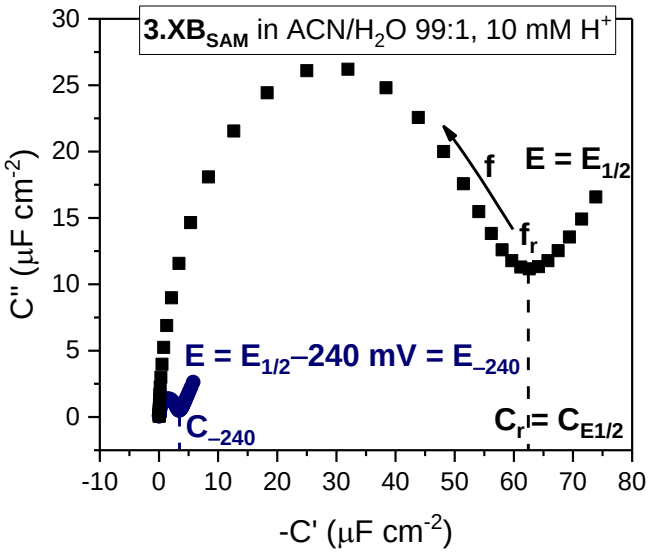


Figure 4.2-3. Capacitive Nyquist plots of **3.XB$_{SAM}$** in ACN/H_2O 99:1, 100 mM $TBAClO_4$, 10 mM $HClO_4$, at $E_{1/2}$ (black squares) and E_{-240} (blue circles). Each data point represents a measurement at a different AC frequency. The film (redox) capacitance is then obtained as the real capacitance C´ at the frequency of the inflection point (f_r), which approximates to the semicircle diameter for the Nyquist recorded at $E_{1/2}$.

Thus, these density of states measurements not only report on the redox capacitive signatures of the redox-active interface, but they also provide some relevant voltammetric parameters (*e.g.*, $E_{1/2}$). In the context of anion sensing, this means that

the voltammetric/redox capacitance density of states distributions are both expected to progressively shift to more cathodic potentials upon anion binding, due to the preferential stabilisation of the Fc^+ oxidation state (further details on this mechanism can be found in Chapter 3 and Section 1.4.2). Indeed, a titration carried out in this manner affords equivalent information regarding ΔE, as shown in Figure 4.2-4, with an excellent agreement between the $\Delta E_{1/2}$ responses of **3.XB$_{SAM}$** to HSO_4^-, as transduced by either voltammetric or redox capacitance DOS measurements. Both voltammetric and redox capacitance DOS response isotherms to increasing concentrations of target (shown for HSO_4^- in Figure 4.2-4) can be obtained with similar practical ease, but the SWV assays can generally be conducted more quickly (1 SWV ≈ 5 s *vs*. 1 capacitive Nyquist plot ≈ 2 min).

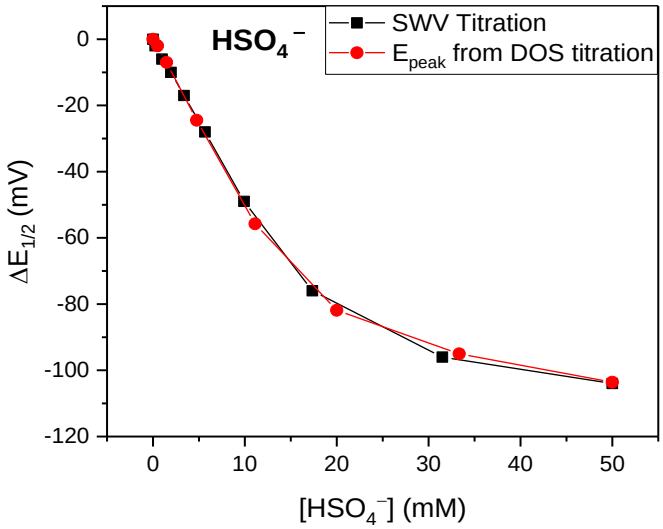


Figure 4.2-4. Voltammetric response isotherms obtained of **3.XB$_{SAM}$** in ACN/H_2O 99:1 (100 mM $TBAClO_4$, 10 mM $HClO_4$), in response to increasing concentrations of HSO_4^- up to 50 mM from standard voltammetric titrations by SWV (black squares), as well as from the peak shift of the redox capacitance DOS distribution (red circles) highlighting that both approaches afford the same voltammetric (potential response) information.

This "shifting redox distribution" mechanism is notably different from the response mechanism that has been observed for large biomolecule redox capacitive sensing in which recruitment of the bulky target sterically restricts electrolyte access to the

electrode surface, thereby reducing C_r. In that case, it is notably difficult to separate specific (target binding), and non-specific (voltammetric degradation, changes in peak shape *etc*.) suppressions of $C_r(E)$, reducing its accuracy. Here, as specific ion recognition is only expected to perturb the $E_{1/2}$ of the electroactive film and not suppress the redox DOS, any observed suppression of $C_r(E)$ can be attributed to voltammetric degradation and can be fully accounted for (visualised in Figure 4.2-5). This is an important distinction to make here as this "shifting redox distribution" transduction mechanism is not only expected to be more accurate than previous redox capacitive methods, but it also underpins the unprecedented control over binding and analytical parameters that is demonstrated later in Section 4.6. This control results from the fact that the binding site is directly electronically coupled to the redox-addressable unit.

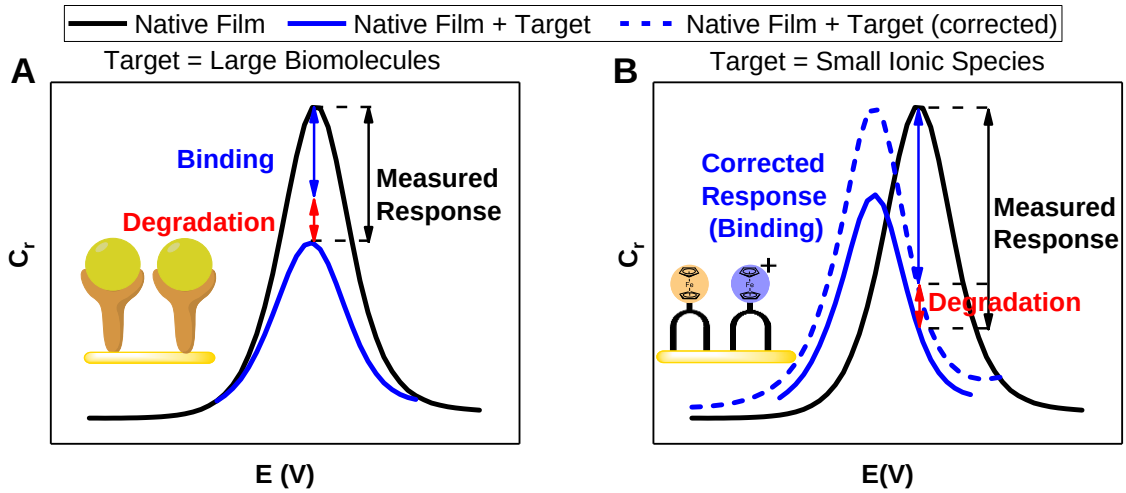


Figure 4.2-5. Schematic depiction of the two transduction mechanisms of redox capacitive sensing for (A) large biomolecules which induce a suppression of the redox DOS and (B) small ionic species which induce a shift in the redox DOS, facilitating correction of the raw, measured responses to account for voltammetric degradation.

In contrast to the transient nature of voltammetry, this redox capacitive approach does not require "sweeps" of the voltage across the redox-active window and can be conducted at any freely-chosen and fixed electrode potential (at a static

equilibrium). Specifically, C_r can be continually measured at a fixed electrode polarisation (and frequency), at any specific point within the Gaussian redox distribution shown in Figure 4.2-2. For example, when the electrode is polarised at $E_{1/2}$, anion binding induces a continuous, monotonic decrease in C_r ($C_{E1/2}$; Figure 4.2-6, red arrow and red trace), as the DOS distribution is continually shifted towards cathodic potentials, away from the sampling potential ($E_{1/2}$, here) such that $C_{E1/2}$ now lies within the anodic tail of the Gaussian distribution. As expected, the binding/sensing isotherm obtained in this manner is similar to that obtained by voltammetric analysis (Figure 4.2-6B, blue trace), however with a somewhat steeper and more quickly plateauing response, arising from a "self-amplification" effect, as discussed in further detail below.

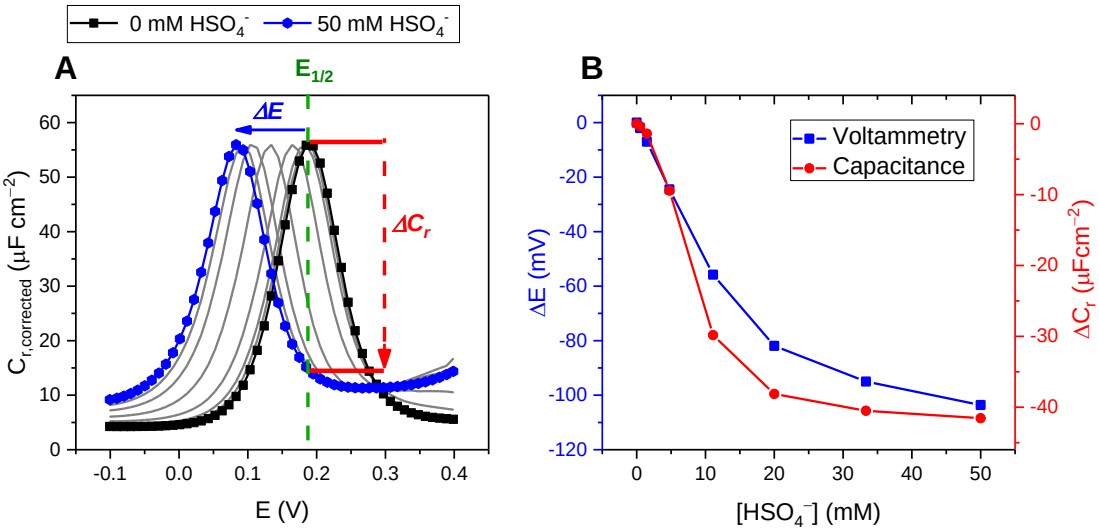


Figure 4.2-6. Response of **3.XB$_{SAM}$** in ACN/H_2O 99:1, 100 mM $TBAClO_4$, 10 mM $HClO_4$, upon exposure to increasing concentrations of HSO_4^-. (A) Normalised C_r as function of potential (the film density of states, DOS). The DOS at each concentration was, for simplicity and illustrative purposes, normalised to the initial $C_{E1/2}$ (i.e. to the initial peak redox capacitance). The raw, absolute redox distributions at each potential are shown in Figure A4.1. The blue arrow indicates the "standard" potential shift as typically resolved voltammetrically. The dashed red arrow indicates the drop in C_r at $E_{1/2}$ (dotted black line). (B) Comparison of the response isotherm obtained from standard voltammetric titrations by SWV (blue squares) with the decrease in C_r at $E_{1/2}$ (red circles), as a result of anion binding-induced cathodic shifting of the DOS such that $C_{E1/2}$ lies in the increasingly smaller tail regime.

To summarise this section:

- Redox capacitance DOS measurements closely resemble those of SW voltammograms as they both represent the redox distribution of the electroactive interface
- Therefore, the ΔE determined from either redox capacitance DOS or SWV measurements are expectedly identical
- However, when the ΔC_r and ΔE isotherms are overlaid, there are clear differences between the two isotherms in that the ΔC_r isotherm is steeper and plateaus more quickly than the ΔE isotherm, suggesting that anion binding is stronger when measured via redox capacitance

4.3 Comparison of Continuous Voltammetric & Redox Capacitive Methods

As alluded to above in Chapter 4.2, there are distinct differences between the voltammetric and redox capacitive (conducted at fixed $E_{1/2}$) anion sensing performance of **3.XB**/**HB**$_{SAM}$, despite otherwise identical conditions. Specifically, Figure 4.2-5 highlights that the C_r response isotherm of **3.XB**$_{SAM}$ for HSO_4^- notably plateaus more quickly with increasing [HSO_4^-] than the standard voltammetric response isotherms, which is indicative of stronger anion binding.

To explain these observations, it is first imperative to note that anion binding to the electroactive interfaces herein is principally governed by two separate binding equilibria. Namely, anion binding to the oxidised receptor **3.XB**$_{SAM}^+$ (K_{Ox}, here ≈1,580 M^{-1}) as well as to the native, neutral receptor **3.XB**$_{SAM}$ (K_{Red}, here ≈20 M^{-1}).[141] The

overall, apparent anion binding strength, K_{App} is dependent on the ratio of the two receptor oxidation states [Ox]/[Red] (*i.e.*, **3.XB$_{SAM}^{+}$/3.XB$_{SAM}$**), and is experimentally determined by fitting response isotherms to a Langmuir-Freundlich model, Equation 3.3-1.

From this relationship, the theoretical, average binding constant, K_{Theo} can be defined as the weighted mean of the binding constants to the fully oxidised/reduced interfaces (K_{Ox} and K_{Red} respectively) and is described by Equation 4.3-1 (derivation provided in Appendices A4, Equations A4.1 – S4.13). Accordingly, K_{Theo} directly reflects the respective molar fractions of oxidised and reduced receptor states (*i.e.*, weighted means of each states, as visualised in Figure 4.3-1), with a 1:1 ratio between oxidised and reduced receptor states when the applied potential = $E_{1/2}$, in accordance with the Nernst equation (Equation 1.4.2-2).

$$K_{Theo} = K_{Ox} * \frac{Ox}{Red+Ox} + K_{red} * \frac{Red}{Red+Ox} \qquad \textbf{Equation 4.3-1}$$

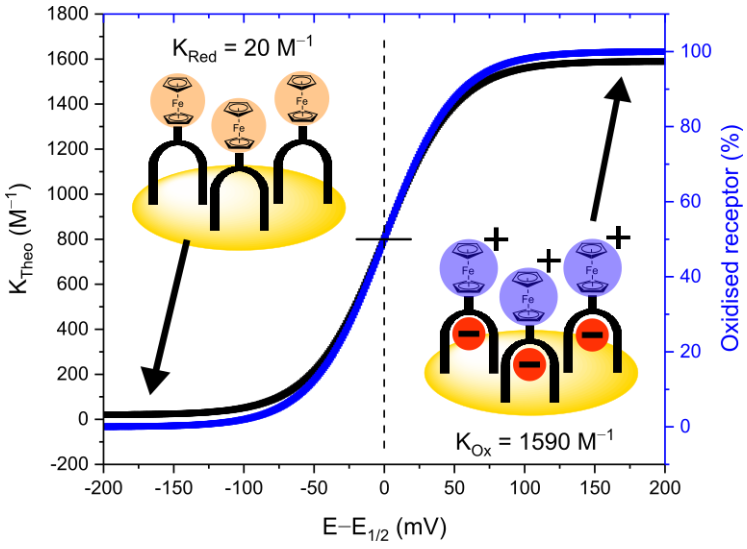


Figure 4.3-1. Theoretical binding constant K_{Theo} (black) and percentage of oxidised receptor (blue) of **3.XB$_{SAM}$** towards HSO_4^- as a function of the electrode potential with respect to $E_{1/2}$ as calculated via Eqn S4.13 and the Nernst equation.

Upon anion binding, the formal potential at which this ratio remains unity shifts cathodically, such that the initial (and constant) electrode polarisation of $E_{1/2}$ now lies in the anodic tail of the Nernstian redox distribution (Figure 4.3-2). Thus, the interface is, as a consequence of anion binding, rendered more cationic at the constantly applied potential (as the ratio of $\mathbf{3.XB_{SAM}^{+}/3.XB_{SAM}}$ increases) and thus displays a higher overall anion binding affinity. In effect, anion binding is, at least phenomenologically "self-amplified". Specifically, the continual, cathodic shift of the redox distribution results in a pseudo-cooperative effect as the increasing dominance of oxidised states (and therefore K_{Ox}) at fixed potential results in stronger anion binding with respect to standard voltammetric methods.

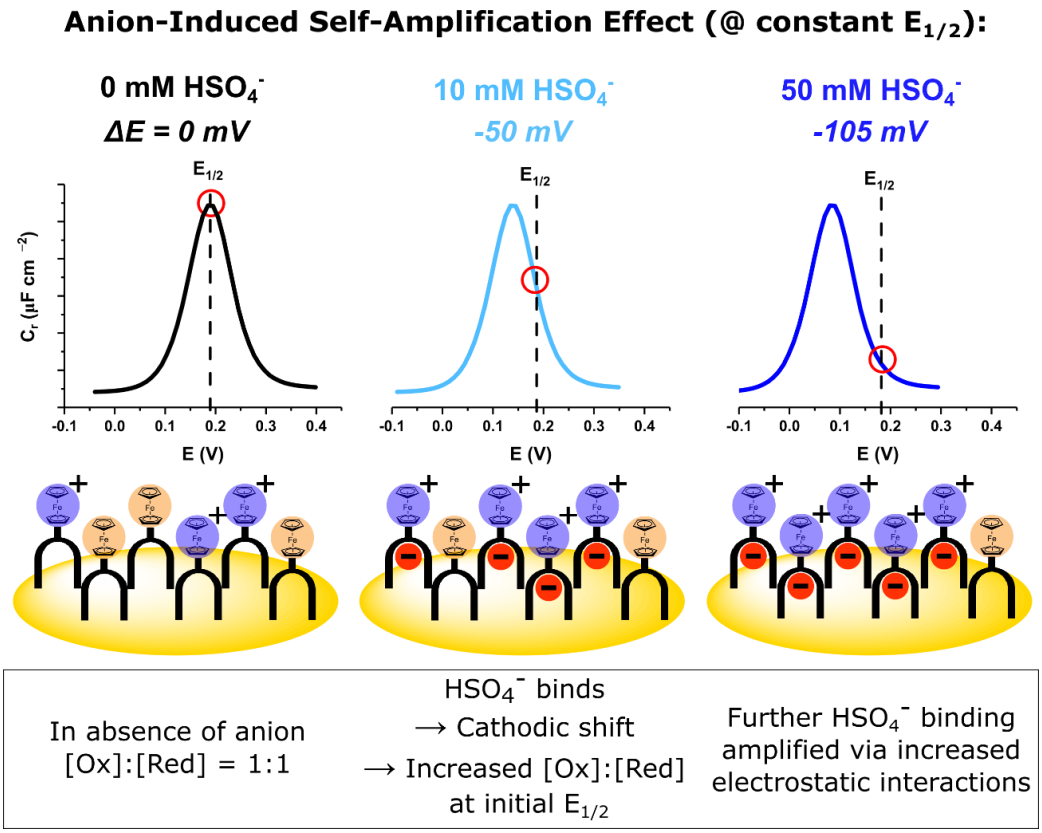


Figure 4.3-2. Schematic depiction of the anion-binding induced cathodic shift of the redox distribution. The red circle depicts the decrease in measured redox capacitance at the constantly applied potential ($E_{1/2}$). Schematically illustrated underneath is the associated ratio of oxidised : neutral (reduced) receptors highlighting the anion binding-induced "oxidation" of the interface, with a concomitantly increased overall anion binding strength ("self-amplification"). It is worth noting that anion binding in the neutral state is essentially negligible (K_{Red} = 20 M^{-1}) and strong in the cationic state (K_{Ox} = 1590 M^{-1}), see also Figure 4.3-1.

Of note is that K_{Theo} and K_{app} are related, but not identical. Firstly, K_{Theo} was calculated based on K_{Ox} = 1590 M^{-1} and K_{Red} = 20 M^{-1}, as obtained from voltammetric isotherm analysis in the presence of only 100 μM acid.[141] However, herein, the higher acid concentration of 10 mM (chosen to minimise voltammetric degradation) induces some degree of protonation of HSO_4^-, such that binding is somewhat attenuated. Secondly, the experimentally determined K_{app} represents an overall sensor performance over a range of anion concentrations. As a result of the self-amplification effect (Figure 4.3-2), the ratio of Ox/Red and thus K_{Theo}, is dependent on the anion concentration such that K_{Theo} is larger in the presence of higher concentrations of anions. In essence, higher [A^-] shifts the redox distribution further cathodically, such that the ratio of $\mathbf{3.XB_{SAM}^+/3.XB_{SAM}}$ rises despite the fact that the initial electrode polarisation has remained constant. K_{app} thus "spans" a range of different K_{Theo}. For example, for measurements at $E_{1/2}$: binding is switched on from an initial theoretical binding constant of $K_{Theo,\ E1/2}$ = 805 M^{-1} to a maximum of K_{Ox} = 1580 M^{-1} (Figure 4.3-1).

In contrast, during standard voltammetric analyses no such "self-amplification" is observed and the overall, apparent binding remains constant (at least as transduced by the shift in half-wave potential). These concepts are borne out in the binding and analytical parameters for both methods. For example, the limit of detection (LOD) of this redox capacitive flow sensor ($\mathbf{3.XB_{SAM}}$, conducted at fixed $E_{1/2}$) towards HSO_4^- was determined to be 44.5 ± 15.5 μM and the apparent binding constant was 121 ± 6 M^{-1} (*cf.* 59.8 ± 5.5 μM and 68.6 ± 17.6 M^{-1}, respectively via the highly optimised voltammetric method detailed in Chapter 3). Without this

optimised analysis, the LOD for a standard voltammetric assay is even worse (825 ± 138 μM).

Crucially, this potential-dependent binding modulation does not arise from any specific interaction of the anion with the electrode itself (*i.e.*, the individual K_{Ox} and K_{Red} remain unaffected), but is purely governed by the potential-dependence of the ratio of the receptor oxidation states. Thus, it follows that it should be possible to further exploit the dependence of K_{app} on the ratio of $\mathbf{3.XB_{SAM}^{+}/3.XB_{SAM}}$ to fine-tune anion binding strength and sensor performance by judicious choice of the electrode potential, as established later in Section 4.6.

4.4 Pseudo-flow Redox Capacitive Anion Sensing

Building on the concepts discussed above and the established redox capacitance DOS response behaviour observed under static conditions, attention then turned to translating static C_r measurements into a continuous redox capacitive readout so that ion binding can be followed in real-time. In order to achieve this, continuous C_r readouts were afforded by performing measurements at a single fixed frequency (f_r, labelled in Figures 4.2-1 and 4.2-3), and fixed potential ($E_{1/2}$, unless otherwise stated). In essence, these continuous measurements only follow C_r at the inflection point of the capacitive Nyquist plot for $\mathbf{3.XB/HB_{SAM}}$, and as only one frequency is recorded the temporal resolution of the redox capacitance measurement is drastically improved from ≈ 2 min per Nyquist plot, to ≤ 2 s per data point measured at fixed f_r. As a result, continuous redox capacitance measurements can be performed in a facile and non-perturbatory manner, affording a continuous sensor readout (C_r) that is sensitive to analyte concentration. The high temporal resolution

of ≤2 s is significantly faster than that of the highly optimised continuous voltammetric method described above in Chapter 3, with a notably direct output that does not require any extensive data processing (*cf.* 3.7 s).

For example, C_r was first continually monitored within a pseudo-flow setup (in a stirred, but otherwise static three-electrode cell) into which sequential anion aliquots were added which are analogous to the static titrations described above in Section 4.2, but allow for continuous monitoring of the induced C_r response at each analyte concentration (Figure 4.4-1, black trace). As expected, the initially stable $C_{E1/2}$ immediately dropped and quickly stabilised to increasingly lower values upon addition of higher concentrations of HSO_4^- (Figure 4.4-1, black trace and Figure A4.2) and $H_2PO_4^-$ (Figure A4.4), affording response isotherms that are identical to those obtained under either fully static or continuous flow conditions (Figure 4.4-2). The progressive decrease in C_r with increasing $[HSO_4^-]$ demonstrates the predicted transduction mechanism discussed above for **3.XB/HB$_{SAM}$** at fixed $E_{1/2}$, whereby target binding induces a cathodic shift of the redox DOS distribution away from the peak C_r, down into the tail of the distribution (see Figure 4.3-2 for a schematic depiction of this mechanism).

Alternatively, continuous analyte additions can be made with the help of a syringe pump to afford sensing isotherms with a very high number of data points (see Figures 4.4-1 & 4.4-2), over a time period of 5 min, see green trace in Figure 4.4-1. Notably this also results in a much shorter measurement duration compared to the sequential addition method in addition to the higher data density. As expected, addition of PF_6^- (control) did not induce a significant capacitance response (Figure

4.4-3). From Figure 4.4-2, it is evident that the relative response isotherms obtained under all three conditions (unstirred + sequential addition, stirred + sequential addition and stirred + continuous addition) are near-identical for the response of **3.XB$_{SAM}$** to increasing [HSO_4^-].

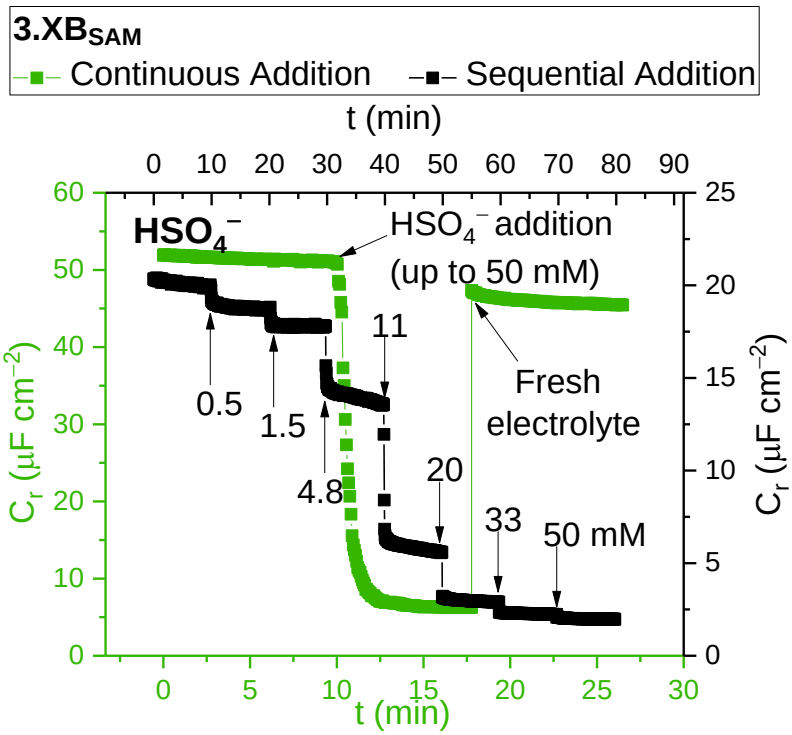


Figure 4.4-1. Continuous capacitance measurement displaying the response of **3.XB$_{SAM}$** under pseudo flow conditions in a stirred three-electrode cell. The trace in black depicts the sequential addition of aliquots of HSO_4^- up to 50 mM. The green trace depicts the response upon continuous addition of up to 50 mM HSO_4^- via a syringe pump (flow rate Q = 0.8 mL min^{-1}, into an initial electrolyte volume of 4 mL), followed by washing and measurement in fresh electrolyte. Note the different time frames (x-axis scaling) for both graphs showing that continuous titration measurements can be conducted up to 3x faster than titrations carried out by sequential additions of target.

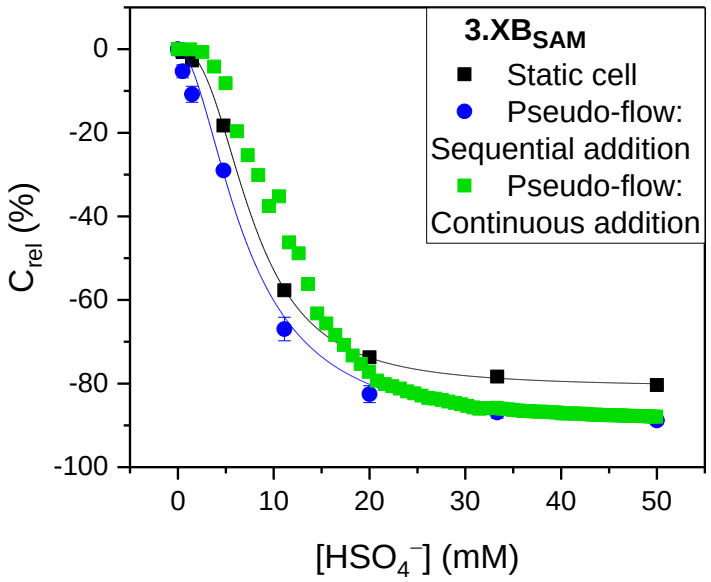


Figure 4.4-2. Capacitance response of **3.XB$_{SAM}$** under completely static conditions (blue squares) and under pseudo flow conditions in a stirred, but otherwise static, three-electrode cell at $E_{1/2}$. The black circles depict the binding isotherm corresponding to the sequential addition of increasing concentrations of up to 50 mM HSO_4^-. Shown in green triangles is the continuous binding isotherm corresponding to the continuous addition of up to 50 mM HSO_4^- via a syringe pump (V_{Sample} = 4 mL, flow rate Q = 0.8 mL min^{-1}, into an initial electrolyte volume of 4 mL). The somewhat later onset of the response under continuous addition arises from a mixing delay.

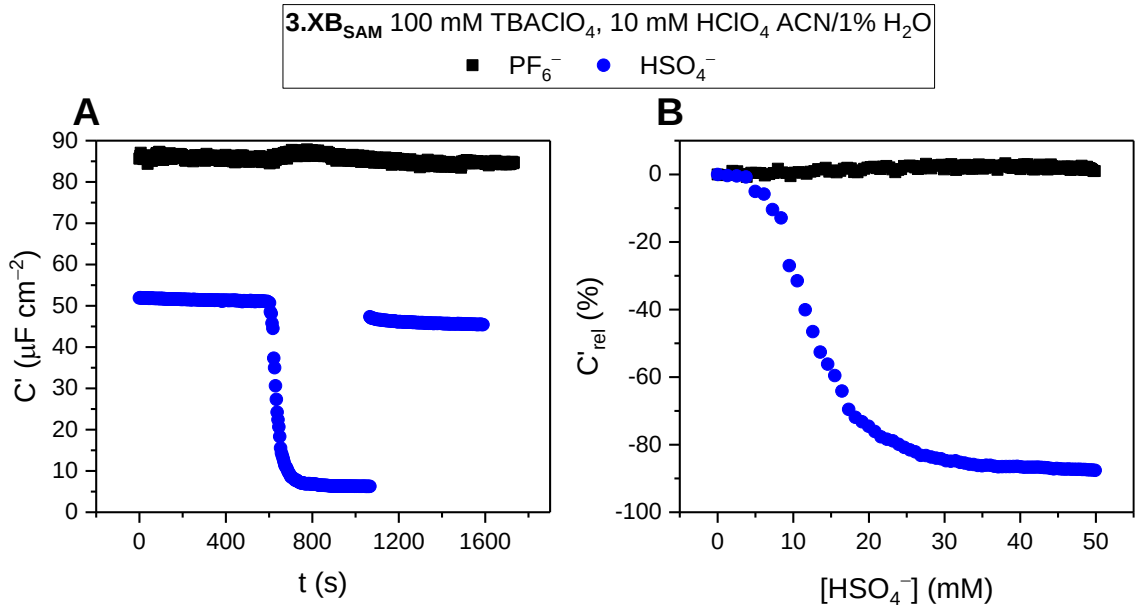


Figure 4.4-3. Capacitance response of **3.XB$_{SAM}$** under pseudo flow conditions in a stirred, but otherwise static, 3-electrode cell at $E_{1/2}$. (A) A comparison is shown for the temporal sensor response upon continuous addition of up to 50 mM HSO_4^- (blue) or PF_6^- (control, black) via a syringe pump (V_{Sample} = 4 mL, flow rate Q = 0.8 mL/min, into an initial electrolyte volume of 4 mL). Following the continuous addition of HSO_4^-, the Au disc electrode functionalised with **3.XB$_{SAM}$** was removed from solution, rinsed with copious amounts of ACN, then placed into a fresh solution of supporting electrolyte only, re-establishing the baseline C_r in the absence of target. (B) The corresponding continuous binding isotherms are depicted, again representing the capacitance response to HSO_4^- (blue) and PF_6^- (black), obtained by conversion of the blue/black trace from the time to the concentration domain.

This approach presents a particularly useful, fast (5 min continuous addition vs. 30 min static or pseudo-flow sequential addition of target) and experimentally straight-forward way of obtaining detailed information about interfacial binding events, an analysis that cannot be easily carried out by standard voltammetric methodologies.

In addition to the practical benefits of the continuous addition method conducted under pseudo-flow conditions, the high density of data points per assay obtained in real-time is also advantageous when elucidating more complex response patterns, such as those observed at different applied, fixed electrode potentials. These results are discussed in greater detail later in Section 4.6 along with predictions and comprehensive analyses for the C_r responses based on different applied, fixed electrode potentials.

In summary:

- A method to conduct continuous redox capacitance measurements in real-time has been presented
- Continuous C_r measurements were associated with a high temporal resolution of ≤2 s
- Continuous C_r measurements can be conducted under pseudo flow conditions (in a stirred solution in a vial) with either sequential or continuous additions of target
- Continuous C_r measurements with continuous addition of target affords response isotherms with a very high number of data points wr.t. to sequential additions (typically ≈ 80 *vs*. 8 data points)

Building on these results, this continuous redox capacitive sensing methodology was then implemented in conjunction with a microfluidic setup (analogous to that of Chapter 3, Figures 3.4-1, 7.9.2-1 and 7.9.2-2) to monitor anion binding in real-time. By translating this continuous C_r method under continuous flow, the reversible nature of the host-guest binding interactions at **3.XB**/$\mathbf{HB_{SAM}}$ can be fully exploited to bind and release anionic targets in a facile manner. This in turn facilitates a fast and simple route to perform systematic assays for anionic targets, and affords a direct output that does not require additional tenuous data processing (*cf*. Chapter 3), as explored below.

4.5 Continuous Redox Capacitive Anion Sensing Under Flow

Utilising a custom-designed electrochemical flow cell (see Section 7.9.2 for more details), measurements under continuous flow were conducted at fixed-frequency (f_r) and fixed-potential ($E_{1/2}$, unless otherwise stated). Electrolyte (ACN/H_2O 99:1, 100 mM $TBAClO_4$, 10 mM $HClO_4$) was continuously pumped through the cell by a syringe pump at a flow rate of 500 µL min^{-1}, and target sample aliquots of defined volume (typically 0.5 mL) were added through the use of a manual injector valve.

Analogously to the voltammetric analyses detailed in Section 3.4, these redox capacitive analyses were tolerant to a large range of flow rates (up to 2 mL min^{-1}, see Figure 4.5-1) and displayed stable, flow rate-independent capacitance responses to target anions.

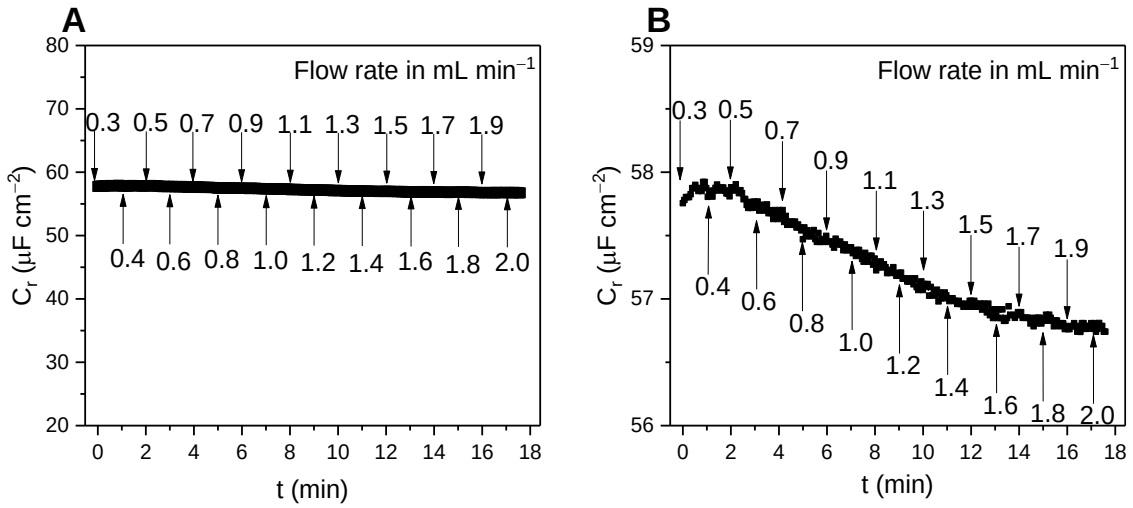


Figure 4.5-1. Dependence of redox capacitance signal (measured at $E_{1/2}$) on flow rate, v over a range of 300 to 2000 μL min^{-1}. (A) Scaled to a range encompassing a typical capacitive response towards anion binding ($\Delta C_{r,max} \approx 50$ μF cm^{-2}) (B) and over a narrower range, highlighting the negligible change in C_r with changing v.

At a constant electrode polarisation of $E_{1/2,}$ exposure of **3.XB/HB$_{SAM}$** to analyte (exemplified in Figure 4.5-2 for the response of **3.XB$_{SAM}$** to HSO_4^-) was expectedly associated with notable response spikes (decrease in C_r), whilst control injections of a non-coordinating, control anion (PF_6^-) did not induce a significant capacitance response (Figure 4.5-3). Injection of the analyte sample was immediately followed by a "washing" step with fresh electrolyte in all cases, such that a (new) C_r baseline is (re)established.

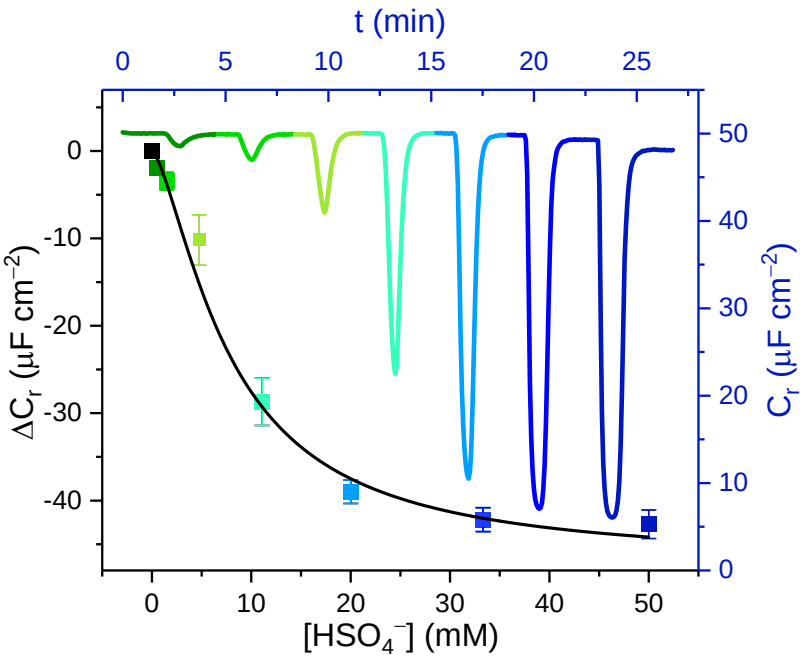


Figure 4.5-2. Redox capacitance response of **3.XB$_{SAM}$** towards HSO_4^- under continuous electrolyte flow in the custom flow cell (cell volume = 100 µL, flow rate Q = 500 µL min^{-1}, E = $E_{1/2}$, f = f_r). Each spike represents the response towards aliquots (V_{Sample} = 0.5 mL) of HSO_4^- of increasing concentrations up to 50 mM. The response isotherm was obtained by normalizing the peak response to the baseline before each addition. The solid line represents a fit according to the Langmuir-Freundlich model (Eqn. 3.3-1). Error bars represent one standard deviation of five independent experiments (independently prepared films across three different electrodes).

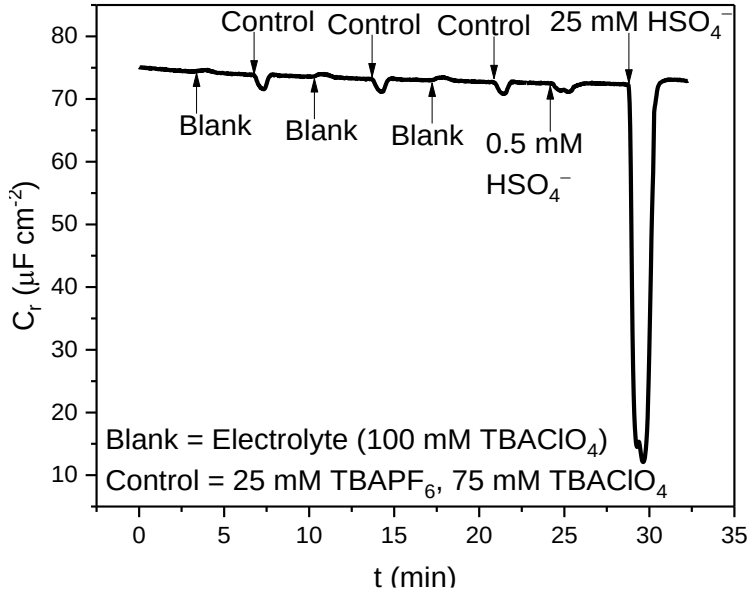


Figure 4.5-3. Redox capacitance response of **3.XB$_{SAM}$** towards blank samples (running electrolyte, 100 mM $TBAClO_4$), control samples (25 mM $TBAPF_6$), 0.5 mM HSO_4^- and 25 mM HSO_4^- under continuous electrolyte flow (flow rate Q = 500 µL min^{-1}, E = $E_{1/2}$, f = f_r). Each spike represents the response towards aliquots (V_{Sample} = 0.5 mL) of the blank, control or HSO_4^- samples, as indicated.

Unless stated otherwise, the flow conditions described above (Q = 500 µL min^{-1} and V_{Sample} = 0.5 mL) were used, which were specifically chosen for two reasons: firstly, to ensure that the maximum possible response at each anion concentration was fully resolved in all cases but also, secondly, to minimise the time **3.XB**/**HB$_{SAM}$** was exposed to the sample aliquots, as voltammetric degradation is expectedly higher in the presence of basic anions (particularly for $H_2PO_4^-$), contributing to signal loss. The first aspect was verified by performing an analogous measurement with double the sample aliquot volume to V_{Sample} = 1 mL (exposing **3.XB**/**HB$_{SAM}$** to target for 2x the length of time), and identical response magnitudes were observed regardless of V_{Sample} (Figure A4.7). The good agreement between both conditions demonstrated that the maximum response was indeed reached under the standard conditions selected here. Empirically, no correlation was found between the magnitude of response and signal loss over time, but to ensure consistency between independent measurements, C_r responses following a baseline signal loss of approximately > 20% were discarded.

By virtue of acidifying the supporting electrolyte (100 mM $TBAClO_4$ + 10 mM $HClO_4$) and polarising at more cathodic potentials (–200 mV w.r.t. $E_{1/2}$ = $E_{–200}$) within the redox active window of **3.XB$_{SAM}$**, signal degradation (resulting from voltammetric degradation) is minimised and long-term anion sensing analyses were supported. Under these conditions, reproducible, positive (by virtue of polarising at $E_{–200}$, discussed in Section 4.6) responses to 20 mM HSO_4^- were observed over a period of more than 4 h (see Figure 4.5-4).

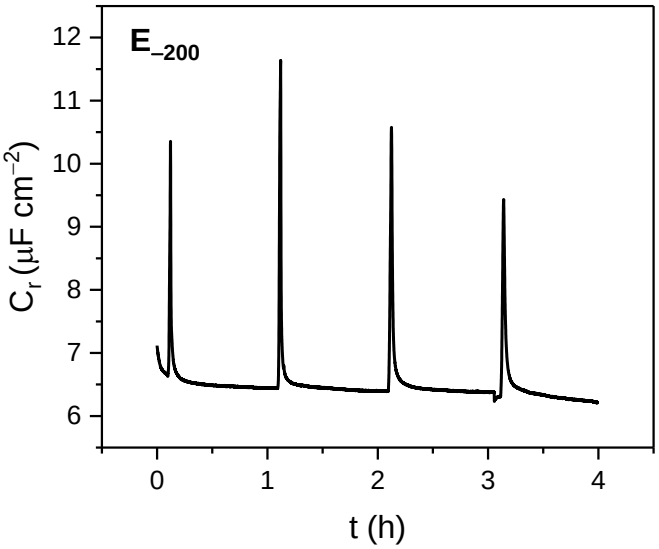


Figure 4.5-4. Redox capacitance response of **3.XB$_{SAM}$** towards HSO_4^- under continuous electrolyte flow (flow rate Q = 200 µL min^{-1}, E = E_{-200}, f = f_r) over 4 h. Each spike in represents the response towards aliquots (V_{Sample} = 0.5 mL) of 20 mM HSO_4^-. Positive responses are observed by virtue of polarising at a potential more cathodic than $E_{1/2}$ (E_{-200}), the origin of this is detailed in Section 4.6.

4.6 Tuning Sensor Performance Through Surface Polarisation

As established above, the addition of anionic targets under continuous flow (*e.g.*, HSO_4^-, $H_2PO_4^-$ or Cl^-) induces significant reductions in the measured C_r of **3.XB/HB$_{SAM}$** when poised at a fixed potential equal to the $E_{1/2}$, as visualised by the response spikes in Figure 4.5-2. Given that the sensing mechanism here is dependent on the redox DOS distribution of **3.XB/HB$_{SAM}$** shifting relative to the applied potential upon anion binding (*e.g.*, at a fixed initial $E_{1/2}$, the distribution shifts cathodically upon addition of anion, resulting in a decrease in C_r from the peak C_r into the anodic tail of the distribution), along with the inherent freedom to choose this fixed, applied potential, one would expect the C_r response to be dependent on this chosen potential. Based on the concepts detailed above, the impact of altering the applied electrode polarisation potential on anion binding/sensing performance was then explored.

For example, when the sensor electrodes are poised anodically with respect to $E_{1/2}$, *e.g.*, at +100 mV (E_{+100}, red trace, Figures 4.6-1 and 4.6-2), anion binding induced a generally similar response to that at $E_{1/2}$ (monotonic signal decrease), however with a smaller overall response magnitude (ΔC_{max}), as the baseline C_r signal at this potential was already smaller (Table 4.6-1). However, the response isotherm was noticeably steeper, which directly reflects enhanced anion binding at the more positively charged **3.XB$_{SAM}$**$^+$ interface (see Figures 4.3-2 and 4.6-2); also reflected in a higher K_{app} of 320 ± 60 M^{-1}.

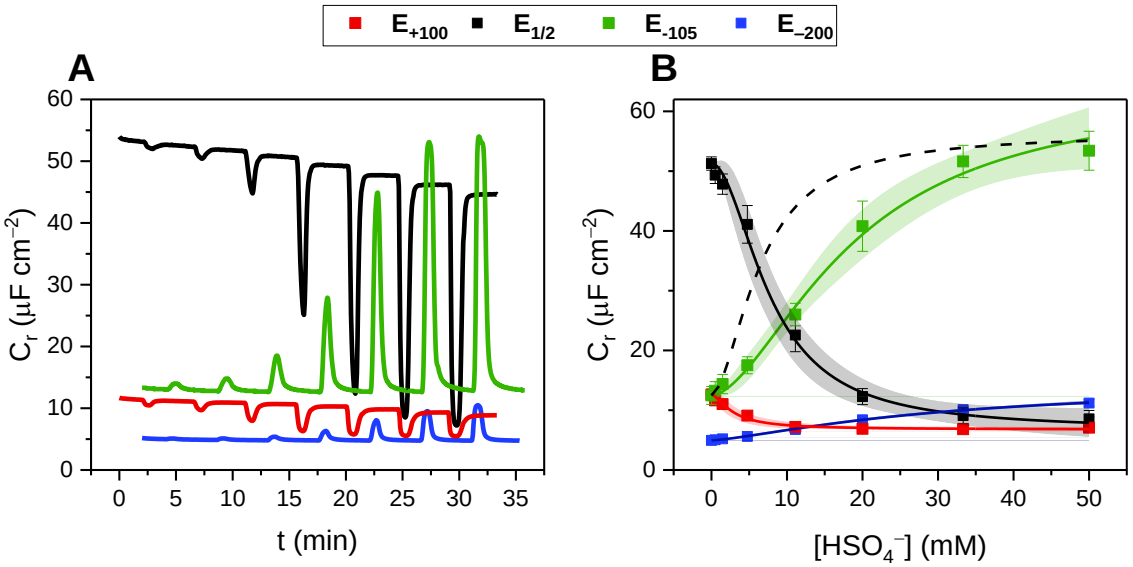


Figure 4.6-1. (A) Redox capacitance response of **3.XB$_{SAM}$** towards HSO_4^- at $E_{1/2}$ (black), E_{-105} (green), E_{-200} (blue) and E_{+100} (red) under continuous electrolyte (B) The corresponding baseline-corrected response isotherms. Solid and dashed lines represent fits according to the Langmuir-Freundlich model (Eqn. 3.3-1). The dashed black line represents, for simpler comparison, the mirrored capacitance response at $E_{1/2}$, highlighting the steeper response slope and enhanced anion binding magnitude at $E_{1/2}$ vs at E_{-105}. Error bars represent one standard deviation from at least three independent experiments. Shaded areas represent the 95% confidence interval.

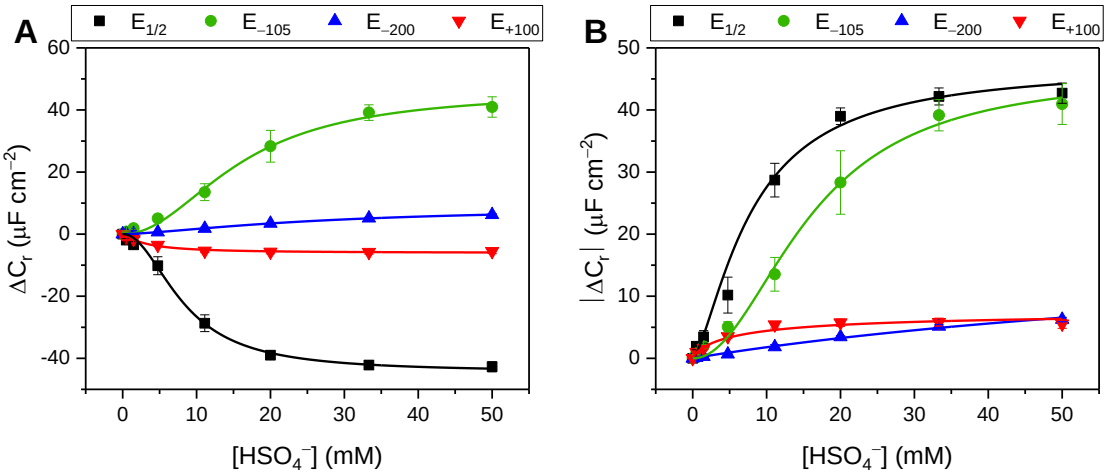


Figure 4.6-2. Baseline-corrected response isotherms corresponding to the sensograms in Figure 4.6-1 showing the response of **3.XB$_{SAM}$** to HSO_4^- (up to 50 mM) as the (A) absolute change in capacitance and (B) the modulus of the change in capacitance. Solid lines represent fits according to the Langmuir-Freundlich model (Eqn. 3.3-1). Error bars represent one standard deviation from at least three independent experiments.

Table 4.6-1. Apparent binding constants Kapp (M^{-1}) and maximum relative response ΔC_{max} (μF cm^{-2}) of **3.XB$_{SAM}$** towards HSO_4^- obtained by fitting of the response isotherms (Figure 4.6-1) at different potentials according to the Langmuir-Freundlich model (Eqn. 3.3-1).

	Redox capacitance				Voltammetry
E_{dc}	**E_{+100}**	**$E_{1/2}$**	**E_{-105}**	**E_{-200}**	n.a.
LOD (μM)	42.4 ± 4.0	44.5 ± 15.5	70.4 ± 18.2	78.9 ± 29.1	59.8 ± 5.5[a]
K_{app} (M^{-1})	320 ± 60	121 ± 6	64.2 ± 7.7	36.2 ± 7.2	68.6 ± 17.6
ΔC_{max} (μF cm^{-2})[b]	-6.09 ± 0.35	-44.4 ± 1.0	46.0 ± 3.05	8.95 ± 1.12	-116 ± 9[c]
Sensitivity (μF mM^{-1})	0.63 ± 0.10	2.06 ± 0.60	1.03 ± 0.17	0.14 ± 0.03	4.89[d]

The limit of detection (LOD) was obtained by analysis of the pseudo-linear region at low concentration (0 – 4.8 mM, see Section 7.10.2). The sensor performance in an optimised voltammetric format (SWV) is also shown for comparison.[271] N.a. – not applicable. Errors represent one standard deviation of at least three independent repeats. a – under highly optimised continuous flow conditions with advanced data processing/fitting. b – at $[HSO_4^-] \rightarrow \infty$ obtained from fitting. c – in mV. d – in mV mM^{-1}.

In contrast, when the sensor is poised at potentials cathodic of $E_{1/2}$, anion binding shifts the redox capacitance such that C_r grows, resulting in a signal "switch-ON". For example, at E_{-105} (the maximum cathodic shift observed, induced upon addition exposure to 50 mM HSO_4^-) a response isotherm is observed that at first glance exactly mirrors that obtained at $E_{1/2}$ (green and black traces, Figures 4.6-1 and 4.6-2). However, upon direct comparison of the resulting isotherms (see Figure 4.6-2), it is evident that whilst the absolute maximum C_r response magnitudes at $E_{1/2}$ and E_{-}

$_{105}$ are almost identical, the response isotherm obtained at E_{-105} is noticeably less steep; indicative of weaker anion binding. This weaker anion binding profile was expected due to the lower proportion of oxidised to reduced receptors at more cathodic potentials. Crucially, this fully corroborates the predictions made above in Section 4.5 that anion binding at a more cathodic applied potential (E_{-105}) is comparably attenuated to that at $E_{1/2}$ (K_{app} = 64 ± 8 M^{-1} and 121 ± 6 M^{-1} at E_{-105} and $E_{1/2}$, respectively) as a result of the initially lower [Ox]/[Red] ratio at E_{-105}. These effects were expectedly even more pronounced at more cathodic potentials (*e.g.*, E_{-200}), where the initial equilibrium is shifted further towards the lower affinity [Red] redox state, thus requiring increasingly higher analyte concentrations to induce a C_r response (K_{app} = 36.2 ± 7.2 M^{-1} and 121 ± 6 M^{-1} at E_{-200} and $E_{1/2}$, respectively). Crucially, these results present a powerful and facile way to modulate anion binding strength by almost ten-fold (*cf*. K_{app}, E_{+100} = 320 M^{-1}). Furthermore, key analytical parameters such as the limit of detection (LOD) were also modulated substantially, (LOD = 42.4 ± 4.0 μM and 78.9 ± 29.1 μM at E_{+100} and E_{-200}, respectively).

The implications of this methodology for host-guest sensing applications more generally are manifold. For example, judicious choice of the applied electrode potential could tune the sensitivity and/or limit of detection (LOD) of the sensor to obtain a threshold sensing response to any precise analyte concentration, for example. Specifically, at sufficiently cathodic potentials, low anion concentrations would not induce sufficient voltammetric shifts of the sampled DOS to induce significant Faradaic activity (*i.e.*, the measured capacitance remains (largely) non-Faradaic, see the isotherm at E_{-200}, Figure 4.6-1). Alternatively, sensing studies with natively redox-active guests could be performed at applied potentials outside of the

guest's electroactive window, thereby enabling analyses that would be otherwise impossible or extremely challenging by other techniques (*e.g.*, voltammetry).

These results were also reproduced under the pseudo flow conditions described above in Section 4.4 (see Figure 4.6-3). Once again, at intermediate potentials (for example see the response isotherms at E_{-50} or E_{-100}), the response is characterised by an initial capacitance increase when the distribution shifts "into" the applied potential followed by a continuous monotonic decreasing response once the distribution shifts further cathodically.

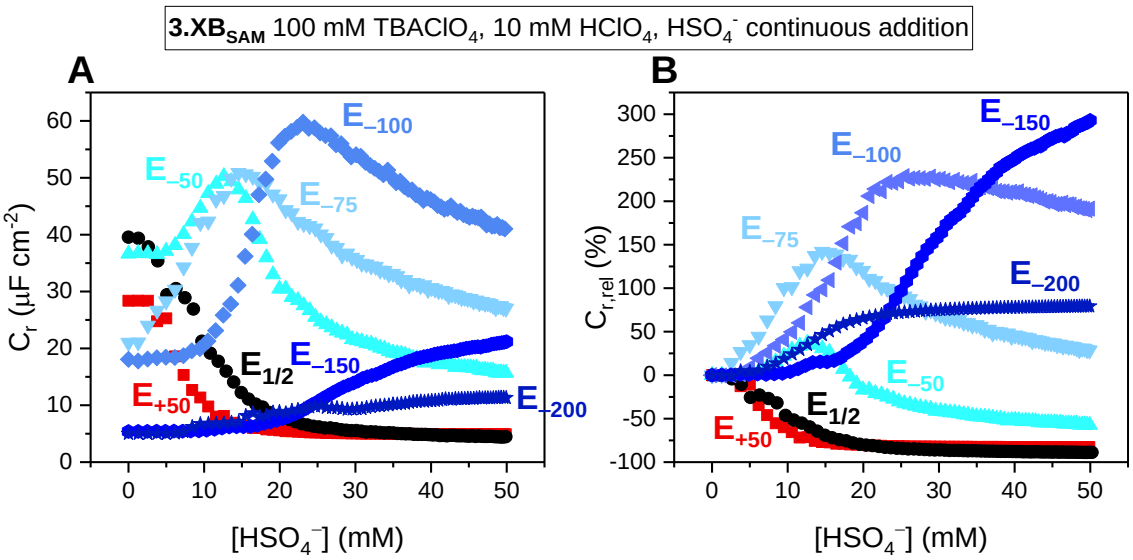


Figure 4.6-3. (A) Absolute and (B) relative capacitance responses of **3.XB$_{SAM}$** towards HSO_4^- (up to a final concentration of 50 mM) at different electrode potentials, as determined by continuous, pseudo-flow experiments (continuous anion addition via syringe-pump into stirred cell). Note that the relative response in B) is normalised to the baseline capacitance at each individual potential and not the baseline capacitance at $E_{1/2}$.

4.7 Redox Capacitive Sensing of Other Anions

This unique control over guest binding strength is, of course, extendable to other anions. For example, binding of $H_2PO_4^-$ to the interface is similarly tuneable by varying the applied electrode potential, with a significantly stronger K_{app} = 401 ± 35 M^{-1} at $E_{1/2}$ than at a cathodic polarisation (132 ± 29 M^{-1} at E_{-200}), as shown in Figures

4.7-1 & 4.7-2. The sensing performance of **3.XB$_{SAM}$** for HSO_4^- and $H_2PO_4^-$ is contrasted in Table 4.7-1. The slightly lower LOD for $H_2PO_4^-$ at E_{-200} in comparison to $E_{1/2}$ arises from a lower standard deviation of the baseline at E_{-200} (*i.e.*, the non-Faradaic capacitive baseline is more stable than the Faradaic baseline). As shown in Table 4.7-1, the sensitivity and K_{app} are significantly higher at $E_{1/2}$. Of further note is that the accuracy of the slopes of the linear range (sensitivities) and LODs is lower for $H_2PO_4^-$ (in comparison to HSO_4^-), as fewer data points fall within the linear sensor response regime.

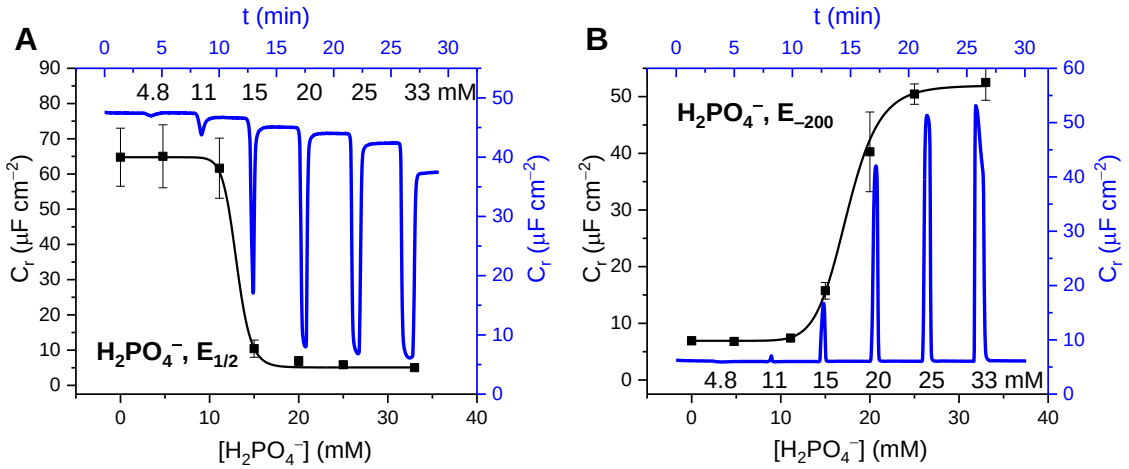


Figure 4.7-1. Redox capacitance response of **3.XB$_{SAM}$** towards $H_2PO_4^-$ under continuous electrolyte flow in a custom flow cell, at (A) E = $E_{1/2}$ and (B) E = E_{-200}. Each spike represents the response towards aliquots of $H_2PO_4^-$ of increasing concentrations up to 33 mM. The solid line represents a fit according to the Langmuir-Freundlich model (Eqn. 3.3-1). Error bars represent one standard deviation of three independent experiments.

Table 4.7-1. Apparent binding constants K_{app} (M^{-1}) and maximum relative response ΔC_{max} (μF cm^{-2}) of **3.XB$_{SAM}$** towards HSO_4^- and $H_2PO_4^-$ obtained by fitting of the response isotherms (Figures 4.7-1 and 4.7-2, respectively) at E_{-200} and $E_{1/2}$ according to the Langmuir-Freundlich model (LFM, Eqn. 3.3-1). The limit of detection (LOD, μM) and sensitivity (μF mM^{-1}) was obtained by analysis of the pseudo-linear region at low concentration (see below and Section 7.10.2).

	HSO_4^-		$H_2PO_4^-$	
E_{dc}	**E_{-200} [a]**	**$E_{1/2}$ [b]**	**E_{-200} [a]**	**$E_{1/2}$ [a]**
LOD (μM)	78.9 ± 29.1	44.5 ± 15.5	4.06 ± 3.29[c]	6.14 ± 0.63[d]
Sensitivity (μF mM^{-1})	0.14 ± 0.03	2.06 ± 0.60	3.75 ± 0.85[c]	13.2 ± 2.81[d]
K_{app} (M^{-1})	36.2 ± 7.2	121 ± 6	132 ± 29	401 ± 35
ΔC_{max} (μF cm^{-2})[e]	8.95 ± 1.12	–44.4 ± 1.0	48.3 ± 4.1	–59.1 ± 8.6

a - 3 b - 5 independent repeats. Obtained from a linear range of c- 11-20 mM $H_2PO_4^-$ or d-11-15 mM $H_2PO_4^-$. e – at $[A^-] = \infty$, as obtained from Langmuir-Freundlich fittings (Eqn. 3.3-1).

As displayed in Figure 4.7-1, negligible responses were observed at **3.XB$_{SAM}$** towards $H_2PO_4^-$ at concentrations below 10 mM, attributable to full protonation of this more basic anion by the acidic electrolyte (consistent with observations in Section 3.3).[271] In order to account for the complete "removal" of $H_2PO_4^-$ from the equilibrium, $H_2PO_4^-$ response isotherms were corrected by omitting all data points between 0 – 10 mM and correcting all remaining data points by -10 mM [$H_2PO_4^-$], resulting in the isotherms shown in Figure 4.7-2. The apparent $H_2PO_4^-$ binding constants and LODs given in Table 4.7-1 were determined from these corrected isotherms.

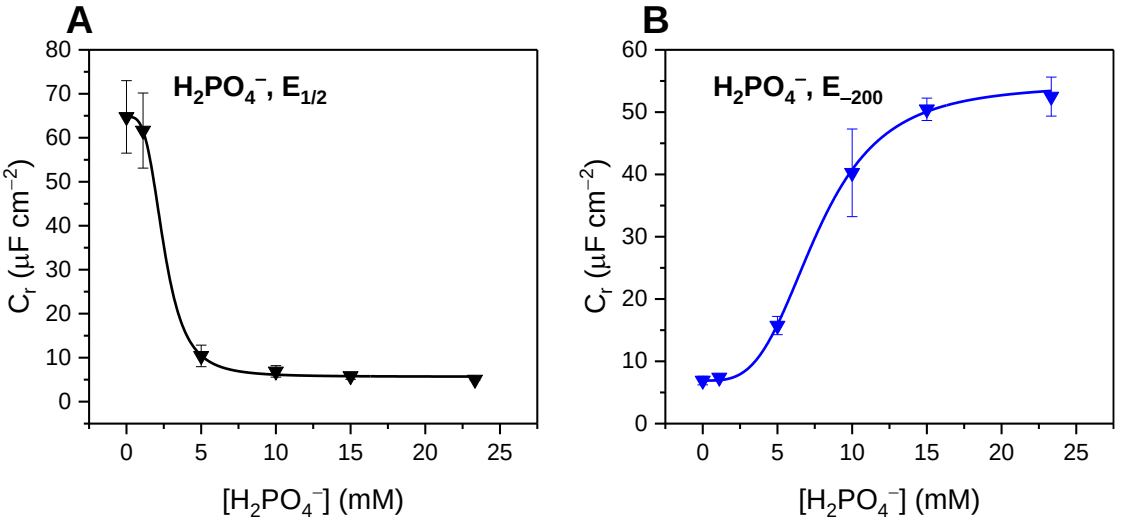


Figure 4.7-2. Redox capacitance response isotherms of the average response of **3.XB$_{SAM}$** towards $H_2PO_4^-$ at (A) $E_{1/2}$ and (B) E_{-200} under continuous electrolyte flow. The response isotherms in (A) and (B) were corrected by –10 mM to account for the suppressed response below 10 mM due to full protonation of $H_2PO_4^-$. Solid lines represent fits according to the Langmuir-Freundlich model (Eqn. 3.3-1). Error bars represent one standard deviation of three independent experiments at independently generated interfaces across three different electrodes.

Preliminary studies were also performed with **3.XB$_{SAM}$** in response to Cl^-, but it should be noted that the standard V_{Sample}= 0.5 mL was insufficient to observe the full extent of the response to Cl^- (*i.e.*, the response to each analyte injection did not plateau), thus V_{Sample} was increased to 1 mL, doubling the duration of time of exposure of Cl^- to the interface. This was shown to be sufficient to observe an equilibrium response for concentrations of Cl^- up to 20 mM, but a noTable

Aharpening of the peaks with increasing [Cl^-], prevented investigation of concentrations above 20 mM (Figure 4.7-3). As shown in Figure 4.7-3, Cl^- induced responses that were also characterised by a significantly slower baseline recovery than observed for the oxoanions, an observation potentially arising from slow anion decomplexation. Interestingly, even slower apparent anion decomplexation was observed at the more cathodic potential (E_{-200}). Fortunately, the high temporal resolution offered by this method appears to be sufficient to resolve interfacial guest association/dissociation kinetics, something that remains particularly challenging in the field of host-guest chemistry.

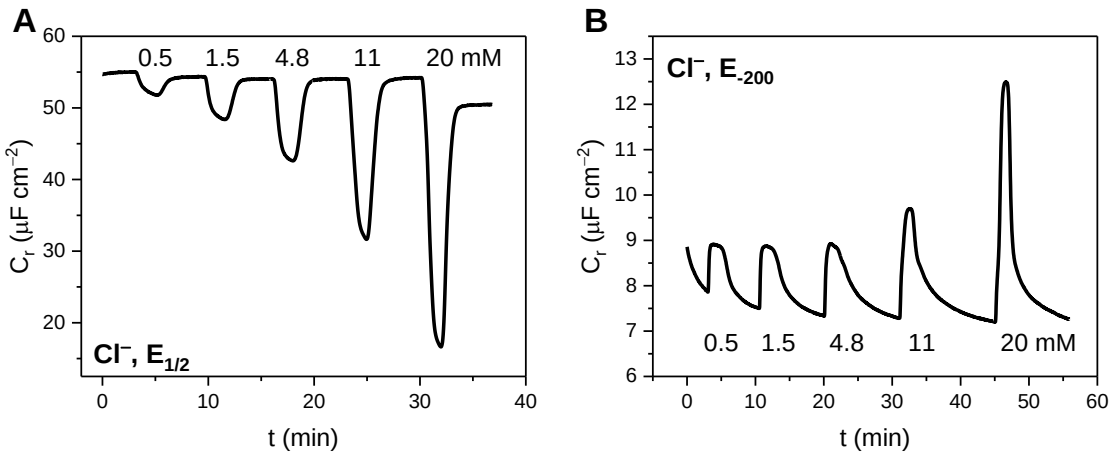


Figure 4.7-3. Redox capacitance response of **3.XB$_{SAM}$** towards Cl^- under continuous electrolyte flow, V_{Sample} = 1 mL at (A) E = $E_{1/2}$ and (B) E_{-200}. Each spike represents the response towards aliquots of Cl^- of increasing concentrations up to 20 mM.

The possibility to elucidate binding kinetics was further investigated through comparative studies of **3.XB$_{SAM}$** in response to HSO_4^- and Cl^-. Figure 4.7-4 shows a side-by-side comparison of responses to HSO_4^- and Cl^- (poised at E_{-100} to reduce voltammetric degradation and extend measurement time), displaying clear differences in the response signatures between these two anions.

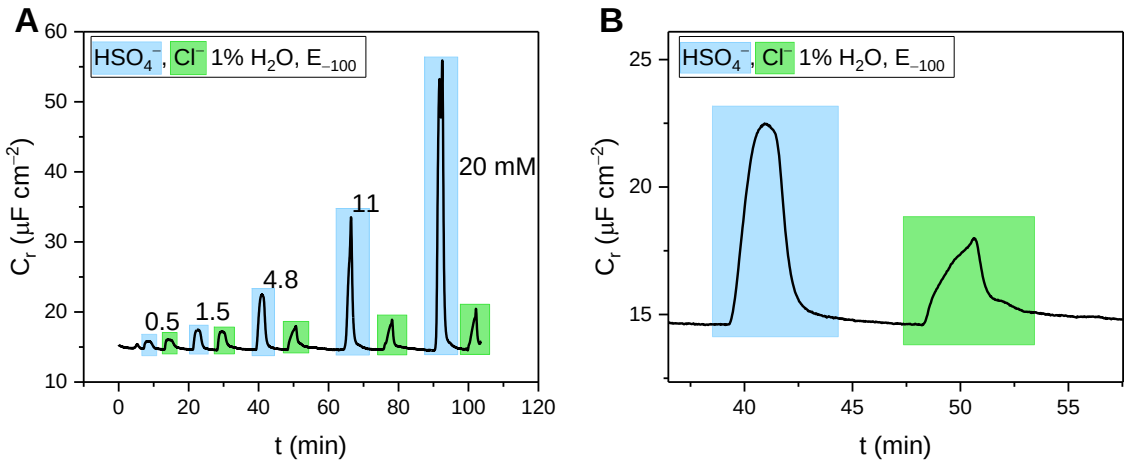


Figure 4.7-4. Redox capacitance response of **3.XB$_{SAM}$** towards HSO_4^- (blue) and Cl^- (green) under continuous electrolyte flow, V_{Sample} = 1 mL at E_{-100} (representing the maximum shift observed for **3.XB$_{SAM}$** towards Cl^-) (A) Each spike in represents the response towards aliquots of HSO_4^- or Cl^- of increasing concentrations up to 20 mM. (B) Comparison of the response towards 4.8 mM HSO_4^- (blue) and Cl^- (green).

The differences resolved for the response signature toward HSO_4^- and Cl^-: namely sharp defined peaks for HSO_4^- and distinctly broader peaks for Cl^-, are especially intriguing given that both anions induce similar voltammetric response magnitudes (assessed under identical continuous flow conditions, as laid out in Chapter 3), as displayed in Figure 4.7-5.

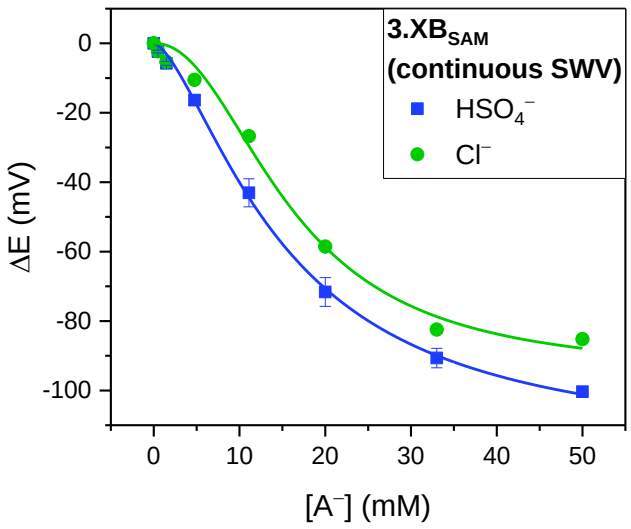


Figure 4.7-5. Voltammetric response isotherms of **3.XB$_{SAM}$** in ACN/H_2O 99:1 (100 mM $TBAClO_4$, 10 mM $HClO_4$), in response to increasing concentrations of HSO_4^- (blue squares) or Cl^- (green circles) up to 50 mM from continuous voltammetric titrations by SWV. Errors bars represent one standard deviation of three independent measurements.

Additionally, considerable differences were observed between the redox capacitance response behaviour of the XB and HB analogues (**3.XB**/**HB**$_{SAM}$) in that **3.XB**$_{SAM}$ exhibited comparatively greater responses for Cl^- with respect to **3.HB**$_{SAM}$ (see Figure 4.7-6). This observation is fully consistent with prior reports of XB *vs*. HB comparative anion binding/sensing studies,[151, 179, 210] indicating that this behaviour results from differences in specific binding via the two different non-covalent interactions.

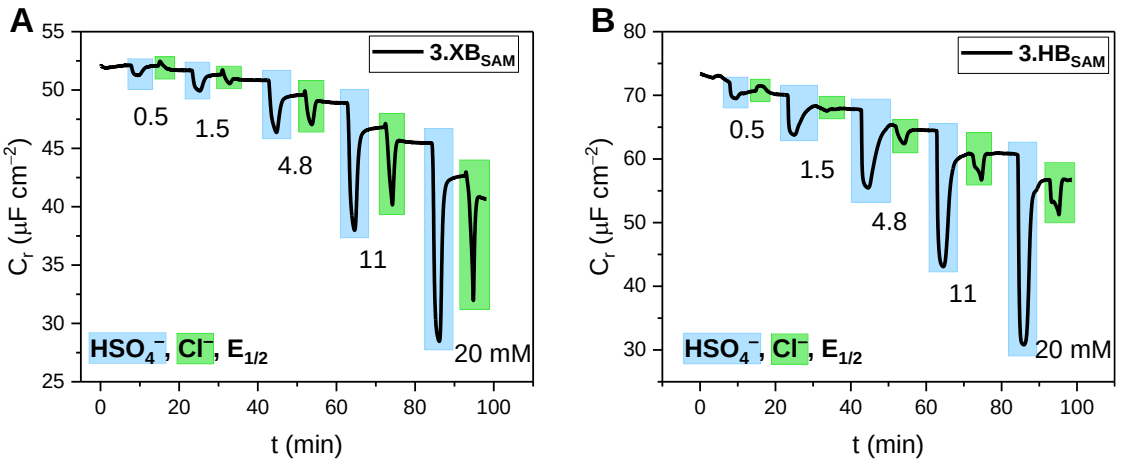


Figure 4.7-6. Redox capacitance response of (A) **3.XB**$_{SAM}$ and (B) **3.HB**$_{SAM}$ towards HSO_4^- (blue) and Cl^- (green) under continuous electrolyte flow, V_{Sample} = 1 mL at $E_{1/2}$. Each spike represents the response towards aliquots of HSO_4^- or Cl^- of increasing concentrations up to 20 mM.

To investigate the observed temporal differences between HSO_4^- and Cl^- responses further, stop-flow experiments were conducted by rapidly flooding the flow cell (V_{sample} = 10 mL, Q = 3 mL min^{-1}) with an aliquot of the target anion (Figure 4.7-7). Flow was then stopped, and the response allowed to plateau before washing the sample out with supporting electrolyte to re-establish the baseline.

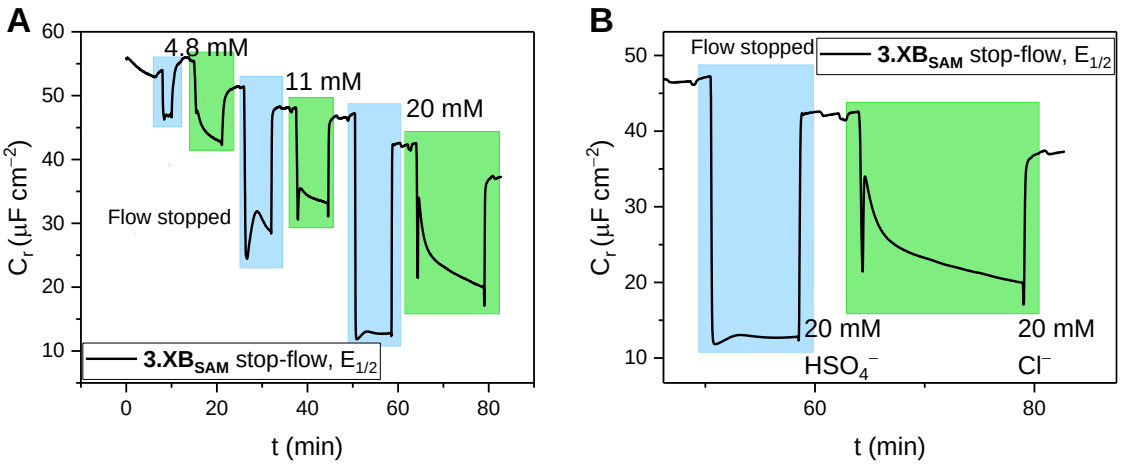


Figure 4.7-7. Redox capacitance response of **3.XB$_{SAM}$** towards HSO_4^- (blue) and Cl^- (green) under stop-flow conditions (initial sample injection: V_{sample} = 10 mL, Q = 3 mL min^{-1}, flow stopped and response allowed to plateau, flow out of cell at Q = 3 mL min^{-1}, all at $E_{1/2}$). (A) Each spike represents the response towards aliquots of HSO_4^- or Cl^- of increasing concentrations up to 20 mM. (B) Magnified section of (A), highlighting the comparison between the response of **3.XB$_{SAM}$** towards 20 mM HSO_4^- (blue) and Cl^- (green).

These experiments were attempted numerous times, but were unfortunately limited by issues of reproducibility between electrodes and unintentional spikes in C_r from switching the manual injector between sample addition and the supporting electrolyte. Nevertheless, qualitative conclusions can still be drawn from comparison of the responses of **3.XB/HB$_{SAM}$** toward HSO_4^- and Cl^-. Specifically, at $E_{1/2}$, Cl^- binding at **3.XB$_{SAM}$** was significantly slower than HSO_4^-, whereas the dissociation of both species appeared to be similar (see Figures 4.7-7B and 4.7-8). However, at E_{-105}, anion binding and dissociation was observed to be almost identical for **3.XB$_{SAM}$** in response to HSO_4^- or Cl^-.

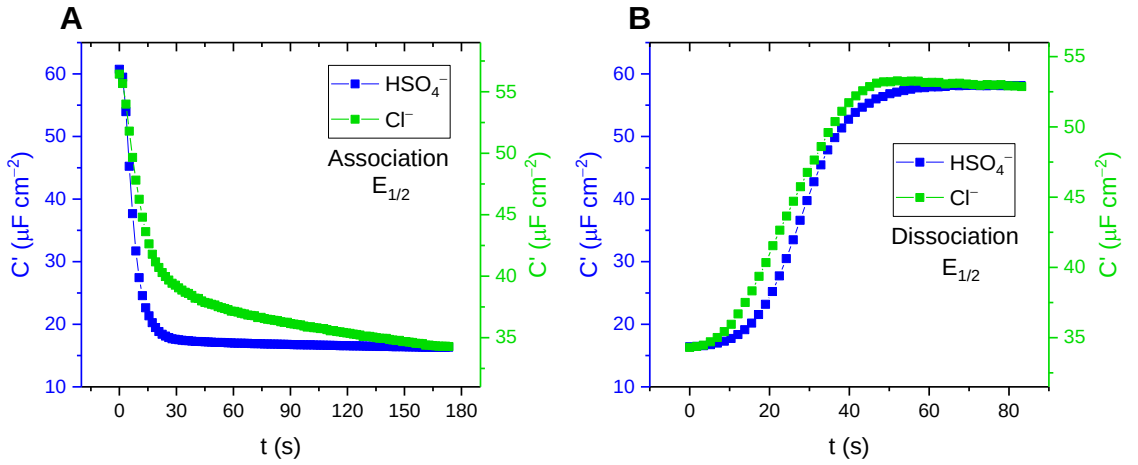


Figure 4.7-8. Comparison of the (A) association and (B) dissociation regimes of 11 mM HSO_4^- (blue) and Cl^- (green) under stop-flow conditions (initial sample injection: V_{sample} = 10 mL, Q = 3 mL min^{-1}, flow stopped and response allowed to plateau, flow out of cell at Q = 3 mL min^{-1}, all at $E_{1/2}$).

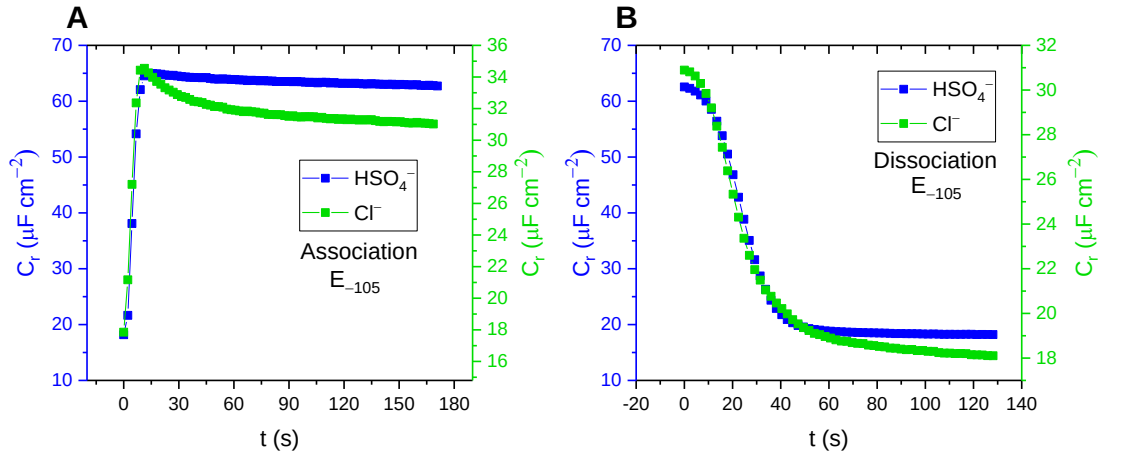


Figure 4.7-9. Comparison of the (A) association and (B) dissociation regimes of 11 mM HSO_4^- (blue) and Cl^- (green) under stop-flow conditions (initial sample injection: V_{sample} = 10 mL, Q = 3 mL min^{-1}, flow stopped and response allowed to plateau, flow out of cell at Q = 3 mL min^{-1}, all at E_{-105}).

Empirically, these observations were reproducibly consistent, however, attempts to accurately quantify the rates of anion binding for both species at **3.XB$_{SAM}$** were not successful. Initially, the association/dissociation traces were fitted to established rate equation models, but were met with poor fits that resulted in inconsistent values for k_{on} or k_{off}.

Following this, an alternative approach was taken to quantify the rate of electron transfer, k_{ET} instead of directly trying to quantify binding rates (k_{on} or k_{off}) to identify whether this parameter differed during anion binding events with HSO_4^- or Cl^-. To

this end, Laviron analyses were performed by acquiring CVs at increasingly high scan rates to induce larger peak separations, ΔE_p. ΔE_p was then be plotted against log(v), from which a linear regime should be resolved at sufficiently high scan rates with an intercept equal to k_{ET}.[288] Unfortunately, this method was limited by both voltammetric degradation and the hardware capabilities of the potentiostats available (scan rates, $v < 100$ V s^{-1}), therefore reliable values for k_{ET} could not be obtained (Figure A4.8).

In conclusion, consistent and substantial differences were observed between the C_r and voltammetric response signatures of **3.XB$_{SAM}$** for HSO_4^- and Cl^-, but values for the binding/dissociation rate constants cannot be accurately quantified with confidence at this time and is the subject of future work (Section 4.9.2).

4.8 Redox Capacitive Measurements at Multiple Potentials & Frequencies

As alluded to a number of times above, this redox capacitive ion sensing methodology is inherently versatile and tunable, and can be adjusted by modulating a wide variety of measurement parameters. This includes, but is not limited to, measurements at different AC amplitudes, potentials or frequencies, or even at multiple different potentials or frequencies. The effect of poising at different applied electrode potentials was discussed in detail above (see Section 4.6), most notably modulating anion binding thermodynamics (*e.g.*, binding affinity tuned by over an order of magnitude).

For example, measurements can be carried out at multiple different AC frequencies, as exemplified for pseudo-flow sensing in Figure 4.8-1, and under continuous flow in Figure 4.8-2. This was achieved by fast switching between the different frequencies, however overtone frequencies, can, depending on the hardware, be obtained simultaneously (*i.e.*, truly simultaneously and without loss of temporal resolution). This affords a higher information density than standard measurements and could potentially be used to further tune the sensor performance. The ability to monitor different frequencies could aid in elucidating the mechanisms underpinning complex interfacial events, as multiple relevant capacitive elements that contribute to the film capacitance can then be monitored.

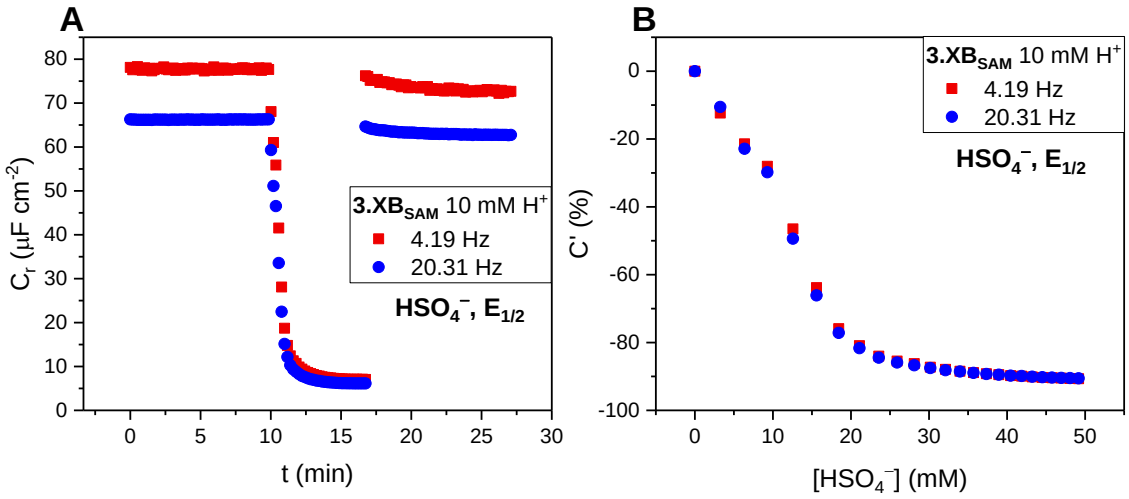


Figure 4.8-1. (A) Comparison of continuous capacitance response of **3.XB$_{SAM}$** under pseudo flow conditions in a stirred, but otherwise static, three-electrode cell at $E_{1/2}$ at f_r (4.2 Hz, red squares) and 20.3 Hz (blue circles). (B) The binding isotherms corresponding to the continuous addition of up to 50 mM HSO_4^- via a syringe pump (V_{Sample} = 4 mL, flow rate Q = 0.8 mL min^{-1}, into an initial electrolyte volume of 4 mL).

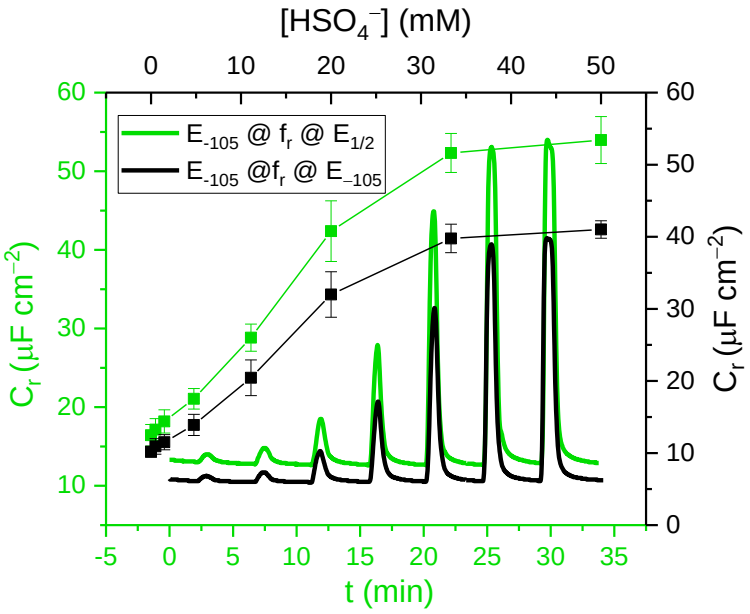


Figure 4.8-2. Redox capacitance response of **3.XB$_{SAM}$** towards HSO_4^- under continuous electrolyte flow in a custom flow cell at E = E_{-105}, and at two different frequencies: (A) f = f_r determined at $E_{1/2}$ and (B) E = f_r determined at E_{-105}. Each spike in represents the response towards aliquots of HSO_4^- of increasing concentrations up to 50 mM. The solid lines are to guide the eye only. Error bars represent one standard deviation of three independent experiments.

Additionally, measurements can be carried out at two (or more) different potentials (Figure 4.8-3). In analogy to the two-frequency approach, this was achieved by alternately determining C_r at two different potentials (*i.e.*, fast switching back and forth), which was associated with a temporal resolution approximately double that of single-potential measurements (≈ 4 s), but afforded double the information density (two full C_r *vs.* t sensograms) within the same experiment/time span. As expected, the sensograms and isotherms obtained in this manner (Figure 4.8-4) were completely identical to those obtained under "standard" conditions when measurements were performed at one fixed potential. Furthermore, if the responses of different targets exhibit characteristic potential-dependent behaviour, then this two-potential approach could also be employed for ratiometric sensing. For example, substantially larger responses are observed at E_{-200} for **3.XB/HB$_{SAM}$**

upon addition of $H_2PO_4^-$ compared to HSO_4^-, and the ratio of responses at E_{-200} *vs.* $E_{1/2}$ could be used to identify which anion is predominantly binding to the interface when mixtures of the two anions are used (see later).

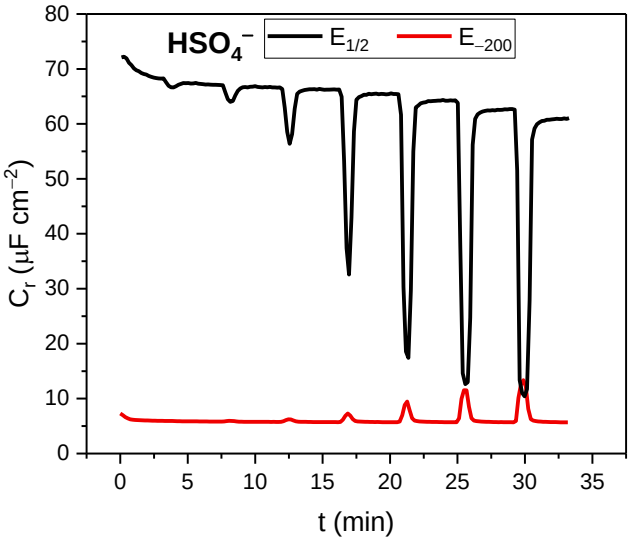


Figure 4.8-3. Redox capacitance response of **3.XB$_{SAM}$** towards HSO_4^- at two alternating potentials under continuous electrolyte flow, E = E_{-200} (red) and E = $E_{1/2}$ (black). Each spike represents the response towards aliquots (V_{Sample} = 0.5 mL) of HSO_4^- of increasing concentrations up to 50 mM.

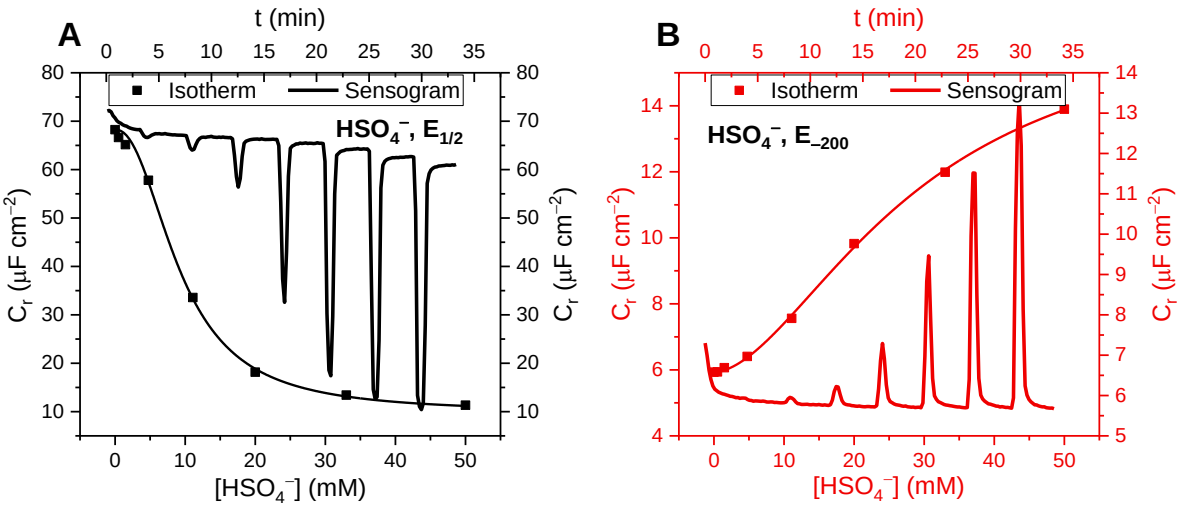


Figure 4.8-4. Redox capacitance response of **3.XB$_{SAM}$** towards HSO_4^- at two alternating potentials – under continuous electrolyte flow (A) E = $E_{1/2}$ and (B) E = E_{-200}. Each spike represents the response towards aliquots of HSO_4^- of increasing concentrations up to 50 mM for sensograms at (A) $E_{1/2}$ and (B) E_{-200}. The solid lines represent fits according to the Langmuir-Freundlich model (Eqn. 3.3-1).

Additionally, this potential dependence of binding strength may be exploited to tune sensor selectivity. For example, the selectivity of **3.XB/HB$_{SAM}$** for $H_2PO_4^-$ over HSO_4^-

would be expected to be improved by poising at potentials more cathodic than that of the maximum ΔE_{max} induced by HSO_4^- (*e.g.*, at E_{-200}). This prediction arises from the maximum voltammetric shifts of **3.XB$_{SAM}$** for HSO_4^- and $H_2PO_4^-$ which are ≈ –105 and –200 mV, respectively. At potentials more cathodic than –105 mV, only small changes in C_r are observed upon addition of HSO_4^- as the point of measurement remains in the tail of the redox distribution. In contrast, substantial changes in C_r are observed towards $H_2PO_4^-$ at E_{-200} (above the protonation threshold: 10 mM), as the potential is poised much closer to the peak of the redox distribution upon addition of increasing concentrations of $H_2PO_4^-$. To investigate whether this hypothesis would hold true in the presence of both anions, preliminary studies were conducted at both $E_{1/2}$ and E_{-200}, whereby 20 mM HSO_4^- and 20 mM $H_2PO_4^-$ were injected in the same sample aliquot (see Figure 4.8-5).

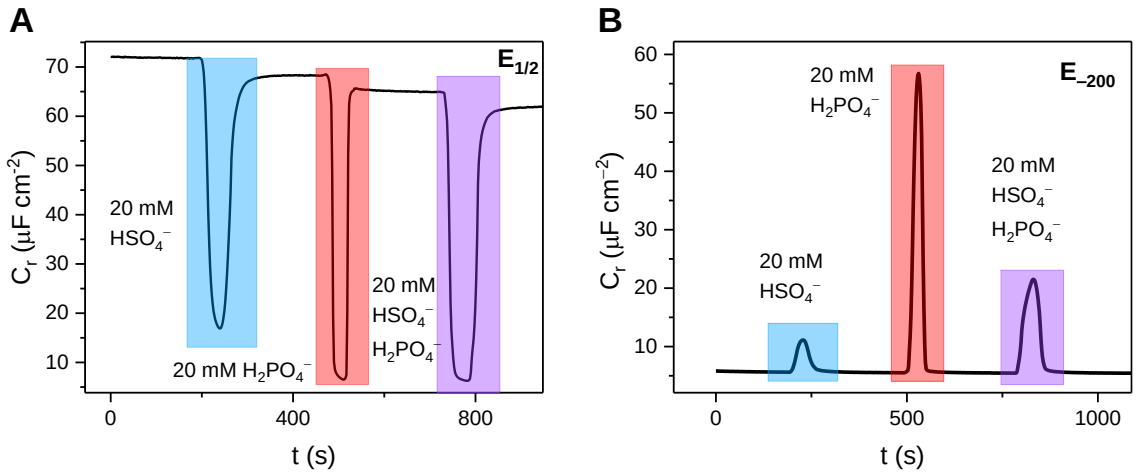


Figure 4.8-5. Redox capacitance responses of **3.XB$_{SAM}$** towards 20 mM HSO_4^- (blue), 20 mM $H_2PO_4^-$ (red) and 20 mM HSO_4^- + 20 mM $H_2PO_4^-$ (purple) under continuous electrolyte flow, V_{Sample} = 0.5 mL at (A) $E_{1/2}$ and (B) E_{-200}.

As depicted in Figure 4.8-5, at $E_{1/2}$ the combined response to HSO_4^- + $H_2PO_4^-$ mostly mirrors that of $H_2PO_4^-$ alone, whereas at E_{-200}, the combined response more closely resembles that of HSO_4^- alone (albeit somewhat higher which likely reflects contributions from $H_2PO_4^-$ binding to some extent). The origin of this anion- and

potential-dependent sensor response is difficult to justify without additional systematic studies, but these interesting results indicate that tuning the potential could indeed modulate the selectivity patterns or preferences of the redox-active, receptive interface.

4.9 Conclusions & Future Work

4.9.1 Conclusions

To conclude, this chapter presents a highly adaptable, novel ion sensing methodology based on changes in the redox capacitance of electroactive, anion-receptive molecular films. The methodology is notably associated with a number of unique advantages over other electrochemical techniques, including high sensitivity, a facile, direct and continuous signal readout, as well as a breadth of versatile ion monitoring modes that can be conducted at any (or multiple) applied electrode potential(s) and AC frequencies. Ion binding-induced shifts in the film redox density of states energy distribution can be monitored from any initially applied, constant electrode polarisation, supporting a "self-amplification" mechanism for anion binding which is otherwise inaccessible via other methods (*e.g.*, voltammetry). Conducting continuous measurements at a judicious choice of the electrode polarisation facilitates assays which are "switch-ON" or "switch-OFF", and additionally supports an ability to tune the thermodynamics of ion recruitment, such as the binding affinity, by over an order of magnitude.

Though exemplified herein with the continuous flow sensing of bisulfate at a redox active halogen-bonding ferrocenyl anion receptive film, this approach is expected to be widely applicable to ion or even neutral guest assaying in general. More

specifically, the methodology presented here for anion sensing is equally translatable to a wide variety of other redox-active interfaces, solvent systems and analytes, wherein the voltammetric profile is reversibly perturbed by guest binding.

4.9.2 Future Work

As alluded to above, the versatility of this methodology offers a broad range of opportunities for future work. For example, further studies in elucidating the capacitive principles governing ion binding at different frequencies could provide a route towards ratiometric sensing for different targets. Additionally, studies of pertinent electroactive ions (*e.g.*, I^-) could be carried out via this method by conducting measurements outside of the redox-active potential window of the ion. Furthermore, in-depth kinetic studies of anion binding would provide much-needed insight into host-guest kinetics, as this is an area of interfacial host-guest chemistry which is almost entirely unexplored.

In addition to explore additional possible modalities of this methodology, extrapolation of the existing powerful modes to other electroactive, receptive interfaces would provide a sensitive, highly adaptable and reagentless detection of target ionic species. Of particular interest would be suitable receptive motifs that could be applied for detecting target ions (K^+, Cl^-, lactate *etc*.) in competitive or even complex aqueous conditions such as biofluids (*e.g.*, sweat or blood), or environmental water sources (*e.g.*, river or ground water).

Chapter 5

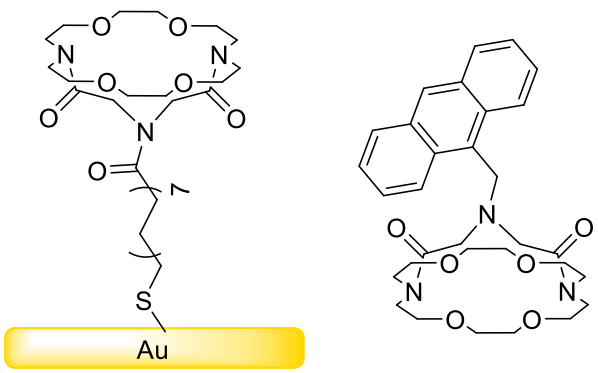
Continuous Non-Faradaic Capacitive Ion Sensing

Chapter 5: Continuous Non-Faradaic Capacitive Ion Sensing

5.1 Introduction & Chapter Aims

As explored in previous chapters, the (further) development of novel and established electrochemical sensing methodologies is a necessary but demanding endeavour to meet the challenge of sensitively and continuously monitoring pertinent ionic species. The methods outlined thus (continuous voltammetry in Chapter 3 and continuous redox capacitance in Chapter 4) far mark a substantial step change towards this objective, but are both associated with the notable drawback of requiring an appended redox-active transducer unit (herein ferrocene) adjacent to an (an)ion binding site in order to transduce (an)ion binding events into a suitable sensory readout ($\Delta E_{1/2}$ or ΔC_r, respectively). As aforementioned, the oxidised, positively-charged ferrocenium state is inherently susceptible to degradation through attacks from adventitious nucleophiles, and therefore an inevitable signal loss is observed due to the progressive loss of redox-addressable units over time. As shown, this signal loss can be mitigated by slightly acidifying the medium in which sensing studies are conducted, but obtaining an equally powerful (sensitive/continuous/tuneable/high temporal resolution etc.) methodology that entirely precludes the need for a redox-active probe has obvious advantages for long-term monitoring applications. To this end, this chapter explores the use of non-Faradaic capacitance spectroscopy for ion sensing under continuous flow.

Despite the numerous benefits of impedance-derived techniques for ion sensing, as previously outlined in Chapter 4, non-Faradaic capacitance spectroscopy has rarely been applied for ion sensing. In the context of capacitive cation sensing, crown ether-based receptive interfaces are among the most commonly reported receptive interfaces. For example, Wanichacheva *et al*. reported the use of an 18-crown-6-based (4,7,13,16-tetraoxa-1,10,21-triazabicyclo[8.8.5]tricosane-19,23-dione) receptive interface, **5.1-1** to selectively sense Li^+ based on changes in the monolayer capacitance upon ion complexation.[289] Interestingly, the selectivity of this sensor was shown to be superior to that of an ISE containing a similar ionophore ($logK_{Li+/Na+} \approx -1.30$ and -0.77, respectively).



5.1-1

Figure 5.1-1. A receptive SAM on gold for capacitive Li^+ sensing based on an 18-crown-6 derivative, and an analogous ionophore used for comparative potentiometric studies with an ISE.[289]

Alternatively, Flink *et al*. presented a family of crown ether-based SAMs (**5.1-2–5**) to investigate the impact on the capacitive response to alkali metal targets when the chain length was varied between the receptive unit and Au electrode surface, and different crown ethers.[184] These crown ether-based SAMs were once again able to bind alkali metals (Na^+, K^+ and Cs^+) in aqueous conditions, which increased the dielectric constant of the film, in turn increasing the monolayer capacitance. An important conclusion from this work was that smaller responses were observed

when an alkyl spacer unit was included between the electrode and receptive unit, due to the invariance of the capacitance of the spacer to target binding.

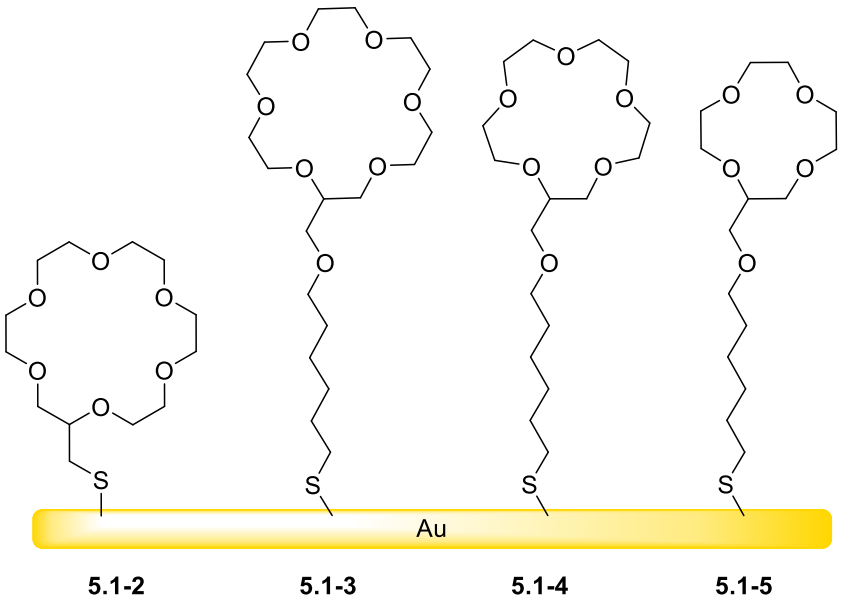


Figure 5.1-2. A family of cation-receptive SAMs on gold based on 18-crown-6 (**5.1-2** and **5.1-3**), 15-crown-5 (**5.1-4**) and 12-crown-4 (**5.1-5**). **5.1-2** and **5.1-3** represent analogues with short and long alkyl spacer units, respectively.[184]

Non-Faradaic capacitive anion sensing is even more rare, with only one example reported by Hein *et al*. based on SAMs of a XB or HB foldameric host, **5.1-6.XB**/**HB**.[136] The solution-phase analogue of **5.1-6.XB**/**HB** was prior mentioned in Section 1.3.2 in the context of solvent exclusion to generate a low ε_r binding microenvironment which potently binds anionic targets.[122] A comparison of solution and interfacial binding again confirmed not only strong anion binding in the film but a retention of this in aqueous solution (*e.g.*, K = 362 M^{-1} (H_2O) for I^- with **5.1-6.XB**). The films are characterised by a low film ε_r (ε_r = 17.6 for **5.1-6.XB**, according to a simple Helmholtz model, detailed later) which is increased upon specific recruitment of charged anionic targets, resulting in an increase in the monolayer capacitance once again.

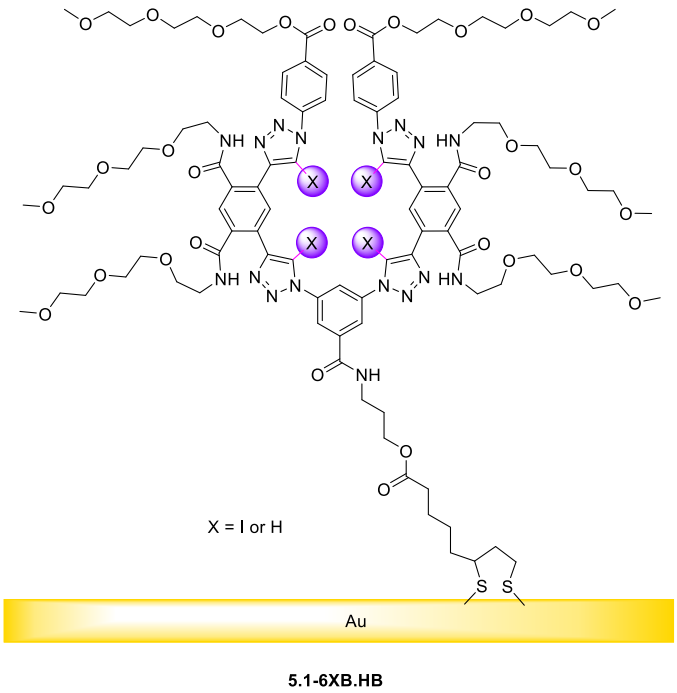


Figure 5.1-3. Schematic depiction of a SAM of XB/HB-based foldameric hosts, **5.1-6XB/HB** on gold for capacitive anion sensing.[136]

Despite the promise of monitoring host-guest binding events through non-Faradaic capacitance measurements, especially in aqueous media, this methodology remains underdeveloped. Therefore, this Chapter builds on the benefits of impedance-derived techniques, as outlined in Chapter 4, to explore the development of a continuous, non-Faradaic capacitive ion sensing methodology. A model benzo-15-crown-5-based receptive molecular film will be utilised to highlight the potential of the approach described below for acquiring a high density of information regarding ion binding kinetics and thermodynamics, in real time and in aqueous media, including real-world-relevant environmental samples.

Key aims for this work include:

1. To build on previous work by translating static non-Faradaic capacitive ion sensing methods into a facile, continuous and direct signal output that can be followed in real-time.

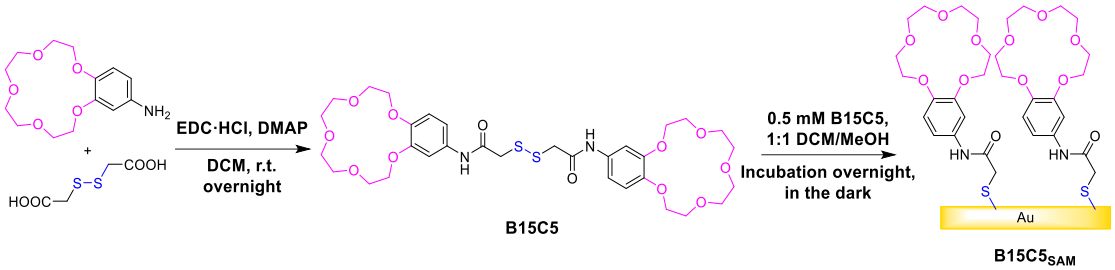
2. To assess the sensitivity, baseline stability and long-term sensing capability of non-Faradaic capacitance for a range of alkali metal cations under continuous flow.
3. To explore the utility of the method in more relevant aqueous media (*e.g.*, river water or an artificial sweat matrix).

5.2 Synthesis of B15C5, Film Formation & Characterisation

5.2.1 Synthesis of B15C5

The synthesis and solution-phase characterisation of **B15C5** was carried out by Dr. Robert Hein (see Section 7.11.3 for further details).

Building on the work described above that is limited to static ion sensing assays only, an exemplary crown ether-based interface was utilised due to its prior-established performance as a sensory interface for non-Faradaic capacitive ion sensing. Specifically, a benzo-15-crown-5 (B15C5) motif (selective for alkali metal cations, particularly Na^+ due to size complementarity) was employed as a representative ion receptive binding unit,[290] and immobilised onto gold sensor surfaces through an adjacent anchoring disulfide moiety. The target receptor, **B15C5** was synthesised in one step from a one-pot reaction between dithioglycolic acid and 4'-aminobenzo-15-crown-5, with 4-dimethylaminopyridine (DMAP) and 1-ethyl-3-(3-dimethylaminopropyl)carbodiimide hydrochloride (EDC·HCl), in anhydrous DCM at room temperature (see Scheme 5.2.1-1, full synthetic protocols can be found in Section 7.11.3). Following purification, **B15C5** was afforded in good yield and characterised by ^1H and ^{13}C NMR (Figures 7.11.3-1 and 7.11.3-2), and high-resolution mass spectrometry (see Section 7.11.3).



Scheme 5.2.1-1. Reaction scheme for **B15C5**, followed by immobilisation as self-assembled monolayers **B15C5$_{SAM}$** on Au electrodes.

5.2.2 B15C5$_{SAM}$ Film Formation & Physical Characterisation

Self-assembled monolayers (SAMs) were formed via incubation of clean gold disc electrodes in 0.5 mM **B15C5** in 1:1 DCM/MeOH overnight in the dark (see Section 7.8.2 for further detail) and extensively characterised by a range of techniques, as detailed below (all characterisation procedures can be found in Chapter 7).

XPS spectra of **B15C5$_{SAM}$** (Figures 5.2.2-1 and 5.2.2-2) were consistent with expectations that only C, N, O and S were present in the film, and there was good agreement between the predicted and obtained atomic ratios based on the chemical formula of **B15C5** (see Tables 5.2.2-1 and 5.2.2-2).

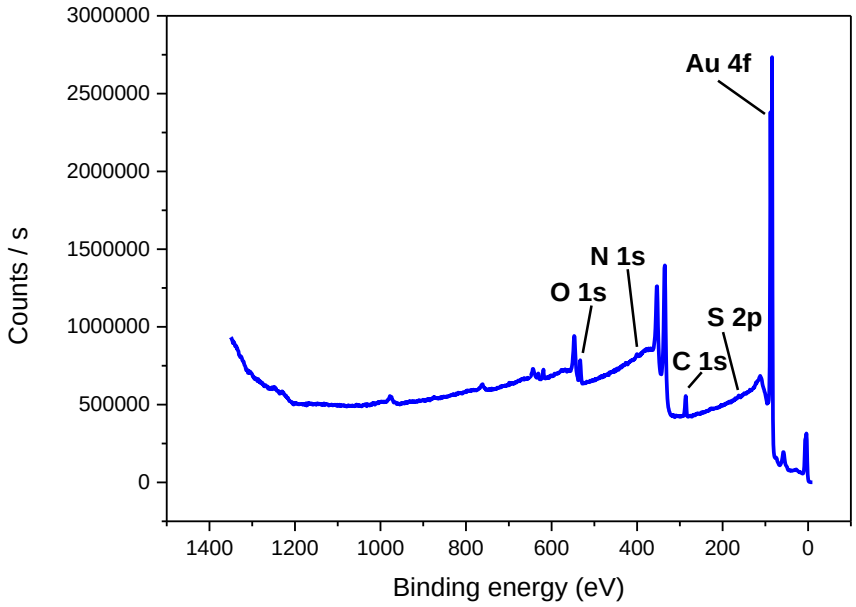


Figure 5.2.2-1. Low resolution survey XPS spectrum of **B15C5$_{SAM}$**.

Table 5.2.2-1. Experimental and theoretical elemental composition of **B15C5$_{SAM}$**, as determined by XPS. Values were normalised to O = 6. Errors represent one standard deviation of triplicate measurements.

Element	Experimental	Theoretical
C	17.18 ± 0.80	16
O	6.00 ± 0.21	6
N	1.71 ± 0.83	1
S	0.55 ± 0.13	1

The slightly poorer agreement observed for N and S presumably arises from an overall low abundance and low sensitivity at these low concentrations, as well as attenuated sensitivity due to their relatively "deeper" location within the film and penetration attenuation of the X-rays. The individual peak fits for C and O are generally good (see Table 5.2.2-2), and the assignments are analogous to those in previous reports.[210] The S binding energies are consistent with chemisorption of the disulfide groups to the Au electrode surface.

Table 5.2.2-2. Peak binding energies and experimental and theoretical ratios for different chemical environments of C, O, N and S of **B15C5$_{SAM}$**. For S only one environment is observed giving rise to two peaks with an area ratio of 2:1 due to spin orbit coupling. / - not relevant as only one environment is present, resulting in 1:1 agreement in all cases.

Element	Chemical Environment	peak BE (eV)	Experimental	Theoretical
C	*C*=C	284.52 ± 0.03	1.72 ± 0.268	3
	C-O, *C*-N, *C*-S	286.18 ± 0.03	8.07 ± 2.24	12
	C=O	288.81 ± 0.39	1	1
O	C=*O*	531.18 ± 0.07	1	1
	C-*O*	532.94 ± 0.01	5.55 ± 0.77	5
N	*N*-C=O	400.03 ± 0.16	/	/
S	*S*-C	162.25 ± 0.07 163.55 ± 0.11	/ /	/ /

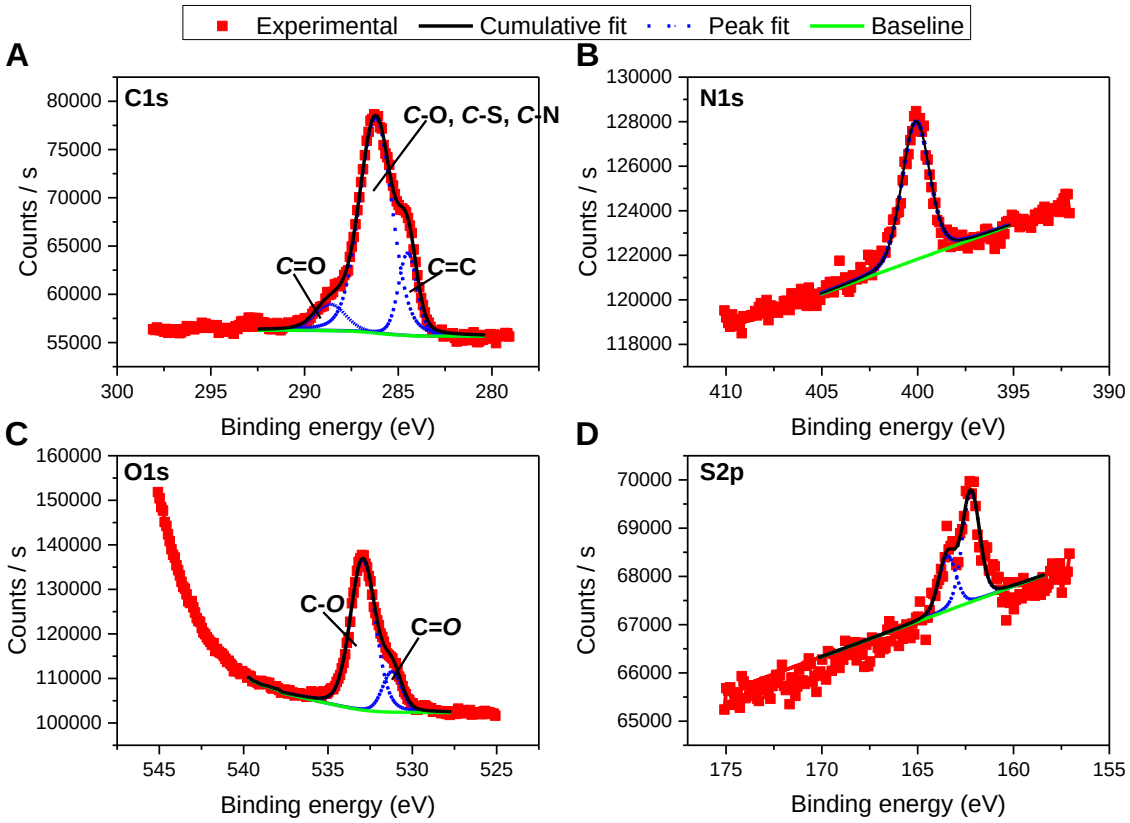


Figure 5.2.2-2. High resolution (A) C1s, (B) N1s, (C) O1s and (D) S2p XPS spectra of **B15C5$_{SAM}$**, including peak fits.

Similarly, the ATR-FTIR spectrum of **B15C5$_{SAM}$** displayed the predicted peaks: a broad amide N-H stretch at 3400 cm^{-1}, aromatic C-H stretches at 2800 cm^{-1} and an amide carbonyl C=O stretch at 1600 cm^{-1} (Figure 5.2.2-3).

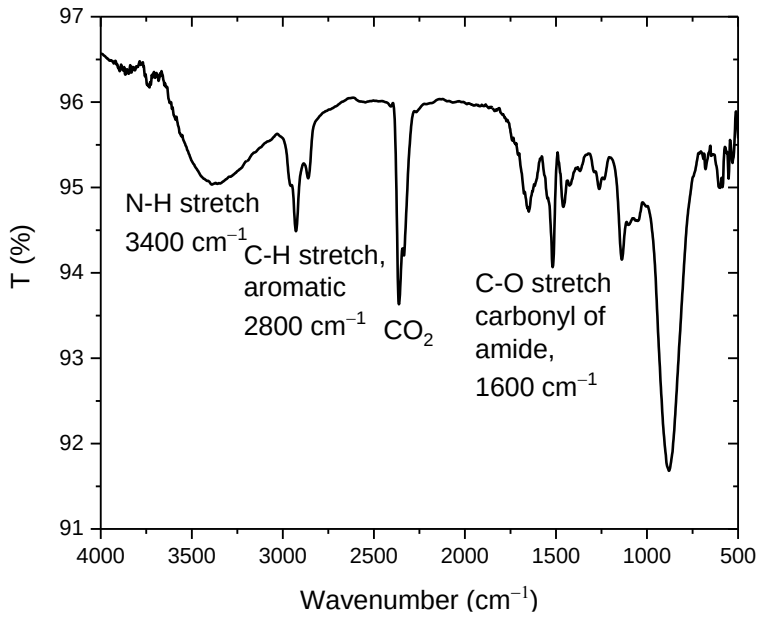


Figure 5.2.2-3. ATR-FTIR of **B15C5$_{SAM}$** on Au.

Water contact angle measurements were representative of a predictably hydrophilic interface (62 ± 1°, *cf*. bare gold = 79 ± 5°); consistent with previous reports of similar 15C5-based SAMs, *c.f.*, 55 ± 1°.[185] Ellipsometry measurements elucidated a film thickness of 1.02 ± 0.2 nm, which is consistent with predicted thicknesses for the receptor in an upright conformation (Appendices A5, Figure A5.1). In summary, homogenous thin films (self-assembled monolayers) with hydrophilic characteristics were confirmed, in line with expectations.

5.2.3 Electrochemical B15C5$_{SAM}$ Film Characterisation

The **B15C5$_{SAM}$** films were then characterised via a number of electrochemical methods (see Section 7.8 for further detail regarding these methods). Firstly, CV measurements were conducted with **B15C5$_{SAM}$** under standard, static cell conditions in 100 mM TEACl (tetraethylammonium chloride) in pure water. As displayed in Figure 5.2.3-1A, no significant Faradaic activity was observed, confirming that the generated **B15C5$_{SAM}$** film is, as expected, redox-inactive. Additionally, even in the presence of high concentrations of a solution-phase redox probe (10 mM $[Fe(CN)_6]^{3+/4+}$) any redox activity is heavily suppressed at **B15C5$_{SAM}$** with respect to a polished, bare Au disc electrode (see Figure 5.2.3-1B), indicating that densely-packed, blocking films are formed.

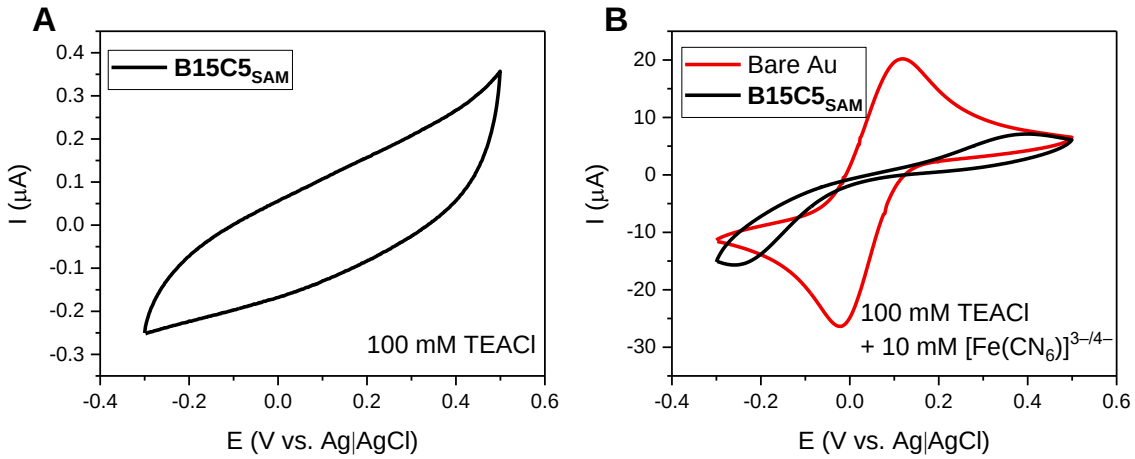


Figure 5.2.3-1. CVs of **B15C5$_{SAM}$** in (A) 100 mM TEACl and (B) 100 mM TEACl + 10 mM $[Fe(CN)_6]^{3-/4-}$ in pure water.

Similarly, other methods confirmed the dense and blocking nature of the **B15C5$_{SAM}$** films including Faradaic impedance measurements, wherein no complete semi-circular region could be defined (Figure 5.2.3-2, R_{ct} > 4 MHz), even at low frequencies of 1 Hz.[136]

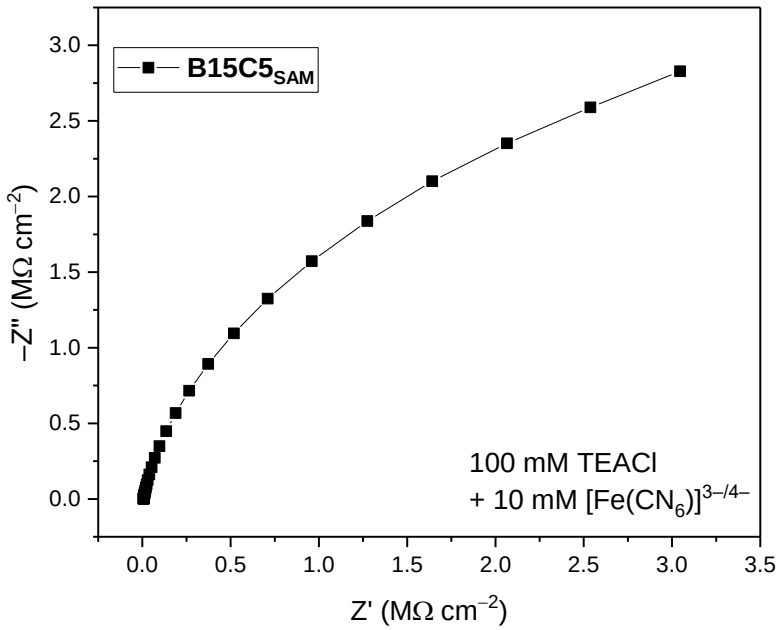


Figure 5.2.3-2. Impedimetric Nyquist plot of **B15C5$_{SAM}$** in 100 mM TEACl + 10 mM $[Fe(CN)_6]^{3-/4-}$ in pure water at a DC bias potential of 0.32 V (corresponding to the $E_{1/2}$ of $[Fe(CN)_6]^{3-/4-}$, determined from SWVs recorded prior to impedimetric measurements) in the AC frequency range of 100 kHz – 1 Hz.

Additionally, reductive thiol stripping resolved high molecular densities of 1.23 ± 0.29 x10^{-10} mol cm^{-2} (*cf.* densely-packed alkane thiol SAMs Γ ≈ 3-5 x10^{-10} mol cm^{-}

^{2}),[291] corresponding to an appropriate molecular footprint of 1.41 ± 0.33 nm. Capacitive bode plot phase angles of ≈85° (see Figure 5.2.3-3, *cf*. an ideal dielectric capacitor = 90°) were also consistent with densely packed film generation.

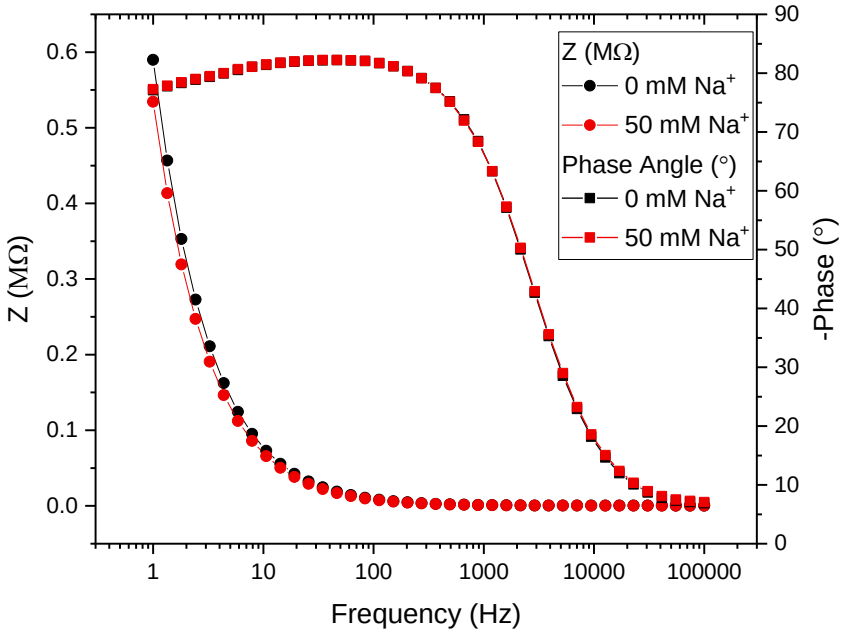


Figure 5.2.3-3. Bode plots of impedance (circles) and phase (squares) vs. frequency of **B15C5$_{SAM}$** in the presence (red) and absence (black) of 50 mM Na^+.

Finally, a film dielectric, ε_r of 4.24 ± 0.21 can be calculated from the film capacitance (3.68 ± 0.18 μF cm^{-2}) and the film thickness (1.02 ± 0.2 nm, as above) when the interface is modelled as a Helmholtz plate capacitor (detailed below in Section 5.3, Equation 5.3-3). The resolved film capacitance for **B15C5$_{SAM}$** is in line with other crown ether-based SAMs (*e.g.*, 4.2 ± 0.1 μF cm^{-2}),[184] and the low film ε_r is also reflective of both a high interfacial molecular density and significant solvent exclusion (*cf*. pure alkane thiol SAMs $\varepsilon_r \approx$ 2-3[292]).[136] As it is this film capacitance, *C*, that will be used to report on ion recognition at **B15C5$_{SAM}$** films, it is crucial to define the capacitive elements which contribute towards *C* in order to understand the underlying transduction mechanism.

5.3 Origin of Non-Faradaic Capacitive Ion Sensing Mechanism

In a similar manner to the redox capacitive method described in Chapter 4, capacitive processes were also probed at a fixed DC potential, upon which a small amplitude AC perturbation (10 mV) across a range of frequencies (1-100,000 Hz). In this instance, though, the fixed, applied potential was the open-circuit potential (OCP: the potential at which no appreciable current flows).[293] This affords capacitive Nyquist plots (Figure 5.3-2B) or Bode plots (Figure 5.3-2C), for example, that describe the non-Faradaic characteristics and resolved film capacitance, *C* of the redox-inactive, receptive interface (*e.g.*, a self-assembled monolayer on gold, as used herein). Namely, the well-defined semi-circular region reports on the film capacitance, *C* which can be obtained by graphically fitting the semicircular regions to a semicircle or ellipse function, by approximation as the real capacitance, C' at the inflection point, or via fitting to an appropriate equivalent circuit. For example, the capacitive signature of a thiol-based SAM on gold, as sampled in a non-Faradaic format can be theoretically described by the equivalent circuit $R_s(C_m[R_tC_t])$ or $R_S(C[R_tQ])$, as proposed previously (further details on these elements are given below).[136, 294] However, equivalent circuit fitting can be challenging and unsuccessful for a number of reasons, including outliers or noise at high or low frequencies, the fitting algorithm becoming stuck at local minima or the non-ideal behaviour of circuit elements. By approximating *C* as the real capacitance, C' at the inflection point, complications arising from circuit fitting and the requirement for

appropriate equivalent circuit models can be avoided. This approach provides a streamlined, facile signal output that is responsive to target ion recruitment (see Figure 5.3-1), which was utilised by Hein *et al.* recently to describe the non-Faradaic capacitance response behaviour of **5.1-6.XB/HB** towards a range of anionic targets in water.[136] An in-depth, theoretical description of this model can be found in a corresponding report from Bueno *et al.*,[294] but the fundamental basis of this model is described below.

Importantly, it should first be noted that the traditional impedance response of **B15C5$_{SAM}$** towards a target ion species (*e.g.*, 50 mM Na^+, as shown in Figure 5.3-1A) is not significant, which is in agreement with the assumption that there is no ion diffusion limiting process (noticeable from the lack of a Warburg diffusive process in the impedance spectra in Figure 5.3-1A).[294] This is also evident in the lack of significant response in the Bode plots shown in Figure 5.2.3-3. In contrast, significant changes are evident once the impedimetric data is transformed into its capacitive components via Equations 5.3-1 and 5.3-2 (see Figure 5.3-1B). Bueno *et al.* attribute this behaviour specifically to changes to the energy state only associated with the capacitive elements of the interface, *i.e.*, there is no ionic transport at lower frequencies, only a single occupancy of the capacitive states.[294]

$$C'(\omega) = \frac{Z''}{\omega|Z|^2} \qquad \textbf{Equation 5.3-1}$$

$$C''(\omega) = \frac{Z'}{\omega|Z|^2} \qquad \textbf{Equation 5.3-2}$$

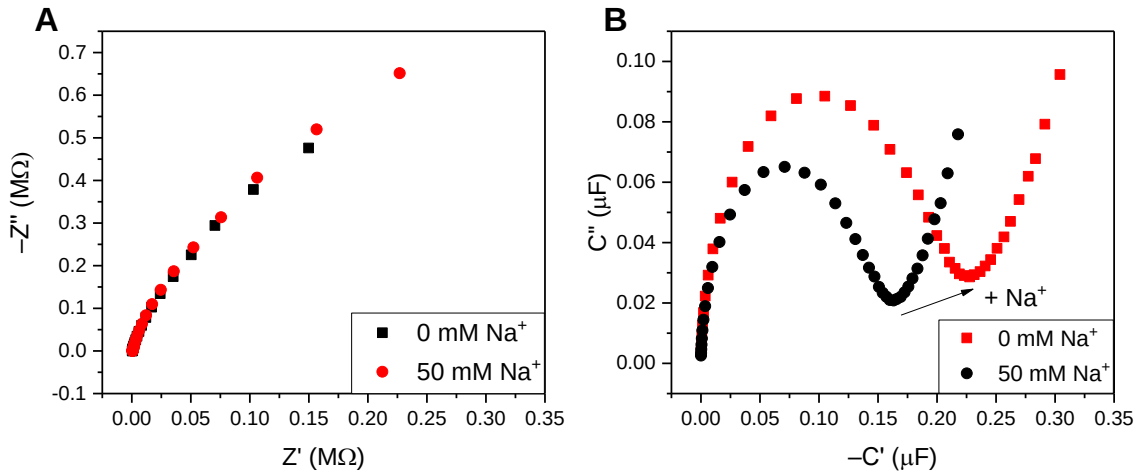


Figure 5.3-1. Impedimetric and capacitive signatures of **B15C5$_{SAM}$** in 100 mM TEACl in H_2O. A) Impedimetric Nyquist plots and B) capacitive Nyquist plots obtained from the impedimetric data which was transformed via Equations 5.3-1 and 5.3-2.

Most simply, this redox-inactive, receptive interface can be described by a plate capacitor Helmholtz model (Equation 5.3-3, where ε_r is film dielectric, A is electrode surface area, and d is receptive film thickness). As ε_0, d and A are expected to remain constant upon ion binding, *C* is therefore directly proportional to the dielectric constant of the film, ε_r, assuming that there is no significant film rearrangement induced by specific target recruitment that would affect d. This is a reasonable assumption here given that the receptive SAMs are very densely-packed (see Section 5.2.3).

$$C = \frac{\varepsilon_r \times \varepsilon_0 \times A}{d}$$ **Equation 5.3-3**

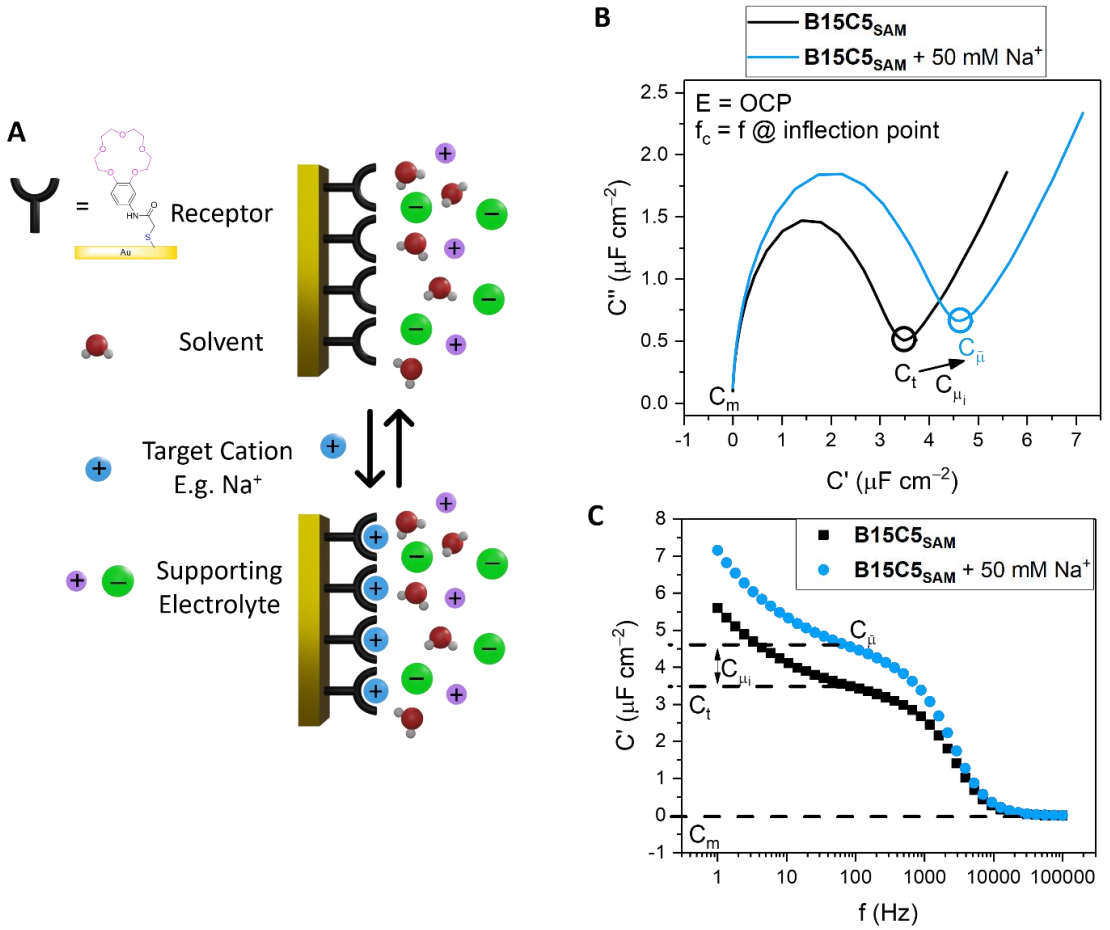


Figure 5.3-2. (A) Schematic depiction of **B15C5$_{SAM}$** in the presence (blue) and absence (black) of a specific target and (B) corresponding capacitive Nyquist and (C) Bode plots. Each data point represents a measurement at a different AC frequency (1-100,000 Hz). The film capacitance, *C* is then obtained as the real capacitance, C' at the frequency of the inflection point (f_c) of the capacitive Nyquist plot, approximately the semicircle diameter.

In the context of this work, one would therefore predict ion (alkali metal cation) recruitment (and any associated enhanced hydration due to introduction of charged species)[136] at the receptive molecular film (**B15C5$_{SAM}$**, described below) to *increase* the film dielectric constant, thus inducing an *increase* in the value of *C* (representatively illustrated in Figure 5.3-2).[136, 294, 295]

Further light can be shed on this model, as the native *C* of the film in the absence of target ions can be separated into its constituent elements, namely C_m (which is itself comprised of two constituent capacitors in series: C_b and C_{dl}) and C_t, which are schematised in Figure 5.3-3. Here, C_m is the native capacitance of the film itself,

with contributions from C_b, the dielectric capacitance of the film in the absence of any ions, and the double layer capacitance, C_{dl}, which accounts for the interactions between the electrolyte and conductive surface (*i.e.*, the gold electrode surface) in this model. Note that a sufficiently short linker group was chosen in the design of **B15C5** to preclude contributions from a so-called linker capacitor ($C_{b,linker}$) in series, which is invariable to ion binding at the SAM and has been shown to dampen specific response magnitudes.[184] C_t describes the capacitance of *non-specific* ion ingress (*i.e.*, the supporting electrolyte, TEACl) into the film.[296, 297] Each of these elements are associated with spectrally-resolved frequency domains, as highlighted in the capacitive Nyquist plots in Figure 5.3-2B and Bode plots in Figure 5.3-2C. Namely, C_m is resolved at high frequencies (> 10,000 Hz), and C_t at intermediate frequencies (typically 50-200 Hz), as represented by the semi-circular region of the capacitive Nyquist plot in Figure 5.3-2B (black trace).

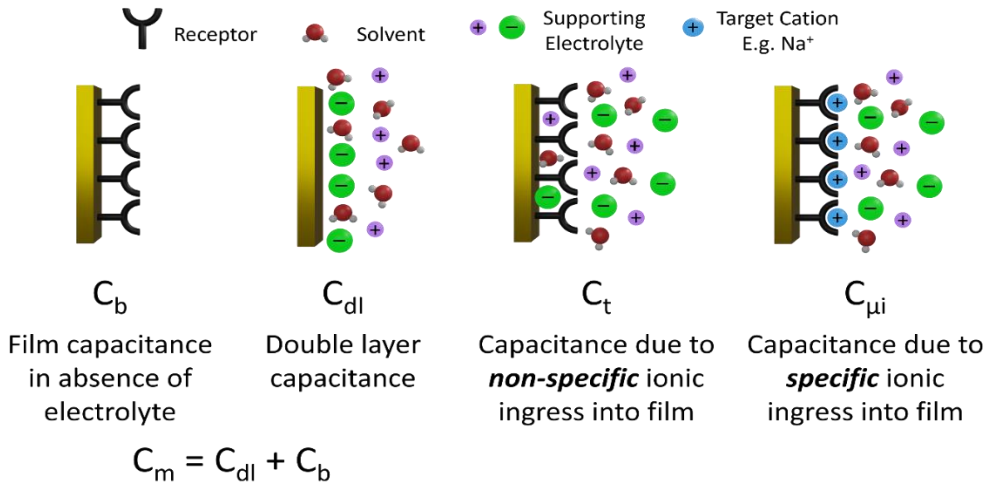


Figure 5.3-3. Schematic depiction of receptive film capacitors in the presence and absence of a specific target.

Upon addition of target ion (herein Na^+, or other alkali metal salts), a so-called ion binding capacitance, denoted $C_{\mu i}$, is additionally introduced which represents *specific* ionic ingress into the film, which can be considered a unique case of, or

contributor to C_t, upon ion binding. C_t and $C_{\mu i}$ are represented as parallel elements, and the entire system, *C* (both in the absence or presence of target ion) can be described by the equivalent circuit $R_s(C_m[R_tC_t])$, as proposed previously.[136, 294]

Importantly, it should be noted that C_m has an essentially negligible contribution to *C* when densely-packed molecular films are utilised, or is at the very least unchanged when target ions are added at constant ionic strength (shown by the minimal change in *C* at the high frequency domain between the black and blue traces in Figure 5.3-2B/C). The film capacitance, *C* can thus be obtained as the real component of the capacitance at the turning point of the hemispherical region of capacitive Nyquist plots, at the corresponding intermediate frequency denoted f_c (i.e., the frequency corresponding to $C_t/C_{\mu i}$, typically 50-150 Hz). It should be noted that the imaginary component was also shown to be sensitive to ion recruitment (Figure 5.3-4) and could therefore equally be used as a sensory readout. However, specific ion binding-induced changes were generally greater for the real component, thus the real component of *C* was chosen as the primary sensory readout to ensure the highest signal-to-noise ratio for these measurements.

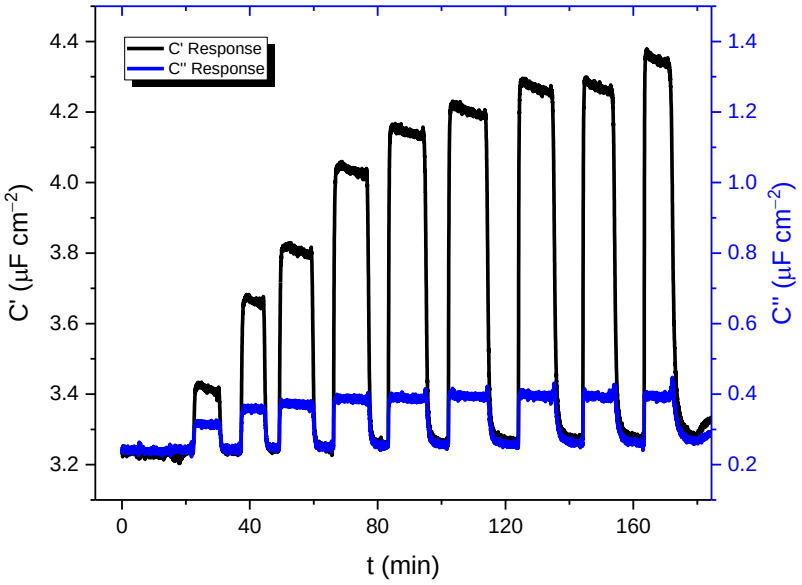


Figure 5.3-4. Comparison of the response of **B15C5$_{SAM}$** induced by increasing [Na^+] (0-50 mM), as assessed by changes in the real (black) and imaginary (blue) components of the film capacitance, conducted under continuous flow (procedure detailed below). Note that the y-axis scaling is identical in both cases, revealing significantly greater changes in the real component of the film capacitance.

5.4 Practical Considerations for Non-Faradaic Capacitive Ion Sensing

For the voltammetric and redox capacitive measurements presented in Chapters 3 & 4, respectively, a 3-electrode electrochemical cell comprised of a Pt counter, Au disc working and Ag|$AgNO_3$ fritted reference electrode was utilised for all static and continuous flow anion sensing studies. Mirroring this setup, a similar cell was initially used which differed only in the composition of the fritted reference electrode to reflect the (major) solvent used with each approach (details regarding the reference electrode composition can be found in Table 5.4-1).

Table 5.4-1. Composition of each of the fritted electrodes used, **or initially used**, for each of the techniques detailed in Chapters 2-5.

Technique (Chapter)	Solvent(s) used for sensing studies	Fritted reference electrode filling solution	Half Cell
Voltammetry (2 & 3)	ACN/H_2O or acetone/H_2O 97.5:2.5	100 mM $TBAClO_4$, 10 mM $AgNO_3$ in ACN	Ag|$AgNO_3$
Redox capacitance (4)	ACN/H_2O 99:1	100 mM $TBAClO_4$, 10 mM $AgNO_3$ in ACN	Ag|$AgNO_3$
Non-Faradaic capacitance (5)	**H_2O**	**3 M KCl in H_2O**	Ag|AgCl

However, notable inconsistencies were observed with this physical setup, with both the baseline *C* (in the absence of target cations), and the *C* response profiles and magnitudes unexpectedly displaying a significant and reproducible flow-rate dependence (*e.g.*, Figures 5.4-2 and 5.4-3). These observations were particularly surprising given that the results presented in either Chapter 3 or Chapter 4 confirmed that moving from static solution to continuous flow conditions had a negligible effect on the characteristics or anion sensing performance of **3.XB**/**HB**$_{SAM}$. This lead to the conclusion that the established physical sensing setup used in Chapters 3 & 4 is not suitable in this specific scenario, which was ultimately postulated to result from K^+ from the filling solution/M^+ ions from the analyte solution being able to diffuse through the frit of the reference electrolyte and interfere with measurements. Alternatively, junction potentials could be established under these specific conditions. It is crucial to note that this does not discredit the results in either Chapter 3 or Chapter 4, as numerous controls were conducted to confirm the integrity of each method and issues with the fritted reference electrode were only observed in the specific case of using alkali metal cations in aqueous media.

To address this, a Ag|AgCl wire pseudoreference electrode was used instead of a fritted reference electrode, and a new flow cell (Design 2) was designed. When this setup was utilised, the flow rate dependence of both the baseline *C* and cation-induced *C* responses of **B15C5$_{SAM}$** were eliminated (Figure 5.4-1, C_{rel} values calculated according to Section 7.10.2).

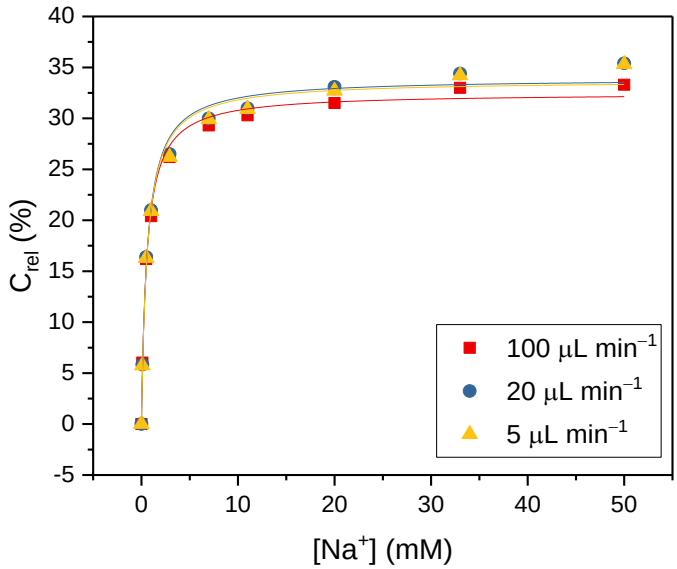


Figure 5.4-1. Relative response isotherms determined from *C* responses, C_{rel} at **B15C5$_{SAM}$** receptive films upon addition of increasing concentrations (0-50 mM) of Na^+ in 100 mM TEACl in H_2O, at flow rates of 100 (red squares), 15 (blue circles) and 5 µL min^{-1} (yellow triangles), utilising a Ag|AgCl pseudoreference electrode. Isotherms were fitted to a Langmuir model (see Section 7.10.2 for further details, and Equation 3.3-2).

Thus, all continuous flow non-Faradaic ion sensing assays from this point onwards were performed using a pseudo-reference electrode in all cases and **Design 2** for continuous sensing assays. Further detail regarding the inconsistencies observed in the results obtained with a fritted reference electrode, and the steps taken to address these issues can be found in the Appendices A5.

5.5 Non-Faradaic Capacitive Cation Sensing

5.5.1 Static Non-Faradaic Capacitive Cation Sensing

With the new practical setup in hand (Au disc working, Pt counter and Ag|AgCl pseudo reference electrode), the cation sensing performance of the **B15C5$_{SAM}$** molecular films was first assessed under static conditions in pure water (with 100 mM TEACl as supporting electrolyte). All responses were determined from the shift in the real component of the inflection point in the capacitive Nyquist plots, *C* (see Figure 5.5.1-1) and are stated relative to the initial *C* in the absence of the target cation ([M^+] = 0 mM). The progressive increase of *C* upon addition of increasing concentrations of M^+ corresponds to specific recruitment of cationic species into the **B15C5$_{SAM}$** interface, which expectedly increases the associated dielectric constant of the molecular films (which are related according to Equation 5.3-3).[184] Cation recruitment is also presumably accompanied by concomitant hydration of the interface to some extent which is also expected to increase film dielectric, as described in previous reports with hosts responsive to both cationic[184] (*e.g.*, **5.1-1 – 5**) and anionic guests (*e.g.*, **5.1-6**).[136]

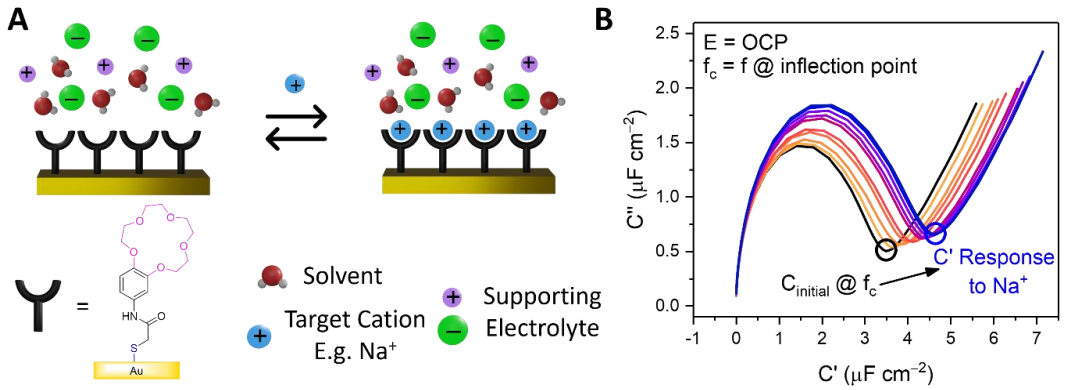


Figure 5.5.1-1. (A) Schematic depiction of **B15C5$_{SAM}$** in the presence and absence of a specific target. (B) Capacitive Nyquist plots of **B15C5$_{SAM}$** in H_2O, 100 mM TEACl conducted at fixed E=OCP. Changes in C are measured at the inflection point of each Nyquist plot (corresponding to frequency, f_c) upon addition of increasing concentrations of NaCl up to 50 mM (blue) in static solution.

In line with previous reports of static analyses of similar 15-crown-5-based SAMs, significant responses (39 ± 5 % modulation, ΔC = 1.7 ± 0.3 μF cm^{-2} towards 50 mM Na^+) were observed with respect to the baseline *C* in the presence of target cations.[184, 185, 298] For example, Figures 5.5.1-2 displays the significant responses of **B15C5$_{SAM}$** to increasing concentrations of Na^+ (Figure 5.5.1-2A) and K^+ (Figure 5.5.1-2B).

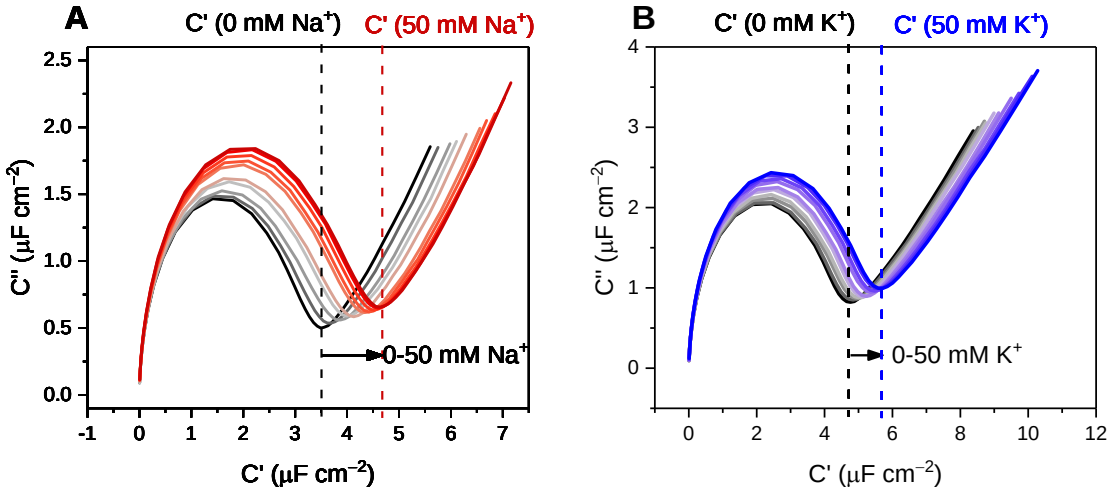


Figure 5.5.1-2. Capacitive Nyquist plots showing the shift in C at **B15C5$_{SAM}$** receptive films induced by addition of increasing concentrations of (A) Na^+ and (B) K^+ in 100 mM TEACl in H_2O, under static conditions.

Negligible responses (ΔC_{max} = 0.007 uF cm^{-2}, C_{rel} = 1.2%) were observed upon exposure of equivalent cation loadings at a non-receptive **1-dodecanethiol$_{SAM}$** interface (see Figure 5.5.1-3), confirming the requirement of specific ion recognition to induce a measurable response.

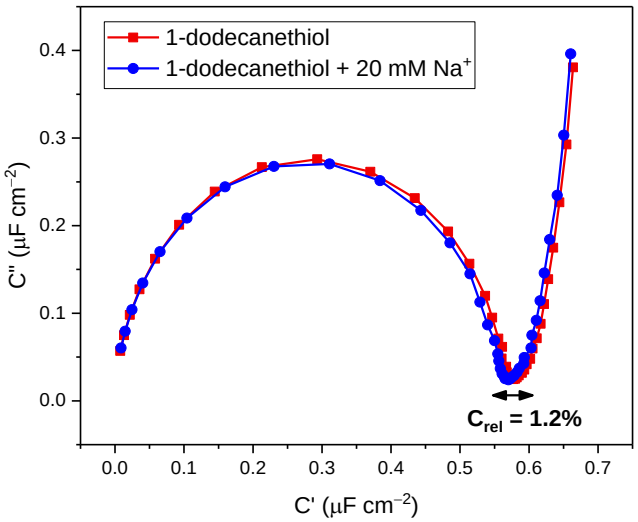


Figure 5.5.1-3. Capacitive Nyquist plots of **1-dodecanethiol$_{SAM}$** in the presence (blue circles) and absence (red squares) of 20 mM NaCl, highlighting the negligible change in *C* at a model non-receptive film in the presence of a significant target cation concentration.

As predicted based on the established size complementarity selectivity preference of 15-crown-5 receptors for Na^+,[185, 298] the resolved selectivity trend of the **B15C5$_{SAM}$** interface correlated with cation ionic size (see Figure 5.5.1-4), with the largest responses observed upon addition of Na^+.[184, 185, 290, 298] These results agree with established solution-phase results, such as those presented by Wagner-Czauderna *et al.*, who observed a selectivity trend of $Na^+ > K^+ > Li^+ > Cs^+$, with corresponding binding constants of 32000 M^{-1}, 16000 M^{-1}, 6300 M^{-1} and 2500 M^{-1}, respectively for B15C5 in ACN.[299] It should be noted, however, that both the selectivity trends of surface-bound 15C5-based receptors for alkali metal cations can vary significantly, and do not necessarily conform to the exact selectivity trends observed in solution.[299, 300] For example, **5.1-4** (a tethered 15C5-based receptive SAM, see Section 5.1) displays a selectivity trend of K^+ (27100 M^{-1}) > Cs^+ (770 M^{-1}) > Na^+ (60 M^{-1}) > Li^+ (30 M^{-1}) in water, which was attributed to sandwich complex formation at the receptive SAM.[184] Another study reported a selectivity trend of K^+ (250 M^{-1}) > Na^+ (120 M^{-1}) > Rb^+ (33 M^{-1}) > Li^+ (13 M^{-1}) > Cs^+ (7.5 M^{-1}) for adsorption constants of these alkali

metal cations to a B15C5 receptive film in water, generated via electrochemical reduction of an in-situ generated B15C5 diazonium salt.[298] This study also attributed the resolved selectivity trend to the formation of 2:1 host-guest sandwich complexes.

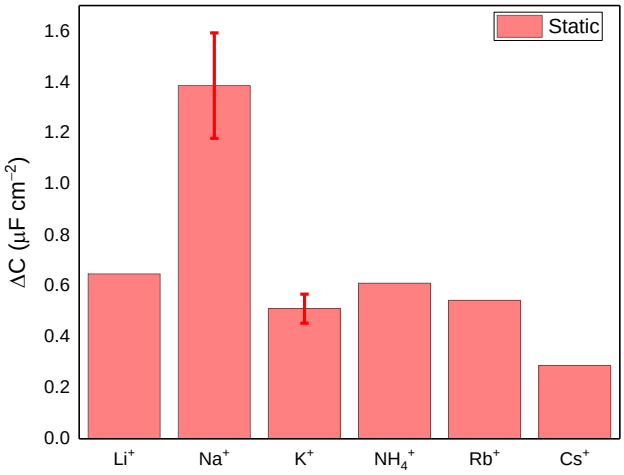


Figure 5.5.1-4. Selectivity studies with **B15C5$_{SAM}$,** as assessed from changes in C (ΔC) upon addition of 20 mM of a range of cations (shown in ascending ionic size order, from left to right: Li^+, Na^+, K^+, NH_4^+, Rb^+ and Cs^+) under static conditions. Where shown, error bars represent one standard deviation of three independent measurements.

Systematic sensing studies were then performed for Na^+ and K^+ as target cations of interest, resulting in the response isotherms shown in Figure 5.5.1-5 which were fitted to a Langmuir model (see Section 7.10.2 for additional information). Unless otherwise stated, all response isotherms were fitted to a standard Langmuir model, (*i.e.*, assuming 1:1 host-guest stoichiometry) in order to facilitate comparisons and discussions regarding the selectivity of **B15C5$_{SAM}$** for each of the cationic guest species. Further discussions on other binding modes such as 2:1 sandwich complex formation and corresponding analytical models can be found in Section 5.5.3. Analysis of these isotherms afforded binding constants of 434 ± 205 M^{-1} and 380 ± 188 M^{-1} for Na^+ and K^+, respectively, which agree well with previous reports of 15-crown-5-based receptors in water.[184, 298] Furthermore, low detection limits of

12.3 ± 3.6 μM and 11.8 ± 3.1 μM were determined for Na^+ and K^+, respectively, signifying the high sensitivity of this method (*cf*. LODs of 10 μM for commercial ISEs; the current industry gold-standard),[301, 302] even in pure water.

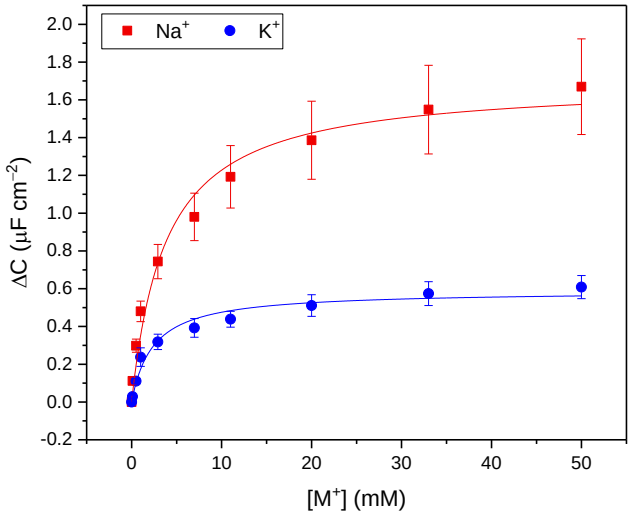


Figure 5.5.1-5. Response isotherms of **B15C5$_{SAM}$** determined from the shift in C' in response to increasing concentrations of Na^+ (red squares) and K^+ (blue circles), under static conditions. Isotherms fitted to Langmuir model (see Section 7.10.2 for further details, and Equation 3.3-2). Errors represent one standard deviation of three independent repeats.

Table 5.5.1-1. Binding constants of **B15C5$_{SAM}$** from Langmuir fitting (Eqn. 3.3-2) of response isotherms with increasing concentrations of Na^+ and K^+ under static conditions. Errors represent one standard deviation of at least three independent repeats. The interface sensitivity was obtained by analysis of the pseudolinear region at low concentration (0–1 mM [M^+]), which was then used to calculate the limit of detection (LOD). Further details on these calculations are included in Section 7.10.2.

	ΔC_{max} (μF cm^{-2})	**K_{Static} (M^{-1})**	**Sensitivity (μF cm^{-2} mM^{-1})**	**LOD (μM)**
Na^+	1.66 ± 0.25	434 ± 205	0.44 ± 0.06	12.3 ± 3.6
K^+	0.61 ± 0.06	380 ± 188	0.23 ± 0.04	11.8 ± 3.1

To summarise, Section 5.5.1 established that non-Faradaic capacitance sensitively reports on specific cation binding events at **B15C5$_{SAM}$** in static solution, in a manner which is fully consistent with previous reports. With these results in hand, the rest of this chapter will explore the novel space of translating non-Faradaic capacitance spectroscopy to a continuous measurement modality. To this end, a derived technique is described below in which capacitive assays are conducted at fixed

frequency and fixed potential, resulting in a facile, continuous sensory readout such that cation levels can be followed in real-time (see below).

5.5.2 Continuous Flow Non-Faradaic Capacitive Cation Sensing

Continuous flow ion sensing assays were facilitated with the generation of an adapted, custom 3D-printed microfluidic chip (Design 2) which was modelled on previous designs[69, 303] to now house a Ag|AgCl wire pseudoreference electrode, as well as a Pt wire counter electrode and receptor-modified Au disc working electrode, as used previously in Chapters 3 and 4 (see Figures 3.4-1 and 5.5.2-1, and Section 7.9.2 for more details). Similarly, the flow cell was combined with a sample injector to introduce sample aliquots of defined volume (typically 1 mL), and a syringe pump to continuously drive electrolyte through the flow system (100 mM TEACl in H_2O). Prior to each measurement, the OCP was determined (typically 0-0.1 V *vs*. Ag|AgCl) and applied as the DC bias potential to acquire a capacitive Nyquist plot, from which f_c was determined (as defined in Figure 5.5.1-1B). Continuous non-Faradaic capacitance measurements were then performed at these fixed OCP and f_c values to afford a continual readout of *C* in real-time with high temporal resolution (≈1.4 s). Introduction of sample cation aliquots induced a significant "spike" in the resulting sensogram (displayed in Figure 5.5.2-1B), followed by a "washing" step whereby electrolyte is continuously flushed over the receptive interface to (re)establish the baseline (denoted by the black lines in Figure 5.5.2-1B). The fidelity of baseline recovery is striking, with an almost negligible drift of $\Delta C = 0.03 \pm 0.04$ μF cm^{-2} h^{-1} (0.5 ± 0.3% h^{-1}, errors correspond to 10 independent repeats across 3 different

electrodes, over measurement timeframes ranging from 5 to 54 h) throughout titrations of a range of relevant cations (Li^+, Na^+, K^+, Rb^+, Cs^+ or NH_4^+).

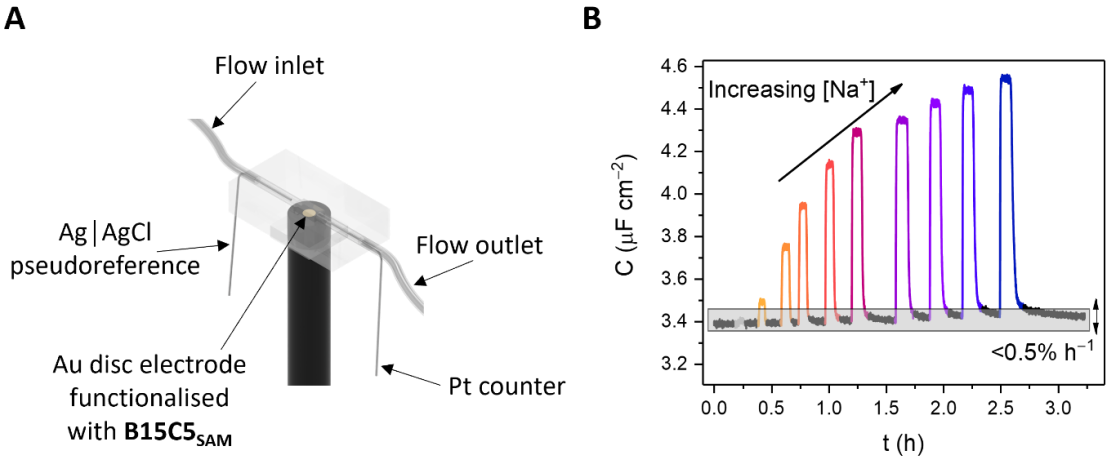


Figure 5.5.2-1. (A) Schematic depiction of the custom-designed, 3D-printed flow cell and electrochemical cell components. (B) Non-Faradaic capacitance response of **B15C5$_{SAM}$** toward Na^+ under continuous electrolyte flow in the custom flow cell (cell volume = 10 µL, flow rate Q = 100 µL min^{-1}, at fixed E = OCP and f = f_c). Each spike represents the response toward aliquots (V_{Sample} = 1 mL) of Na^+ of concentration increasing up to 50 mM. Subsequent washing of the interface with supporting electrolyte re-establishes the baseline (black lines) with excellent recovery (0.5 ± 0.3% h^{-1}, as highlighted within figure).

Corroborating the observations made under static conditions (see Section 5.5.1), the addition of the alkali metals (Li^+, Na^+, K^+, Rb^+ and Cs^+) and NH_4^+ under continuous flow induced significant changes in *C* (up to ΔC = 1.1 ± 0.1 µF cm^{-2}, or 33%, see Figure 5.5.2-2). Once again, a clear selectivity preference for Na^+ was observed, with Figure 5.5.2-3 highlighting the consistency in resolved selectivity trends under static and continuous flow conditions, as assessed by comparison of the responses induced at **B15C5$_{SAM}$** towards 20 mM of each cation in both cases.

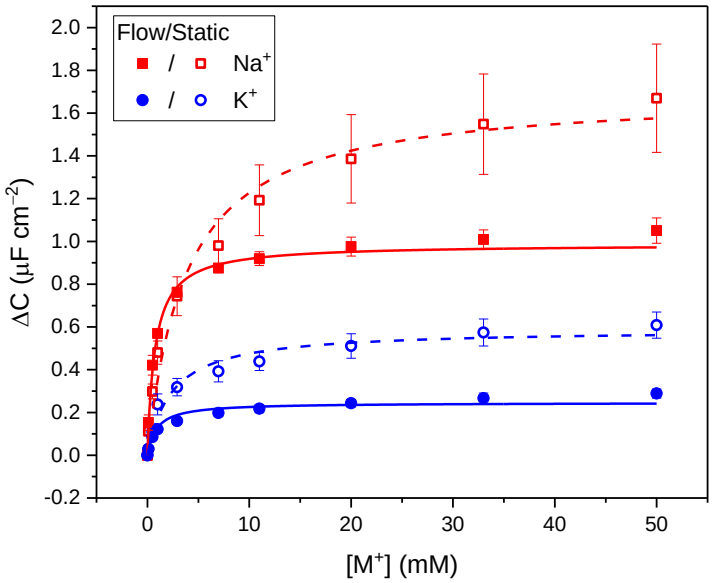


Figure 5.5.2-2. Comparison of the *C* response isotherms determined at **B15C5$_{SAM}$** in response to increasing concentrations of Na+ (red squares) and K+ (blue circles), under static conditions (open symbols) and under continuous flow at 100 μL min^{-1} (filled symbols). Isotherms fitted to Langmuir model (see Section 7.10.2 for further details, and Equation 3.3-2). Errors represent one standard deviation of three independent repeats. An analogous plot comparing the relative response magnitudes can be found in the Appendices A5 (Figure A5.11).

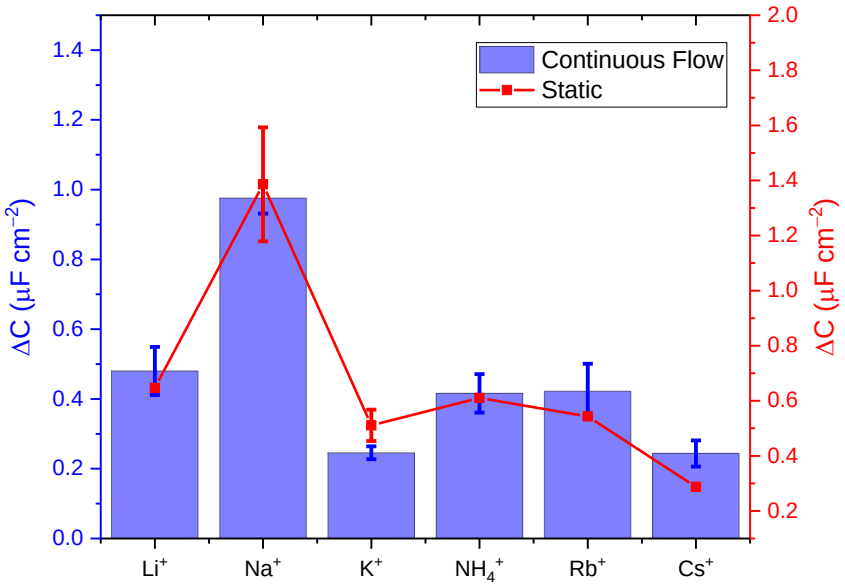


Figure 5.5.2-3. Selectivity studies with 20 mM of alkali metals and NH_4^+, assessed from changes in C (ΔC) at **B15C5$_{SAM}$** receptive films under static (red) and continuous flow (blue) conditions, illustrating the excellent agreement in selectivity trends resolved under static and continuous flow conditions. Where shown, error bars represent one standard deviation of three independent measurements. An analogous plot comparing the response magnitudes with identical y-scaling can be found in the Appendix (Figure A5.12).

In general, the response magnitudes determined under static and continuous flow conditions agreed well (particularly when the relative response magnitudes are contrasted; Figure A5.11, as predicted based on the results obtained via the continuous voltammetric and redox capacitive ion sensing methods. The slight discrepancies in overall response magnitude observed between static and continuous flow conditions were attributed to the fact that all continuous flow responses were normalised with respect to each new baseline established prior to each sample addition. In doing so, any baseline drift can be fully accounted for, preventing additive errors in the measured response under static conditions which would manifest in larger discrepancies between the two conditions with each successive addition of target (herein at higher concentrations, evidenced in Figure 5.5.2-2). Re-establishing the baseline following each sample addition under continuous flow conditions is a facile and rapid feat by virtue of the microfluidic setup used herein, but replicating this under static conditions would be extremely challenging experimentally. Specifically, the **B15C5$_{SAM}$**-functionalised working electrode would have to be removed from solution, rinsed with copious quantities of pure water, then resubmerged in fresh electrolyte and the baseline *C* restabilised for at least 1 h prior to each addition. A conservative estimate for the length of time to complete a static assay in this manner (9 additions) would be at least 12 h, (*cf*. a typical continuous flow Na^+ assay ≈ 3h, which avoids the lengthy washing and re-stabilisation procedures required following each addition under static conditions), highlighting the practical ease afforded by performing ion sensing assays under continuous flow.

To verify that all significant responses measured under continuous flow resulted from specific ion recruitment events, control experiments were once again conducted at a non-receptive **1-dodecanethiol$_{SAM}$** interface. Consistent with the results under static conditions, negligible changes in *C* (ΔC < 1% in all cases) were observed at **1-dodecanethiol$_{SAM}$** upon injection of mM target cation levels (ΔC < 2%, see Figure 5.5.2-4).

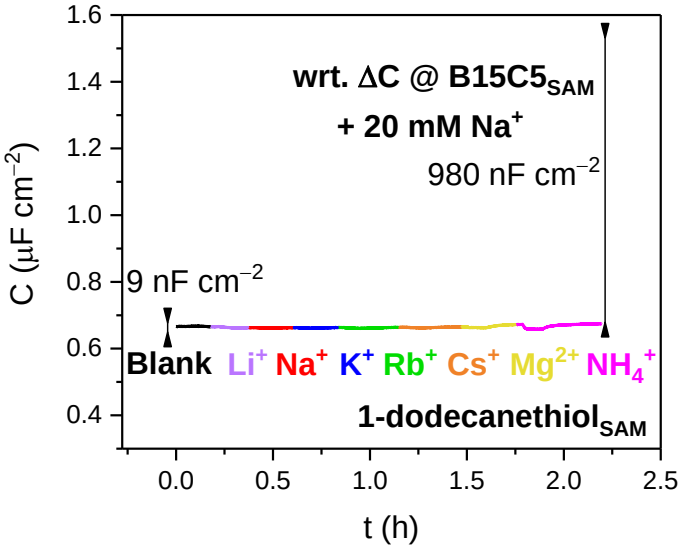


Figure 5.5.2-4. C responses induced at a non-receptive control interface, **1-docanethiol$_{SAM}$** upon addition of a blank sample (100 mM TEACl), and 20 mM Li^+, Na^+, K^+, Rb^+, Cs^+, Mg^{2+} and NH_4^+, added as MCl salts. As shown, the control interface exhibits negligible responses to any of the cations investigated (ΔC < 9 nF cm^{-2}, C_{rel} < 0.2% cf. ΔC = 980 nF cm^{-2} for the response of **B15C5$_{SAM}$** to 20 mM Na^+).

Additionally, injection of "blank" samples of 100 mM TEACl at **B15C5$_{SAM}$** did not induce a significant response (exemplified as the grey line at *ca*. 0.25 h in Figure 5.5.2-1). Furthermore, markedly attenuated responses were observed during competition studies when either Na^+ or K^+ were precomplexed with excess [2.2.2]-cryptand ($K(Na^+)$ = 8000 M^{-1} in H_2O)[304] compared to the responses of **B15C5$_{SAM}$** to Na^+ or K^+ alone (see Figures 5.5.2-5 and 5.5.2-6, sensogram shown in Figure A5.13), in line with expectations for competitive recruitment.

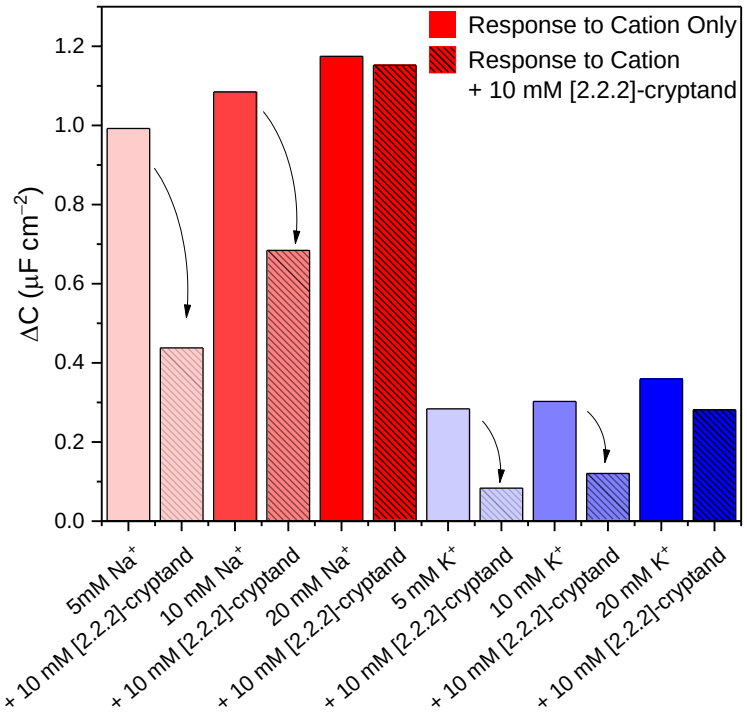


Figure 5.5.2-5. Competition studies of **B15C5$_{SAM}$** with [2.2.2]-cryptand for Na^+ (red) and K^+ (blue). Solid bars represent the responses to aliquots of M^+ alone (5, 10 or 20 mM), and dashed bars denote responses to M^+ (5, 10 and 20 mM) + 10 mM [2.2.2]-cryptand (precomplexed).

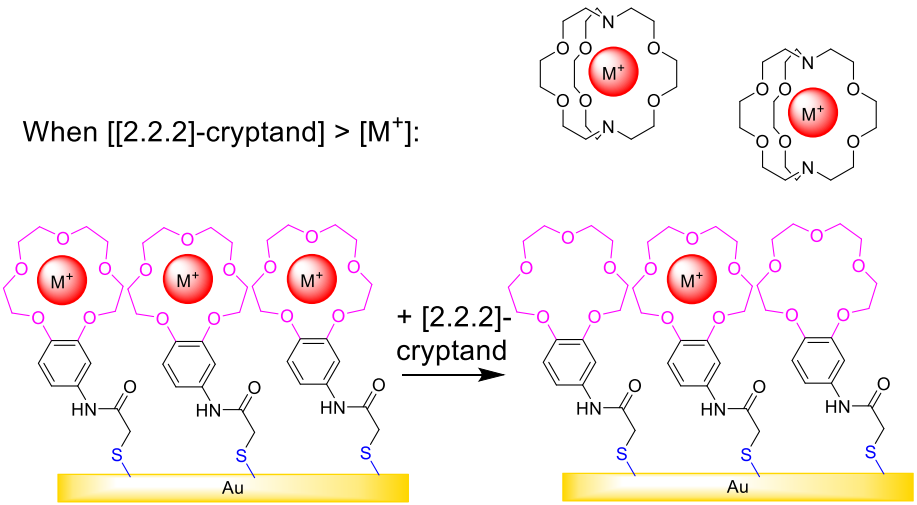


Figure 5.5.2-6. Schematic depiction of competition studies of **B15C5$_{SAM}$** with [2.2.2]-cryptand, predicting lower C responses with higher ratios of [[2.2.2]-cryptand]:[M^+].

Systematic sensing studies were conducted for a range of cations under continuous flow by titrating in increasing concentrations of MCl salts (at a constant ionic strength of 100 mM to mitigate non-specific electrolyte effects on *C* response). Representative sensograms for all the target cations, and the corresponding

response isotherms are shown in Figures A5.13 and 5.5.2-6, respectively. Derived response isotherms afforded a range of binding and analytical parameters, including the apparent binding constant, maximum response in *C*, sensitivity and LOD which are summarised in Table 5.5.2-1.

Table 5.5.2-1. Binding constants of **B15C5$_{SAM}$** from Langmuir fitting (Eqn. 3.3-2) of response isotherms with increasing concentrations of a range of alkali metals (Li^+, Na^+, K^+, Rb^+, Cs^+ and NH_4^+) under continuous flow at 100 µL min^{-1}. Errors represent one standard deviation of at least three independent repeats. Details on how the interface sensitivity and limit of detection (LOD) were calculated can be found in Section 7.10.2. Analogous analyses with a Langmuir-Freundlich model (Eqn. 3.3-1) are tabulated in the Appendices A5, Table A5.3.

	ΔC_{max} (µF cm^{-2})	K (M^{-1})	Sensitivity (µF cm^{-2} mM^{-1})	LOD (µM)
Li^+	0.63 ± 0.09	133 ± 12	0.11 ± 0.02	14.7 ± 2.7
Na^+	1.03 ± 0.06	1252 ± 341	0.52 ± 0.05	4.0 ± 1.2
K^+	0.29 ± 0.02	555 ± 58	0.09 ± 0.01	27.4 ± 4.7
Rb^+	0.48 ± 0.09	763 ± 197	0.18 ± 0.02	9.3 ± 0.8
Cs^+	0.24 ± 0.07	1929 ± 640	0.12 ± 0.01	18.2 ± 7.5
NH_4^+	0.47 ± 0.06	1232 ± 357	0.21 ± 0.04	11.0 ± 0.8

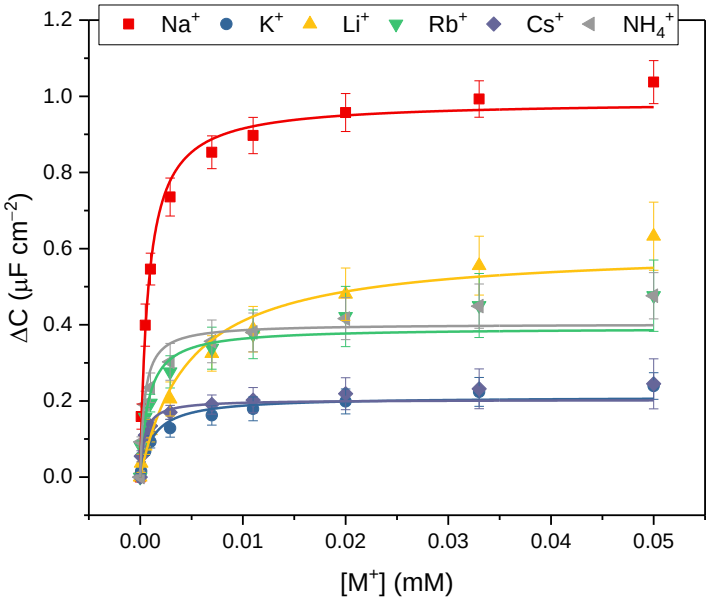


Figure 5.5.2-6. Response isotherms determined from the shift in *C* of **B15C5$_{SAM}$** in response to increasing concentrations of Na^+ (red squares), K^+ (blue circles), Li^+ (yellow triangles), Rb^+ (green inverted triangles), Cs^+ (purple diamonds) and NH_4^+ (grey stars) under continuous flow at 100 µL min^{-1}. Isotherms were fitted to a Langmuir model (see Section 7.10.2 for further details, and Equation 3.3-2). Errors represent one standard deviation of three independent repeats.

As is apparent from the acquired data, the crown SAM sensor is consistently most sensitive to Na^+, demonstrating a high sensitivity of 0.52 ± 0.05 μF cm^{-2} mM^{-1} under continuous flow, correlating to a highly competitive limit of detection of 4.0 ± 1.2 μM. This exceeds that typical of most commercial ISEs, the industry standard for in-the-field Na^+ sensing, which typically quote a limit of detection around 10 μM.[301, 302] Not only does the sensitivity of this methodology match that of commercial ISEs, but it also does not require any recalibration or the use of basic conditions to achieve this, unlike certain commercial ISEs.

Supported by the previously noted high baseline capacitive stability of this **B15C5$_{SAM}$** interface, the long-term sensing capability was then assessed by continually monitoring responses to repeat 3 mM Na^+ injections over the course of 54 h. The resulting sensogram is displayed in Figure 5.5.2-7, and highlights the high reproducibility of response over significant measurement time, with an average response of ΔC =0.68 ± 0.08 μF cm^{-2} (C_{rel} = 17.9 ± 2.7%) across 15 additions. It should be noted that the impressive baseline stabilities mentioned earlier still persist over this entire timeframe (0.2% h^{-1}), fully consistent with the shorter-term measurements (*cf.* 0.5 ± 0.3% h^{-1}). Of further note, is that this 54 h duration of sensing was performed in one continuous, undisturbed measurement, without re-conditioning or calibration; this is in stark contrast to the majority of commercial ion-selective electrodes which typically require re-calibration after a few hours in order to achieve their stated sensitivity and accuracy.[302, 305]

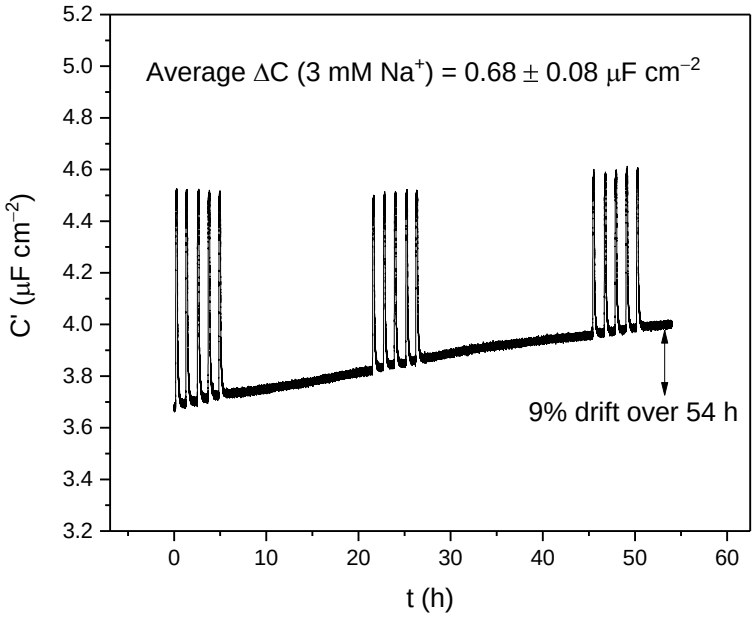


Figure 5.5.2-7. Long term cation sensing experiment conducted over 54 h in water (100 mM TEACl as supporting electrolyte). Responses to 3 mM Na^+ are shown as spikes in the sensogram.

Furthermore, excellent agreement was observed between predicted and determined responses toward a blinded range of samples of unknown [Na^+] (six samples between 0.03-3 mM Na^+) in both pure water (Figure 5.5.2-8) and a simple artificial sweat matrix (11.3 mM lactic acid, 21.6 mM urea in water, Figure 5.5.2-9), both containing 100 mM TEACl as supporting electrolyte for consistency with the results obtained above. Three additional samples (9.47, 15.38 and 42.91 mM) were analysed in the artificial sweat matrix, corresponding to concentrations of Na^+ that fall within a relevant range for Na^+ levels in sweat (typically between 10-100 mM).[306] The correlation between predicted and measured values in both cases was determined through cross reference to a prior acquired calibration curve in both cases, which are shown in Figure 5.5.2-8B and 5.5.2-9B, respectively.

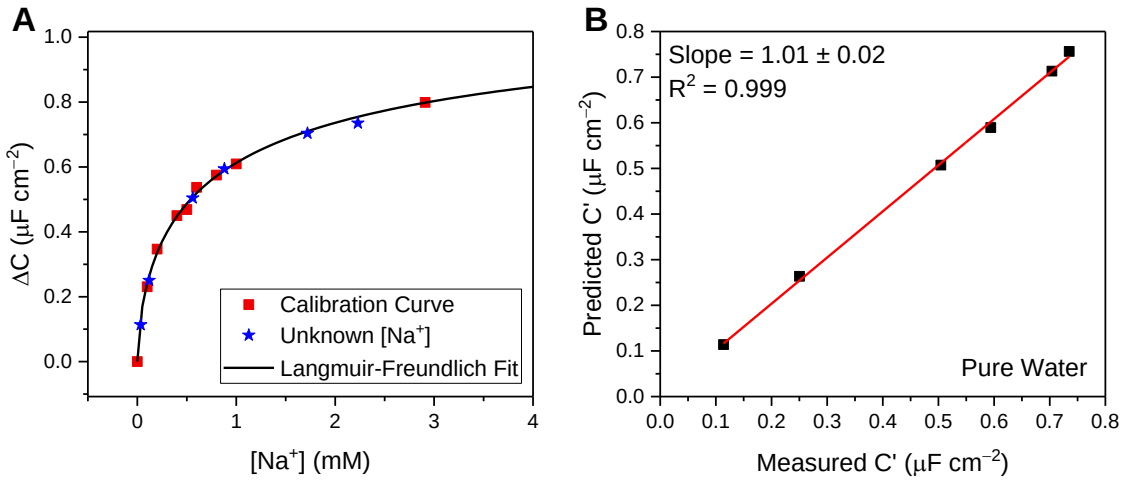


Figure 5.5.2-8. (A) Responses to samples of unknown concentration in pure water superimposed onto a calibration curve fitted to a Langmuir-Freundlich model (Eqn. 3.3-1), recorded prior to blind studies. (B) Correlation plot showing the excellent agreement between determined and predicted capacitance response magnitudes for a range of blinded unknown concentrations in pure water (100 mM TEACl as supporting electrolyte). Predicted response magnitudes were obtained from comparison to the calibration curve shown in Figure 5.5.2-8A.

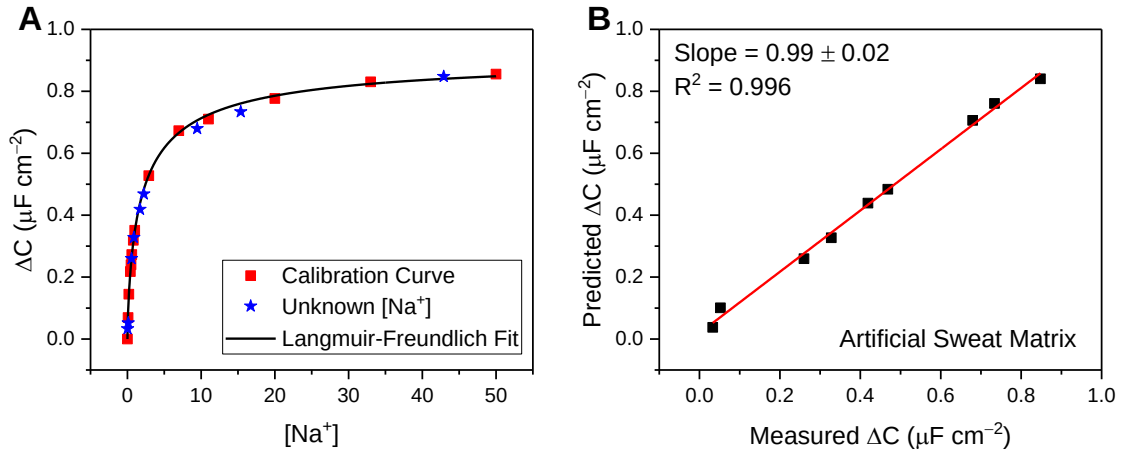


Figure 5.5.2-9. (A) Responses to samples of unknown concentration in artificial sweat (100 mM TEACl, 11.3 mM lactic acid, 21.6 mM urea in DI water) superimposed onto a calibration curve fitted to a Langmuir-Freundlich model (Eqn. 3.3-1), recorded prior to blind studies. (B) Correlation plot showing the excellent agreement between measured and predicted capacitance response magnitudes for a range of blinded unknown concentrations. Predicted response magnitudes were estimated from comparison to the calibration curve shown in Figure 5.5.2-9A.

Encouraged by these results, the performance of **B15C5$_{SAM}$** for cation sensing was then assessed in a range of real aqueous samples varying from freshwater to tap water samples (details of each real aqueous sample can be found in Table 7.8.1-1). As exemplified in Figure 5.5.2-10A for Freshwater Sample 1, well-defined capacitive Nyquist plots were obtained in these samples (spiked with 100 mM TEACl for consistency) that closely resembled those in pure water. Subsequently, Na^+

sensing studies were performed which displayed significant dose-dependent responses in freshwater and tap water samples (see Figures 5.5.2-10B, S5.15 and S5.16), which once again generally reflected the results measured in pure water, albeit with lower (half that of the response magnitudes in pure water) magnitudes of response (Figure 5.5.2-11).

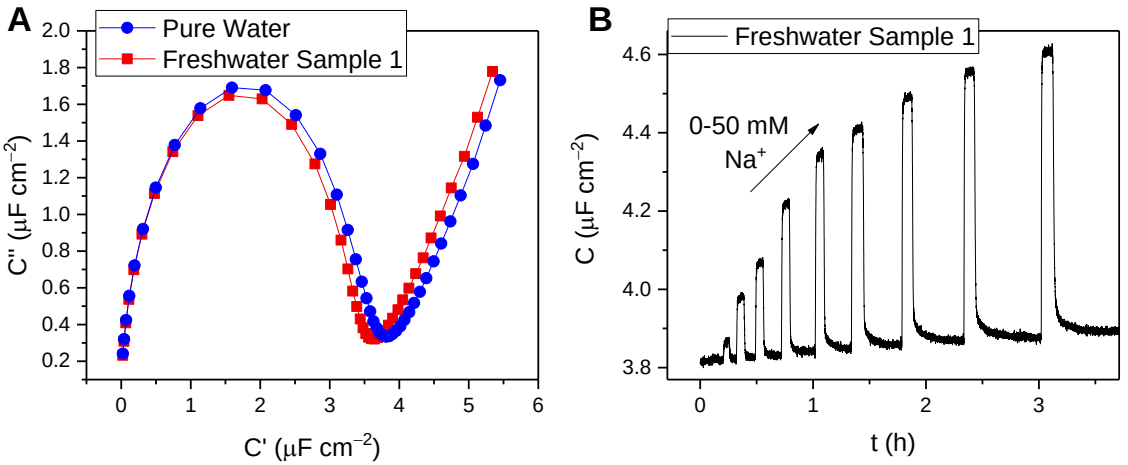


Figure 5.5.2-10. Capacitive Nyquist plots of **B15C5$_{SAM}$** acquired in pure water (blue circles) and Freshwater Sample 1 (red squares). (B) Sensogram displaying the response of **B15C5$_{SAM}$** to increasing concentrations of Na^+ up to 50 mM in Freshwater Sample 1 (with 100 mM TEACl as supporting electrolyte).

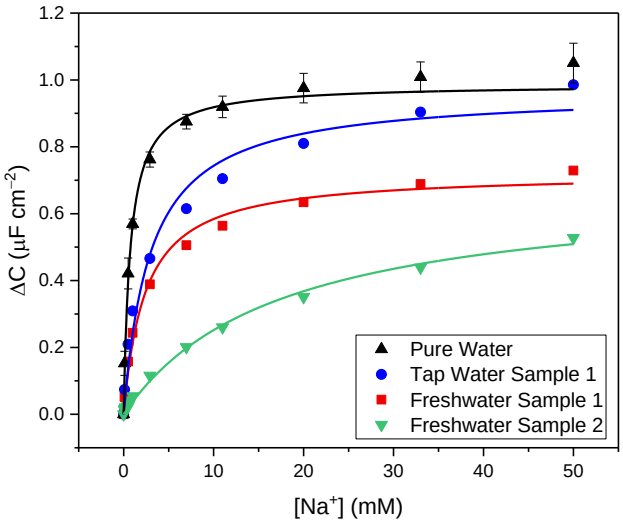


Figure 5.5.2-11. Response isotherms determined from the shift in *C* of **B15C5$_{SAM}$** in response to increasing concentrations of Na^+ in pure water (black triangles), Tap Water Sample 1 (blue circles), Freshwater Sample 1 (red squares), and Fresh Water Sample 2 (green inverted triangles), under continuous flow at 100 µL min^{-1}. Isotherms were fitted to a Langmuir model (see Section 7.10.2 for further details, and Equation 3.3-2). Where shown, error bars represent one standard deviation of three independent repeats (for results in pure water only).

The lower response magnitudes observed in real samples in Figure 5.5.2-11 were attributed to competitive binding at **B15C5$_{SAM}$** with background levels of pertinent interferants such as K^+. Indeed, the suppression of both the maximum response magnitude and Na^+ binding affinity generally correlated with higher background [K^+]; from pure water ([K^+] = negligible), to Fresh Water Sample 1 ([K^+] = 0.009 mM), then to Fresh Water Sample 2 ([K^+] = 0.159 mM), as shown in Table 5.5.2-2. Efforts were also made to quantify native [Na^+] in the real, aqueous samples via established standard addition methods, but a poor agreement was generally obtained between the measured native [Na^+] and the predicted native [Na^+] based on previous reports (Table 5.5.2-2). The inconsistencies between these values likely arise for two reasons: firstly, the true [Na^+] in each of these samples are expected to fluctuate slightly due to external factors (*e.g.*, the fresh water samples will be affected by recent rainfall), and secondly, the standard addition method is only accurate when the measured responses result from recruitment of the target in question (*i.e.*, for Na^+ alone). As established in Figure 5.5.2-11, the response of **B15C5$_{SAM}$** in the absence (black line) and presence of background interferants (e.g., K^+ or Ca^{2+}) (blue, red or green lines) are clearly different, presumably due to recruitment/interaction of **B15C5$_{SAM}$** with these interferants to some extent. This is not an unexpected observation; whilst crown ether-based SAMs often exhibit size-dependent selectivity preferences that are consistent with solution-phase observations, other ions (other than alkali metal cations) will often still bind to some extent and induce a measurable response. Nevertheless, it should be noted that these issues are not inherently related to the methodology; rather the selectivity of the receptive interface. Therefore, these results still show promise for quantification of targets in

real, aqueous media, and more selective receptive interfaces are envisaged to improve the accuracy of this methodology.

Table 5.5.2-2. Binding constants and maximum responses (ΔC_{max}) of **B15C5$_{SAM}$** from Langmuir fitting (Eqn. 3.3-2) of response isotherms with increasing concentrations of Na^+ under continuous flow at 100 µL min^{-1}, in a range of real samples. a- Errors represent one standard deviation of at least three independent repeats. b- Errors result from mathematical fittings to response isotherms. N/A- not applicable.

	ΔC_{max} (µF cm^{-2})	K (M^{-1})	Measured Native [Na^+] (mM)	Expected Native [Na^+] (mM)
Pure Water	1.03 ± 0.06[a]	1252 ± 341[a]	N/A	N/A
Freshwater Sample 1[307]	0.73	421 ± 54.2[b]	0.198	0.079
Freshwater Sample 2[308]	0.53	58.3 ± 5.65[b]	1.567	0.143
Tap Water Sample 1[309]	0.99	336 ± 65.9[b]	0.918	0.099

5.5.3 Temporal Resolution of Cation-Dependent Binding Modes

In addition to cation quantification in pure water, the high temporal resolution of this continuous non-Faradaic capacitive ion sensing modality resolved both association and dissociation regimes of binding, which appeared to differ considerably between the cations of interest. As noted previously, kinetic analyses are rare in host-guest recognition, in part due to the lack of methodologies capable of monitoring association/dissociation in real-time. Thus, elucidating different behaviour for the recruitment of different targets would provide critical insight for the kinetics of host-guest chemistry in general, and inform future host design choices.

In this case, two distinct temporal populations were observed which correlated with ionic size. Namely, the smaller cations (Li^+ and Na^+) exclusively exhibit the first

behaviour whereby a single, defined plateau is quickly established. In contrast, a second signature is only observed for the larger cations (K^+, Rb^+, Cs^+ and NH_4^+, to an extent) whereby an initial plateau is once again rapidly established but then gradually drifts to a lower *C*. Crucially, it should be noted that all titration studies were performed in an identical and systematic manner for each of the cations, precluding physical or experimental disparities from inducing this different behaviour.

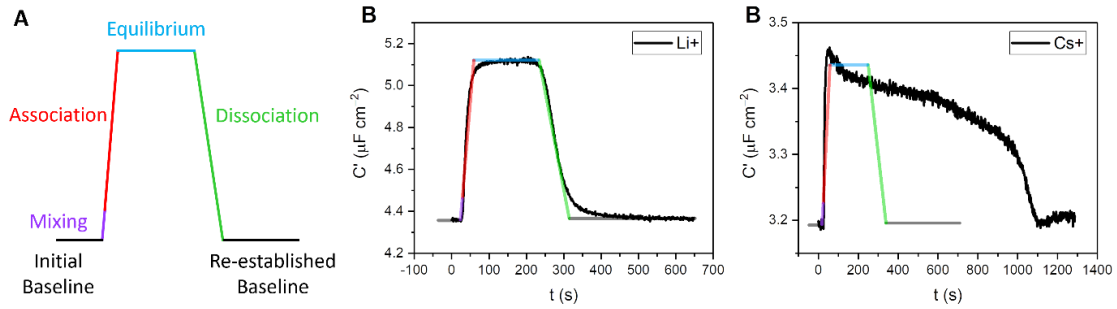


Figure 5.5.3-1. (A) Representative response signature expected for specific binding at a receptive interface, representing the capacitance determined prior to target injection (baseline, black lines), and following injection which comprises a short mixing period (purple), association (red) and subsequent dissociation upon washing (green). This predicted signature is superimposed (with consistent scaling with respect to time) onto the measured responses of **B15C5$_{SAM}$** to 50 mM (B) Li^+ and (C) Cs^+.

In order to quantify this behaviour, the rates of the association (upon injection) and dissociation (upon washing) of five representative concentrations of the target cations were approximated by fitting a linear model to the first 10 data points following a change of > 0.03 μF cm^{-2} with respect to the baseline (corresponding to the smallest change in *C* which can be confidently attributed to specific binding). At a flow rate of 100 μL min^{-1} and a cell volume of ≈ 10 μL, any mixing of the supporting electrolyte and analyte solution within the cell would be expected to conclude within 2 s of the analyte solvent front reaching the cell (*i.e.*, the point at which a measurable change in *C* is observed). Therefore, given the high temporal resolution,

the data used for this analysis of kinetics can be assumed to predominantly reflect binding, and not artefacts of mixing. Each of the association and dissociation traces for each concentration (0.1, 1, 3, 11 and 50 mM) of cation, as well as the linear fits to the first 10 data points in the association/dissociation regime can be found in the Appendix, Figures A5.16-S5.21 and Tables A5.4 and S5.5. Interestingly, the binding rate constants for each of the cations (at $[M^+]$ = 50 mM) appear to be broadly consistent, and lie in the range of 13-66 nF cm^{-2} s^{-1} with the lowest rate attributed to Cs^+ and the highest to Na^+. Contrasting Li^+ and Cs^+ as representative small and large cations, respectively, the "on-rate" for Li^+ was 3x faster than Cs^+ (37.2 *vs*. 12.9 nF cm^{-2} s^{-1}, respectively). The dissociation rate constants, however, differ substantially, with Li^+ and Na^+ exhibiting broadly similar dissociation rates at 50 mM $[M^+]$ (6.7 and 4.8 nF cm^{-2} s^{-1}, respectively), but significantly slower rates were observed for K^+ (2.6 nF cm^{-2} s^{-1}) and particularly Cs^+ (0.2 nF cm^{-2} s^{-1}). This equates to a 42-fold faster "off-rate" for Li^+ compared to Cs^+, which is visualised in Figure 5.5.3-1.

Although a direct chemical interpretation of these dissociation regimes is challenging, the stark differences between the "off-rates" for the different alkali metals could report on different ion binding modes Specifically, the significantly slower dissociation kinetics exhibited for the larger cations (K^+, Rb^+, Cs^+ and NH_4^+) may result from a 2:1 host-guest binding stoichiometry at the surface (schematically depicted in Figure 5.5.3-2). The formation of 2:1 host-guest sandwich complexes have been alluded to in previous reports to justify deviations from predicted selectivity trends based on size complementarity at 1:1 host-guest complexes.[185, 298]

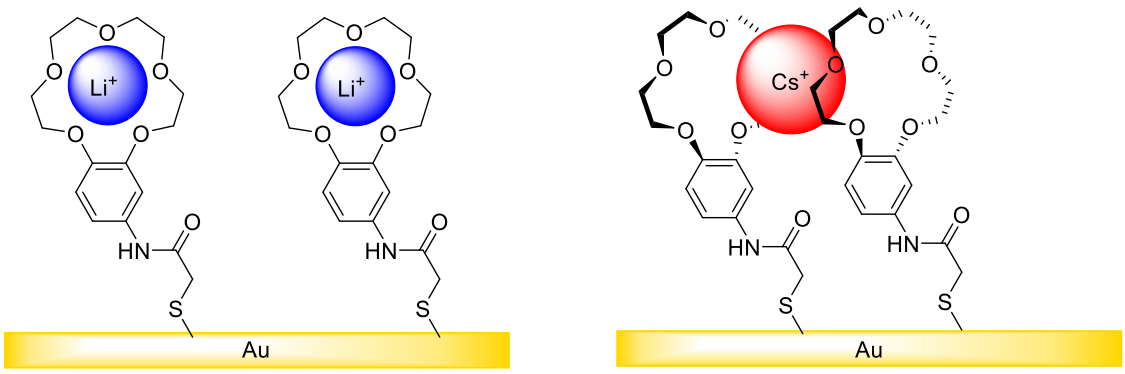


Figure 5.5.3-2. Schematic depiction of 1:1 (left) and 2:1 (right) host-guest cation binding modes at **B15C5$_{SAM}$**.

To try and gain a better understanding of these effects, all response isotherms for the systematic studies of the alkali metal cations were additionally fitted to a Langmuir-Freundlich model (Equation 3.3-1, results can be found in Table A5.3). As described earlier in Section 3.3, the Langmuir-Freundlich model differs from the classical Langmuir model by including a heterogeneity factor, n. Here, it was hypothesised that any deviation away from the expected 1:1 host-guest binding mode (n = 1) towards a 2:1 host-guest binding mode or any other more complex binding mode, would be expected to be borne out in an n value closer to 0. Unfortunately, no clear relationship could be observed between n and the size of the alkali metal guest, but future work could include Hill analyses of the acquired data to determine whether there is any degree of cooperativity during cation binding with the larger alkali metal cations.

5.6 Conclusions & Future Work

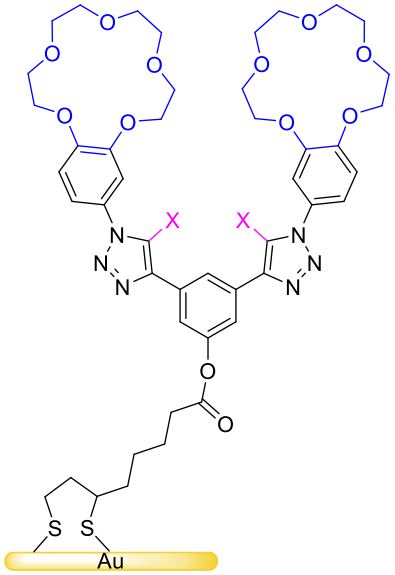
5.6.1 Conclusions

A proof-of-principle, reagentless ion sensing methodology based on non-Faradaic capacitance for continuous, real-time cation sensing with a benzo-15-crown-5

receptive molecular film is reported. The low baseline capacitance of these interfaces supports high sensitivity (LODs as low as 5 μM for Na^+) reagentless cation detection with baseline stabilities sufficiently good to enable ion sensing across extended periods of time. Analyses conducted in real world media marks this work as considerable progress towards ion monitoring over practically-relevant time scales for environmental monitoring in groundwater, for example. Previously inaccessible temporal ion binding and unbinding information is resolvable and herein may be reflective of different interfacial binding modes. Though exemplified here with benzo-15-crown-5 (B15C5) molecular films, the methodology is envisioned to be widely extendable to a range of ion-receptive interfacial hosts.

5.6.2 Future Work

The high reproducibility of responses to cationic targets marks **B15C5$_{SAM}$** an ideal model interface for comparison with other derived receptive interfaces, such as **4.XB/HB-B15C5$_{SAM}$** for ion pair sensing studies. As **4.XB/HB-B15C5$_{SAM}$** contains the same cation binding site as **B15C5$_{SAM}$** (benzo-15-crown-5 units) in addition to anion binding sites ((iodo)-triazole units), cation, anion and ion pair binding and sensing can be independently investigated.[179]



X = I, 4.XB-B15C5$_{SAM}$
X = H, 4.HB-B15C5$_{SAM}$

Scheme 5.6-1. Ion pair receptive film **4.XB/HB-B15C5$_{SAM}$**

Preliminary experiments were performed to assess the viability of these assays with **4.XB/HB-B15C5$_{SAM}$**, starting with analogous cation sensing studies to those performed with **B15C5$_{SAM}$**. As predicted based on the identical B15C5-based cation binding sites, the observed responses of **4.XB-B15C5$_{SAM}$** and **4.HB-B15C5$_{SAM}$** to increasing concentrations of Na^+ and K^+ were very similar in magnitude (see Figure 5.6-1). For example, the maximum *C* response for Na^+ was determined to be 0.39 ± 0.05 μF cm^{-2} and 0.41 μF cm^{-2} for **4.XB-B15C5$_{SAM}$** and **4.HB-B15C5$_{SAM}$**, respectively.

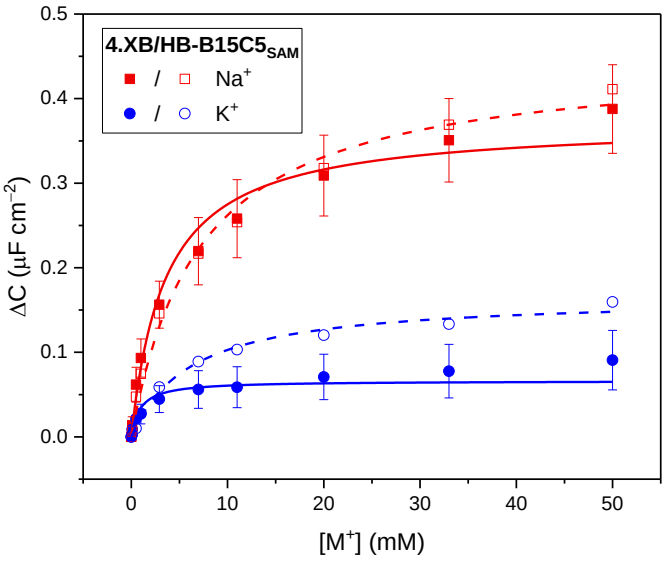


Figure 5.6-1. Response isotherms determined from the shift in *C* of **4.XB-B15C5$_{SAM}$** (solid symbols) and **4.HB-B15C5$_{SAM}$** in response to increasing concentrations of Na^+ (red squares) and K^+ (blue circles) under continuous flow at 100 μL min^{-1}. Isotherms were fitted to a Langmuir model (see Section 7.10.2 for further details, and Equation 3.3-2). Where shown, errors represent one standard deviation of two independent repeats.

Following cation sensing studies, preliminary ion pair sensing assays were performed to explore the selectivity preferences of both **4.XB**/**HB-B15C5$_{SAM}$** interfaces as well as their relative abilities to recruit both anionic and cationic guests. The results of this are displayed in Figure 5.6-2, and highlight a number of interesting conclusions.

1. **4.HB-B15C5$_{SAM}$** typically outperforms **4.XB-B15C5$_{SAM}$** in terms of *C* response magnitude to anionic targets, although there is some indication that the XB sensor generally outperforms the HB sensor in response to the halides. For example, the response of **4.XB-B15C5$_{SAM}$** is larger for Br^- than that of **4.HB-B15C5$_{SAM}$**, and the same is true for the addition of NaCl. Further studies with I^- would aid these investigations.
2. Significant differences were observed between the response magnitudes of **4.XB-B15C5$_{SAM}$** and **4.HB-B15C5$_{SAM}$** towards all of the salts used here, suggesting that ion pair recruitment is mediated by specific non-covalent interactions at the iodo-triazole- and proto-triazole-based anion binding sites, respectively.
3. In general, the selectivity preference of both **4.XB**/**HB-B15C5$_{SAM}$** generally reflects expectations based on Hofmeister trends. *I.e.*, the least strongly solvated anions (*e.g.*, SCN^-) are preferentially bound/induce the largest responses, as the high solvation energies of the more charge dense anions (*e.g.*, Cl^-) are prohibitive.

4. Notably different response magnitudes were observed towards salts of Na^+, K^+ and NH_4^+, consistent with expectations that specific cation binding contributes significantly to the measured response.

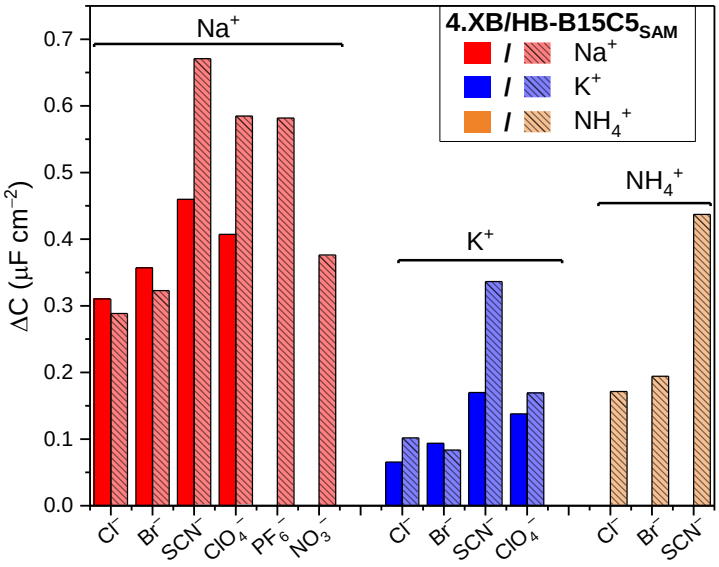


Figure 5.6-2. Ion pair sensing studies of **4.XB-B15C5$_{SAM}$** (solid bars) and **4.HB-B15C5$_{SAM}$** (dashed bars) for 20 mM of a range of Na^+ (red), K^+ (blue) and NH_4^+ (orange) salts in pure water (100 mM TEACl as supporting electrolyte), under continuous flow at 100 μL min^{-1}.

In order to comprehensively assess the ion pair performance of **4.XB/HB-B15C5$_{SAM}$**, systematic cation, anion and ion pair sensing studies must be undertaken. The resulting sensograms may also provide further insight into the unexpected response signatures and kinetics of binding observed at **B15C5$_{SAM}$** for different cationic targets.

Chapter 6

Conclusions & Future Outlook

Chapter 6: Conclusions & Future Outlook

In summary, this thesis details a comprehensive analysis of the impact of generating binding microenvironment with low local ε_r within polymeric architectures. Then, multiple novel ion sensing methodologies including voltammetric, redox capacitive and non-Faradaic capacitive approaches were outlined that are capable of producing continuous sensor outputs to monitor ion binding in real-time with high temporal resolution.

The systematic characterisation and comparison of the anion binding and electrochemical sensing performance of monomeric and polymeric hosts based on XB or HB-mediated binding was detailed, for the first time, in Chapter 2. These analyses revealed profound solvent exclusion effects such that the incorporation of relatively simple XB binding motifs into a co-polymeric architecture enabled a substantial augmentation of anion binding strength in highly competitive organic-aqueous solvent systems of up to 47x. Importantly, this polymeric enhancement effect can be tuned based on the characteristics of the chosen co-monomer(s) (15x at **pDEGA-1.XB** and 47x at **pDEGA-BuA-1.XB**, w.r.t. **1.XB**). These effects are particularly pronounced for the XB polymers, and the more shielded, low ε_r binding microenvironment established within the copolymeric scaffold also offered a greater tolerance for anion binding strength to increasing bulk solution polarity. Resolved $E_{1/2}$ values of the ferrocene transducers appended to the hosts also provides a semi-quantitative assessment of the local dielectric constants within the polymeric structures. This approach to augmenting ionic host-guest recognition

with polymeric architectures was unprecedented and represents a promising approach to engineering microenvironments to support more effective ion binding (and thus sensing) in real-world-relevant media. The synthetic versatility of this route will also support a tuning of receptive site preorganisation, multivalent effects, and a robust device integration (with polymers spun coat onto sensing substrates, for example).

A novel continuous voltammetric ion sensing method was developed and applied with self-assembled anion-receptive molecular films in Chapter 3. Within this, a custom-designed, 3D-printed flow cell housing a standard 3-electrode electrochemical cell was produced to facilitate continuous square wave voltammetry measurements, resulting in hundreds of square wave voltammograms over a typical sensing period of ≈ 30 min (corresponding to a temporal resolution of ≈ 3.7 s). Custom MATLAB scripts were applied to handle the resulting large data sets in order to semi-automate the analysis of the raw voltammograms and determine the $E_{1/2}$ of each with accuracy. Excellent agreement was observed between the cathodic perturbations of the $E_{1/2}$s of ferrocenyl-isophalamide-(iodo)triazole-based SAMs, **3.XB**/**HB**$_{\mathbf{SAM}}$ in response to HSO_4^-, $H_2PO_4^-$ and Cl^- under continuous flow and static conditions. Reproducible responses of **3.XB**$_{\mathbf{SAM}}$ to HSO_4^- were observed over a period of over 4.5 h, marking an important step in the translation of such sensors from lab to real-life applications. Importantly, this voltammetric flow methodology is widely applicable to sensing of any analyte that can reversibly induce a voltammetric response of an electroactive interface.

Chapter 4 presents a highly adaptable, novel ion sensing methodology based on changes in the redox capacitance of the same electroactive, anion-receptive molecular films, **3.XB**/$\mathbf{HB_{SAM}}$. Notably, this method is associated with a number of unique advantages over more standard (voltammetric) electrochemical techniques, including a facile, direct and continuous signal readout (precluding lengthy data analysis methods), as well as a breadth of versatile ion monitoring modes that can be conducted at any (or multiple) applied electrode potential(s). Most notably, it is possible to tune the thermodynamics of ion recruitment (*e.g.*, the binding affinity) by over an order of magnitude whilst monitoring anion binding at specific, fixed electrode polarisations. This approach is, again, equally translatable to any redox-coupled host interface and its associated analytes.

Finally, a proof-of-principle, reagentless ion sensing methodology based on non-Faradaic capacitance for continuous, real-time ion sensing is outlined in Chapter 5. This method notably excludes the requirement for an appended redox-active transducer, which concomitantly broadens the scope of applicable hosts and drastically extends measurement time by avoiding voltammetric degradation entirely. In fact, the baseline stability of an exemplary benzo-15-crown-5 receptive molecular film was sufficiently good to enable ion sensing across extended periods of time of up to 54 h. The low baseline capacitance of these interfaces supports high sensitivity (LODs as low as 5 μM for Na^+) reagentless cation detection, as well as an ability to both map out the expected ion specificity preferences of the interface and resolve ion binding kinetics. Namely, the associated temporal fingerprints, across cations of different size, give some indication of an ability to resolve ion binding

modes. The methodology, with strikingly simple interfaces, translated successfully to the analysis of ion binding in river water and artificial sweat. Of further interest, would be the application of this reagentless approach in conjunction with more selective receptive film designs. This could be achieved, for example, by optimising a procedure to produce mixed SAMs to isolate each **B15C5** binding unit at the surface which would interfere with 2:1 host-guest binding modes, forcing a stricter adherence to the size-dependent selectivity trends observed for 1:1 host-guest binding in solution.[299] Alternatively, more potent supramolecular ion receptive motifs (see Section 1.2.2 for supramolecular design principles which could be utilised) could be used to tailor this approach towards a specific target (*e.g.*, [2.2.2]cryptand for K^+, $K = 2 \times 10^5\ M^{-1}$).[310] Whilst these approaches might initially be more synthetically taxing, enhancing the selectivity of the receptive film is envisioned to drastically improve the feasibility of translating this sensing approach into practical applications. Namely, a more selective sensor should negate the impact of inorganic and organic contaminants present in real aqueous samples such as river water or sweat that may directly compete with the target species for the binding site, substantially improving sensor performance.

In essence, this thesis provides a technical electrochemical toolbox to fully exploit the reversible nature of supramolecular hosts and aid in their translation to sensing applications. Furthermore, the novel methodologies presented here are widely applicable to a broad range of host-guest configurations. The demonstrated abilities to tune anion binding via dielectric engineering or modulate anion binding thermodynamics via judicious choice of applied potential, as well as reagentless

approaches with high temporal resolution, are particularly promising in the context of exploring interfacial binding events more generally. The analysis of host-guest binding kinetics remains highly undeveloped and presents a significant opportunity for impactful future work. Though exemplified herein for ion sensing, which of course has countless applications in medical and environmental monitoring scenarios, neutral species (*e.g.*, perfluoroalkyls or perfluoroaryls) would also be interesting targets for future work.

Chapter 7

Experimental

Chapter 7: Experimental

7.1 General Considerations

All experiments were performed in the presence of air, at room temperature, unless otherwise stated. All commercially available chemicals and solvents were used as received without further purification, other than di(ethylene glycol) ethyl ether acrylate (DEGA) and n-butyl acrylate (BuA) monomers which were passed through a basic alumina column immediately prior to use to remove inhibitors. All hygroscopic tetrabutylammonium (TBA) salts and $[Cu(CH_3CN)_4]PF_6$ were stored in vacuum desiccators at room temperature. Supporting electrolyte ($TBAClO_4$ from Sigma Aldrich or TEACl from Sigma Aldrich) was of electrochemical grade. Where mixtures of solvents were used, ratios are reported by volume (*v*/*v*). Ultrapure water was obtained from a Milli-Q system (18.2 MΩcm) and was used for all aqueous solutions. Anhydrous solvents were acquired from an MBraun MPSP-800 column.

7.2 NMR Spectroscopy & High-Resolution Mass-Spectrometry

Routine NMR spectra were recorded on Bruker NMR spectrometers AVIII HD 400, with ^1H NMR anion binding titrations recorded on a Bruker AVIII HD 500 spectrometer. Chemical shifts are given in parts per million (ppm) relative to the residual solvent peak. Unless otherwise stated, a 50 mM solution of the chosen TBA salt of an anion was added to 0.5 mL containing 1 mM of the binding unit (**1.XB/HB**) in the same solvent media as the TBA salt. Each titration isotherm comprises 17

data points, corresponding to 0.0, 0.2, 0.4, 0.6, 0.8, 1.0, 1.2, 1.4, 1.6, 1.8, 2, 2.5, 3.0, 4.0, 5.0, 7.0, 10.0 equivalents of added guest anion. All anion binding events were found to be fast on the NMR timescale; consistent with expectations based on anion binding studies with similar hosts.[209, 311] Chemical shifts of polymer proton signals were determined using the MestReNova (v. 14.2.0) peak picking algorithm, ensuring that the value corresponds to the centre of the signal. Binding constants were determined using BindFit,[312] applying a 1:1 host-guest binding model in all cases. Fitting using 2:1 host-guest model failed in all cases. Addition of the solution containing the guest caused dilution of the host, which was accounted for in calculations.

Mass spectra were recorded on a Bruker μTOF spectrometer.

7.3 Gas Permeation Chromatography (GPC) Measurements

GPC was carried out with a Shimadzu LC-20AD GPC instrument equipped with two PSS SDV 5 μm linear M columns and a refractive index (RI) detector, calibrated with an Agilent EasiVial PS 2 mL pre-weighed calibration kit. Samples were prepared by dissolving approximately 5 mg of each polymer in 1 mL HPLC grade THF (inhibitor free), then filtered through 2 μm PTFE syringe filters. Each sample was then injected into the GPC instrument where an eluent of HPLC grade THF (inhibitor free) was used at a flow rate of 1.0 mL min^{-1} (heated to 30 °C). RI and UV detectors were calibrated using narrow molecular weight polystyrene standards covering a M_w range of 900-360,000 g mol^{-1}. Analysis of GPC data was completed with Shimadzu GPC post-run program.

7.4 Water Contact Angle Measurements

Water contact angles measurements were acquired with a FTA1000B goniometer (First Ten Ångstroms), equipped with a manually-operated µL syringe to dispense a sessile drop of deionised water to use as the wetting liquid. A point grey USB camera in combination with a Navitar lens was used to record video at 61 frames per second. Data analysis was performed with FTA32 software in which all droplets were fitted to a symmetrical, spherical model.

7.5 Ellipsometry

All ellipsometry measurements were performed by Dr. Robert Jacobs on a Beaglehole Instruments Picometer equipped with a 2 mW Helium-Neon laser (632.8 nm). Average film thicknesses were determined by fitting the acquired data to a one-layer model, taking a bare gold substrate as a reference and 1.45 as the refractive index of the SAM. The standard deviation of the average film thickness was calculated from five different measurements on the same substrate.

7.6 Fourier-Transform Infrared Attenuated Total Reflection (FTIR-ATR) Spectroscopy

FTIR-ATR spectra were measured in transmission mode between 500 and 4000 cm^{-1} on an IRTracer-100 (Shimadzu).

During ATR-IR spectroscopy, the IR beam is directed through a crystal with a reflective index higher than the sample (herein germanium), and at an angle greater than the critical angle so that there is total internal reflection of the beam at the surface of the crystal which is in direct contact with the sample, before then being

detected.[313] At the crystal-sample boundary, evanescent waves are caused which penetrate into the sample (typically a few microns, though this is dependent on the crystal used). The IR radiation absorbed by the sample will cause the reflected evanescent waves to be attenuated, providing chemical information about the sample.

For **1.XB**, **1.HB**, **pDEGA-1.XB** and **pDEGA-1.HB**, approximately 1-2 mg of solid sample was placed onto the measurement platform (germanium crystal) for analysis. For all surface bound samples (**B15C5$_{SAM}$**), each sample was prepared onto 1x1 cm gold on silica chips with an identical procedure to that used for the preparation of the corresponding SAMs on the gold disc electrodes used throughout this thesis. *I.e.*, **B15C5$_{SAM}$** was prepared by incubating a 1x1 cm gold on silica chip in a solution of 0.5 mM **B15C5** in 1:1 DCM/MeOH overnight, which was then rinsed with copious amounts of DCM and MeOH and dried under a stream of N_2. The prepared chip with the receptive SAM of interest was then placed onto the measurement platform for analysis.

7.7 X-ray Photoelectron Spectroscopy

Interfacial samples were analysed using a Thermo Scientific K-Alpha XPS instrument equipped with a microfocussed, monochromated Al X-ray source. The source was operated at 12 keV, utilising a 400 μm spot size. The analyser was operated at a constant analyser energy (CAE) of either 200 eV or 50 eV for survey and detailed scans, respectively. Charge neutralisation was applied using a combined low energy electron/ion flood source. The errors stated in this thesis were

calculated based on measurements of three independent areas within the same sample. Data acquisition was carried out by Dr. Philip Holdway.

All data analysis was carried out with CasaXPS (v2.3) where Linear or Tougaard backgrounds were used in all cases. Peak fitting was carried out without any restrictions of the peak position, line shape, area or full width half maximum (FWHM) of the peak.

7.8 Electrochemical Measurements

7.8.1 Considerations for Electrochemical Measurements

All electrochemical measurements were conducted using an Autolab Potentiostat (Metrohm) or PalmSens4 Potentiostat. A standard three-electrode cell was used in all cases, comprised of a working electrode, reference electrode and counter electrode. The exact components of each three-electrode cell are detailed for the work described in each chapter below:

Chapter 2: Working electrode- glassy carbon disc electrode (BaSi, 2 mm diameter), counter electrode- platinum wire, reference electrode- a non-aqueous $Ag|AgNO_3$ reference electrode with an inner filling solution of 10 mM $AgNO_3$, 100 mM $TBAClO_4$ in ACN. Solvent- range of organic/aqueous mixtures, supporting electrolyte-100 mM $TBAClO_4$.

Chapters 3 & 4: Working electrode- gold disc electrode (BaSi, 1.6 mm diameter) functionalised with **3.XB/HB_{SAM},** counter electrode- platinum wire, reference electrode- a non-aqueous $Ag|AgNO_3$ reference electrode with an inner filling

solution of 10 mM $AgNO_3$, 100 mM $TBAClO_4$ in ACN. Solvent- ACN/H_2O 99:1, supporting electrolyte-100 mM $TBAClO_4$ + 10 mM $HClO_4$ (unless stated otherwise).

Chapter 5: Working electrode- gold disc working electrode (BaSi, 1.6 mm diameter) functionalised with **B15C5$_{SAM}$** or **3.XB/HB$_{SAM}$**, counter electrode- platinum wire, reference electrode- initially an aqueous Ag|AgCl reference electrode with an inner filling solution of 3 M KCl, then subsequently replaced with a Ag|AgCl pseudoreference electrode which was used for all sensing studies in Chapter 5 from Section 5.5 and onwards. The Ag|AgCl pseudoreference electrode was generated by submerging silver wire in 0.5 M HCl, and connecting both working and counter connectors. A platinum wire counter electrode was added and connected to the counter terminal, then a current of 5 mA was applied for 15 s via chronopotentiometry (or until the wire visibly darkens and becomes matte). Solvent- H_2O, supporting electrolyte-100 mM TEACl (unless stated otherwise).

Previous studies have shown that both the identity and concentration of the supporting electrolyte can have a profound impact on the ion binding and sensing performance of ion-receptive hosts. For example, Oliveira *et al.* showed that the voltammetric anion sensing performance of a methylated iodo-TTF receptor varied significantly depending on which electrolyte was used, even those which are often assumed to be "non-coordinating".[314] The maximum cathodic shift displayed for this methylated iodo-TTF receptor in response to 100 equiv. Cl^- varied by up –13 mV, and the best performance (*i.e.*, the greatest voltammetric shift magnitude, ΔE = –49 mV) was observed with the use of ([tetrakis[3,5-bis(trifluoromethyl)phenyl]borate) $BArF^-$ as a supporting electrolyte, closely followed by ClO_4^- (ΔE = –47.5 mV). These

results imply that the largest counterions typically interfere with binding/signal transduction the least, therefore $TBAClO_4$ was selected as the supporting electrolyte of choice for anion sensing studies. TEACl was selected as a fully water-soluble (at 100 mM) supporting electrolyte for cation sensing studies. Sufficiently high background electrolyte concentrations (≥100 mM) were chosen so as to minimise errors associated with solution-phase resistance (*i.e.*, ohmic drop). Additionally, in all cases, including characterisation and sensing studies, a constant ionic strength was maintained at a fixed 100 mM throughout to ensure that changes in the overall electrolyte concentration didn't interfere with measurements.

Real, aqueous sample information:

All real, aqueous samples were filtered through syringe filters of 0.22 µm to remove any debris from solution.

Table 7.8.1-1. Tabulated data regarding the location, date of acquisition and native target (Na^+) and interferent (K^+) concentrations of each of the real, aqueous samples collected. N/A- not applicable, as data was not available.

Sample Name	Sample Location	Date of Sample Acquisition (dd/mm/yyyy)	Native [Na^+] (mM)	Native [K^+] (mM)	Source
Freshwater Sample 1	Blue Lough in Mourne Mountains	07/04/2023	0.198	0.009	[307]
Freshwater Sample 2	Cherwell River, University Parks, Oxford	09/10/2023	1.567	0.159	[308]
Tap Water Sample 1	Tap from lab 10-35 in the Physical and Theoretical Chemistry Laboratory, University of Oxford	06/04/2023	0.918	N/A	[309]- Accessed 18/03/2024

7.8.2 Electrode Cleaning Procedure & SAM Formation

Au disc electrodes and glassy carbon electrode were both polished mechanically with a 0.05 μm alumina slurry for 2 mins, followed by sonication in 1:1 EtOH/H_2O for several minutes. Au disc electrodes were also chemically polished via submersion in freshly made piranha acid (3:1 concentrated H_2SO_4/30% H_2O_2), and subsequently electrochemically polished in 0.5 M potassium hydroxide (KOH) from –0.7 V to –1.7 V, then in 0.5 M H_2SO_4 from –0.15 V to –1.35 V for at least 1 hour each (at a scan rate of 100 mV s^{-1}).

Immediately following the cleaning procedure, the Au disc electrodes were rinsed thoroughly with water and ethanol, dried under N_2 and then submerged in the appropriate incubation solution (see below) overnight, in the dark. Following this, the Au disc electrodes were rinsed with copious amounts of the solvent they were immersed in, dried with N_2, then used immediately

Chapters 3 & 4: A solution of 0.25 mM **3.XB** in ACN.

Chapter 5: A solution of 0.5 mM **B15C5** in 1:1 DCM/MeOH. A solution of 0.25 mM **4.XB/HB-B15C5** in ACN/H_2O 1:1.

7.8.3 Molecular Surface Coverage Determination

Molecular surface coverages, Γ were determined either via voltammetric methods by integrating the peak area from a cyclic voltammogram of a redox-active SAM (Figure 7.8.3-1A) to obtain the charge, Q, which can then be applied to Equations 7.8.3-1 – 3), or via reductive thiol stripping for a redox in-active or redox-active SAM (Figure 7.8.3-1B). Reductive thiol stripping involved sweeping from 0 to -1.3 V via CV

(vs. Ag|AgCl) in 0.5 M KOH solution (cell = Pt wire counter, Ag|AgCl reference electrode and receptor-modified Au disc working electrode), from which the resulting desorption peak was integrated and again related to Equations 7.8.3-1 – 3 to determine the surface coverage.

$$Q = \frac{A_p}{\upsilon}$$ **Equation 7.8.3-1**

$$A_{EA} = \frac{Q}{M_{O_2}}$$ **Equation 7.8.3-2**

$$\Gamma = \frac{Q}{(A_{EA^\circ} \times n \times F)}$$ **Equation 7.8.3-3**

(where the calculated charge required to reduce a monolayer of chemisorbed O_2 on polycrystalline Au, M_{O2}=482 μC cm^{-2}).[315]

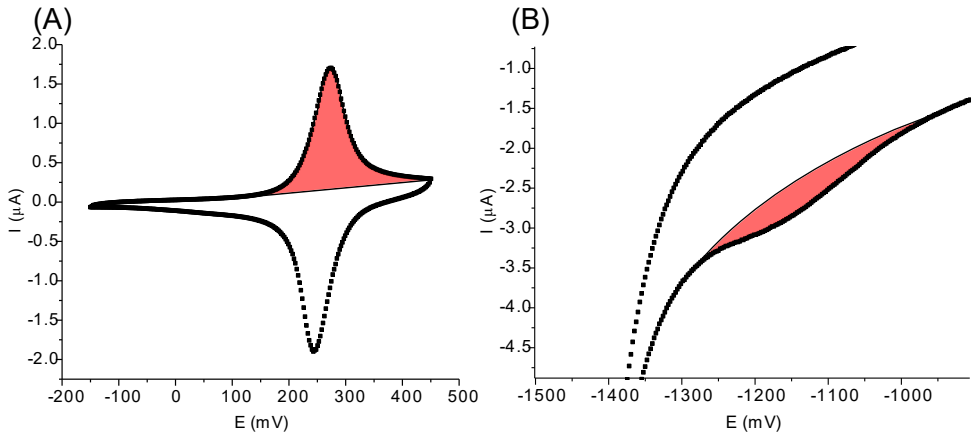


Figure 7.8.3-1. Schematic of integrating under peak for surface coverage determination by (A) CV and (B) reductive thiol stripping.

Randles-Sevcik Equation: υ: scan rate, *n*: number of electrons transferred, *A*: electrode surface area, D_0: diffusion coefficient of the oxidised analyte, C_0: bulk concentration of analyte

$$i_p = 0.446nFAC_0\left(\frac{nF\upsilon D_0}{RT}\right)^{1/2}$$ **Equation 2.6.1-1**

7.8.4 Square Wave Voltammetry (SWV)

Static square wave voltammetry (SWV) measurements were conducted between in an appropriate range (*e.g.*, –0.1 to 0.45 V for **3.XB**/**HB$_{SAM}$**) with a step potential of 2 mV, amplitude of 20 mV and frequency of 25 Hz and were used to determine the $E_{1/2}$ of the redox-active host in question. Continuous flow SWV measurements were carried out between –0.25 to 0.3 V with a step potential of 2 or 5 mV (typically 5 mV, unless otherwise indicated), amplitude of 20 mV and frequency of 50 Hz, with all pre/post-equilibration times set to 0 s.

7.8.5 Capacitance Measurements

Chapter 4: The film capacitance, *C* was obtained by electrochemical impedance spectroscopy (EIS).[182] Measurements were carried out between 100 kHz and 0.1 Hz over 40 frequencies (logarithmically stepped), using a 10 mV AC amplitude and no equilibrium time. The DC potential applied was the $E_{1/2}$ of **3.XB$_{SAM}$,** as determined by SWV (see above), unless otherwise stated. The redox capacitance, C_r was determined from the diameter of the semicircle of the capacitive Nyquist plot (approximated as C' at the inflection point), and the corresponding frequency at this capacitance was denoted as f_r (typically 4 - 10 Hz). Density of state (DOS) experiments were performed at fixed frequency, f_r over a potential range of –0.1 to 0.4 V, with an equilibrium time of 1 s.

Continuous capacitive measurements were performed with a time scan at fixed potential ($E_{1/2}$, unless otherwise stated) and fixed frequency (f_r, unless otherwise stated).

Chapter 5: The film capacitance, *C* was again obtained by electrochemical impedance spectroscopy (EIS).[182] Measurements were carried out between 100 kHz and 0.1 Hz over 40 frequencies (logarithmically stepped), using a 10 mV AC amplitude and no equilibrium time. The DC potential applied was the OCP measured for each capacitive Nyquist plot, unless otherwise stated. The non-Faradaic film capacitance, *C* was determined from the diameter of the semicircle of the capacitive Nyquist plot (approximated as C' at the inflection point), and the corresponding frequency at this capacitance was denoted as f_r (typically 50 - 150 Hz). Continuous capacitive measurements were performed with a time scan at fixed potential (OCP, unless otherwise stated) and fixed frequency (f_c, unless otherwise stated).

For both Chapters 4 and 5, the impedimetric data was transformed into its capacitive components via Equations 7.8.5-1 and 7.8.5-2, where C' and C'' are the real and imaginary capacitance.[136, 294] Plotting C'' vs. –C' affords the capacitive Nyquist plots used throughout this thesis.

$$C'(\omega) = \frac{Z''}{\omega|Z|^2} \qquad \textbf{Equation 5.3-1}$$

$$C''(\omega) = \frac{Z'}{\omega|Z|^2} \qquad \textbf{Equation 5.3-2}$$

7.9 Continuous Electrochemical Measurements & Microfluidics

7.9.1 Pseudo-flow Set-up

A standard three-electrode cell (as described above in Section 7.8.1), filled with 4 mL of electrolyte (ACN/H_2O 99:1, 100 mM $TBAClO_4$, 10 mM $HClO_4$) was continuously stirred with a small stirrer bar. A syringe pump (Harvard Apparatus PHD 2000 Infuse/Withdraw) with PEEK tubing (Cole-Parmer) was used to inject 4 mL of the analyte solution (100 mM TBAX where X= target anion in the same solvent as above) at a flow rate of 800 µL min^{-1} (injection duration is 5 min), leading to a final anion concentration, [A^-] = 50 mM. Continuous capacitive measurements at a fixed frequency were performed as stated above in Section 7.8.5.

7.9.2 Flow Cell Designs

Design 1 flow cells were produced with an Elegoo Mars 3D printer or a FormLabs Form 2 3D printer using FormLabs Tough 2000 resin, which is chemically resistant to a range of organic solvents (Figure 7.9.2-1). General designs were produced with Autodesk Fusion 360 (see Figure 7.9.2-2 for annotated blueprint of design), which were then rendered into compatible (printable) designs in CHITUBOX. A Pt wire (counter electrode) was held in place in a channel adjacent to the main chamber with epoxy resin (Araldite Rapid), and the non-aqueous Ag|$AgNO_3$ reference electrode and Au disc electrode functionalised with **3.XB/HB** were inserted before each experiment, giving an airtight cell with an approximate inner chamber volume of 100 µL.

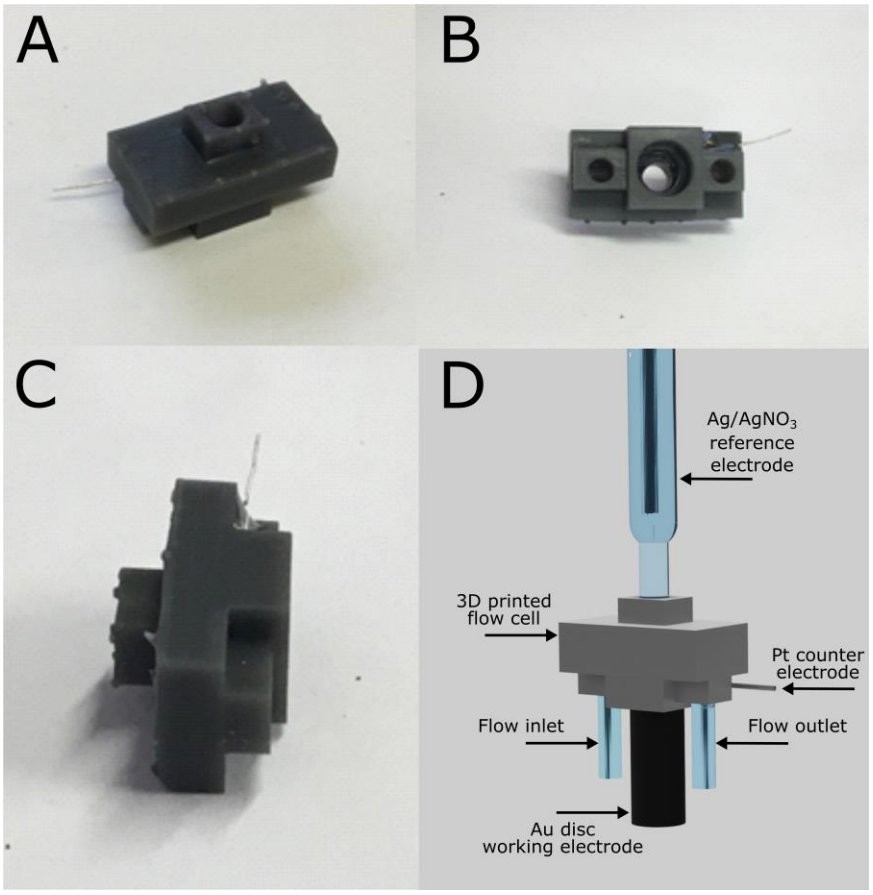


Figure 7.9.2-1. (A-C) Photos and (D) schematic of **Design 1** of 3D-printed microfluidic cell.

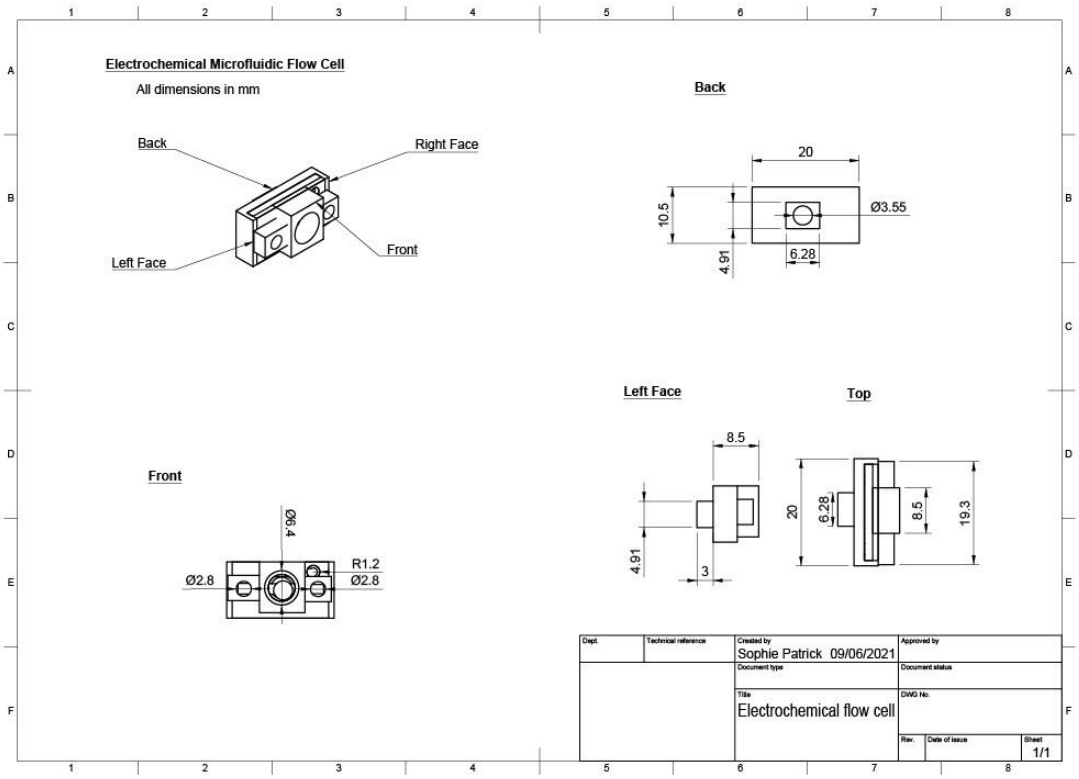


Figure 7.9.2-2. Blueprint of **Design 1** of 3D-printed microfluidic cell displaying all relevant dimensions in mm. R = radius, Ø = diameter.

Design 2 flow cells were generated with Autodesk Fusion 360 (see Figure 7.10.1-3 for annotated blueprint of design), which were then rendered into compatible (printable) designs in CHITUBOX. **Design 2** flow cells were produced with an Elegoo Mars 3D printer using ANYCUBIC 3D Printing UV Sensitive Resin Basic (Clear). A Pt wire (counter electrode) and a Ag|AgCl pseudoreference wire electrode were held in place in a channel adjacent to the main chamber with epoxy resin (Araldite Rapid), and the Au disc electrode functionalised with **B15C5$_{SAM}$** was inserted before each experiment, giving an airtight cell with an approximate inner chamber volume of 10 µL.

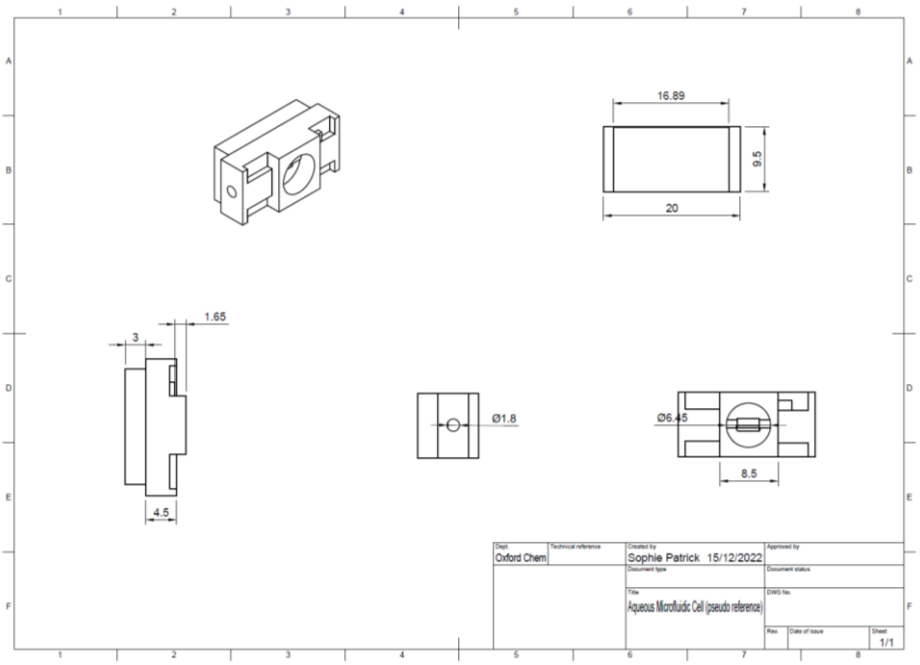


Figure 7.9.2-3. Blueprint schematic of new flow cell design.

7.9.3 Continuous Flow Set-up

A 3D-printed microfluidic cell (**Design 1** for Chapters 3 & 4, or **Design 2** for Chapter 5) was utilised for continuous flow experiments. Electrolyte (see Section 7.8.3) was continuously pushed through the cell with a syringe pump at a flow rate of 500 µL

min^{-1} for Chapters 3 & 4, or 100 µL min^{-1} for Chapter 5, unless otherwise stated. Integrated into the flow line was an injector system (Rheodyne® Model 9725) through which the analyte solutions (of identical overall ionic strength, and acid concentration in the same solvent) were injected into the continuous flow. The majority of tubing used was Cole-Parmer PEEK tubing other than a small connecting section from the main tubing line to the cell, which was Cole-Parmer MasterFlex Peristaltic tubing.

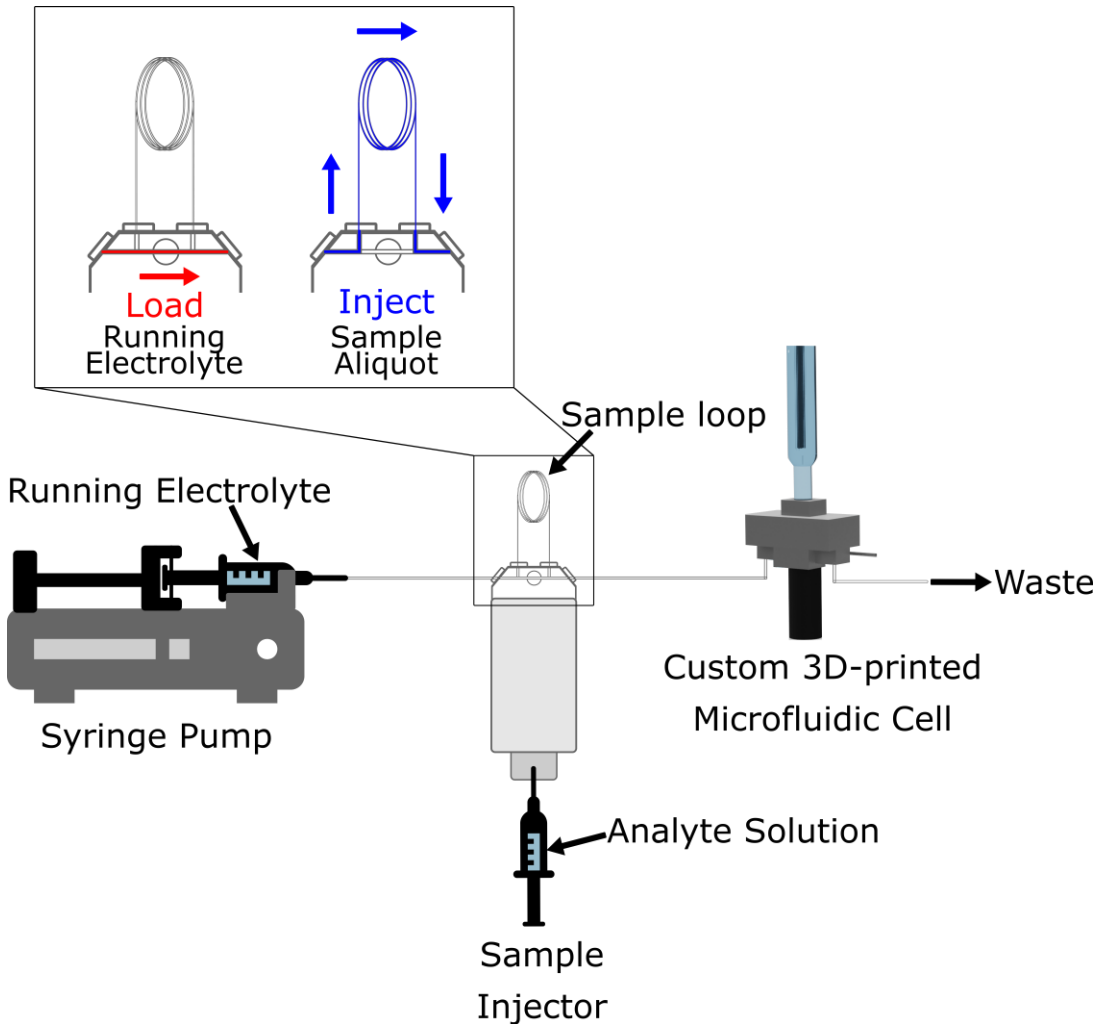


Figure 7.9.3-1. Schematic of microfluidic set-up. Inset depicts the two running modes for the microfluidic system: load and inject. Running electrolyte is continuously pumped throughout. When in load mode, only fresh running electrolyte passes through the system but when switched to inject mode, electrolyte passes through the sample loop which was filled with the analyte solution prior to switching.

7.10 Data Analysis & Model Fitting

7.10.1 Analysis of Errors Associated with Determining Binding Constants at Polymeric Hosts

As detailed above, the relevant polymeric signals used to follow anion binding were significantly broader than those of the monomers. To determine the uncertainty of assessing chemical shifts from broader signals, two parallel approaches were taken: (1) repeat data processing and sampling and (2) intentional applied error.

In the first test, a standard ^{1}H NMR signal data processing and sampling method was applied a total of 5 times for each titration data set (for titrations of **pDEGA-1.XB** with TBA^{+} halide salts in all three solvent systems, 9 titration data sets total) to obtain 5 binding constants which were then averaged and collated into Table 7.10.1-1. The resulting error corresponds to that of the human error in accurately determining the centre of each of the relevant polymer signals during data processing, and the impact of this on resolved anion binding constants. This error was evaluated as <10% in all cases, *ca*. 5%, confirming that this human error in analysing the broader signals of the polymeric hosts does not induce further uncertainty in K in comparison to the monomeric hosts.

Table 7.10.1-1. Binding constants of polymeric receptor **pDEGA-1.XB** in response to the halides in different solvent systems obtained from repeated independent processing (resampling five times, N = 1 to 5) of titration data. Standard error reported as a numerical value and percentage of the mean in parentheses.

ACN-d_3:D_2O 97.5:2.5			
	I^-	**Br^-**	**Cl^-**
1	1413	849	191
2	1658	1060	275
3	1614	803	202
4	1627	860	211
5	1436	912	173
Mean	1550	897	210
St. Dev (σ_{N-1})	116	99	39
Standard error of the mean (%)	52 (3.3%)	44 (4.9%)	17 (8.2%)
Acetone-d_6:ACN-d_3:D_2O 48.75:48.75:2.5			
	I^-	**Br^-**	**Cl^-**
1	2164	1607	305
2	1866	1181	297
3	1576	1197	356
4	1946	1189	327
5	1354	1164	294
Mean	1781	1268	316
St. Dev (σ_{N-1})	318	190	26
Standard error of the mean (%)	140 (8.0%)	85 (6.7%)	12 (3.6%)
Acetone-d_6:D_2O 97.5:2.5			
	I^-	**Br^-**	**Cl^-**
1	3030	2204	911
2	2288	2880	1063
3	2808	2746	1137
4	3124	3594	1157
5	3598	2404	1124
Mean	2970	2766	1078
St. Dev (σ_{N-1})	478	535	100
Standard error of the mean (%)	210 (7.2%)	240 (8.7%)	45 (4.1%)

The second approach involved inducing systematic errors to each of the polymer chemical shifts used to follow anion binding by applying random noise (0.005 ppm, *ca*. 5% of the maximum signal shift displayed during titrations) to two representative data sets for **pDEGA-1.XB** (upon titration of Cl^- in acetone-d_6/D_2O 97.5:2.5 and I^- in acetonitrile-d_3/D_2O 97.5:2.5). This procedure was repeated a total of 10 times for each data set (see Table 7.10.1-2), affording binding constants that typically deviated from the originally determined value for K by < 17%, in good agreement with the predicted magnitude of error for K at the polymeric hosts (Table 7.10.1-1, 20%). Therefore, even with substantial applied error in determining the centre of each relevant polymer signal, errors in K are still modest.

Table 7.10.1-2. Comparison of the experimentally determined (real) binding constant for **pDEGA-1.XB** and the binding constants determined from the original isotherm with a random error added to the chemical shifts (0.005 ppm) of the followed signals. Deviation from the original value is reported in parentheses as percentage of the original value.

Binding constants of pDEGA-1.XB and I^- in ACN-d_3/D_2O 97.5:2.5					
Real Determined K (M^{-1})	**Repeat 1**	**Repeat 2**	**Repeat 3**	**Repeat 4**	**Repeat 5**
1887	1478 (22%)	2854 (51%)	1556 (18%)	1771 (6.2%)	2042 (8.2%)
Average Deviation	**Repeat 6**	**Repeat 7**	**Repeat 8**	**Repeat 9**	**Repeat 10**
17%	1657 (12%)	1650 (12%)	1415 (25%)	2123 (13%)	1901 (0.7%)
Binding constants of pDEGA-1.XB and Cl^- in acetone-d_6/D_2O 97.5:2.5					
Real Determined K (M^{-1})	**Repeat 1**	**Repeat 2**	**Repeat 3**	**Repeat 4**	**Repeat 5**
911	934 (2.5%)	972 (6.7%)	1104 (21%)	842 (7.6%)	1194 (31%)
Average Deviation	**Repeat 6**	**Repeat 7**	**Repeat 8**	**Repeat 9**	**Repeat 10**
13%	944 (3.6%)	1187 (30%)	859 (5.8%)	975 (7.0%)	1013 (11%)

Comparison of the ratio of integrals from characteristic polymer and TBA^+ signals further confirmed that the correct number of equivalents of guest (*i.e.*, 1:1) were added during titrations, utilising TBA^+ as an internal standard. Three well-resolved polymer signals were used for integrations: protons H_a, H_b, and $H_{c'}$ (the integral of proton H_b was used for normalisation, 2H; protons H_a and $H_{c'}$ served as controls), as well as at least two signals of TBA^+, typically two terminal signals: $-CH_2CH_3$ and/or NCH_2-. To limit the influence of any overlap of the TBA^+ signals with polymer (backbone) signals, all TBA^+ signals were normalised to the baseline (by subtracting the integral of the same region) prior to the addition of any TBA^+ salts.

The ratio of polymer:TBA^+ (host:guest) signal integrals were calculated after each successive TBA^+ salt addition for each titration point, then compared to the predicted ratio based on the initial host/guest concentrations and averaged over all followed signals and additions. These comparative analyses afforded a parameter representing the average deviation from the expected host:guest ratio throughout a titration (*i.e.*, with 1 corresponding to perfect agreement, and 1.1 denoting a 10% deviation from ideal). For example, throughout titrations of **1.XB** with TBA^+ halide salts, all four TBA^+ signals were well-resolved meaning that 64 TBA^+ data points (4·16 additions) could be compared to polymer signal H_b and averaged. Standard errors, α for each of these calculations were calculated from the standard deviation, σ_{N-1} of averaging over the number of additions, N (equal to 16 in all cases) according to $\alpha = \frac{\sigma_{N-1}}{\sqrt{N}}$.

The results of these analyses for titrations of **1.XB** and **pDEGA-1.XB** with TBA^+ halide salts are collated in Table 7.10.1-3, and are notably consistent regardless of the

monomeric/polymeric nature of the host, or the anionic guest or solvent system utilised. The systematic positive deviation of the guest-to-host ratio (magnitudes of > 1 in all cases) results from the difference in relaxation times between aromatic signals of the host and aliphatic signals of TBA^+, but low concentrations (< 1 mM regime) also likely contribute to the uncertainty of the determined integrals. Crucially, this shows that there was no additional uncertainty in the determination of binding unit concentration for the polymeric hosts compared to the monomeric hosts (both exhibit average deviations of ≈1.2), which in turn validates the observed differences between these hosts beyond simple variations in [host]:[guest].

Table 7.10.1-3. Average deviations from the expected guest-to-host ratio in titrations of monomeric host **1.XB** and polymeric host **pDEGA-1.XB** with halides in different solvent systems. Random error estimated with 95% confidence level.

	Acetone-d_6:D_2O 97.5:2.5		**Acetone-d_6:ACN-d_3:D_2O 48.75:48.75:2.5**		**ACN-d_3:D_2O 97.5:2.5**	
	1.XB	**pDEGA-1.XB**	**1.XB**	**pDEGA-1.XB**	**1.XB**	**pDEGA-1.XB**
Cl^-	1.18 ± 0.02	1.16 ± 0.04	1.20 ± 0.02	1.16 ± 0.02	1.17 ± 0.02	1.19 ± 0.04
Br^-	1.33 ± 0.02	1.22 ± 0.04	1.15 ± 0.02	1.23 ± 0.04	1.14 ± 0.02	1.24 ± 0.02
I^-	1.27 ± 0.02	1.18 ± 0.04	1.18 ± 0.02	1.12 ± 0.04	1.12 ± 0.02	1.16 ± 0.02

As discussed above, minimal errors in K (*ca*. 10%) were found to be associated with analysing the broader polymeric signals. Nevertheless, as the integrals of these relevant polymer signals were utilised to estimate polymer composition and effective binding unit concentration, it was imperative to confirm that any error in host concentration does not significantly impact the resulting anion binding constants with the polymeric hosts. For completeness, the effect of errors in both host *and* guest concentration on K were simulated by introducing intentional error to either [host] or [guest] during isotherm analyses with BindFit software, affording

new, modified binding constant values. It should be noted that these purposefully applied errors also in essence account for potential errors in M_n values (determined by GPC), which would also, of course, impact the calculated effective binding unit concentrations. As displayed in Tables 7.10.1-4 and 7.10.1-5, these errors are typically < 20%, but variation in host concentration, which is most pertinent here, only results in errors of *ca*. < 10%.

Table 7.10.1-4. Comparison of the determined binding constants for **pDEGA-1.XB** and I^- in ACN-d_3/D_2O 97.5:2.5, and the binding constants determined from the original isotherm with an intentional error of 10% or 20% in host and/or guest concentration. Deviation from the original value reported in parentheses as percentage of the original value.

	K from isotherms with intentional errors added to c_{host} (M^{-1})			
Initial K Value	**c_{host} + 20%**	**c_{host} + 10%**	**c_{host} – 10%**	**c_{host} – 20%**
1887	2191 (16%)	2031 (7.6%)	1756 (6.9%)	1637 (13%)
	K from isotherms with intentional errors added to c_{guest} (M^{-1})			
	c_{guest} + 20%	**c_{guest} + 10%**	**c_{guest} – 10%**	**c_{guest} – 20%**
	1396 (26%)	1606 (14%)	2276 (20%)	2846 (51%)
	K from isotherms with intentional errors added to c_{host} and c_{guest} (M^{-1})			
	c_{host} + 10% c_{guest} + 20%	**c_{host} + 10% c_{guest} + 10%**	**c_{host} + 10% c_{guest} – 10%**	**c_{host} + 10% c_{guest} – 20%**
	1481 (22%)	1715 (10%)	2476 (31%)	3142 (66%)
	c_{host} – 10% c_{guest} + 20%	**c_{host} – 10% c_{guest} + 10%**	**c_{host} – 10% c_{guest} – 10%**	**c_{host} – 10% c_{guest} – 20%**
	1317 (30%)	1507 (20%)	2097 (11%)	3142 (37%)

Table 7.10.1-5. Comparison of the determined binding constant for **pDEGA-1.XB** and Cl^- in acetone-d_6/D_2O 97.5:2.5, and the binding constants determined from the original isotherm with an intentional error of 10% or 20% in host and/or guest concentration. Deviation from the original value reported in parentheses as percentage of the original value.

	K from isotherms with intentional errors added to c_{host} (M^{-1})			
Initial K Value	**c_{host} + 20%**	**c_{host} + 10%**	**c_{host} – 10%**	**c_{host} – 20%**
911	993 (9.0%)	951 (4.4%)	874 (4.1%)	839 (7.9%)
	K from isotherms with intentional errors added to c_{guest} (M^{-1})			
	c_{guest} + 20%	**c_{guest} + 10%**	**c_{guest} – 10%**	**c_{guest} – 20%**
	708 (22%)	797 (13%)	1062 (17%)	1270 (39%)
	K from isotherms with intentional errors added to c_{host} and c_{guest} (M^{-1})			
	c_{host} + 10% c_{guest} + 20%	**c_{host} + 10% c_{guest} + 10%**	**c_{host} + 10% c_{guest} – 10%**	**c_{host} + 10% c_{guest} – 20%**
	733 (20%)	828 (9.1%)	1115 (22%)	1343 (47%)
	c_{host} – 10% c_{guest} + 20%	**c_{host} – 10% c_{guest} + 10%**	**c_{host} – 10% c_{guest} – 10%**	**c_{host} – 10% c_{guest} – 20%**
	685 (25%)	768 (16%)	1013 (11%)	1202 (32%)

Based on all the analysis presented above, the error of binding constant values was estimated by combining contributions from the resampling analysis (< 10%) and the analysis of concentration perturbations (< 10%). The propagation formula results in an estimate of $u < \sqrt{(10\%)^2 + (10\%)^2} = 14\%$. According to this, the standard error of determining anion binding constants with this system can be approximated conservatively as 20%. It is worth stressing here that despite any differences observed with the data processing of the polymeric hosts compared to the monomeric hosts, the analysis resulted in consistent results, e.g. the selectivity trend remained unaltered across different solvent systems (and reflects the trend observed for the monomer). Furthermore, repeat titrations of representative data sets for **pDEGA-1.XB** with the halides confirmed that these predicted errors are consistent (< 10% error, Table 7.10.1-6).

Table 7.10.1-6. Anion binding constant values (M^{-1}) determined for polymeric host **pDEGA-1.XB** in acetonitrile-d_3/D_2O 97.5:2.5 in independent experiments.

	K (M^{-1})		
	Repeat 1	**Repeat 2**	**Average**
Cl^-	210	260	240
Br^-	900	860	880
I^-	1500	1800	1650
$H_2PO_4^-$	56	110	80

7.10.2 Response Isotherm and Sensogram Analysis

All analysis and fitting of electrochemical data was carried out with OriginPro 2017.

Chapter 2:

Analysis of the voltammetric sensor responses was carried out via Equations 1.4.2-1 and 1.4.2-3. Fitting of the voltammetric sensing isotherms according to Equation 1.4.2-3 was carried out without any restriction of the parameters, unless stated otherwise. In some cases, nonsensical values were obtained from fits with Equation 1.4.2-3 (*e.g.*, negative values for K_{red}) which is chemically not possible, and is purely the result of the fitting (affording the best mathematical fit to Equation 1.4.2-3), which can be restricted to $K_{Red} = 0$ to afford similar fits.

$$\Delta E = -\frac{RT}{nF}\ln\left(\frac{K_{Ox}}{K_{Red}}\right) \qquad \textbf{Equation 1.4.2-2}$$

$$\Delta E = -\frac{RT}{nF}\ln\left(\frac{1+K_{Ox}[A^-]}{1+K_{Red}[A^-]}\right) \qquad \textbf{Equation 1.4.2-3}$$

Chapter 3:

All anion-induced shifts are reported with respect to the potential in the baseline preceding each injection for flow experiments or with respect to the initial SWV preceding the first addition for static titrations. All binding constants are rounded to three significant figures and were obtained by fitting of the sensing isotherms to the Langmuir-Freundlich model (Equation 3.3-1). Note that the Langmuir-Freundlich model simplifies to the classic Langmuir model when n = 1 (Equation 3.3-2).

$$\theta = \frac{(K_{app} * [A^-])^n}{1 + (K_{app} * [A^-])^n} \qquad \textbf{Equation 3.3-1}$$

$$\theta = \frac{K_{app} * [A^-]}{1 + K_{app} * [A^-]} \qquad \textbf{Equation 3.3-2}$$

For quantitative analysis, the sensing isotherms for $H_2PO_4^-$ were corrected for full protonation of $H_2PO_4^-$ by the acidified electrolyte, by correcting isotherms by –10 mM.

LODs were calculated according to Equation 7.10-1 where σ is the standard deviation of the baseline/blank and S is the slope of the linear region of the sensor response (herein also referred to as “sensitivity”). For continuous voltammetric measurements under flow, σ was determined from the root-mean-square deviation of a linear fit of ten data points ($E_{1/2}$ values) in the initial baseline of the sensograms (determined by the respective analysis method as used for the measurement, PeakPick or AsymFit), immediately preceding the response to the first addition of analyte. For static voltammetric measurements, σ was determined as the standard deviation of ten data points ($E_{1/2}$ values) from ten SWVs performed immediately preceding the first analyte addition. S was determined from the slope of a linear fit

to the pseudo-linear regime of each respective binding isotherm, with a range between 0-11 mM for HSO_4^- and Cl^-, and either 9.5-13.4 or 10.5-13.4 mM for $H_2PO_4^-$ (for static and continuous voltammetric measurements, respectively).

$$LOD = \frac{3\sigma}{S} \qquad \textbf{Equation 7.10-1}$$

Chapter 4:

Continuous Flow Sensogram Analysis

Continuous capacitive responses from measurements under flow were corrected for baseline degradation by linear scaling of all data points to the initial baseline recorded before the addition of the first anion aliquot. All sensograms shown represent the raw data without baseline corrections, but are in some cases offset in the x-axis (time domain) for illustrative purposes (in order to reduce overlap between sensograms obtained at different potentials). All sensing isotherms are baseline corrected and all quantitative analyses were carried out on baseline-corrected isotherms.

Binding Isotherm Analysis

All binding constants are rounded to three significant figures and were obtained by fitting of the sensing isotherms to the Langmuir-Freundlich model (Equation 3.3-1). For quantitative analysis, the sensing isotherms for $H_2PO_4^-$ were corrected for full protonation of $H_2PO_4^-$ by the acidified electrolyte. Of note is that K_{app} represents an apparent binding constant and neither reflects anion binding to the oxidised receptor (K_{Ox}) nor the native, neutral receptor (K_{Red}), but can be interpreted as a general measure of sensor performance and anion binding strength. Similarly, no

specific physico-chemical interpretation can be assigned to “n”, but it is typically interpreted as a measure of non-ideality/inhomogeneity, herein arising from partial protonation of the anions at low anion concentrations as well as the self-amplification effect.

Relative responses (in %) were calculated according to $C_{rel} = (C_{A^-} - C_0)/C_0 \times 100$.

Chapter 5:

Relative responses (in %) were calculated according to $C_{rel} = (C_{M^+} - C_0)/C_0 \times 100$.

Limit of Detection (LOD) and Sensitivity Determination

LODs were calculated according to a standard equation given by Equation 7.10-1. For continuous capacitive or voltammetric measurements, σ was determined from the root-mean-square deviation of a linear fit of 10 data points in the initial baseline of the sensograms, immediately preceding the response of the first addition. S was determined from the slope of a linear fit to the linear regime of each respective binding isotherm, with a linear range between 0-4.8 mM for HSO_4^-, and either 11-15 mM (@ $E_{1/2}$) or 11-20 mM (@ E_{-200}) for $H_2PO_4^-$.

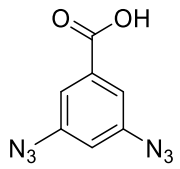
7.11 Synthesis

7.11.1 Synthesis for Chapter 2

The synthetic routes for the monomers (**1.XB**/**HB**) and polymers (**pDEGA**, **pDEGA-1.XB**/**HB**, **pDEGA-BuA-1.XB** and **pDEGA-1.XB$_{0.5}$**) are shown in Schemes 2.2-1 and 2.3.3-1, respectively.

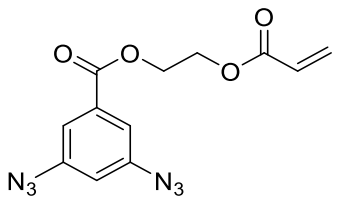
The synthesis and characterisation of all compounds was carried out by Dr. Krzysztof Bąk, other than the synthesis of **pDEGA**.

Synthesis of Monomeric Hosts:



A

3,5-diazidobenzoic acid, **A** was prepared from 3,5-diaminobenzoic acid following previously reported procedure.[316] ^{1}H NMR is in accordance with the published data.



B

2-(Acryloyloxy)ethyl 3,5-diazidobenzoate B: 3,5-Diazidobenzoic acid, **A** (500 mg, 2.45 mmol) was dissolved in dry CH_2Cl_2 (50 mL) and dry DMF (3 mL). 2-Hydroxyethyl acrylate (1.14 g, 9.80 mmol) was added to the solution followed by EDC·HCl (563 mg, 2.94 mmol) and DMAP (359 mg, 2.94 mmol). The solution was stirred at RT for

48 h under N_2. The reaction mixture was then washed with 5% aq. citric acid solution (3 x 20 mL), saturated aq. $NaHCO_3$ solution (20 mL) and brine (20 mL). Organic layer was dried over $MgSO_4$ and solvent was removed in vacuo. Purification by column chromatography (SiO_2; DCM/MeOH 99:1) afforded product **B** as white solid (293 mg, 40% yield).

^{1}H NMR (600 MHz, $CDCl_3$), δ: 7.48 (d, J = 2.05 Hz, 2H), 6.81 (t, J = 2.05 Hz, 1H), 6.45 (dd, 1H), 6.16 (dd, 1H) 5.88 (dd, 1H), 4.58 (m, 2H), 4.51 (m, 2H).

^{13}C NMR (151 MHz, $CDCl_3$), δ: 166.01, 164.78, 142.50, 133.06, 131.77, 128.03, 116.55, 114.18, 63.50, 62.11.

HRMS (ESI+ve) m/z: 325.0643 ($[M+Na]^+$, $C_{12}H_{10}N_6O_4Na$ requires 325.0656)

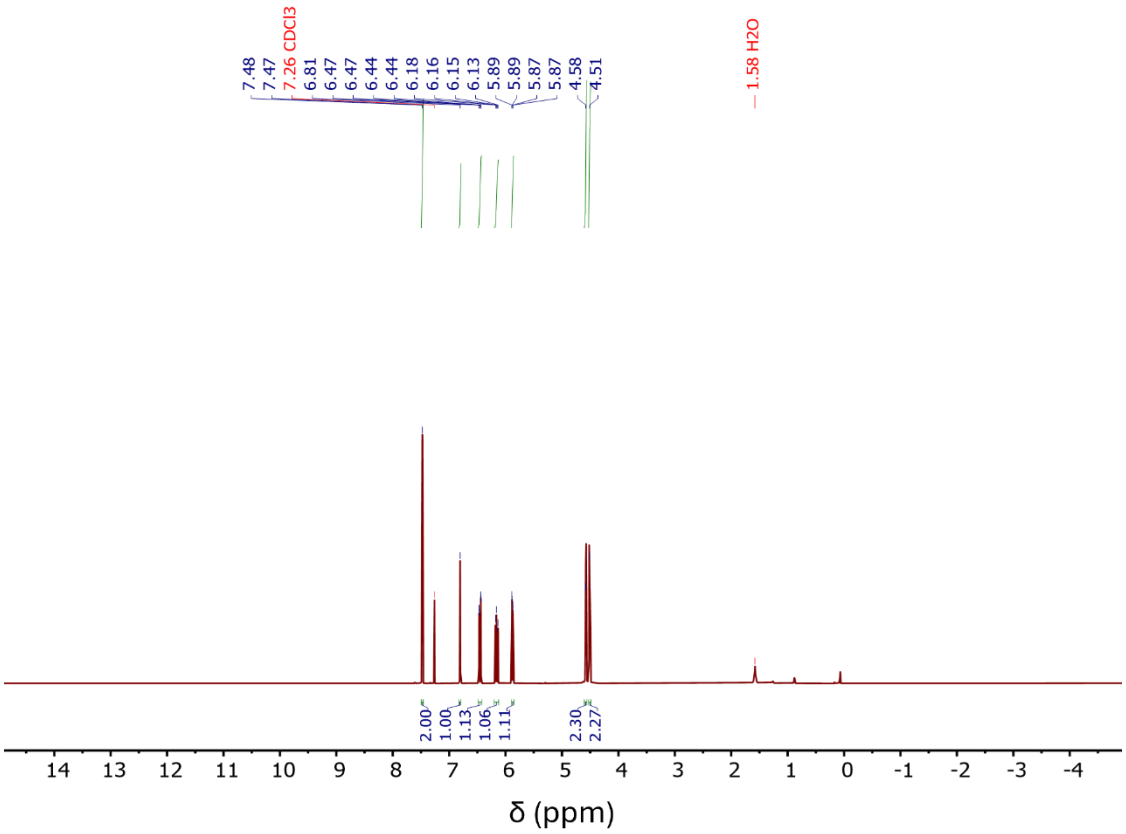


Figure 7.11.1-1. ^{1}H NMR spectrum of **B** ($CDCl_3$, 298K, 600 MHz).

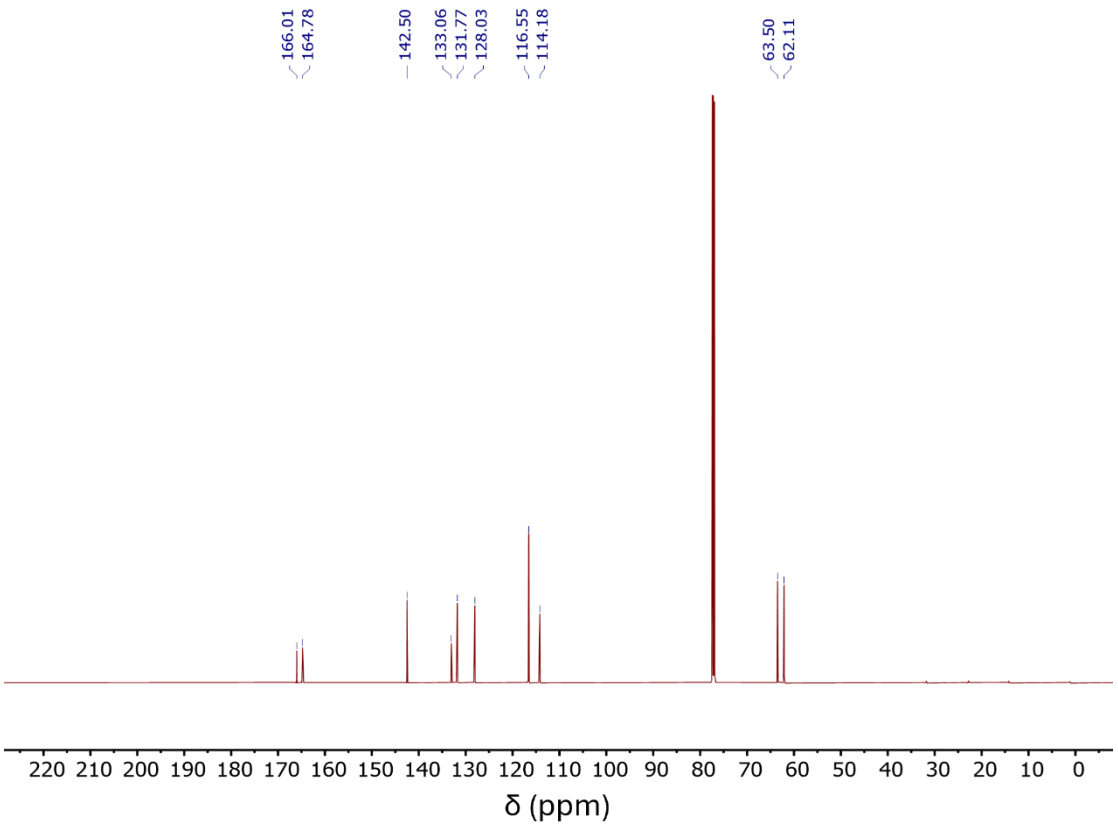
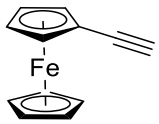


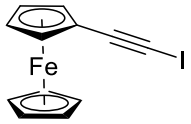
Figure 7.11.1-2. ^{13}C NMR spectrum of **B** in ($CDCl_3$, 298K, 151 MHz).



C.HB

Ethynylferrocene C.HB was prepared following previously published procedure.[317] A stirred solution of 2-formyl-1-chlorovinyl-ferrocene **D** (1.56 g, 5.69 mmol) in 1,4-dioxane (15 mL) was refluxed for 5 min under N_2. A 0.5 M sodium hydroxide solution (35 mL, 17.5 mmol) was added in one portion to the reaction mixture. The mixture was refluxed for 30 min. The solution was allowed to cool down to RT, poured onto ice, and then it was neutralised to pH = 7 by 2 M hydrochloric acid. The crude mixture was extracted with petroleum ether (2 x 50 mL). The organic phase was separated and washed with saturated $NaHCO_3$ solution (2 × 20 mL), and water (2 × 20 mL). The

organic layer was dried over Na_2SO_4 and solvent was removed *in vacuo*. Purification by column chromatography (SiO_2, hexane/DCM 9:1) afforded product **C.HB** as an orange solid (820 mg, 69% yield). ^{1}H NMR and MS in accordance with previously published data.



C.XB

Iodoethynylferrocene C.XB. An aqueous solution of KOH (5.2 M, 1.7 mL) was added at 0°C to a methanol solution (10 mL) of ethynylferrocene **C.HB** (500 mg, 2.38 mmol). The mixture was stirred for 10 min, after which iodine (664 mg, 2.62 mmol) was added in one portion. The solution was warmed to room temperature, protected from light and stirred for 2 h. The solution was poured into water (20 mL) and extracted with Et_2O (20 mL x 3). The organic layers were combined and washed with 10% aq. $Na_2S_2O_3$ solution (20 mL), brine (20 mL) and then dried with $MgSO_4$. The solvent was removed *in vacuo* to afford the product **C.XB** as an orange solid (776 mg, 97% yield). ^{1}H NMR and MS in accordance with previously published data.

^{1}H NMR (400 MHz, $CDCl_3$), δ: 4.44 (t, J = 1.825, 2H), 4.22 (s, 5H), 4.18 (t, J = 1.825, 2H).

^{13}C NMR (151 MHz, $CDCl_3$), δ: 92.19, 72.03, 70.35, 69.00, 66.00.

HRMS (ESI+ve) m/z: 335.9085 ($[M+]^+$, $C_{12}FeH_9I$ requires 335.9171)

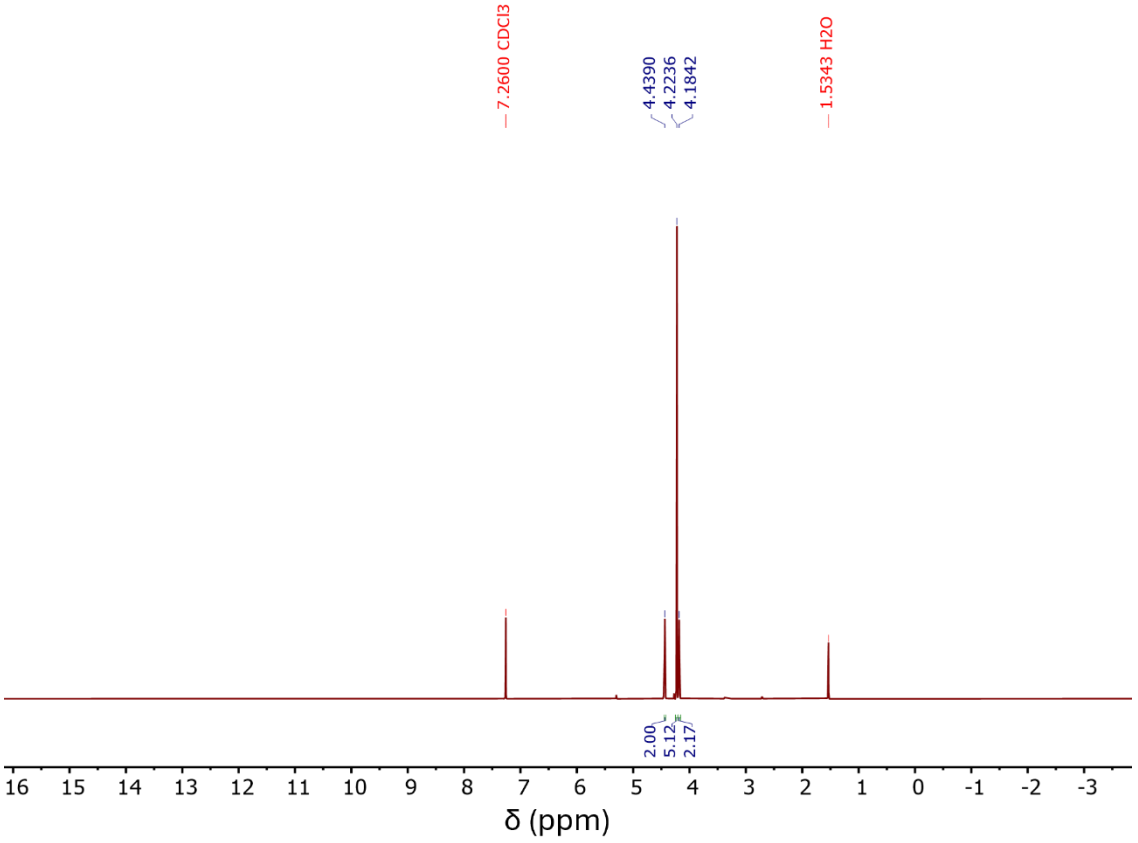


Figure 7.11.1-3. ^{1}H NMR spectrum of **C.XB** ($CDCl_3$, 298K, 400 MHz).

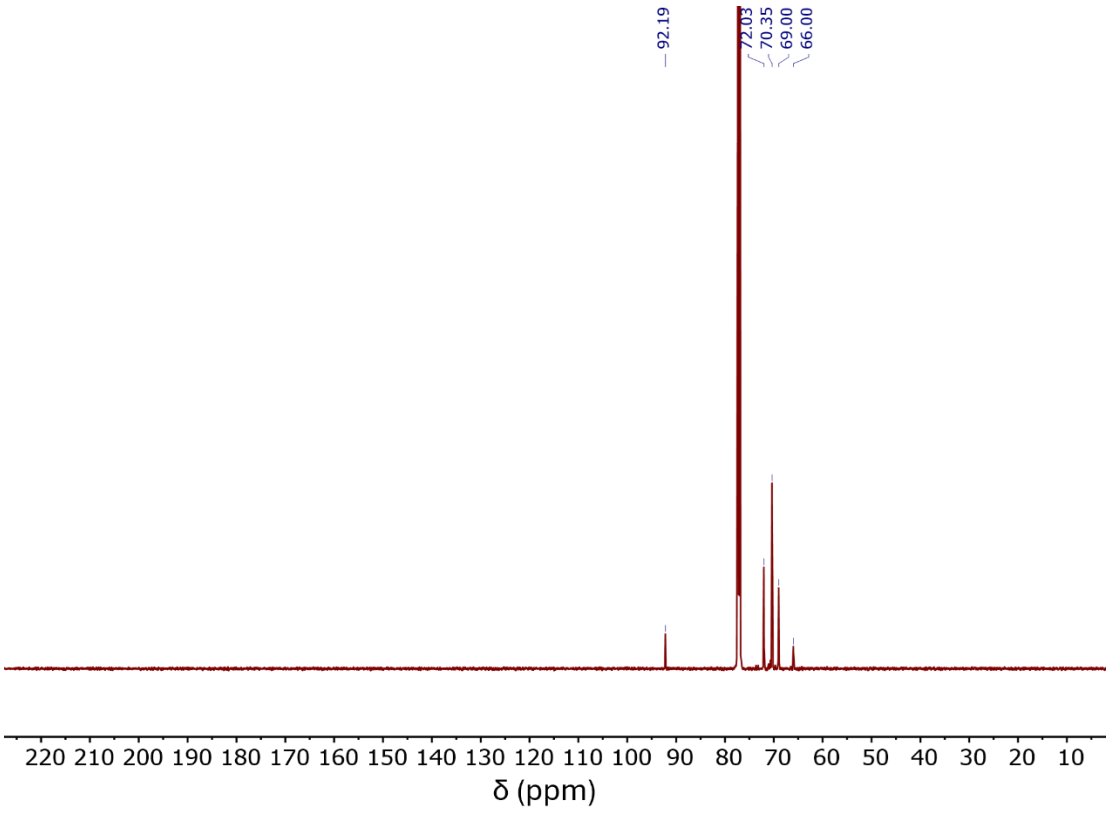
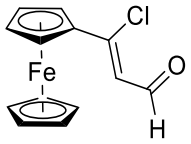
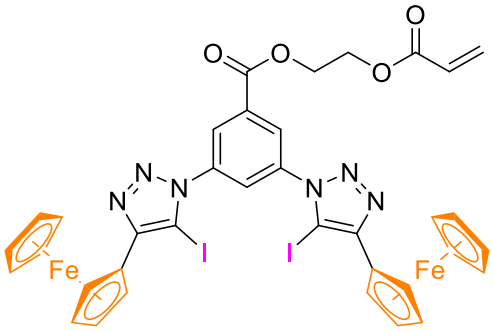


Figure 7.11.14. ^{13}C NMR spectrum of **C.XB** ($CDCl_3$, 298K, 151 MHz).



D

(2-Formyl-1-chlorovinyl)-ferrocene, D was prepared following previously published procedure.[317] A stirred solution of acetylferrocene (2.00 g, 8.77 mmol) in dry DMF (25 mL) was purged with N_2 for 15 min and then cooled to 0 °C in an ice bath. The solution was stirred for 15 min under an N_2 atmosphere. In a separate flask, dry DMF (5.0 mL) was cooled in an ice bath, to which phosphorus oxychloride (2.6 mL) was added under N_2. The prepared mixture was transferred to the vigorously stirred solution of the acetylferrocene. The addition was completed within 10 min and the stirring was continued at 0°C under N_2 for 1.5 h. 20% aqueous sodium acetate (65 mL) was cautiously added to the reaction mixture in one portion and stirring was continued for 1 h at RT. The organic phase was separated and the aqueous phase was extracted with CH_2Cl_2. The combined organic phase was dried over anhydrous $MgSO_4$ and solvent was removed *in vacuo*. Purification by column chromatography (SiO_2; hexane/ethyl ether 3:1) afforded product **D** as dark purple powder (1.48 g, 65% yield). ^{1}H NMR and MS in accordance with previously published data.[317]



1.XB

$[Cu(CH_3CN)_4]PF_6$ (123 mg, 0.33 mmol) and tris((1-benzyl-4-triazolyl)methyl)amine (TBTA, 176 mg, 0.331 mmol) were dissolved in DCM (anhydrous, 2 mL). The mixture was stirred for 30 min under N_2. Then iodoethynylferrocene, **C.XB** (445 mg, 1.33 mmol) and **B** (200 mg, 0.66 mmol) were added. The reaction mixture was protected from light and stirred overnight under N_2. Next, it was washed with aqueous EDTA (10%)/NH_3 (2%) solution (3 x 20 mL), followed by brine (20 mL). Organic layers were combined and dried over $MgSO_4$. The solvent was removed in vacuo to give the crude product. Purification by flash chromatography (SiO_2, DCM/MeOH 99:1) afforded product **1.XB** as a crystalline orange solid (420 mg, 65% yield).

^{1}H NMR (400 MHz, $CDCl_3$), δ: 8.50 (d, J = 2.03 Hz, 2H), 8.14 (t, J = 2.03 Hz, 1H), 6.46 (dd, 1H), 6.17 (dd, 1H) 5.88 (dd, 1H), 5.10 (t, J = 1.85 Hz, 4H) 4.68 (m, 2H), 4.56 (m, 2H), 4.41 (t, J = 1.85 Hz, 4H), 4.20 (s, 10H).

^{13}C NMR (151 MHz, $CDCl_3$), δ: 165.98, 163.81, 151.52, 137.91, 132.56, 131.98, 128.41, 128.19, 127.99, 75.08, 74.51, 70.10, 69.62, 67.86, 64.07, 62.10.

HRMS (ESI+ve) m/z: 974.9033 ($[M+H]^+$, $C_{36}H_{29}Fe_2I_2N_6O_4$ requires 974.9033)

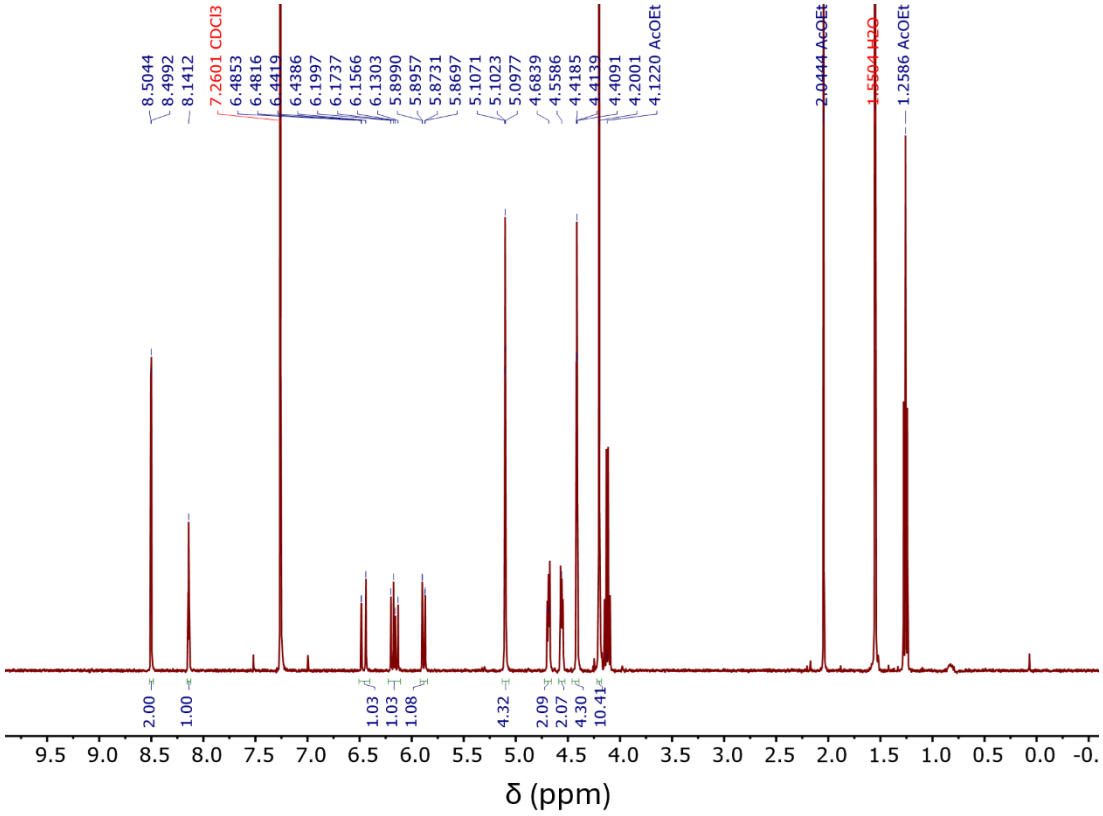


Figure 7.11.1-5. ^{1}H NMR spectrum of **1.XB** ($CDCl_3$, 298K, 400 MHz).

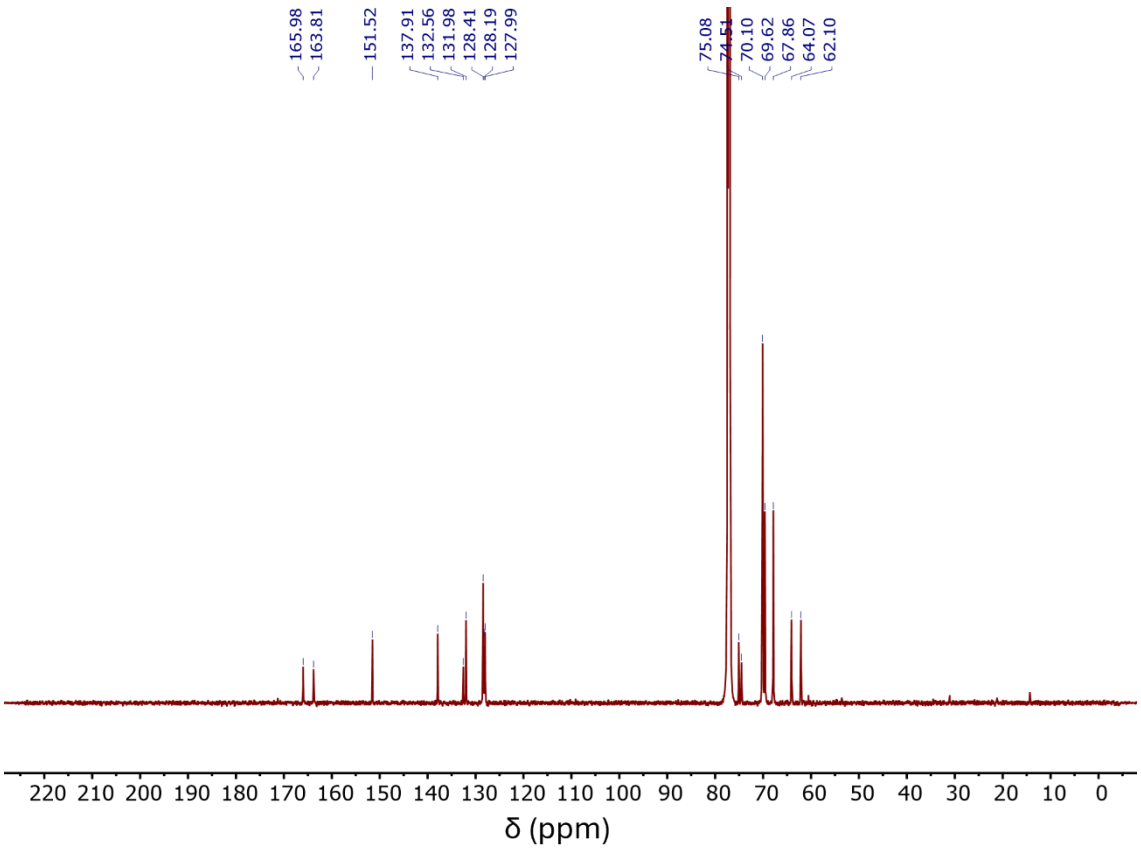
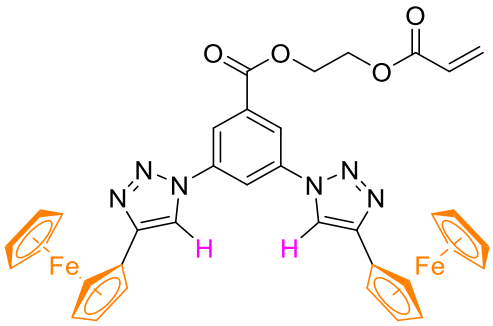


Figure 7.11.1-6. ^{13}C NMR spectrum of **1.XB** in ($CDCl_3$, 298K, 151 MHz).



1·HB

$[Cu(CH_3CN)_4]PF_6$ (99 mg, 0.266 mmol) and tris((1-benzyl-4-triazolyl)methyl)amine (TBTA, 132 mg, 0.266 mmol) were dissolved in DCM (anhydrous, 2 mL). The mixture was stirred for 30 min under N_2. Then ethynylferrocene, **C.HB** (209 mg, 1.00 mmol) and **B** (150 mg, 0.500 mmol) were added. The reaction mixture was protected from light and stirred overnight under N_2. Next, it was washed with aqueous EDTA (10%)/NH_3 (2%) solution (3 x 20 mL), followed by brine (20 mL). Organic layers were combined and dried over $MgSO_4$. The solvent was removed in vacuo to give the crude product. Purification by flash chromatography (SiO_2, DCM/MeOH 99:1) afforded product **1.HB** as a crystalline orange solid (320 mg, 56% yield).

^{1}H NMR (400 MHz, $CDCl_3$), δ: 8.64 (t, J = 2.02 Hz, 1H), 8.48 (d, J = 2.02 Hz, 2H), 8.10 (s, 2H), 6.49 (dd, 1H), 6.20 (dd, 1H) 5.90 (dd, 1H), 4.84 (t, J = 1.83 Hz, 4H) 4.69 (m, 2H), 4.61 (m, 2H), 4.39 (t, J = 1.83 Hz, 4H), 4.14 (s, 10H).

^{13}C NMR (151 MHz, $CDCl_3$), δ: 166.02, 164.15, 148.86, 138.27, 133.20, 131.86, 127.95, 119.99, 117.40, 116.12, 71.35, 70.44, 68.08, 64.05, 61.99.

HRMS (ESI+ve) m/z: 723.1077 ($[M+H]^+$, $C_{36}H_{31}Fe_2N_6O_4$ requires 723.1100)

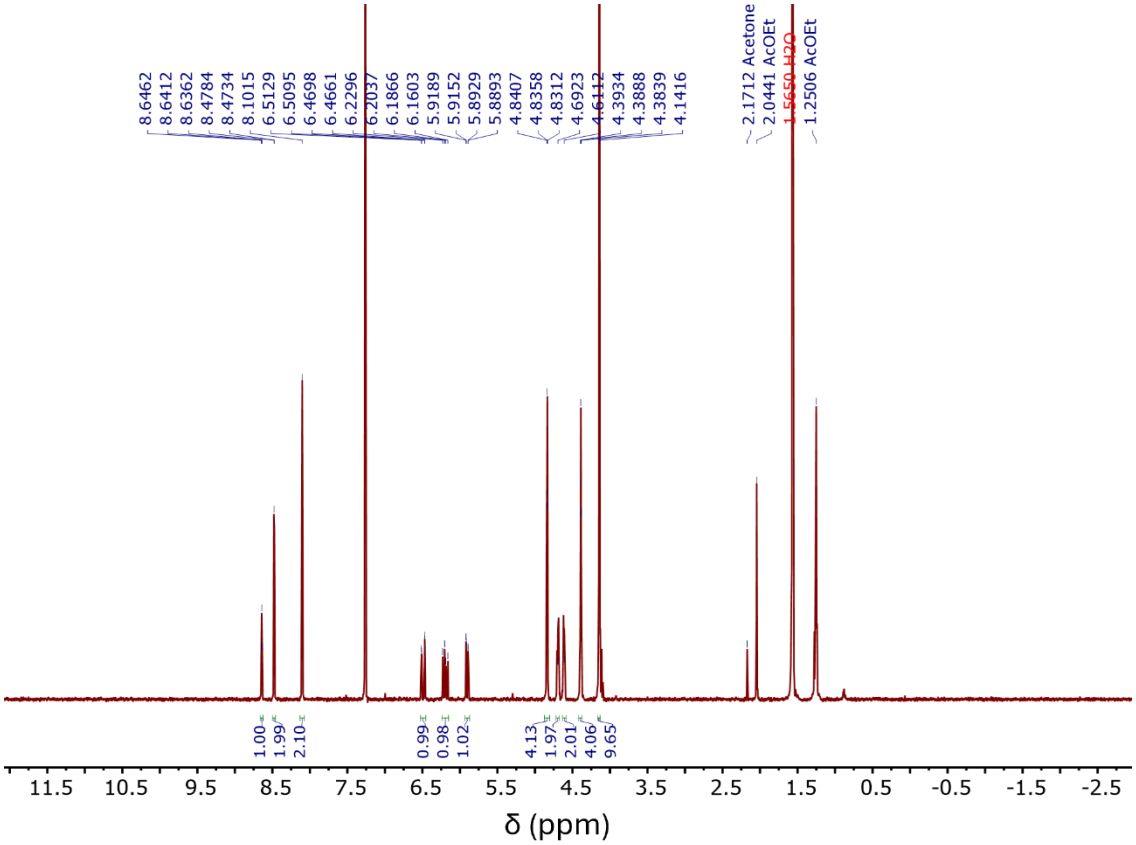


Figure 7.11.1-7. ^{1}H NMR spectrum of **1.HB** ($CDCl_3$, 298K, 400 MHz).

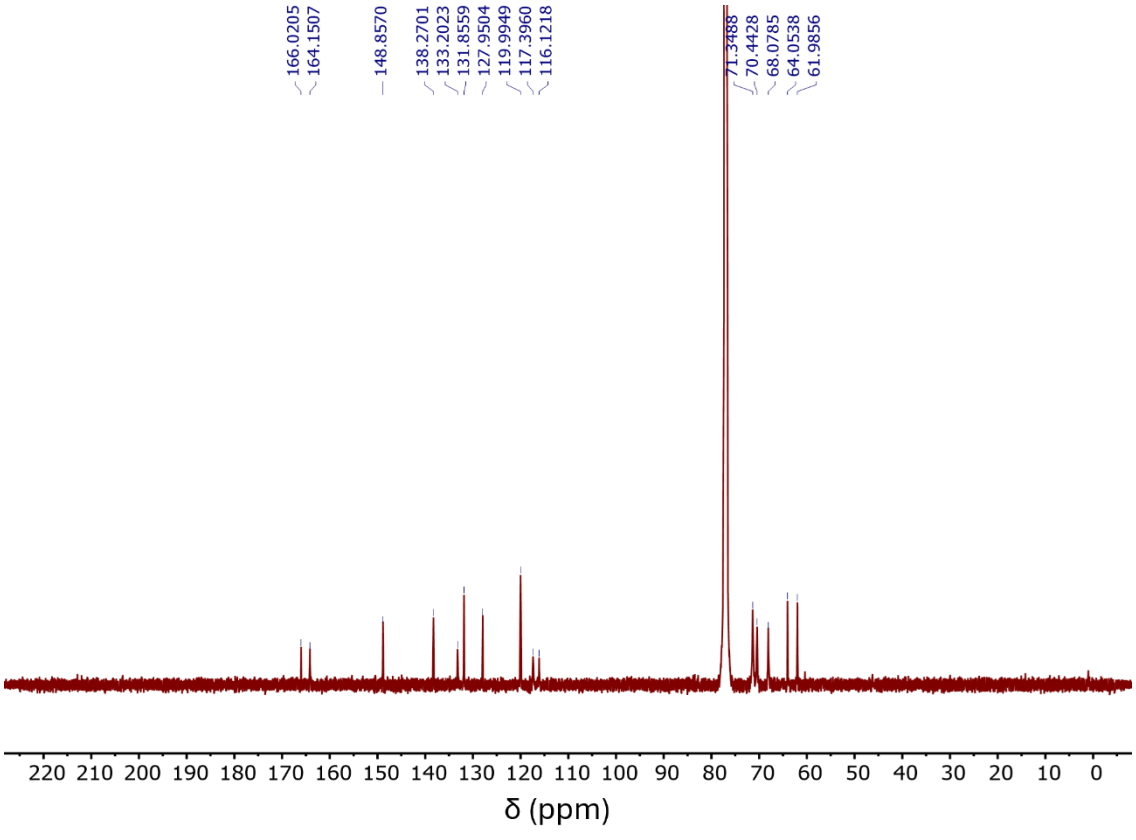
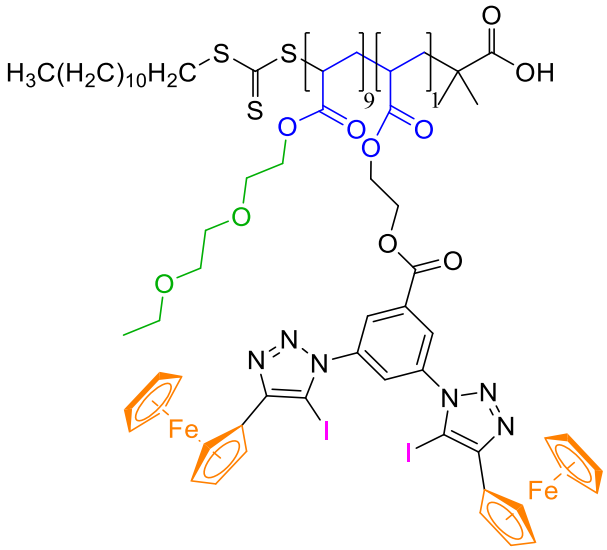


Figure 7.11.1-8. ^{13}C NMR spectrum of **1.HB** in ($CDCl_3$, 298K, 151 MHz).

Synthesis of Polymeric Hosts:

A Kessil® PR-160-390nm lamp was used for all UV-initiated RAFT polymerisations, which emits light with a wavelength of 390 nm.



pDEGA-1.XB

^{1}H NMR (400 MHz, $CDCl_3$), δ: 8.52 (bs, 2H), 8.13 (bs, 1H), 5.10 (bs, 4H) 4.62 (bs, 2H), 4.39 (bs, 6H), 4.19 (bs, 28H), 3.72-3.44 (bs, 72H), 2.32 (bs, polymer backbone), 1.91 (bs, polymer backbone), 1.62 (bs, polymer backbone), 1.20 (bt, 27H)

^{13}C NMR (151 MHz, $CDCl_3$), δ: 174.31, 70.65, 69.90, 68.98, 66.70, 63.57, 41.28, 15.27.

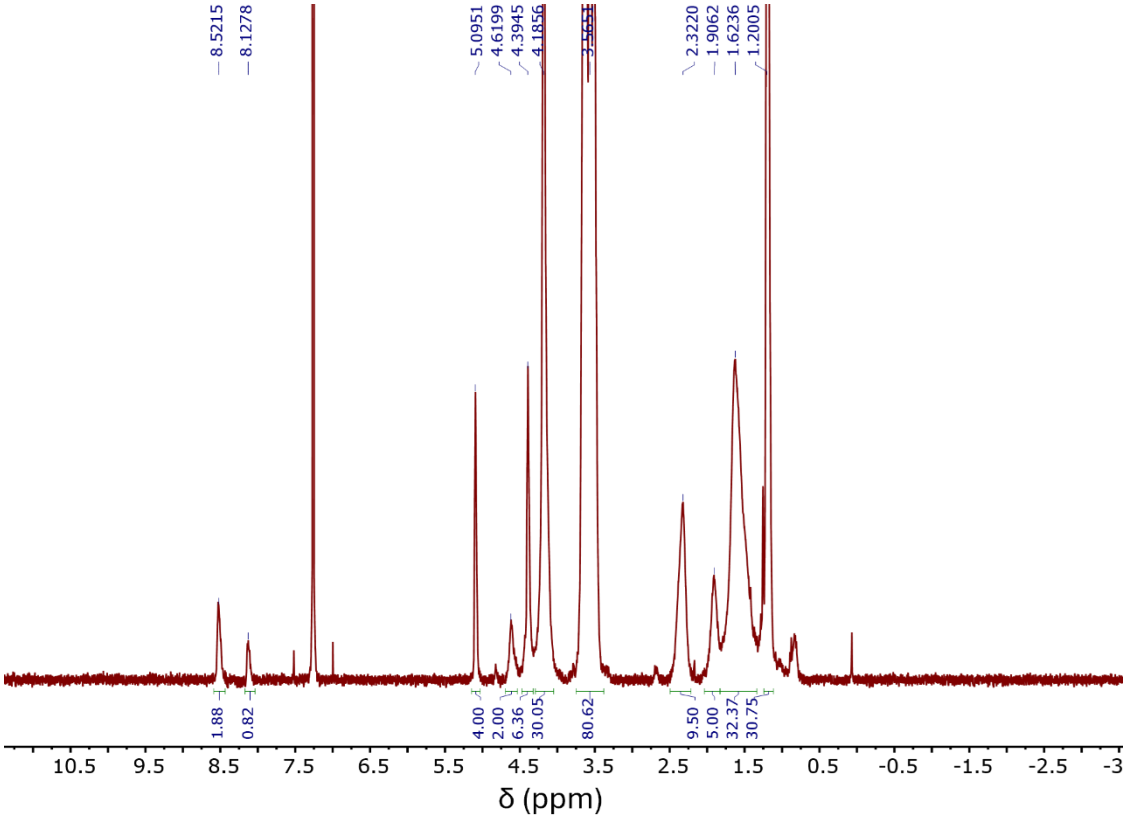


Figure 7.11.1-9. ^{1}H NMR spectrum of **pDEGA-1.XB** ($CDCl_3$, 298K, 400 MHz).

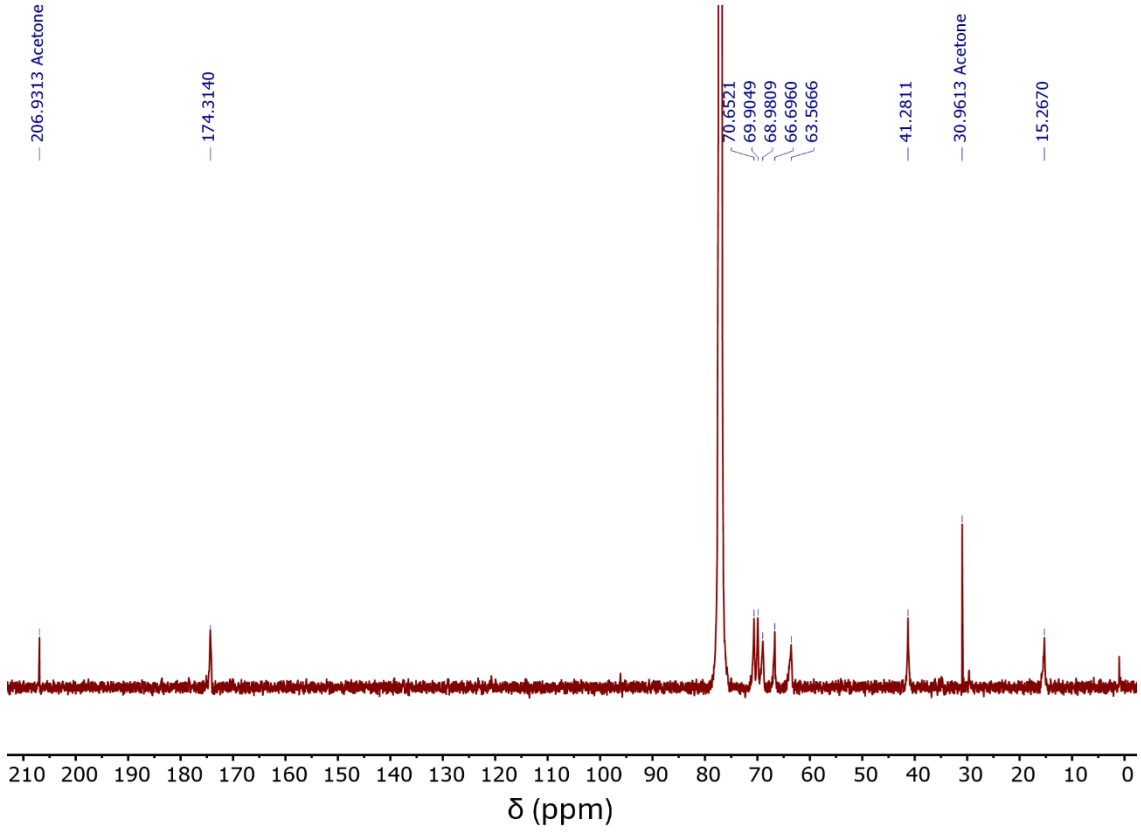
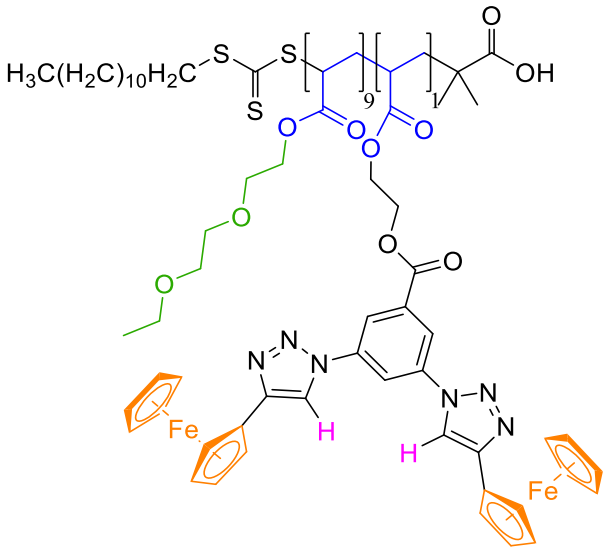


Figure 7.11.1-10. ^{13}C NMR spectrum of **pDEGA-1.XB** ($CDCl_3$, 298K, 151 MHz).



pDEGA-1.HB

^{1}H NMR (400 MHz, $CDCl_3$), δ: 8.72 (bs, 1H), 8.50 (bs, 2H), 8.30 (bs, 2H), 4.82 (bs, 4H) 4.64 (bs, 2H), 4.46 (bs, 2H), 4.35 (bs, 4H), 4.18 (bs, 10H), 4.11 (bs, 18H) 3.73-3.43 (bs, 72H), 2.32 (bs, polymer backbone), 1.89 (bs, polymer backbone), 1.19 (bt, 27H)

^{13}C NMR (151 MHz, $CDCl_3$), δ: 174.25, 70.57, 69.87, 68.88, 66.62, 63.49, 41.28, 15.25.

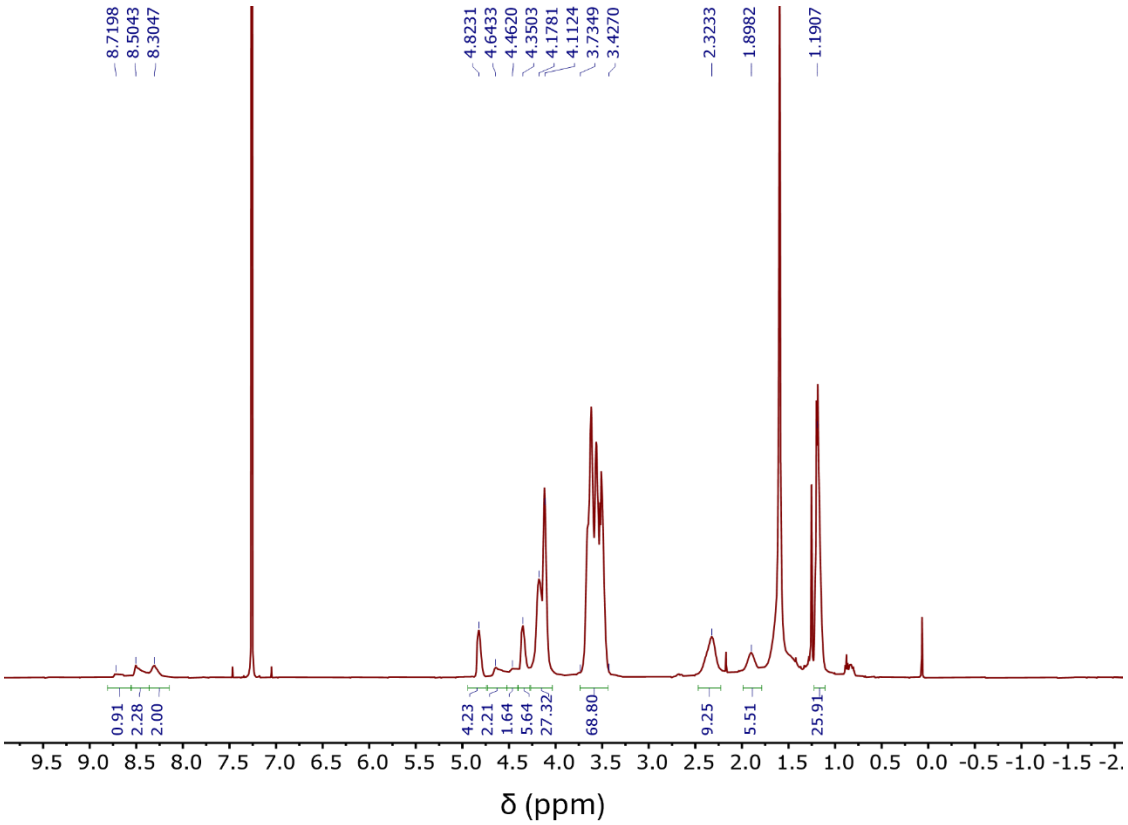


Figure 7.11.1-11. ^{1}H NMR spectrum of **pDEGA-1.HB** ($CDCl_3$, 298K, 400 MHz).

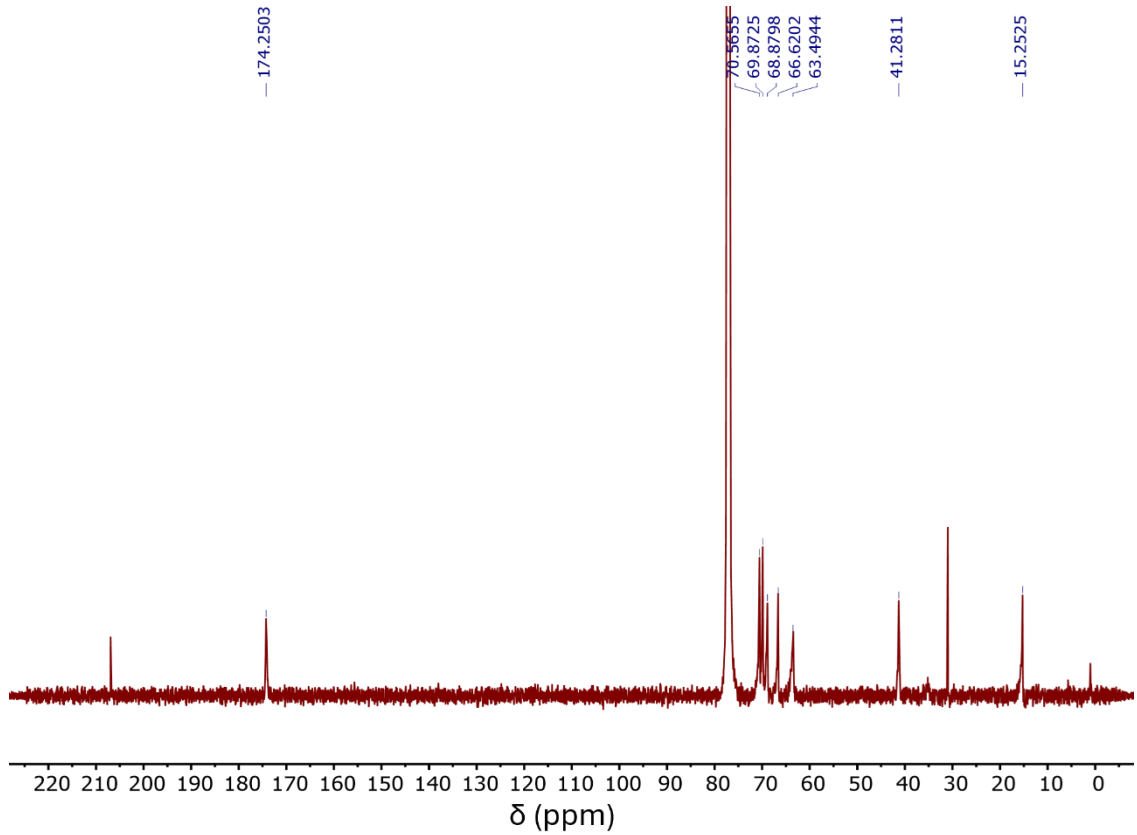
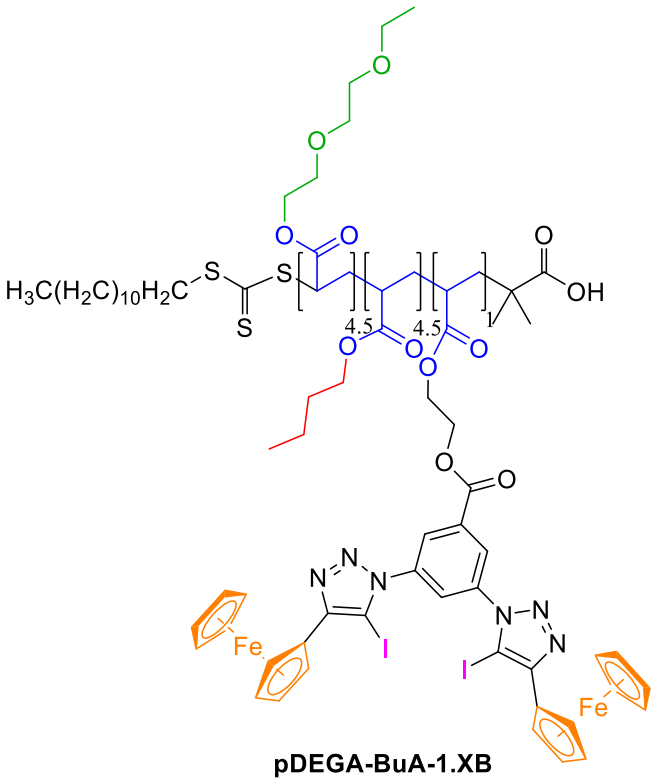


Figure 7.11.1-12. ^{13}C NMR spectrum of **pDEGA-1.HB** ($CDCl_3$, 298K, 151 MHz).



pDEGA-BuA-1.XB

^{1}H NMR (400 MHz, $CDCl_3$), δ: 8.52 (bs, 2H), 8.14 (bs, 1H), 5.09 (bs, 4H) 4.62 (bs, 2H), 4.39 (bs, 6H), 4.24 (bt, 9H) 4.18 (bs, 10H), 4.03 (bt, 9H) 3.71-3.44 (bs, 36H), 2.32 (bs, polymer backbone), 1.90 (bs, polymer backbone), 1.36 (bs, polymer backbone), 1.20 (bs, polymer backbone), 0.93 (bs, 13.5H), 0.83 (bs, 9H)

^{13}C NMR (151 MHz, $CDCl_3$), δ: 174.32, 70.64, 69.90, 68.92, 66.71, 64.50, 63.65, 41.36, 30.65, 19.14, 15.29, 13.81.

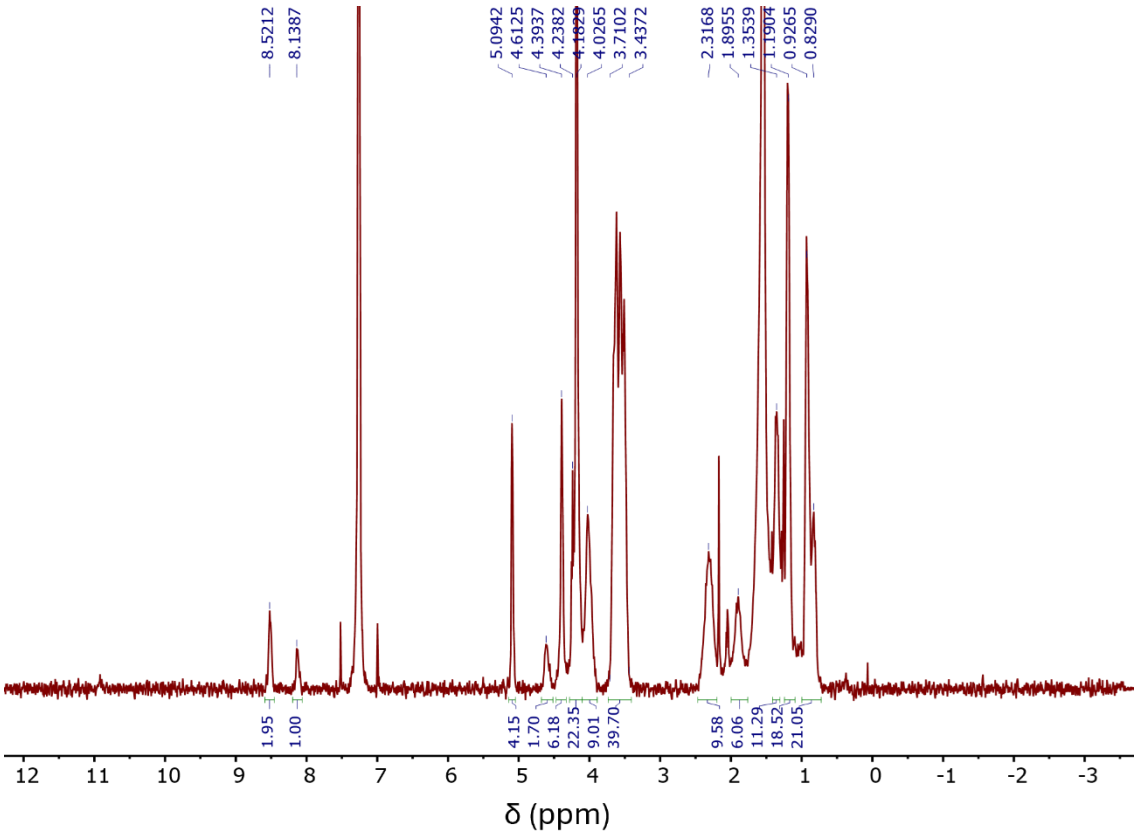


Figure 7.11.1-13. ^{1}H NMR spectrum of **pDEGA-BuA-1.XB** ($CDCl_3$, 298K, 400 MHz).

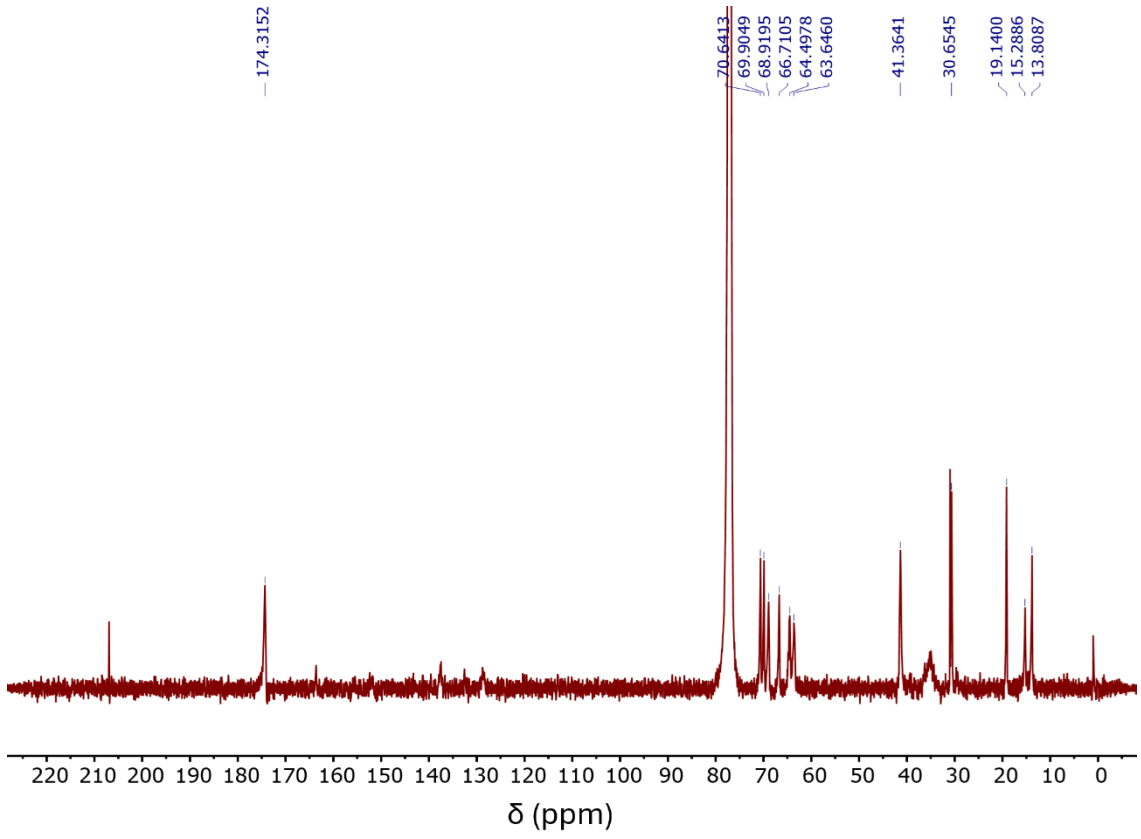
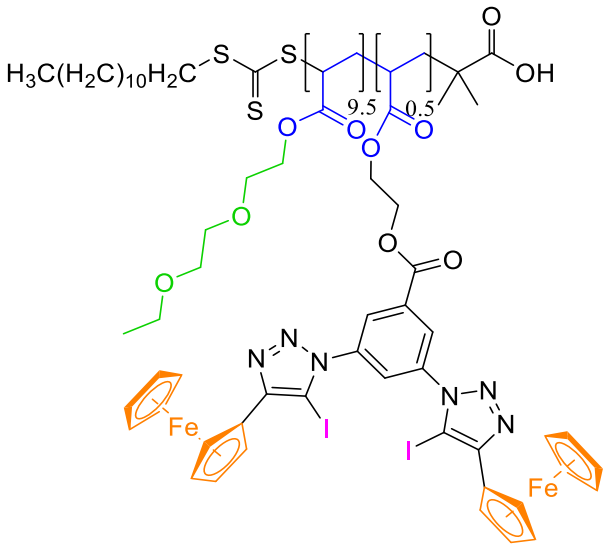


Figure 7.11.1-14. ^{13}C NMR spectrum of **pDEGA-BuA-1.XB** ($CDCl_3$, 298K, 151 MHz).



pDEGA-1.XB$_{0.5}$

^{1}H NMR (400 MHz, CDCl$_3$), δ: 8.53 (bs, 2H), 8.14 (bs, 1H), 5.10 (bs, 4H) 4.62 (bs, 2H), 4.34 (bs, 6H), 4.19 (bs, 38H), 3.72-3.44 (bs, 152H), 2.33 (bs, polymer backbone), 1.91 (bs, polymer backbone), 1,64 (bs, polymer backbone), 1.20 (bt, 57H)

^{13}C NMR (151 MHz, CDCl$_3$), δ: 174.32, 70.61, 69.91, 68.94, 66.67, 63.54, 41.31, 15.28.

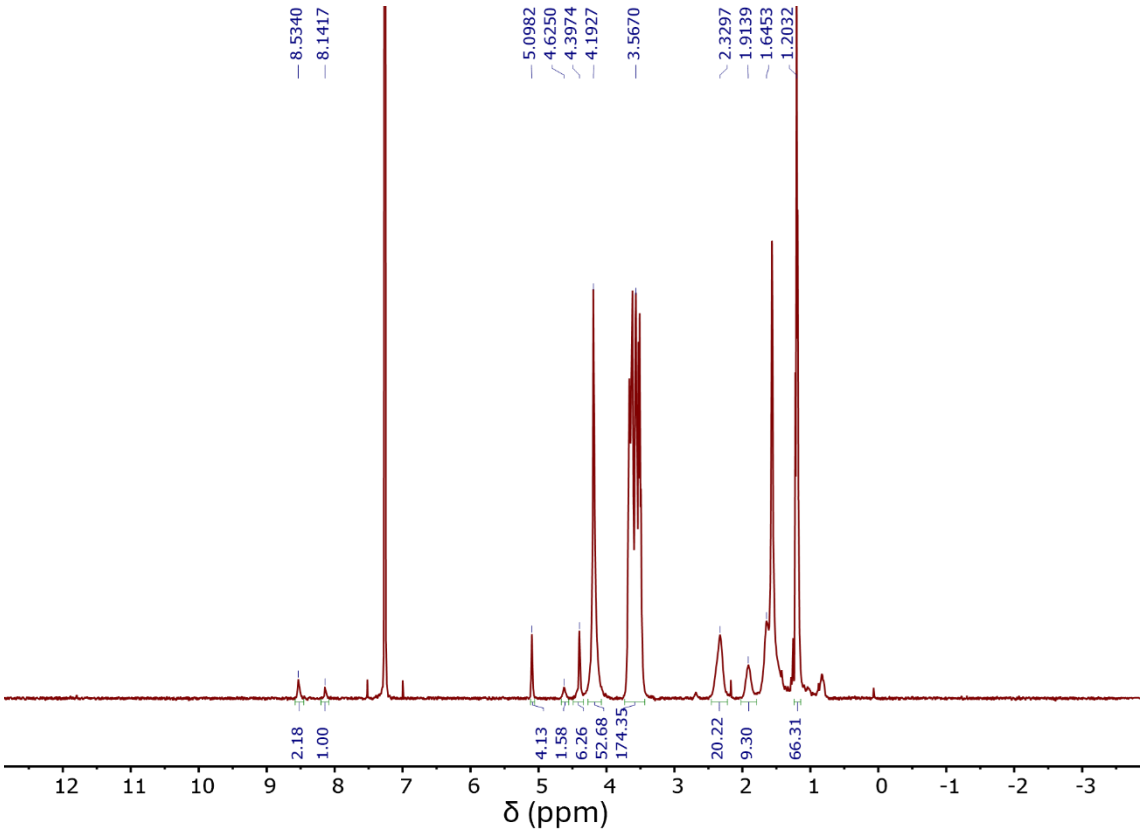


Figure 7.11.1-15. ^{1}H NMR spectrum of **pDEGA-1.XB$_{0.5}$** ($CDCl_3$, 298K, 400 MHz).

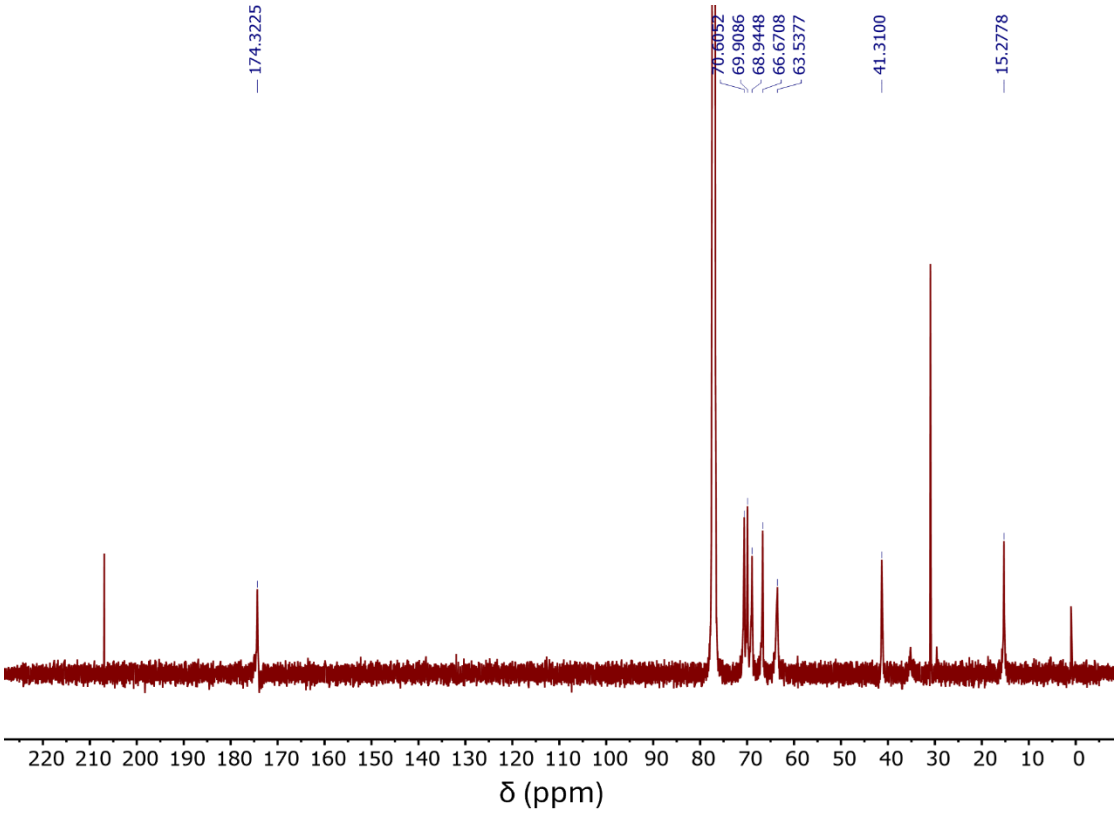
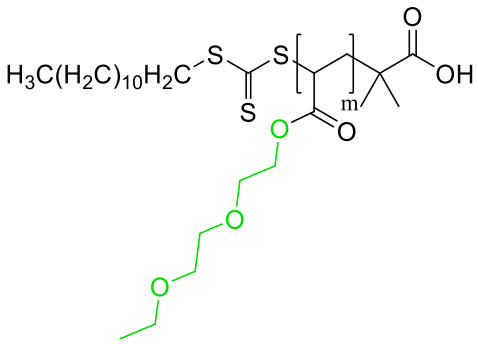


Figure 7.11.1-16. ^{13}C NMR spectrum of **pDEGA-1.XB** ($CDCl_3$, 298K, 151 MHz).



pDEGA

^{1}H NMR (600 MHz, $CDCl_3$), δ: 4.20 (bs, 2H), 3.67 (bs, 2H), 3.63 (bs, 2H), 3.57 (bs, 2H), 3.52 (q, 2H) 2.33 (bs, polymer backbone), 1.92 (bs, polymer backbone), 1.70 (bs, polymer backbone), 1.65 (bs, polymer backbone), 1.5 (bs), 1.20 (t, 3H)

^{13}C NMR (151 MHz, $CDCl_3$), δ: 174.39, 70.68, 69.99, 69.00, 66.74, 63.73, 63.56, 41.41, 15.3.

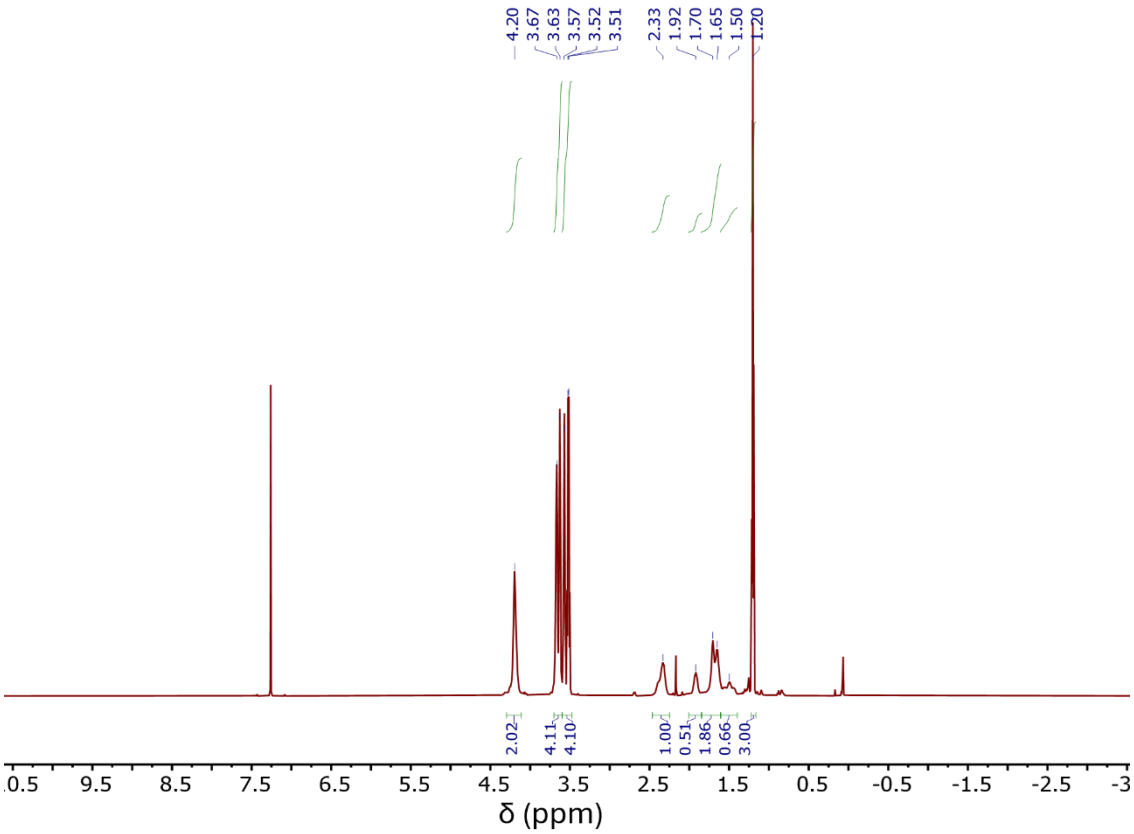


Figure 7.11.1-17. ^{1}H NMR spectrum of **pDEGA** ($CDCl_3$, 298K, 600 MHz).

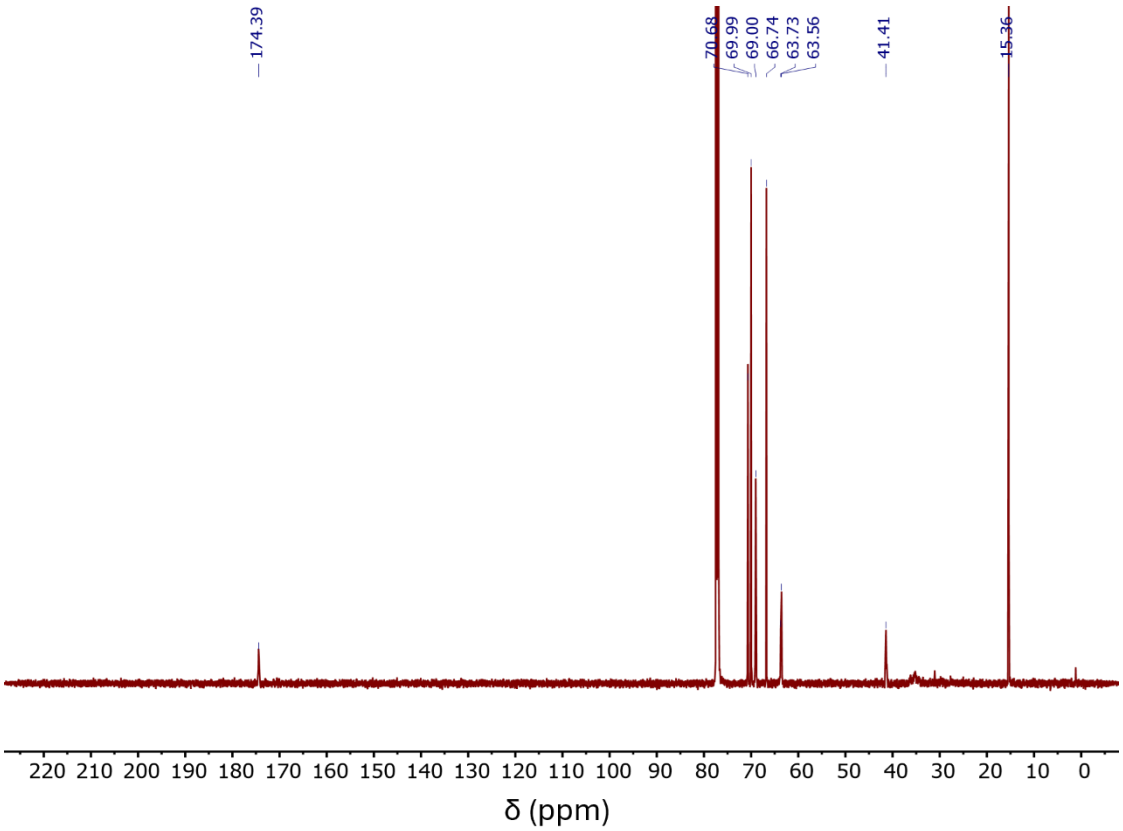


Figure 7.11.1-18. ^{13}C NMR spectrum of **pDEGA** ($CDCl_3$, 298K, 151 MHz).

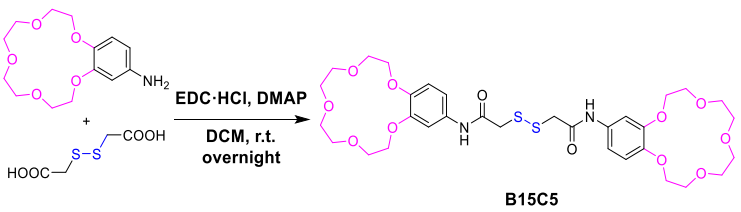
7.11.2 Synthesis for Chapters 3 & 4

The synthesis and characterisation of both XB/HB-Fc-isophthalamide (**3.XB**/**HB**) receptors was carried out by Dr. Robert Hein.

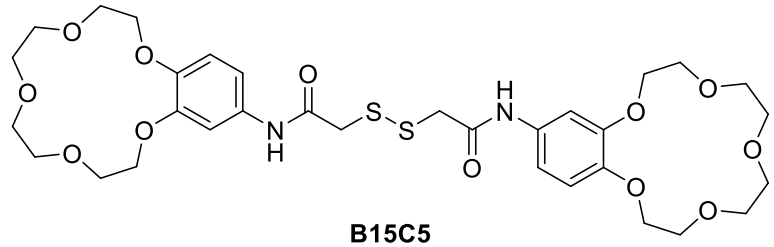
The synthetic schemes, procedures and characterisation data for **3.XB**/**HB** can be found in the thesis of Dr. Robert Hein[179] and in a published report.[210]

7.11.3 Synthesis for Chapter 5

The synthesis and characterisation of **B15C5** was carried out by Dr. Robert Hein.



Scheme 7.11.3-1. Reaction scheme to form **B15C5**.



B15C5

Procedure: Dithioglycolic acid (32 mg, 0.177 mmol, 1 equiv.), 4'-aminobenzo-15-crown-5 (100 mg, 0.354 mmol, 2 equiv.), 4-dimethylaminopyridine (59 mg, 0.531 mmol, 3 equiv.) and 1-ethyl-3-(3-dimethylaminopropyl)carbodiimide hydrochloride (0.425 mmol, 2.4 equiv.) were dissolved in 5 mL of anhydrous DCM and reacted at room temperature overnight. Subsequently, 25 mL DCM were added and the organic phase was washed 3 times with 5% aqueous HCl and then once with H_2O. Following drying over $MgSO_4$ and removal of the solvent in vacuo, the product was purified by alumina column chromatography (DCM to 3.5% MeOH in DCM gradient). The product was obtained as a yellow solid (83 mg, 0.116 mmol, 66%).

^{1}H NMR (600 MHz, $CDCl_3$/MeOD 2:1 (v/v)): δ 7.30 (d, *J* = 2.4 Hz, 2H), 7.05 (dd, *J* = 8.6, 2.4 Hz, 2H), 6.82 (d, *J* = 8.6 Hz, 2H), 4.08 (ddd, *J* = 8.8, 5.1, 3.3 Hz, 8H), 3.86 (tt, *J* = 6.7, 3.6 Hz, 8H), 3.75 – 3.68 (m, 16H), 3.59 (s, 4H).

^{13}C NMR (151 MHz, $CDCl_3$/MeOD 2:1 (v/v)) δ 167.81, 149.10, 145.86, 132.23, 114.65, 112.84, 107.09, 70.71, 70.65, 70.31, 69.52, 69.40, 69.34, 68.68, 43.56.

HRMS (ESI+ve): m/z: 735.2221 ($[M+Na]^+$, $C_{32}H_{44}O_{12}N_2NaS_2$ requires 735.2228).

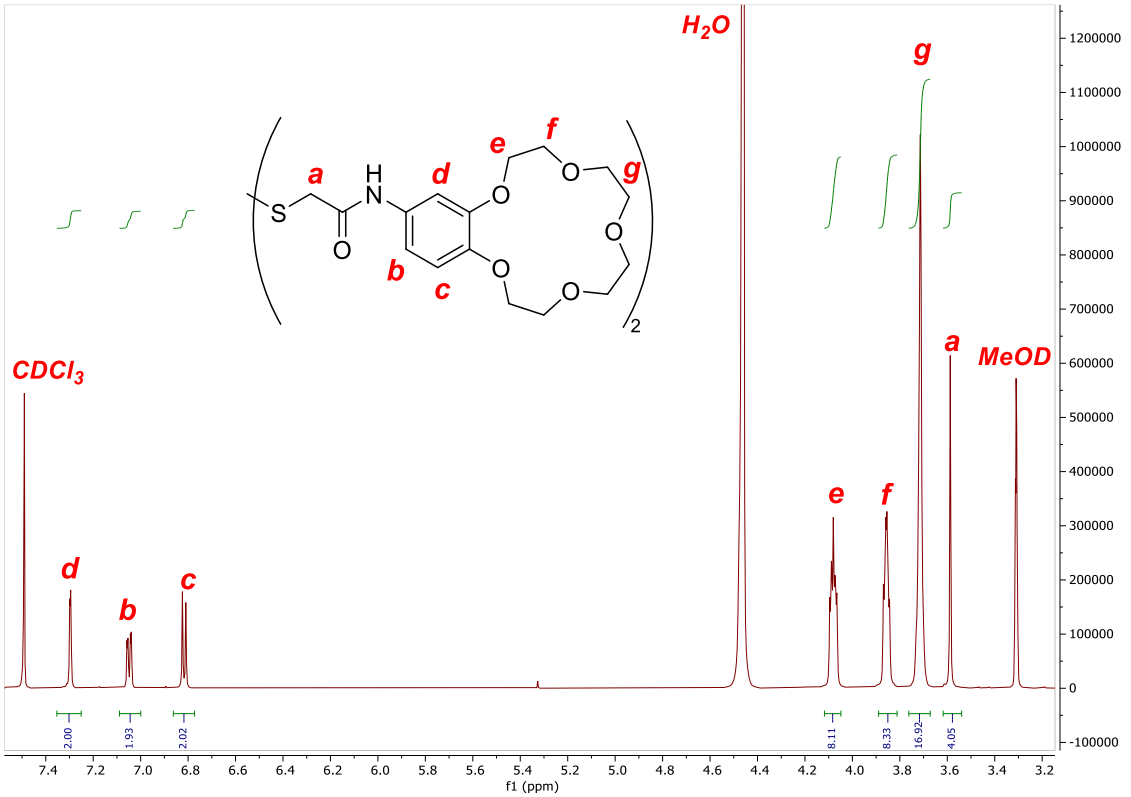


Figure 7.11.3-1. ^{1}H NMR of **B15C5** in $CDCl_3$/MeOD 2:1 (v/v).

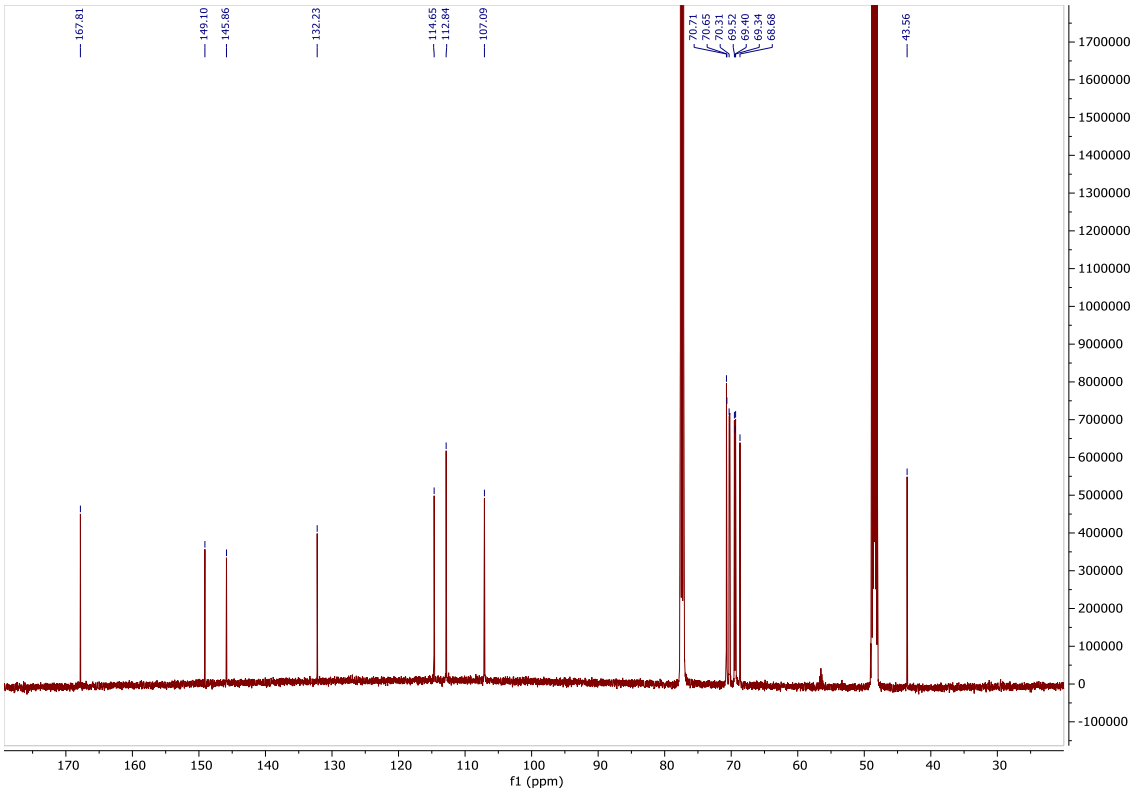


Figure 7.11.3-2. ^{13}C NMR of **B15C5** in $CDCl_3$/MeOD 2:1 (v/v).

The synthesis and characterisation of both XB/HB-ion pair receptors (**4.XB/HB-B15C5**) receptors was carried out by Dr. Andrew Docker.

The synthetic schemes, procedures and characterisation data for **4.XB/HB-B15C5** can be found in the thesis of Dr. Robert Hein.[179]

Chapter 8

References

Chapter 8: References

1. Busschaert, N.; Caltagirone, C.; Van Rossom, W.; Gale, P. A., *Chem. Rev.* **2015,** *115* (15), 8038-8155.
2. Gale, P. A.; Caltagirone, C., *Chem. Soc. Rev.* **2015,** *44* (13), 4212-4227.
3. Macreadie, L. K.; Gilchrist, A. M.; McNaughton, D. A.; Ryder, W. G.; Fares, M.; Gale, P. A., *Chem* **2022,** *8* (1), 46-118.
4. Packer, M. J.; Hunter, C. A., *J. Mol. Biol.* **1998,** *280* (3), 407-420.
5. Pohl, H. R.; Wheeler, J. S.; Murray, H. E., Sodium and Potassium in Health and Disease. In *Interrelations between Essential Metal Ions and Human Diseases*, Sigel, A.; Sigel, H.; Sigel, R. K. O., Eds. Springer Netherlands: Dordrecht, 2013; pp 29-47.
6. Haygarth, P. M., *Sci. Total Environ.* **2005,** *344* (1), 1-3.
7. Li, D.; Seaman, J. C.; Kaplan, D. I.; Heald, S. M.; Sun, C., *Chem. Eng. J.* **2019,** *360*, 1-9.
8. Katayev, E. A.; Kolesnikov, G. V.; Sessler, J. L., *Chem. Soc. Rev.* **2009,** *38* (6), 1572-1586.
9. Ghelani, D. P.; Schneider-Futschik, E. K., *ACS Pharmcol. Transl. Sci.* **2020,** *3* (1), 4-10.
10. Hoffmann, E. K.; Lambert, I. H., *Philos. Trans. R. Soc. London, Ser. B* **2014,** *369* (1638), 20130109.
11. Leri, A. C.; Myneni, S. C. B., *Geochim. Cosmochim. Acta.* **2012,** *77*, 1-10.
12. Leung, A.; Pearce, E. N.; Braverman, L. E., *Expert Rev. Endocrinol. Metab.* **2010,** *5* (4), 593-602.
13. Diauudin, F. N.; Rashid, J. I. A.; Knight, V. F.; Wan Yunus, W. M. Z.; Ong, K. K.; Kasim, N. A. M.; Abdul Halim, N.; Noor, S. A. M., *Sensing and Bio-Sensing Research* **2019,** *26*, 100305.
14. He, J. J.; Quiocho, F. A., *Science* **1991,** *251* (5000), 1479-1481.
15. Hao, T.-w.; Xiang, P.-y.; Mackey, H. R.; Chi, K.; Lu, H.; Chui, H.-k.; van Loosdrecht, M. C. M.; Chen, G.-H., *Water Res.* **2014,** *65*, 1-21.
16. Kaur, K.; Saini, R.; Kumar, A.; Luxami, V.; Kaur, N.; Singh, P.; Kumar, S., *Coord. Chem. Rev.* **2012,** *256* (17), 1992-2028.
17. Evans, N. H.; Beer, P. D., *Angew. Chem. Int. Ed.* **2014,** *53* (44), 11716-11754.
18. Brown, A.; Beer, P. D., *Chem. Commun.* **2016,** *52* (56), 8645-8658.
19. Carnegie, R. S.; Gibb, C. L. D.; Gibb, B. C., *Angew. Chem. Int. Ed.* **2014,** *53* (43), 11498-11500.
20. Marcus, Y., *J. Chem. Soc., Faraday Trans. 1* **1987,** *83* (2), 339-349.
21. Marcus, Y., *Journal of the Chemical Society, Faraday Transactions* **1991,** *87* (18), 2995-2999.
22. Kavallieratos, K.; Bertao, C. M.; Crabtree, R. H., *J. Org. Chem.* **1999,** *64* (5), 1675-1683.
23. Klein, H. A.; Beer, P. D., *Chem. Eur. J.* **2019,** *25* (12), 3125-3130.
24. von Krbek, L. K. S.; Schalley, C. A.; Thordarson, P., *Chem. Soc. Rev.* **2017,** *46* (9), 2622-2637.
25. Cram, D. J., *Angew. Chem. Int. Ed.* **1988,** *27* (8), 1009-1020.
26. Wittenberg, J. B.; Lyle, I., Complementarity and Preorganization. In *Supramol. Chem.*, 2012.
27. Frausto da Silva, J. J. R., *J. Chem. Educ.* **1983,** *60* (5), 390.
28. Jia, C.; Wang, Q.-Q.; Begum, R. A.; Day, V. W.; Bowman-James, K., *Org. Biomol. Chem.* **2015,** *13* (25), 6953-6957.
29. Hancock, R. D.; Martell, A. E., *Chem. Rev.* **1989,** *89* (8), 1875-1914.
30. Lindoy, L. F., *The Chemistry of Macrocyclic Ligand Complexes*. Cambridge University Press: Cambridge, 1989.
31. Pedersen, C. J., *J. Am. Chem. Soc.* **1967,** *89* (10), 2495-2496.
32. Pedersen, C. J., *Angew. Chem. Int. Ed.* **1988,** *27* (8), 1021-1027.
33. Dietrich, B.; Lehn, J. M.; Sauvage, J. P., *Tetrahedron Lett.* **1969,** *10* (34), 2885-2888.
34. Wilmore, J. T.; Beer, P. D., *Adv. Mater. n/a* (n/a), 2309098.
35. Wisner, J. A.; Beer, P. D.; Drew, M. G. B.; Sambrook, M. R., *J. Am. Chem. Soc.* **2002,** *124* (42), 12469-12476.
36. Mercer, D. J.; Loeb, S. J., *Chem. Soc. Rev.* **2010,** *39* (10), 3612-3620.
37. Molina, P.; Zapata, F.; Caballero, A., *Chem. Rev.* **2017,** *117* (15), 9907-9972.
38. Lim, J. Y. C.; Beer, P. D., *Chem* **2018,** *4* (4), 731-783.
39. Schottel, B. L.; Chifotides, H. T.; Dunbar, K. R., *Chem. Soc. Rev.* **2008,** *37* (1), 68-83.
40. Langton, M. J.; Serpell, C. J.; Beer, P. D., *Angew. Chem. Int. Ed.* **2016,** *55* (6), 1974-1987.

41. Schmidtchen, F. P., *Angew. Chem. Int. Ed.* **1977,** *16* (10), 720-721.
42. Graf, E.; Lehn, J. M., *J. Am. Chem. Soc.* **1976,** *98* (20), 6403-6405.
43. Bazzicalupi, C.; Bencini, A.; Giorgi, C.; Valtancoli, B.; Lippolis, V.; Perra, A., *Inorg. Chem.* **2011,** *50* (15), 7202-7216.
44. Dietrich, B.; Fyles, T. M.; Lehn, J.-M.; Pease, L. G.; Fyles, D. L., *J. Chem. Soc., Chem. Commun.* **1978,** (21), 934-936.
45. Kuchelmeister, H. Y.; Schmuck, C., *Chem. Eur. J.* **2011,** *17* (19), 5311-5318.
46. Kataev, E. A.; Müller, C.; Kolesnikov, G. V.; Khrustalev, V. N., *Eur. J. Org. Chem.* **2014,** *2014* (13), 2747-2753.
47. Ngo, H. T.; Liu, X.; Jolliffe, K. A., *Chem. Soc. Rev.* **2012,** *41* (14), 4928-4965.
48. Butler, S. J.; Parker, D., *Chem. Soc. Rev.* **2013,** *42* (4), 1652-1666.
49. Pouessel, J.; Le Bris, N.; Bencini, A.; Giorgi, C.; Valtancoli, B.; Tripier, R., *Dalton Trans.* **2012,** *41* (35), 10521-10532.
50. Liu, Y.; Sengupta, A.; Raghavachari, K.; Flood, A. H., *Chem* **2017,** *3* (3), 411-427.
51. Bhattacharjee, N.; Gao, X.; Nathani, A.; Dobscha, J. R.; Pink, M.; Ito, T.; Flood, A. H., *Chem. Eur. J.* **2023,** *29* (68), e202302339.
52. Shang, J.; Zhao, W.; Li, X.; Wang, Y.; Jiang, H., *Chem. Commun.* **2016,** *52* (24), 4505-4508.
53. Lim, J. Y. C.; Cunningham, M. J.; Davis, J. J.; Beer, P. D., *Chem. Commun.* **2015,** *51* (78), 14640-14643.
54. Carroll, C. N.; Berryman, O. B.; Johnson, C. A.; Zakharov, L. N.; Haley, M. M.; Johnson, D. W., *Chem. Commun.* **2009,** (18), 2520-2522.
55. Bhattacharjee, N.; Gao, X.; Nathani, A.; Dobscha, J. R.; Pink, M.; Ito, T.; Flood, A. H., *Chem. Eur. J. n/a* (n/a), e202302339.
56. Patrick, S. C.; Beer, P. D.; Davis, J. J., *Nat. Rev. Chem.* **2024,** *8*, 256-276.
57. Gilli, G.; Gilli, P., *The Nature of the Hydrogen Bond: Outline of a Comprehensive Hydrogen Bond Theory*. Oxford University Press: 2009.
58. Amendola, V.; Fabbrizzi, L.; Mosca, L., *Chem. Soc. Rev.* **2010,** *39* (10), 3889-3915.
59. Beer, P. D.; Gale, P. A., *Angew. Chem. Int. Ed.* **2001,** *40* (3), 486-516.
60. Cockroft, S. L., *Chem* **2017,** *3* (3), 383-384.
61. Cavallo, G.; Metrangolo, P.; Milani, R.; Pilati, T.; Priimagi, A.; Resnati, G.; Terraneo, G., *Chem. Rev.* **2016,** *116* (4), 2478-2601.
62. Brown, A.; Beer, P. D., *Chem. Commun.* **2016,** *52* (56), 8645-8658.
63. Beale, T. M.; Chudzinski, M. G.; Sarwar, M. G.; Taylor, M. S., *Chem. Soc. Rev.,* **2013,** *42* (4), 1667-1680.
64. Taylor, M. S., *Coord. Chem. Rev.* **2020,** *413*, 213270.
65. Hein, R.; Docker, A.; Davis, J. J.; Beer, P. D., *J. Am. Chem. Soc.* **2022,** *144* (19), 8827-8836.
66. Clark, T.; Hennemann, M.; Murray, J. S.; Politzer, P., *J. Mol. Model.* **2007,** *13* (2), 291-296.
67. Clark, T.; Hennemann, M.; Murray, J. S.; Politzer, P., *J. Mol. Model.* **2007,** *13* (2), 291-296.
68. Docker, A.; Guthrie, C. H.; Kuhn, H.; Beer, P. D., *Angew. Chem. Int. Ed.* **2021,** *60* (40), 21973-21978.
69. Patrick, S. C.; Hein, R.; Beer, P. D.; Davis, J. J., *J. Am. Chem. Soc.* **2021,** *143* (45), 19199-19206.
70. Hijazi, H.; Vacher, A.; Groni, S.; Lorcy, D.; Levillain, E.; Fave, C.; Schöllhorn, B., *Chem. Commun.* **2019,** *55* (13), 1983-1986.
71. Vargas Jentzsch, A.; Emery, D.; Mareda, J.; Metrangolo, P.; Resnati, G.; Matile, S., *Angew. Chem. Int. Ed.* **2011,** *50* (49), 11675-11678.
72. Jentzsch, A. V.; Emery, D.; Mareda, J.; Nayak, S. K.; Metrangolo, P.; Resnati, G.; Sakai, N.; Matile, S., *Nat. Commun.* **2012,** *3* (1), 905.
73. Vargas Jentzsch, A.; Matile, S., *J. Am. Chem. Soc.* **2013,** *135* (14), 5302-5303.
74. Pancholi, J.; Beer, P. D., *Coord. Chem. Rev.* **2020,** *416*, 213281.
75. Mascal, M.; Armstrong, A.; Bartberger, M. D., *J. Am. Chem. Soc.* **2002,** *124* (22), 6274-6276.
76. Zheng, X.; Shuai, Z.; Wang, D., *J. Phys. Chem. A* **2013,** *117* (18), 3844-3851.
77. Berryman, O. B.; Hof, F.; Hynes, M. J.; Johnson, D. W., *Chem. Commun.* **2006,** (5), 506-508.
78. Mascal, M., *Angew. Chem. Int. Ed.* **2006,** *45* (18), 2890-2893.
79. Giese, M.; Albrecht, M.; Rissanen, K., *Chem. Commun.* **2016,** *52* (9), 1778-1795.
80. Guha, S.; Saha, S., *J. Am. Chem. Soc.* **2010,** *132* (50), 17674-17677.

81. Biedermann, F.; Nau, W. M.; Schneider, H.-J., *Angew. Chem. Int. Ed.* **2014,** *53* (42), 11158-11171.
82. Abraham, M. H., *J. Am. Chem. Soc.* **1982,** *104* (8), 2085-2094.
83. Wei, W., *Adv. Sci.* **2023,** *10* (22), 2302057.
84. Wilming, F. M.; Becker, J.; Schreiner, P. R., *J. Org. Chem.* **2022,** *87* (3), 1874-1878.
85. Barendt, T. A.; Ferreira, L.; Marques, I.; Félix, V.; Beer, P. D., *J. Am. Chem. Soc.* **2017,** *139* (26), 9026-9037.
86. Gibb, C. L. D.; Gibb, B. C., *Journal of the American Chemical Society* **2011,** *133* (19), 7344-7347.
87. Zhang, Y.; Furyk, S.; Bergbreiter, D. E.; Cremer, P. S., *J. Am. Chem. Soc.* **2005,** *127* (41), 14505-14510.
88. Assaf, K. I.; Nau, W. M., *Org. Biomol. Chem.* **2023,** *21* (33), 6636-6651.
89. Biedermann, F.; Uzunova, V. D.; Scherman, O. A.; Nau, W. M.; De Simone, A., *J. Am. Chem. Soc.* **2012,** *134* (37), 15318-15323.
90. Oleinikova, A.; Brovchenko, I., *J. Phys. Chem. B* **2012,** *116* (50), 14650-14659.
91. Hummer, G.; Rasaiah, J. C.; Noworyta, J. P., *Nature* **2001,** *414* (6860), 188-190.
92. Sommer, F.; Marcus, Y.; Kubik, S., *ACS Omega* **2017,** *2* (7), 3669-3680.
93. Kubik, S.; Goddard, R.; Kirchner, R.; Nolting, D.; Seidel, J., *Angew. Chem. Int. Ed.* **2001,** *40* (14), 2648-2651.
94. Smithrud, D. B.; Wyman, T. B.; Diederich, F., *J. Am. Chem. Soc.* **1991,** *113* (14), 5420-5426.
95. Van Zee, N. J.; Adelizzi, B.; Mabesoone, M. F. J.; Meng, X.; Aloi, A.; Zha, R. H.; Lutz, M.; Filot, I. A. W.; Palmans, A. R. A.; Meijer, E. W., *Nature* **2018,** *558* (7708), 100-103.
96. Andersen, N. N.; Eriksen, K.; Lisbjerg, M.; Ottesen, M. E.; Milhøj, B. O.; Sauer, S. P. A.; Pittelkow, M., *J. Org. Chem.* **2019,** *84* (5), 2577-2584.
97. Setny, P.; Baron, R.; McCammon, J. A., *J. Chem. Theory Comput.* **2010,** *6* (9), 2866-2871.
98. Assaf, K. I.; Ural, M. S.; Pan, F.; Georgiev, T.; Simova, S.; Rissanen, K.; Gabel, D.; Nau, W. M., *Angew. Chem. Int. Ed.* **2015,** *54* (23), 6852-6856.
99. Assaf, K. I.; Gabel, D.; Zimmermann, W.; Nau, W. M., *Org. Biomol. Chem.* **2016,** *14* (32), 7702-7706.
100. Jungwirth, P.; Cremer, P. S., *Nature Chem.* **2014,** *6* (4), 261-263.
101. Thilgen, C., *Angew. Chem. Int. Ed.* **2012,** *51* (3), 587-589.
102. Tang, D.; Dwyer, T.; Bukannan, H.; Blackmon, O.; Delpo, C.; Barnett, J. W.; Gibb, B. C.; Ashbaugh, H. S., *J. Phys. Chem. B* **2020,** *124* (23), 4781-4792.
103. Chandler, D., *Nature* **2005,** *437* (7059), 640-647.
104. Lum, K.; Chandler, D.; Weeks, J. D., *J. Phys. Chem. B* **1999,** *103* (22), 4570-4577.
105. Pflugrath, J. W.; Quiocho, F. A., *Nature* **1985,** *314* (6008), 257-260.
106. Pflugrath, J. W.; Quiocho, F. A., *J. Mol. Biol.* **1988,** *200* (1), 163-180.
107. Chakrabarti, P., *J. Mol. Biol.* **1993,** *234* (2), 463-482.
108. Kauzmann, W., Some Factors in the Interpretation of Protein Denaturation. In *Advances in Protein Chemistry*, Anfinsen, C. B.; Anson, M. L.; Bailey, K.; Edsall, J. T., Eds. Academic Press: 1959; Vol. 14, pp 1-63.
109. Fernández, A.; Crespo, A., *Chem. Soc. Rev.* **2008,** *37* (11), 2373-2382.
110. Liu, Y.; Parks, F. C.; Sheetz, E. G.; Chen, C.-H.; Flood, A. H., *J. Am. Chem. Soc.* **2021,** *143* (8), 3191-3204.
111. Custelcean, R., *Chem. Soc. Rev.* **2014,** *43* (6), 1813-1824.
112. Liu, Y.; Zhao, W.; Chen, C.-H.; Flood, A. H., *Science* **2019,** *365* (6449), 159-161.
113. Fiala, T.; Sleziakova, K.; Marsalek, K.; Salvadori, K.; Sindelar, V., *J. Org. Chem.* **2018,** *83* (4), 1903-1912.
114. Bruns, C. J., Stoddart, J.F., An Introduction to the Mechanical Bond. In *The Nature of the Mechanical Bond*, Wiley: 2016; pp 1-54.
115. Wilmore, J. T.; Beer, P. D., *Adv. Mater. n/a* (n/a), 2309098.
116. Langton, M. J.; Robinson, S. W.; Marques, I.; Félix, V.; Beer, P. D., *Nat. Chem.* **2014,** *6* (12), 1039-1043.
117. Zhukov, A.; Karlsson, R., *J. Mol. Recognit.* **2007,** *20* (5), 379-385.
118. Lutolli, A.; Che, M.; Parks, F. C.; Raghavachari, K.; Flood, A. H., *J. Org. Chem.* **2023,** *88* (11), 6791-6804.
119. Suk, J.-m.; Jeong, K.-S., *J. Am. Chem. Soc.* **2008,** *130* (36), 11868-11869.

120. Hua, Y.; Liu, Y.; Chen, C.-H.; Flood, A. H., *J. Am. Chem. Soc.* **2013,** *135* (38), 14401-14412.
121. Borissov, A.; Lim, J. Y. C.; Brown, A.; Christensen, K. E.; Thompson, A. L.; Smith, M. D.; Beer, P. D., *Chem. Commun.* **2017,** *53* (16), 2483-2486.
122. Borissov, A.; Marques, I.; Lim, J. Y. C.; Félix, V.; Smith, M. D.; Beer, P. D., *J. Am. Chem. Soc.* **2019,** *141* (9), 4119-4129.
123. Nicola, J. P.; Carrasco, N.; Mario Amzel, L., *Nat. Commun.* **2014,** *5* (1), 3948.
124. Sethumadhavan, V.; Rudd, S.; Switalska, E.; Zuber, K.; Teasdale, P.; Evans, D., *BMC Mater.* **2019,** *1* (1), 4.
125. Adhikari, B.; Majumdar, S., *Prog. Polym. Sci.* **2004,** *29* (7), 699-766.
126. Lange, U.; Roznyatovskaya, N. V.; Mirsky, V. M., *Anal. Chim. Acta* **2008,** *614* (1), 1-26.
127. Pensa, E.; Cortés, E.; Corthey, G.; Carro, P.; Vericat, C.; Fonticelli, M. H.; Benítez, G.; Rubert, A. A.; Salvarezza, R. C., *Acc. Chem. Res.* **2012,** *45* (8), 1183-1192.
128. Hetemi, D.; Noël, V.; Pinson, J., *Biosensors* **2020,** *10* (1), 4.
129. Romieu, A.; Massif, C.; Rihn, S.; Ulrich, G.; Ziessel, R.; Renard, P.-Y., *New J. Chem.* **2013,** *37* (4), 1016-1027.
130. Dong, J.; Davis, A. P., *Angew. Chem. Int. Ed.* **2021,** *60* (15), 8035-8048.
131. Johnson, R. D.; Gavalas, V. G.; Daunert, S.; Bachas, L. G., *Anal. Chim. Acta* **2008,** *613* (1), 20-30.
132. Gooding, J. J.; Mearns, F.; Yang, W.; Liu, J., *Electroanalysis* **2003,** *15* (2), 81-96.
133. Mandler, D.; Turyan, I., *Electroanalysis* **1996,** *8* (3), 207-213.
134. Yi, R.; Mao, Y.; Shen, Y.; Chen, L., *J. Am. Chem. Soc.* **2021,** *143* (33), 12897-12912.
135. Patrick, S. C.; Hein, R.; Docker, A.; Beer, P. D.; Davis, J. J., *Chem. Eur. J.* **2021,** *27* (39), 10201-10209.
136. Hein, R.; Borissov, A.; Smith, M. D.; Beer, P. D.; Davis, J. J., *Chem. Commun.* **2019,** *55* (33), 4849-4852.
137. Beer, P. D.; Davis, J. J.; Drillsma-Milgrom, D. A.; Szemes, F., *Chemical Communications* **2002,** (16), 1716-1717.
138. Cormode, D. P.; Evans, A. J.; Davis, J. J.; Beer, P. D., *Dalton Trans.* **2010,** *39* (28), 6532-6541.
139. Beer, P. D.; Davis, J. J.; Drillsma-Milgrom, D. A.; Szemes, F., *Chem. Commun.* **2002,** (16), 1716-1717.
140. Hijazi, H.; Vacher, A.; Groni, S.; Lorcy, D.; Levillain, E.; Fave, C.; Schöllhorn, B., *Chem. Commun.* **2019,** *55* (13), 1983-1986.
141. Hein, R.; Li, X.; Beer, P. D.; Davis, J. J., *Chem. Sci.* **2021,** *12* (7), 2433-2440.
142. Bickerton, L. E.; Johnson, T. G.; Kerckhoffs, A.; Langton, M. J., *Chem. Sci.* **2021,** *12* (34), 11252-11274.
143. Doyle, E. L.; Hunter, C. A.; Phillips, H. C.; Webb, S. J.; Williams, N. H., *J. Am. Chem. Soc.* **2003,** *125* (15), 4593-4599.
144. Voskuhl, J.; Ravoo, B. J., *Chem. Soc. Rev.* **2009,** *38* (2), 495-505.
145. Neal, J. F.; Zhao, W.; Grooms, A. J.; Flood, A. H.; Allen, H. C., *J. Phys. Chem. C* **2018,** *122* (46), 26362-26371.
146. Wu, X.; Wang, P.; Lewis, W.; Jiang, Y.-B.; Gale, P. A., *Nat. Commun.* **2022,** *13* (1), 4623.
147. Lou, B.; Chen, C.; Zhou, Z.; Zhang, L.; Wang, E.; Dong, S., *Talanta* **2013,** *105*, 40-45.
148. Bakker, E.; Telting-Diaz, M., *Anal. Chem.* **2002,** *74* (12), 2781-2800.
149. Privett, B. J.; Shin, J. H.; Schoenfisch, M. H., *Anal. Chem.* **2010,** *82* (12), 4723-4741.
150. Hein, R.; Beer, P. D.; Davis, J. J., *Chem. Rev.* **2020,** *120* (3), 1888-1935.
151. Hein, R.; Beer, P. D.; Davis, J. J., *Chem. Rev.* **2020,** *120* (3), 1888-1935.
152. Xiao, K. P.; Bühlmann, P.; Nishizawa, S.; Amemiya, S.; Umezawa, Y., *Anal. Chem.* **1997,** *69* (6), 1038-1044.
153. Nishizawa, S.; Bühlmann, P.; Xiao, K. P.; Umezawa, Y., *Anal. Chim. Acta* **1998,** *358* (1), 35-44.
154. Carey, C. M.; Riggan, W. B., *Anal. Chem.* **1994,** *66* (21), 3587-3591.
155. Zahran, E. M.; Hua, Y.; Lee, S.; Flood, A. H.; Bachas, L. G., *Anal. Chem.* **2011,** *83* (9), 3455-3461.
156. Zahran, E. M.; Fatila, E. M.; Chen, C.-H.; Flood, A. H.; Bachas, L. G., *Anal. Chem.* **2018,** *90* (3), 1925-1933.
157. Antonisse, M. M. G.; Reinhoudt, D. N., *Electroanalysis* **1999,** *11* (14), 1035-1048.
158. Bakker, E.; Bühlmann, P.; Pretsch, E., *Chem. Rev.* **1997,** *97* (8), 3083-3132.

159. Sun, R.; Wang, L.; Yu, H.; Abdin, Z.-u.; Chen, Y.; Huang, J.; Tong, R., *Organometallics* **2014,** *33* (18), 4560-4573.
160. Beer, P. D.; Chen, Z.; Goulden, A. J.; Graydon, A.; Stokes, S. E.; Wear, T., *J. Chem. Soc., Chem. Commun.* **1993,** (24), 1834-1836.
161. Beer, P. D.; Keefe, A. D., *J. Organomet. Chem.* **1989,** *375* (1), C40-C42.
162. Canevet, D.; Sallé, M.; Zhang, G.; Zhang, D.; Zhu, D., *Chem. Commun.* **2009,** (17), 2245-2269.
163. Schröder, H. V.; Schalley, C. A., *Beilstein J. Org. Chem.* **2018,** *14*, 2163-2185.
164. Nielsen, K. A.; Jeppesen, J. O.; Levillain, E.; Becher, J., *Angew. Chem. Int. Ed.* **2003,** *42* (2), 187-191.
165. Lee, M. H.; Cao, Q.-Y.; Kim, S. K.; Sessler, J. L.; Kim, J. S., *J. Org. Chem.* **2011,** *76* (3), 870-874.
166. Biesaga, M.; Pyrzyńska, K.; Trojanowicz, M., *Talanta* **2000,** *51* (2), 209-224.
167. Bhaumik, C.; Saha, D.; Das, S.; Baitalik, S., *Inorg. Chem.* **2011,** *50* (24), 12586-12600.
168. Bhaumik, C.; Maity, D.; Das, S.; Baitalik, S., *Polyhedron* **2013,** *52*, 890-899.
169. Lehr, J.; Lang, T.; Blackburn, O. A.; Barendt, T. A.; Faulkner, S.; Davis, J. J.; Beer, P. D., *Chem. Eur. J.* **2013,** *19* (47), 15898-15906.
170. Beer, P. D.; Berry, N.; Drew, M. G. B.; Fox, O. D.; Padilla-Tosta, M. E.; Patell, S., *Chem. Commun.* **2001,** (2), 199-200.
171. Clare, J. P.; Statnikov, A.; Lynch, V.; Sargent, A. L.; Sibert, J. W., *J. Org. Chem.* **2009,** *74* (17), 6637-6646.
172. Mullaney, B. R.; Cunningham, M. J.; Davis, J. J.; Beer, P. D., *Polyhedron* **2016,** *116*, 20-25.
173. Creste, G.; Groni, S.; Fave, C.; Branca, M.; Schöllhorn, B., *Faraday Discuss.* **2017,** *203* (0), 301-313.
174. Astruc, D., *Eur. J. Inorg. Chem.* **2017,** *2017* (1), 6-29.
175. Beer, P. D.; Gale, P. A.; Chen, G. Z., *Coord. Chem. Rev.* **1999,** *185-186*, 3-36.
176. D. Beer, P.; A. Gale, P.; Z. Chen, G., *J. Chem. Soc., Dalton Trans.* **1999,** (12), 1897-1910.
177. Cao, Q.-Y.; Pradhan, T.; Kim, S.; Kim, J. S., *Org. Lett.* **2011,** *13* (16), 4386-4389.
178. Oliveira, R.; Groni, S.; Fave, C.; Branca, M.; Mavré, F.; Lorcy, D.; Fourmigué, M.; Schöllhorn, B., *Phys. Chem. Chem. Phys.* **2016,** *18* (23), 15867-15873.
179. Hein, D. R. Electrochemical Anion Sensing in Solution and at Receptive Interfaces. University of Oxford, 2020.
180. Lim, J. Y. C.; Cunningham, M. J.; Davis, J. J.; Beer, P. D., *Chem. Commun.* **2015,** *51* (78), 14640-14643.
181. Lim, J. Y. C.; Beer, P. D., *Eur. J. Inorg. Chem.* **2017,** *2017* (2), 220-224.
182. Hein, R.; Borissov, A.; Smith, M. D.; Beer, P. D.; Davis, J. J., *Chem. Commun.* **2019,** *55* (33), 4849-4852.
183. Ebdelli, R.; Rouis, A.; Mlika, R.; Bonnamour, I.; Jaffrezic-Renault, N.; Ben Ouada, H.; Davenas, J., *J. Electroanal. Chem.* **2011,** *661* (1), 31-38.
184. Flink, S.; van Veggel, F. C. J. M.; Reinhoudt, D. N., *J. Phys. Chem. B* **1999,** *103* (31), 6515-6520.
185. Flink, S.; Boukamp, B. A.; van den Berg, A.; van Veggel, F. C. J. M.; Reinhoudt, D. N., *J. Am. Chem. Soc.* **1998,** *120* (19), 4652-4657.
186. Wanichacheva, N.; Soto, E. R.; Lambert, C. R.; McGimpsey, W. G., *Analytical Chemistry* **2006,** *78* (20), 7132-7137.
187. Zhang, S.; Echegoyen, L., *J. Am. Chem. Soc.* **2005,** *127* (6), 2006-2011.
188. Zhang, S.; Palkar, A.; Echegoyen, L., *Langmuir* **2006,** *22* (25), 10732-10738.
189. Zhi, F.; Lu, X.; Yang, J.; Wang, X.; Shang, H.; Zhang, S.; Xue, Z., *J. Phys. Chem. C* **2009,** *113* (30), 13166-13172.
190. Wei, J.; Guo, Z.; Chen, X.; Han, D.-D.; Wang, X.-K.; Huang, X.-J., *Anal. Chem.* **2015,** *87* (3), 1991-1998.
191. Piccoli, J.; Hein, R.; El-Sagheer, A. H.; Brown, T.; Cilli, E. M.; Bueno, P. R.; Davis, J. J., *Anal. Chem.* **2018,** *90* (5), 3005-3008.
192. Santos, A.; Bueno, P. R.; Davis, J. J., *Biosens. Bioelectron.* **2018,** *100*, 519-525.
193. Bueno, P. R., *Anal. Chem.* **2018,** *90* (12), 7095-7106.
194. Garrote, B. L.; Santos, A.; Bueno, P. R., *ACS Sens.* **2019,** *4* (9), 2216-2227.

195. Ion, A. C.; Moutet, J.-C.; Pailleret, A.; Popescu, A.; Saint-Aman, E.; Siebert, E.; Ungureanu, E. M., *J. Electroanal. Chem.* **1999,** *464* (1), 24-30.
196. Dong, Y.-D.; Zhang, H.; Zhong, G.-J.; Yao, G.; Lai, B., *J. Chem. Eng.* **2021,** *405*, 126980.
197. Chandel, N.; Jain, K.; Jain, A.; Raj, T.; Patel, A. K.; Yang, Y.-H.; Bhatia, S. K., *Ind. Crops Prod.* **2023,** *201*, 116929.
198. Rostami, A.; Taylor, M. S., *Macromol. Rapid Commun.* **2012,** *33* (1), 21-34.
199. Huang, F.; Scherman, O. A., *Chem. Soc. Rev.* **2012,** *41* (18), 5879-5880.
200. Huo, Y.; He, Z.; Wang, C.; Zhang, L.; Xuan, Q.; Wei, S.; Wang, Y.; Pan, D.; Dong, B.; Wei, R.; Naik, N.; Guo, Z., *Chem. Commun.* **2021,** *57* (12), 1413-1429.
201. Liu, Y.; Wang, Z.; Zhang, X., *Chem. Soc. Rev.* **2012,** *41* (18), 5922-5932.
202. McDonald, K. P.; Qiao, B.; Twum, E. B.; Lee, S.; Gamache, P. J.; Chen, C.-H.; Yi, Y.; Flood, A. H., *Chem. Commun.* **2014,** *50* (87), 13285-13288.
203. Rogers, B. A.; Okur, H. I.; Yan, C.; Yang, T.; Heyda, J.; Cremer, P. S., *Nat. Chem.* **2022,** *14* (1), 40-45.
204. Rembert, K. B.; Okur, H. I.; Hilty, C.; Cremer, P. S., *Langmuir* **2015,** *31* (11), 3459-3464.
205. Kakuchi, R.; Nagata, S.; Sakai, R.; Otsuka, I.; Nakade, H.; Satoh, T.; Kakuchi, T., *Chem. Eur. J.* **2008,** *14* (33), 10259-10266.
206. Sakai, R.; Okade, S.; Barasa, E. B.; Kakuchi, R.; Ziabka, M.; Umeda, S.; Tsuda, K.; Satoh, T.; Kakuchi, T., *Macromolecules* **2010,** *43* (18), 7406-7411.
207. Aydogan, A.; Coady, D. J.; Kim, S. K.; Akar, A.; Bielawski, C. W.; Marquez, M.; Sessler, J. L., *Angew. Chem. Int. Ed.* **2008,** *47* (50), 9648-9652.
208. Tong, H.; Wang, L.; Jing, X.; Wang, F., *Macromolecules* **2003,** *36* (8), 2584-2586.
209. Bickerton, L. E.; Docker, A.; Sterling, A. J.; Kuhn, H.; Duarte, F.; Beer, P. D.; Langton, M. J., *Chem. Eur. J.* **2021,** *27* (45), 11738-11745.
210. Hein, R.; Li, X.; Beer, P. D.; Davis, J. J., *Chem. Sci.* **2021,** *12* (7), 2433-2440.
211. Perrier, S., *Macromolecules* **2017,** *50* (19), 7433-7447.
212. Beckwith, A. L. J.; Leydon, R. J., *Tetrahedron Letters* **1963,** *4* (6), 385-388.
213. Nuyken, O.; Pask, S. D., *Polymers* **2013,** *5* (2), 361-403.
214. Matyjaszewski, K.; Xia, J., *Chem. Rev.* **2001,** *101* (9), 2921-2990.
215. Moad, G.; Rizzardo, E.; Thang, S. H., *Polymer* **2008,** *49* (5), 1079-1131.
216. Vancoillie, G.; Frank, D.; Hoogenboom, R., *Prog. Polym. Sci.* **2014,** *39* (6), 1074-1095.
217. Herfurth, C.; Voll, D.; Buller, J.; Weiss, J.; Barner-Kowollik, C.; Laschewsky, A., *J. Polym. Sci. A Polym. Chem.* **2012,** *50* (1), 108-118.
218. George, M. H.; Hayes, G. F., *Journal of Polymer Science: Polymer Chemistry Edition* **1975,** *13* (5), 1049-1070.
219. Jiang, X.; Li, R.; Feng, C.; Lu, G.; Huang, X., *Polym. Chem.* **2017,** *8* (18), 2773-2784.
220. Saleem, M.; Wang, L.; Yu, H.; Zain ul, A., *Arab. J. Chem.* **2019,** *12* (6), 800-815.
221. Nguema Edzang, R. W.; Lejars, M.; Brisset, H.; Raimundo, J. M.; Bressy, C., *RSC Adv.* **2015,** *5* (94), 77019-77026.
222. Tian, C.; Wang, P.; Ni, Y.; Zhang, L.; Cheng, Z.; Zhu, X., *Angew. Chem. Int. Ed.* **2020,** *59* (10), 3910-3916.
223. Marcus, Y., *Inc, New York* **1997**, 1-33.
224. Bąk, K. M.; Patrick, S. C.; Li, X.; Beer, P. D.; Davis, J. J., *Angew. Chem. Int. Ed.* **2023,** *62* (14), e202300867.
225. Wolters, L. P.; Schyman, P.; Pavan, M. J.; Jorgensen, W. L.; Bickelhaupt, F. M.; Kozuch, S., *WIREs Comput. Mol. Sci.* **2014,** *4* (6), 523-540.
226. Lim, J. Y. C.; Beer, P. D., *Eur. J. Inorg. Chem.* **2017,** *2017* (2), 220-224.
227. Patrick, S. C.; Hein, R.; Docker, A.; Beer, P. D.; Davis, J. J., *Chemistry – A European Journal* **2021,** *27* (39), 10201-10209.
228. Beer, P. D.; Gale, P. A.; Chen, G. Z., *Coord. Chem. Rev.* **1999,** *185-186*, 3-36.
229. Miller, S. R.; Gustowski, D. A.; Chen, Z. H.; Gokel, G. W.; Echegoyen, L.; Kaifer, A. E., *Analytical Chemistry* **1988,** *60* (19), 2021-2024.
230. Oliveira, R.; Groni, S.; Fave, C.; Branca, M.; Mavre, F.; Lorcy, D.; Fourmigue, M.; Schollhorn, B., *Phys. Chem. Chem. Phys.* **2016,** *18* (23), 15867-15873.
231. Busschaert, N.; Caltagirone, C.; Van Rossom, W.; Gale, P. A., *Chemical Reviews* **2015,** *115* (15), 8038-8155.
232. Langton, M. J.; Serpell, C. J.; Beer, P. D., *Angew. Chem. Int. Ed.* **2016,** *55* (6), 1974-1987.

233. Bakker, E.; Telting-Diaz, M., *Analytical Chemistry* **2002,** *74* (12), 2781-2800.
234. Bobacka, J.; Ivaska, A.; Lewenstam, A., *Chemical Reviews* **2008,** *108* (2), 329-351.
235. Zdrachek, E.; Bakker, E., *Analytical Chemistry* **2019,** *91* (1), 2-26.
236. Parrilla, M.; Cuartero, M.; Crespo, G. A., *TrAC, Trends Anal. Chem.* **2019,** *110*, 303-320.
237. Bühlmann, P.; Pretsch, E.; Bakker, E., *Chemical Reviews* **1998,** *98* (4), 1593-1688.
238. Bakker, E.; Bühlmann, P.; Pretsch, E., *Electroanalysis* **1999,** *11* (13), 915-933.
239. Etkind, S. I.; Vander Griend, D. A.; Swager, T. M., *The Journal of Organic Chemistry* **2020,** *85* (15), 10050-10061.
240. Evans, N. H.; Serpell, C. J.; White, N. G.; Beer, P. D., *Chem. Eur. J.* **2011,** *17* (44), 12347-12354.
241. Romero, T.; Orenes, R. A.; Tarraga, A.; Molina, P., *Organometallics* **2013,** *32* (20), 5740-5753.
242. Reynes, O.; Maillard, F.; Moutet, J.-C.; Royal, G.; Saint-Aman, E.; Stanciu, G.; Dutasta, J.-P.; Gosse, I.; Mulatier, J.-C., *J. Organomet. Chem.* **2001,** *637*, 356-363.
243. Lim, J. Y. C.; Beer, P. D., *Eur. J. Org. Chem.* **2019,** *2019*, 3433-3441.
244. Lim, J. Y. C.; Beer, P. D., *Eur. J. Inorg. Chem.* **2017,** *2017* (2), 220-224.
245. Zapata, F.; Caballero, A.; Molina, P., *Eur. J. Inorg. Chem.* **2017,** *2017* (2), 237-241.
246. Tse, Y. C.; Hein, R.; Mitchell, E. J.; Zhang, Z.; Beer, P. D., *Chem. Eur. J.* **2021**, DOI: 10.1002/chem.202102493.
247. Zaleskaya, M.; Jagleniec, D.; Karbarz, M.; Dobrzycki, Ł.; Romański, J., *Inorganic Chemistry Frontiers* **2020,** *7* (4), 972-983.
248. Alfonso, M.; Espinosa Ferao, A.; Tárraga, A.; Molina, P., *Inorg. Chem.* **2015,** *54* (15), 7461-7473.
249. Reynes, O.; Bucher, C.; Moutet, J.-C.; Royal, G.; Saint-Aman, E., *Chemical Communications* **2004,** (4), 428-429.
250. Lehr, J.; Lang, T.; Blackburn, O. A.; Barendt, T. A.; Faulkner, S.; Davis, J. J.; Beer, P. D., *Chem. Eur. J.* **2013,** *19* (47), 15898-15906.
251. Beer, P. D.; Davis, J. J.; Drillsma-Milgrom, D. A.; Szemes, F., *Chem. Commun.* **2002,** (16), 1716-1717.
252. Adam, C.; Faour, L.; Bonnin, V.; Breton, T.; Levillain, E.; Sallé, M.; Gautier, C.; Canevet, D., *Chem. Commun.* **2019,** *55* (58), 8426-8429.
253. Hijazi, H.; Vacher, A.; Groni, S.; Lorcy, D.; Levillain, E.; Fave, C.; Schollhorn, B., *Chem. Commun.* **2019,** *55* (13), 1983-1986.
254. Kaur, B.; Erdmann, C. A.; Daniëls, M.; Dehaen, W.; Rafiński, Z.; Radecka, H.; Radecki, J., *Analytical Chemistry* **2017,** *89* (23), 12756-12763.
255. Blanchard, P.-Y.; Boisard, S.; Dias, M.; Breton, T.; Gautier, C.; Levillain, E., *Langmuir* **2012,** *28* (33), 12067-12070.
256. Kasprzak, A.; Kowalczyk, A.; Jagielska, A.; Wagner, B.; Nowicka, A. M.; Sakurai, H., *Dalton Trans.* **2020,** *49* (29), 9965-9971.
257. Evans, N. H.; Rahman, H.; Davis, J. J.; Beer, P. D., *Analytical and Bioanalytical Chemistry* **2012,** *402* (5), 1739-1748.
258. Popenoe, D. D.; Deinhammer, R. S.; Porter, M. D., *Langmuir* **1992,** *8* (10), 2521-2530.
259. Prins, R.; Korswagen, A. R.; Kortbeek, A. G. T. G., *J. Organomet. Chem.* **1972,** *39* (2), 335-344.
260. Valincius, G.; Niaura, G.; Kazakevičienė, B.; Talaikytė, Z.; Kažemėkaitė, M.; Butkus, E.; Razumas, V., *Langmuir* **2004,** *20* (16), 6631-6638.
261. Zhang, L.; Godínez, L. A.; Lu, T.; Gokel, G. W.; Kaifer, A. E., *Angew. Chem. Int. Ed.* **1995,** *34* (2), 235-237.
262. Kütt, A.; Rodima, T.; Saame, J.; Raamat, E.; Mäemets, V.; Kaljurand, I.; Koppel, I. A.; Garlyauskayte, R. Y.; Yagupolskii, Y. L.; Yagupolskii, L. M.; Bernhardt, E.; Willner, H.; Leito, I., *J. Org. Chem.* **2011,** *76* (2), 391-395.
263. Swenson, H.; Stadie, N. P., *Langmuir* **2019,** *35* (16), 5409-5426.
264. Ayawei, N.; Ebelegi, A. N.; Wankasi, D., *J. Chem.* **2017,** *2017* (1), 3039817.
265. Osteryoung, J. G.; Osteryoung, R. A., *Anal. Chem.* **1985,** *57* (1), 101-110.
266. Alévêque, O.; Levillain, E., *Electrochem. Commun.* **2015,** *51*, 137-143.
267. Alévêque, O.; Levillain, E., *Electrochem. Commun.* **2016,** *67*, 73-79.
268. Suman, S.; Singh, R., *Microchem. J.* **2019**, 104045.
269. Gale, P. A.; Caltagirone, C., *Chem. Soc. Rev.* **2015,** *44* (13), 4212-4227.

270. Evans, N. H.; Serpell, C. J.; Christensen, K. E.; Beer, P. D., *Eur. J. Inorg. Chem.* **2012,** *2012* (6), 939-944.
271. Sophie C. Patrick, R. H., Mohamed Sharafeldin, Xiaoxiong Li, Paul D. Beer, Jason J. Davis, *ChemRxiv* **2021**, DOI: 10.33774/chemrxiv-2021-2nqwc.
272. Choi, S. J.; Yoon, B.; Ray, J. D.; Netchaev, A.; Moores, L. C.; Swager, T. M., *Adv. Funct. Mater.* **2020,** *30* (7), 1907087.
273. Bueno, P. R.; Hein, R.; Santos, A.; Davis, J. J., *Phys. Chem. Chem. Phys.* **2020,** *22* (7), 3770-3774.
274. Zhang, S.; Echegoyen, L., *J. Am. Chem. Soc.* **2005,** *127* (6), 2006-2011.
275. Zhang, S.; Palkar, A.; Echegoyen, L., *Langmuir* **2006,** *22* (25), 10732-10738.
276. Shervedani, R. K.; Pourbeyram, S., *Biosens. Bioelectron.* **2009,** *24* (7), 2199-2204.
277. Zhi, F.; Lu, X.; Yang, J.; Wang, X.; Shang, H.; Zhang, S.; Xue, Z., *J. Phys. Chem. C* **2009,** *113* (30), 13166-13172.
278. Wei, J.; Guo, Z.; Chen, X.; Han, D.-D.; Wang, X.-K.; Huang, X.-J., *Anal. Chem.* **2015,** *87* (3), 1991-1998.
279. Daniels, J. S.; Pourmand, N., *Electroanalysis* **2007,** *19* (12), 1239-1257.
280. Chang, B.-Y.; Park, S.-M., *Annu. Rev. Anal. Chem.* **2010,** *3*, 207-229.
281. Xu, Q.; Davis, J. J., *Electroanalysis* **2014,** *26* (6), 1249-1258.
282. Kanyong, P.; Patil, A. V.; Davis, J. J., *Annu. Rev. Anal. Chem.* **2020,** *13*, 183-200.
283. Laschuk, N. O.; Easton, E. B.; Zenkina, O. V., *RSC Advances* **2021,** *11* (45), 27925-27936.
284. Piccoli, J.; Hein, R.; El-Sagheer, A. H.; Brown, T.; Cilli, E. M.; Bueno, P. R.; Davis, J. J., *Anal. Chem.* **2018,** *90* (5), 3005-3008.
285. Santos, A.; Bueno, P. R.; Davis, J. J., *Biosens. Bioelectron.* **2018,** *100*, 519-525.
286. Baradoke, A.; Hein, R.; Li, X.; Davis, J. J., *Anal. Chem.* **2020,** *92* (5), 3508-3511.
287. Lehr, J.; Fernandes, F. C. B.; Bueno, P. R.; Davis, J. J., *Anal. Chem.* **2014,** *86* (5), 2559-2564.
288. Chatterjee, S.; Sengupta, K.; Bandyopadhyay, S.; Dey, A., *J. Mater. Chem. A* **2016,** *4* (18), 6819-6823.
289. Wanichacheva, N.; Soto, E. R.; Lambert, C. R.; McGimpsey, W. G., *Anal. Chem.* **2006,** *78* (20), 7132-7137.
290. Izatt, R. M.; Bradshaw, J. S.; Nielsen, S. A.; Lamb, J. D.; Christensen, J. J.; Sen, D., *Chem. Rev.* **1985,** *85* (4), 271-339.
291. Rouhana, L. L.; Moussallem, M. D.; Schlenoff, J. B., *J. Am. Chem. Soc.* **2011,** *133* (40), 16080-16091.
292. Porter, M. D.; Bright, T. B.; Allara, D. L.; Chidsey, C. E. D., *J. Am. Chem. Soc.* **1987,** *109* (12), 3559-3568.
293. Bard, A. J.; Faulkner, L. R.; White, H. S., *Electrochemical methods: fundamentals and applications*. John Wiley & Sons: 2022.
294. Bueno, P. R.; Hein, R.; Santos, A.; Davis, J. J., *Phys. Chem. Chem. Phys.* **2020,** *22* (7), 3770-3774.
295. Cram, D. J., *Angew. Chem. Int. Ed.* **1988,** *27* (8), 1009-1020.
296. Góes, M. S.; Rahman, H.; Ryall, J.; Davis, J. J.; Bueno, P. R., *Langmuir* **2012,** *28* (25), 9689-9699.
297. Lehr, J.; Weeks, J. R.; Santos, A.; Feliciano, G. T.; Nicholson, M. I. G.; Davis, J. J.; Bueno, P. R., *Phys. Chem. Chem. Phys.* **2017,** *19* (23), 15098-15109.
298. Morita, K.; Yamaguchi, A.; Teramae, N., *J. Electroanal. Chem.* **2004,** *563* (2), 249-255.
299. Wagner-Czauderna, E.; Koczorowska, A.; Kalinowski, M. K., *J. Coord. Chem.* **1999,** *46* (3), 265-276.
300. Pedersen, C. J.; Frensdorff, H. K., *Angew. Chem. Int. Ed.* **1972,** *11* (1), 16-25.
301. Lim, H.-R.; Kim, Y.-S.; Kwon, S.; Mahmood, M.; Kwon, Y.-T.; Lee, Y.; Lee, S. M.; Yeo, W.-H., *Sensors* **2020,** *20* (11), 3297.
302. Midgley, D., *Transactions of the Institute of Measurement and Control* **1987,** *9* (1), 25-36.
303. Patrick, S. C.; Hein, R.; Sharafeldin, M.; Li, X.; Beer, P. D.; Davis, J. J., *Chem. Eur. J.* **2021,** *27* (70), 17700-17706.
304. Lehn, J. M.; Sauvage, J. P., *J. Chem. Soc. D* **1971,** (9), 440-441.
305. Dimeski, G.; Badrick, T.; John, A. S., *Clin. Chim. Acta.* **2010,** *411* (5), 309-317.
306. Baker, L. B.; Chavez, P. J. D. D.; Nuccio, R. P.; Brown, S. D.; King, M. A.; Sopeña, B. C.; Barnes, K. A., *J. Appl. Physiol.* **2022,** *133* (6), 1250-1259.

307. Monteith, D.; Norris, D.; Murphy, J.; Jones, I.; Juggins, S.; Shilland, E.; Battarbee, R.; Henderson, G.; Pretty, J.; Tomlinson, S., **2022**.
308. Bowes, M. J.; Armstrong, L. K.; Harman, S. A.; Wickham, H. D.; Nicholls, D. J.; Scarlett, P. M.; Roberts, C.; Jarvie, H. P.; Old, G. H.; Gozzard, E., *Earth Syst. Sci. Data* **2018,** *10* (3), 1637-1653.
309. Water, T. Water Quality Report for OX1 3QZ. https://www.thameswater.co.uk/help/water-quality/check-your-water-quality#/results/OX13QZ (accessed 18/03/2024).
310. Lehn, J.; Sauvage, J., *J. Chem. Soc. D* **1971,** (9), 440-441.
311. Min Tay, H.; Docker, A.; Cheong Tse, Y.; Beer, P. D., *Chem. Eur. J.* **2023,** *29* (43), e202301316.
312. Brynn Hibbert, D.; Thordarson, P., *Chem. Commun.* **2016,** *52* (87), 12792-12805, http://supramolecular.org.
313. Blum, M.-M.; John, H., *Drug Test Anal.* **2012,** *4* (3-4), 298-302.
314. Oliveira, R.; Groni, S.; Vacher, A.; Barrière, F.; Lorcy, D.; Fourmigué, M.; Maisonhaute, E.; Schöllhorn, B.; Fave, C., *ChemistrySelect* **2018,** *3* (31), 8874-8880.
315. Hoogvliet, J. C.; Dijksma, M.; Kamp, B.; van Bennekom, W. P., *Anal. Chem.* **2000,** *72* (9), 2016-2021.
316. Zill, A. T.; Zimmerman, S. C., *Isr. J. Chem.* **2009,** *49* (1), 71-78.
317. Wu, X.; Wu, W.; Cui, X.; Zhao, J.; Wu, M., *J. Mat. Chem. C* **2016,** *4* (14), 2843-2853.
318. Bąk, K. M.; Patrick, S. C.; Li, X.; Beer, P. D.; Davis, J. J., *Angew. Chem. Int. Ed.* **2023,** *62* (14), e202300867.

Appendices

Appendices:

A1 Appendices for Chapter 1

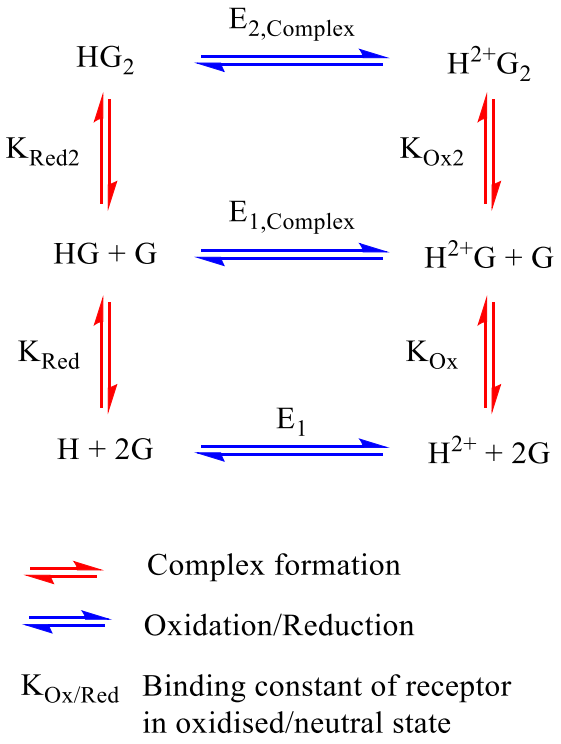


Figure A1.1. Square scheme describing the binding and redox equilibria involved in 1:2 host-guest binding with a host bearing two, one-electron redox transducers.

Derivation of 1:2 host-guest binding isotherm based on the Nernst equation and square scheme shown in Figure A1.1. Assuming that the binding reactions happen on an extremely fast timescale with respects to the electrochemical perturbation, the binding reaction equilibria are always at dynamic equilibrium during the electrochemical perturbation. Therefore, each binding reaction can be described by the Nernst equation as a single redox couple with an apparent standard potential, E˚ in Nernst equation (Eqn A1.1).

$$E = E^{\circ} + \frac{RT}{nF}\ln\left(\frac{[H_{Ox}]+[HG_{Ox}]+[H2G_{Ox}]}{[H_{Red}]+[HG_{Red}]+[H2G_{Red}]}\right) \qquad \textbf{Equation A1.1}$$

Another assumption is that that mass action laws are always satisfied for all binding equilibria.

$$K_{Ox} = \frac{[HG_{Ox}]_{eq}}{[H_{Ox}]_{eq}[G]_{eq}} \quad \textbf{Equation A1.2}$$

$$K_{Ox2} = \frac{[H2G_{Ox}]_{eq}}{[HG_{Ox}]_{eq}[G]_{eq}} \quad \textbf{Equation A1.3}$$

$$K_{Red} = \frac{[HG_{Red}]_{eq}}{[H_{Red}]_{eq}[G]_{eq}} \quad \textbf{Equation A1.4}$$

$$K_{Red2} = \frac{[H2G_{Red}]_{eq}}{[HG_{Red}]_{eq}[G]_{eq}} \quad \textbf{Equation A1.5}$$

Applying (Eqn A1.3) and (Eqn A1.5) into (Eqn A1.1) leads to

$$E = E^{\circ} + \frac{RT}{nF}\ln\left(\frac{[H_{Ox}]_{eq}+[HG_{Ox}]_{eq}+K_{Ox2}[HG_{Ox}]_{eq}[G]_{eq}}{[H_{Red}]_{eq}+[HG_{Red}]_{eq}+K_{Red2}[HG_{Red}]_{eq}[G]_{eq}}\right) \quad \textbf{Equation A1.6}$$

$$E = E^{\circ} + \frac{RT}{nF}\ln\left(\frac{[H_{Ox}]_{eq}+[HG_{Ox}]_{eq}(1+K_{Ox2}[G]_{eq})}{[H_{Red}]_{eq}+[HG_{Red}]_{eq}(1+K_{Red2}[G]_{eq})}\right) \quad \textbf{Equation A1.7}$$

Applying (Eqn A1.2) and (Eqn A1.4) into (Eqn A1.7) gives

$$E = E^{\circ} + \frac{RT}{nF}\ln\left(\frac{[H_{Ox}]_{eq}+K_{Ox}[H_{Ox}]_{eq}[G]_{eq}(1+K_{Ox2}[G]_{eq})}{[H_{Red}]_{eq}+K_{Red}[H_{Red}]_{eq}[G]_{eq}(1+K_{Red2}[G]_{eq})}\right) \quad \textbf{Equation A1.8}$$

$$E = E^{\circ} + \frac{RT}{nF}\ln\left(\frac{[H_{Ox}]_{eq}\left(1+K_{Ox}[G]_{eq}(1+K_{Ox2}[G]_{eq})\right)}{[H_{Red}]_{eq}\left(\left(1+K_{Red}[G]_{eq}(1+K_{Red2}[G]_{eq})\right)\right)}\right) \quad \textbf{Equation A1.9}$$

The Nernst equation also applies for the H_{Ox}/H_{Red} couple in equation (Eqn A1.10)

$$E = E_{H_{Ox}/H_{Red}}{}^{\circ} + \frac{RT}{nF}\ln\frac{[H_{Ox}]}{[H_{Red}]} \quad \textbf{Equation A1.10}$$

By subtracting (Eqn A1.10) from (Eqn A1.9) gives equation (Eqn A1.11)

$$\Delta E = -\frac{RT}{nF}\ln\left(\frac{1+K_{Ox}[G]_{eq}(1+K_{Ox2}[G]_{eq})}{1+K_{Red}[G]_{eq}(1+K_{Red2}[G]_{eq})}\right) \quad \textbf{Equation A1.11}$$

Assuming that [G] is in excess compared to [H] ($[G]_0$>>$[H]_0$) for the titration conditions then the amount of G associated with complex formation can be neglected and so the assumption that $[G]_{eq}$≈$[G]_0$ stands, resulting in equation (Eqn A1.12), which is used for fitting anion titrations throughout for 1:2 host-guest fittings.

$$\Delta E = -\frac{RT}{nF}\ln\left(\frac{1+K_{Ox}[G]_0(1+K_{Ox2}[G]_0)}{1+K_{Red}[G]_0(1+K_{Red2}[G]_0)}\right) \qquad \textbf{Equation A1.12}$$

A2 Appendices for Chapter 2

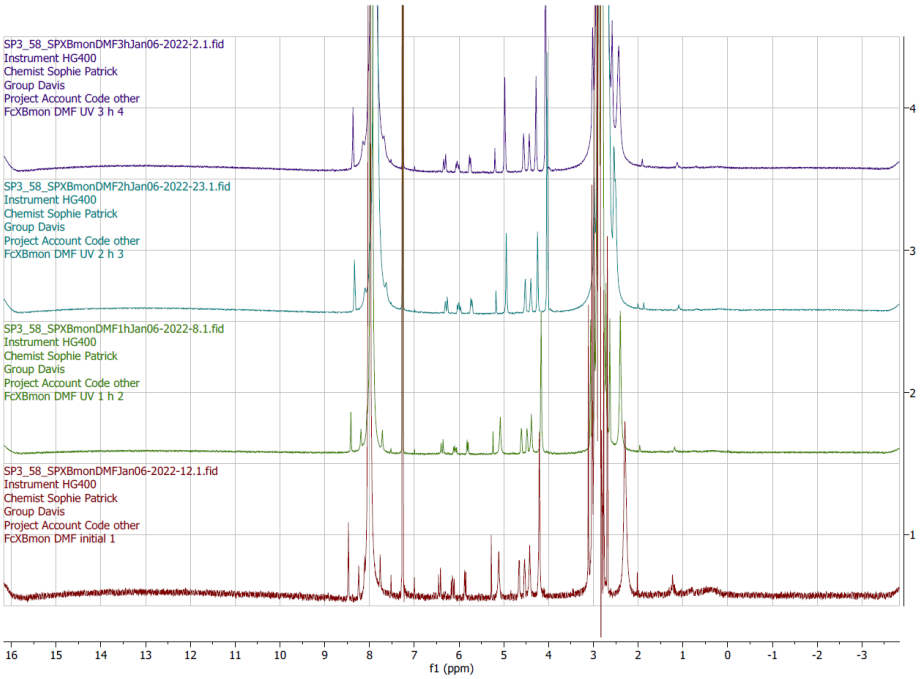


Figure A2.1. ^{1}H NMR spectra in $CDCl_3$ of aliquots of 50 mM **1.XB** in DMF with increasing durations of irradiation with UV light (390 nm).

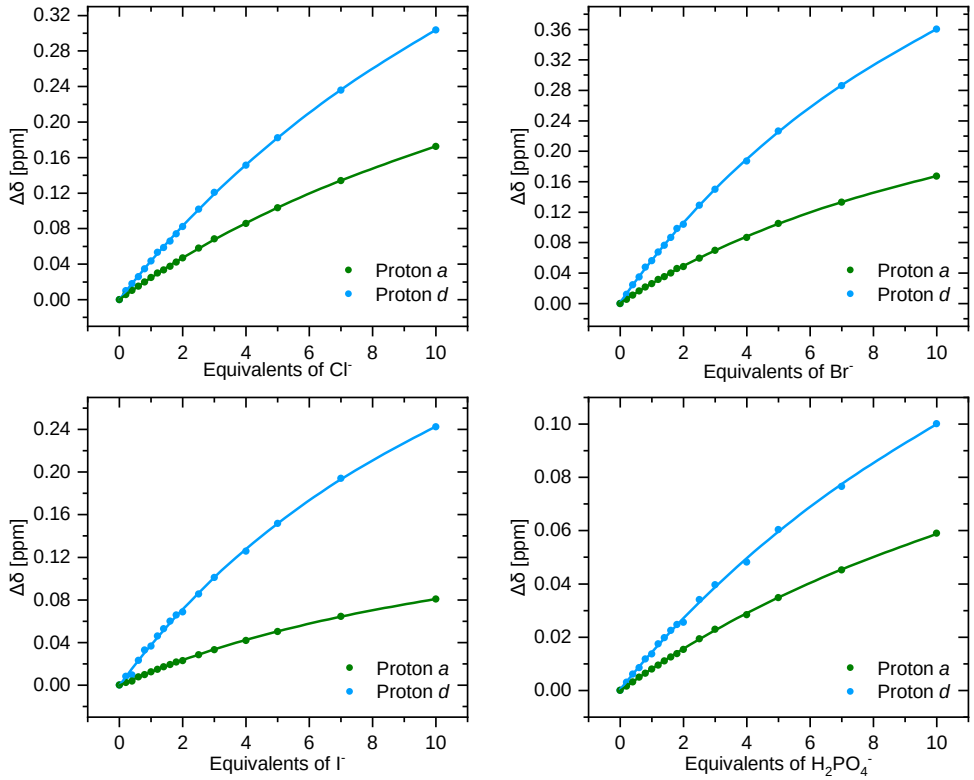


Figure A2.2. Anion binding isotherms for **1.HB** in acetone-d_6:D_2O (97.5:2.5, v/v), where circles represent experimental data and the lines represent the fitted isotherm.

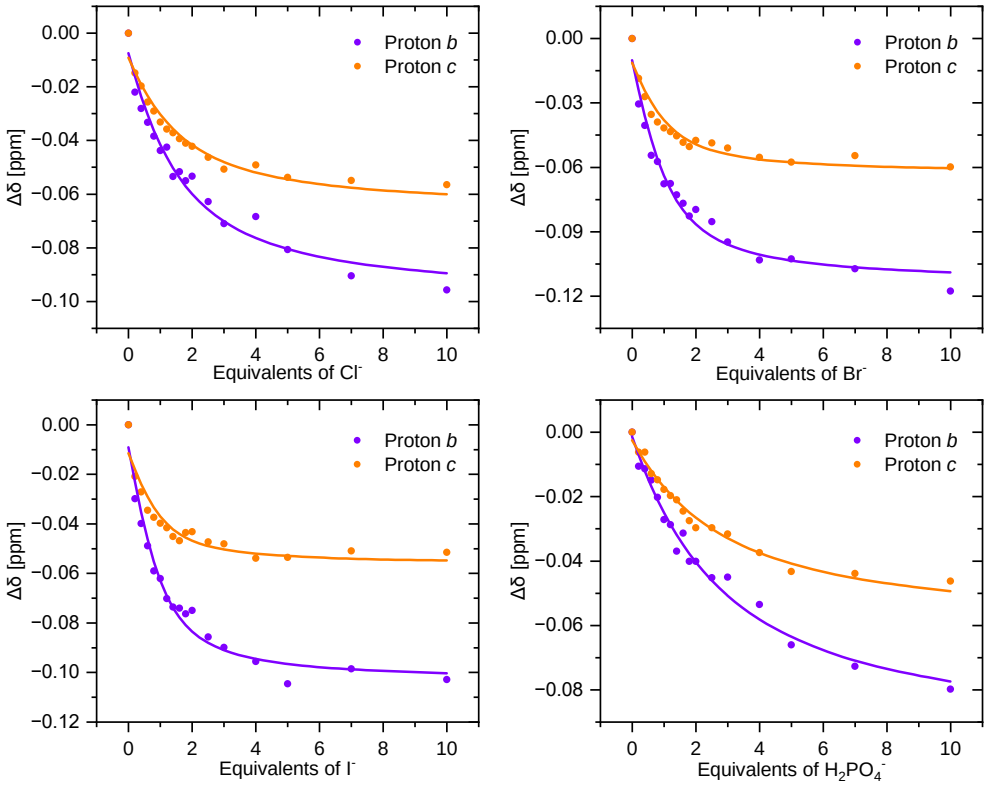


Figure A2.3. Anion binding isotherms for **pDEGA-1.XB** in acetone-d_6:D_2O (97.5:2.5, v/v), where circles represent experimental data and the lines represent the fitted isotherm.

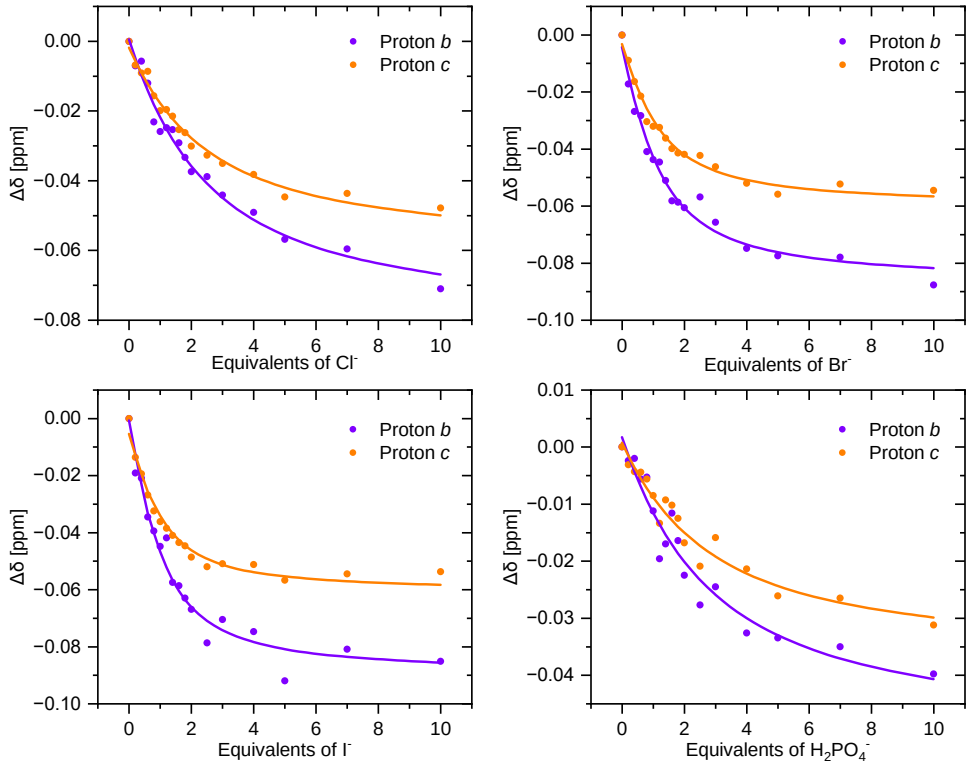


Figure A2.4. Anion binding isotherms for **pDEGA-1.XB** in acetone-d_6:acetonitrile-d_3:D_2O (48.75:48.75:2.5, v/v/v), where circles represent experimental data and the lines represent the fitted isotherm.

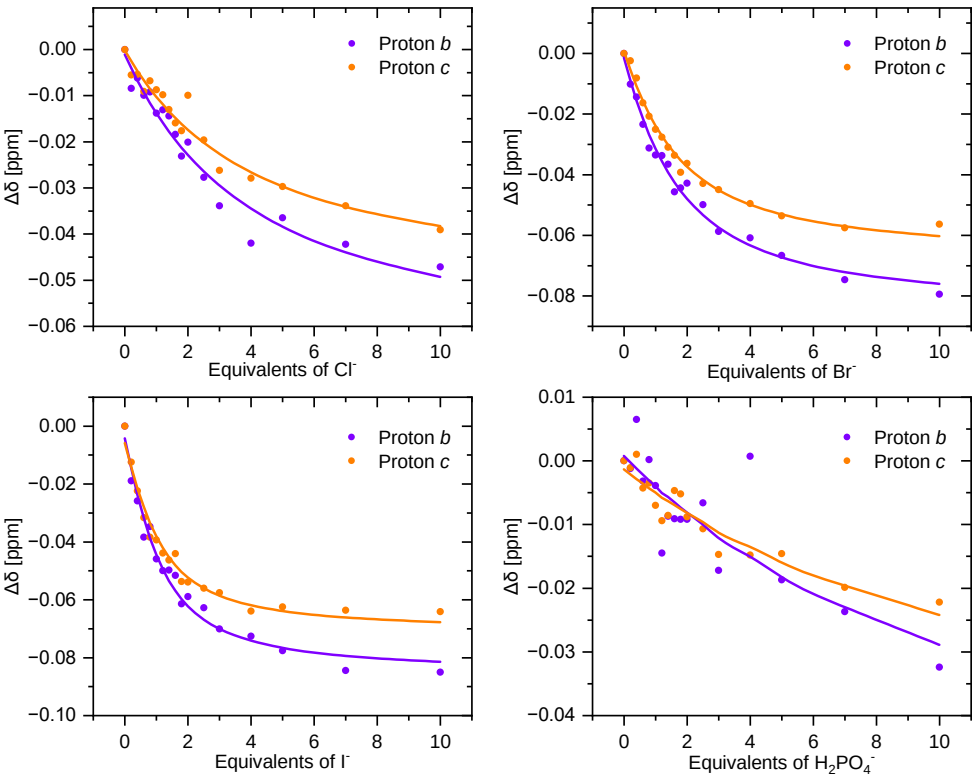


Figure A2.5. Anion binding isotherms for **pDEGA-1.XB** in acetonitrile-d_3:D_2O (97.5:2.5, v/v), where circles represent experimental data and the lines represent the fitted isotherm.

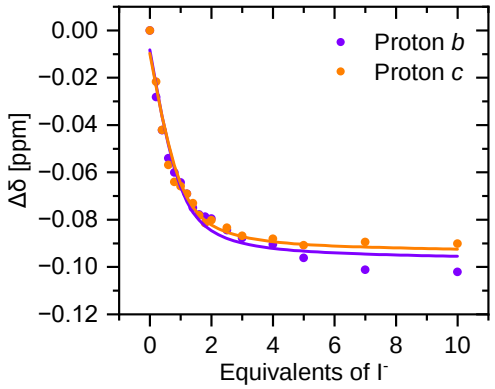


Figure A2.6. Anion binding isotherms for **pDEGA-BuA-1·XB** in acetonitrile-d_3:D_2O (97.5:2.5, v/v), where circles represent experimental data and the lines represent the fitted isotherm.

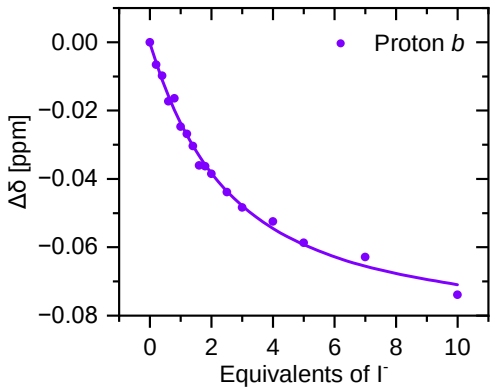


Figure A2.7. Anion binding isotherms for **pDEGA-1.XB$_{0.5}$** in acetonitrile-d_3:D_2O (97.5:2.5, v/v), where circles represent experimental data and the lines represent the fitted isotherm.

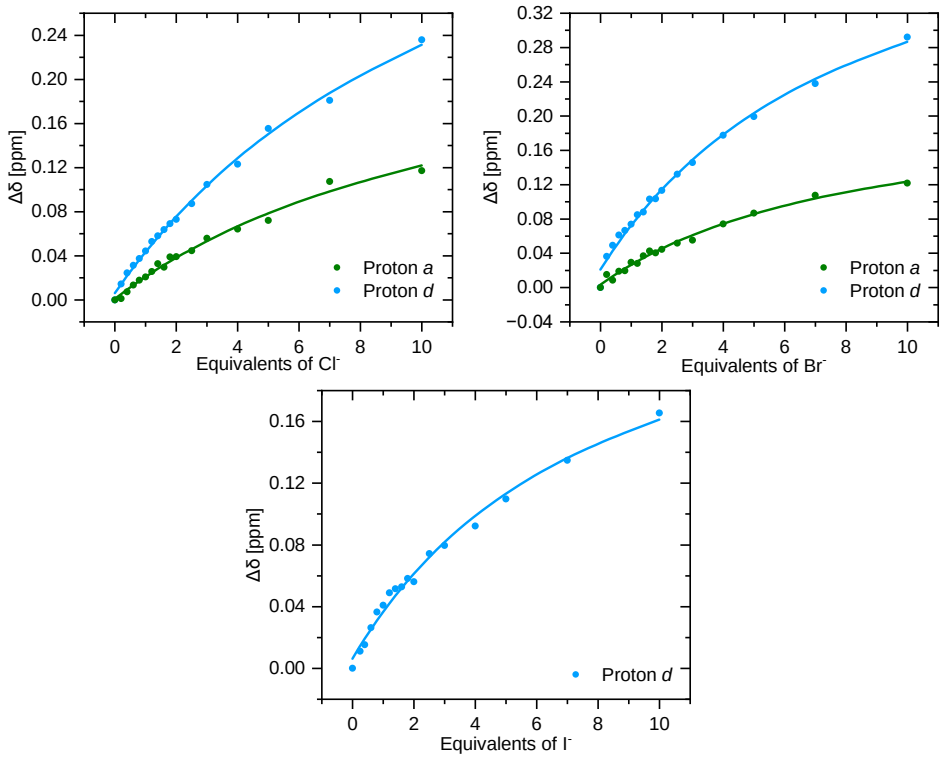


Figure A2.8. Anion binding isotherms for **pDEGA-1.HB** in acetone-d_6:D_2O (97.5:2.5, v/v), where circles represent experimental data and the lines represent the fitted isotherm.

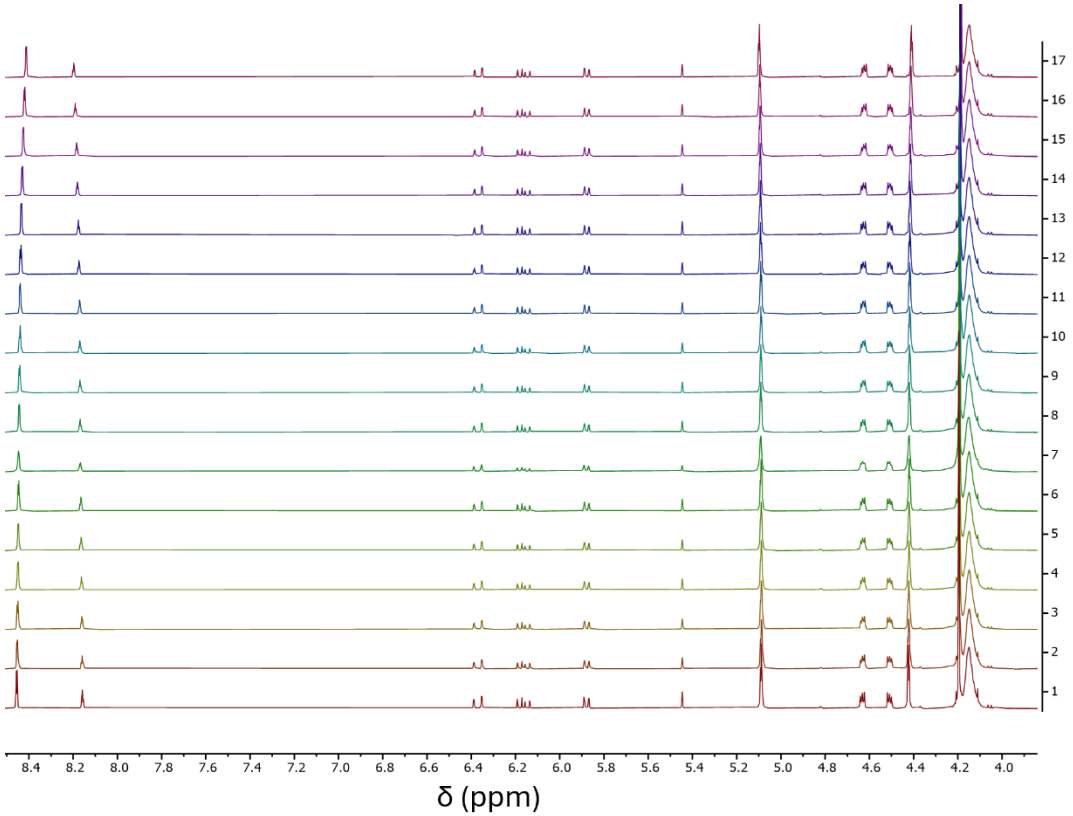


Figure A2.9. Stacked ^{1}H NMR spectra from titration of **1.XB** with TBAI in presence of homopolymer **pDEGA** (concentration of DEGA units 0.009 mM, or 1:9 ratio of **1.XB** to DEGA) in acetonitrile-d_3:D_2O (97.5:2.5, v/v), 500 MHz, 298 K. Spectrum no. 1 – 0 equivalents of the guest; spectrum no. 17 – 10 equivalents of the guest.

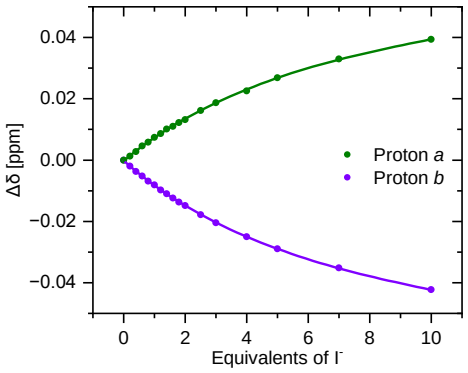


Figure A2.10. Anion binding isotherms for **1.XB** in presence of homopolymer **pDEGA** (concentration of DEGA units 0.009 mM, or 1:9 ratio of **1.XB** to DEGA) in acetonitrile-d_3:D_2O (97.5:2.5, v/v), where circles represent experimental data and the lines represent the fitted isotherm.

All other ^{1}H NMR spectra acquired during anion titrations for all monomeric and polymeric hosts can be found in the Supporting Information associated with the publication of the work detailed in Chapter 2.[318]

Electrochemical Characterisation of Monomeric and Polymeric Hosts:

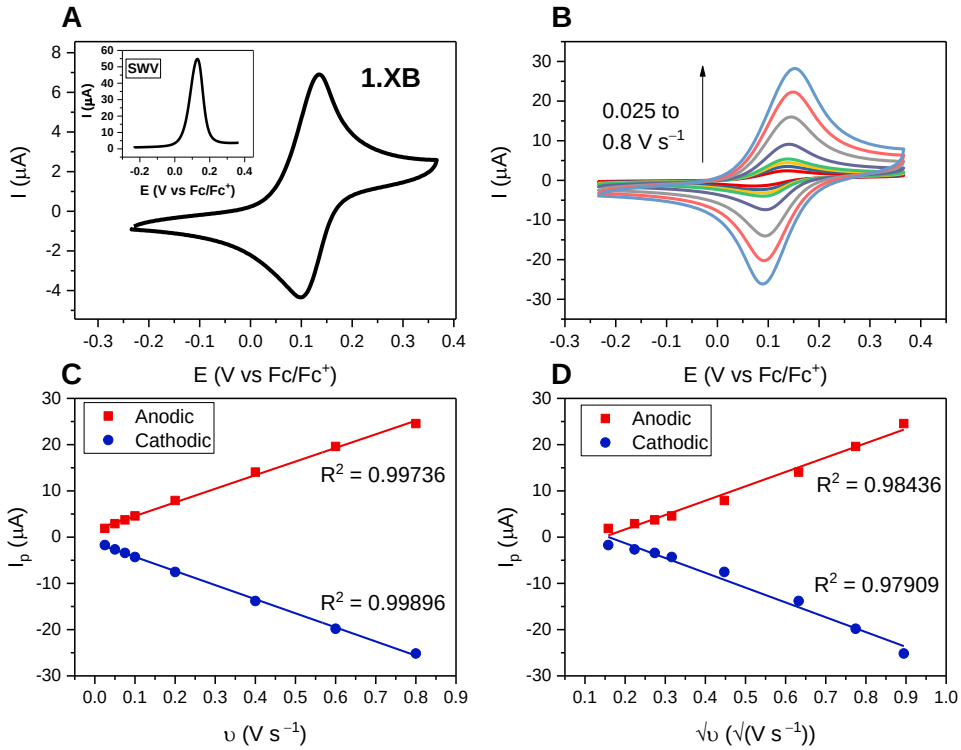


Figure A2.4. (A) Cyclic voltammogram and square wave voltammogram (inset) of 0.1 mM **1.XB** in 97.5:2.5 ACN/H_2O, 100 mM $TBAClO_4$, at a scan rate of 0.1 V s^{-1}. (B) Cyclic voltammograms of the same system at varying scan rates from 0.025 to 0.8 V s^{-1}, and plots of peak current vs. (C) scan rate (D) the square-root of the scan rate in the same solvent system. All potentials wrt. external $Fc|Fc^+$ couple.

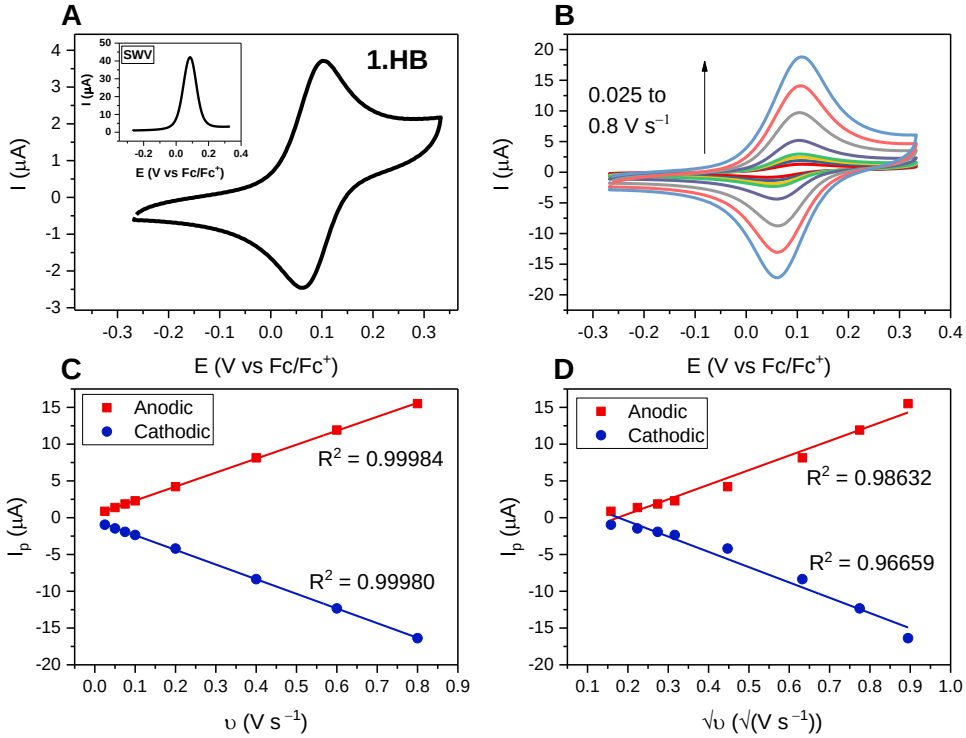


Figure A2.5. A) Cyclic voltammogram and square wave voltammogram (inset) of 0.1 mM **1.HB** in 97.5:2.5 ACN/H_2O, 100 mM $TBAClO_4$, at a scan rate of 0.1 V s^{-1}. B) Cyclic voltammograms of the same system at varying scan rates from 0.025 to 0.8 V s^{-1}, and plots of peak current vs. C) scan rate D) the square-root of the scan rate in the same solvent system. All potentials wrt. external $Fc|Fc^+$ couple.

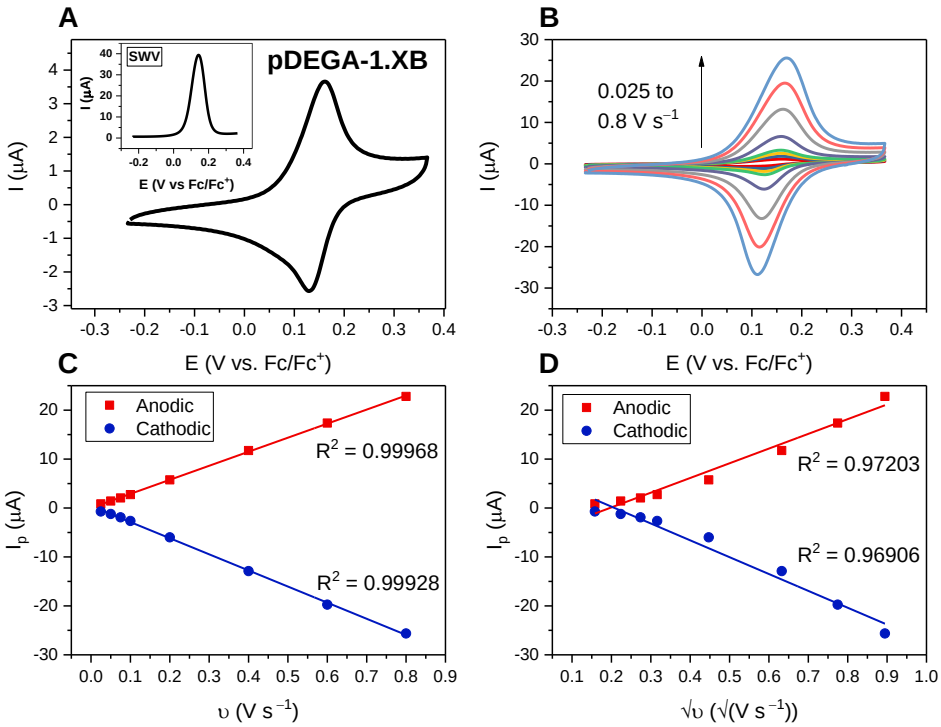


Figure A2.6. A) Cyclic voltammogram and square wave voltammogram (inset) of 0.1 mM **pDEGA-1.XB** in 97.5:2.5 ACN/H_2O, 100 mM $TBAClO_4$, at a scan rate of 0.1 V s^{-1}. B) Cyclic voltammograms of the same system at varying scan rates from 0.025 to 0.8 V s^{-1}, and plots of peak current vs. C) scan rate D) the square-root of the scan rate in the same solvent system. All potentials wrt. external $Fc|Fc^+$ couple.

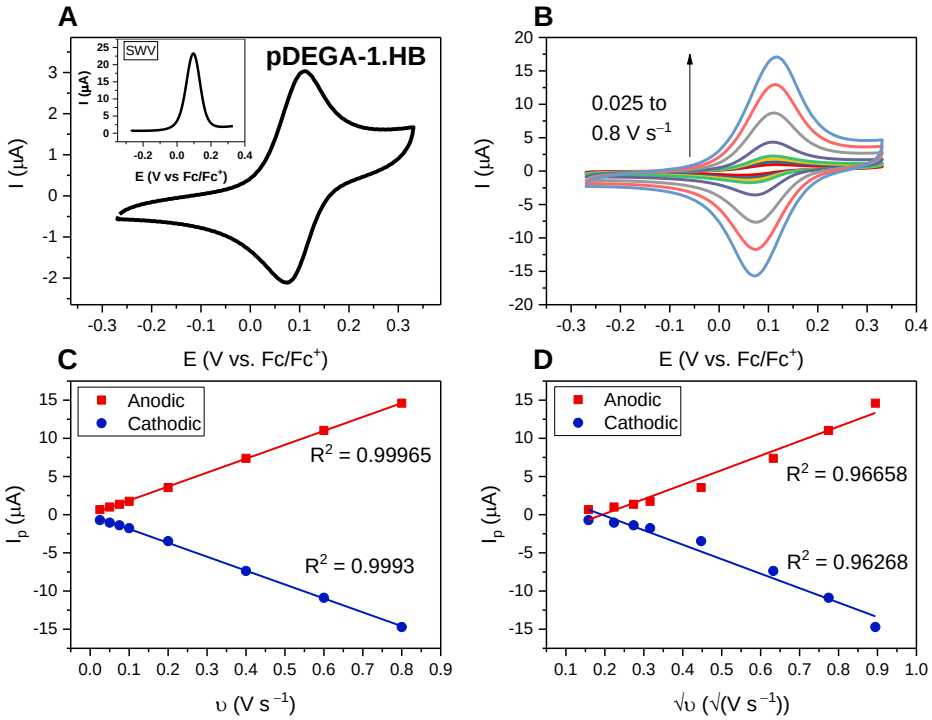


Figure A2.7. A) Cyclic voltammogram and square wave voltammogram (inset) of 0.1 mM **pDEGA-1.HB** in 97.5:2.5 ACN/H_2O, 100 mM $TBAClO_4$, at a scan rate of 0.1 V s^{-1}. B) Cyclic voltammograms of the same system at varying scan rates from 0.025 to 0.8 V s^{-1}, and plots of peak current vs. C) scan rate D) the square-root of the scan rate in the same solvent system. All potentials wrt. external $Fc|Fc^+$ couple.

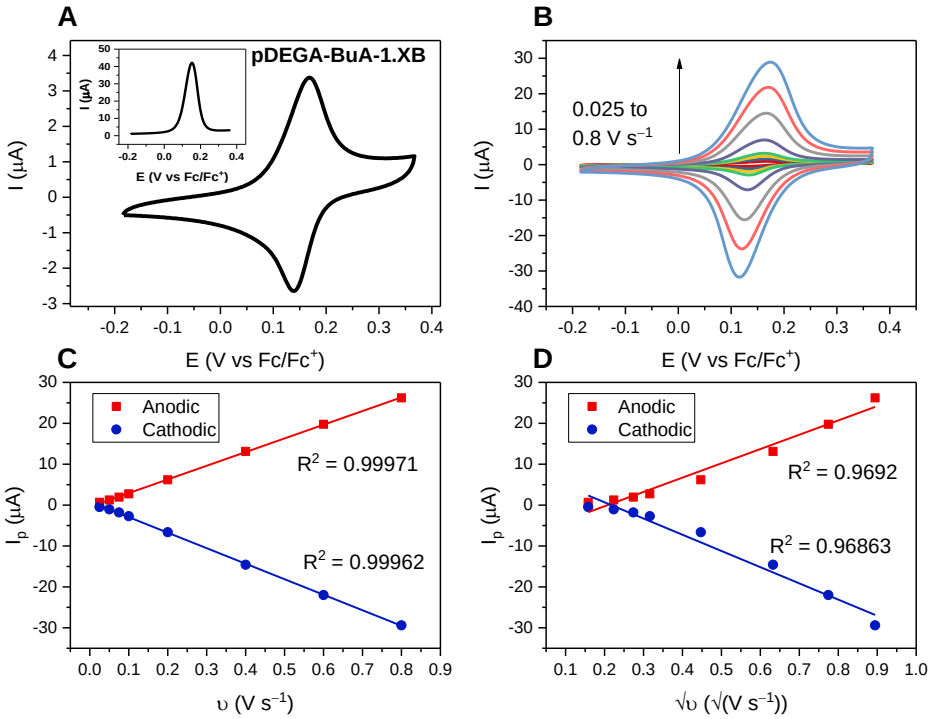


Figure A2.8. A) Cyclic voltammogram and square wave voltammogram (inset) of 0.1 mM **pDEGA-BuA-1.XB** in 97.5:2.5 ACN/H_2O, 100 mM $TBAClO_4$, at a scan rate of 0.1 V s^{-1}. B) Cyclic voltammograms of the same system at varying scan rates from 0.025 to 0.8 V s^{-1}, and plots of peak current vs. C) scan rate D) the square-root of the scan rate in the same solvent system. All potentials wrt. external $Fc|Fc^+$ couple.

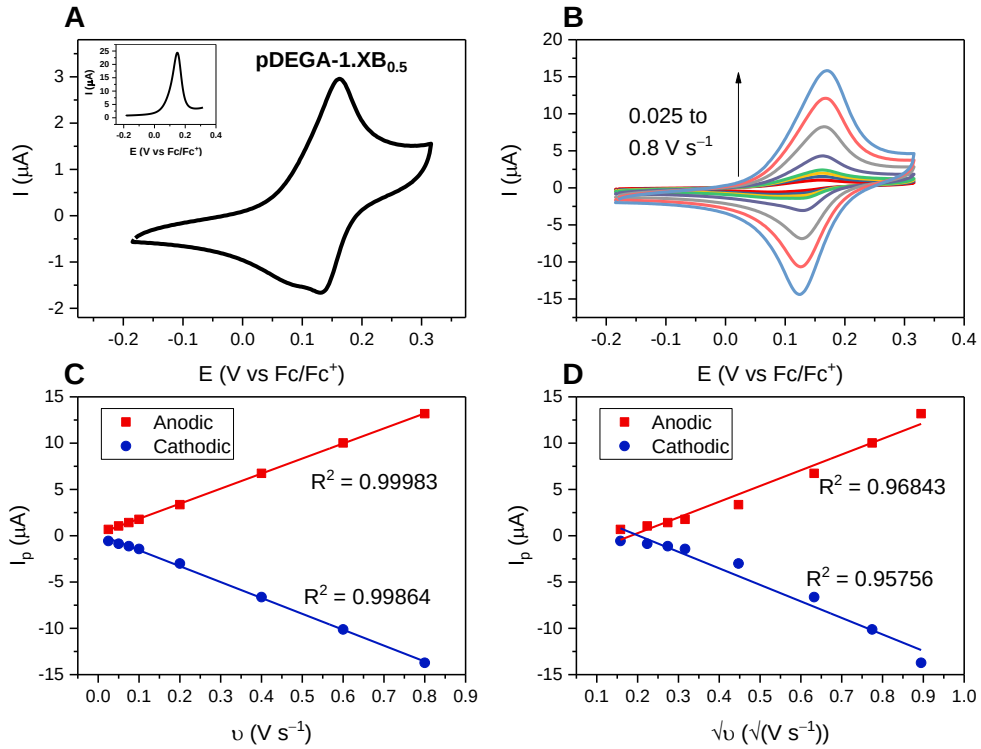


Figure A2.9. A) Cyclic voltammogram and square wave voltammogram (inset) of 0.1 mM **pDEGA-1.XB$_{0.5}$** in 97.5:2.5 ACN/H_2O, 100 mM $TBAClO_4$, at a scan rate of 0.1 V s^{-1}. B) Cyclic voltammograms of the same system at varying scan rates from 0.025 to 0.8 V s^{-1}, and plots of peak current vs. C) scan rate D) the square-root of the scan rate in the same solvent system. All potentials wrt. external $Fc|Fc^+$ couple.

Table A2.1. Diffusive binding constants of the oxidised (K_{Ox}) and neutral (K_{Red}) hosts (M^{-1}), and BEFs in response to HSO_4^-, as determined from fitting isotherms with a 1:1 host-guest Nernst model (K_{Ox}/K_{Red}, Eqn. 2) or the maximum shift (Eqn. 1) in response to 50 mM [X^-].

HSO_4^- Host	Solvent	K_{Ox} (M^{-1})	K_{Red} (M^{-1})	R^2	BEF (isotherm)	BEF (max shift)
1.XB	97.5:2.5 ACN/H_2O	301 ± 35.4	21.9 ± 6.26	0.992	13.7	8.05
pDEGA-1.XB	97.5:2.5 ACN/H_2O	1040 ± 84.0	37.9 ± 6.61	0.996	27.4	19.6
1.HB	97.5:2.5 ACN/H_2O	1580 ± 91.0	37.1 ± 4.85	0.998	42.5	28.8
pDEGA-1.HB	97.5:2.5 ACN/H_2O	2280 ± 121	48.3 ± 5.35	0.998	47.2	34.9
1.XB	97.5:2.5 Acetone/H_2O	903 ± 81.5	30.8 ± 6.54	0.995	29.3	20.3
pDEGA-1.XB	97.5:2.5 Acetone/H_2O	2740 ± 585	46.5 ± 21.3	0.975	58.9	44.8
1.HB	97.5:2.5 Acetone/H_2O	1860 ± 191	9.41 ± 5.08	0.994	197	62.4
pDEGA-1.HB	97.5:2.5 Acetone/H_2O	5703 ± 887	14.3 ± 9.36	0.987	339	164

Table A2.2. Diffusive binding constants of the oxidised (K_{Ox}) and neutral (K_{Red}) hosts (M^{-1}), and BEFs in response to $H_2PO_4^-$, as determined from fitting isotherms with a 1:1 host-guest Nernst model (K_{Ox}/K_{Red}, Eqn. 2) or the maximum shift (Eqn. 1) in response to 50 mM [X^-].

$H_2PO_4^-$ Host	Solvent	K_{Ox} (M^{-1})	K_{Red} (M^{-1})	R^2	BEF (isotherm)	BEF (max shift)
1.XB	97.5:2.5 ACN/H_2O	10800 ± 2490	159 ± 56.8	0.973	68.0	88.3
pDEGA-1.XB	97.5:2.5 ACN/H_2O	23100 ± 3140	95.3 ± 18.7	0.995	305	304
1.HB	97.5:2.5 ACN/H_2O	26900 ± 5700	203 ± 64.5	0.982	132	177
pDEGA-1.HB	97.5:2.5 ACN/H_2O	104000 ± 12200	193 ± 57.1	0.996	543	696
1.XB	97.5:2.5 Acetone/H_2O	22800 ± 4700	59.5 ± 25.9	0.981	383	447
pDEGA-1.XB	97.5:2.5 Acetone/H_2O	115000 ± 12200	35.6 ± 10.1	0.996	3220	2490
1.HB	97.5:2.5 Acetone/H_2O	72400 ± 13200	47.5 ± 20.2	0.988	1520	1540
pDEGA-1.HB	97.5:2.5 Acetone/H_2O	242000 ± 22600	59.3 ± 11.9	0.998	4080	3710

Table A2.3. Diffusive binding constants of the oxidised (K_{Ox}) and neutral (K_{Red}) hosts (M^{-1}), and BEFs in response to Cl^-, as determined from fitting isotherms with a 1:1 host-guest Nernst model (K_{Ox}/K_{Red}, Eqn. 2) or the maximum shift (Eqn. 1) in response to 50 mM [X^-].

Cl^- Host	Solvent	K_{Ox} (M^{-1})	K_{Red} (M^{-1})	R^2	BEF (isotherm)	BEF (max shift)
1.XB	97.5:2.5 ACN/H_2O	421 ± 44.1	38.5 ± 7.73	0.993	10.9	8.05
pDEGA-1.XB	97.5:2.5 ACN/H_2O	472 ± 131	18.4 ± 14.7	0.948	25.6	14.9
1.HB	97.5:2.5 ACN/H_2O	71.4 ± 4.19	4.34 ± 1.40	0.999	16.4	3.72
pDEGA-1.HB	97.5:2.5 ACN/H_2O	96.4 ± 9.81	2.15 ± 2.48	0.995	44.9	5.06
1.XB	97.5:2.5 Acetone/H_2O	1240 ± 289	170 ± 52.9	0.966	7.33	8.05
pDEGA-1.XB	97.5:2.5 Acetone/H_2O	1360 ± 48.6	54.7 ± 3.72	0.999	24.8	18.8
1.HB	97.5:2.5 Acetone/H_2O	285 ± 20.0	21.5 ± 3.67	0.997	13.3	7.45
pDEGA-1.HB	97.5:2.5 Acetone/H_2O	650 ± 131	1.80 ± 7.00	0.977	361.5	6.90

Table A2.4. Diffusive binding constants of the oxidised (K_{Ox}) and neutral (K_{Red}) hosts (M^{-1}), and BEFs in response to Br^-, as determined from fitting isotherms with a 1:1 host-guest Nernst model (K_{Ox}/K_{Red}, Eqn. 2) or the maximum shift (Eqn. 1) in response to 50 mM [X^-].

Br^- Host	Solvent	K_{Ox} (M^{-1})	K_{Red} (M^{-1})	R^2	BEF (isotherm)	BEF (max shift)
1.XB	97.5:2.5 ACN/H_2O	791 ± 122	101 ± 22.8	0.986	7.84	7.45
pDEGA-1.XB	97.5:2.5 ACN/H_2O	519 ± 121	58.1 ± 22.5	0.967	8.94	8.05
1.HB	97.5:2.5 ACN/H_2O	88.0 ± 19.0	17.1 ± 7.84	0.983	5.13	2.95
pDEGA-1.HB	97.5:2.5 ACN/H_2O	106 ± 14.0	13.5 ± 4.64	0.992	7.86	3.86
1.XB	97.5:2.5 Acetone/H_2O	810 ± 99.4	124.4 ± 21.1	0.992	6.51	5.91
pDEGA-1.XB	97.5:2.5 Acetone/H_2O	1222 ± 188	58.1 ± 16.4	0.986	21.0	18.1
1.HB	97.5:2.5 Acetone/H_2O	261 ± 16.4	32.0 ± 3.90	0.998	8.15	5.47
pDEGA-1.HB	97.5:2.5 Acetone/H_2O	160 ± 10.3	6.35 ± 2.06	0.998	25.1	6.90

A3 Appendices for Chapter 3: Continuous Voltammetric Anion Sensing

MATLAB Code

Function “f3” refers to the function given by Equation 3.6-1.

PeakPick Code:

```
result = [];
AllPeaks = [];
AllPeaks2 = [];
%For loop to apply analysis to n SWVs
for v = 1:n
   i = (2*v) - 1;

   % Extracting the data from the table into variables
   x1 = DataTable{i,:};
   y1 = DataTable{i+1,:};

   % Extracting E and I data for each SWV into separate table
   PeakTable1 = [x1(:),y1(:)];
   % Finding Emax values from maximum I value
   [~,x1] = max(PeakTable1(:,2));
   Peak1 = PeakTable1(x1,:);
   %Combining all Emax values into one table as final result
   AllPeaks = [AllPeaks; Peak1];
```

AsymFit Code:
(run in addition to the PeakPick Code above)

```
%Taking values for I
Y = DataTable{i+1,:};

%Identify maximum I
maximum = max(Y);

%Find location of maximum I in matrix
[a,b] = find(Y==maximum);

%Cut main table down to ±50 mV either side of Emax for each SWV trace
CutTable = DataTable([i:i+1],[(b-12):(b+12)]);

   % Extracting the data from the table into new variables
   x = CutTable{1,:};
   y = CutTable{2,:};

%Curve Fit
%Initialisation parameters
```

```
    Guessxpeak = Peak1(1,1);
    alpha = y(1,1);
    beta = maximum-Peak1(1,1);
    fwhm = x(1,16) - x(1,6);

  x0 = [alpha beta Guessxpeak fwhm fwhm fwhm];

%Curve fitting options
options = optimoptions('lsqcurvefit','Algorithm','levenberg-
marquardt','MaxIterations',10000,'MaxFunctionEvaluations',20000,'FunctionTolerance',1e-
9,'StepTolerance',1e-10,'FiniteDifferenceType','central');
lb = [0 0 0 0 0 0];
ub = [];
constant = lsqcurvefit(@f4,x0,x,y,lb,ub,options);

%Defining each constant to be optimised
y0 = constant(1);
A = constant(2);
xc = constant(3);
c1 = constant(4);
c2 = constant(5);
c3 = constant(6);

%Extracting final results into one table
result = [result; y0, A, xc, c1, c2, c3];

xmin = min(x);
xmax = max(x);

%Variables of Asymfit
xfit = xmin:0.00001:xmax;
yfit = f3(constant,xfit);

    % Extracting Efit and Ifit data for each SWV into separate table
    PeakTable2 = [xfit(:),yfit(:)];
    % Finding peak values from maximum Ifit value
    [~,xfit] = max(PeakTable2(:,2));
    Peak2 = PeakTable2(xfit,:);
    %Combining all E1/2 values into one table as final result
    AllPeaks2 = [AllPeaks2; Peak2];


end
AllPeaks
AllPeaks2
result
```

Static AsymFit: Langmuir-Freundlich Fitting Data

Table A3.1. Apparent binding constants (K_{app}), heterogeneity factors (n) and R^2 values from Langmuir-Freundlich fitting (Eqn. 3.3-1) for sensing studies with **1.XB/HB$_{SAM}$** under static conditions in response to HSO_4^-, $H_2PO_4^-$ and Cl^-, which were analysed via the AsymFit method. All errors are mathematical errors from fitting.

	Notes	1.XB/HB	K_{app} (M^{-1})	n	R^2
HSO_4^-		XB	91.7 ± 4.0	1.72 ± 0.10	0.999
		HB	80.8 ± 2.3	1.58 ± 0.05	0.999
	Repeat	XB	82.3 ± 7.0	1.49 ± 0.13	0.998
	Repeat	HB	74.1 ± 3.4	1.43 ± 0.06	0.999
	Repeat	XB	81.0 ± 4.6	1.64 ± 0.11	0.999
	Repeat	HB	70.9 ± 3.7	1.48 ± 0.07	0.999
$H_2PO_4^-$	Full range up to 23.4 mM	XB	93.1 ± 1.7	15.1 ± 4.0	0.979
	Full range up to 23.4 mM	HB	95.7 ± 1.4	20.4 ± 5.5	0.981
	Corrected by -10 mM	XB	989 ± 224	0.648 ± 0.087	0.999
	Corrected by -10 mM	HB	2120 ± 427	0.708 ± 0.176	0.997
Cl^-	Up to 33 mM	XB	52.9 ± 7.7	1.97 ± 0.27	0.997
	Up to 33 mM	HB	54.3 ± 5.8	2.37 ± 0.32	0.997

Static AsymFit: LODs and Sensitivities

Table A3.2. Sensitivities (slope of linear region at low concentrations, including R^2), baseline standard deviations and limits of detection (LODs) for sensing studies with **1.XB/HB$_{SAM}$** under static conditions, which were analysed via the AsymFit method. All errors are mathematical errors from fitting.

	Linear Range (mM)	1.XB/HB	Sensitivity ($mV\ mM^{-1}$)	R^2	Baseline s.d. (mV)	LOD (µM)
HSO_4^-	0-11	XB	4.81 ± 0.14	0.997	0.0916	57.2
	0-11	HB	5.35 ± 0.12	0.998	0.110	61.7
	0-11	XB	4.72 ± 0.08	0.999	0.162	103
	0-11	HB	5.29 ± 0.03	0.999	0.0763	43.2
	0-11	XB	4.51 ± 0.13	0.998	0.0641	42.7
	0-11	HB	5.13 ± 0.08	0.999	0.0492	28.8
$H_2PO_4^-$	9.5-13.4	XB	36.0 ± 10.3	0.859	0.0906	20.1
	9.5-13.4	HB	41.8 ± 14.4	0.808	0.0479	8.58
Cl^-	0-11	XB	2.71 ± 0.25	0.975	0.189	210
	0-11	HB	2.08 ± 0.19	0.975	0.135	195

Flow AsymFit (5 mV): Langmuir-Freundlich Fitting Data

Table A3.3. Apparent binding constants (K_{app}), heterogeneity factors (n) and R^2 values from Langmuir-Freundlich fitting (Eqn. 3.3-1) for sensing studies with **1.XB/HB$_{SAM}$** under continuous flow conditions (E_{step} = 5 mV) in response to HSO_4^-, $H_2PO_4^-$ and Cl^-, which were analysed via the AsymFit method. All errors are mathematical errors from fitting.

	Notes	1.XB/HB	K_{app} (M^{-1})	n	R^2
HSO_4^-		XB	73.0 ± 4.3	1.60 ± 0.10	0.999
		XB	69.8 ± 6.1	1.56 ± 0.14	0.998
	Repeat	XB	53.6 ± 4.5	1.49 ± 0.10	0.999
	Repeat	HB	69.6 ± 2.8	1.55 ± 0.06	0.999
	Repeat	HB	70.5 ± 6.1	2.07 ± 0.29	0.995
	Repeat	HB	63.7 ± 7.0	2.26 ± 0.44	0.991
$H_2PO_4^-$	Full range up to 23.4 mM	XB	78.5 ± 0.7	25.5 ± 3.2	0.997
	Full range up to 23.4 mM	HB	79.0 ± 0.2	31.0 ± 1.1	0.999
	Corrected by -10 mM	XB	385 ± 20	4.63 ± 0.72	0.997
	Corrected by -10 mM	HB	401 ± 5	5.74 ± 0.19	0.999
Cl^-	Up to 33 mM	XB	61.2 ± 8.1	2.35 ± 0.44	0.994
	Up to 33 mM	HB	60.4 ± 4.4	2.65 ± 0.33	0.997

Flow AsymFit (5 mV): LODs and Sensitivities

Table A3.4. Sensitivities (slope of linear region at low concentrations, including R^2), baseline standard deviations and limits of detection (LODs) for sensing studies with **1.XB/HB$_{SAM}$** under continuous flow conditions (E_{step} = 5 mV), which were analysed via the AsymFit method. All errors are mathematical errors from fitting.

	Linear Range (mM)	1.XB/HB	Sensitivity (mV mM^{-1})	R^2	Baseline s.d. (mV)	LOD (µM)
HSO_4^-	0-11	XB	4.21 ± 0.15	0.996	0.0917	65.4
	0-11	XB	3.96 ± 0.12	0.997	0.0717	54.3
	0-11	XB	3.33 ± 0.11	0.997	0.0617	55.5
	0-11	HB	4.80 ± 0.13	0.998	0.0903	56.4
	0-11	HB	3.71 ± 0.21	0.991	0.0204	16.5
	0-11	HB	3.02 ± 0.12	0.995	0.0322	32.0
$H_2PO_4^-$	10.5-13.4	XB	49.9 ± 14.5	0.922	0.0628	3.77
	10.5-13.4	HB	59.3 ± 17.1	0.923	0.0177	0.894
Cl^-	0-11	XB	2.27 ± 0.20	0.977	0.0678	89.6
	0-11	HB	1.93 ± 0.20	0.968	0.0308	48.0

Flow AsymFit (2 mV): Langmuir-Freundlich Fitting Data

Table A3.5. Apparent binding constants (K_{app}), heterogeneity factors (n) and R^2 values from Langmuir-Freundlich fitting (Eqn. 3.3-1) for sensing studies with **1.XB$_{SAM}$** under continuous flow conditions (E_{step} = 2 mV) in response to HSO_4^-, $H_2PO_4^-$ and Cl^-, which were analysed via the AsymFit method. All errors are mathematical errors from fitting.

	Notes	1.XB	K_{app} (M^{-1})	n	R^2
HSO_4^-		XB	74.2 ± 8.0	1.43 ± 0.14	0.998
	Repeat	XB	57.5 ± 5.7	1.69 ± 0.17	0.998
	Repeat	XB	88.4 ± 6.3	1.59 ± 0.13	0.998

Flow AsymFit (2 mV): LODs and Sensitivities

Table A3.6. Sensitivities (slope of linear region at low concentrations, including R^2), baseline standard deviations and limits of detection (LODs) for sensing studies with **1.XB$_{SAM}$** under continuous flow conditions (E_{step} = 2 mV), which were analysed via the AsymFit method. All errors are mathematical errors from fitting.

	Linear Range (mM)	1.XB	Sensitivity (mV mM^{-1})	R^2	Baseline s.d. (mV)	LOD (µM)
HSO_4^-	0-11	XB	4.46 ± 0.08	0.999	0.0431	29.0
	0-11	XB	3.21 ± 0.06	0.999	0.0922	86.1
	0-11	XB	4.81 ± 0.04	0.999	0.0738	46.0

Peak Pick (2 mV): Langmuir-Freundlich Fitting Data

Table A3.7. Apparent binding constants (K_{app}), heterogeneity factors (n) and R^2 values from Langmuir-Freundlich fitting (Eqn. 3.3-1) for sensing studies with **1.XB$_{SAM}$** under continuous flow conditions (E_{step} = 2 mV) in response to HSO_4^-, $H_2PO_4^-$ and Cl^-, which were analysed via the PeakPick method. All errors are mathematical errors from fitting.

	Notes	1.XB	K_{app} (M^{-1})	n	R^2
HSO_4^-		XB	65.8 ± 10.4	1.25 ± 0.13	0.997
	Repeat	XB	57.5 ± 5.7	1.69 ± 0.17	0.998
	Repeat	XB	86.9 ± 6.4	1.49 ± 0.11	0.998

Peak Pick (2 mV): LODs and Sensitivities

Table A3.8. Sensitivities (slope of linear region at low concentrations, including R^2), baseline standard deviations and limits of detection (LODs) for sensing studies with **1.XB/HB$_{SAM}$** under continuous flow conditions (E_{step} = 2 mV), which were analysed via the PeakPick method. All errors are mathematical errors from fitting.

	Linear Range (mM)	1.XB	Sensitivity (mV mM^{-1})	R^2	Baseline s.d. (mV)	LOD (µM)
HSO_4^-	0-11	XB	4.36 ± 0.17	0.995	1.19	819
	0-11	XB	3.25 ± 0.13	0.995	0.895	825
	0-11	XB	4.83 ± 0.07	0.999	1.02	633

A4 Appendices for Chapter 4: Redox Capacitive Anion Sensing

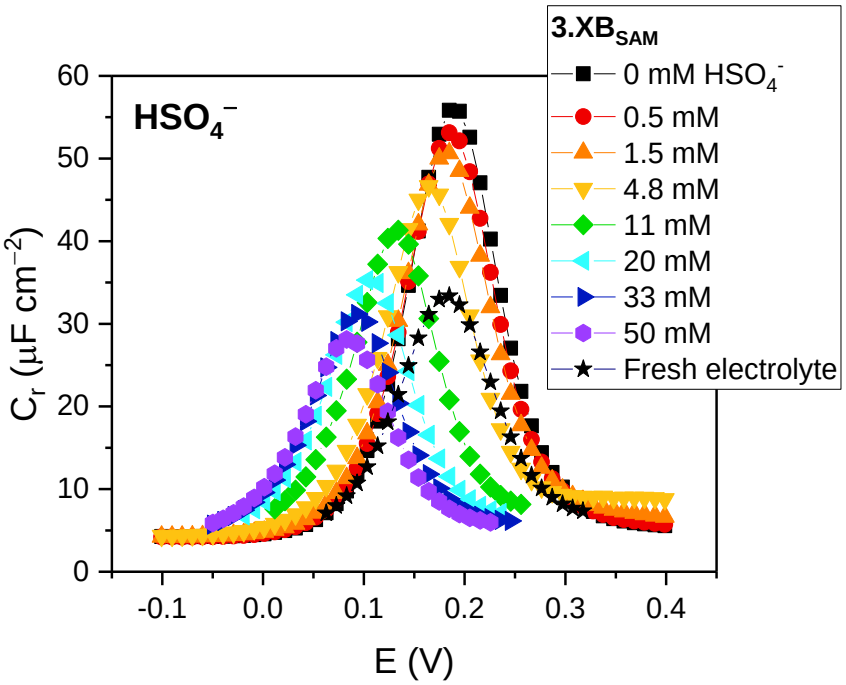


Figure A4.1. Raw, absolute redox distributions showing redox capacitance C_r of **3.XB$_{SAM}$** in ACN/H_2O 99:1 (100 mM $TBAClO_4$, 10 mM $HClO_4$) as function of potential (density of states, DOS), in response to increasing concentrations of HSO_4^- up to 50 mM.

Derivation of K_{Theo}:

Starting from the Nernst equation (Eqn. 1.4.2-2), an approximation of $-\frac{RT}{nF} = 59\ \text{mV}$ is first made to simplify Eqn. 1.4.2-2 to Eqn. A4.1, which can be rearranged to give Eqn. A4.2.

$$\Delta E = -\frac{RT}{nF}\ln\left(\frac{Ox}{Red}\right) \qquad \textbf{Equation 1.4.2-2}$$

$$\Delta E = -59\ \text{mV} * \log\left(\frac{Ox}{Red}\right) \qquad \textbf{Equation A4.1}$$

$$\frac{Ox}{Red} = 10^{\frac{\Delta E}{-0.059\ \text{V}}} \qquad \textbf{Equation A4.2}$$

The theoretical, average binding constant K_{Theo} is defined by Eqn. 4.3-1, as the weighted mean of the binding constants to the oxidised and reduced interfaces, given by K_{Ox} and K_{red} respectively, and the respective molar fractions of oxidized and reduced receptor states. K_{Theo} can alternatively be described by Eqn. A4.5, where the proportions of oxidized and reduced receptors at the interface have been replaced with the variables $\%Red$ and $\%Ox$ (Eqn. A4.3 and A4.4).

$$K_{Theo} = K_{Ox} * \frac{Ox}{Red+Ox} + K_{red} * \frac{Red}{Red+Ox} \qquad \textbf{Equation 4.3-1}$$

$$\%Red = \frac{Red}{Ox+Red} \qquad \textbf{Equation A4.3}$$

$$\%Ox = \frac{Ox}{Ox+Red} \qquad \textbf{Equation A4.4}$$

$$K_{Theo} = K_{Ox} * \%Ox + K_{red} * \%Red \qquad \textbf{Equation A4.5}$$

As $\%Ox$ and $\%Red$ add up to 1, $\%Ox$ can be substituted for (1-$\%Red$) in Eqn. A4.5, affording Eqn. A4.6.

$$K_{Theo} = K_{Ox} * (1 - \%Red) + K_{red} * \%Red \qquad \textbf{Equation A4.6}$$

Eqn. A4.3 can be rearranged as shown in the steps described by Eqns. A4.7-A4.9. Substitution of Eqn. A4.2 into Eqn. A4.9 then affords Eqn. A4.10.

$$\frac{1}{\%Red} = \frac{Ox+Red}{Red}$$ **Equation A4.7**

$$\frac{1}{\%Red} = \frac{Ox}{Red} + \frac{Red}{Red} = \frac{Ox}{Red} + 1$$ **Equation A4.8**

$$\%Red = \left(\frac{Ox}{Red} + 1\right)^{-1}$$ **Equation A4.9**

$$\%Red = \left(10^{\frac{\Delta E}{-0.059}} + 1\right)^{-1}$$ **Equation A4.10**

Eqn. A4.11 is afforded by substituting Eqn. A4.10 into Eqn. A4.6, and undergoes final simplifications to result in Eqn. A4.13 which correlates K_{Theo} to the applied potential (ΔE with respect to $E_{1/2}$), as shown in Figure 4.3-1. The upper and lower bounds are K_{Ox}= 1590 M^{-1} and K_{Red}= 20 M^{-1} which were obtained as described previously.[141]

$$K_{Theo} = K_{Ox} * \left(1 - \left(10^{\frac{\Delta E}{-0.059}} + 1\right)^{-1}\right) + K_{red} * \left(10^{\frac{\Delta E}{-0.059}} + 1\right)^{-1}$$ **Equation A4.11**

$$K_{Theo} = K_{Ox} - K_{Ox}\left(10^{\frac{\Delta E}{-0.059}} + 1\right)^{-1} + K_{red} * \left(10^{\frac{\Delta E}{-0.059}} + 1\right)^{-1}$$ **Equation A4.12**

$$K_{Theo} = K_{Ox} + (K_{Red} - K_{Ox})\left(10^{\frac{\Delta E}{-0.059}} + 1\right)^{-1}$$ **Equation A4.13**

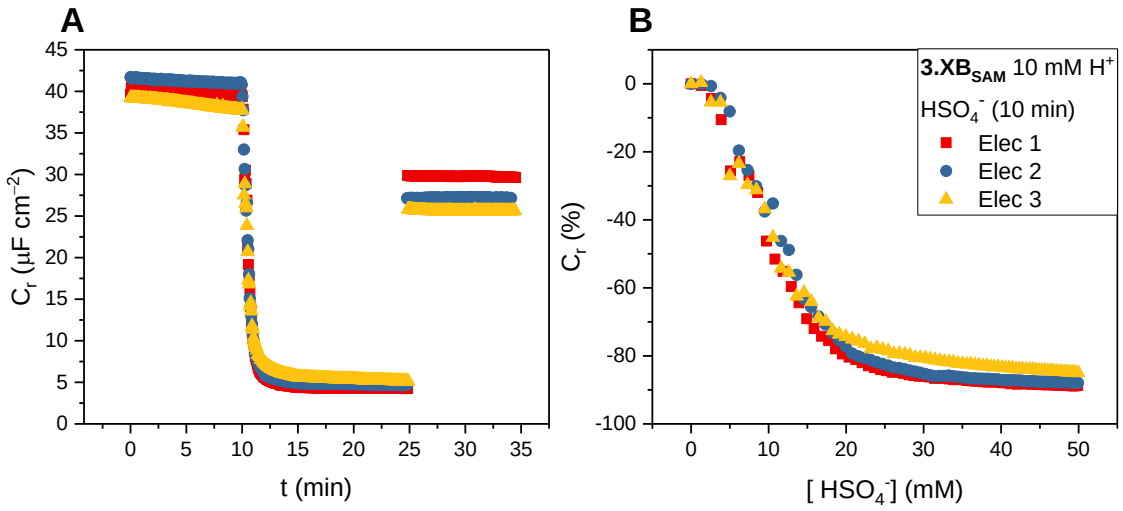


Figure A4.2. Triplicate, independent repeats of capacitance responses of **3.XB$_{SAM}$** under pseudo flow conditions in a stirred, but otherwise static, 3-electrode cell at $E_{1/2}$. (A) A comparison is shown for the temporal sensor responses upon continuous addition of up to 50 mM HSO_4^- via a syringe pump (V_{Sample} = 4 mL, flow rate Q = 0.8 mL min^{-1}, into an initial electrolyte volume of 4 mL). (B) The corresponding continuous binding isotherms are depicted, representing the capacitance response to HSO_4^-, obtained by conversion of the traces from the time to the concentration domain.

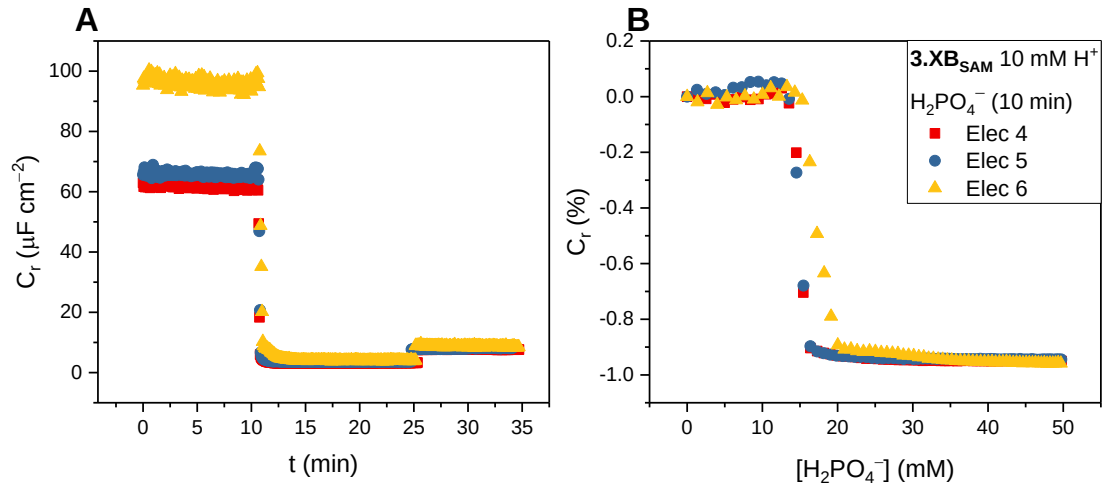


Figure A4.3. Triplicate, independent repeats of capacitance responses of **3.XB$_{SAM}$** under pseudo flow conditions in a stirred, but otherwise static, 3-electrode cell at $E_{1/2}$. (A) A comparison is shown for the temporal sensor responses upon continuous addition of up to 50 mM $H_2PO_4^-$ via a syringe pump (V_{Sample} = 4 mL, flow rate Q = 0.8 mL min^{-1}, into an initial electrolyte volume of 4 mL). (B) The corresponding continuous binding isotherms are depicted, representing the capacitance response to $H_2PO_4^-$, obtained by conversion of the traces from the time to the concentration domain.

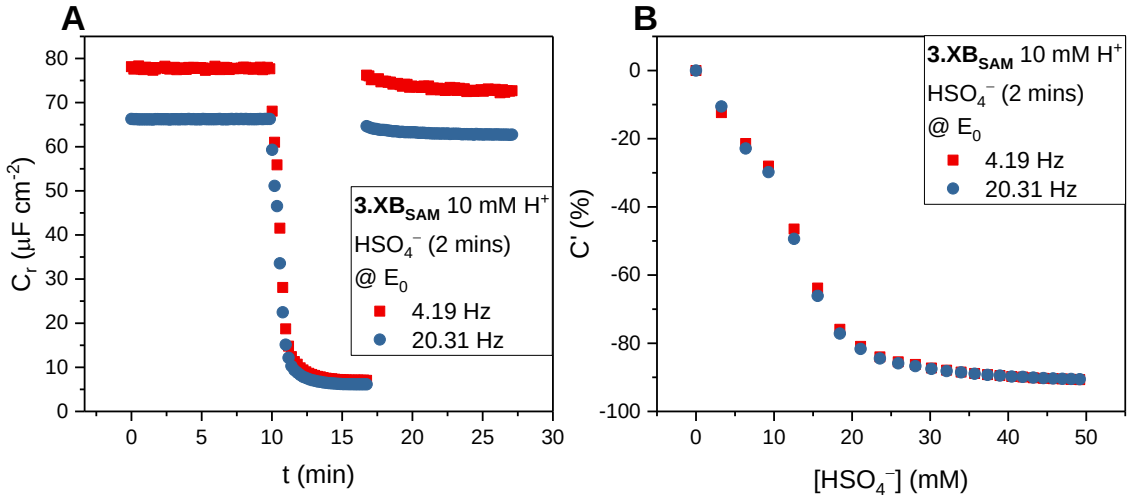


Figure A4.4. Triplicate, independent repeats of capacitance responses of **3.XB$_{SAM}$** under pseudo flow conditions in a stirred, but otherwise static, 3-electrode cell at $E_{1/2.}$ (A) A comparison is shown for the temporal sensor responses at a fixed frequency of 4.19 Hz (f @ inflection point of semicircular region of capacitive Nyquist plot, red squares) or 20.31 Hz (f @ apex of semicircular region of capacitive Nyquist plot, blue circles) upon continuous addition of up to 50 mM HSO_4^- via a syringe pump (V_{Sample} = 4 mL, flow rate Q = 0.8 mL min^{-1}, into an initial electrolyte volume of 4 mL). (B) The corresponding continuous binding isotherms are depicted, representing the capacitance response to HSO_4^-, obtained by conversion of the traces from the time to the concentration domain.

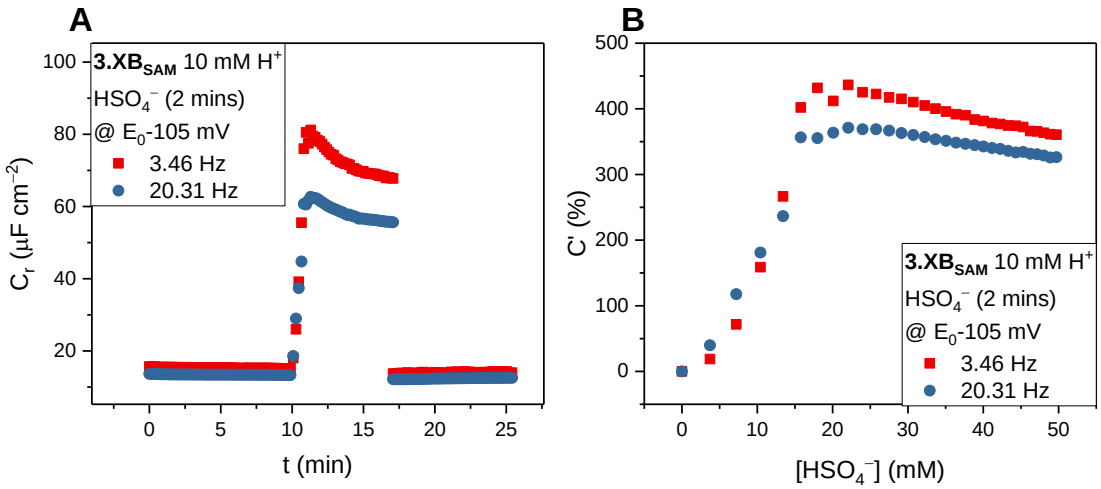


Figure A4.5. Triplicate, independent repeats of capacitance responses of **3.XB$_{SAM}$** under pseudo flow conditions in a stirred, but otherwise static, 3-electrode cell at E_{-105}. (A) A comparison is shown for the temporal sensor responses at a fixed frequency of 3.46 Hz (f @ inflection point of semicircular region of capacitive Nyquist plot, red squares) or 20.31 Hz (f @ apex of semicircular region of capacitive Nyquist plot, blue circles) upon continuous addition of up to 50 mM HSO_4^- via a syringe pump (V_{Sample} = 4 mL, flow rate Q = 0.8 mL min^{-1}, into an initial electrolyte volume of 4 mL). (B) The corresponding continuous binding isotherms are depicted, representing the capacitance response to HSO_4^-, obtained by conversion of the traces from the time to the concentration domain.

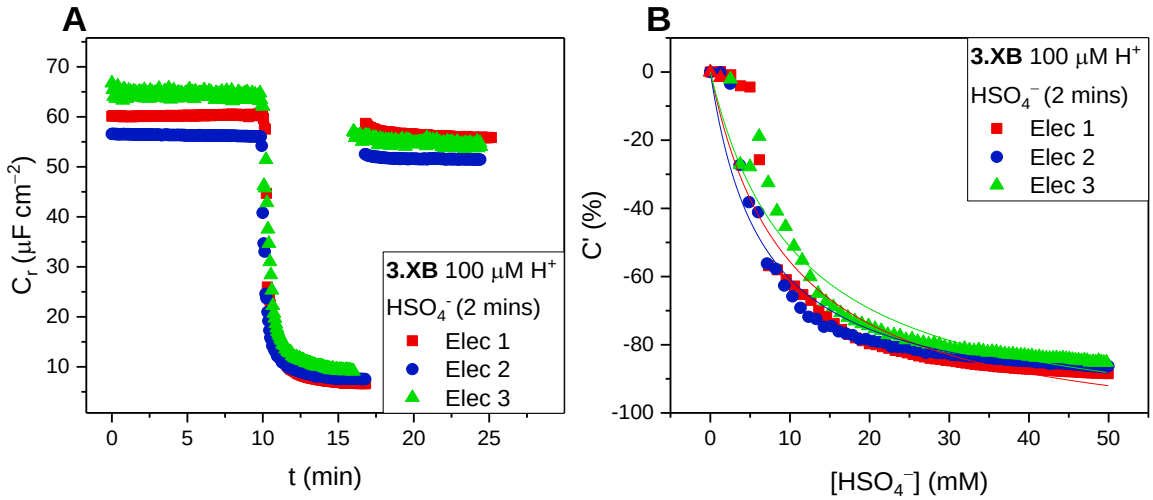


Figure A4.6. Triplicate, independent repeats of capacitance responses of **3.XB$_{SAM}$** under pseudo flow conditions in a stirred, but otherwise static, 3-electrode cell at $E_{1/2}$. Note that the $HClO_4$ concentration used here is 100 µM. (A) A comparison is shown for the temporal sensor responses upon continuous addition of up to 50 mM HSO_4^- via a syringe pump (V_{Sample} = 4 mL, flow rate Q = 0.8 mL min^{-1}, into an initial electrolyte volume of 4 mL). (B) The corresponding continuous binding isotherms are depicted, representing the capacitance response to HSO_4^-, obtained by conversion of the traces from the time to the concentration domain.

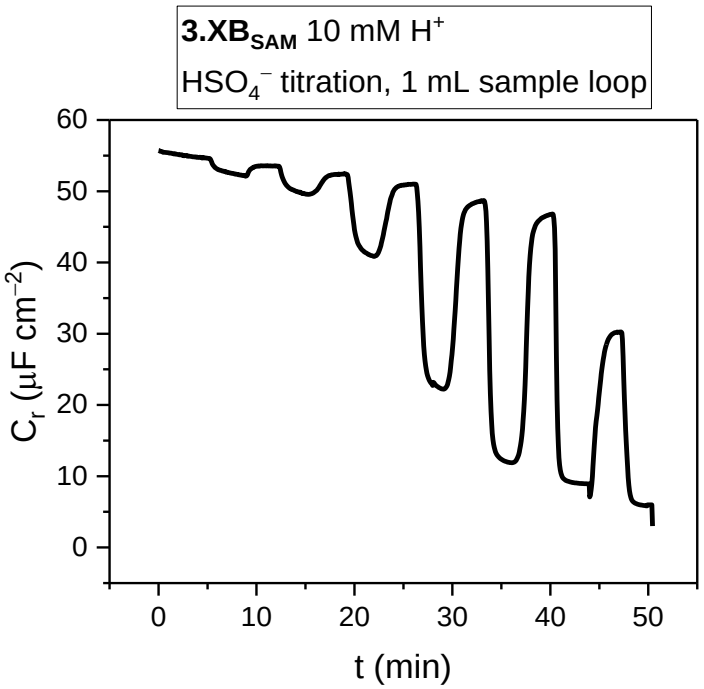


Figure A4.7. Redox capacitance response of **3.XB$_{SAM}$** towards HSO_4^- under continuous electrolyte flow in a custom flow cell (cell volume = 100 µL, flow rate Q = 300 µL min^{-1}, E = $E_{1/2}$, f = f_r). Each spike in represents the response towards aliquots (V_{Sample} = 1 mL) of HSO_4^- of increasing concentrations up to 50 mM. These conditions highlight the ability to reach a longer plateau for each response but inevitably suffer from higher signal loss in comparison to the "typical" chosen conditions of (Q = 500 µL min^{-1} and V_{sample} = 0.5 ml) due to the longer duration of this analogous experiment.

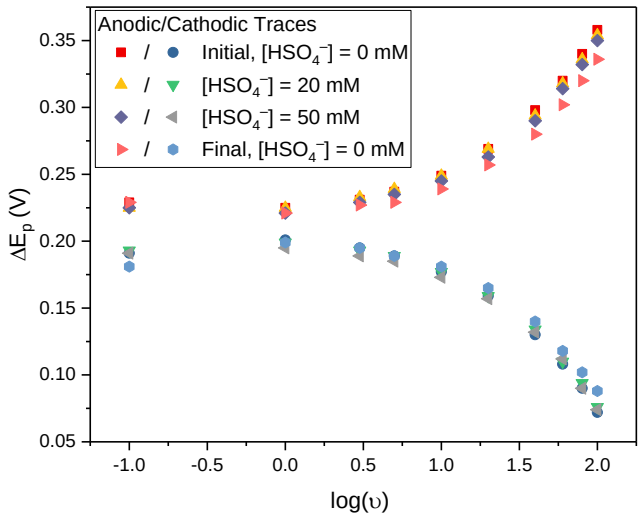


Figure A4.8. Laviron analyses of **3.XB$_{SAM}$**. CVs at increasingly high scan rates (v = 0.1 – 100 V s^{-1}) were obtained from which the peak separation, ΔE_p was plotted against log(v). At sufficiently high scan rates, a linear regime should be resolved which can be fitted and k_{ET} extracted from its intercept.[288]

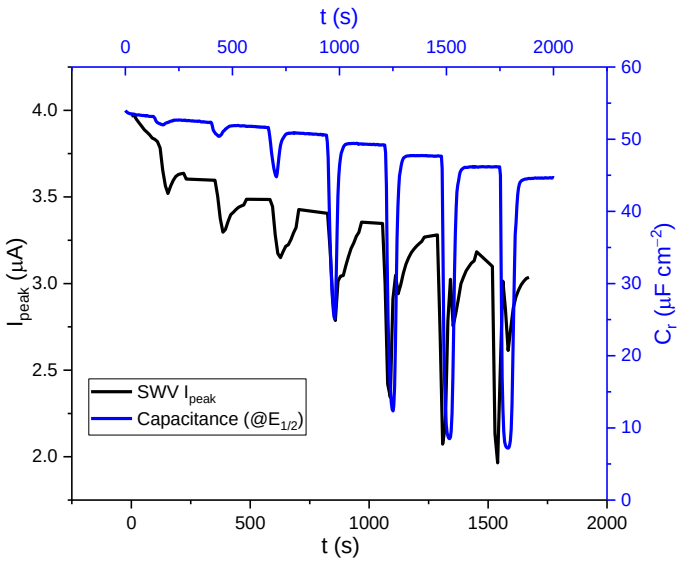


Figure A4.9. Comparison of the signal degradation resulting from standard HSO_4^- voltammetric (black) and redox capacitive (blue) assays, carried out over same duration.

- ~30% signal loss (current) for voltammetric titration
- ~15% signal loss (redox capacitance) with capacitive titration

A5 Appendices for Chapter 5: Continuous Non-Faradaic Capacitive Ion Sensing

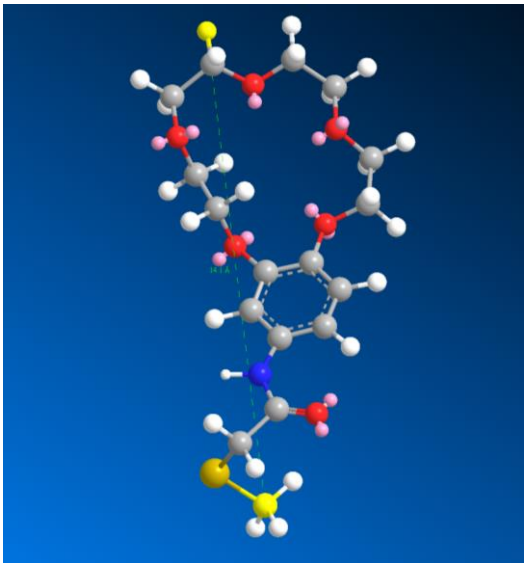


Figure A5.1. Simulated length of **B15C5** (1.41 nm), as determined by Chem3D software, which agrees well with film thicknesses determined via ellipsometry (1.02 ± 0.2 nm).

Non-Faradaic Capacitive Cation Sensing with a Fritted Reference Electrode

Initial studies to assess the cation sensing performance of **B15C5$_{SAM}$** were first conducted under static conditions, which were expected to reflect the established results of those discussed in Chapter 5.1. Namely, a substantial increase in *C* (depicted by a shift in C' in resolved Nyquist plots, see Figure A5.2) should be observed upon exposure of **B15C5$_{SAM}$** to the alkali metals, with particularly large responses expected for Na^+ due to the established 1:1 host-guest size complementarity of 15-crown-5 for Na^+. Indeed, this behaviour was observed, as evidenced by the *C* responses induced by increasing concentrations of Na^+ (Figure A5.2A) and K^+ (Figure A5.2B). The measured Δ*C* can then be translated to response isotherms and fitted to a Langmuir model (see Figure A5.3 and Equation 3.3-2) to afford binding constants of 49.8 ± 7.8 M^{-1} and 110 ± 24 M^{-1}, respectively.

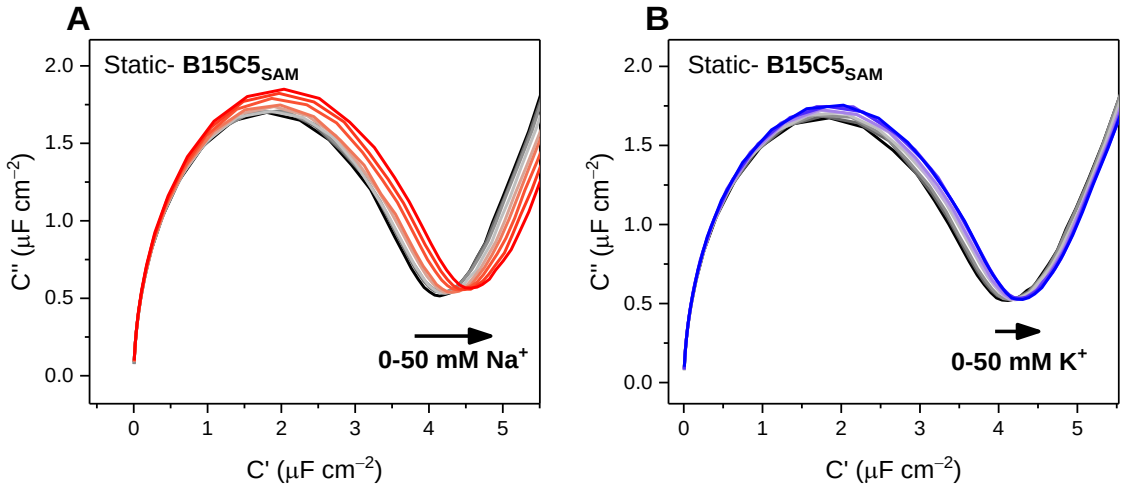


Figure A5.2. Capacitive Nyquist plots displaying the shift in C at **B15C5$_{SAM}$** receptive films upon addition of increasing concentrations (0-50 mM) of (A) Na^+ and (B) K^+ in 100 mM TEACl in H_2O, under static conditions utilising a Ag|AgCl (3M KCl) fritted reference electrode.

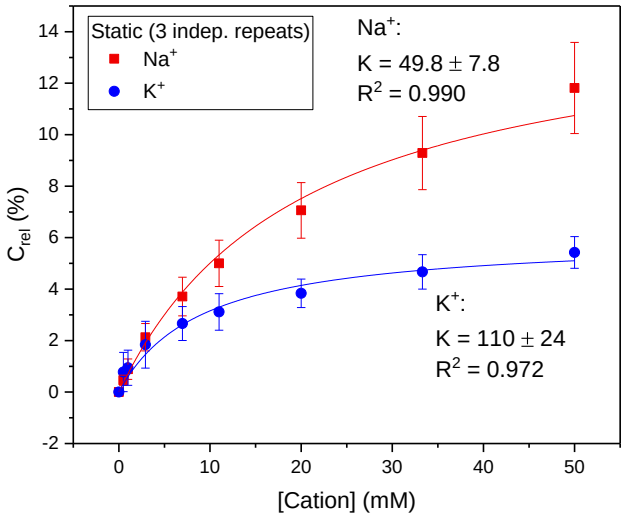


Figure A5.3. Relative response isotherms corresponding to the C response of **B15C5$_{SAM}$** upon addition of increasing concentrations (0-50 mM) of Na^+ (red squares) and K^+ (blue circles) in 100 mM TEACl in H_2O, under static conditions, utilising a Ag|AgCl (3M KCl) fritted reference electrode. Isotherms were fitted to a Langmuir model (see Section 7.10.2 for further details, and Equation 3.3-2). Errors represent one standard deviation of three independent repeats.

The resolved selectivity preference of **B15C5$_{SAM}$** was also generally consistent with previous reports and expectations based on size complementarity trends ($Na^+ \approx NH_4^+ > Cs^+ \approx K^+ > Mg^{2+} > Li^+$, see Figure A5.4).

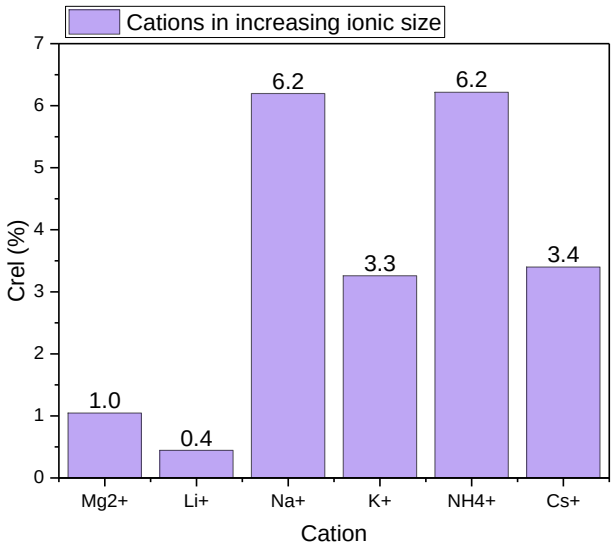


Figure A5.4. Selectivity studies of **B15C5$_{SAM}$** under static conditions, shown by the relative response to 20 mM of MCl salts where M^+ = alkali metals, NH_4^+ and Mg^{2+} (listed by increasing ionic size from left to right).

However, upon moving to a continuous flow setup with **Design 1**, both the baseline *C* in the absence of target cations, and the *C* response profiles and magnitudes to a range of targets unexpectedly exhibited a substantial and reproducible flow-rate dependence. Namely:

1. In the absence of target, *decreasing* the flow rate generally *increased* the baseline *C* from ≈ 20 to 0 μL min^{-1}. At flow rates > 20 μL min^{-1}, baseline *C* remained constant (Figure A5.5).

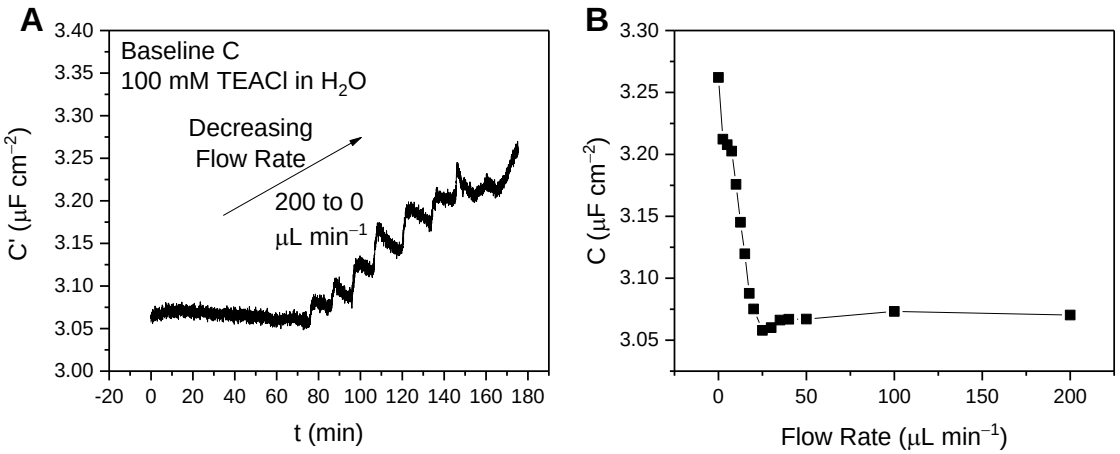


Figure A5.5. (A) Sensogram depicting the dependence of the baseline *C* of **B15C5$_{SAM}$** on flow rate (from 200 to 0 μL min^{-1}) in 100 mM TEACl in H_2O, utilising a Ag|AgCl (3M KCl) fritted reference electrode and (B) the corresponding baseline *C* vs. flow rate plot. (B) highlights that increasing the flow rate from 0 to ≈ 20 μL min^{-1} decreases baseline *C*, but flow rates > 20 μL min^{-1} do not induce further changes.

2. *Increasing* the flow rate from 5 to 100 μL min^{-1} significantly *enhanced* the *C* response magnitude (Figures A5.6 and S5.7). At flow rates > 100 μL min^{-1}, no further enhancement in *C* was observed.

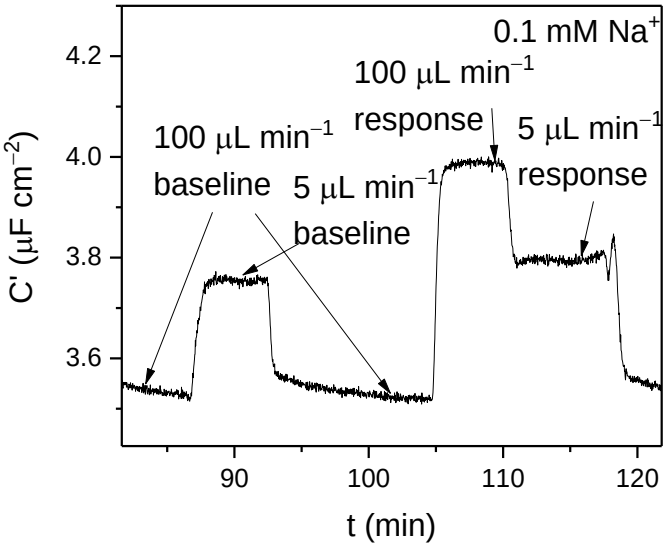


Figure A5.6. Representative flow sensogram showing the flow rate dependence of both the C baseline, and the C response magnitude of **B15C5$_{SAM}$** to 0.1 mM Na^+, in 100 mM TEACl in H_2O, utilising a Ag|AgCl (3M KCl) fritted reference electrode.

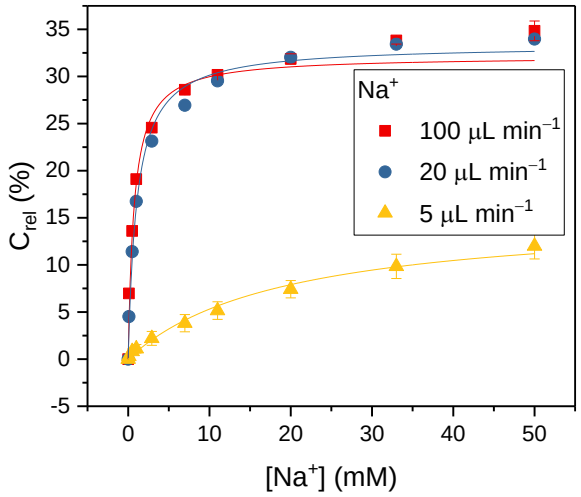


Figure A5.7. Relative response isotherms determined from C responses at **B15C5$_{SAM}$** receptive films upon addition of increasing concentrations (0-50 mM) of Na^+ in 100 mM TEACl in H_2O, at flow rates of 100 (red squares), 20 (blue circles) and 5 µL min^{-1} (yellow triangles), utilising a Ag|AgCl (3M KCl) fritted reference electrode. Isotherms were fitted to Langmuir model (see Section 7.10.2 for further details, and Equation 3.3-2). Error bars on the data sets for 100 and 5 µL min^{-1} represent one standard deviation of at least two independent repeats.

3. The flow rate dependence on the response magnitude to a constant target concentration appeared to be ion-dependent. Some ions were more affected by changes in flow rate than others (Figures A5.8-S5.11, and Table A5.1).

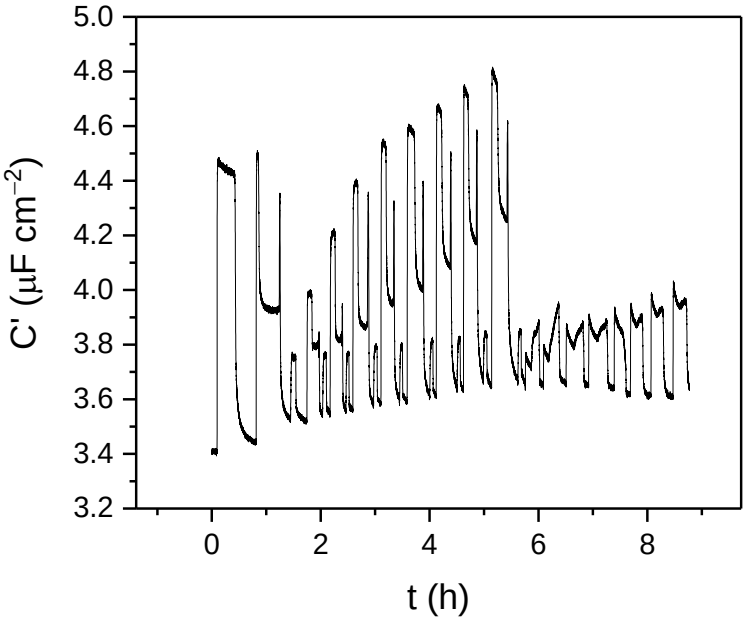


Figure A5.8. Representative flow sensogram showing a titration at **B15C5$_{SAM}$** receptive films at different flow rates (5-100 µL min^{-1}) in response to increasing concentrations of Na^+, then K^+ in 100 mM TEACl in H_2O, utilising a Ag|AgCl (3M KCl) fritted reference electrode.

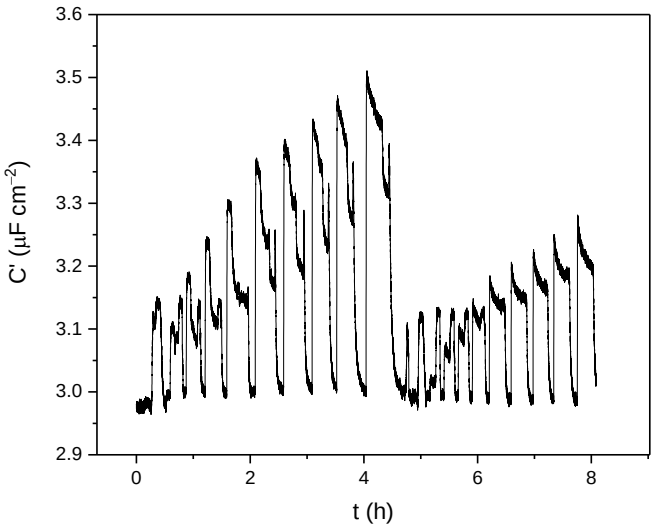


Figure A5.9. Representative flow sensogram showing a titration at **B15C5$_{SAM}$** receptive films at different flow rates (5-100 µL min^{-1}) in response to increasing concentrations of NH_4^+, then Rb^+ in 100 mM TEACl in H_2O, utilising a Ag|AgCl (3M KCl) fritted reference electrode.

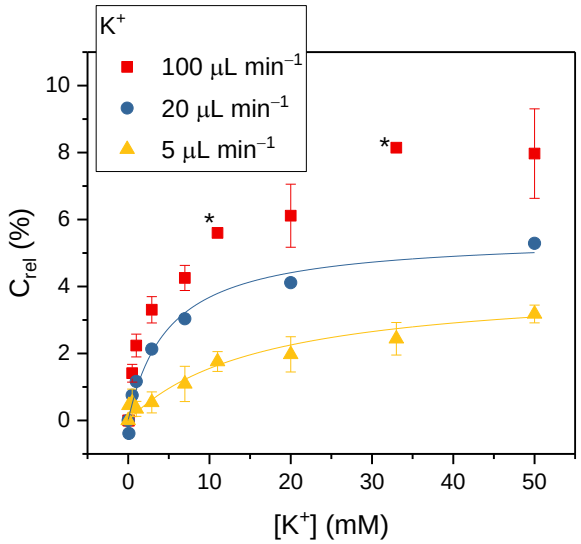


Figure A5.10. Relative response isotherms determined from C responses at **B15C5$_{SAM}$** receptive films upon addition of increasing concentrations (0-50 mM) of K^+ in 100 mM TEACl in H_2O, at flow rates of 100 (red squares), 20 (blue circles) and 5 µL min^{-1} (yellow triangles), utilising a Ag|AgCl (3M KCl) fritted reference electrode. Isotherms were fitted to Langmuir model (see Section 7.10.2 for further details, and Equation 3.3-2). Error bars on the data sets for 100 and 5 µL min^{-1} represent one standard deviation of at least two independent repeats unless annotated with "*", in which case only one data set was gathered at this concentration.

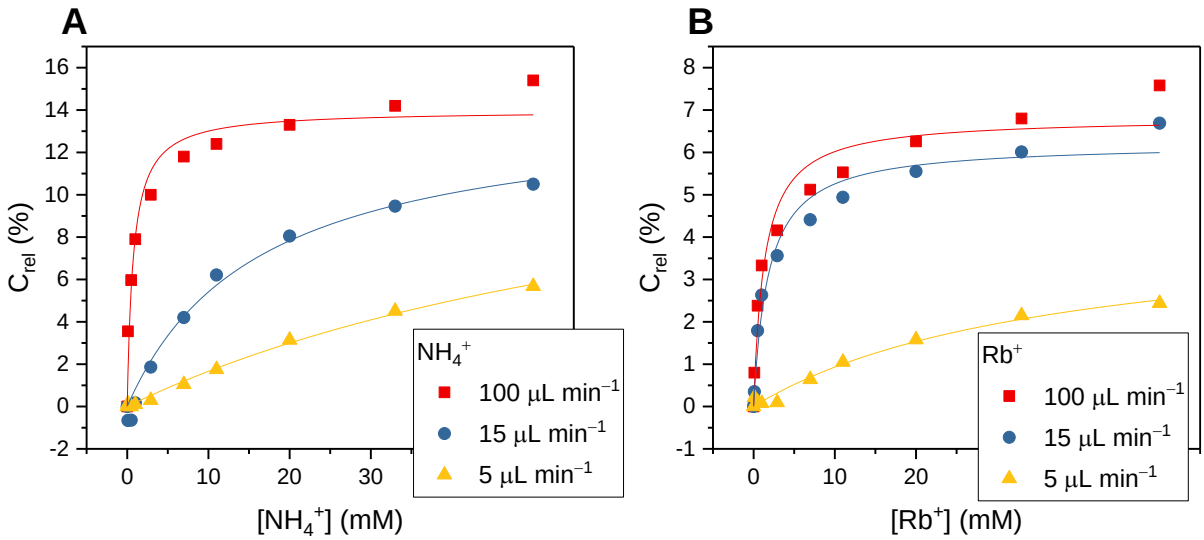


Figure A5.11. Relative response isotherms determined from C responses at **B15C5$_{SAM}$** receptive films upon addition of increasing concentrations (0-50 mM) of (A) NH_4^+ and (B) Rb^+ in 100 mM TEACl in H_2O, at flow rates of 100 (red squares), 20 (blue circles) and 5 µL min^{-1} (yellow triangles), utilising a Ag|AgCl (3M KCl) fritted reference electrode. Isotherms were fitted to Langmuir model (see Section 7.10.2 for further details, and Equation 3.3-2).

Table A5.1. Binding constants (M^{-1}) of **B15C5$_{SAM}$** from Langmuir fitting (Eqn. 3.3-2) of response isotherms with increasing concentrations of various cations (Na^+, K^+, NH_4^+ and Rb^+) at different flow rates: high (100 µL min^{-1}), intermediate (20 or 15 µL min^{-1}) and low (5 µL min^{-1}) flow rates, utilising a Ag|AgCl (3M KCl) fritted reference electrode.

	K (M^{-1})		
	100 µL min^{-1}	**20(15) µL min^{-1}**	**5 µL min^{-1}**
Na^+	1380 ± 99	933 ± 110	52 ± 13
K^+	549 ± 124	201 ± 44	61 ± 14
NH_4^+	1330 ± 310	(62 ± 13)	12 ± 2
Rb^+	753 ± 189	(549 ± 118)	27 ± 7

4. Good agreement between the response magnitudes determined under static conditions and continuous flow conditions could not be obtained. The closest agreement was displayed when a very slow flow rate of 5 µL min^{-1} was utilised (Figure A5.12), but additional inconsistencies were observed at this pseudo-static flow rate (see below and Figures A5.13 and S5.14).

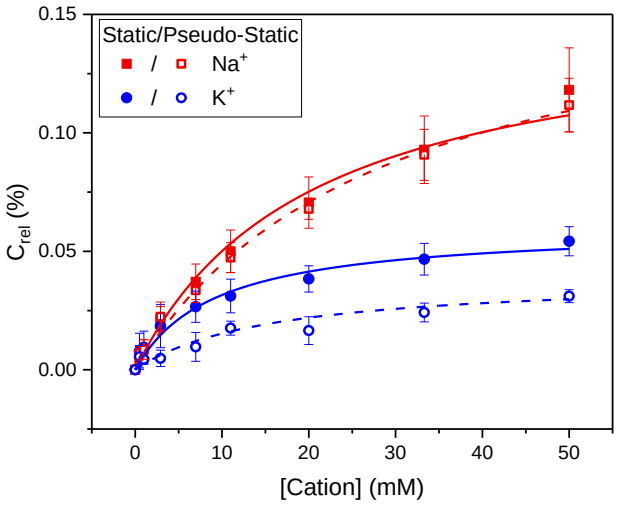


Figure A5.12. Relative response isotherms determined from the shift in C at **B15C5$_{SAM}$** upon addition of increasing concentrations of Na^+ (red squares) and K^+ (blue circles) in 100 mM TEACl in H_2O, under static conditions (solid symbols) or pseudo-static conditions (flow rate of 5 µL min^{-1}, empty symbols), utilising a Ag|AgCl (3M KCl) fritted reference electrode. Isotherms fitted to Langmuir model (see Section 7.10.2 for further details, and Equation 3.3-2). Errors represent one standard deviation of three independent repeats.

5. Studies performed at a *constant* 5 µL min^{-1} displayed an unexpected response profile with two separate response plateaus (Figures A5.10 and S5.11). Note that the flow rate was not changed at any point during the duration of these experiments.

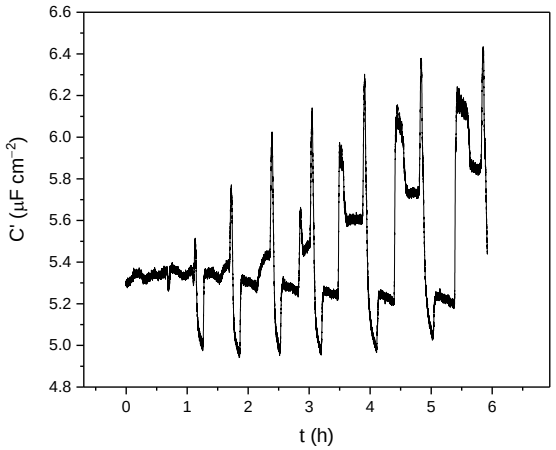


Figure A5.10. Representative flow sensogram showing the C response of **B15C5$_{SAM}$** to increasing concentrations of Na^+ in 100 mM TEACl in H_2O at 5 µL min^{-1} (at a pseudo-static flow rate), utilising a Ag|AgCl (3M KCl) fritted reference electrode.

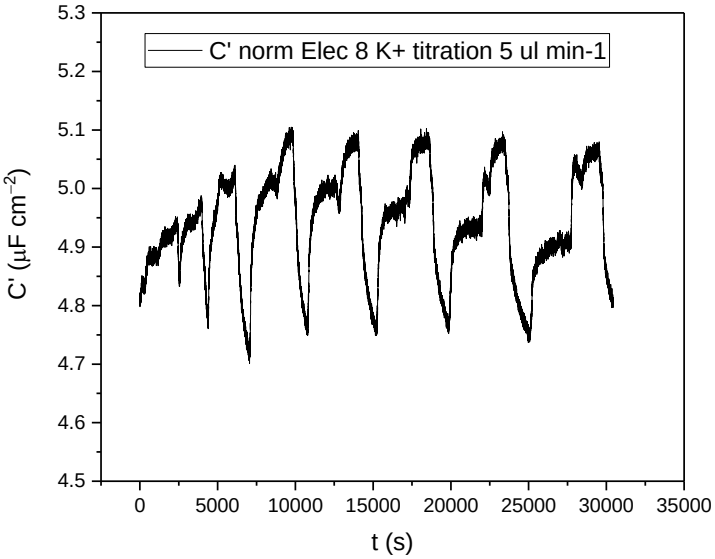


Figure A5.11. Representative flow sensogram showing the C response of **B15C5$_{SAM}$** to increasing concentrations of K^+ in 100 mM TEACl in H_2O at 5 µL min^{-1} (at a pseudo-static flow rate), utilising a Ag|AgCl (3M KCl) fritted reference electrode.

Hypotheses for Flow Rate Dependence of C with Fritted Reference Electrode

1. **Inefficient mixing**

To ensure efficient mixing and a continuous throughout the initial flow cell **Design 1** was adjusted as follows:

a. Remove corners of cell to prevent reservoirs of static electrolyte which are not being flushed through properly
b. Add spherical obstacles to the walls of the inlet and outlet to induce turbulence
c. Reduce volume of flow cell chamber from 100 µL to 10 µL

Results:

a. Removing the corners of the cell did not affect the resolved flow rate dependence seen above, there were still significant discrepancies in the determined response magnitudes and binding constants from fits of the response isotherms at different flow rates.
b. Adding 3 half-sphere obstacles each in a triangle arrangement in the inlet and/or outlet of the cell did not affect the resolved flow rate dependence seen above. Once again, there were still significant discrepancies in the determined response magnitudes and binding constants from fits of the response isotherms at different flow rates.
c. Reducing the volume of the flow cell chamber from 100 µL to 10 µL seemed to reduce the magnitude of the effect but a significant flow rate dependence was still observed.

2. **Impurities/contaminants/interferents**

A few approaches were taken to mitigate the effect of any residual, trace impurities that may result from the equipment/glassware used.

a. Brand new glassware for sample storage and new wash bottles to contain deionised water for sample preparation

b. Extensive cleaning procedure performed on injector and all components

c. pH tests of cationic targets and supporting electrolyte

Results:

a/b. Neither of these steps had a measurable impact on *C*.

c. The pH of all of the solutions containing 20 mM MCl + 80 mM TEACl or 100 mM MCl (100 mM constant ionic strength) was measured but did not correlate in any meaningful way to the resulting flow rate dependence trends (see Table A5.2).

Table A5.2. pH of target samples containing 20 mM MCl + 80 mM TEACl or 100 mM MCl (100 mM constant ionic strength) in water.

Sample	pH
H_2O blank control	8.5
100 mM TEACl	6.9
20 mM Li^+	7.3
100 mM Li^+	6.6
20 mM Na^+	6.7
100 mM Na^+	6.0
20 mM K^+	6.0
100 mM K^+	5.4
20 mM Rb^+	6.0
100 mM Rb^+	5.5
20 mM Cs^+	6.2
100 mM Cs^+	4.8
20 mM NH_4^+	5.5
100 mM NH_4^+	5.1
20 mM Mg^{2+}	5.5
100 mM Mg^{2+}	5.6

3. **Role of the supporting electrolyte**

   a. Change the supporting electrolyte from TEACl to more sterically bulky TBACl. Less likely to penetrate within interface.

   b. Change the supporting electrolyte concentration from 100 mM to 50 mM.

   Results:

a/b. Neither changing the identity (TEACl replaced with TBACl), or the concentration (100 mM replaced with 50 mM) significantly affected the flow rate-dependent responses of **B15C5$_{SAM}$** to Na^+ (Figures A5.8-S5.10)

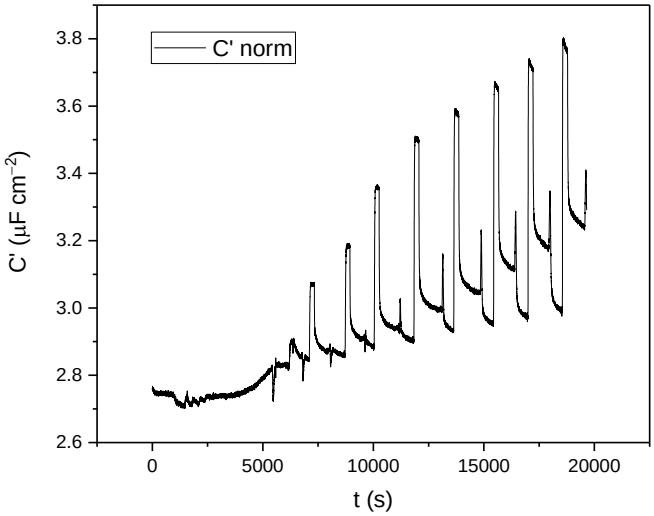


Figure A5.8. Representative flow sensogram showing the C response of **B15C5$_{SAM}$** to increasing concentrations of Na^+ in 100 mM TBACl in H_2O at a flow rate of 100, 15 or 5 μL min^{-1}, utilising a Ag|AgCl (3M KCl) fritted reference electrode.

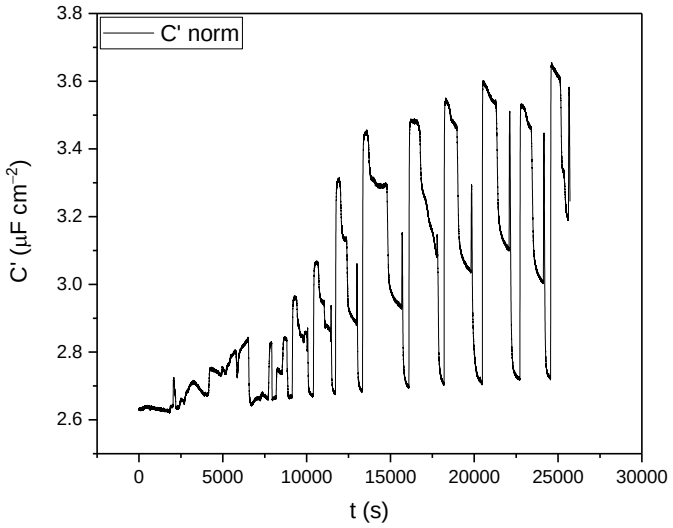


Figure A5.9. Representative flow sensogram showing the C response of **B15C5$_{SAM}$** to increasing concentrations of Na^+ in 50 mM TEACl in H_2O at a flow rate of 100, 15 or 5 μL min^{-1}, utilising a Ag|AgCl (3M KCl) fritted reference electrode.

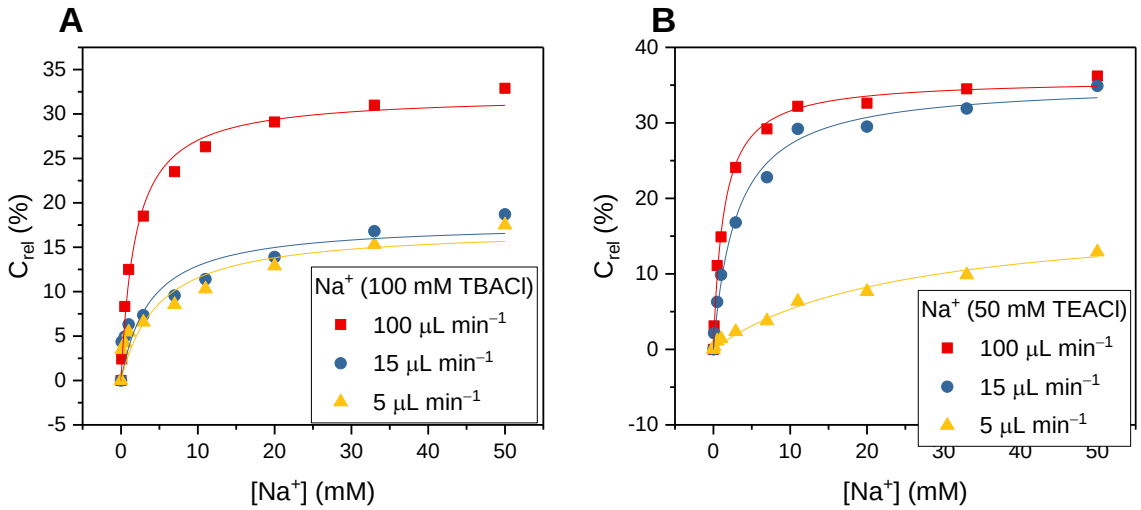


Figure A5.10. Relative response isotherms determined from the shift in C at $B15C5_{SAM}$ receptive films with addition of increasing concentrations of Na^+ in A) 100 mM TBACl and B) 50 mM TEACl in H_2O, at flow rates of 100 (red squares), 15 (blue circles) and 5 µL min^{-1} (yellow triangles). Isotherms fitted to Langmuir model (see Section 7.10.2 for further details, and Equation 3.3-2).

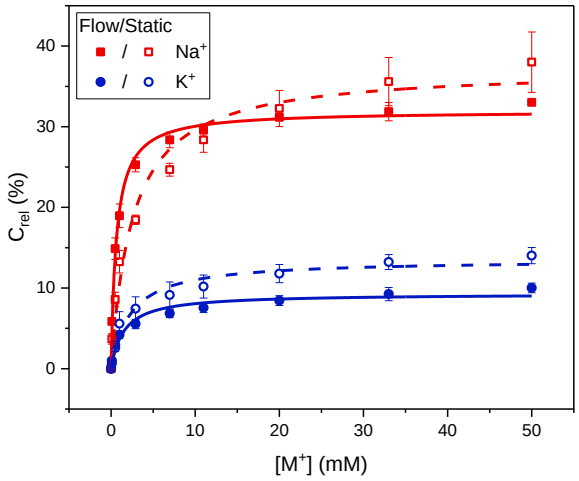


Figure A5.11. Relative response isotherms determined from the shift in C' (Crel (%)) in response to increasing concentrations of Na+ (red squares) and K+ (blue circles), under static conditions (open symbols) and under continuous flow at 100 µL min–1 (filled symbols). Isotherms fitted to Langmuir model (see Section *7.10.2* for further details, and Equation *3.3-2*). Errors represent one standard deviation of three independent repeats.

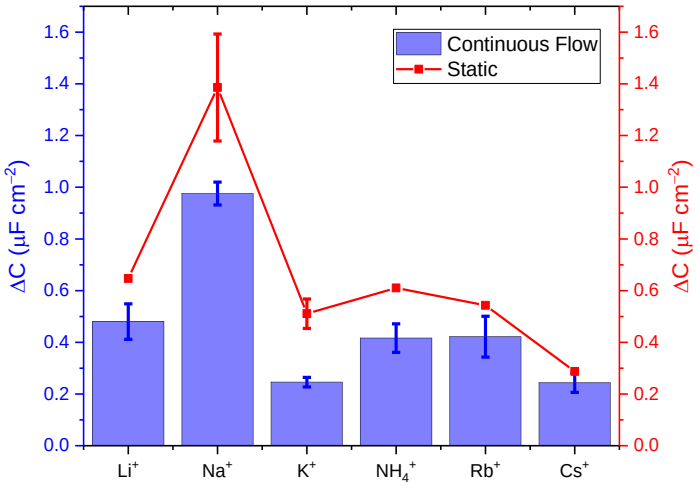


Figure A5.12. Selectivity studies with 20 mM of alkali metals, NH_4^+ and Mg^{2+} assessed from changes in *C* (**Δ**C) at **B15C5$_{SAM}$** receptive films under static (red) and continuous flow (blue) conditions**,** illustrating the excellent agreement in selectivity trends resolved under static and continuous flow conditions. Where shown, error bars represent one standard deviation of three independent measurements. Note identical y-scaling for both plots.

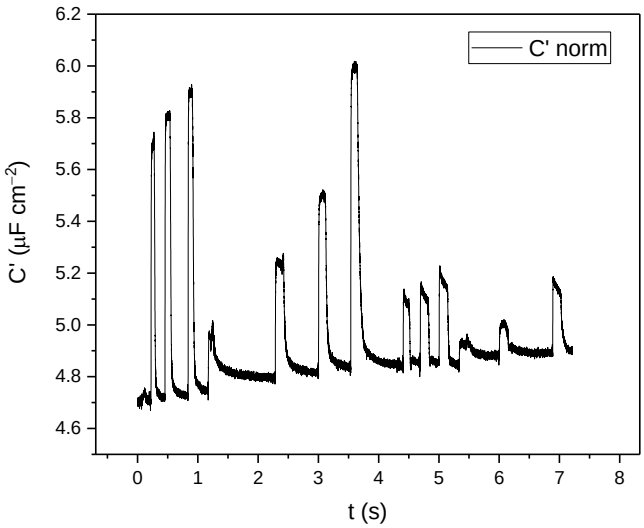


Figure A5.13. Sensogram displaying the response of **B15C5$_{SAM}$** to: 5 mM Na^+, 10 mM Na^+, 20 mM Na^+, 10 mM [2.2.2]-cryptand, 5 mM Na^+ + 10 mM [2.2.2]-cryptand, 10 mM Na^+ + 10 mM [2.2.2]-cryptand, 20 mM Na^+ 10 mM [2.2.2]-cryptand. Then 5 mM K^+, 10 mM K^+, 20 mM K^+, 5 mM K^+ + 10 mM [2.2.2]-cryptand, 10 mM K^+ + 10 mM [2.2.2]-cryptand, 20 mM K^+ 10 mM [2.2.2]-cryptand.

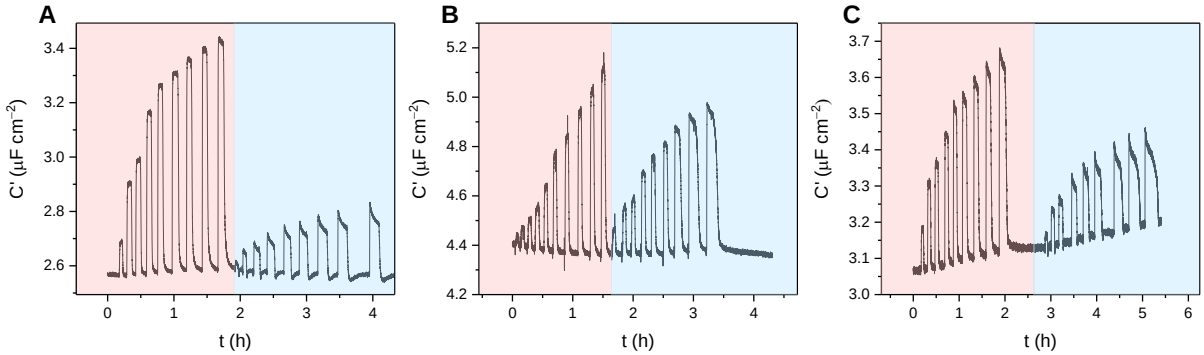


Figure A5.14. Representative sensograms of the response of **B15C5$_{SAM}$** to increasing concentrations (in order: 0.1, 0.5, 1, 3, 7, 11, 20, 33 and 50 mM MCl) of (A) Na^+ (left, red) and K^+ (right, blue), (B) Li^+ (left, red) and Rb^+ (right, blue) and (C) NH_4^+ (left, red) and Cs^+ (right, blue).

Table A5.3. Binding constants of **B15C5$_{SAM}$** from Langmuir-Freundlich (Eqn. 3.3-1) fitting of response isotherms with increasing concentrations of a range of alkali metals (Li^+, Na^+, K^+, Rb^+, Cs^+ and NH_4^+) under continuous flow at 100 µL min^{-1}. Errors represent one standard deviation of at least three independent repeats. The interface sensitivity was obtained by analysis of the pseudolinear region at low concentration (0–1 mM [M^+]), which was then used to calculate the limit of detection (LOD). Further detail on these calculations are included in the Supporting Information.

	ΔC_{max} (µF cm^{-2})	K (M^{-1})	n	Sensitivity (µF cm^{-2} mM^{-1})	LOD (µM)
Na^+ (static)	1.67 ± 0.25	72 ± 42	0.61 ± 0.04	0.44 ± 0.06	12.3 ± 3.6
K^+ (static)	0.61 ± 0.06	248 ± 164	0.66 ± 0.07	0.23 ± 0.04	11.8 ± 3.1
Li^+	0.63 ± 0.09	39 ± 16	0.63 ± 0.07	0.11 ± 0.02	14.7 ± 2.7
Na^+	1.03 ± 0.06	1012 ± 382	0.72 ± 0.07	0.52 ± 0.05	4.0 ± 1.2
K^+	0.29 ± 0.02	210 ± 34	0.57 ± 0.01	0.09 ± 0.01	27.4 ± 4.7
Rb^+	0.48 ± 0.09	262 ± 151	0.50 ± 0.03	0.18 ± 0.02	9.3 ± 0.8
Cs^+	0.24 ± 0.07	1335 ± 544	0.57 ± 0.09	0.12 ± 0.01	18.2 ± 7.5
NH_4^+	0.47 ± 0.06	491 ± 439	0.47 ± 0.07	0.21 ± 0.04	11.0 ± 0.8

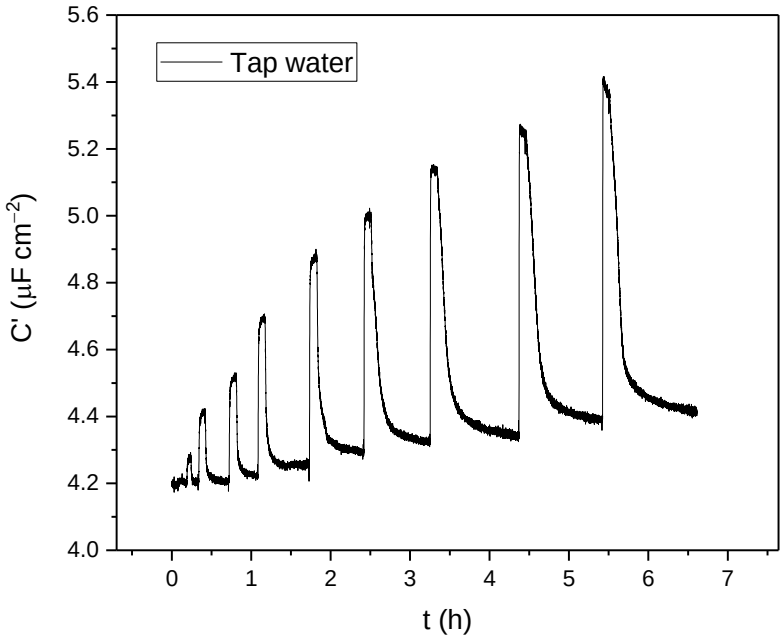


Figure A5.15. Sensogram displaying the response of **B15C5$_{SAM}$** to increasing concentrations of Na^+ up to 50 mM in Tap Water Sample 1 (with 100 mM TEACl as supporting electrolyte).

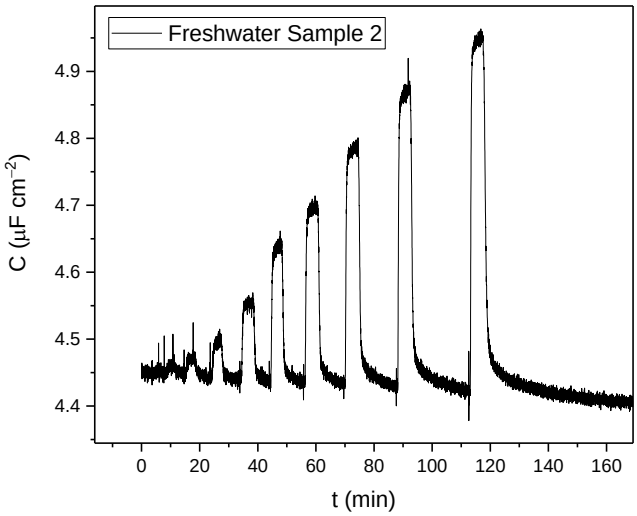


Figure A5.16. Sensogram displaying the response of $B15C5_{SAM}$ to increasing concentrations of Na^+ up to 50 mM in Freshwater Sample 2 (with 100 mM TEACl as supporting electrolyte).

Table A5.4. Slopes determined from linear fits to the first 10 data points of the association regime of binding/recovery with 1, 3 and 50 mM of Li^+, Na^+, K^+, Rb^+, Cs^+ and NH_4^+ (corresponding to the linear fits shown in Figures A5.16-S5.21A, C, E, G and I).

	Initial Response Slope (nF cm^{-2} s^{-1})					
[M$^+$] (mM)	**Li^+**	**Na^+**	**K^+**	**Rb^+**	**Cs^+**	**NH_4^+**
0.1	1.28 ± 0.43	3.88 ± 0.41	N/A	2.63 ± 0.57	N/A	4.22 ± 0.38
1	4.15 ± 0.51	21.9 ± 0.46	3.50 ± 0.22	8.85 ± 0.58	6.38 ± 0.67	12.8 ± 0.52
3	8.01 ± 0.56	34.7 ± 0.65	6.55 ± 0.38	15.2 ± 0.56	9.74 ± 0.69	18.6 ± 0.46
11	16.7 ± 0.40	52.2 ± 2.63	8.96 ± 0.63	24.1 ± 1.48	10.5 ± 2.93	28.2 ± 1.29
50	37.2 ± 1.22	66.0 ± 7.37	14.9 ± 2.02	34.0 ± 2.70	12.9 ± 2.01	32.5 ± 3.42

Table A5.5. Slopes determined from linear fits to the first 10 data points of the dissociation regime of binding/recovery with 1, 3 and 50 mM of Li^+, Na^+, K^+, Rb^+, Cs^+ and NH_4^+ (corresponding to the linear fits shown in Figures A5.16-S5.21B, D, F, H and J).

	Initial Washing Slope (nF cm^{-2} s^{-1})					
[M$^+$] (mM)	**Li^+**	**Na^+**	**K^+**	**Rb^+**	**Cs^+**	**NH_4^+**
0.1	1.06 ± 0.43	3.42 ± 0.54	1.10 ± 0.20	2.17 ± 0.40	N/A	3.15 ± 0.41
1	3.64 ± 0.51	9.03 ± 0.41	2.66 ± 0.25	5.25 ± 0.37	3.13 ± 0.34	5.52 ± 0.44
3	4.06 ± 0.45	9.16 ± 0.95	2.54 ± 0.19	5.38 ± 0.56	2.93 ± 0.20	4.89 ± 0.46
11	6.76 ± 0.51	8.28 ± 0.79	2.39 ± 0.28	4.03 ± 0.36	0.16 ± 0.27	3.53 ± 0.35
50	6.67 ± 0.53	4.79 ± 0.48	2.57 ± 0.21	3.81 ± 0.32	0.16 ± 0.21	0.71 ± 0.35

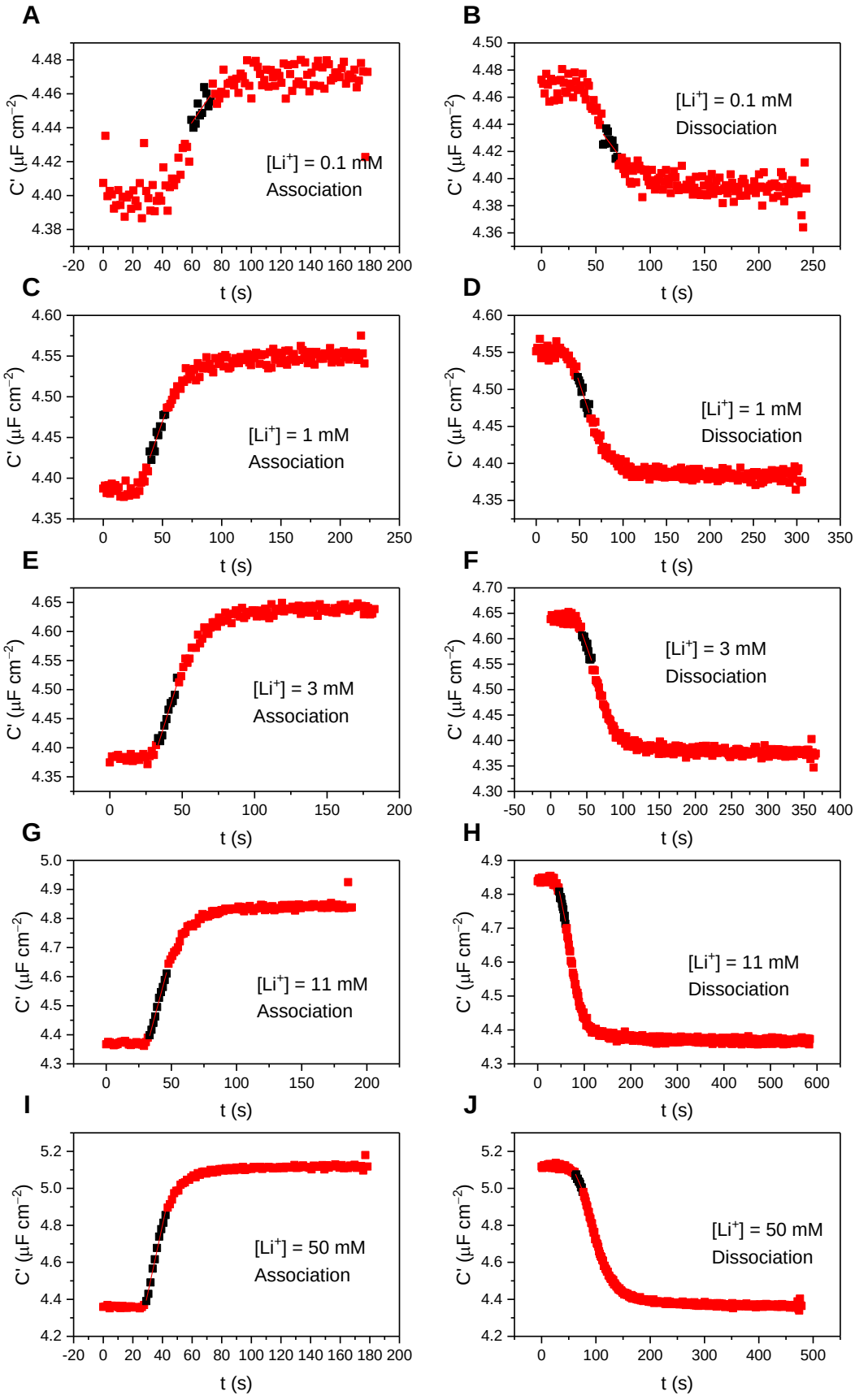


Figure A5.17. Association (left) and dissociation (right) traces, respectively, for a range of concentrations of Li^+: 0.1 mM (A and B), 1 mM (C and D), 3 mM (E and F), 11 mM (G and H) and 50 mM (I and J). Linear fits to the first 10 data points in the association/dissociation regime are shown in red.

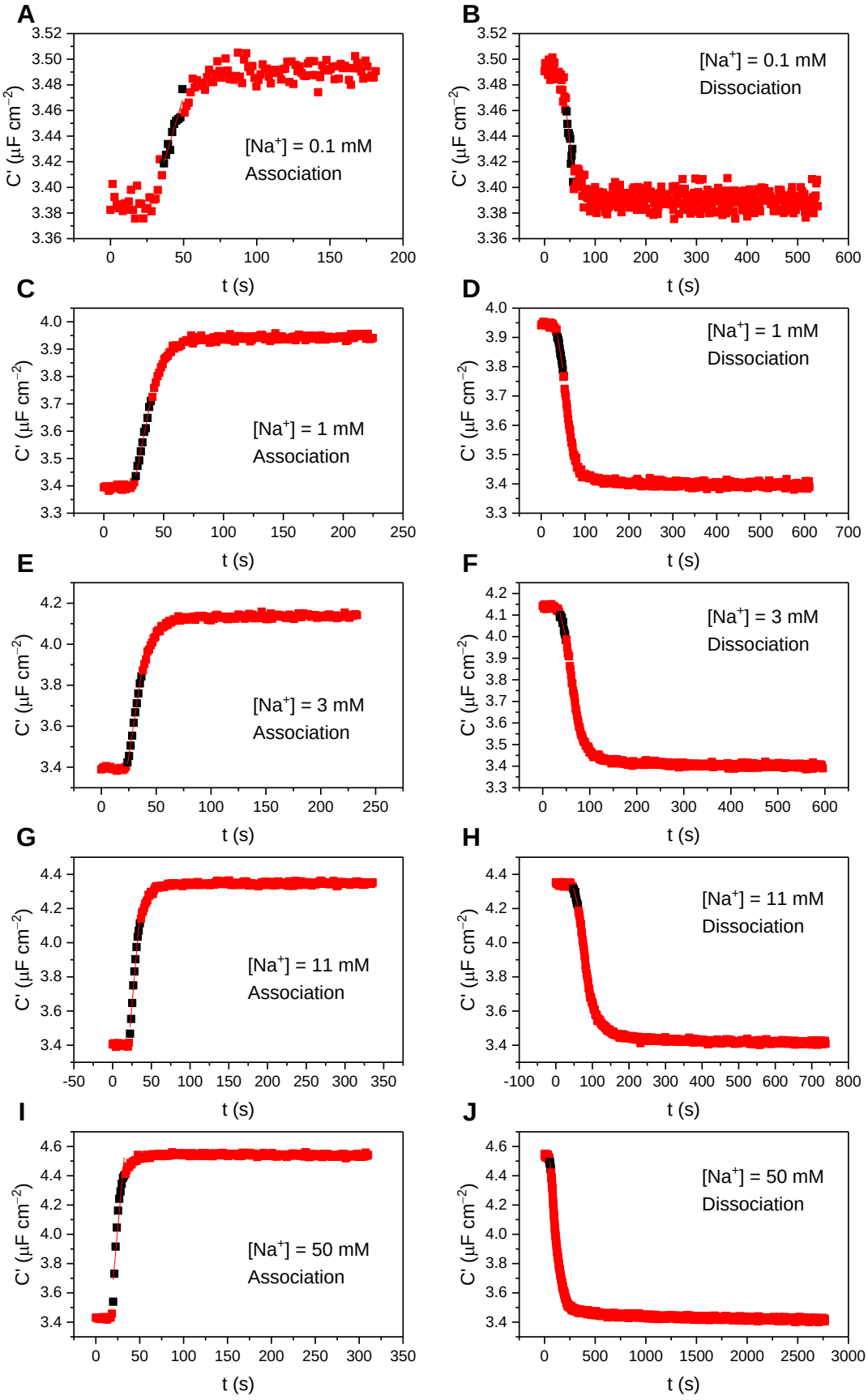


Figure A5.18. Association (left) and dissociation (right) traces, respectively, for a range of concentrations of Na^+: 0.1 mM (A and B), 1 mM (C and D), 3 mM (E and F), 11 mM (G and H) and 50

mM (I and J). Linear fits to the first 10 data points in the association/dissociation regime are shown in red.

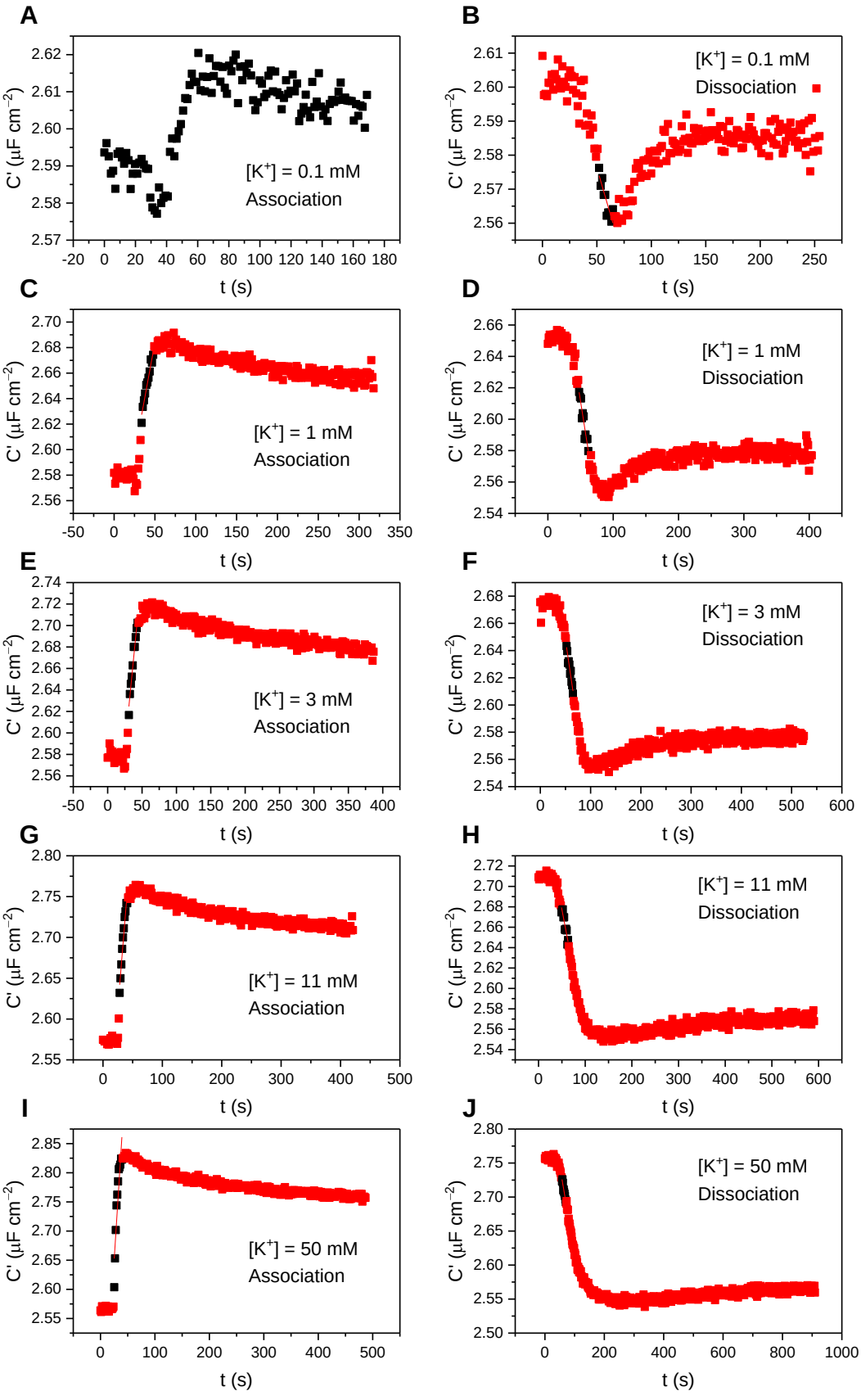


Figure A5.19. Association (left) and dissociation (right) traces, respectively, for a range of concentrations of K^+: 0.1 mM (A and B), 1 mM (C and D), 3 mM (E and F), 11 mM (G and H) and 50 mM (I and J). Linear fits to the first 10 data points in the association/dissociation regime are shown in red.

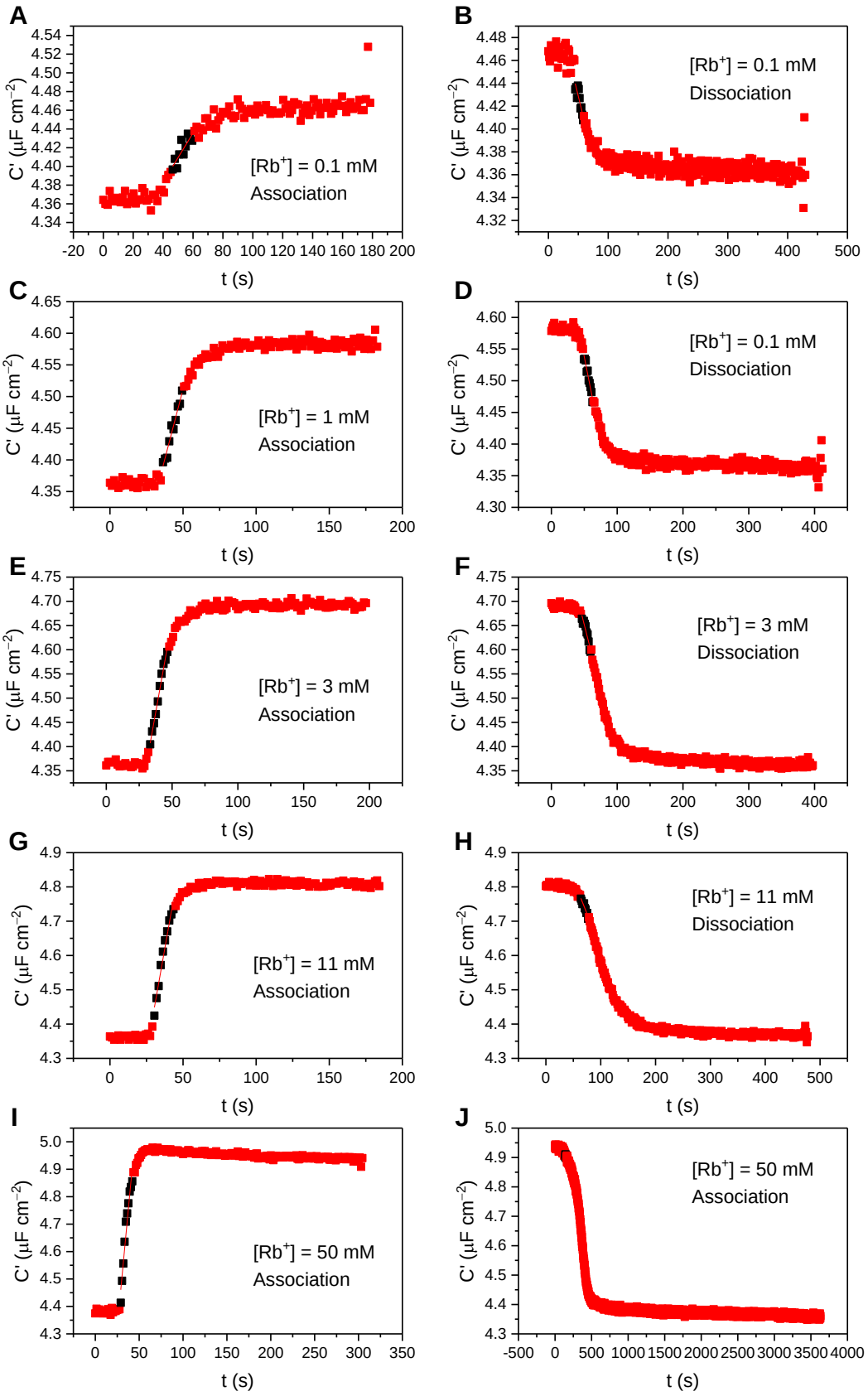


Figure A5.20. Association (left) and dissociation (right) traces, respectively, for a range of concentrations of Rb^+: 0.1 mM (A and B), 1 mM (C and D), 3 mM (E and F), 11 mM (G and H) and 50 mM (I and J). Linear fits to the first 10 data points in the association/dissociation regime are shown in red.

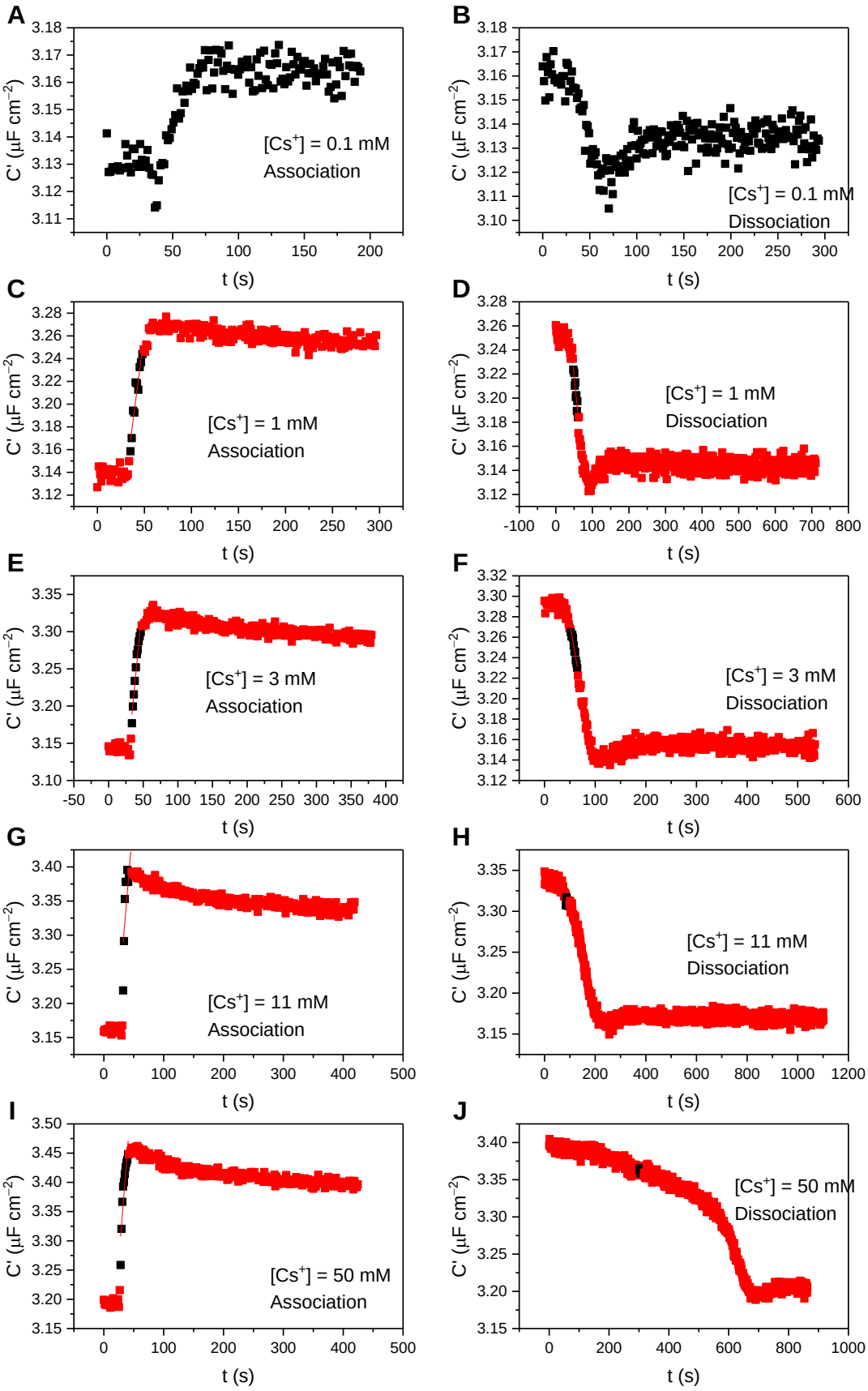


Figure A5.21. Association (left) and dissociation (right) traces, respectively, for a range of concentrations of Cs^+: 0.1 mM (A and B), 1 mM (C and D), 3 mM (E and F), 11 mM (G and H) and 50

mM (I and J). Linear fits to the first 10 data points in the association/dissociation regime are shown in red.

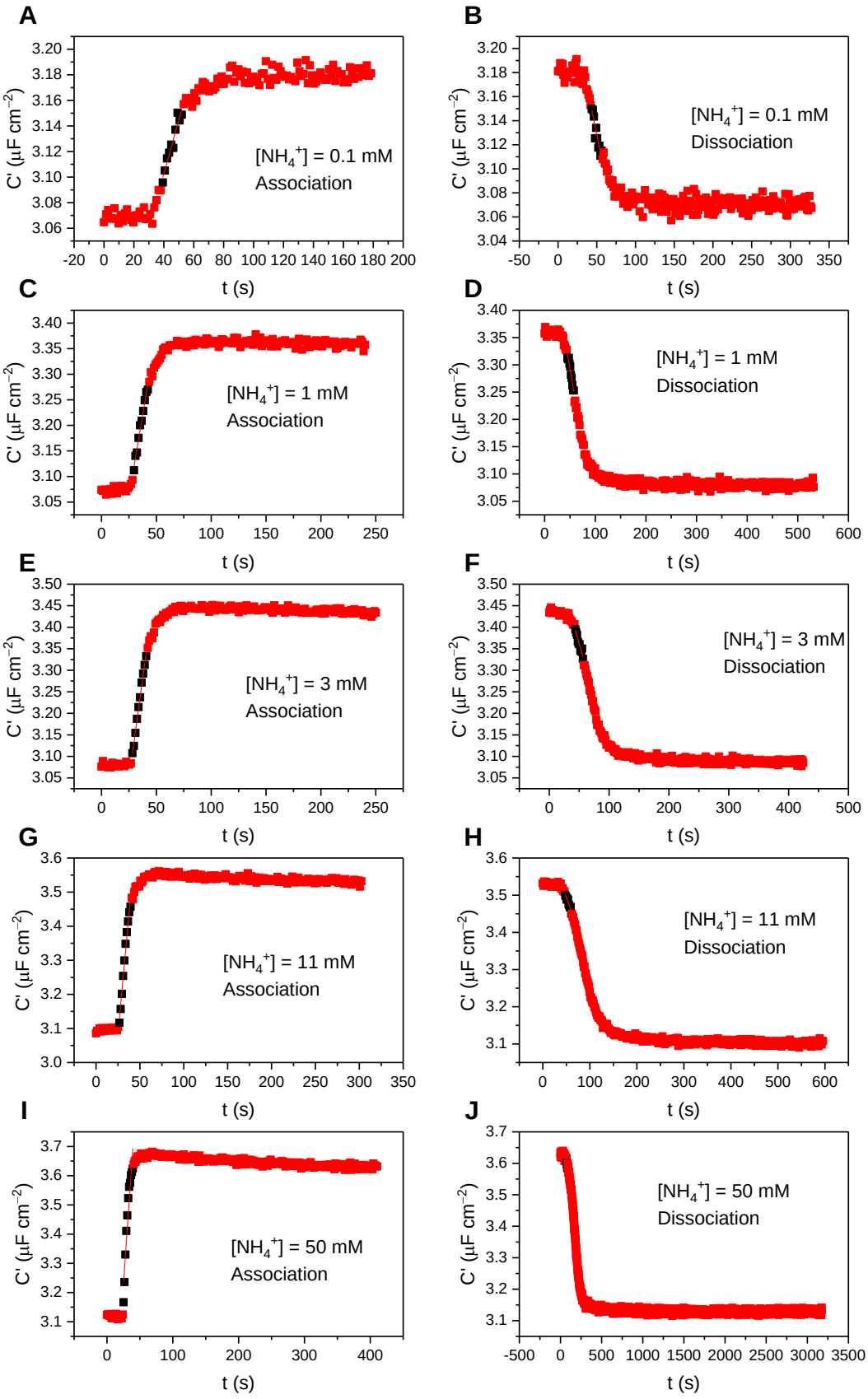


Figure A5.22. Association (left) and dissociation (right) traces, respectively, for a range of concentrations of NH_4^+: 0.1 mM (A and B), 1 mM (C and D), 3 mM (E and F), 11 mM (G and H) and 50 mM (I and J). Linear fits to the first 10 data points in the association/dissociation regime are shown in red.

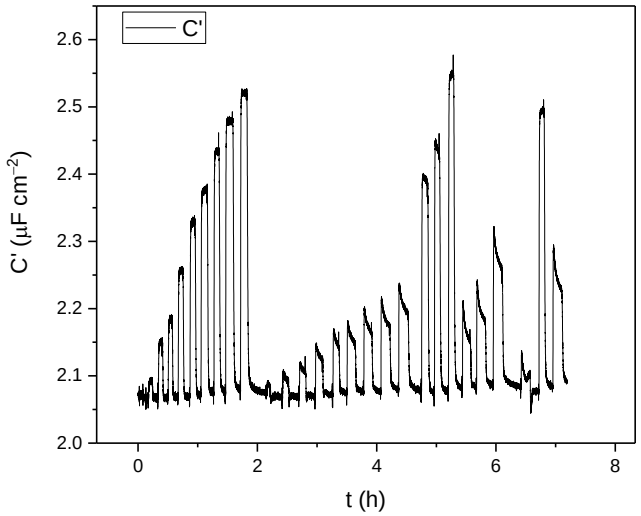


Figure A5.23. Representative sensograms of the response of **4.XB-B15C5$_{SAM}$** to increasing concentrations of Na^+ and K^+, then to 20 mM of a range of salts: NaCl, NaBr, NaSCN, $NaClO_4$, KCl, KBr, KSCN and $KClO_4$.

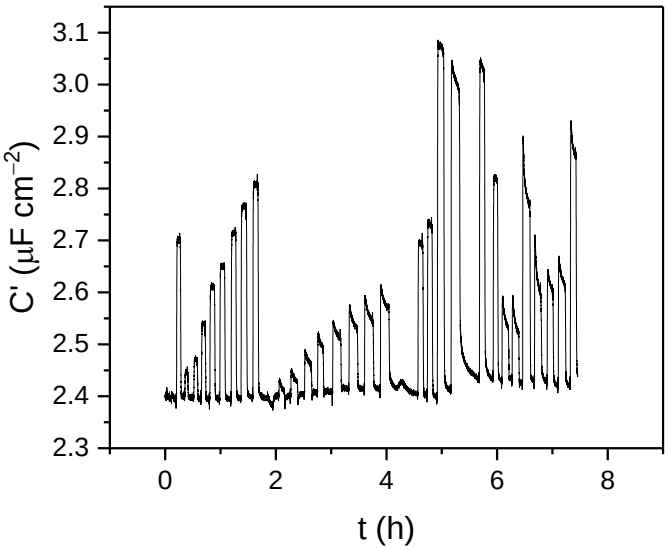


Figure A5.24. Representative sensograms of the response of **4.HB-B15C5$_{SAM}$** to increasing concentrations of Na^+ and K^+, then to 20 mM of a range of salts: NaCl, NaBr, NaSCN, $NaClO_4$, $NaPF_6$, $NaNO_3$, KCl, KBr, KSCN, $KClO_4$, NH_4Cl, NH_4Br and NH_4SCN.